

OBSERVATOIRE DE PARIS

SYSTÈMES DE RÉFÉRENCE TEMPS-ESPACE

UMR8630 / CNRS, PSL



JOURNÉES 2019 ☆

**Astrometry, Earth Rotation, and Reference Systems
in the GAIA era**

☆ **PARIS, 7-9 OCTOBER**



OBSERVATOIRE DE PARIS

SYSTÈMES DE RÉFÉRENCE TEMPS-ESPACE

UMR8630 / CNRS, PSL

61 avenue de l'Observatoire, 75014 Paris, FRANCE

Edited by

Actes publiés par

C. BIZOUARD

JOURNÉES 2019 ☆

**Astrometry, Earth Rotation, and Reference Systems
in the GAIA era**

☆ **PARIS, 7-9 OCTOBER**

TABLE OF CONTENTS

PREFACE	vi
ORGANIZING COMMITTEE	vii
LIST OF PARTICIPANTS	viii
SCIENTIFIC PROGRAM	xi
LIST OF POSTERS	xv
SESSION I: GAIA mission	1
Lindegren L.: The bright reference frame of GAIA and VLBI observations of radio stars	3
Liu N., Lambert S., Zhu Z. and Liu J.-C.: Is there an interest in bringing Gaia-CRF into VLBI data reduction ?	9
Secrest N., Frouard J., Hennessy G.: Quasar selection techniques going into the Gaia era	15
Damljanović G., Taris F., Jovanović M.D.: Short-term and long-term flux variability of extragalactic objects useful for the future Gaia CRF	21
Robert V., Desmars J., Arlot J.-E.: The NAROO digitization center	27
Rocca-Volmerange B., Godinaud L.: Continuous UV-IR Spectral Energy Distributions of quasars	33
Hobbs D.: Future space astrometry	37
Høg E. and Hobbs D. : Gaia successor with international participation	43
Lunz S., Heinkelmann R., Anderson J., Johnson M., Fey A., Titov O.: GAIA-VLBI: phase-referencing continuum emission observations of optically bright stars with the VLBA (planned proposal)	49
Malkin Z.: Spherical Rectangular Equal-Area Grid (SREAG)— some features	55
Marco F.J., Martínez M.J., López J.A.: An example to analyze discrete vector fields on the sphere using quantitative and qualitative methods	61
SESSION II: Earth rotation and geodynamics 1 (observations and analysis)	65
Capitaine N.: The IAU commission “Earth rotation” and the IAU definition of the pole and UT1	67
Capitaine N., Arias F., Boucher C.: Tribute to Bernard Guinot (1925-2017)	73
Nastula J., Brzeziński A., Kryński J.: Tribute to Professor Barbara Kołaczek (1931-2017)	75
Karbon M., Lambert S., Bizouard C., Richard J.Y.: Impact of the Parameterization of the source positions on the Free Core Nutation	79
Fodor CS., Heinkelmann R., Modiri S., Raut S., Schuh H., Varga P.: On the mutual interrelation between earth rotation and earthquake activity	85
Rosat S., Gillet N., Boy J.-P.: On the possible sources to interannual deformations at the Earth’s surface	91
Stamatakos N., Davis M., Shumate N.: IERS rapid service / prediction center products and services: improvements, changes, and challenges, 2017 to 2019.	99
Cheng Y.-T., Liu J.-C., Zhu Zi: Analyses of celestial pole offsets with VLBI, LLR, and optical observations	107
Malkin Z., Miller N., Soboleva T.: Outstanding Pulkovo latitude observers Lidia Kostina and Natalia Persiyaninova	113
Martínez M.J., Marco F.J.: A revision of ΔT values for the 5, 6 and 7th centuries	119
Nurul Huda I., Bizouard C., Lambert S., Ziegler Y.: Estimation of Earth rotation resonance parameters through VLBI analysis	123
Park H.-E., Roh K. M., Yoo S.-M., Cho J.: The development of the GNSS-based products service system	129

Pasynok S., Bezmenov I., Ignatenko I., Tcyba E., Zharov V.: Operative EOP activities in VNIIFTRI	135
Raut S., Heinkelmann R., Modiri S., Schuh H.: Effect of VLBI intensive sessions on daily and sub-daily erp determined from CONT17 IVS data	141
Richard J-Y., Bizouard C., Lambert S., Becker O., Karbon M.: New earth orientation parameters by combination of GNSS and VLBI	147
Skurikhina E.: Estimation of the accuracy of prediction of the Earth Orientation Parameters at the IAA data analysis center	153
Tcyba E. N., Volkova O. A.: Determination of Earth Orientation Parameters by SLR at MMC SSTF / FSUE VNIIFTRI	159
SESSION III: ICRF and astrogeodesy	163
Dorland B., Secrest N., Johnson M., Fischer T., Zacharias N., Souchay J., Lambert S., Barache C., Taris F.: The Fundamental Reference AGN Monitoring Experiment (FRAMEX)	165
Titov O., Shu F., Chen W.: Observations of radio stars in geodetic VLBI experiments	173
Zacharias N., Finch C., Dorland B., Secrest N., Johnson M.: Deep south telescope	179
Johnson M., Hunt L., Fey A., Gordon D., Spitzak J.: VLBA imaging of ICRF3 sources	183
Gomez G.E., Charlot P., Campbell R., Kettenis M., Keimpema A.: Geodesy at K-band with the European VLBI Network	185
Gattano C., Karbon M.: Parametrization of the source coordinates and its astrophysical interpretation	189
Trofimov D., Petrov S., Smirnov S., Zheltova K., Chekunov I.: Total electron content over Vostok antarctic station	195
Yatskiv Ya. S., Khoda O.: On the consistency between local ties and space geodesy estimates in the Simeiz–Katzively co-location site	201
SESSION IV: Earth Rotation and Geodynamics 2 (models)	207
Salstein D.: Atmospheric angular momentum related to earth rotation studies: history and modern developments	209
Sliwinska J., Nastula J.: Prograde and retrograde terms of gravimetric polar motion excitation estimates from the newest grace gravity field models	215
Escapa A., Getino J., Ferrandiz J. M., Baena T.: Second order effects in IAU2000 nutation model	221
Liu J.-C , Capitaine N., Cheng Y.-T.: Testing the improvement of the iau precession using different J_2 variation with time	227
Dehant V., Triana S.A, Requier J., Trinh A., Zhu P., Laguerre R., Houliez A., Van hoolst T.: Progress in understanding nutations	233
Naghibi S. E., Karabasov S. A.: Excitation of the Earth’s Chandler wobble by the north atlantic double-gyre	237
Sidorenkov N., Dionis E., Bizouard C., Zotov L.: Decadal fluctuations in Earth’s rotation as evidences of lithospheric drift over the asthenospere	243
Zotov L., Bizouard C., Sidorenkov N., Shen WB., Guo ZL.: On the variability of the Chandler wobble	249
Vondrák J., Ron C.: Determination of FCN parameters from different VLBI solutions, considering geophysical excitations	255
Bizouard C., Nurul Huda I., Ziegler Y., Lambert S.: Polar motion resonance in the retrograde diurnal band	261

Dill R., Dobslaw H.: The importance of seasonal sea-level variations from geophysical models and satellite gravimetry for excitation of Length-Of-Day	267
Fernández L.I., Böhm S.: Influence of the 2015-2016 enso event on Length-Of-Day variations	273
Lambert S.: Atmospheric excitation of the Chandler wobble along the 20th century: insights from ECMWF ERA-20c reanalysis	279
Perepelkin V., Filippova A., Krylov S.: Dynamic effects of the spatial movement of the Earth-Moon system in the Earth's pole oscillation	285
Böhm S., Salstein D.: Next generation of coupled climate models and the predicted atmospheric excitation of Length Of Day	287
SESSION V: Space navigation and solar system dynamics	291
Fienga A., Viswanathan V., Deram P., Di Ruscio A., Bernus L., Laskar J., Gastineau M., Rambaux N., Minazzoli O., Durante D., Less L.: INPOP new release: INPOP19a .	293
Hilton J.L., Stewart S.G.: Implementation of improved magnitude parameters for solar system planetary ephemerides	299
Rambaux N., Viswanathan V., Fienga A., Laskar J., Gastineau M.: A new dynamical model of the lunar core and improved observational constraints from lunar laser ranging	303
Pavlov D.: Solid body tides in the dynamical model of the Moon	309
Pashkevich V. V., Vershkov A.N.: Geodetic (Relativistic) rotation of the Mars satellites system	315
Zschocke S.: Post-linear metric of a solar system body	321
Teyssandier P.: Recent improvements in the determination of time transfer functions . .	329
Movsesian P., Petrov S., Trofimov D.: Analysis and normalization of GNSS onboard clocks	335
Melnikov A.V., Pashkevich V.V., Vershkov A.N., Karelin G.M.: Chaos and relativistic effects in the rotational dynamics of minor planetary satellites	339
PREVIOUS JOURNEES	345

PREFACE

Two years after the Journées 2017 at Alicante University, the Journées 2019 *Astrometry, Earth Rotation and Reference Systems in the Gaia Era* were organized by the Observatoire de Paris, and took place at the Campus of the Pierre and Marie Curie University (Paris 6), France, from October 7 to 9, 2019. During three decades the Journées saga (as said Y. Yatskiv in Alicante), held in Paris and in other European cities was lead by N. Capitaine, since 2017 its organisation was entrusted to new faces. This is an unique forum devoted to space-time reference systems, involving both the techniques that allow to realize them and their fundamental or practical applications, sweeping astrometry, Earth rotation changes and geodynamics in light of the various processes affecting the Earth. Its organization has been the result of an active and continuing cooperation between the *Systèmes de Référence Temps Espace* Department (SYRTE) of Paris Observatory and other European institutions.

Journées 2019 have been marked by record numbers of participants and communications. There were 118 attendants coming from 21 countries over the 5 continents. The scientific program included 58 oral presentations and 38 posters. Presentations were split into five sessions, alternating astrometry (sessions I and III), Earth rotation changes (Session II/IV) and solar system dynamics (session V). Of particular interest were the communications dedicated to the results of the Gaia mission and its possible future prolongation in IR band (Session I), the realization of the International Celestial Frame III (session III). In session II, many interesting talks were devoted to the centennial of the "Earth rotation" IAU commission.

For the second time, the Journées proceedings are not in paper format but limited to an electronic edition, that can be downloaded from: https://syrte.obspm.fr/astro/journees2019/index.php?page=presentation_pdf along with the slides of the oral presentations and posters. Having estimated that their results are too preliminary or were already published in peer-reviewed journal, some authors did not submit paper. Moreover, for some posters, tributes, and introductory talks, the corresponding slides or poster have been judged more appropriate. They can be found on the Journées 2019 web site. The number of papers that have been collected for the proceedings amounts 61. Each of them has been referenced in ADS bibliographic database by Zinovy Malkin.

The proceedings are available on the website of the Journées 2019, that will be maintained for years. Anyway they will be put on an electronic archive. All submitted paper have been carefully reviewed and corrected accordingly. We are especially grateful to Sergei Klioner, Laura Fernandez and Maria Karbon for having largely contributed to this review. Alberto Escapa and Zinovy Malkin brought valuable corrections pertaining to formal aspects of the proceedings. Olivier Becker set up the upolad system and the LaTeX layout.

We want to thank all the participants in these Journées, particularly the invited speakers and the SOC members for their excellent presentations and their invaluable commitment.

A video and audio support was insured by a technician of the Pierre and Marie Curie University. The organization of the coffee breaks as well as the poster sessions was highly facilitated by finding out, a few weeks before the meeting, the "Tipi space" 5 minutes by feet from the Charpak amphitheater. In this regard, we acknowledge the support received from the Pierre and Marie Curie University. But, before all, we congratulate the members of the Local Organizing Committee who faced, in reason of the exceptional number of participants, a very heavy logistic pertaining to installation and transport of the material, especially poster grids, registration, and conference diner at "La Coupole".

Christian BIZOUARD, Chair of the SOC - Jean SOUCHAY, Chair of the LOC
15 September 2020

Scientific Organizing Committee

ARIAS Elisa Felicitas, *Observatoire de Paris*, France
BIZOUARD Christian, **Chair**, *Observatoire de Paris, IERS*, France
BROWN Anthony, *Leiden Observatory*, Netherlands
DELVA Pacôme, *Sorbonne Universit - Observatoire de Paris*, France
ESCAPA Alberto, *University of León*, Spain
FERNÁNDEZ Laura Isabel, *Laboratorio MAGGIA. FCAG. Univ. Nacional de La Plata*, Argentina
FOLGUEIRA Marta, *Faculty of Mathematics, Complutense University of Madrid*, Spain
JACOBS Christopher, *JPL*, USA
KARBON Maria, *SYRTE, Observatoire de Paris*, France
KLIONER Sergei, *Lohrmann Observatorium, Technische Universität Dresden*, Germany
MALKIN Zinovy, *Pulkovo Observatory*, Russia
NASTULA Jolanta, **Co-chair**, *Centrum Badan Kosmicznych PAN*, Poland
PARK Ryan, *Jet Propulsion Laboratory*, USA
SCHUH Harald, *GFZ (German Research Centre for Geosciences)*, Germany
SEITZ Florian, *DGFI-TUM*, Germany
SOUCHAY Jean, *Observatoire de Paris*, France

Local Organizing Committee

BARACHE Christophe, *Observatoire de Paris*, France
BAUDOIN Pascale, *Observatoire de Paris*, France
BECKER Olivier, *Observatoire de Paris*, France
BIZOUARD Christian, *Observatoire de Paris*, France
GATTANO César, *Observatoire de Bordeaux*, France
LAMBERT Sébastien, *Observatoire de Paris*, France
SOUCHAY Jean, **Chair**, *Observatoire de Paris*, France
TARIS Francois, *Observatoire de Paris*, France

LIST OF PARTICIPANTS

AKSIM Dan, *Institute of Applied Astronomy of the RAS*, Russia
ARIAS Elisa Felicitas, *Observatoire de Paris*, France
ARLOT Jean-Eudes, *IMCCE/Paris observatory*, France
BARACHE Christophe, *Observatoire de Paris*, France
BAUDOIN Pascale, *Observatoire de Paris*, France
BECKER Olivier, *Observatoire de Paris*, France
BELL Steve, *UK Hydrographic Office*, United Kingdom
BIZOUARD Christian, *Observatoire de Paris*, France
BÖHM Sigrid, *TU Wien*, Austria
BONNEFOND Pascal, *Observatoire de Paris*, France
BROWN Anthony, *Leiden Observatory*, Netherlands
BUDNIK Frank, *ESOC/ESA*, Germany
CAPITAINE Nicole, *Observatoire de Paris*, France
CARLUCCI Teddy, *Observatoire de Paris*, France
CHARLOT Patrick, *Laboratoire d'Astrophysique de Bordeaux*, France
CHENG Yu-Ting, *Nanjing University*, China
CHO Jungho, *Korea Astronomy and Space Science Institute*, South Korea
DAMLJANOVIC Goran, *Astronomical Observatory*, Serbia
DE WITT Aletha, *South African Radio Astronomy Observatory*, South Africa
DÉBARBAT Suzanne, *Observatoire de Paris*, France
DEHANT Veronique, *Royal Observatory of Belgium*, Belgium
DELVA Pacôme, *Sorbonne Université- Observatoire de Paris*, France
DILL Robert, *GFZ*, Germany
DORLAND Bryan, *USNO*, USA
ESCAPA Alberto, *University of León and University of Alicante*, Spain
EUBANKS Marshall, *Space Initiatives Inc*, USA
FERNÁNDEZ Laura Isabel, *Univ. Nacional de La Plata*, Argentina
FERRÁNDIZ José M., *University of Alicante*, Spain
FIENGA Agnès, *Observatoire de la Côte d'Azur*, France
FODOR Csilla, *Eötvös Loránd Univ.*, Hungary
FOLGUEIRA Marta, *Faculty of Mathematics, Complutense University of Madrid*, Spain
FROUARD Julien, *USNO*, USA
GAMBIS Daniel, *Observatoire de Paris*, France
GATTANO César, *Laboratoire d'Astrophysique de Bordeaux*, France
GERLACH Enrico, *Lohrmann Observatorium, TU Dresden*, Germany
GODARD Bernard, *ESOC / ESA*, Germany
GOMEZ Maria Eugenia, *Laboratoire d'Astrophysique de Bordeaux*, France
GROSS Richard, *Jet Propulsion Laboratory*, USA
HEINKELMANN Robert, *GFZ Potsdam*, Germany
HILTON James, *US Naval Observatory*, USA
HOBBS David, *Lund Observatory*, Sweden
HOHENKERK Catherine, *Formerly HM Nautical Almanac Office*, UK
HØG Erik, *Copenhagen University, Niels Bohr Institute*, Denmark
IVANTSOV Anatoliy, *Akdeniz University*, Turkey
JACOBS Christopher, *JPL*, USA
JIANG Nan, *Nanjing University*, China
JOHNSON Megan, *USNO*, USA
KARBON Maria, *Observatoire de Paris*, France

KLIONER Sergei, *Lohrmann Observatorium, TU Dresden, Germany*
 LAMBERT Sébastien, *Observatoire de Paris, France*
 LINDEGREN Lennart, *Lund Observatory, Sweden*
 LIU Jia-Cheng, *Nanjing University, China*
 LIU Niu, *Nanjing University, China*
 LUNZ Susanne, *GFZ Potsdam, Germany*
 MALKIN Zinovy, *Pulkovo Astronomical Observatory of the RAS, Russia*
 MAMMADALIYEV Nijat, *TU Berlin, Germany*
 MARCO Francisco J., *Universitat Jaume I, Spain*
 MARTIN-MUR Tomas, *Caltech/JPL, USA*
 MARTÍNEZ María J., *Universidad Politécnica de Valencia, Spain*
 MÉTIVIER Laurent, *IPGP-IGN, France*
 MIGNARD Francois, *Observatoire de la Côte d'Azur, France*
 MORLEY Trevor, *ESOC / ESA, Germany*
 MOVESIAN Pavel, *St. Petersburg State University, Russia*
 NAGHIBI Elnaz, *Imperial College London, UK*
 NASTULA Jolanta, *Centrum Badan Kosmucznych PAN, Poland*
 NICKOLA Marisa, *HartRAO, South Africa*
 NURUL HUDA Ibnu, *Observatoire de Paris, France*
 PARK Han Earl, *KASI, South Korea*
 PARK Ryan, *Jet Propulsion Laboratory, USA*
 PASHKEVICH Vladimir, *Pulkovo Astronomical Observatory of the RAS, Russia*
 PASYNOK Sergey, *VNIIFTRI, Russia*
 PAVLIS Erricos, *Joint Center for Earth Systems Tech., Univ. of Maryland, USA*
 PAVLOV Dmitry, *Institute of Applied Astronomy of the RAS, Russia*
 PEREPELKIN Vadim, *Moscow Aviation Institute, Russia*
 PETROV Sergey, *St. Petersburg State University, Russia*
 PETROV Leonid, *NASA Goddard Space Flight Center, USA*
 PITJEV Nikolay, *St. Petersburg University, Russia*
 PITJEVA Elena, *Institute of Applied Astronomy of the RAS, Russia*
 PUENTE Víctor, *National Geographic Institute of Spain, Spain*
 RAMBAUX Nicolas, *IMCCE, France*
 RAUT Shrishail, *Technische Universität Berlin, Germany*
 RICHARD Jean-Yves, *Observatoire de Paris, France*
 ROBERT Vincent, *IMCCE - Observatoire de Paris - IPSA, France*
 ROCCA VOLMERANGE Brigitte, *Institut d'astrophysique de Paris, France*
 ROLAND Jacques, *IAP, France*
 RON Cyril, *Astronomical Institute CAS Czech, Republic*
 ROSAT Severine, *IPGS-EOST, France*
 SALSTEIN David, *Atmospheric and Environmental Research, USA*
 SCHUH Harald, *GFZ (German Research Centre for Geosciences), Germany*
 SECREST Nathan, *U.S. Naval Observatory, USA*
 SEITZ Florian, *DGFI-TUM, Germany*
 SIDORENKOV Nikolay, *Hydrometcenter of the Russian Federation, Russia*
 SKURIKHINA Elena, *Institute of Applied Astronomy of the RAS, Russia*
 ŚLIWIŃSKA Justyna, *Centrum Badan Kosmucznych PAN, Poland*
 SOUCHAY Jean, *Observatoire de Paris, France*
 SPOTO Federica, *Observatoire de la Cte d'Azur, France*
 STEWART Susan, *US Naval Observatory, USA*
 TANGA Paolo, *Observatoire de la Cte d'Azur, France*

TARIS Francois, *Observatoire de Paris*, France
TCYBA Efim, *FSUE VNIIFTRI*, Russia
TEYSSANDIER Pierre, *Observatoire de Paris*, France
THUILLOT William, *IMCCE / Paris Observatory*, France
TITOV Oleg, *Geoscience Australia*, Australia
TROFIMOV Dmitrii, *St. Petersburg State University*, Russia
VAHER Eero, *Lund Observatory*, Sweden
VAQUERO Pedro A., *Instituto Geografico Nacional*, Spain
VONDRÁK Jan, *Astronomical Institute CAS, Prague* Czech, Republic
WHITTAKER James, *UK Hydrographic Office* United, Kingdom
WILMOT Toni, *UK Hydrographic Office*, UK
WINSKA Malgorzata, *Warsaw University of Technology*, Poland
YATSKIV Yaroslav S., *Main Astronomical Observatory*, Ukraine
ZACHARIAS Norbert, *US Naval Observatory*, USA
ZHELTOVA Kseniya, *St. Petersburg State University*, Russia
ZOTOV Leonid, *Lomonosov Moscow State University*, Russia
ZSCHOCKE Sven, *Lohrmann Observatorium, TU Dresden*, Germany

SCIENTIFIC PROGRAMME

Monday October 7 9h-12h30: ORAL SESSION I

8h15-9h00: REGISTRATION

9h00- 9h15: OPENING (LOC, IAU,SOC: J. SOUCHAY, F. SEITZ, C. BIZOUARD)

SESSION I: GAIA mission

Chair : David HOBBS (Lund Observatory, Sweden)

9h15-9h30: Lennart LINDEGREN: *The bright reference frame of Gaia and VLBI observations of radio stars*

9h30- 9h45: Federica SPOTO: *Asteroid astrometry in the Gaia era*

9h45-10h00: Paolo TANGA: *Correcting archive asteroid astrometry by Gaia DR2*

10h00-10h30 COFFEE BREAK (TIPI)

Chair: Felicitas ARIAS (Observatoire de Paris)

10h30-10h45: Niu LIU, Z. ZHU, S. B. LAMBERT and J.-C. LIU: *Is it possible to bring the Gaia-CRF2 into the VLBI data reduction?*

10h45-11h00: Nathan SECREST, J. FROUARD: *Quasar Selection Techniques going into the Gaia Era*

11h00-11h30: (invited) François MIGNARD: *Space astrometry from Hipparcos to Gaia : a tribute to JEAN KOVALEVSKY*

11h30-11h45: Goran DAMLJANOVIC, F. TARIS, M.D. JOVANOVIC: *Short-term and long-term flux variability of extragalactic objects useful for the future Gaia CRF*

11h45-12h00: V. ROBERT, J. DESMARS, Jean-Eudes ARLOT: *The NAROO digitization centre*

12h00-12h15: Brigitte ROCCA VOLMERANGE, L. GODINAUD: *Continuous UV to far-IR Spectral Energy Distributions of Quasars*

12h15-12h30: David HOBBS: *Future space astrometry*

12h30-14h00: LUNCH BREAK

Monday October 7 14h-17h30: ORAL SESSION II

SESSION II: Earth Rotation and Geodynamics I (observations and analysis)

100 YRS. CELEBRATION OF COMMISSION " ROTATION OF THE EARTH"

Chair: Jan VONDRAK (Astronomical Institute of the Czech Academy of Science)

14h00-14h15: Florian SEITZ: *Introduction to the Centennial Celebration of IAU Commission A2/19*

14h15-14h45: (invited) Zinovy MALKIN, A. BRZEZINSKI, N. CAPITAINE, V. DEHANT, R. GROSS, C. HUANG, D. MCCARTHY: *overview of the 100 year history of IAU commission 19/A2.*

14h45-15h00: Nicole CAPITAINE: *the IAU Commission ?Earth Rotation? and the IAU definition of the pole and UT1*

15h00-15h15: Richard GROSS, A. BRZEZINSKI: *The International Astronomical Union and Polar Motion*

15h15-15h45: N. Capitaine, S. Klioner, Z. Malkin, J. Nastula: *Tribute to B. GUINOT, B. KO-LACZEK, V. ABALAKIN, V. VITYAZEVA*

15h45-16h15 - COFFEE BREAK (TIPI)

Chair: Yaroslav YATSKIV (Main Astronomical Observatory of the Ukraine)

16h15-16h30: Leonid PETROV, R. RAY: *Combined analysis of free and forced nutations from VLBI group delays*

16h30-16h45: Maria KARBON: *Impact of the parameterisation of the source positions on the Free Core Nutation*

16h45-17h00: Csilla FODOR, R. HEINKELMANN, S. MODIRI, S. RAUT, H. SCHUH and P. VARGA: *Impact of major earthquakes on variations of Earth rotation*

17h00-17h15: Severine ROSAT, N. GILLET, J.-P. BOY: *On the possible detection of inter-annual deformation signal at the Earth's surface due to the fluid core dynamics*

17h15-17h30: Nicholas STAMATAKOS, M. DAVIS, N. SHUMATE: *IERS Rapid Service Prediction Center Products and Services: Improvements, Changes and Challenges, 2017 to 2019.*

17h30-18h30: POSTER SESSION with focus on sessions I, II & V (TIPI)

Tuesday October 8 8h30-12h30h & 14h00-14h15: ORAL SESSION III

SESSION III: ICRF and astrogeodesy

Chair : Maria KARBON (Observatoire de Paris)

8h30-8h45: Patrick CHARLOT, C. GARCIA-MIRO, T. AN, B. sCAMPBELL, F.COLOMER, A. de WITT, P. EDWARDS, S. LAMBERT: *Looking into the future of the radio reference frame with SKA*

8h45-9h00: Marshall EUBANKS, L. PETROV: *COMPASS: Applications of VLBI Beacons in Cis-lunar Space*

9h00-9h10: Anatoliy IVANTSOV: *Astronomical refraction in the Earth's ellipsoidal atmosphere*

9h15-9h30: Chris JACOBS: *Advancing the X/Ka-band Celestial Frame: Roadmap to the Future*

9h30-9h45: Aletha de WITT, C. JACOBS, D. GORDON, H. KRASNA, K. LE BAIL, MCCALLUM, QUICK, SOJA, HORIUCHI: *The K-Band Celestial Reference Frame Roadmap*

10h00-10h30 PHOTO, COFFEE BREAK (TIPI)

Chair : Aletha de WITT (South African Radio Astronomy Observatory)

10h30-10h45: Bryan DORLAND, N. SECREST, JOHNSON, N. ZACHARIAS, A. FEY, C. FINCH, T. FISCHER, L. HUNT, J. SOUCHAY: *The Fundamental Reference AGN Monitoring Experiment (FRAMEx) collaboration*

10h45-11h00: Megan JOHNSON: *A volume-limited AGN Survey for the FRAMEx Project*

11h00-11h15: Nijat MAMMADALIYEV, P.A. SCHREINER, S. GLASER, K. BALIDAKIS, K.H. NEUMAYER, J. M. ANDERSON, R. HEINKELMANN, R. KOENIG, H. SCHUH: *On a possible*

contribution of VLBI to geocenter realization via satellites assessed by simulation study

11h15-11h30: Erricos PAVLIS, V. LUCERI, M. KUZMICZ-CIESLAK, and G. BIANCO: *The ILRS Planned Contribution to ITRF2020*

11h30-11h45: Victor PUENTE, M. FOLGUEIRA, E. AZCUE: *Analysis of VLBI and GNSS ties in CONT campaigns*

11h45-12h00: Jacques ROLAND, C. GATTANO, S. LAMBERT, F. TARIS: *Structure and variability of quasars*

12h00-12h15: Oleg TITOV, F. SHU: *Observations of radio stars with geodetic VLBI*

12h15-12h30: Norbert ZACHARIAS, C. FINCH: *Deep South Telescope*

12h30-14h00 LUNCH BREAK

14h00-14h15: Megan JOHNSON, L. HUNT, A. FEY, D. GORDON, and J. SPITZAK: *VLBA imaging of ICRF3 sources*

Tuesday October 8 14h15-17h30: ORAL SESSION IV

SESSION IV: Earth Rotation and Geodynamics II (models)

Chair: Jose Manuel FERRANDIZ (University of Alicante VLBI Analysis Centre)

14h15-14h45: (invited) David SALSTEIN: *Atmospheric angular momentum related to Earth rotation studies: history and modern developments*

14h45-15h00 J. NASTULA and Justina SLIWINSKA: *Prograde and retrograde terms of gravimetric polar motion excitation estimates from the newest GRACE gravity field models*

15h00-15h15 Alberto ESCAPA, J. GETINO, J.M. FERRANDIZ, T. BAENAS: *Second-order effects in IAU2000 nutation model*

15h15-15h30: Jia-Cheng LIU, N. CAPITAINE: *A possible improvement of IAU 2006 precession model*

15h30-16h00 COFFEE BREAK / POSTER SESSION (TIPI)

Chair: Laura FERNANDEZ (Universidad Nacional de La Plata)

16h00-16h15 Véronique DEHANT: *Progress in understanding nutations*

16h15-16h30: Elnaz NAGHIBI, S.A. KARABASOV: *Excitation of the Earth's Chandler wobble by the North Atlantic double gyre*

16h30-16h45: Nikolay SIDORENKOV, E. DIONIS, C. BIZOUARD, L. ZOTOV: *Decade fluctuations in Earth's rotation as evidences of lithospheric drift over the asthenosphere*

16h45-17h00: Leonid ZOTOV, C. BIZOUARD, N. SIDORENKOV: *Chandler wobble variability*

17h00-17h15: Jan VONDRAK, C. RON: *Determination of FCN parameters from different VLBI solutions, considering geophysical excitations*

17h15-17h30: José Manuel FERRANDIZ, R.S. GROSS, A. ESCAPA, J. GETINO, A. BRZEZINSKI, R. HEINKELMAN: *Joint Working Group on Theory of Earth rotation and validation*

17h30-18h30 POSTER SESSION with focus on sessions III, IV (TIPI)

19h30 MEETING DINNER AT "LA COUPOLE"

Wednesday October 9 8h30-12h30: ORAL SESSION V

SESSION V: Space navigation and solar system dynamics

Chair: Sergei KLIONER (Lohrmann Observatorium, TU Dresden)

8h30-8h45: Agnès FIENGA, L. BERNUS, P. DERAM, A. Di RUSCIO, O. MINAZZOLI, J. LASKAR, M. GASTINEAU: *The new planetary ephemerides INPOP19a and applications*

8h45-9h00: James HILTON, S.G. STEWART: *Implementation of Improved Magnitude Parameters for Solar System Planetary Ephemerides*

9h00-9h15: Elena V. PITJEVA, N. P. PITJEV, D. A. PAVLOV: *Estimates of changes of the gravitational constant G and the gravitational parameter of the Sun GM_{\odot} Sun based on new data and observations of spacecraft and on updated the EPM2019 ephemeris*

9h15-9h30: Nicolas RAMBAUX, V. VISWANATHAN, A. FIENGA, J. LASKAR, M. GASTINEAU: *Dynamical model of lunar core and observational constraint from Lunar Laser Ranging*

9h30-9h45: Pacôme DELVA, N. PUCHADES: *A gravitational redshift test using eccentric Galileo satellites*

9h45-10h00: Tomas MARTIN-MUR, J. LAZIO, S. BHASKARAN, R. PARK, C. JACOBS: *Leveraging Gaia Data for Deep Space Navigation*

10h00-10h30 COFFEE BREAK

Chair: Jean SOUCHAY (Observatoire de Paris)

10h30-10h45: Dmitri PAVLOV: *Solid body tides in the dynamical model of the Moon*

10h45-11h00: Dan AKSIM, D. PAVLOV: *On the Extension of Adams-Bashforth-Moulton for Numerical Integration of Delay Differential Equations and Application to the Moon's Orbit*

11h00-11h15: Vladimir V. PASHKEVICH, A.N. VERSHKOV: *Geodetic (Relativistic) rotation of the Mars satellites system*

11h15-11h30: Sven ZSCHOCKE: *On the post-linear metric of a solar system body*

11h30-11h45: Pierre TEYSSANDIER: *Unified approach of Shapiro and lensing effects in the field of an axisymmetric spinning body*

11h45-12h00 CLOSING (LOC, SOC, Proceedings, announcement of next Journées)

12h30-14h00 MEETING COCKTAIL AT PARIS OBSERVATORY, SALLE CASSINI

LIST OF POSTERS

Session I: GAIA mission

- I.1 Eric HOEG: Gaia Successor with International Participation
- I.2 Susanne LUNZ, R. HEINKELMANN, J. ANDERSON, M. JOHNSON, A. FEY, O. TITOV: Gaia-VLBI: phase-referencing continuum emission observations of optically bright stars with the VLBA (planned proposal)
- I.3 Zinovy MALKIN: A new equal-area grid on the sphere
- I.4 Francisco J. MARCO, MARTÍNEZ M-J., LÓPEZ J.A.: An example to analyse discrete vector fields on the sphere using quantitative and qualitative methods

Session II: Earth Rotation and Geodynamics I (observations and analysis)

- II.1 Yu-Ting CHENG, J.-C. LIU, and Z. ZHU: Analyses of celestial pole offsets with VLBI, LLR, and optical observations
- II.2 Maria DAVIS, N. STAMATAKOS, C. BIZOUARD, S. LAMBERT, D. McCARTHY, Toward IERS Conventions 2022
- II.3 Robert HEINKELMANN, S. MODIRI, S. BELDA, M. HOSEINI, Z. MALKIN, J.-M. FERRAN-DIZ, H. SCHUH: On the correlation of Celestial Pole Offsets and geomagnetic field variations (recent achievements)
- II.4 Zinovy MALKIN, T. SOBOLEVA, N. MILLER: Outstanding Pulkovo latitude observers Lidia Kostina and Natalia Persiyaninova
- II.5 Maria J. MARTINEZ, F.J. MARCO: A revision of \dot{T} and LOD values for the fifth, sixth and seventh centuries
- II.6 Ibnu NURUL HUDA, C. BIZOUARD, S. LAMBERT, Y. Ziegler: Estimation of Earth rotation resonance parameters through VLBI analysis
- II.7 Han Earl PARK, K.-M. ROH, S.-M. YOO, J. CHO: The Development of the GNSS-based Products Service System
- II.8 Sergey PASYNOK, I. BEZMENOV, I. IGNATENKO, E. T.YBA: Operative EOP activities in VNIIFTRI
- II.9 Shrishail RAUT, R. HEINKELMANN, S. MODIRI, H. SCHUH: Effect of VLBI intensive sessions on daily and sub-daily ERP determined from CONT17 IVS data.
- II.10 Jean-Yves RICHARD: Earth Orientation Parameters by GNSS & VLBI
- II.11 Elena SKURIKHINA: Estimation of the accuracy of prediction of the Earth orientation parameters at the IAA data analysis center
- II.12 Efim TCYBA, O. VOLKOVA: Determination of Earth Orientation Parameters by SLR in MMC SSTF FSUE VNIIFTRI

Session III: ICRF and astrogeodesy

- III.1 Dan AKSIM, A. MELNIKOV, D. PAVLOV, S. KURDUBOV: On the Investigations of the Electron Density in the Solar Corona with Very Long Baseline Interferometry
- III.2 Maria Eugenia GOMEZ, P. CHARLOT, R. CAMPBELL, M. KETTENIS, A. KEIMPEMA, Geodesy at K band with the European VLBI Network

- III.3 Maria KARBON, C. GATTANO: Parametrization of the source coordinates and its astrophysical interpretation
- III.4 Marisa NICKOLA: Improving HartRAO performance at K-Band
- III.5 Victor PUENTE, E. AZCUE, S. GARCIA-ESPADA, Y. GARCIA-ESPADA, P.A. VAQUERO : Status of the geodetic VLBI analysis at the National Geographic Institute of Spain
- III.6 Dimitri TROFIMOV, S.D. PETROV, Y.A. SEROV, I.V. CHEKUNOV, S.S. SMIRNOV, K.V. ZHELTOVA, O.A. TROSHICHEV: Total electron Content over Vostok Antarctic station
- III.7 Aletha de WITT, C. JACOBS, NICKOLA, D. GORDON, H. KRASNA, K. LE BAIL, MCCALLUM, J.QUICK, SOJA, HORIUCHI: The K-Band celestial reference Frame : First imaging results
- III.8 Yaroslav S. YATSKIV, O. O. KHODA: On the consistency between local ties and space geodesy estimates in the Simeiz-Katzively co-location site

Session IV: Earth Rotation and Geodynamics II (models)

- IV.1 Christian BIZOUARD, Ibnu NURUL HUDA: Polar motion resonance parameter in the diurnal band
- IV.2 Jungho CHO, S-H. NA, K-W. SEO, K-H. YOUM, W. SHEN: The annual wobble excitation due to the seasonal atmospheric loading on continents
- IV.3 Robert DILL, H. DOBSLAW: The importance of seasonal sea-level variations from geophysical models and satellite gravimetry for excitation of length-of-day
- IV.4 Laura Isabel FERNANDEZ, S. BØHM: Influence of the 2015-2016 ENSO event on length of day variations
- IV.5 Marta FOLGUEIRA, J. SOUCHAY and D. GOMEZ: 30 years-evolution in the modelling of the rotation of the rigid Earth: new effects and developments
- IV.6 Sébastien LAMBERT: Atmospheric excitation and torques over the 20th century: how was driven the Chandler wobble?
- IV.7 Vadim PEREPELKIN, S. KRYLOV, A. FILIPPOVA: Dynamic effects of the spatial movement of the Earth-moon system in the Earth's pole oscillation
- IV.8 Yavor CHAPANOV, Cyril RON, J. VONDRAK: Chandler period variations due to solar activity
- IV.9 Malgorzata WINSKA : Improved geodetic-hydrological residual time series constrained by polar motion observations and geophysical models
- IV.10 Sigrid BØHM and D. SALSTEIN: Next generation of coupled climate models and the predicted atmospheric excitation of length of day

Session V: Space navigation and solar system dynamics

- V.1 Suzanne DEBARBAT: Le système solaire selon Cassini I
- V.2 A.A. CHICHARRO, Victor PUENTE and M. FOLGUEIRA and J. SOUCHAY: Influence on Earth satellites due to the close approach of 99942 Apophis
- V.3 S.DOMENECH and Marta FOLGUEIRA : Rotation of Mars and Venus: influence of the zonal harmonic J3
- V.4 Serguei KUDRYATSEV : Updated harmonic development of tide-generating potential of Mars
- V.5 Pavel MOVSESIAN, S. PETROV, D. TROFIMOV, I. CHEKUNOV: Analysis and normalization of GNSS onboard clock
- V.6 Vladimir V. PASHKEVICH, A.V.MELNIKOV, A.N.VERSHKOV and G.M.KARELIN: Chaos and relativistic effects in the rotational dynamics of minor planetary satellites

Session I

GAIA MISSION

THE BRIGHT REFERENCE FRAME OF GAIA AND VLBI OBSERVATIONS OF RADIO STARS

L. LINDEGREN

Lund Observatory, Lund University - Sweden - lennart@astro.lu.se

ABSTRACT. The *Gaia* Celestial Reference Frame is defined by faint quasars, and it is assumed that the positions and proper motions of other sources are expressed in the same frame. For *Gaia* DR2, position differences for Hipparcos stars at epoch J1991.25 show that the proper motion system of the bright ($G < 13$) sources in DR2 rotate by about 0.15 mas yr^{-1} . This is confirmed by Lindegren (2020), using a new algorithm to compare DR2 data with published VLBI astrometry for 41 radio stars. The spin of the bright reference frame of *Gaia* DR2 is caused by the different modes of observation in *Gaia* and related calibration issues unresolved in DR2. To validate the bright reference frame of *Gaia* in future data releases will require accurate positional VLBI observations to be acquired in the next 5–10 years for the largest possible set of suitable radio stars.

1. THE GAIA CELESTIAL REFERENCE FRAME

The second release of *Gaia* data (DR2; Gaia Collaboration et al., 2018a) provides full astrometric information (positions, parallaxes, and proper motions) for 1331 million sources at the reference epoch J2015.5. Their magnitudes in the integrated *Gaia* band range from $G \simeq 3$ to 21, although the astrometry is unreliable for $G \lesssim 6$ due to detector saturation. The positions and proper motions of all sources are formally given in the second realisation of the *Gaia* Celestial Reference Frame, *Gaia*-CRF2 (Gaia Collaboration et al., 2018b).

The primary realisation of *Gaia*-CRF2 is the list of positions, as given in DR2, for a subset of 556 869 sources identified as quasi-stellar objects (QSOs), i.e. the optical emission from active galactic nuclei (AGNs) at cosmological distances. Their proper motions, also given in DR2, are usually insignificant and the reference frame was adjusted so that their global rotation (spin) is zero to within 0.02 mas yr^{-1} . 2820 of the QSOs were identified as the optical counterparts of ICRF sources in a prototype version of ICRF3 (Jacobs et al., 2018), and were used to align the positional system of *Gaia*-CRF2 with the ICRF to within about 0.02 mas at the epoch J2015.5.

An implicit assumption is that the positions and proper motions of all DR2 sources are on the same reference frame, providing a secondary, much denser realisation of *Gaia*-CRF2 for all magnitudes in the range $G \simeq 3$ –21. However, the quality of the reference frame cannot easily be checked except for the QSOs, which are all fainter than $G \simeq 13$, and 99.9% fainter than $G = 16$ mag. The QSOs are, in every respect, observed and treated exactly as ordinary stars of similar magnitude and colour, and it is therefore reasonable to assume that the levels of non-rotation and alignment errors quoted above apply also to the stellar part of *Gaia*-CRF2 fainter than $G \simeq 16$. As shown below, they do not apply, though, to stars brighter than $G \simeq 13$.

An important question is then how *Gaia*-CRF2, and indeed all future versions of the *Gaia* CRF, can be validated for sources brighter than $G \simeq 16$. In this paper I argue that accurate VLBI astrometry of radio stars can be used for this purpose, but that a concerted and well-planned programme of such observations in the next 5–10 years is needed to match the expected improvements in future versions of the *Gaia* CRF.

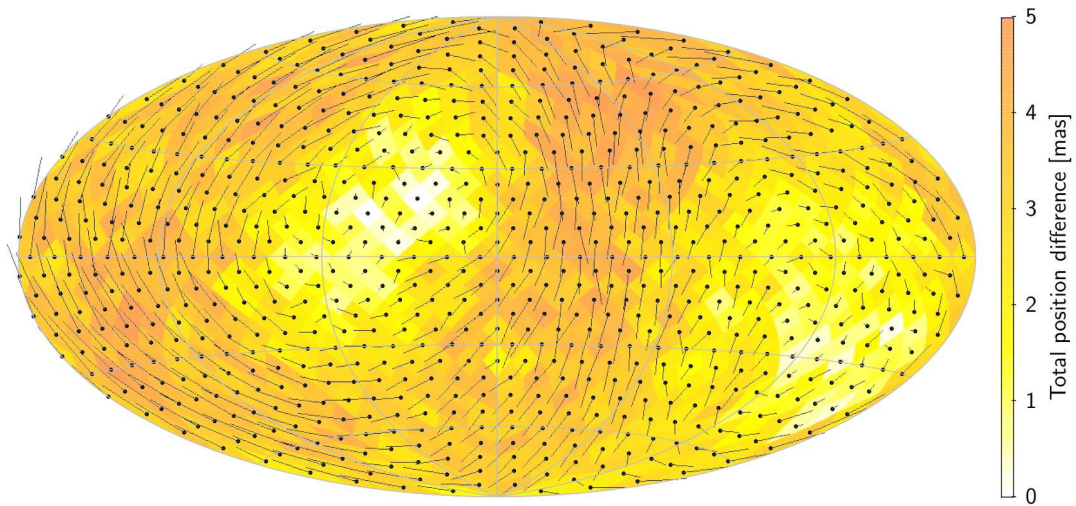


Figure 1: Position differences at epoch J1991.25 between *Gaia* DR2 and the Hipparcos Catalogue. The fans show the median displacements ($\alpha_{\text{DR2}} - \alpha_{\text{Hip}}$, $\delta_{\text{DR2}} - \delta_{\text{Hip}}$), magnified a factor 10^7 , in cells of $\simeq 54 \text{ deg}^2$ solid angle. The cells are coloured according to the total median displacement in the cell. The map uses the Hammer–Aitoff projection in equatorial (ICRS) coordinates with $\alpha = \delta = 0$ at the centre, north up, and α increasing from right to left.

2. THE BRIGHT REFERENCE FRAME OF GAIA DR2

Already at the time when *Gaia* DR2 was published, it was known that the reference frame for the bright sources ($G \lesssim 13$) has a significant ($\simeq 0.15 \text{ mas yr}^{-1}$) spin relative to the quasars. This was seen from a comparison (Figure 4 in Lindegren et al., 2018) with proper motions from the *Tycho–Gaia* Astrometric Solution (TGAS) of DR1. In TGAS the proper motions were obtained by incorporating positions from the Hipparcos and *Tycho*-2 catalogues in the solution, thus benefiting from the $\sim 24 \text{ yr}$ epoch difference (Michalik et al., 2015).

The issue is illustrated in Figure 1. This shows the systematic differences in the positions of Hipparcos stars between *Gaia* DR2 and the Hipparcos Catalogue (van Leeuwen, 2007). The position comparison is made at the reference epoch of the Hipparcos Catalogue, J1991.25, by propagating the *Gaia* DR2 positions back to this epoch, using the proper motions in DR2. The pattern shows a very clear signature of rotation, by about 3.6 mas around the direction $(\alpha, \delta) = (53^\circ, +15^\circ)$. There are three possible explanations for this global pattern: (i) a misalignment of the Hipparcos Catalogue at J1991.25 with respect to the ICRS by 3.6 mas; (ii) a similar but opposite misalignment of the *Gaia* DR2 positions at J2015.5; or (iii) a spin of the DR2 proper motions relative to ICRS by about $(3.6 \text{ mas}) / (24.25 \text{ yr}) \simeq 0.15 \text{ mas yr}^{-1}$. From the way the Hipparcos Catalogue was aligned with ICRS (Kovalevsky et al., 1997), explanation (i) is very unlikely (formally, the probability is $< 10^{-6}$), and (ii) can be ruled out on similar grounds (cf. Sect. 3). Although a minor part of the effect could be explained by a combination of (i) and (ii), we must conclude that (iii) is the main cause, i.e. that the bright reference frame of DR2 rotates with respect to ICRS at a rate of about 0.15 mas yr^{-1} .

To further quantify this rotation, Figure 2 shows the equatorial components of the global spin vector $[\omega_X, \omega_Y, \omega_Z]$ calculated in bins of the G magnitude. For $G \gtrsim 16$ the reference frame is non-rotating to $< 0.02 \text{ mas yr}^{-1}$. Between $G = 14$ and 16 some deviation in ω_Y is indicated, although the number of QSOs is too small to allow a firm conclusion. For $G \lesssim 13$ the spin is very significant, and almost constant between $G = 7$ and 11. From $G = 11$ to 13 the data are too noisy to tell with certainty if there is a progressive transition to the faint reference frame. The combined

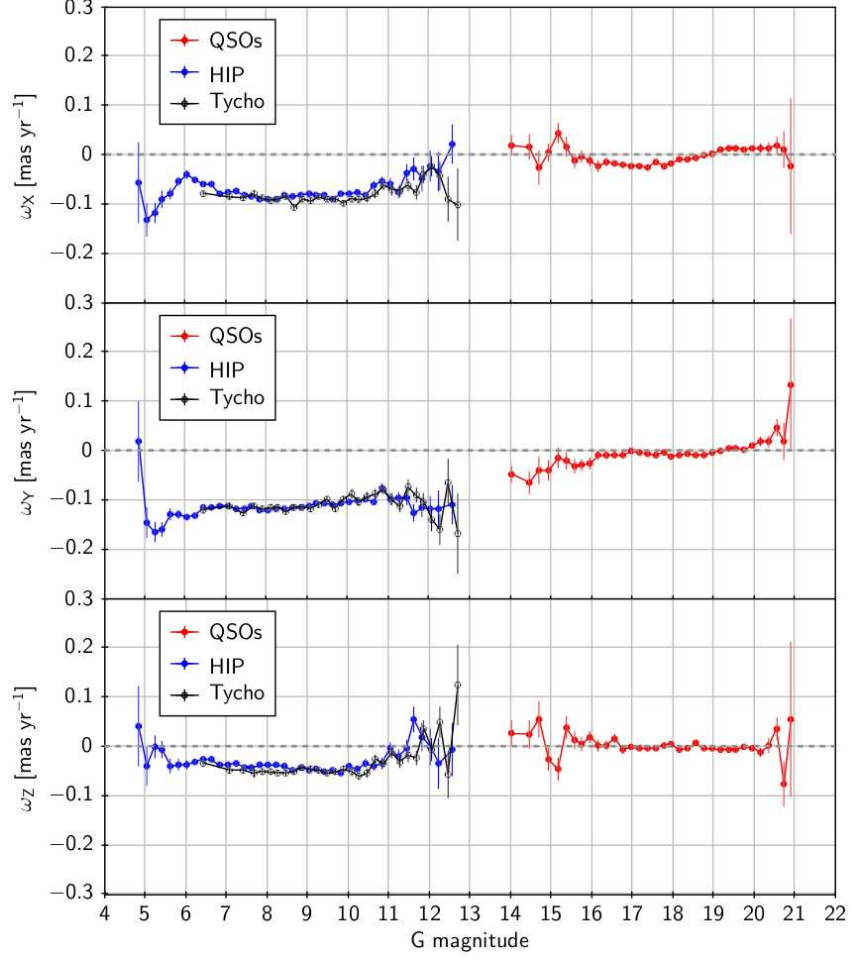


Figure 2: Estimates of the global spin of the *Gaia*-CRF2 as a function of G . For sources fainter than $G \simeq 14$ (in red), the spin is estimated from the proper motions of QSOs; for brighter sources it is computed from the differences between the *Gaia* DR2 proper motions of Hipparcos stars (blue) and *Tycho*-2 stars (black) and their proper motions derived from the position differences DR2 – Hip and DR2 – Tyc, divided by the epoch difference of 24.25 yr.

result, using the $\sim 90\,000$ best-fitting Hipparcos stars, is:

$$\boldsymbol{\omega} \equiv \begin{bmatrix} \omega_X \\ \omega_Y \\ \omega_Z \end{bmatrix} = \begin{bmatrix} -0.085 \pm 0.025 \\ -0.113 \pm 0.025 \\ -0.039 \pm 0.025 \end{bmatrix} \text{ mas yr}^{-1}, \quad (1)$$

where the uncertainties follow from the estimated RMS alignment error of the Hipparcos Catalogue at J1991.25 (0.6 mas per axis; Kovalevsky et al., 1997) divided by the epoch difference. The vector (1) is a correction to the DR2 proper motions in the following sense:

$$\left. \begin{aligned} \mu_{\alpha^*}^{\text{ICRF}} &= \mu_{\alpha^*}^{\text{DR2}} + \omega_X \cos \alpha \sin \delta + \omega_Y \sin \alpha \sin \delta - \omega_Z \cos \delta \\ \mu_{\delta}^{\text{ICRF}} &= \mu_{\delta}^{\text{DR2}} - \omega_X \sin \alpha + \omega_Y \cos \alpha \end{aligned} \right\} \quad (2)$$

Note that this correction only applies to sources brighter than $G \simeq 13$.

3. USING VLBI ASTROMETRY OF RADIO STARS

The classical method to estimate the spin ($\boldsymbol{\omega}$) of a catalogue is to derive absolute proper motions for some objects, e.g. using VLBI, calculate the proper motion differences with respect to the catalogue, and finally use equations like (2) to solve the components ω_x , ω_y , ω_z by least squares (e.g. Bobylev, 2019). This method does not use any positional information contained in the VLBI data, except for the differential measurements from which proper motions are derived.

But even without any associated proper motions, positional VLBI observations can contribute to the determination of $\boldsymbol{\omega}$, just like the Hipparcos positions did for (1), provided that they are made at an epoch sufficiently different from the *Gaia* epoch. The greater the epoch difference, the more weight is contributed by the VLBI positions to the determination of $\boldsymbol{\omega}$. The early phase-referencing VLBI observations by Lestrade et al. (1999) are thus particularly valuable, as their mean epochs in the early 1990s provide a time baseline of more than two decades to the *Gaia* observations. Future VLBI observations, even many years after the *Gaia* mission has ended, will for the same reason be extremely valuable for the determination of the spin. Note that the VLBI positions at various epochs need not refer to the same sources, since the information on $\boldsymbol{\omega}$ comes from their positional differences with respect to *Gaia*.

Lindegren (2020) describes a general algorithm to estimate the spin ($\boldsymbol{\omega}$) and orientation error ($\boldsymbol{\epsilon}$) of a stellar catalogue by means of VLBI observations. It determines by least squares the six constants in the linear expression

$$\boldsymbol{\epsilon}(t) = \boldsymbol{\epsilon}(T) + (t - T)\boldsymbol{\omega} \quad (3)$$

for the orientation error relative to the ICRS as a function of time, where T is the reference epoch of the *Gaia* data. Applied to *Gaia* DR2 ($T = 2015.5$), using VLBI data for 41 radio stars collected from the literature, the result is

$$\boldsymbol{\epsilon}(2015.5) = \begin{bmatrix} -0.35 \pm 0.14 \\ +0.36 \pm 0.25 \\ +0.05 \pm 0.05 \end{bmatrix} \text{ mas}, \quad \boldsymbol{\omega} = \begin{bmatrix} -0.077 \pm 0.051 \\ -0.096 \pm 0.042 \\ -0.002 \pm 0.036 \end{bmatrix} \text{ mas yr}^{-1}. \quad (4)$$

In this solution only 26 of the 41 radio stars were retained; 15 were iteratively rejected based on a goodness-of-fit criterion. Most of the rejected sources are known to have significantly non-uniform motions due to perturbing companions.

Within its uncertainty, the result for $\boldsymbol{\omega}$ in Eq. (4) agrees with the spin (1) obtained from the Hipparcos positions. It therefore supports the conclusion in Sect. 2 concerning the rotation of the bright reference frame of *Gaia* DR2. The two determinations of $\boldsymbol{\omega}$ are in fact not entirely independent: the alignment of the Hipparcos Catalogue at J1991.25 to the ICRS mainly relied on the VLBI observations of 12 radio stars made by Lestrade et al. between 1984 and 1994 (Kovalevsky et al., 1997), and several of them also contribute heavily to (4), as discussed below.

4. THE VALUE OF OLD (AND FUTURE) VLBI OBSERVATIONS

The algorithm described in Lindegren (2020) also computes quantities E_i and Ω_i representing the statistical weights contributed by the VLBI data on each radio star (i) to the determination of $\boldsymbol{\epsilon}(2015.5)$ and $\boldsymbol{\omega}$, respectively (or, in the case of a rejected object, the potentially contributed weight). Figure 3 shows these quantities plotted against the mean epoch of the VLBI observations. From Figure 3a it is evident that the orientation at epoch J2015.5 is almost entirely determined by VLBI observations made close to this epoch. This is expected, since the older VLBI data only contribute to $\boldsymbol{\epsilon}(2015.5)$ if their proper motions are good enough to provide positions at J2015.5 of competitive precision, which is usually not the case.

By contrast, in Figure 3b more than half of the total weight contributed towards the determination of $\boldsymbol{\omega}$ comes from the six accepted objects with pre-1995 VLBI data, thanks to their large

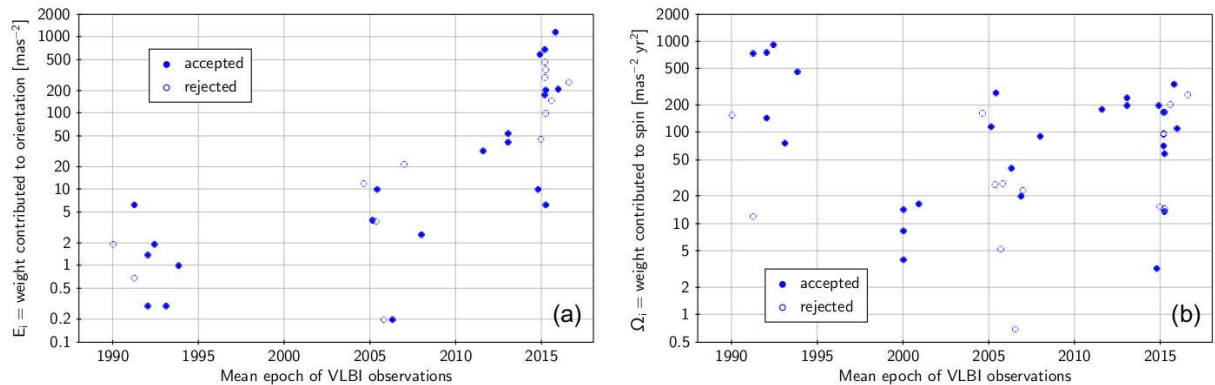


Figure 3: Weights contributed by the VLBI data for the 41 radio stars considered by Lindegren (2020) to the estimation of **(a)** the orientation at J2015.5, and **(b)** the spin of the bright reference frame of *Gaia* DR2. Filled and open circles denote sources accepted and rejected in the solution.

epoch differences with respect to the *Gaia* data. In order of decreasing Ω_i , these objects are: AR Lac, LS I +61 303, Cyg X-1, HD 199178, HD 22468, and BH CVn (HR 5110). All of them were observed by Lestrade et al. (1999) with typical positional uncertainties of 0.3–0.5 mas at their respective mean epoch. Recent programmes such as the GOBELINS survey (e.g. Kounkel et al., 2017) often reach positional uncertainties that are ten times smaller, but because their mean epochs are close to the *Gaia* DR2 epoch they mainly contribute (in this analysis) to the determination of ϵ (2015.5), as shown in Figure 3a. However, as more observations of a similar accuracy will surely be added to the analysis in coming years, the determination of ω will increasingly rely on the recent data.

Nevertheless, in spite of expected improvements in future VLBI data, the old observations will not become obsolete. Most of the radio stars are close binaries (e.g. of RS CVn type), and many have a third component in a long-period orbit causing a significant acceleration in the motion of the close pair. This is the case e.g. for σ^2 CrB and UX Ari, two well-observed objects in the Lestrade et al. programme that were rejected in the present analysis due to their bad goodness-of-fit statistics. With a more sophisticated modelling of their motions, these objects could well be included in future analyses, in which case the early data will be extremely valuable.

For the present analysis it was sometimes possible to increase, by a large factor, the weight of an early VLBI position simply by recalculating it, using the most recent (ICRF3) position for the calibrator source (the quasar used for the phase referencing). One example is Cyg X-1, where the positional uncertainty at 1991.25 was reduced from $\simeq 1.5$ mas, as given in Lestrade et al. (1999), to the $\simeq 0.35$ mas used in this analysis. This is of course only possible when the identity and position of the calibrator, as used in the original VLBI reduction, have been documented.

5. CONCLUSION

Based on a comparison with accurate VLBI astrometry of radio stars, it is concluded that the bright ($G \lesssim 13$ mag) reference frame of *Gaia* DR2 is rotating with respect to quasars at a rate of about 0.15 mas yr^{-1} . This supports a similar conclusion based on a comparison with Hipparcos positions at the epoch J1991.25. On the other hand, QSO data show that the faint ($G \gtrsim 16$) reference frame of *Gaia* DR2 is non-rotating at $< 0.02 \text{ mas yr}^{-1}$. The difference between the bright and faint reference frames is related to the different modes of observation (CCD sampling) in *Gaia*, and associated calibration issues that will only be resolved in future releases (see Appendix B in Lindegren, 2020, for details).

The comparison of *Gaia* DR2 data with VLBI astrometry uses a new algorithm that incorporates in an optimal way both positional information and proper motions in a single solution of the orientation (ϵ) and spin (ω) of the *Gaia* reference frame with respect to the ICRS.

It is expected that the the celestial reference frame will be an order of magnitude more precise in the final release of *Gaia* data than it is in DR2. To validate the bright reference frame of future releases to a matching accuracy will be challenging. Clearly it will not be enough to compare with the Hipparcos reference frame, which will not improve with time. Instead, the validation must rely mainly on existing and future VLBI astrometry of radio stars. This will require many more positional measurements to be obtained in the next 5–10 years, on an absolute accuracy level of $\simeq 0.1$ mas or better, with direct links to the ICRF frame. To minimise the impact of multiplicity, it will be prudent to use as many different sources as possible. While most of the new positional VLBI data could materialise as a by-product of various astrophysical programmes, it may be necessary to complement them with dedicated observations targeting specific objects, such as astrometrically “clean” radio stars (ideally single main-sequence stars), objects with a long history of accurate VLBI observations, and radio stars with optical magnitudes in the range 13 to 16, which are rare in current programmes.

Irrespective of their original scientific motivation, it is important that astrometric VLBI observations are published in sufficient detail, and with adequate meta-information, so that they can be used in the future to address other scientific questions, including those related to the radio-optical reference frame. As a minimum, the positions derived from the individual observing sessions should be given, with their mean epochs of observation, as well as the assumed positions of the calibrators. Most, but not all recent publications already provide this information.

Acknowledgement. This work made use of data from the ESA mission *Gaia*, processed by the *Gaia* Data Processing and Analysis Consortium (DPAC). Funding for DPAC has been provided by national institutions, in particular those participating in the *Gaia* Multilateral Agreement.

6. REFERENCES

- Bobylev, V.V., 2019, “Parameters of the Link between the Optical and Radio Frames from *Gaia* DR2 Data and VLBI Measurements”, *Astronomy Letters* 45, pp. 10–19.
- Gaia* Collaboration et al., 2018a, “*Gaia* Data Release 2. Summary of the contents and survey properties”, *A&A* 616, A1.
- Gaia* Collaboration et al., 2018b, “*Gaia* Data Release 2. The celestial reference frame (*Gaia*-CRF2)”, *A&A* 616, A14.
- Jacobs, C., Charlot, P., Arias, E.F., et al., 2018, “ICRF-3: An overview of the proposed next generation Multi-wavelength ICRF”, *COSPAR Meeting* 42, B2.1-0031-18.
- Kounkel, M., Hartmann, L., Loinard, L., et al., 2017, “The Gould’s Belt Distances Survey (GOBELINS). II. Distances and structure toward the Orion molecular clouds”, *ApJ* 834, p. 142.
- Kovalevsky, J., Lindegren, L., Perryman, M.A.C., et al., 1997, “The HIPPARCOS catalogue as a realisation of the extragalactic reference system”, *A&A* 323, pp. 620–633.
- Lestrade, J.-F., Preston, R.A., Jones, D.L., et al., 1999, “High-precision VLBI astrometry of radio-emitting stars”, *A&A* 344, pp. 1014–1026.
- Lindegren, L., 2020, “The *Gaia* reference frame for bright sources examined using VLBI observations of radio stars”, *A&A* 633, A1.
- Lindegren, L., Hernández, J., Bombrun, A., et al., 2018, “*Gaia* Data Release 2. The astrometric solution”, *A&A* 616, A2.
- Michalik, D., Lindegren, L., Hobbs, D., 2015, “The Tycho-*Gaia* astrometric solution. How to get 2.5 million parallaxes with less than one year of *Gaia* data”, *A&A* 574, A115.
- van Leeuwen, F., 2007, “Hipparcos, the New Reduction of the Raw Data”, *ASSL* 350.

IS THERE AN INTEREST IN BRINGING GAIA-CRF INTO VLBI DATA REDUCTION ?

N. LIU¹, S. LAMBERT², Z. ZHU¹, and J.-C. LIU¹

¹ School of Astronomy & Space Science, Nanjing University - China - zhuzi@nju.edu.cn

² SYRTE, Observatoire de Paris - France - sebastien.lambert@obspm.fr

ABSTRACT. The very long baseline interferometry (VLBI) and *Gaia* mission provide two main realizations of the celestial reference frame, which are the International Celestial Reference Frame (ICRF) and *Gaia*-CRF, with similar precision. One weakness in the ICRF is the large-scale systematics which is not supposed to be seen in the *Gaia*-CRF. It is, thus, possible to consider the *Gaia*-CRF as another option besides the ICRF in the VLBI data reduction. We generate several VLBI global solutions with different configurations on the celestial frame and compare VLBI products. Our preliminary results show that different a priori catalogs only introduce an orientation offset in the celestial frame together with corresponding bias in the UT1 and nutation series. If we fix the defining source position to *Gaia* DR2, the estimated celestial frame will be brought closer to the *Gaia*-CRF in terms of dipolar terms.

1. INTRODUCTION

The celestial reference frame (CRF) now has several realizations at an accuracy level of tens of micro-arc second (μas) since publications of the *Gaia* Data Release 2 (DR2, Gaia Collaboration et al. 2016, 2018a, 2018b) and the third generation of International Celestial Reference Frame (ICRF, Charlot et al. 2019). The International Celestial Reference Frame (ICRF) is realized through positions of a set of radio sources measured by the very long baseline interferometry (VLBI) in the radio domain, while the *Gaia* celestial frame (*Gaia*-CRF) is constructed via positions and proper motions of extra-galactic objects in the optical domain.

One weakness in the ICRF is that it contains large scale systematics due to the north-south network asymmetry. A systematic position error of about $50 \mu\text{as}$ in the South (around $\delta = -30^\circ$) in the ICRF2 was reported in, e.g., Liu et al 2018 but is now partly accounted for by modeling of the Galactic aberration. These systematics are not supposed to be present in *Gaia*-CRF because the scanning law of *Gaia* allows a more uniform sky coverage. The current precision of *Gaia* data is only comparable to that of VLBI but one should note that the *Gaia* DR2 used only less than half of data collected during the whole mission. As a result, the final *Gaia*-CRF could be potentially more precise (lower position error) and more accurate (lower systematics) than the radio frame. Under this situation, it would be interesting to consider the *Gaia*-CRF as an option for the VLBI data reduction. Besides, analyzing the VLBI observations within the *Gaia*-CRF could be a possible way for the radio-optic frame link. The remaining problem is the radio-to-optical distance but, except for a few sources, it should not produce any global systematics and affect the maintenance of the celestial frame datum.

For these reasons, we propose to test the possibility of considering the *Gaia*-CRF in the VLBI data reduction, to look at to which extent one could use the *Gaia*-CRF (i.e., an independent datum) as a priori and how such an a priori perturbed the VLBI products: celestial reference frame (CRF), Earth Orientation Parameters (EOP), and terrestrial reference frame (TRF).

2. METHOD AND MATERIALS

In the VLBI data reduction, a set of equations is added to the normal equation before solving it to fix the reference frame (both CRF and TRF) and reduce the degeneracies among CRF, TRF, and EOP. These special equations are called constraints. To fix the celestial frame, a so-called No-Net-Rotation (NNR) constraint is applied to a priori positions of a special ensemble of radio sources, that is, defining sources. This NNR constraint permits no (or as low as possible) rotation between the a priori and a posteriori catalogs (CRFs). In the state-of-art VLBI global solution, the NNR constraint is applied to the ICRF3 position of 303 defining sources to maintain the celestial reference frame. Instead, if we apply the NNR constraint to the *Gaia* position of an ensemble of well-selected sources, VLBI observations are then analyzed within the frame of *Gaia*-CRF. This is our implementation of *Gaia*-CRF in the VLBI data reduction.

For illustration purposes, we chose the 250 sources in the ICRF3-prototype subset of *Gaia* DR2 (`gaiadr2.aux_iers_gdr2_cross_id`¹) common to the 303 ICRF3 defining sources. These sources represent the most precise positions in the current ICRF3 catalog but not in the *Gaia*-CRF2 (since the *Gaia* position error is quite uniform) and consist of the defining source list used in this work.

To check if the radio-optical position offset is significant, we calculated the angular separation ρ and normalized separation X between *Gaia* and ICRF3 S/X position for these 250 sources following the methods in Mignard et al. (2016). These two quantities are depicted in Figure 1. The angular separation is less than $\rho_0 = 0.71$ mas (indicated by the horizontal red line) for the bulk (95%) of sources. In an ideal case, X is expected to follow a Rayleigh distribution, then the theoretical number of sources whose normalized separation X is greater than a certain value X_0 falls below one for $X_0 = 3.3$ (indicated by the vertical red line). If we take ρ_0 and X_0 as upper limits, most sources (about 90%) do not present a genius radio-optical offset.

Figure 2 demonstrates the dependency of the difference between *Gaia* DR2 and ICRF3 positions on the declination for 250 common sources, in the sense of *Gaia* DR2 minus ICRF3. We expanded these position differences onto a set of vector spherical harmonics (VSH; Mignard and Klioner, 2013) of the first degree to study the global difference. The model is given as followed.

$$\begin{aligned}\Delta\alpha \cos\delta &= -R_1 \cos\alpha \sin\delta - R_2 \sin\alpha \sin\delta + R_3 \cos\delta - G_1 \sin\alpha + G_2 \cos\alpha, \\ \Delta\delta &= +R_1 \sin\alpha - R_2 \cos\alpha - G_1 \cos\alpha \sin\delta - G_2 \sin\alpha \sin\delta + G_3 \cos\delta.\end{aligned}\quad (1)$$

The rotation vector R characterizes the orientation between celestial frames while the glide vector G reveals the dipolar deformation or zonal errors in the celestial frame. A weighted least-squares fit of Eq.(1) gives an orientation offset of $\sim -70 \mu\text{as}$ on the X-axis (R_1) and glide terms at a level of $50 \mu\text{as}$.

We ran four global solutions using VLBI observations made at S/X-band during 1979-2019 with identical parameterizations except for the CRF. Solution A and C used the *Gaia* DR2 positions as the a priori source positions while B and D used the ICRF3 SX positions. The positions of defining sources (only 250 defining sources here) were adjusted in the solution A and B but fixed in solution C and D. The option of estimating adjustments to the position of defining sources means that the celestial frame will be adjusted in the VLBI analysis process. If not, the new celestial frame will be fixed tightly to the a priori frame. The number of global parameters is same between A and B as well as between C and D, later pair having about 500 less.

Table 1 summarizes the configuration and post-fit statistical information on these solutions. We find that the post-fit root-mean-square (RMS) and reduced- χ^2 would slightly increase if fixing the defining source positions to their a priori position; they were greater when fixing the defining source positions to the *Gaia* position. This result indicates that the ICRF3 positions suit VLBI data better than the *Gaia* DR2 positions in the case of fixing defining source positions.

¹<http://gea.esac.esa.int/archive/>

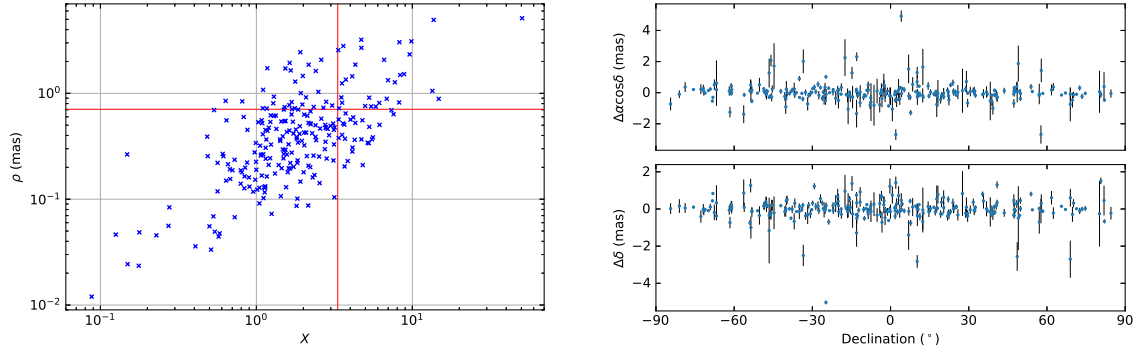


Figure 1: Angular separation and normalized Figure 2: Positional difference between the separation between the *Gaia* DR2 and ICRF3 *Gaia* DR2 and ICRF3 SX positions for the 250 common sources for the 250 common sources. common sources and their ICRF3 positions as a function of declination.

Table 1: Configurations of VLBI solutions.

Label	A priori catalog	Defining Source position	Post-fit RMS ps	Reduced- χ^2
A	<i>Gaia</i> DR2	adjusted	26.37	1.19
B	ICRF3 SX	adjusted	26.37	1.19
C	<i>Gaia</i> DR2	fixed	28.03	1.34
D	ICRF3 SX	fixed	26.44	1.20

3. COMPARISON OF VLBI SOLUTIONS

3.1 Celestial Reference Frame

When we only changed the a priori catalog, it is the case for solution A and B. Figure 3 depicts the positional difference between solution A and B for 4600 common radio sources as a function of the right ascension and declination. Both diagrams present a nearly perfect pattern of rotation. The fitting to the first order of VSH shows that only a dominant component of $R_1 \sim -55 \mu\text{as}$, possibly inherited from the rotation between a priori positions, as well as R_2 and R_3 on the same order of $\sim +20 \mu\text{as}$. No significant terms of glide are reported. It indicates that using different positions of the same ensemble of defining sources in the VLBI global solution would only alter the orientation of the estimated celestial frame but will not influence the zonal property.

The impact of fixing the defining source position to different a priori position on the resulted estimations of (other) source positions is presented in Figure 4. A small rotation-like pattern shows up from the noisy residuals whose weighted RMS is about $50 \mu\text{as}$ both in right ascension and declination. The rotation is estimated to be as large as $+150 \mu\text{as}$ in R_1 and $-90 \mu\text{as}$ in R_2 . Meanwhile, dipole terms are found to be larger than $80 \mu\text{as}$ for all three components.

Besides the inter-comparison amongst solutions, we also compare these solutions to the *Gaia* DR2. It is intended to check if using *Gaia* DR2 as the a priori catalog would bring the celestial reference frame to the *Gaia*-CRF, the latter supposed to be free of declination-dependent errors. The rotation between each solution and *Gaia* DR2 highly agrees with the others, except the R_1 component of the solution D. The dipole parameter between solution C and *Gaia* DR2 is smaller than D in Y- and Z- component, but greater in X-component. It inspires us that the zonal-like error in the ICRF, if existing, could be minimized via the option of fixing the defining source positions to *Gaia* DR2.

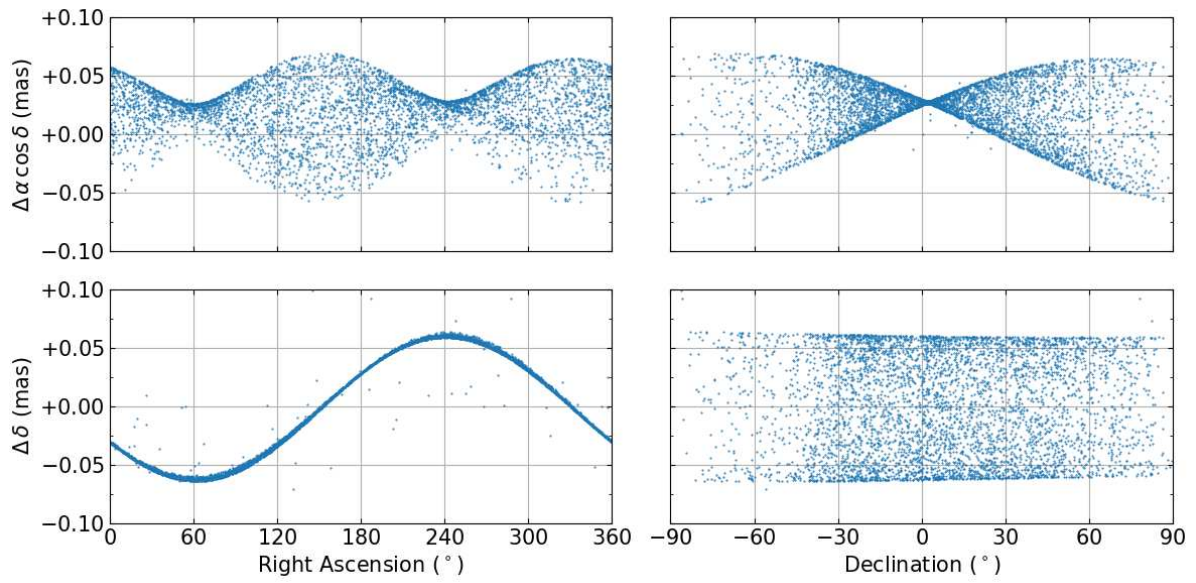


Figure 3: Positional difference for 4600 common sources between solution A and B as a function of the right ascension (left) and declination (right), in the sense of “A–B”.

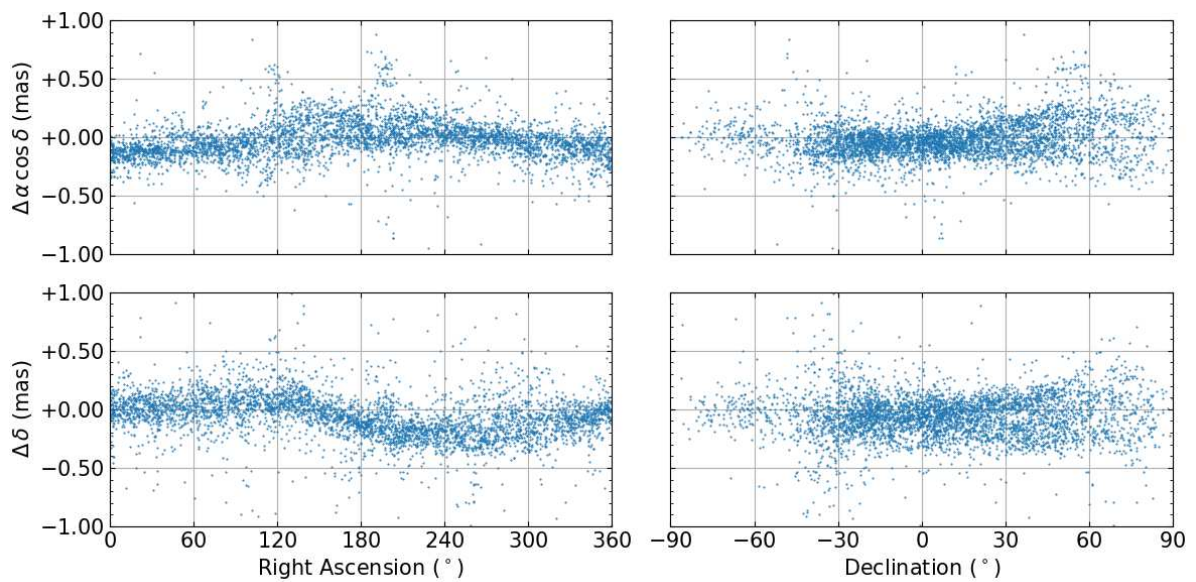


Figure 4: Positional difference for 4356 common sources between solution C and D as a function of the right ascension (left) and declination (right), in the sense of “C–D”.

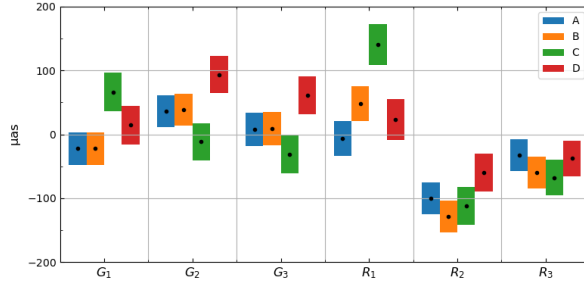


Figure 5: VSH parameters fitted to position differences between various solutions and *Gaia* DR2. The black dot indicate the estimate while the bar shows the 1-sigma.

3.2 Earth Orientation Parameters

In this section, we studied the impact of different CRF parameterization choices on the EOP series, which are the polar motion (x_p and y_p), UT1, length-of-day (LOD), and offset of Celestial Intermediate Pole (dX and dY).

Figure 6 demonstrates constant EOP offsets between solutions A and B: nearly zero in polar motion and LOD, $\sim 2 \mu\text{s}$ in UT1, about $\sim +80 \mu\text{as}$ in dX, and $\sim +60 \mu\text{as}$ in dY, the last three terms matching the rotation component R_3 , R_2 , and R_1 between celestial frames.

In the case of fixing the defining source positions to their a priori, the impact of different a priori catalogs on the EOP, as shown in Figure 7, is more complicated. From the running medians (red line) one can still find a rough corresponding relation between EOP and orientation of CRFs as found between solutions A and B, but other signals are mixed, especially a period pattern in LOD before 1995. These signals require further investigation which will be carried out in the future.

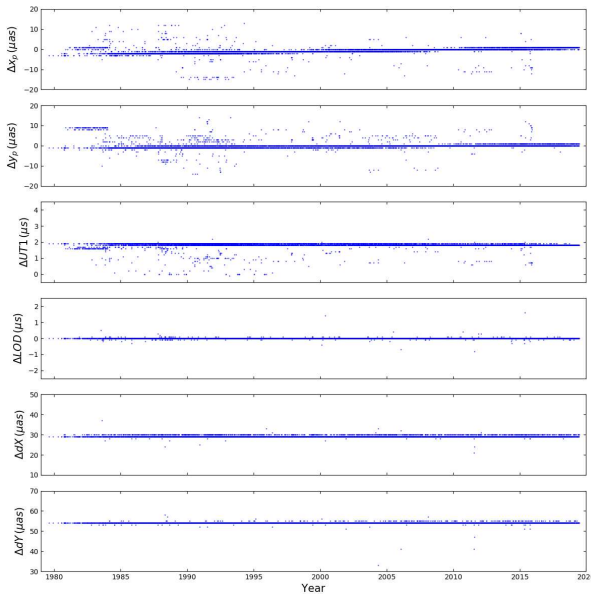


Figure 6: Difference of EOP series between solution A and B, in the sense of “A–B”.

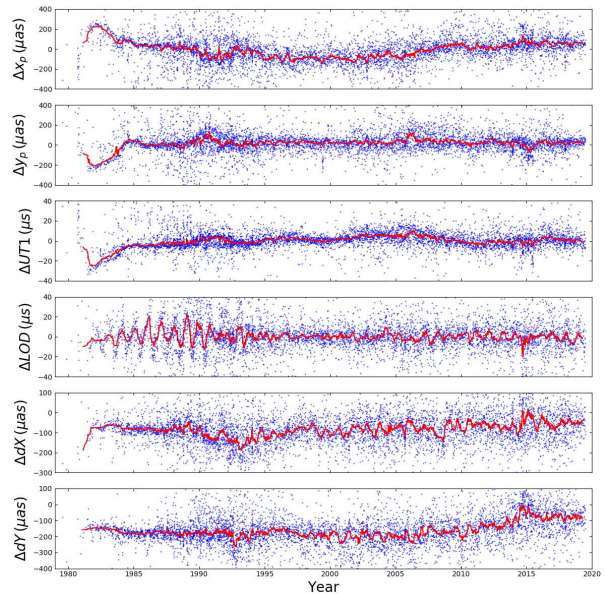


Figure 7: Difference of EOP series between solution C and D, in the sense of “C–D”. The red line indicates the running median.

3.3 Terrestrial Reference Frame

We compared the station positions and velocities for these four solutions. The difference between solution A and B is less than 0.1 mm for station positions and almost zero for velocities. In the case of “C–D”, the difference is larger: about 0.5 mm and 0.1 mm/yr for station positions and velocities, respectively.

4. CONCLUSION

We explore the possibility of analyzing VLBI data within the frame of the *Gaia*-CRF2. We found that the orientation of CRF axes would be influenced if we used different a priori catalogs but adjusted the position of defining sources. Meanwhile, the estimated EOP would have some bias that corresponds to the orientation between estimated CRFs. The terrestrial frame is slightly perturbed by different CRF parameterizations. If we fixed the positions of defining sources to be their positions in the *Gaia* DR2, both rotation and dipole term of estimated source positions would be influenced, the later brought closer to *Gaia*-CRF2. This analysis strategy offers us the option of reducing the declination-dependent errors in the ICRF only when the *Gaia* frame is ideally free of declination-dependent systematics. Limited by the precision of the *Gaia* DR2, we could not draw any constructive conclusions. The main question of this work should be re-tested with upcoming releases of *Gaia*.

Acknowledgement. We are funded by the National Natural Science Foundation of China (NSFC) under grant No. 11833004. This work has made use of data from the European Space Agency (ESA) mission *Gaia* (<https://www.cosmos.esa.int/gaia>), processed by the *Gaia* Data Processing and Analysis Consortium (DPAC, <https://www.cosmos.esa.int/web/gaia/dpac/consortium>). Funding for the DPAC has been provided by national institutions, in particular the institutions participating in the *Gaia* Multilateral Agreement.

4. REFERENCES

- Charlot P., et al., 2020, "The third realization of the International Celestial Reference Frame by VLBI", A&A , doi: 10.1051/0004-6361/202038368.
- Gaia Collaboration, Brown, et al., 2018b, Gaia Data Release 2. Summary of the contents and survey properties, A&A 616, A1.
- Gaia Collaboration, Mignard, et al., 2018a, Gaia Data Release 2. The celestial reference frame (Gaia-CRF2), A&A 616, A14.
- Gaia Collaboration, Prusti, et al., 2016, The Gaia mission, A&A 595, A1.
- Liu, N., et al., 2018, A&A 609, A19.
- Mignard, F., Klioner, S., 2012, Analysis of astrometric catalogues with vector spherical harmonics, A&A 547, A59.
- Mignard, F., et al., 2016, Gaia Data Release 1. Reference frame and optical properties of ICRF sources, A&A 595, A5.

QUASAR SELECTION TECHNIQUES GOING INTO THE GAIA ERA

N. SECREST¹, J. FROUARD², G. HENNESSY³

U.S. Naval Observatory - USA

¹nathan.j.secrest.civ@mail.mil, ²julien.h.frouard.civ@navy.mil, ³gregory.s.hennessy.civ@mail.mil

ABSTRACT. In the last five years, there has been an explosion in the number of known active galactic nuclei (AGN) and quasars, thanks largely to the *Wide-field Infrared Survey Explorer* (WISE). This has been a major boon for celestial reference frame (CRF) work, which requires a quasi-inertial reference frame by which positions and proper motions can be defined and self-consistently measured. In this work, we describe new developments in the pursuit of a maximally dense, maximally uniform all-sky sample of AGN and quasars, as well as how the improved CRF may in turn benefit quasar work.

1. WHY QUASARS?

How is motion defined? When discussing the positions of astronomical objects, we must be precise about exactly with respect to *what* we are defining these positions, which determines how independently we can measure any associated motion that we observe. When we observe an astronomical object, our measurement of its apparent motion is affected by the Earth's rotation about its axis, the Earth's orbit around the Sun, the Sun's motion through the Galaxy (the secular aberration), the Galaxy's motion with respect to the Local Group, the Local Group's motion induced by the inhomogeneous distribution of local matter in the universe (the "clustering dipole" in cosmology parlance), and finally any inhomogeneity that may exist in the distribution and motion of matter at the largest observable scales. Fortunately, the success of Λ CDM at describing the universe on the largest ($> 100h^{-1}$ Mpc) scales suggests that this latter term is negligible (although see Colin et al. 2017; Rameez et al. 2018; and references therein), and so distant extragalactic objects are the best, and likely final, choice to realize a quasi-inertial reference system, i.e. the International Celestial Reference System (ICRS; e.g., Arias et al. 1995). The most distant (and therefore most ideal) extragalactic objects, quasars, are fortunately also powerful sources of compact radio emission, allowing us to take advantage of VLBI's exquisite astrometric precision both to produce a realization of the ICRS, the International Celestial Reference Frame (Ma et al. 1998; Fey et al. 2015; Charlot et al. 2020) and to tie it to the International Terrestrial Reference Frame (ITRF; e.g., Altamimi et al. 2016).

2. FINDING QUASARS

While efforts to realize the ICRS have been successful, several issues remain, such as a relative under-density of sources below declinations of $\sim -30^\circ$, despite efforts to increase the uniformity of the *defining* sources (Figure 1), caused by relatively few southern baselines in the global VLBI network. A related issue, which is the focus of this work, is the effect of defining a fundamental CRF at one wavelength (i.e., in the radio *S* and *X* bands) on the tie to CRFs at other wavelengths. This issue has become especially pressing with the advent of *Gaia*, which for the first time has produced a CRF at visual (optical) wavelengths comparable in precision to VLBI measurements. Alignment of the *Gaia* reference frame to the ICRS was done with a subset of 2843 sources identified as optical counterparts to the ICRF3 prototype (Lindgren et al. 2018), but to ensure that this aligned CRF is

non-rotating a much larger, all-sky, and uniform catalog of quasars is preferred. As faint stars and quasars are often photometrically indistinguishable in the optical, spectroscopic confirmation of the presence of redshifted broad Balmer and high-ionization narrow emission lines has generally been required in the absence of a strong radio counterpart, which has so far been too observationally expensive to produce a proper all-sky sample as needed. The launch of the mid-infrared *Wide-field Infrared Survey Explorer* (WISE; Wright et al. 2010) in 2009 provided a serendipitous solution to this problem. In the mid-infrared, AGN and quasars occupy a distinct region of photometric color-color space (i.e., $[3.4 \mu\text{m}]-[4.6 \mu\text{m}]$, $[4.6 \mu\text{m}]-[12 \mu\text{m}]$ for WISE) because of their power-law spectral energy distributions, and these colors are nearly insensitive to heavy obscuration (e.g., Donley et al. 2012). Using the WISE color-color selection wedge of Mateos et al. (2012), Secrest et al. (2015) produced an all-sky sample of 1.4 million AGN, which they showed to contain few to no star contaminants that would be detectable by *Gaia*. This sample of AGN, which has half a million *Gaia* counterparts, after applying a few astrometric quality cuts, was subsequently used for the *Gaia*-CRF (Lindgren et al. 2018).

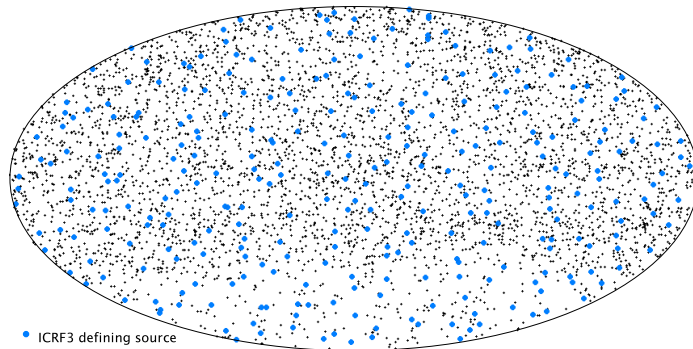


Figure 1: Aitoff projection of ICRF3, in equatorial coordinates.

While WISE data has been hugely beneficial for CRF work, there are two problems that we discuss here. The first is non-uniformity in the distribution of WISE sources across the sky (see Figure 1 in Secrest et al. 2015; Figure 2 in this work). This is caused by an over-density of sources at the ecliptic poles due to the WISE scanning pattern, which is easily remedied with a simple magnitude cut, and an under-density of sources along the Galactic plane due to source confusion. This latter issue cannot be remedied using WISE data alone, and so we have begun exploring other methods of filling in the decrement of sources along the Galactic plane.

It is not possible, even in principle, to find AGN with *Gaia* counterparts lying behind much of the Galactic plane, as no optical counterpart exists for sight lines with $E(B - V) \gtrsim 2$. However, a significant portion of the Galactic plane in the zone of WISE confusion has sight lines with $E(B - V) < 2$, suggesting that it is worthwhile to look at alternate methods to identify AGN with *Gaia* counterparts (Figure 2). While mid-infrared color-based diagnostics are the ideal method to photometrically identify AGN and quasars, the near-infrared, which carries the advantage of much higher angular resolution ($< 1''$ for facilities such as UKIRT, versus $\sim 6''$ to $8''$ for WISE), shows promise. Moreover, the proposed *GaiaNIR* mission (e.g., Hobbs et al. 2019) will operate at roughly the near-infrared *H*-band, where the extinction coefficient $A/E(B - V)$ is a factor of ~ 4 times smaller than in the *Gaia* *G* band (e.g., Yuan et al. 2013), allowing background AGN counterpart identification to $E(B - V) \lesssim 8$, freeing up significantly more of the Galactic plane (Figure 2).

We have developed a machine learning-based method to identify likely AGN candidates along the Galactic plane that folds in prior information, specifically the Galactic extinction, with optical photometry from *Gaia* and near-infrared photometry from the UKIDSS Galactic Plane Survey (GPS;

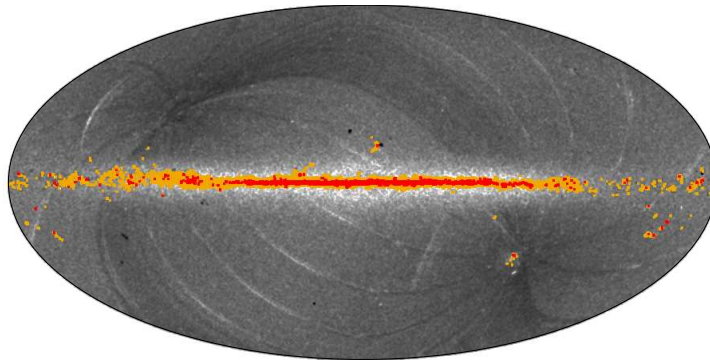


Figure 2: Aitoff projection of AGN from Secret et al. (2015), shaded by density. Gold regions denote $E(B - V) > 2$, where *Gaia* is insensitive to background AGN, while red regions denote $E(B - V) > 8$, where *GaiaNIR* will be insensitive to background AGN.

Lucas et al. 2008). Using `scikit-learn`,¹ we train a k -NN classifier with AGN selected from the AllWISE catalog at high Galactic longitude, where source confusion is less of an issue, in order to sample a similar parameter space in $E(B - V)$ and representative stellar populations. We use photometry from *Gaia* DR2 and the UKIDSS GPS, and $E(B - V)$ from Schlafly & Finkbeiner (2011). By validating against our training sample, we found reliability and completeness values of $\sim 70\%$ and $\sim 30\%$. Given that the percentage of AGN in the training set is only 0.45%, this means that our classifier is performing ~ 160 times better than random chance. In order to validate our classifier, we have an accepted program to spectroscopically confirm our AGN candidates in the near-IR, where optical strong emission lines should exist given the typical redshifts of mid-IR AGN, using the UIST instrument on UKIRT, although logistical problems have prevented this program from being executed thus far. We show a sample of our Galactic plane AGN candidates in Figure 3.

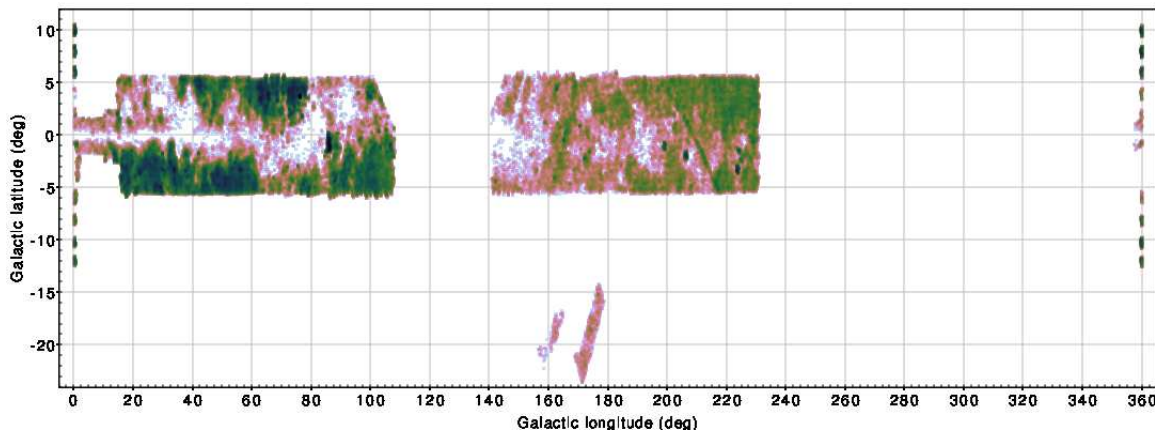


Figure 3: Cutout of the Galactic plane, with darker shading indicating a higher density of AGN candidates (arbitrary scaling).

3. RECIPROCITY

We have shown how massive photometric catalogs have been and may continue to be used to assist with CRF work in the *Gaia* era. This benefit is not one-way, however, and CRF work provides

¹<https://scikit-learn.org/stable>.

reciprocal benefit to photometric catalogs in the form of refined astrometric reference catalogs. In the case of WISE and *Gaia*, we have begun re-deriving the astrometry of the AllWISE catalog, as well as the deeper unWISE catalog (Schlafly et al. 2019), using astrometry from *Gaia*. The WISE catalog astrometry is based on 2MASS (Skrutskie et al. 2006) with proper motion corrections from UCAC4 (Zacharias et al. 2006)² that, while of excellent astrometric quality, do nonetheless exhibit residual position-dependent astrometric offsets (zonal errors), which could potentially be alleviated by using *Gaia* data (e.g., Spoto et al. 2017). In Figure 4, we show the signed (\pm) astrometric offsets (in mas) between reference sources in the AllWISE catalog and their *Gaia* counterparts, using the default catalog AllWISE positions. In Figure 5, we show the offsets using our re-derived positions.

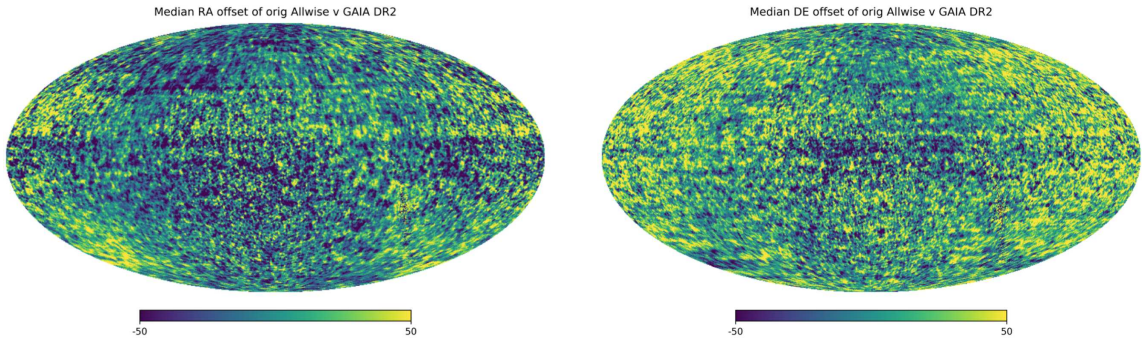


Figure 4: Offsets (in mas) in R.A. and Decl. between AllWISE and *Gaia* counterparts using default AllWISE catalog source positions.

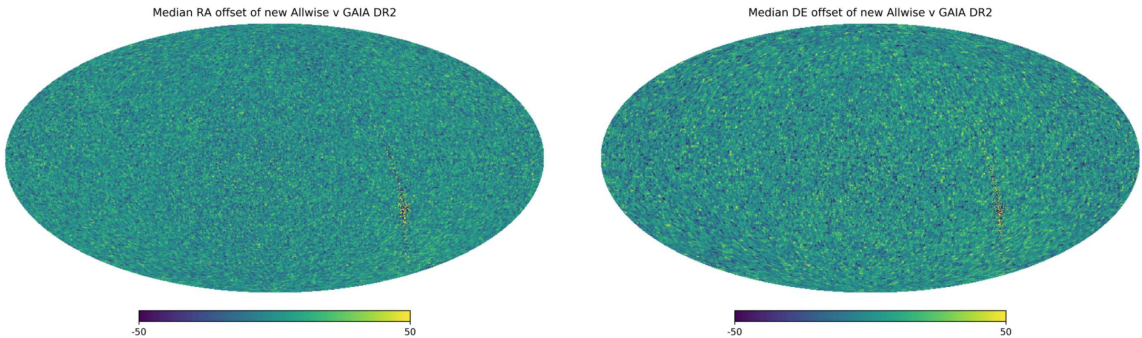


Figure 5: Offsets (in mas) in R.A. and Decl. between AllWISE and *Gaia* counterparts using re-derived AllWISE catalog source positions.

As can be seen, the new version of the AllWISE catalog is now on the *Gaia* coordinate system after using *Gaia* as the astrometric reference catalog. This essentially de-biases the WISE data with respect to position, allowing for large, all-sky studies using catalog data unaffected by positional systematics. We emphasize that these results are preliminary, and we are currently working on further validating them. Nonetheless, with the impressive depth of WISE data (over 2 billion objects in the latest unWISE release; Schlafly et al. 2019) and its wide-ranging utility, from quasar and AGN studies to studies of brown dwarfs and asteroids, efforts to produce optimized astrometry are of utmost importance. Serendipitously, in the preparation of this work the new CatWISE catalog (Eisenhardt et al. 2020) was released,³ which uses *Gaia* for astrometric validation, further underscoring the reciprocity between these two missions.

²http://wise2.ipac.caltech.edu/docs/release/allwise/expsup/sec2_5.html.

³<https://catwise.github.io>.

4. REFERENCES

- Altamimi, Z., Rebischung, P., Métivier, L., et al., 2016, *Journal of Geophysical Research (Solid Earth)*, 121, 6109
- Arias, E. F., Charlot, P., Feissel, M., et al., 1995, *A&A* , 303, 604
- Colin, J., Mohayaee, R., Rameez, M., et al., 2017, *MNRAS* , 471, 1045
- Charlot, P., et al., 2020, "The third realization of the International Celestial Reference Frame by very long baseline interferometry", *A&A* , doi: 10.1051/0004-6361/202038368.
- Donley, J. L., Koekemoer, A. M., Brusa, M., et al., 2012, *ApJ* , 748, 142
- Eisenhardt, P. R., Marocco, F., Fowler, J. W., et al., 2020, *ApJS* , 247, 69
- Fey, A. L., Gordon, D., Jacobs, C. S., et al., 2015, *AJ* , 150, 58
- Hobbs, D., Brown, A., Høgg, E., et al., 2019, arXiv e-prints, arXiv:1907.12535
- Lindegren, L., Hernández, J., Bombrun, A., et al., 2018, *A&A* , 616, A2
- Lucas, P. W., Hoare, M. G., Longmore, A., et al., 2008, *MNRAS* , 391, 136
- Ma, C., Arias, E. F., Eubanks, T. M., et al., 1998, *AJ* , 116, 516
- Mateos, S., Alonso-Herrero, A., Carrera, F. J., et al., 2012, *MNRAS* , 426, 3271
- Rameez, M., Mohayaee, R., Sarkar, S., et al., 2018, *MNRAS* , 477, 1772
- Schlafly, E. F., & Finkbeiner, D. P., 2011, *ApJ* , 737, 103
- Schlafly, E. F., Meisner, A. M., & Green, G. M., 2019, *ApJS* , 240, 30
- Secrest, N. J., Dudik, R. P., Dorland, B. N., et al., 2015, *ApJS* , 221, 12
- Skrutskie, M. F., Cutri, R. M., Stiening, R., et al., 2006, *AJ* , 131, 1163
- Spoto, F., Tanga, P., Bouquillon, S., et al., 2017, *A&A* , 607, A21
- Wright, E. L., Eisenhardt, P. R. M., Mainzer, A. K., et al., 2010, *AJ* , 140, 1868
- Yuan, H. B., Liu, X. W., & Xiang, M. S., 2013, *MNRAS* , 430, 2188
- Zacharias, N., Finch, C. T., Girard, T. M., et al., 2013, *AJ* , 145, 44

SHORT-TERM AND LONG-TERM FLUX VARIABILITY OF EXTRA-GALACTIC OBJECTS USEFUL FOR THE FUTURE GAIA CRF

G. DAMLJANOVIĆ¹, F. TARIS², M.D. JOVANOVIĆ¹

¹ Astronomical Observatory, Belgrade - Serbia - gdamljanovic@aob.rs - miljana@aob.rs

² SYRTE, Observatoire de Paris - France - francois.taris@obspm.fr

ABSTRACT. Some Active Galactic Nuclei (AGN) objects (quasars - QSOs, blazars, for example) are well known for their rapid flux variability across the whole electromagnetic spectrum. They are variable on diverse time-scales, from minutes through months to even decades. There are three classes of variability: intraday - IDV (from a few minutes to several hours), short-term - STV (from several days to months), and long-term variability - LTV (from months to decades). In case of IDV, the flux changes is by a few tenths of magnitude, but in cases of STV and LTV it could be more than magnitude (even few magnitudes). Photometry is a powerful tool to investigate AGNs by measuring their variability time-scales, amplitude and duty cycle. Quasars have got a fundamental role in the evolution of their host galaxies, and they are used to build the International Celestial Reference Frame (ICRF). It is of importance that their proper motions are negligible because of their extreme distances. The visual-wavelength Gaia astrometry of the micro-arcsecond domain has got significant positional offsets with the radio VLBI positions of QSOs. We did optical observations of QSOs (visible in both, optical and radio domain, and important for ICRF - Gaia CRF link) to study their flux and color variability on short-term and long-term time-scales. Some results of five objects (1535+231, 1556+335, 1607+604, 1722+119, and 1741+597) are presented, here.

1. INTRODUCTION

The Hipparcos Catalog - High Precision PARallax Collecting Satellite of European Space Agency (ESA) mission (ESA 1997) with positions, proper motions, and parallaxes for about 118000 stars on the International Celestial Reference System (ICRF), equator J2000, and epoch 1991.25, replaced the FK5 at 1997 after IAU XXIII General Assembly in Kyoto. Last few years, it is going on the Gaia ESA space astrometry mission (Global Astrometric Interferometer for Astrophysics): astrometrically, photometrically, and spectroscopically surveying the full sky. The plan was to observe about one billion sources for astrometry (until 20 magnitude in V band), and about 150 million ones for spectroscopy (until 16 mag); see paper (Prusti 2012). The goal is the Gaia Celestial Reference Frame (Gaia CRF) in the future, quasars based one. Until now, there are two solutions: the Gaia DR1 which was appeared in September 2016, and Gaia DR2 (in April 2018). The first one was the Tycho-Gaia astrometric solution for about two million stars (using 14 months of observations), and the second one was based just on Gaia data for about 1.3 billion stars at J2015.5 plus 0.4 billion faint sources (using 22 months of Gaia satellite observations).

The Gaia optical astrometry is going to the dawn of micro-arcsecond level, but at that level there is the appearance of positional offsets between the radio and optical positions of quasars (QSOs) that define the ICRF. The radio positions of QSOs are determined using VLBI data. Mentioned offsets are of importance for astrometry and reference frame, they currently put a limit for the accuracy and definition of the CRF at non-radio wavelengths. It is limiting research in different topics (proper motions, Earth orientation and ephemerides, geodesy, secular aberration, trajectories of stars in our galaxy, etc.). The reasons for optical/radio offsets could be due to real astrophysical processes associated with the Active Galactic Nuclei (AGN) that power quasars (jet

launching/orientation), or real physical offsets between the AGN and its host galaxy. It is necessary to investigate AGNs properties which could affect apparent positions, and it is of importance to understand: physical nature of quasar optical/radio offsets, AGN/source galaxy physics (jet launching, obscuration, luminosity/obscuration variability, dual/binary AGN, AGN-source galaxy effects and interactions, etc.), lensed QSOs, and other effects. One of important task is to produce highly reliable and statistically complete multi-wavelength samples of AGN and their host galaxies, and it is in line with our investigation. The AGNs (mostly QSOs in the case of ICRF objects) are well known for their flux variability at diverse time-scales: intraday (IDV, from a few minutes to several hours), short-term (STV, from several days to months), and long-term variability (LTV, from months to decades). Using optical observations of QSOs and relative photometry, we investigated their flux and color variability on short-term and long-term time-scales to support ICRF - Gaia CRF link.

2. INSTRUMENTS AND RESULTS

For investigation of photometry of QSOs useful for the link ICRF - Gaia CRF (Bourda et al. 2011) we realized the "Serbian-Bulgarian mini-network telescopes" from 2013 to use six telescopes at three sites: Rozhen National Astronomical Observatory (NAO) and Belogradchik AO in Bulgaria, and Astronomical Station Vidojevica (ASV) of Astronomical Observatory in Belgrade (Serbia). Also, to support our cooperation, two SASA-BAS joint research projects between Serbian (SASA) and Bulgarian (BAS) Academy of Sciences are established: "Observations of ICRF radio-sources visible in optical domain" (during period 2014-2016), and "Study of ICRF radio-sources and fast variable astronomical objects" (2017-2019). The telescopes are:

- 1.) 60 cm ASV (from 2010, Cassegrain, CCD Apogee Alta U42 and E47, CCD SBIG ST10 XME),
- 2.) 1.4 m ASV (from mid-2016 via Belissima project, Ritchey-Chrétien, CCD Apogee Alta U42, CCD Andor iKon-L),
- 3.) 2m Rozhen (Ritchey-Chrétien, CCD VersArray 1300B, CCD Andor iKon-L),
- 4.) 60 cm Rozhen (Cassegrain, CCD FLI PL09000),
- 5.) Schmidt-camera 50/70 cm at Rozhen (CCD FLI PL16803),
- 6.) 60 cm Belogradchik (Cassegrain, CCD FLI PL09000).

Also, telescopes Joan Oró 0.8 m - TJO (robotic one, the Montsec Astronomical Observatory, Catalonia, Spain, Cassegrain, CCD FLI PL4240-1-B, CCD Andor iKon-L), and Leopold Figl 1.5 m (the University of Vienna, Austria, R.C., CCD SBIG ST10 XME) were used. All data were done using Johnson UBV and Cousins R_cIc filters. The CCD images were reduced by subtracting bias and dark, and divided by flat field (also, frames were corrected for bad pixels, etc.). After that, the relative photometry was applied via few comparison stars. Magnitudes of V-band and R-band of these stars were calculated via *ugriz* SDSS Catalog ones and suitable transformations between V, R filters and *ugriz* SDSS (Chonis and Gaskell 2008). And we took some comparison stars of 1722+119 from the paper (Doroshenko et al. 2014). For example, the V-band and R-band data of the object 1741+597 are presented on Figs. 1 and 2, respectively: VBRL (Vidojevica, Belogradchik, Rozhen, and Leopold Figl) data during 2013-2015, TJO - Joan Oró data during 2014-2015, and MJ data using 60 cm and 1.4 m ASV telescopes from mid-2016 to mid-2019; MJ means data which were collected by Miljana D. Jovanović (PhD student at Belgrade University). All in all, it is about six years long data set. Mentioned three groups of data are consistent between each other (see Figs. 1 and 2). The F-test was applied to investigate variability of V-band and R-band light-curves of objects and their comparison stars; there is no variability of comparison stars and object 1556+335. Other objects (1535+231, 1607+604, 1722+119, and 1741+597) show flux variability. The object 1741+597 is presented in Figs. 1-4 because its big flux variability (about 2 magnitudes in V and R bands). Some points of light-curves were rejected by applying the

3σ criteria; the reason for that was the bad tracking during observations, bad weather conditions, etc. For relative photometry, we used our finding charts of presented objects with their comparison stars.

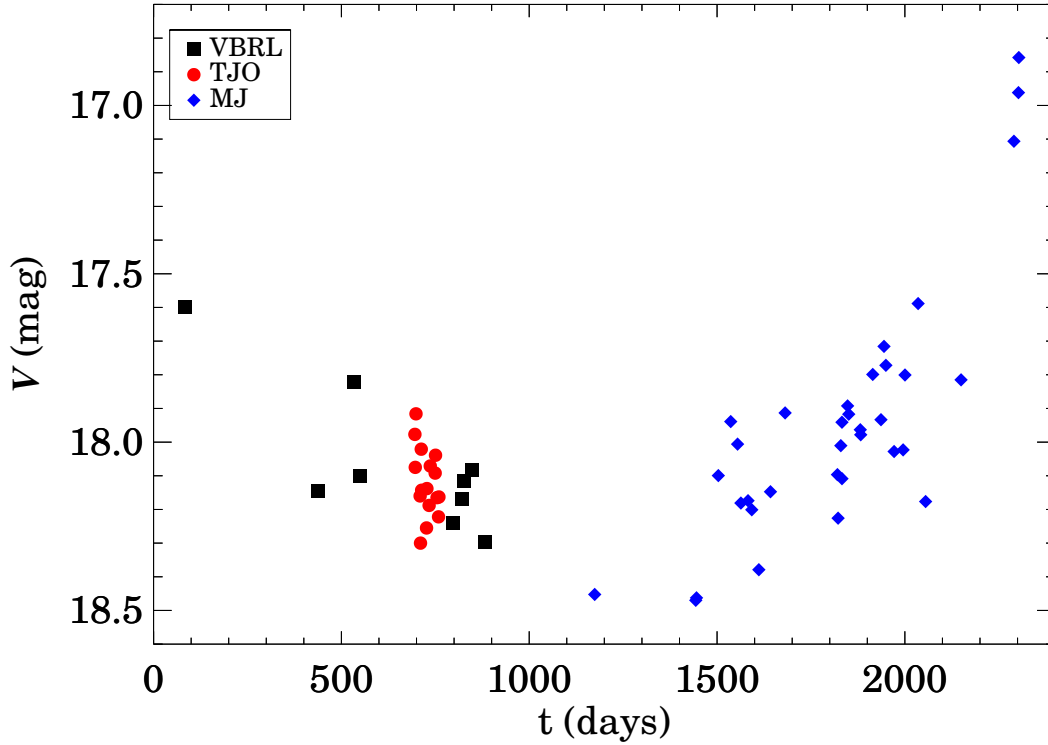


Figure 1: Data of V (mag); object 1741+597, $t = JD - 2456400.0$.

To determine the period, phase, and amplitude of sinusoidal term we used the Least Squares Method (LSM). The minimum period for LSM is about 0.3 yr (in line with the Nyquist frequency), and the maximum one is about 12 yr (double observational period) with step of 0.1 yr; observational period is about 6 yr. The linear, semiannual, and annual terms were removed (Rani et al. 2009, Kesteven et al. 1976) to get the input data for LSM; see residuals of V and R on Figs. 3 and 4 (points), respectively. The solution of our interest is the best fit using LSM, or associated with a minimum standard deviation of differences between curve (see Figs. 3 and 4) and input data; that solution for each object is done in Table 1. The presented curve is combination of few obtained sinusoids of our interest here (see Table 1), and the final residuals (Figs. 3 and 4) are differences between that curve and the input data. The results are presented in Table 1: object, filter, period, and amplitude (with standard deviation). There are few periods per object. For the same object, in V-band some quasiperiods are slightly different from R-band results because of different number of input points, not enough input data for LSM, etc. With more data (in the future) it is possible to get more precise results. Some of presented quasiperiods (in Table 1) could be artificial ones; it is necessary to investigate the physics of these quasiperiods for each object separately. As criterion to present calculated period (in Table 1), we took into account each harmonic which period in V-band is close to R-band one, and which value of A is bigger than suitable σ_A value. The final residuals were investigated using Abbe's criterion, and it was concluded that the final residuals could be explained with random variations.

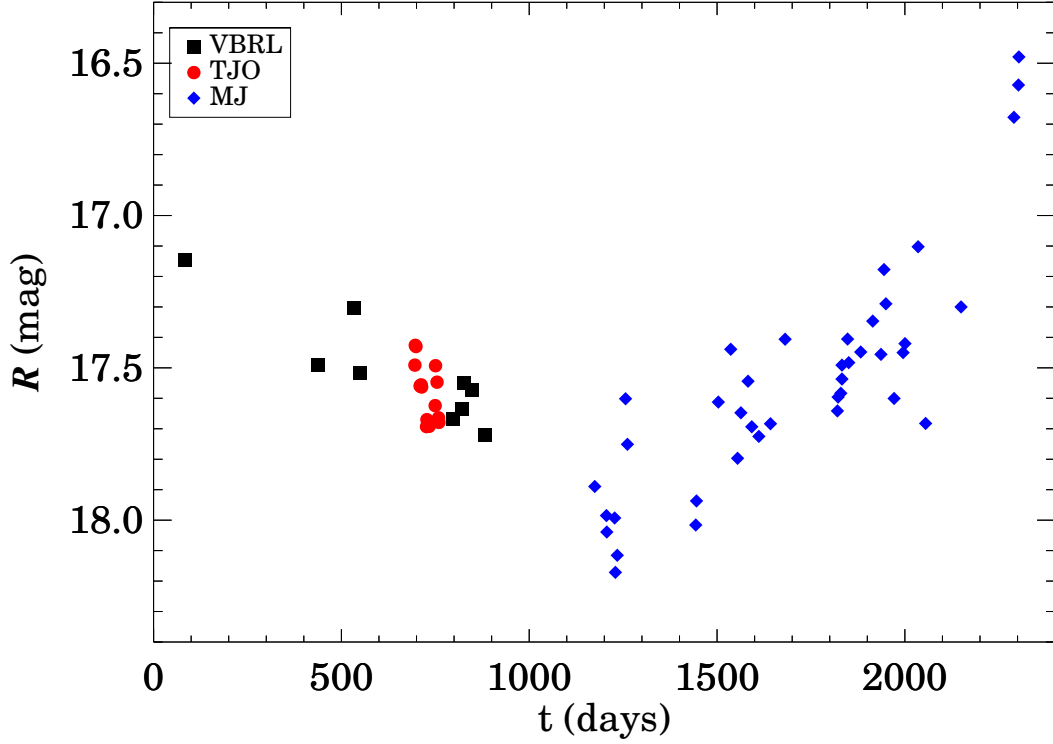


Figure 2: Data of R (mag); object 1741+597, $t = JD - 2456400.0$.

Object	Filter	Period (y)	$A \pm \sigma_A$ (mag)
1535+231	V	0.57, 0.88, 1.21	0.158(0.028), 0.132(0.025), 0.133(0.022)
	R	0.57, 0.87, 1.21	0.233(0.028), 0.143(0.024), 0.122(0.022)
1607+604	V	0.94, 1.89, 4.10	0.051(0.017), 0.088(0.014), 0.047(0.013)
	R	0.87, 1.99, 3.69	0.045(0.012), 0.067(0.010), 0.062(0.009)
1722+119	V	0.83, 0.88, 1.08,	0.392(0.052), 0.126(0.030), 0.122(0.028),
		1.52, 1.77, 3.43,	0.461(0.037), 0.169(0.024), 0.217(0.032),
	4.43	0.150(0.021)	
	R	0.82, 0.88, 1.10,	0.399(0.049), 0.122(0.024), 0.134(0.017),
1.52, 1.90, 3.55,	0.386(0.039), 0.184(0.034), 0.139(0.020),		
4.76	0.265(0.026)		
1741+597	V	0.70, 0.90, 1.17,	0.178(0.023), 0.119(0.033), 0.205(0.027),
		1.59, 3.07, 4.97	0.110(0.018), 0.159(0.020), 0.119(0.017)
	R	0.67, 0.85, 1.18,	0.131(0.021), 0.177(0.025), 0.214(0.030),
	1.58, 3.49, 5.66	0.121(0.017), 0.140(0.019), 0.102(0.015)	

Table 1: The amplitudes of quasiperiods for objects: 1535+231, 1607+604, 1722+119, 1741+597.

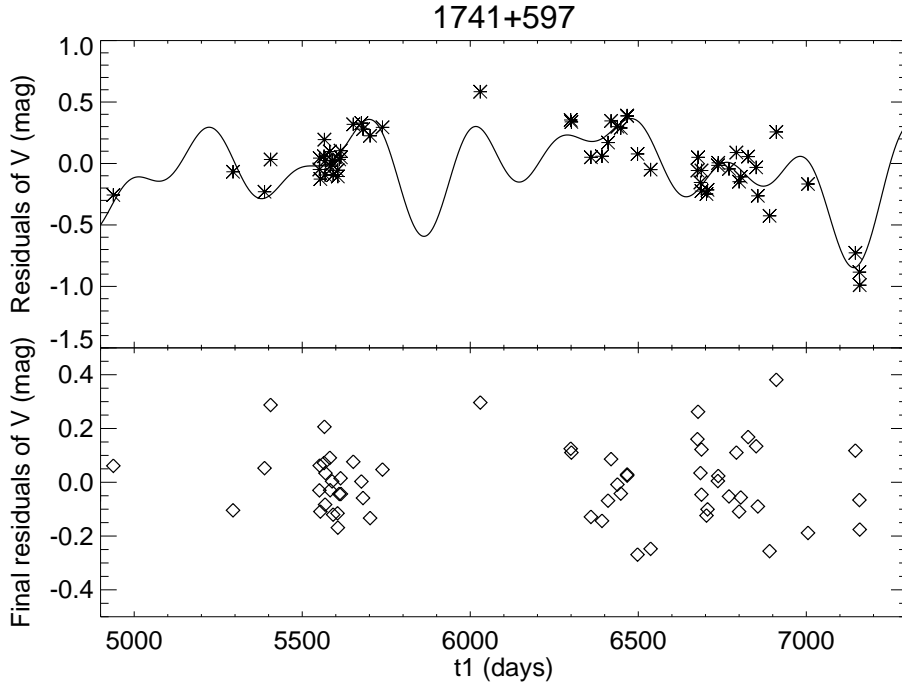


Figure 3: Residuals of V (mag); object 1741+597, $t_1 = JD - 2451544.5$.

3. CONCLUSION

Between the visual-wavelength Gaia astrometry of the micro-arcsecond domain and radio VLBI positions of QSOs has got significant positional offsets. It is of importance to investigate these offsets for precise ICRF - Gaia CRF link. Because of it, we did optical observations of QSOs, visible in optical and radio domains (about 47 objects), important for mentioned link (Bourda et al. 2011) to study their flux and color variability on short-term and long-term time-scales. Here, we presented some results for five objects: 1535+231, 1556+335, 1607+604, 1722+119, and 1741+597. After F-test, one object (1556+335) and comparison stars of all objects did not show flux variability. Some results of mentioned objects are presented in Table 1: periods, and amplitudes (with standard deviations). The input three sets of data for the object 1741+597 in V and R bands (as an example) are on Figs. 1 and 2. The curves (using few sinusoids as results determined via LSM) with residuals are on Figs. 3 and 4. After Abbe's criterion, the final residuals could be explained with random variations. Some of presented quasiperiods in Table 1 could be artificial ones. For now, we presented quasiperiods (in Table 1) which result (calculated period) in V-band is close to R-band one, and that value of A is bigger than suitable σ_A value. Also, semiannual and annual terms were removed (Rani et al. 2009, Kesteven et al. 1976). It is important to continue mentioned investigation via physics of calculated quasiperiods, and using more data for LSM.

Acknowledgement. This work was supported by the Ministry of Education, Science and Technological Development of the Republic of Serbia through the project 176011 "Dynamics and kinematics of celestial bodies and systems". Also, we gratefully acknowledge the observing grant support from the Institute of Astronomy and Rozhen National Astronomical Observatory, Bulgarian Academy of Sciences, via bilateral joint research project "Study of ICRF radio-sources and fast variable astronomical objects".

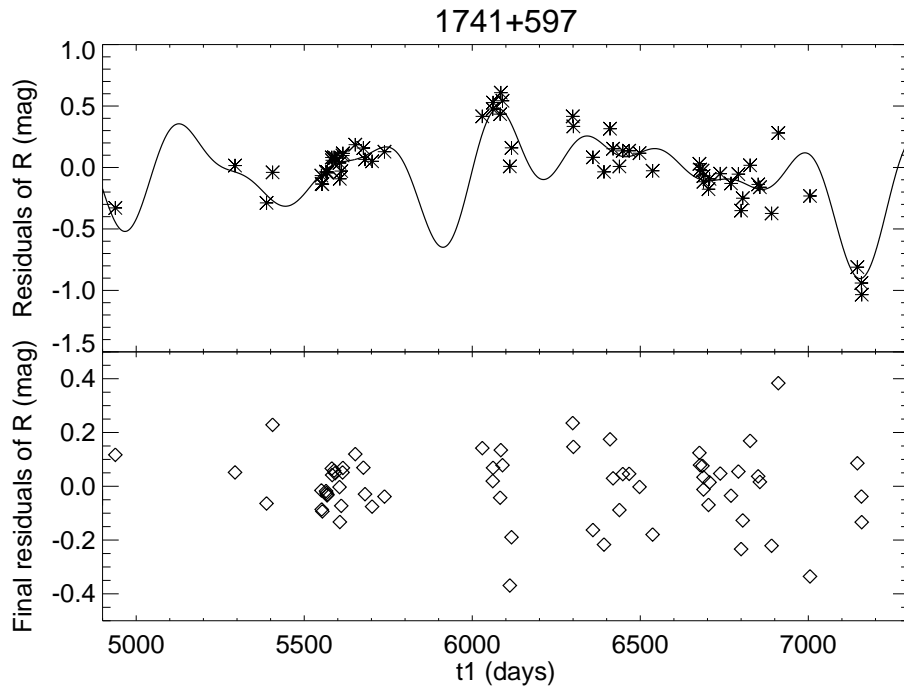


Figure 4: Residuals of R (mag); object 1741+597, $t_1 = JD - 2451544.5$.

4. REFERENCES

- Bourda, G., Callioud, A., Charlot, P., Porcas, R., and Garrington, S., 2011, "VLBI observations of optically-bright extragalactic radio sources for the alignment of the radio frame with the future Gaia frame. II. Imaging candidate sources ", *A&A* 526, A102.
- Chonis, T.S., and Gaskell, C.M., 2008, "Setting UBVRI Photometric Zero-Points Using Sloan Digital Sky Survey ugriz Magnitudes", *AJ* 135, pp. 264–267.
- Doroshenko, V.T., Efimov, Yu.S., Borman, G.A., and Pulatova, N.G., 2014, "BVRI CCD-Photometry of Comparison Stars in the Fields of Galaxies with Active Nuclei. VII", *Astrophysics* 57, 176.
- ESA, 1997, *The Hipparcos and Tycho Catalogues*, ESA SP-1200 (Noordwijk: ESA Publications Division).
- Kesteven, M.J.L., Bridle, A.H., Brandie, G.W., 1976, "Variability of extragalactic sources at 2.7 GHz. I. Results of a 2-yr monitoring program, *AJ* 81, 11.
- Prusti, T., 2012, "The promises of Gaia", *Astron. Nachr.* 333, p. 453.
- Rani, B., Wiita, P.J., Gupta, A.C., 2009, "NEARLY PERIODIC FLUCTUATIONS IN THE LONG-TERM X-RAY LIGHT CURVES OF THE BLAZARS AO 0235+164 AND 1ES 2321+419", *AJ* 696, p. 2170.

THE NAROO DIGITIZATION CENTER

V. ROBERT^{1,2}, J. DESMARS^{1,2}, J.-E. ARLOT¹

¹ IMCCE, Institut de Mécanique céleste et de calcul des éphémérides, Observatoire de Paris, PSL - France - arlot@imcce.fr, desmars@imcce.fr

² IPSA Institut polytechnique des sciences avancées - France - vincent.robert@obspm.fr

ABSTRACT. The study of transient events or motion of stars and solar system bodies uses old data in order to modelize the evolution of the studied object. In all models strongly depending on time, data from the past are of great interest. Unfortunately, old data are, most of time, of a poor accuracy, the references used at the time of the reduction being not confident. The arrival of the new reference star Gaia was the opportunity of a new reduction of old data allowing observation in the past with today accuracy. However, a new reduction means that we have digitized images of the old observations which were made for most of them on photographic plates from 1890 to 1980. For such a purpose, we started the NAROO project joining digitization and reduction of old plates. A new sub-micrometric scanner has been built in Meudon observatory and we are now starting the scientific program.

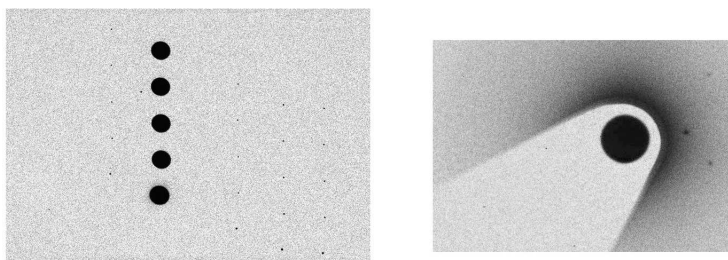


Figure 1: Examples of plates for Solar system dynamics studies: left, the Jupiter system (5 exposures) showing the bright planet and the faint satellites; right, the planet Mars and its two faint satellites Phobos and Deimos. The bright light from Mars is decreased thanks to a metallic filter.

1. PRESENTATION OF THE PROJECT

The old observations of the bodies of the solar system are of great interest: they make possible to better evaluate the dynamics and physical evolution of these bodies. To build the dynamical models of the solar system, observations are necessary to adjust the constants of the motions. For this purpose, observation sampling must be sufficiently extensive to determine the small effects that accumulate over time but are difficult to detect on close observations. Thus, the astrometric observations published at the end of the nineteenth century are still useful and used for the current models. Unfortunately, these old observations did not benefit from accurate star catalogs for their reduction, and this biased these data. It appeared to us that a new reduction with recent catalogs could improve their accuracy. For this, it was necessary to find the original observation as the photographic plates. A new measurement based on a sub-micrometric digitization of these plates and an advanced image processing could then be used in a new reduction using the latest catalogs of reference stars. The GAIA catalog whose proper motions will allow to go up to the late nineteenth century justified our approach allowing to observe in the past with today accuracy. A work of inventory and backup of the available plates, of selection of the best old observations and

the building of a sub-micrometric scanner for the digitization of the photographic plates allowed our project to start. Besides the study of astrometry and dynamics in the solar system, our digitizing device may be useful for other purposes such as photometry, spectroscopy of transient objects the evolution of which with time being essential to understand. These works will require specific calibrations but will benefit from photographic plates allowing to extend their database towards past.

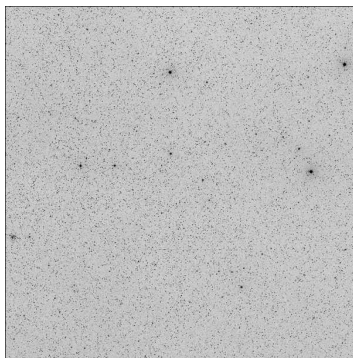


Figure 2: A Schmidt plate may contain thousands objects with a lot of small bodies of the Solar system. Prediscoveries of objects unknown at the time of the observation are possible adding observations from the past for the understanding of the dynamics of their motion.

2. OLD OBSERVATIONS

Old observations compared with new ones allow to detect, measure and model the evolution of the objects. For example, the solar system objects are moving and the modelization of their motion benefit of observations spread on a large interval of time. All the periodic terms and perturbations are better described and taken into account. More, some suspected effects such as dissipation due to tides and cumulative on a long interval of time may be out into evidence (cf. Figure 7). Even with accurate data made on a too short interval of time, such as space data, may not detect such effects.

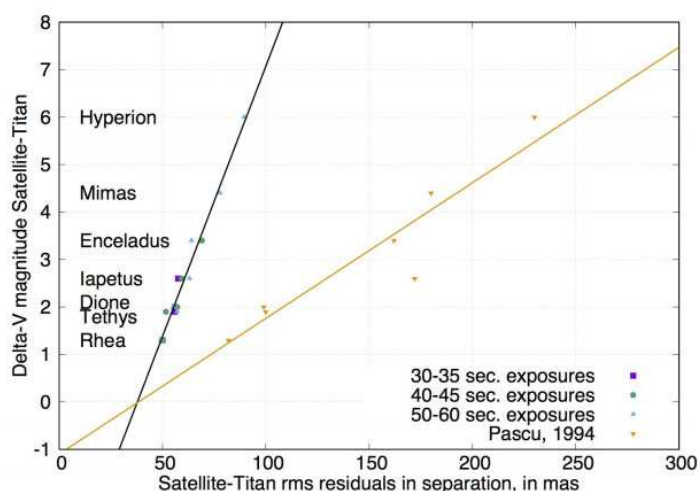


Figure 3: Comparison between old classical reduction showing a worst accuracy compared with the new one for Saturnian satellites.

Old observations are still available since published at the time of their making. However, they

were reduced using old reference catalogues not enough accurate for today purposes. A new reduction of these old observations using the Gaia reference star catalogue will allow to get the old data with today accuracy. We then are able to observe in the past. For such a reduction, a digitizing of the photographic plates is necessary in order to be able to analyze the original image with modern tools. Note that the proper motions of the Gaia stars have an accuracy of one mas one century ago that is sufficient for our purpose.

3. PREVIOUS TESTS WITH BELGIAN DIGITIZER

Thanks to a similar device in Belgium, we were able to demonstrate the validity of our project of digitizing photographic plates. We made a new reduction, using new astrometric catalogs that provided final accurate positions. We applied this to the Galilean satellites and their astrometric positions were not only more accurate than those previously derived from manual measurements, but provided new information due to the star link reduction: we obtained equatorial RA and Dec positions of the Galileans, allowing us to deduce positions of Jupiter indirectly through accurate ephemerides of the Galilean satellites. Finally, we compared these astrometric positions of Jupiter to the best current ephemerides of the planet. Depending on the ephemeris, we obtained residuals between a few tens of mas, to better than 100 mas. We also demonstrate the interest of a new reduction based on a sub-micrometric digitization comparing old and recent reduction of the positions of the satellites of Saturn (cf. Figure 3).

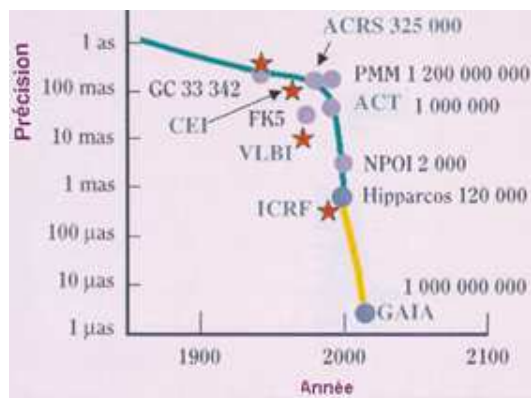


Figure 4: Progresses of astrometric accuracy of reference star catalogues. All the old observations still used nowadays were reduced with 100 mas accuracy catalogues making necessary a new reduction with the Gaia reference catalogue.

4. SCIENCE WITH NAROO

4.1 Astrometry in the Gaia era

In the context of long-term dynamic studies, the old observations are all the more interesting because they are indispensable for the modeling of transient events or observable periodic behavior. Also, the first objective of the NAROO project is to achieve a new astrometric reduction of old observations (astro-photographic plates and CCD) using the last release of the Gaia-DR reference catalog to ensure the best measurement accuracy. The Figure 5 shows the positioning accuracy of the Gaia reference stars versus time. An important result: the stars present on the oldest plates, typically a century old, will have an astrometric precision of 1 mas, allowing the same reduction as for today observations. More, all observations will now be in the same reference frame.

The interest for a new analysis and reduction.- The Figure 3 show the interest of a new reduction of old observations. The figure proposes a comparison two reductions: the one made by D. Pascu

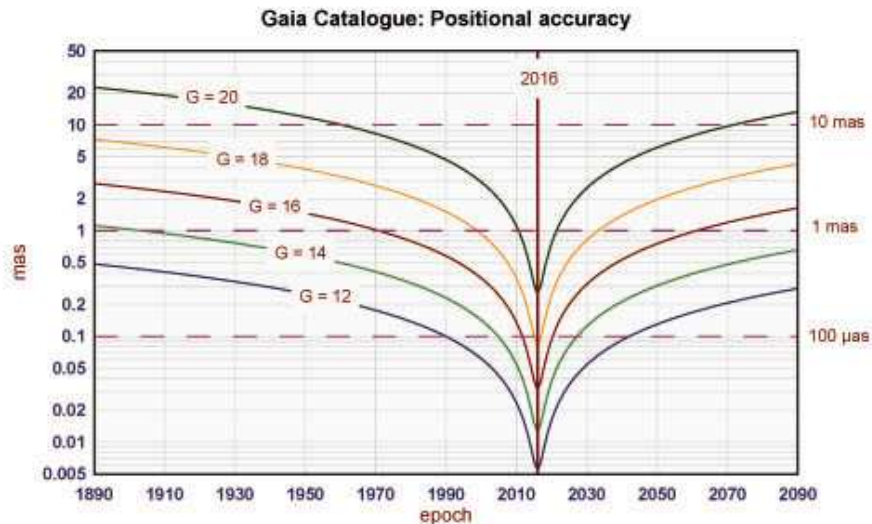


Figure 5: The accuracy of Gaia reference stars versus time (c) F. Mignard. Most of stars on old plates have a magnitude smaller than 15 having a positional accuracy better than one mas one century ago.

(1994), and the one made by V. Robert et al. (2016) after digitization. The plots RMS vs ΔV magnitude show the decreasing trend of the accuracy in positioning the satellites having different magnitudes. The new analysis led to an increase of the accuracy.



Figure 6: The sub-micrometric scanner in Meudon Observatory.

4.2 Solar system dynamics

Asteroids and comets.- Old observations of comets and asteroids had a very poor astrometric accuracy because of the reference star catalogues used at that time. A new astrometric reduction after digitization will be very useful putting all data in the same reference frame with the same accuracy. The main goals are : - analysis of Schmidt plates which contains a large number of objects still unknown (cf. Figure 2) - pre-discoveries of TNO, comets and Near Earth objects NEA/NEO; - increasing the time interval of the observations made and used in the theoretical models being

then able to detect and quantify the non-gravitational and/or cumulative effects.

The natural satellites of planets.- The interest of increasing the time interval for which we have observations, is to allow in particular the quantification of the effects of tides. These effects, due to energy transfers between satellite and planet, lead to orbital accelerations or decelerations (cf. Figure 7). These movement variations generate cumulative effects that become easily detectable over a century of observations. The old photographic plates are therefore essential for this research.

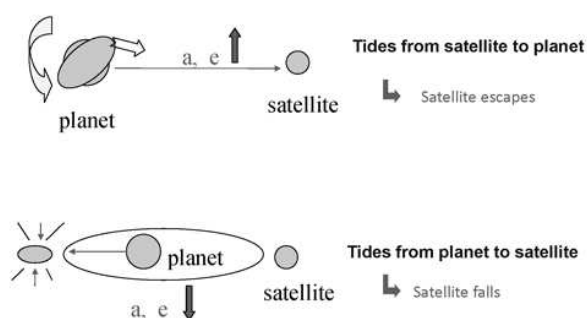


Figure 7: Influence of tides on satellite motion: satellites have an acceleration in their motion which is detectable and measurable through observations made during a long interval of time since the effects are cumulative with time.

Planets.- Planets are objects that are difficult to observe directly, especially because of their apparent brightness that disturbs images. Planetary dynamical models are adjusted on astrometric positions derived from those of natural satellites. We have shown that old observations, unfortunately inaccurate and used in the adjustments, could introduce biases in the results (V. Robert et al., 2015, 2016). A new reduction of old photographic plates is therefore essential to correct those already used, to complete and improve the existing models, to allow a better estimation of the internal structure.

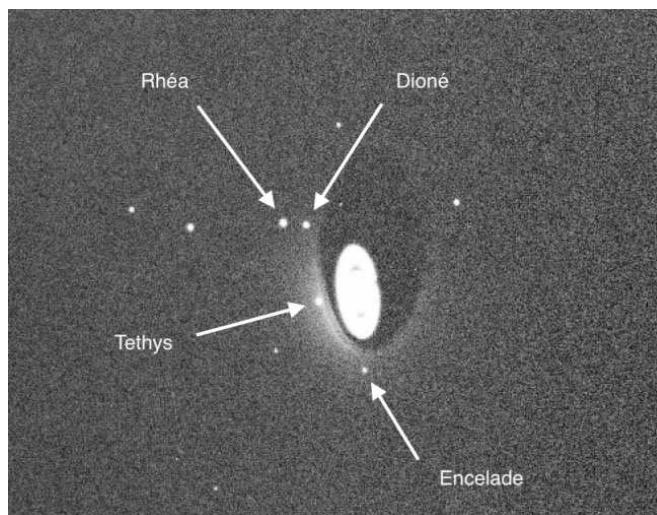


Figure 8: The first light from NAROO: the digitization of a plate of the Saturnian system.

5. THE DIGITIZING DEVICE

The astronomical plates and the quality of the results require a digitizing machine of a particular

precision because of the importance of the relative positions of the measured objects (Robert et al. 2011). Our project is based on the installation at the Paris observatory of such an instrument that we acquired and which was built in France by Newport-Microcontrol (cf. Figure 6). Note that the significant resistance to time of photographic plates has been demonstrated (Hendriks 1983). Admittedly, "ideal" archiving conditions are recommended, but emulsions and supports can remain intact and therefore usable as long as they do not undergo rapid temperature variations or extreme humidity conditions. The machine has a granite base on which an XY table rests on an air cushion. The plate holders can support plates up to 350 mm side. The position of the XY table is determined by Heidenhein encoders. Stability and repeatability are on the order of 50 nanometers. The XY table is powered by two frictionless linear motors that avoid zero problems and has progressive accelerations optimized to avoid vibrations. The XY table is completed by an optical system composed of a 1: 1 telecentric objective and an illumination system, both specially dimensioned by the Observatory's Instrumental Pole in order to accommodate, on the Z axis, a Andor SCMOS camera.

6. CONCLUSION

The reduction of old photographic plates has been tested first with the UCAC2 reference star catalogue. It was not possible to analyse data older than those of 1980s but the arrival of the Gaia reference star catalogue allows to go further in the past. Even one century ago, the astrometric accuracy will reach one mas. Our project of a new reduction of old plates is now running and is able to digitize and reduce any photographic plate in good shape (cf. the first light of our scanner on Figure 8). One may have more information on the NAROO web site at naroo.imcce.fr

7. REFERENCES

- Hendricks, J. S.; Booth, T. E., 1985, "MCNP Variance Reduction Overview", Monte-Carlo Methods and Applications in Neutronics, Photonics, and Statistical Physics. Proceedings of the Joint Los Alamos National Laboratory - Commissariat l'Energie Atomique Meeting, held at Cadarache Castle, Provence, France, April 22-26, 1985. Lecture Notes in Physics 240, edited by R. Alcouffe, R. Dautray, A. Forster, G. Ledonois, and B. Mercier. Springer-Verlag, Berlin, 1985., p. 83, doi: 10.1007/BFb00490371.
- Pascu, D., 1994, "An appraisal of the USNO program for photographic astrometry of bright planetary satellites", Galactic and Solar System Optical Astrometry, Proceedings of the Royal Greenwich Observatory and the Institute of Astronomy Workshop, held in Cambridge, June 21-24, 1993. Edited by L.V. Morrison and G.F. Gilmore. Cambridge: Cambridge University Press, 1994., p. 304
- Robert, V.; de Cuyper, J. -P.; Arlot, J. -E.; de Decker, G.; Guibert, J.; Lainey, V.; Pascu, D.; Winter, L.; Zacharias, N., 2011, "A new astrometric reduction of photographic plates using the DAMIAN digitizer: improving the dynamics of the Jovian system", MNRAS 415, pp. 701–708.
- Robert, V.; Lainey, V.; Pascu, D.; Pasewaldt, A.; Arlot, J. -E.; De Cuyper, J. -P.; Dehant, V.; Thuillot, W., 2015, "A new astrometric measurement and reduction of USNO photographic observations of Phobos and Deimos: 1967-1997", A&A 582, pp. 36–43.
- Robert, V.; Pascu, D.; Lainey, V.; Arlot, J. -E.; De Cuyper, J. -P.; Dehant, V.; Thuillot, W., 2016, "New astrometric measurement and reduction of USNO photographic observations of the main Saturnian satellites: 1974-1998", A&A 596, pp. 37–46.

CONTINUOUS UV-IR SPECTRAL ENERGY DISTRIBUTIONS OF QUASARS

B. ROCCA-VOLMERANGE¹, L. GODINAUD²

¹ Institut d'Astrophysique de Paris, CNRS and Sorbonne Université,
98bis Bd Arago, F-75014, Paris- France - brigitte.rocca@iap.fr

² Université Paris-Saclay, Orsay - France

ABSTRACT. In the present research, we propose continuous UV to IR SED templates of quasars derived from the AGN torus emission. The IR emission of the active nucleus is extracted from observations of distant 3CR radio galaxies after subtraction of their star, gas and dust galaxy components with our galaxy model. This IR emission continues in the far-UV to optical emission with the help of a classical model of AGN from Selsing et al, 2016. The galaxy templates are from the evolution code Pégase.3 by Fioc and Rocca-Volmerange, 2019 and the AGN clumpy dust models from Siebenmorgen et al, 2015. The final UV-IR templates of quasars, depending on z and inclination, will be tools to interpret magnitudes and colors of galaxies and quasars at various redshifts, the physical link of the star formation-AGN activities as the contribution of the IGM with Gaia, ALMA, SPITZER and the future telescopes JWST, EUCLID and others (work in progress).
Keywords: Galaxies (quasars): general, torus, infrared: galaxies, ISM: dust, emission

1. THE AGN TORUS FROM DUST MODELS

Multiwavelength hybrid spectral energy distributions SEDs (Drouart et al., 2016) are built to follow the evolution of distant radiogalaxies with the host galaxy and an evolving starburst of the code Pégase3 (Fioc & Rocca-Volmerange, 2019, www2.iap.fr/pegase) plus a clumpy AGN torus model from Siebenmorgen et al., 2015. Pégase3 predicts from 0 to 20 Gyrs, the stellar and nebular emissions, corrected for metallicity-dependent dust attenuation, updated from Fioc & Rocca-Volmerange, 1997, and coherently extended by radiative transfer MonteCarlo simulations to the IR dust emission, respecting the energy balance. The best-fit procedures are testing these multiple synthetic libraries on UV-to-far-IR observations of 3CR galaxies. An example of the decomposition (Figure 1) for the radiogalaxy 3C356 identifies three components: the AGN torus in the midIR (green line), the evolved galaxy component (orange line) and the young starburst (blue line). The synthetic global sum is the light black line. The references are given for other 3CR radiogalaxies including 3C266 (Drouart et al., 2016, Podigachoski et al., 2016, see also Figure 3) applying the hybrid method to the 3CR catalog at various z . Three components (AGN, old galaxy and evolved starburst) are found in all cases, even at higher redshifts.

2. THE UV-IR QUASAR TEMPLATES

Selsing et al. 2016 extracts the ultraviolet-blue to near-IR composite spectrum of quasars from various QSO samples, observed at different epochs with different instruments, in particular on selected observations at $1 \leq z \leq 2.1$ from the Sloan Digital Sky Survey (SDSS). After subtractions of X-ray attenuation and the galaxy host contribution, a power-law continuum for the composite spectrum on the rest-frame range from $\text{Ly}\beta$ to 11350\AA is proposed. The continuum of a single quasar spectrum is then modeled as a power law, $f_\lambda = A \lambda^{\alpha(\lambda)}$ with a spectral slope of $\alpha = 1.70\lambda \pm 0.01\text{\AA}$.

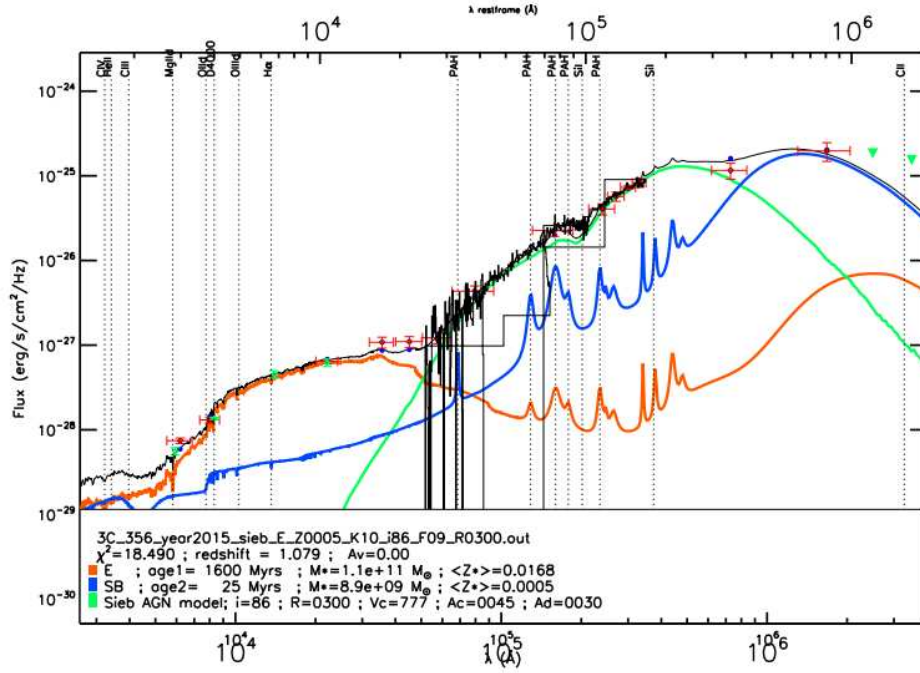


Figure 1: The UV-farIR best-fit of the radio galaxy 3C356 ($z=1.079$, $i=86$ deg) with hybrid models of AGN and Pégase3, shows the IR torus emission (green) and synthetic stellar young (blue), old (orange) populations and total (light black line), (Drouart et al., 2016, Podigaschoski et al., 2016). The observations are from HST and SPITZER/IRAC filters (red squares) and the IRS spectrum (dark black line): in particular, this best-fit is considered as robust due to its consistency with this observed *SPITZER/IRS* spectrum.

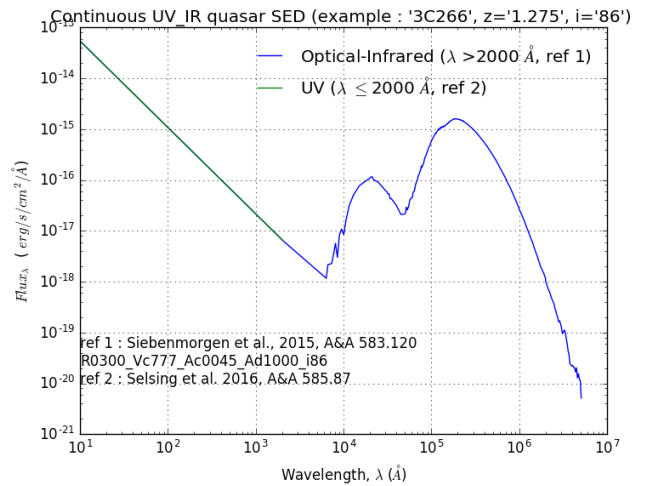
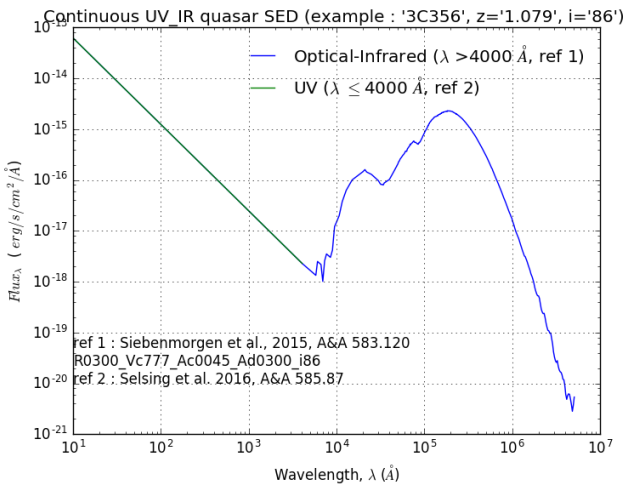


Figure 2: The UV - IR SED of quasars is presented by connecting the two UV (green line) to IR (blue line) components of the torus emission for, as examples, the two 3CR radiogalaxies 3C356 and 3C266. This last galaxy and other 3CR galaxies (see Figure 3 from Podigaschoski et al, 2016) show the surprising continuity of the two components at the respective junction wavelength (4000Å for 3C356 and 2000Å for 3C266). The templates depend on z and on the AGN-axis inclination on the line of sight.

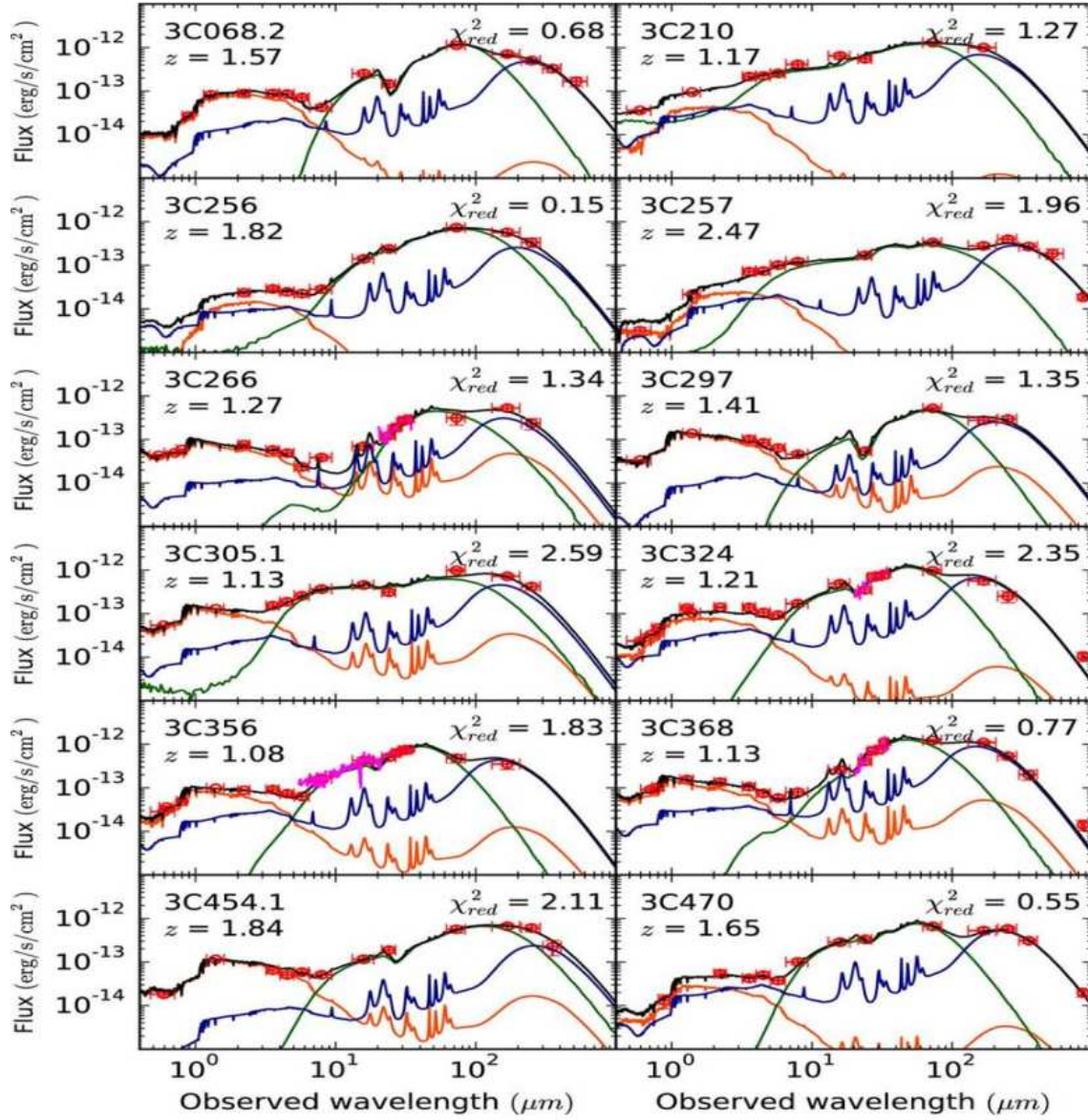


Figure 3: The three components (AGN, old galaxy and recent burst) of the 3CR radiogalaxies (Podigachoski et al, 2016). Identified with Pégase3 and Siebenmorgen et al. 2015, all show the same 3-component distribution for various redshifts

This UV-near-IR infrared slope, typical of quasars, is connected with the IR torus emission from the observed SED of the 3CR radiogalaxies (see section 1). While Figure 2 presents two examples (3C356 and 3C266) chosen for their *IRS – Spitzer* spectrum fitting, the disentangling is applied to the 3CR sample (Figure 3). The most surprising result is the continuity of the two slopes of the AGN models at the junction domain: 2000Å for 3C356 and 4000Å for 3C266. These templates mainly depend on z and inclination, and also other physics parameters adopted by Siebenmorgen et al., 2015 through their library of 7000 SEDs for a broad range of luminosities, sizes and obscurations. The radiative transfer is tested on nearby galaxies in spherical symmetry for a stellar cluster permeated by an interstellar medium with standard (Milky Way) dust properties. Similarly the subtracted IR dust emission of galaxy components (host galaxy and burst) with Pégase.3 is coherent through MonteCarlo simulations with the absorbed energy by dust grains with local observed galaxies.

3. CONCLUSION AND FUTURE

For the 3CR galaxies, a continuous and significant link from the UV to IR domains of the torus emission is observed in the 3CR galaxy sample. The relation depends on the distance z and on inclination of the torus axis. These templates, assimilated to quasar templates, may be convolved through the pass-bands of the filters to better analyze the high spatial resolution of quasar data from the satellite Gaia, the relation between star formation and AGN activities hinted by the different thermal peaks in the far-IR. In the mid-IR, these templates will be helpful for data analyzes with better spatial and spectral resolutions of the *JWST/NIRcam*, *MIRI*, *NIRspec* instruments. We plan to build Pégase.3 template libraries and corresponding synthetic colors to help the community for the future data.

4. REFERENCES

- Drouart, G., Rocca-Volmerange, B., De Breuck, C., Fioc, M., Lehnert, M., Seymour, N., Stern, D., & Vernet, J., 2016, *A&A* , 593, 109.
- Fioc, M., Rocca-Volmerange, B., 2019, *A&A* 623, 143.
- Fioc, M., & Rocca-Volmerange, B., 1997, *A&A* 326, 950.
- Podigachoski, P., Rocca-Volmerange, B., Barthel, P., Drouart, G., & Fioc, M., 2016, *MNRAS* , 462, 4183.
- Selsing J., Fynbo, J. P. U., Christensen, L., Krogager, J. K., 2016, *A&A* 585, 87.
- Siebenmorgen, D., Heymann, F., Efstathiou, A., 2015, *A&A* 583, 120.

FUTURE SPACE ASTROMETRY

D. HOBBS

Lund Observatory, Box 43, 22100, Lund - Sweden - david@astro.lu.se

ABSTRACT. With Gaia's second data release in April of 2018 Europe entered a new era of space astrometry. Further data releases are also planned for the coming years. Despite this great progress astronomers are already looking towards the future. Gaia had an advantage over pointed missions in being a global survey which provided absolute parallaxes and addressed a very broad range of science cases. However, Gaia only operates at optical wavelengths while much of the Galactic centre and the spiral arm regions are obscured by interstellar extinction. One clear option for space astrometry is to shift to the infra-red where new science cases immediately become apparent. This can, of course, be achieved with a pointed mission performing relative astrometry, such as the Japanese small-Jasmine concept, focused on the Galactic plane. However, I would argue that much more can be achieved by essentially replicating an all-sky Gaia-like mission with Near-InfraRed (NIR) detectors.

1. THE SCIENTIFIC MOTIVATION

The second Gaia data release contained astrometric data for ~ 1.7 billion sources with tens of microarcsec (or microarcsec per year) accuracy in a vast volume of the Milky Way and future data releases will further improve on this. Gaia has just completed its nominal 5 year mission (July 2019), but is expected to continue operations for an extended period of an additional 5 years through to mid 2024. Its final catalogue to be released ~ 2027 will provide astrometry for ~ 2 billion sources, with astrometric precisions reaching 10 microarcsec.

In our recent white paper to the European Space Agency's (ESA's) Voyage2050 call we have outlined the detailed science cases for a new all-sky visible and NIR astrometry mission (Hobbs *et al.*, 2019a). With a wavelength cutoff in the K-band the new mission is not just focused on a single or small number of key science cases. Instead, it is extremely broad, answering key science questions in nearly every branch of astronomy while also providing a dense and accurate visible-NIR reference frame needed for future astronomy facilities. Such a new mission will require new types of detectors to scan the entire sky and measure global absolute parallaxes. The spacecraft must have a constant rotation to scan the sky which results in a moving image that must be compensated for by, for example, operating the detectors in Time Delayed Integration (TDI) mode.

For around 2 billion common stars the combination of two all-sky space observatories would provide an astrometric foundation for all branches of astronomy – from the solar system and stellar systems, including exoplanet systems, to compact galaxies, quasars, neutron stars, binaries and dark matter (DM) substructures. The addition of NIR will result in up to 8 billion newly measured stars in some of the most obscured parts of our Galaxy, and crucially reveal the very heart of the Galactic bulge region (see Figure 1).

In this paper I argue that rather than improving on the accuracy to answer specific science questions, a greater overall science return can be achieved by going deeper than Gaia and by expanding the wavelength range to the NIR. A new mission could expand and improve on the science cases of Gaia using basic astrometry. Key topics are focused on what dark matter is and how is it distributed, how the Milky Way was formed and how has it been impacted by mergers and collisions? How do stars form and how does stellar feedback affect star formation; what are

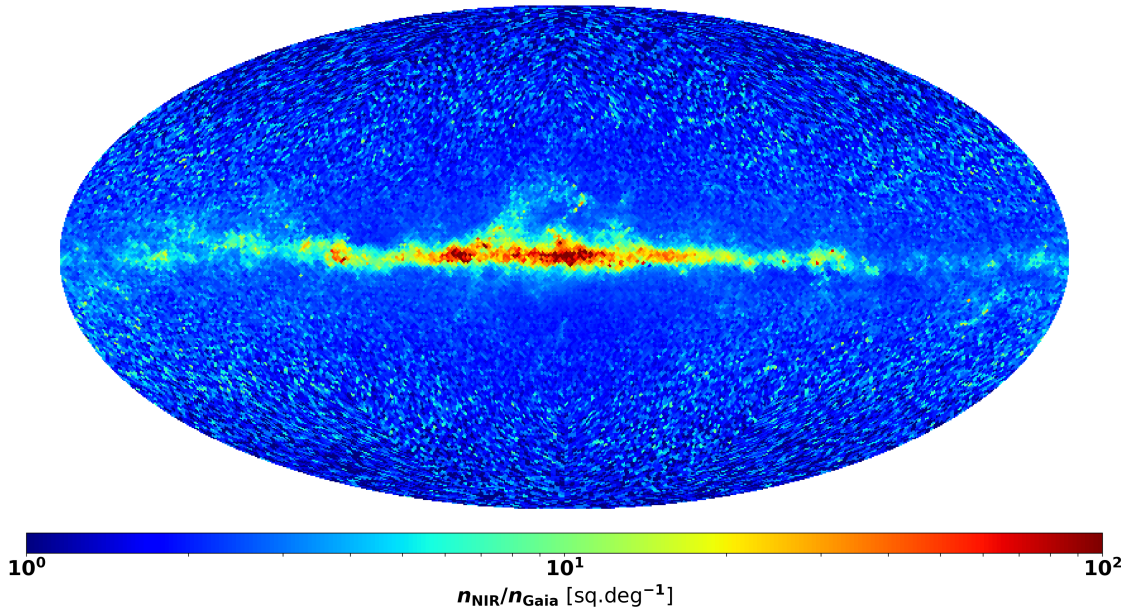


Figure 1: All-sky projection in Galactic coordinates of the star count ratio per square degree between GaiaNIR and Gaia (G-band limit of 20.7th mag giving 1.5 billion Gaia sources). In total 5 times more stars could be observed, especially in the disk where extinction is highest, by GaiaNIR for the H-band limit of 20th mag (left figure) and 6 times more stars could be observed by including the K-band limit of 20th mag. Crowding is not taken into account here and will limit the increase in numbers in the densest areas. From Hobbs *et al.*, 2019a.

the properties of stars, particularly those shrouded in dust, and small solar system bodies; how are they distributed and what is their motion? How many co-planar systems like ours (with Earth-sized and giant planets) are there and what fraction have planets with long period orbits? To answer these questions there are three main science challenges for a new all-sky astrometry mission (The following is a brief summary of the discussion in Hobbs *et al.*, 2019a where more detailed arguments are given):

1.1 NIR astrometric science cases

NIR astrometry (and simultaneous photometry) is crucial for penetrating obscured regions and for observing intrinsically red objects when implemented with sufficient accuracy. Peering through the dust of the Milky Way to obtain a dense sampling of the phase space necessary to study the bulge, bar, bar-disk interface and spiral arms. Spiral structure can excite stars to radially migrate and induce disk heating and accurate measurements of the 3-D motion and properties of these obscured stars are needed to trace the dynamical history and evolution of our Galaxy. Preliminary estimates show that a new NIR astrometry mission would observe at least 5 times as many stars as Gaia, assuming the same magnitude range, giving a huge increase in the catalogue size and would dramatically increased phase space sampling of the disk, especially of the innermost regions where co-existing populations require better statistics.

Since Gaia was proposed, it has become clear that the evolution of the Milky Way is far more complex than had been realized. Not only is it not in equilibrium, its stars actually move away from their birth places, a process called radial migration which can vary with time and distance from the Galactic centre. Stars can be strongly influenced by the bulge and bar regions and their interaction with spiral arms and also by minor mergers. All of this implies that the local volume near the Sun

cannot be understood in isolation, without a proper description of the innermost regions of the Milky Way and its merger history. A new NIR astrometry mission would allow us to probe this vast region and accurately determine the dynamics of the stars there.

The Milky Way presents our best opportunity to study the nature of dark matter, the gravitational force at different points in the inner disk of the Milky Way is not well known and many sources will not have been observed by Gaia so a new NIR mission would give unique measurements with similar accuracy to Gaia. The parallaxes, and proper motions at the Galactic centre distances will thus not be very accurate for many new sources. However, double epoch observations for bright stars will give a smaller sample of very accurate parallaxes and proper motions. The very unique all-sky astrometry that a new NIR mission can offer constrains the detailed dynamical and orbital structure of many more stars and at greater distances around the central black hole region than other surveys such as GRAVITY and Small-JASMINE.

Gaia has already shown that the Galactic plane itself shows clear signs of a warp and this means that conceptions of our Galaxy having a simple rotation curve which is a function of radius must be discarded, and we must map the velocity field across the Galactic plane. A future astrometric mission will allow us to do this far more accurately than Gaia alone, because of the improved proper motions, and working in the NIR will alleviate the selection effects caused by dust extinction revealing the stars in the midplane of the Galaxy that are not seen by Gaia.

Stars are continuously formed in clusters of tens to thousands and evolve together for a shorter (~ 100 Myr) or longer time (a few Gyr) in associations or open clusters, respectively, depending on whether they are gravitationally bound or unbound. Clusters are often located in the spiral arms of the Milky Way and are composed of young stars that have recently formed in the disk. The stars belonging to a cluster have roughly the same age and metallicity and can be used to probe the Galactic disk structure and formation rate, to study young star properties and their formation process as well as probing radial migration.

The spiral structure of the Milky Way is surprisingly poorly known, radio measurements are providing good constraints on the fundamental parameters of the Galaxy, including the distance to the Galactic centre, but are very limited in number. Spiral arms are also the main areas of star formation in the Milky Way, and are responsible for a significant portion of radial migration and disk heating. A new NIR astrometry mission can provide many more samples of stars in the disk plane with enough astrometric accuracy up to about the distance of 8 kpc, and can uncover the stellar motion around the Outer, Perseus, Local, Sagittarius, and Scutum-Centaurus arms over a large range of Galactocentric radii and azimuthal angles. This will provide an ultimate answer for the origin of the spiral arms and will be key to resolving questions regarding the nature of dark matter, by showing us whether the Galaxy has a cored or cusped dark matter halo, whether there are any thin, disc-like components to the dark matter distribution, and whether spiral arms have their own dark matter component.

1.2 Improved proper motion science cases

A new mission could be combined with the older Gaia catalogue (currently ~ 1.7 billion sources) with a 20 year interval to give a much longer baseline of 25–35 years, with very accurate proper motions (a factor of 14–20 better in the two components) and improved parallaxes needed to measure larger distances. While Gaia is making much progress it will not be sufficient to discover and characterise most of the stream-like structures in the halo. Improvements in the accuracy of proper motions would allow a new mission to resolve tangential motions in streams and local dwarf galaxies, with a potential accuracy of $2\text{--}3 \text{ km s}^{-1}$ for specific samples out to ~ 100 kpc. Additionally, improved proper motions will also be crucial to help disentangle the mixed populations in the bulge region. This is only possible by exploiting the long time baseline allowed by combining Gaia measurements with those from a future astrometric mission. This will provide great insight into the gravitational potential in the outer reaches of the Milky Way where halo streams are

sensitive probes.

Streams in the Milky Way halo are formed when satellite galaxies or globular clusters are pulled apart in the tidal potential of the Milky Way. The stars then drift apart because they are on different orbits and form a (typically thin) band of stars across the sky. Improving proper motion measurements for stars in Milky Way streams will allow “gaps” in the streams to be identified more easily, we might see the influence of dark matter sub-haloes in the Milky Way’s halo even though they contain no stellar matter. All this will allow us to determine the dark matter distribution at large radii, including any flattening of the potential, and the total mass of the Galaxy. A future astrometry mission would provide highly accurate proper motions and more accurate distances to these stars, which will allow much more precise determination of the potential of the Milky Way at these large radii.

A full understanding of the internal dynamics of dwarf spheroidal galaxies still remains beyond our reach. There is a trade-off between dark matter content and tangential anisotropy and/or repeated tidal heating by encounters with the Milky Way which can masquerade as a highly dark matter dominated galaxy. The only way to be sure of the true dark matter content is to measure the internal proper motions of the stars in the dwarf galaxy, not only the bulk proper motion of the system (feasible with Gaia). Only the combination of Gaia and GaiaNIR can hope to achieve this challenging goal.

Astrometrically resolving internal dynamics of nearby galaxies, such as M31, dwarf spheroidal galaxies, globular clusters, the Large and Small Magellanic Clouds (LMC, SMC), sets requirements on the accuracy. For example, the LMC has a parallax of $20 \mu\text{as}$ and an accuracy of about 10% is needed, which is just within the reach of Gaia. Precise mapping of dark matter (sub-) structure in the local group (for instance Cen-A) and beyond is possible with accurate proper motions. Gaia can only just directly measure internal motions of nearby galaxies. Combining proper motions from two Gaia-like missions opens up the tantalising possibility of accurately measuring their internal motions and thus resolving the dynamics within the Local Group.

Proper motions and parallaxes, especially of binaries, will be much improved when astrometric data from two missions are combined and the detection of planets with significantly longer periods than by Gaia alone can be achieved. A significant population of stars with planetary system architectures similar to our Sun’s (so long period, massive gas giants, like Jupiter and Saturn, in the outer reaches, shielding Earth type planets in the star’s habitable zone) will be discovered. Another strong impact is on the study of the population of small Solar System bodies, asteroids, comets, and planetary satellites. Solar System bodies are easily perturbed and repeated high accuracy astrometry and photometry are needed improve our knowledge here.

1.3 Maintenance of the celestial reference frame

A new mission would allow the slowly degrading accuracy of the Gaia visible reference frame, which will become the fundamental Celestial Reference Frame (CRF) and the basis for all modern astronomical measurements, to be re-initialised back to a maximal precision. This degradation is due to errors in its spin and due to small proper motion patterns which are not accounted for. The catalogue accuracy itself will decay more rapidly due to errors in the measured proper motions. However, the million or so quasars expected in the Gaia-CRF represents a tiny fraction of the Gaia sources. With the typical angular distance between the quasars of about 6 arcminutes the Gaia-CRF is not dense enough to provide a suitable reference grid needed for forthcoming Extreme, Giant and Overwhelming telescopes but also for smaller instruments currently operating or being planned. Moreover, most of the quasars of the Gaia-CRF are rather faint (between magnitudes $G = 19$ and 21) so that the accessibility of the reference frame is given only in the optical and almost exclusively in that interval of magnitudes. The extension of the Gaia visible reference frame into the NIR is an important step given that so many new space and ground based observatories will have infrared sensitive instruments. A new mission would provide better accuracy to explore

proper motion patterns, for example, from the Sun's Galactic acceleration to gravitation waves, real time cosmology and fundamental physics.

In summary, the new mission proposed to ESA in the Voyage2050 call (Hobbs, *et al.*, 2019a), will observe many new stars in obscured regions. We estimate at least 5 times as many stars will be observed, giving up to 8 billion new objects. NIR opens up a new wavelength range which allows us to probe the dusty obscured regions of the Galactic disk with high-precision astrometry and broad-band high-resolution photometry, while out of the Galactic plane a new mission will go deeper to enhance the halo science cases and provide complementary legacy data to ground based surveys such as LSST. A common astrometric solution for the two missions will give greatly improved proper motions but also improve the parallaxes, for up to 2 billion common stars. Long term maintenance and expansion of the dense and very accurate celestial reference frame with a new mission is necessary for future precise astronomical observations and provides an essential service for the astronomical community. These features ensure that a new mission is not simply an increment on the previous one but will create an astrometric revolution in itself!

2. THE TECHNICAL CHALLENGE

In 2016 Hobbs *et al.* proposed to ESA a new all-sky NIR astrometry mission, called GaiaNIR, which could realise the science cases discussed above. Such a NIR space observatory is however not possible today: it requires a new type of Time Delay Integration (TDI) NIR detector to scan the entire sky and to measure global absolute parallaxes. In 2017, an ESA study¹ of the GaiaNIR proposal already hinted that a US-European collaboration would be a possible route to make GaiaNIR science and technology a reality and subsequently McArthur *et al.* 2019 and Hobbs *et al.* 2019b submitted white papers to the US decadal survey (Astro2020) outlining the science cases and a possible US-European collaboration. The Australian National University is also developing NIR astronomical detector technology with TDI capabilities and are very interested in becoming part of this endeavour. The Japanese are currently working in a different direction with small-JASMINE, which has been recently selected by ISAS/JAXA for their M-3 mission with a current scheduled launch in mid-2020s, to do relative (to Gaia) astrometry in the NIR, but only focusing on the small region within ~ 100 pc from the Galactic centre and relatively bright ($H_w < 15$ mag) stars. With their experience from small-JASMINE they are clearly interested in collaborating on the new mission outlined here.

In the Astro2020 APC white paper (Hobbs *et al.*, 2019b) investigated four different technologies which could be used to achieve our goals. Astronomical-grade infrared detectors are well established for both ground- and space-based applications. At shorter IR wavelengths, the premium detectors are HgCdTe devices, especially those fabricated by Teledyne in the USA. Unlike CCD detectors, the state-of-the-art for optical wavelengths, the HgCdTe devices cannot be used in a scanning mode, in which the image is transferred within the device synchronously with the scanning motion of the optical system (i.e. TDI). TDI is useful in many applications, and particularly for surveys, as individual exposures are not required, and data simply pour out of the detector array in a continuous stream. An example of TDI in ground-based astronomical applications is the Sloan Digital Sky Survey (SDSS), one of the most influential astronomy initiatives ever while a space-based example is ESA's Gaia mission mentioned above. Such surveys could not have been achieved without TDI operation but have been limited to the optical band.

This is a significant limitation. The importance of NIR in modern astronomy and cosmology is abundantly clear with most major ground-based facilities operating powerful infrared instrument suites, and major upcoming missions such as James Webb Space Telescope, Euclid and WFIRST

¹<http://sci.esa.int/future-missions-department/60028-cdf-study-report-gaianir/>.

are either completely or significantly orientated to infrared observations. There is a compelling case, therefore, for an infrared detector that can operate in TDI. There are a number of possible approaches to developing TDI-NIR detectors:

1. Using HgCdTe Avalanche Photodiodes (APDs) with TDI-like signal processing capability. The challenge here is to scale the technology to large format arrays and ensure the dark current does not introduce unwanted noise at temperatures above 100 K.
2. Ge detectors due to the lower band gap can detect NIR radiation of longer wavelengths than possible with Si detectors. Clearly this technology is new but many of the manufacturing techniques developed for Si are also applicable to Ge and further development is needed to see if they can be used for our application with low noise in large format arrays.
3. A hybrid solution which uses a HgCdTe NIR detector layer bump bonded to a Si CCD. The idea is that the photons are detected in the surface NIR layer and transferred to the Si buried channel at each pixel. Charge can then be easily moved along the pixels of the same column in sync with the charge generation, thus achieving TDI. What is not known yet is how efficiently the charge can be transferred from the NIR detection layer to the Si CCD and if both materials can be operated at the same temperature.
4. Microwave Kinetic Inductance Detectors (MKIDs) are cooled, multispectral, single photon counting, multiplexed devices, capable of observation in the UV through to NIR. They measure the energy of photons at high frequency to within several percent making them ideal for TDI like operation. Whilst relatively new, small MKID arrays have already been utilised on ground-based telescopes for astronomy, demonstrating their potential.

The above list of has been ordered to reflect the suitability of each option; the APD detectors are currently seen as the best option; the Ge detectors are limited in wavelength to 1600 nm; the hybrid solution is technically complex; and the MKID solution requires cryogenic cooling. The APD solution is most promising and rapid progress is being made in developing large format arrays suitable for our application (see Gilbert *et al.*, 2019). Nevertheless there are still some technical challenges, namely 1) they exhibit large dark currents even at low gain while conventional HgCdTe detectors do not and 2) the visible response of the devices needs to be enhanced - normally achieved through substrate removal. It remains to be seen if these challenges can be overcome but APD development looks promising at this point.

3. REFERENCES

- Hobbs, D., *et al.*, 2019a, ESA, Voyage 2050 White Paper, arXiv:1907.12535.
Hobbs, D., *et al.*, 2016, Response to ESA's call for new "Science Ideas", arXiv:1609.07325.
Hobbs, D., *et al.*, 2019b, NAS Astro2020 Decadal Survey APC White Paper, arXiv:1907.05191.
McArthur, B., *et al.*, 2019, NAS Astro2020 Decadal Survey White Paper, arXiv:1904.08836.
Gilbert, J., *et al.*, 2019, 70th International Astronautical Congress, Washington D.C., arXiv:1911.04684.

Gaia SUCCESSOR WITH INTERNATIONAL PARTICIPATION

E. HØG¹ and D. HOBBS²

¹ Niels Bohr Institute, Blegdamsvej 17, 2100 Copenhagen Ø, Denmark - ehoeg@hotmail.dk

² Lund Observatory, Box 43, 22100, Lund - Sweden - david@astro.lu.se

ABSTRACT. Astrometric data from Gaia are already revolutionizing astronomy in all branches from the solar system and stellar structure to cosmic distances and the dynamics of the Milky Way. In April 2018, the second data release based on 22 months of observations gave 5-parameter astrometry for more than 1.3 billion sources and a further 0.4 billion sources with 2-parameter solutions; while subsequent releases will give increasingly accurate and comprehensive sets of astrophysical data. The final Gaia data set will presumably be based on 10 years of observations thus providing a new astrometric foundation of all astronomy. It is however clear that a Gaia successor in twenty years is required for observation of the same stars (estimated to be ~ 2 billion), providing improved parallaxes and improved proper motions with 10–20 times better accuracy, in order to maintain and strengthen the astrometric foundation of astronomy. By adding a Near-InfraRed (NIR) capability to the new mission we will be able to peer into the obscured regions of the Galaxy and measure up to 8 billion new objects and reveal many new sciences in the process.

1. MOTIVATION FOR GaiaNIR

The current Gaia mission has only just begun to revolutionize our understanding of the Galaxy. The first Gaia data release gave 5 parameter astrometry for more than 2 million sources but this gave just a hint of what was about to come in the second release. In April 2018 we released 5 parameter astrometry for more than 1.3 billion sources and a further 0.4 billion sources with 2-parameter solutions. The nominal Gaia mission of 5 years will eventually provide positions, absolute parallaxes and proper motions, to unprecedented accuracies ($20\text{--}25 \mu\text{as (yr}^{-1}\text{)}$) at the magnitude $G=15$), with the addition of all-sky homogeneous multi-colour photometry and spectroscopy. The extended mission of up to 10 years will further improve on this with increasingly accurate and comprehensive sets of astrophysical data. These unique capabilities go well beyond and are complementary to the science cases being addressed by ground based surveys (such as RAVE, SDSS, Pan-Starrs, APOGEE, LSST, etc).

The most obvious way to improve on Gaia’s capabilities is to extend them to all-sky absolute Near-InfraRed (NIR) astrometry allowing the new mission to probe through the Galactic dust to observe the structure and kinematics of the star forming regions in the disk, the spiral arms and the bulge region to give model independent distances and proper motions in these obscured parts of the sky. A new mission launched with an interval of 20 years (around 2040) would allow new measurements of objects already in the Gaia catalogue to be combined with older data giving improved proper motions with 10–20 times smaller errors. Parallaxes would also be improved in such joint solutions by a factor of $\sqrt{2}$ assuming the two missions are of equal duration. After the publication of the final Gaia catalogue the positions of stars will be accurately known at the chosen reference epoch and linked to the VLBI reference frame. However, this accurate positional information will slowly degrade due to the small uncertainties in the proper motions of the stars. Hence, it is necessary to repeat the measurements of Gaia after about 20 years to maintain the positional accuracy and the optical reference frame.

The accuracy of the new mission should be at least that of Gaia using tried and trusted

instrumentation, techniques, and lessons learned from Gaia. To achieve these goals we need to explore the feasibility and technological developments needed to manufacture space qualified and passively cooled optical and NIR (400–2500 nm) Time Delay Integration (TDI) sensors needed to compensate for rotation. To maintain ESA's leadership in all-sky space astrometry it is highly desirable to develop such detector technology within Europe. The most promising NIR sensors today seem to be Avalanche PhotoDiode (APD) HgCdTe sensors which can also support TDI mode. In 2016 we successfully proposed such a technology study to ESA (Hobbs et al., 2016) in a call for "New Science Ideas" to be investigated for technologies not yet sufficiently mature. It is hoped that these ideas may become candidates for future missions in the ESA Science Program.

A new mission would also multiply the number of observed objects by a factor of 5-6 giving up to 8-10 billion newly measured objects depending on the cutoff wavelength of 1800 nm or 2500 nm. In 2017 ESA studied¹ such a NIR space observatory (GaiaNIR). The outcome was that in order to achieve the very demanding science goals it requires new types of NIR TDI detectors to scan the entire sky and to measure global absolute parallaxes. Gaia is an ESA-only mission as Hipparcos was and we thought a Gaia successor should be the same. Recently however, we have strengthened our efforts by international collaboration. Together with US, Japanese and Australian colleagues we have submitted a proposal outlining the detailed science cases to ESA's Voyage2050 call (Hobbs, et al., 2019a) and two proposals for study in the US Astro2020 Decadal Survey (McArthur, et al., 2019 and Hobbs, et al., 2019b). Such an international collaboration would help to keep the overall cost of the Mission for ESA within the Medium-class (M-class) envelope and thus make its selection more feasible.

2. ESA TELESCOPE IN 2017

In 2017 ESA studied¹ the GaiaNIR concept at its Concurrent Design Facility (CDF). GaiaNIR was one of the 26 proposals received from the New Science Ideas call in 2016 (Hobbs et al., 2016) and its purpose was to:

- enlarge the achievement of Gaia to astronomical sources which are only visible in NIR;
- improve the stellar parallax and proper motion accuracy by revisiting the common sources 20 years after Gaia;
- maintain the accuracy of the Gaia optical reference frame and to extend it to the NIR.

The ESA study for GaiaNIR resulted in a new telescope design which is not un-similar to Gaia as many key ideas were reused. The optical path of the telescope is composed of:

- A primary, a secondary and a tertiary curved mirror.
- Four flat mirrors:
 - two at the entrance pupil, one for each sky direction;
 - at the exit pupil which can accommodate a de-scanning mechanism for conventional NIR detectors (static image) or a simple flat mirror for TDI like NIR detectors (moving image);
 - a folding mirror after the exit pupil located to the side of the Korsch tertiary mirror to make the overall mechanical envelope more compact.

Figure 1 shows the GaiaNIR optical surfaces and light path. Support structures of all optical instruments are directly connected to the torus structure to avoid obstructions of the light path.

¹<http://sci.esa.int/future-missions-department/60028-cdf-study-report-gaianir/>.

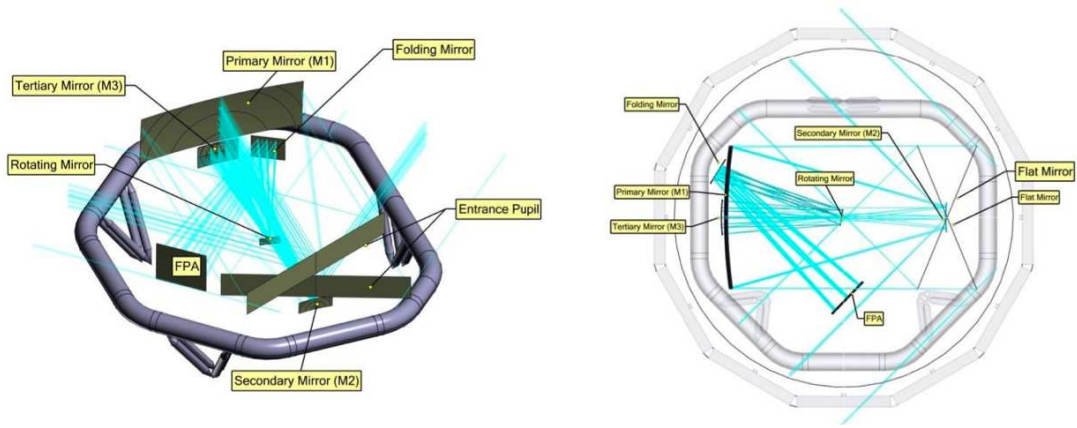


Figure 1: *GaiaNIR optical surfaces and the light path (left) and Top view of the GaiaNIR Light path (right). Images from the ESA CDF study report.*

Note the de-rotation mirror that is located in the middle of the torus structure, this is required for conventional non-TDI NIR detectors to produce a static image on the focal plane but can be replaced with a simple flat mirror when using TDI NIR detectors which give a moving image on the focal plane.

For GaiaNIR ESA designed an off-axis Korsch telescope, as it is in Gaia. But it differs from Gaia with regard to two important optical features: 1) The mirror surfaces are simple conics. This simplifies manufacturing alignment and test; and 2) The entrance pupil is at the flat folding mirror in front of the primary instead of on the primary mirror itself. This does not have a significant effect on image quality. Gaia's mirrors are conics with high order aspheric coefficients and used off axis, which made manufacture and test of these elements very challenging.

The entrance pupil area was equivalent to $1600 \times 250 \text{ mm}^2$, where the long side of the pupil is in the direction of rotation and the field-of-view was $0.6^\circ \times 0.47^\circ$ and the effective focal length was 35 m similar to Gaia.

Star magnitude [Gaia-band magnitude]	Gaia NIR with TDI			Gaia NIR baseline		
	G2V	M0V	M3III	G2V	M0V	M3III
7 (bright)	9	9	9	9	9	9
15	48	34	19	165	81	27
21	4129	1881	426	38660*	16843	2919

* Indicates that the detection limit has been reached.

Figure 2: *Summary of the astrometric performance comparison in micro-arcsecs between the GaiaNIR with TDI and GaiaNIR baseline (with de-rotation mirror) and for three stellar types and a 5 year mission. Table from the ESA CDF study report.*

During the CDF study the baseline mission concept used conventional non-TDI NIR detectors together with a de-rotation mirror to remove the image motion as the spacecraft rotates. This baseline astrometric solution was compared to using the same detectors but with a TDI mechanism and the results of the CDF study are presented in Table 2. It is clear that the baseline solution with conventional detectors gave very poor astrometric performance for faint stars (up to a factor of 10) while a TDI detector solution gave performances comparable to Gaia. The difference in results is mainly due to the reset time for the de-rotation mechanism which does not allow the star

light to be integrated for long enough. The science performance for the faint stars is critical for this mission - most stars are faint and most of the GaiaNIR science cases are aimed at the faint stars. In conclusion this mission concept requires that we use a TDI like approach to integrate the light as it passes across the focal plane - this important and obvious conclusion was unfortunately ignored in the ESA CDF study report.

3. DETECTORS AND FILTERS

In the recent APC white paper in Astro2020 Hobbs, *et al.*, 2019b investigated 4 different detector technologies which could be used to achieve TDI in NIR detectors. From these four approaches we identified electron initiated Avalanche PhotoDiodes (e-APDs) as the most promising for our application. APDs are semiconductor electronic devices which exploit the photoelectric effect and can be considered the semiconductor analogue of the photomultiplier. They are very promising technology with the limitation of increasing the dark current at temperatures above 100K. The very fast read out of these devices makes APDs inherently suited to a TDI like signal processing mode.

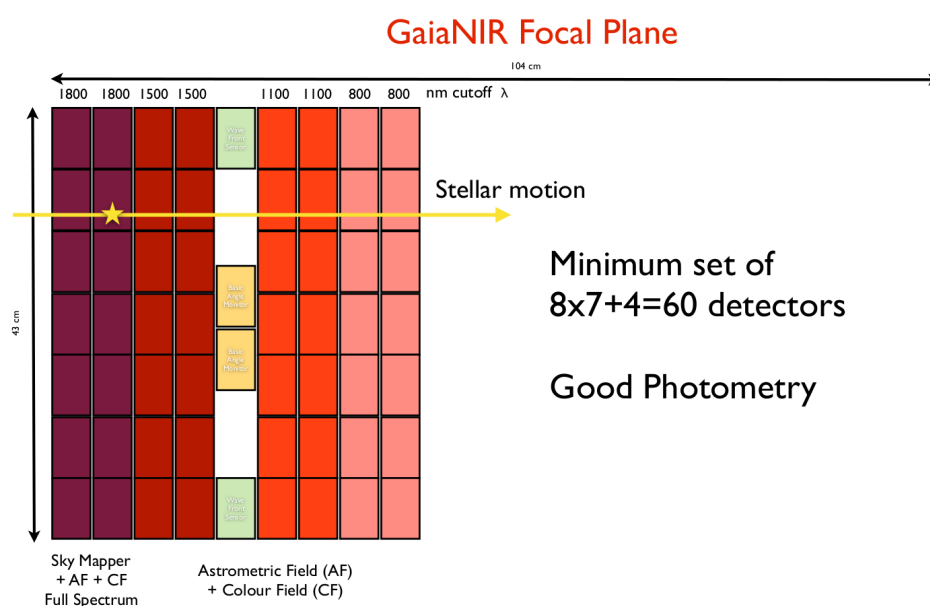


Figure 3: Overview of the minimal focal plane array design for GaiaNIR with 4 pass bands from 400 nm to the indicated cut-off wavelength. The arrowed line on top indicates the 104 cm size of the Gaia focal plane. The new design is less than half the size of Gaia's and could be expanded to include more detectors if affordable. If the cut-off wavelength is selected to be 2500 nm it would be ideal to add a fifth band of filters on the left giving 74 detectors in total.

One of the reasons e-APD arrays have matured so quickly in recent years is that they can be constructed using near-standard manufacturing processes. e-APDs offer voltage controlled gain at the point of photon absorption, electron gain values up to 1000, virtually zero power consumption, bandwidths to GHz, high stability, high uniformity, no impact on the pixel design and non-destructive readout schemes with subpixel sampling are possible with negligible added noise. Nevertheless there are still some technical challenges, namely 1) they exhibit large dark currents even at low gain while conventional HgCdTe detectors do not and 2) the visible response of the devices needs to be enhanced - normally achieved through substrate removal. It remains to be seen if these challenges can be overcome but APD development looks promising at this point.

The focal plane design used in the ESA CDF study is shown in Figure 3 and was a minimal focal

plane designed to meet the science requirements but also to reduce the costs given that the new detectors were expected to be more expensive than the 'conventional' CCDs used for Gaia. Crucial differences between the GaiaNIR focal plane and Gaia's are that:

1. The sky mapper field has been removed and dissemination between the two fields-of-view (FoVs) will be done by on-board tracking of the motions of stars (which are different) for each FoV across the focal plane.
2. The photometric and astrometric FoV are combined into a single field.
3. The radial-velocity spectrometer is removed and not considered necessary given the large number of planned ground based surveys.

The design consisted of 60 NIR detectors, arranged in 7 along-scan rows and 9 across-scan strips (8 are for the astrometric/photometric field, the other is used for monitoring purposes), divided into 4 photometric fields each with different upper cut-off wavelengths. The design can easily be extended to 2500 nm by adding one extra photometric field. Stars enter the focal plane from both FoV on the left and will move in slightly different directions depending on the which FoV they originate from, on-board software can then anticipate their motion across the rest of the focal plane. The leftmost photometric band is the broadest to detect all stars and subsequent bands are narrower. Spectral filtering can be achieved by depositing filter material directly on the detectors which is a relatively new technique to simplify the optics and reduce costs.

4. SO WHAT DO WE DO?

The study by ESA in 2017 concluded that the GaiaNIR mission would be Large-class (L-class) even after reducing costs. However to enhance our chances of being selected we need to fit in the M-class cost category for ESA. This can only be achieved by attracting external partners who could help fund the project (US, Japan, Australia, etc. have indicated interest) and we plan to intensify our efforts in this direction in the coming years.

We are currently closely following the SAPHIRA e-APD being developed by Leonardo MW Ltd. (see Gilbert, *et al.*, 2019). On-sky performance has been demonstrated in imaging mode a number of times and early success with one such system at the Australian National University (ANU) has led to a space-based TDI mission for astronomy. The Emu mission will demonstrate space-flight readiness for SAPHIRA with a ~ 100 mm telescope deployed on the International Space Station (ISS) which mitigates many of the technical hurdles associated with deploying small payloads, instead focusing on technology demonstration. A prototype system was successfully demonstrated on-sky in April 2019. While the current generation SAPHIRA e-APD has only a modest scale (320x256 pixels, but with a high pixel operability, approaching 100%), a number of active collaborations are underway to deliver large format (1kx1k) devices more relevant for the extended focal plane mosaics typically needed for large survey missions. ESA have recently issued tenders for the development of 2kx2k APD devices and it is this large format that would be suitable for our mission.

5. REFERENCES

- Hobbs, D., *et al.*, 2019a, ESA, Voyage 2050 White Paper, arXiv:1907.12535.
Hobbs, D., *et al.*, 2016, Response to ESA's call for new "Science Ideas", arXiv:1609.07325.
Hobbs, D., *et al.*, 2019b, NAS Astro2020 Decadal Survey APC White Paper, arXiv:1907.05191.
McArthur, B., *et al.*, 2019, NAS Astro2020 Decadal Survey White Paper, arXiv:1904.08836.
Gilbert, J., *et al.*, 2019, 70th International Astronautical Congress, Washington D.C., arXiv:1911.04684.

GAIA-VLBI: PHASE-REFERENCING CONTINUUM EMISSION OBSERVATIONS OF OPTICALLY BRIGHT STARS WITH THE VLBA (PLANNED PROPOSAL)

S. LUNZ¹, R. HEINKELMANN¹, J. ANDERSON², M. JOHNSON³, A. FEY³, O. TITOV⁴

¹ GFZ German Research Centre for Geosciences - Germany - susanne.lunz@gfz-potsdam.de, robert.heinkelman@gfz-potsdam.de

² Technische Universität Berlin - Germany - james.anderson@gfz-potsdam.de

³ USNO United States Naval Observatory - USA - megan.johnson@navy.mil, alan.fey@navy.mil

⁴ Geoscience Australia - Australia - oleg.titov@ga.gov.au

ABSTRACT. For independent verification of the global orientation and spin of optically bright objects obtained from the Gaia mission, positional VLBI observations of radio stars are identified as being the most precise technique for the upcoming data releases (Lindgren, 2019). Here, we propose three radio star surveys in the continuum emission phase-referencing mode with the VLBA for the (re-)detection of stars with promising characteristics for the VLBI-Gaia link to meet the demand of more VLBI data for this task. In the first proposal we revisit stars that have been detected by continuum VLBI/VLA observations in the past. To optimize the sky distribution we plan to find new radio stars in the second and third proposal, either by searching for radio emission of suitable nearby single stars that have never been observed at radio wavelengths before or by observing stars that already have detected radio emission.

1. NECESSITY OF NEW VLBI-OBSERVATIONS OF RADIO STARS IN THE VIEW OF GAIA

Gaia's ability to determine an accurate optical frame and a distance scale is important for many scientific topics, such as the study of star and Galaxy kinematics, better calibration of the cosmic distance ladder and constraining physical properties of a wide range of celestial objects. Since satellite navigation systems, such as GPS, are not available beyond the immediate vicinity of the Earth, the Gaia catalog will play a key role in the navigation and attitude control of spacecraft in the future. The Gaia data already outperform any other optical realization today and will most likely remain the most accurate source for optical positions for several decades in the future. Verifying Gaia's orientation and spin accuracy, especially for the optically bright objects, is essential for high-precision astro-navigation and orientation, particularly in the post-mission period when spin and proper motion errors dominate the position errors. Gaia Data Release 2 (DR2, Gaia Collaboration et al. (2018)) comprises around 1.7 billion objects gathered during the first 22 months of Gaia's operational phase. For astrometry, it provides an independent reference frame with an accuracy that is comparable to the Third International Celestial Reference Frame (ICRF3, Charlot et al. (2018)) derived from geodetic VLBI measurements of extragalactic radio sources, providing a unique historical opportunity to identify systematics in both measurement techniques as well as to study scientific subjects including frequency-dependent time varying core-shifts using common objects.

The orientation of Gaia DR2 is tied to the radio frame through quasars. The orientation was constrained to the ICRF3 prototype whereas the spin parameters were constrained to the ICRF3 prototype and AllWISE data of quasars (Secrest et al., 2015), as described in Gaia Collaboration et al. (2018). In terms of calibration, Gaia data are separated into several magnitude dependent parts

due to instrumental reasons (Lindegren et al., 2018). The faint part of the Gaia reference frame behaves as expected in both orientation and spin when validating it against external data (Lindegren et al., 2018). For the verification of the orientation and spin of the bright (<13 mag) Gaia frame, stars can be used that are also visible in radio frequencies. The Gaia team used VLBI data of around 20 radio stars from the literature to verify the orientation, but because of the sparseness of the data, the large epoch differences and the non-linear motions of many of the stars the orientation could not be determined sufficiently well (Lindegren et al., 2018). Clearly, systematic errors in individual objects as well as in the measurement techniques are limiting the ability to determine an accurate tie. In contrast, the spin of the bright reference frame was calculated from proper motion differences of 88,091 bright stars in DR2 and the Tycho-Gaia astrometric solution (TGAS, Lindegren et al. (2016)) in Gaia DR1 (Gaia Collaboration et al., 2016). The proper motions of DR2 were derived from the 22 months of Gaia observations only, whereas the proper motions of DR1 (TGAS) were computed with the help of Hipparcos positions of stars at epoch 1991.25, a time span of about 24 years. The spin shows a significant deviation from the spin calculated from data of fainter objects of about 0.15 mas/yr, and thus disagrees at more than a 5 sigma significance (see Figure 4 in Lindegren et al. (2018)). The spin difference results not from bad data in DR1 (TGAS), but instead from DR2, due to uncalibrated instrumental effects on proper motions of bright objects. These could be effects in the gated observations or the observations of window class 0, which are also clearly related to the dependence of the change of difference in parallax as a function of magnitude (Lindegren et al., 2018). In future Gaia DRs, analysis methods will be used that should minimize the difference between the bright and faint frame. The improved positions, parallaxes and proper motions expected for subsequent Gaia DRs will not be comparable to Hipparcos data in terms of accuracy anymore. Then, only VLBI measurements will provide sufficient accuracy to enable the verification of future Gaia DRs.

Unfortunately VLBI data of radio stars are sparse till today and more observations would be very beneficial for this task. The effect of more VLBI data was studied by Lindegren (2019). Using only VLBI data, he simultaneously estimated six spin and orientation parameters from VLBI and Gaia data of 26 best fitting stars, also based on single-epoch measurements. The calculations resulted in a similar rotation of the bright reference frame at a rate of 0.1 mas/yr relative to the faint reference frame. Still, one of the limitations of his calculations is the sparseness of available VLBI observations of (suitable) radio stars. Also the resulting orientation parameters are biased by the heterogeneous sky distribution of the stars observed in more recent years, as their data contribute most to these parameters.

Lindegren (2019) shows, that new single-epoch measurements of positions of the best fitting stars will most of all improve the determination of spin parameters, if they are taken in later years (rather in 2030 than in 2020). From our point of view, taking measurements now can already improve and validate earlier data releases, and thus will be valuable for the scientific community right away. His study also shows that the error of spin parameters significantly decreases with subsequent Gaia data releases even without additional VLBI observations, which is due to smaller uncertainties in the Gaia proper motions due to a longer time span of available observations, whereas for the orientation new VLBI data will present a significant improvement for current and later Gaia data releases. We propose three approaches to fulfill the various needs of new radio star observations.

2. PLANNED PROPOSALS

Our proposals are planned to be observed with the VLBA network. All stars for proposed observations are within its declination limit and are optically brighter than 13 mag, as required for the bright Gaia frame. The sky coverage for the various proposals is shown in Figure 1 and the respective brightness histograms in Figure 2. The selected stars are well represented in Gaia

data having a full valid 5-parameter solution in DR2 if not stated otherwise. In addition, they show a good fit to a single star model from this data, which is expressed by parameter RUWE (re-normalized unit weight error, calculated from Gaia DR2 data, Lindegren (2018)) being smaller than 1.4, which indicates that they are not resolved as binary stars in Gaia DR2. The stars were additionally selected to provide a good sky coverage, i.e., in areas with many stars we selected only the radio-brightest ones.

2.1 Re-observation of already known radio stars

A re-observation of radio stars that have already been observed by VLBI not only has the advantage to get refined proper motions and parallaxes as well as positions during the observation time of Gaia with few input of new observing time, but also a high probability of successful detection. The optically bright stars are highly variable and faint in radio frequencies if compared to extragalactic radio sources that are usually used for geodetic VLBI. For this proposal, we excluded stars with radio spectral-line observations, since we want to focus on continuum emission only. We further consider the suitable spectral types for the link between optical and radio frequencies. This leads to main sequence stars with the exception of stars of type O and B, since the probability of radio-optical offsets is higher for these types due to stellar winds and complex structures, as well as to the exclusion of M and L type stars due to the higher possibility of resolved binaries in VLBI observations. As recommended by Lindegren (2019), they are neither Mira type nor red supergiants. We took the information of spectral classes from the SIMBAD database (Wenger et al., 2000).

The final selection of 46 stars consists of seventeen stars that are from the list of recommended candidates for Gaia-VLBI link by Lindegren (2019). Four of them are of spectral type O or B but they are still selected because they fit a single-star model well and thus a higher priority was given to the precious longer data set that is available when combining the new data with data from the archive. One of the 17 stars (V2248 Oph) is known to be a triple star system, but shows a low discrepancy between VLBI and Gaia. More observations are useful for an enhanced study of the VLBI and Gaia offset for this object. With a view to future Gaia DRs and the availability of orbits for some objects as well as the verification of these orbits, four additional stars were selected which show the probability of a binary companion but are promising for orbital modeling. Two more stars were selected from the list of Xu et al. (2019). One of them, β Per, was chosen because it is the only one of the eleven link stars for the Hipparcos mission that was not yet in the selected sample. This is because it does not have a full astrometry solution in DR2 yet. We made an exception for this star and took it into our selection of stars to be observed, because again, new observations for this star would provide a long positional time series when combined with the observations from the 1980s and 1990s, and in addition we will be able to do tests using the same set of stars as for Hipparcos comparisons. It is a future task to look for more possible candidate stars for the Gaia/VLBI link that have extensive VLBI observation history and were detected by Gaia but do not have a full astrometric solution in DR2 yet. Using the same general approach, we additionally selected 23 radio stars of Boboltz et al. (2003) and Boboltz et al. (2007), who did phase-referenced continuum observations in X-band of in total 52 radio stars for the Hipparcos CRF link using the VLA and Pie Town telescopes.

2.2 Detection of nearby stars

Our second proposal aims to increase the number of radio-optical counterparts in order to improve the sky distribution. We selected optically-bright stars that are both in Hipparcos and Gaia DR2 subsets, in order to have a good chance of accurate Gaia data at the end of the mission. We excluded stars that were identified as double or multiple star systems by Hipparcos. We further filtered for main sequence stars that are of suitable spectral types using data from SIMBAD. From the r-squared law, we assume that the nearest such stars would be the brightest, so if these stars

produce any significant radio emission, the nearest would be the best objects to observe. Our final selection contains stars that are within 20 pc of the Earth.

It consists of 102 stars that to our knowledge have not been observed by VLBI yet. The set was chosen to provide a rather uniform sky coverage and a variety of spectral classes that are most suitable for the tie (see Figure 3).

2.3 VLBI-observation of previously detected stars

The third proposal aims to re-observe stars that have already been detected by continuum radio observations in the past. The catalog of Wendker (2015), a collection of radio detections until the late 1990s, was used to find promising objects for re-observation with the VLBA. The 75 selected stars were detected with a minimum flux density of 0.5 mJy in a frequency range from 1 to 100 GHz. We chose a somewhat lower detection limit than our observations will allow, since we assume that variability in the brightness of the stars can be great, and therefore we do not want to exclude a star prematurely. Also, we assume that the possibility of detection does not vary dramatically within the frequency range. The stars have not been observed in phase-referencing mode before. Therefore, there is no overlap with proposal 1. We prioritized the non-binarity and higher number of possible new candidates for a successful search survey, which is why the proposed candidates can belong to various spectral classes as seen in Figure 3. It is certainly possible to filter for preferred spectral classes, if desired.

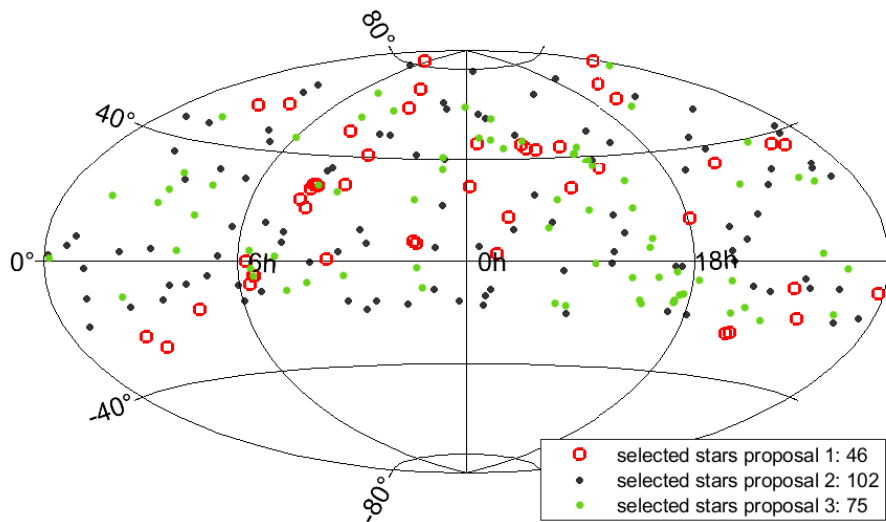


Figure 1: Stars selected for observations with color-coding according to the type of proposal.

3. SUMMARY

VLBI observations of optically bright radio stars will be the only method to improve the validation of the orientation and spin of the Gaia bright reference frame in future Gaia DRs. So far there are too few observations for this purpose, and the sky distribution of these is not homogeneous enough to get sufficient results. We present three different strategies for observations to improve the determination of the spin as well as the orientation parameters using the VLBA network. It is clearly promising to re-observe already known radio stars and to make use of longer observation intervals by adding data from the archive for improved estimates of the star's parameters. But this is not enough for the precise alignment in both orientation and spin, because there are not enough

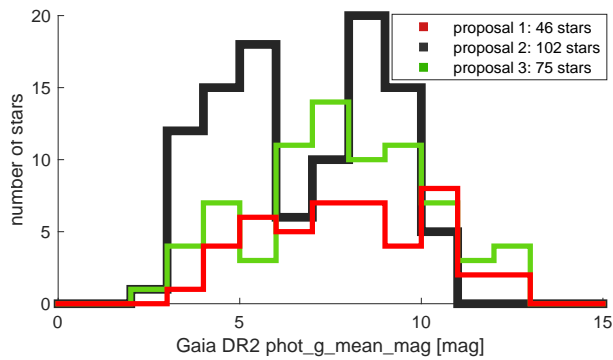


Figure 2: Histogram of G-magnitude of the stars selected for the observations.

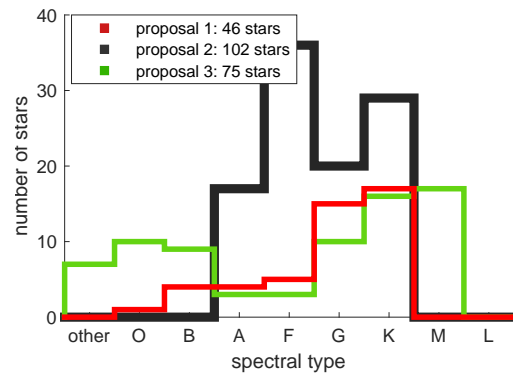


Figure 3: Histogram of the spectral types of the stars selected for the observations. For proposal 3, a stricter selection for the most suitable spectral types would be possible.

suitable stars known yet, as discussed in Lindegren (2019). Therefore, radio stars have to be found which have not been observed by VLBI in the past. We offer two approaches for a selection of suitable candidates to be observed.

For each of the proposals, we would like to conduct a search survey to find stars that are visible for the VLBA in phase-referencing mode. In a second step, more observations need to be carried out to get precise positions, proper motions and parallax for those objects which could be detected in the surveys. In addition, precious data from the archive should get collected and re-processed if necessary.

This project is supported by the DFG grant (HE5937/2-2). This work has made use of the data from the European Space Agency (ESA) mission Gaia processed by the Gaia Data Processing and Analysis Consortium as well as from the mission HIPPARCOS. Funding for the DPAC has been provided by national institutions, in particular the institutions participating in the Gaia Multilateral Agreement. This research has made use of the VizieR catalogue access tool, CDS, Strasbourg, France and the SIMBAD database, operated at CDS, Strasbourg, France.

4. REFERENCES

- Boboltz et al., 2003, “Astrometric Positions and Proper Motions of 19 Radio Stars”, *AJ* 126, 484.
- Boboltz et al., 2007, “Very Large Array plus Pie Town Astrometry of 46 Radio Stars”, *AJ* 133, pp. 906–916.
- Charlot et al., 2020, “The Third Realization of the International Celestial Reference Frame by Very Long Baseline Interferometry”, *A&A*, doi: 10.1051/0004-6361/202038368.
- Gaia Collaboration, Brown, A.G.A. et al., 2016, “Gaia Data Release 1. Summary of the astrometric, photometric, and survey properties”, *A&A* 595, A2.
- Gaia Collaboration, Brown, A.G.A., et al., 2018, “Gaia Data Release 2. Summary of the contents and survey properties”, *A&A* b16, A1.
- Gaia Collaboration, Mignard, F., et al., 2018, “Gaia Data Release 2. The celestial reference frame (Gaia-CRF2)”, *A&A* 616, A14.
- Lindegren et al., 2016, “Gaia Data Release 1. Astrometry: one billion positions, two million proper motions and parallaxes”, *A&A* 595, A4.
- Lindegren et al., 2018, “Gaia Data Release 2. The astrometric solution”, *A&A* 616, A2.

- Lindegren, 2020, "The Gaia reference frame for bright sources examined using VLBI observations of radio stars", *A&A* 633, A1.
- Secret, N. J., Dudik, R. P., Dorland, B. N., et al., 2015, "Identification of 1.4 Million Active Galactic Nuclei in the Mid-Infrared using WISE Data", *ApJS*, 221, 12.
- Wendker, 2015, "VizieR Online Data Catalog: Catalogue of Radio Stars (Wendker, 2001)".
- Wenger et al., 2000, "The SIMBAD astronomical database", *A&AS* 143, 9.
- Xu et al., 2019, "Comparison of Gaia DR2 Parallaxes of Stars with VLBI Astrometry", *ApJ* 875, 114.

SPHERICAL RECTANGULAR EQUAL-AREA GRID (SREAG)—SOME FEATURES

Z. MALKIN

Pulkovo Observatory - Russia - malkin@gaoran.ru

ABSTRACT. A new method Spherical Rectangular Equal-Area Grid (SREAG) was proposed in Malkin (2019) for splitting spherical surface into equal-area rectangular cells. In this work, some more detailed features of SREAG are presented. The maximum number of rings that can be achieved with SREAG for coding with 32-bit integer is $N_{ring}=41068$, which corresponds to the finest resolution of $\sim 16''$. Computational precision of the SREAG is tested. The worst level of precision is $7 \cdot 10^{-12}$ for large N_{ring} . Simple expressions were derived to calculate the number of rings for the desired number of cells and for the required resolution.

1. INTRODUCTION

A new approach to pixelization of a spherical surface Spherical Rectangular Equal-Area Grid (SREAG) was proposed in Malkin (2019). It is aimed at constructing of a grid that best satisfies the following properties:

1. it consists of rectangular cells with the boundaries oriented along the latitudinal and longitudinal circles;
2. it has uniform cell area over the sphere;
3. it has uniform width of the latitudinal rings;
4. it has near-square cells in the equatorial rings;
5. it allows simple realization of basic functions such as computation of the cell number given object position, and computation of the cell center coordinates given the cell number.

In this paper, some more details of the SREAG pixelization method are discussed in addition to Malkin (2019).

2. SREAG METHOD

Let's briefly repeat the description of the SREAG pixelization method presented in Malkin (2019). The basic parameter of this method is the number of rings N_{ring} , which must be an even number. The sphere is first split into latitudinal N_{ring} rings of constant width $dB = 180^\circ/N_{ring}$. Then each ring is split into several cells of equal size. The longitudinal span of cells in each ring is computed as $dL_i = dB \sec b_0^i$, where i is the ring number, and b_0^i is the central latitude of the ring. This provides near-square cells in the equatorial rings. Then the number of cells in each ring equal to $360/dL_i$ is rounded to the nearest integer value. This procedure results in the initial grid. In fact, only the total number of cells in the grid, N_{cell} , and the number of cells in each ring are used in the final grid construction. Given N_{cell} , we can compute the area of each cell $A = 4\pi/N_{cell}$.

Then the latitudinal boundaries of the rings are to be adjusted as follows. Let us start from the North pole. Let b^u be the upper (closer to the pole) boundary of the ring in the final grid, and b^l be the lower boundary. Then, taking into account that the cell area is $A = dL * (\sin b^u - \sin b^l)$, the simple loop will allow to compute all the final ring boundaries (Malkin, 2019):

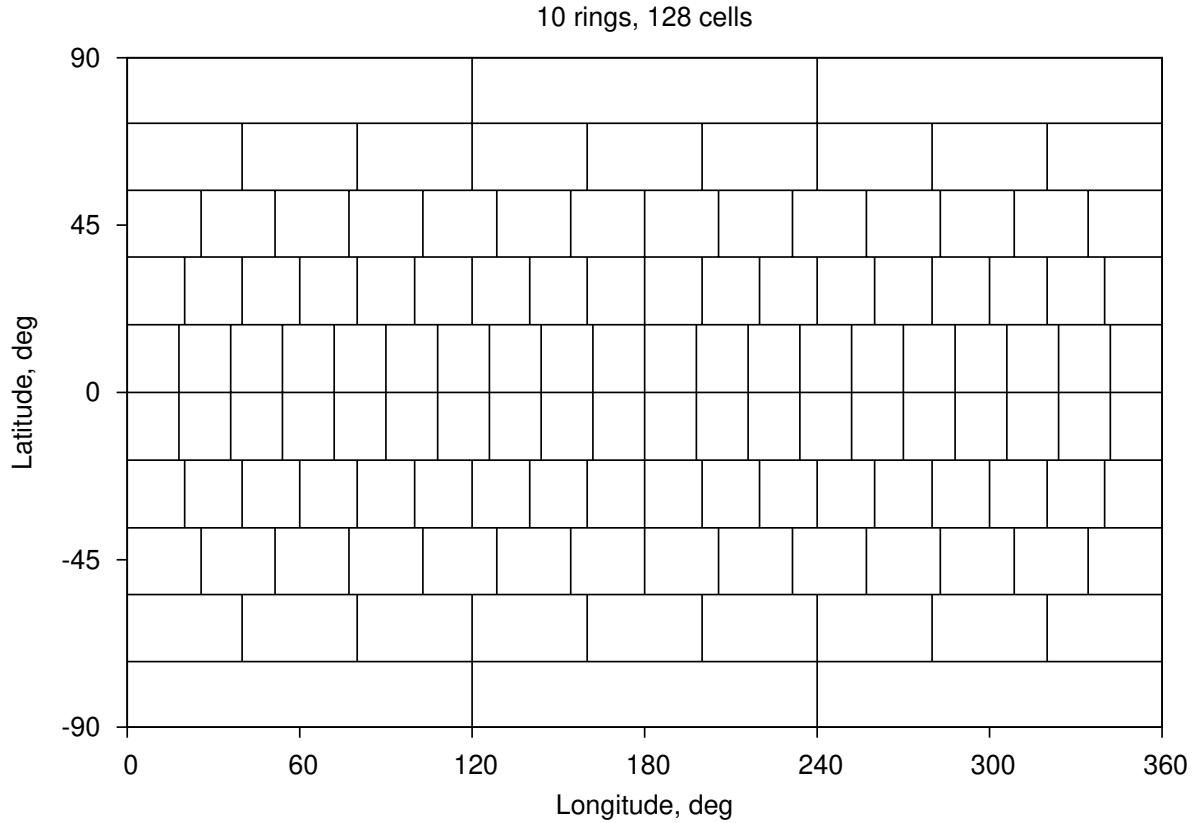


Figure 1: Example: 10-ring SREAG grid.

```

 $b_1^u = \pi/2$ 
do i=1,  $N_{ring}/2$ 
   $b_i^l = \arcsin(\sin b_i^u - A/dL_i)$ 
   $b_{i+1}^u = b_i^l$ 
end do

```

The last value $b_{N_{ring}/2}^l$ corresponds to the equator and therefore must be equal to zero, which verifies the correctness of the computation. The latitudinal boundaries for the rings in the South hemisphere are just copied from the North hemisphere with negative sign. Figure 1 presents an examples of grids constructed making use of the proposed method. Figure 2 shows the precision of the computation, which is determined by the deviation of the absolute value of the computed equatorial latitude $b_{N_{ring}/2}^l$ from zero.

The number of cells in the grid depending on N_{ring} is shown in Figure 3. For 32-bit integer, maximum available N_{ring} is 41068, which corresponds to $N_{cell} = 2'147'421'180$. A larger N_{ring} corresponds to N_{cell} larger than $2^{31}-1=2'147'483'647$, the maximum value for a 32-bit signed integer. This limitation can be extended using a 64-bit integer.

Thus, the SREAG method provides detailed choice of the grid resolutions to satisfy a wide range of user requirements. For $N_{ring} = 4 \dots 41068$ grid resolution varies from $\sim 45^\circ$ to $\sim 16''$ (Figure 4). Analysis of the literature showed that the resolution used in practice lies in the range 7.3° to $26''$, which is fully covered by the SREAG resolution range.

If one starts with the desired N_{cell} , one can easily calculate the corresponding number of rings by $N'_{ring} = 0.886227 \sqrt{N_{cell}}$ with further rounding the result to the nearest even integer.

Another simple but accurate expression allows to approximate the grid resolution (in arcmin) as $10800/N_{ring}$ and thus obtain the required number of rings to provide the desired resolution.

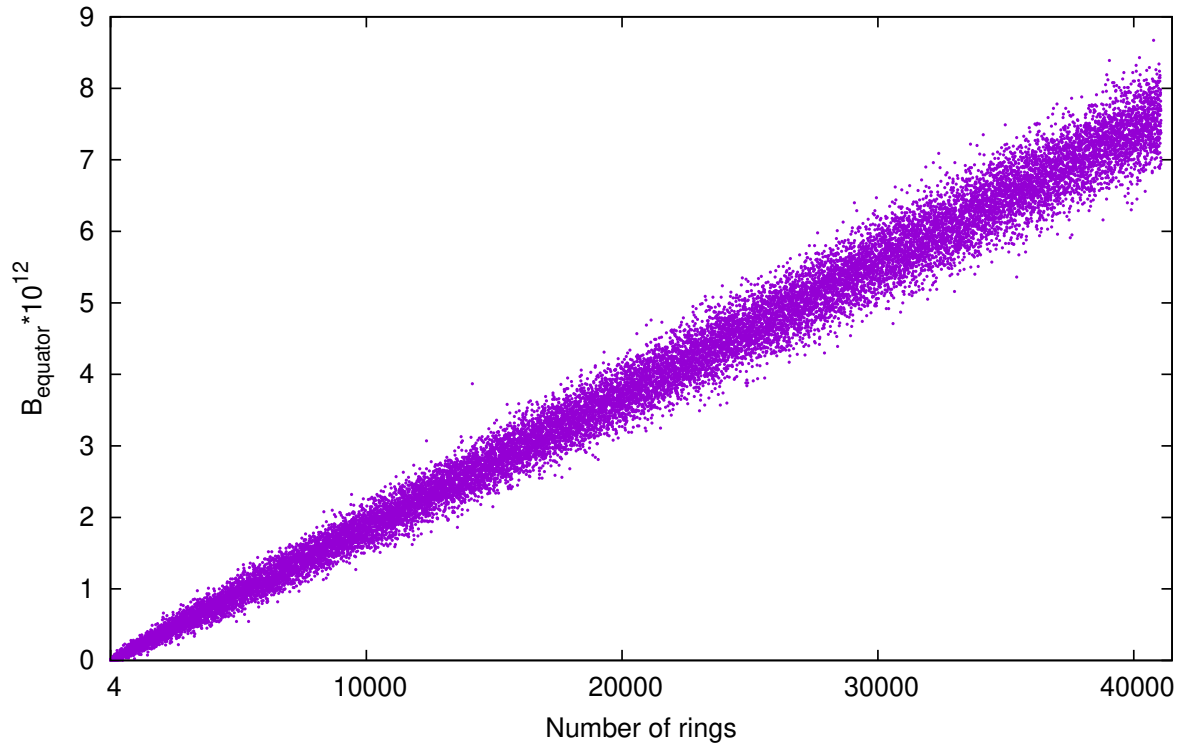


Figure 2: Computational precision (see text for explanation).

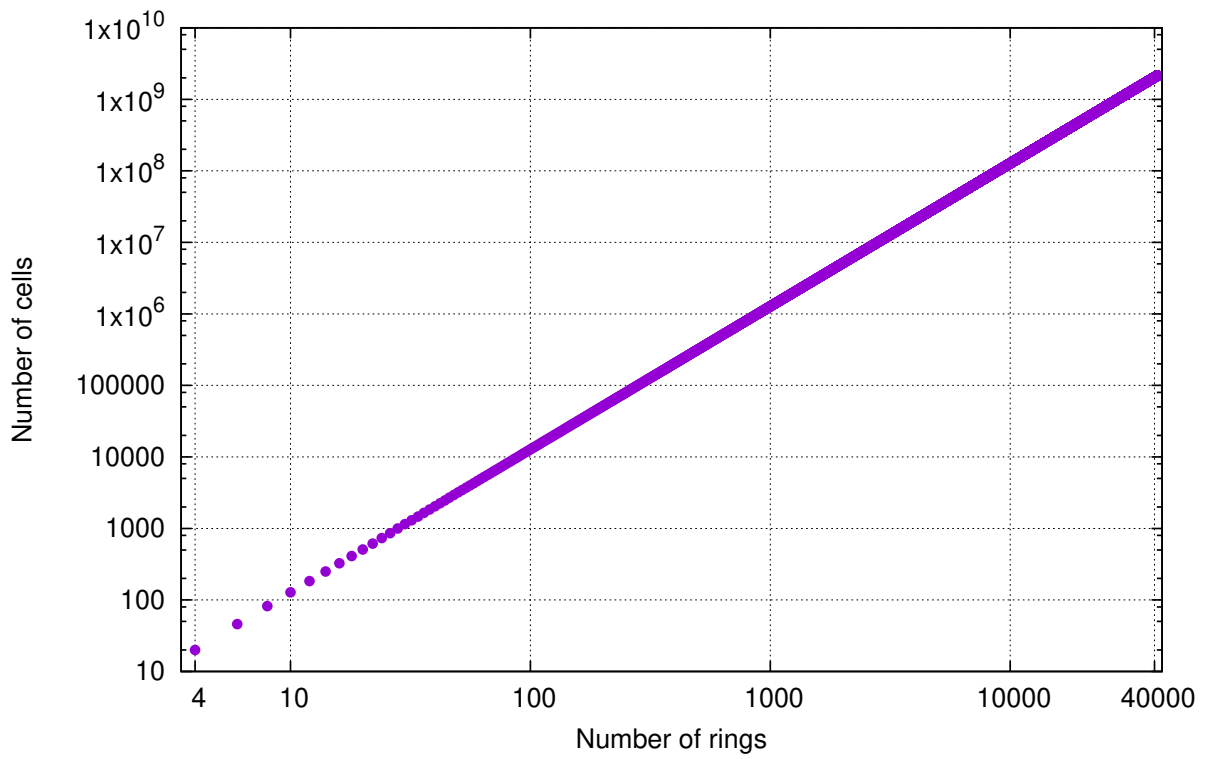


Figure 3: The number of cells in the grid as function of N_{ring} .

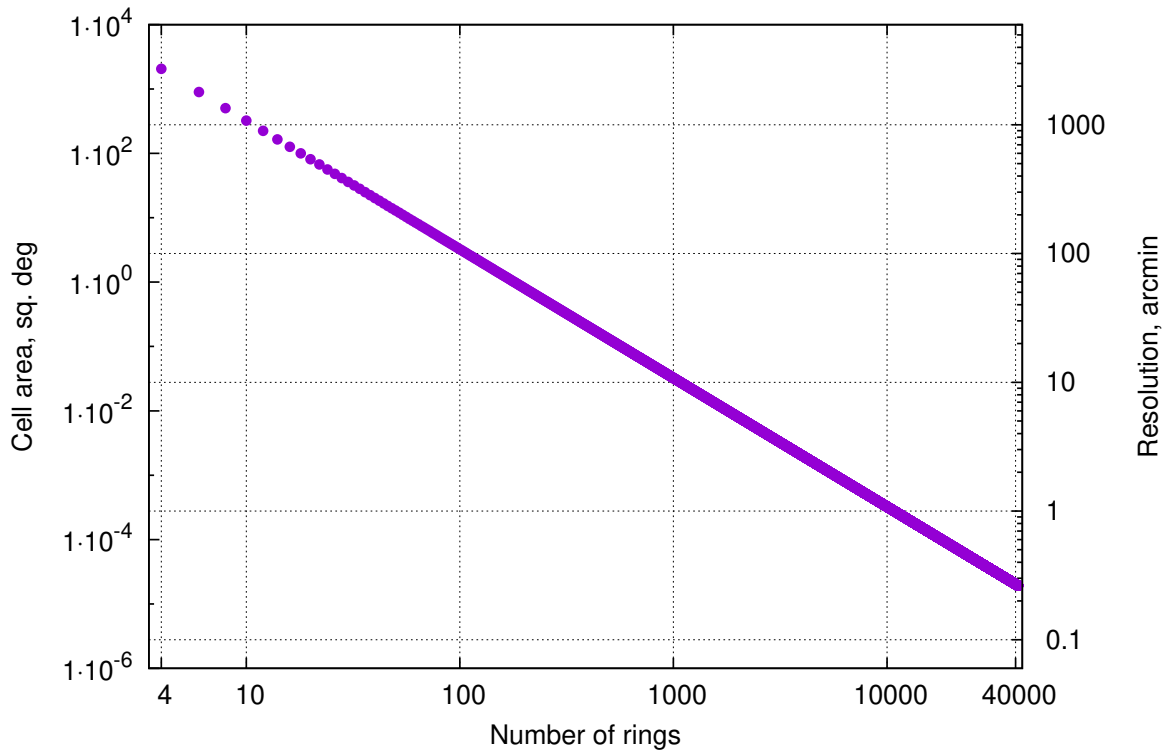


Figure 4: Cell area and grid resolution.

3. CONCLUSION

The new method SREAG is developed for subdividing a spherical surface into equal-area cells. The main features of the proposed approach are:

- it provides an isolatitudinal rectangular grid cells with the latitude- and longitude-oriented boundaries with near-square cells in the equatorial rings;
- it provides a strictly uniform cell area;
- it provides a near-uniform ring width (although the ring width in the final grid is not strictly uniform, the deviation of the central latitude of the rings from the uniform distribution is much smaller for SREAG than for other popular pixelization methods as was shown in Malkin (2019));
- it provides a wide range of grid resolution with a possibility of detailed choice of desirable cell area;
- the binned data is easy to visualize and interpret in terms of the longitude-latitude (right ascension-declinations) rectangular coordinate system, natural for astronomy and geodesy;
- it is simple in realization and use.

Proposed approach to pixelization of a celestial or terrestrial spherical surface allows to construct a wide range of grids for analysis of both large-scale and tiny-scale structure of data given on a sphere. The number of cells is theoretically unlimited and is constrained in practice only by the precision of machine calculations.

The SREAG method can be hopefully useful for various practical applications in different research fields in astronomy, geodesy, geophysics, geoinformatics, and numerical simulation. In particular, it can be used in further analyses of the celestial reference frame, for selection of uniformly distributed reference sources in the next ICRF realizations, and for evaluation of the systematic errors of the source position catalogs.

4. SUPPORTING SOFTWARE

Several Fortran routines to perform basic operations with SREAG are provided at http://www.gaoran.ru/english/as/ac_vlbi/#SREAG. They include:

GRIDPAR.FOR	Compute parameters of the grid for a given number of rings
CELLPAR.FOR	Compute the cell parameters for a given cell number
POS2CN2.FOR	Compute the cell number for a given point position
CN2POS2.FOR	Compute the cell center coordinates for a given cell number
NR2NC.FOR	Compute the number of cells for a given number of rings
NC2NR.FOR	Compute the nearest number of rings for a given number of cells

The authors is grateful to Sergey Klioner for useful comments on the manuscript.

5. REFERENCES

Malkin, Z., 2019, "A new equal-area isolatitudinal grid on a spherical surface", AJ 158, id. 158, doi: 10.3847/1538-3881/ab3a44.

AN EXAMPLE TO ANALYZE DISCRETE VECTOR FIELDS ON THE SPHERE USING QUANTITATIVE AND QUALITATIVE METHODS

F.J. MARCO¹, M.J. MARTÍNEZ², J.A. LÓPEZ¹

¹ Universidad Jaume I. IMAC, Dept. Matemàtiques, Castellón - Spain
marco@mat.uji.es, lopez@mat.uji.es

² Universidad Politècnica de Valencia, IUMPA, Dept. Matemàtica Aplicada - Spain
mjmartin@mat.upv.es

ABSTRACT. Our aim is to compatibilize the correction of massive ground-based catalogs and the study of properties that are missed in DR2. Two advantages justify these studies. On the one hand, it is usual to suppose that in the correction process the signal and the noise are accurately detected, but this is not necessary true if the statement "with respect to me adjustment model and a precision order" is not added to the assertion. The improvement of two ground-based catalogs and their comparison may explain a common part in the residuals depending on certain physical properties. On the other hand a question arises: the observation from the Earth involves some intrinsic errors but is it possible to align them to the ICRF while conserving the above-mentioned intrinsically terrestrial properties? This is not possible, but we can seek for quantitative improvements that eliminate bias and determine qualitative properties of the residual vector field on the celestial sphere with radius r considering magnitudes and spectral types. This is applied to assign a proper motion vector field in the domain of work.

1. INITIAL STEPS

Choice of a set of stars common to the Hipparcos and the massive catalog 2MASS. Denote this set as Ω_0 . Now, we consider different properties such as the spectral type (splitting the data into a KM set and a no-KM set), H-magnitudes (splitting the data into $m_4 = [5.750, 7.153)$, $m_5 = [7.153, 8.556)$, $m_6 = [8.556, 9.959)$ and $m_7 = [9.959, 11.363)$) and also the distances assigning the data to sets, following Astraatmadja and Bailer-Jones (2016) in DR1. We can build different subsets of stars as, for instance, Ω_{KM, m_4} for KM stars with m_4 magnitude; or $\Omega_{m_5|_{r=200}}$, containing m_5 stars in the slice $[100pc, 300pc]$, for example. The intervals for r $[25pc, 200pc]$, $[100pc, 300pc]$, $[200pc, 400pc]$, are named after their "center" $r = 100, 200, 300, \dots pc$. We will denote as Ω any of these possible data work sets.

2. STEP 2: OBTENTION OF THE VECTOR FIELDS

From each set of data points Ω , we suppose a relation $Y_i = m(X_i)$ where $X_i \in \Omega$ is a random vector and we assume that:

$$m(\mathbf{X}_i) \simeq m(\mathbf{x}) + (D^1 m)_x(\mathbf{X}_i - \mathbf{x}) \quad (1)$$

with x near some X_i . We obtain the estimator for the vector field and the estimators for the first derivatives of the vector field: $\hat{m}(x)$, $\hat{m}_1(x)$, $\hat{m}_2(x)$, ... as the solution of the problem described in:

$$\begin{aligned} \{\hat{m}(x), \hat{m}_1(x), \hat{m}_2(x)\} &= \{b_{00}(\mathbf{x}), b_{11}(\mathbf{x}), b_{12}(\mathbf{x})\} = \\ &= \min_{\{b_k(x)\}} \{Y_i - b_0(\mathbf{x}) - b_{11}(\mathbf{x})(X_{i,1} - x_1) - b_{12}(\mathbf{x})(X_{i,2} - x_2)\}^2 K_{h,ix} \end{aligned}$$

$$K_{h,ix} = \frac{1}{h_1} K\left(\frac{X_{i,1} - x_1}{h_1}\right) \frac{1}{h_2} K\left(\frac{X_{i,2} - x_2}{h_2}\right) \quad (2)$$

3. STEP 3: USING VECTOR FIELDS TO OBTAIN QUANTITATIVE DATA

Suppose that the vector of the residuals is developed in vector spherical harmonics depending on r, α, δ by means of:

$$\mathbf{X}(r, \alpha, \delta) = \sum_{n, |m| \leq n} [r_{nm} \mathbf{R}_{nm} + s_{nm} \mathbf{S}_{nm} + t_{nm} \mathbf{T}_{nm}] \quad (3)$$

where $\mathbf{R}_{nm}, \mathbf{S}_{nm}, \mathbf{T}_{nm}$ are the vectors (orthogonal and complete system of the functions with integrable square in the sphere of radius r) whose coefficients represent the radial, spheroidal and toroidal parts, respectively of the field \mathbf{X} . These vectors are given by the expressions:

$$\mathbf{R}_{nm} = Y_{nm} \mathbf{r}, \mathbf{S}_{nm} = r \nabla Y_{nm}, \mathbf{T}_{nm} = -\mathbf{r} \times \nabla Y_{nm} \quad (4)$$

Using inner product $\langle \cdot, \cdot \rangle$ in the Hilbert Space of the spherical S^2 -vector, the coefficient for the normalized basis vector ϕ_k , are $\alpha_k = \langle \hat{m}, \phi_k \rangle$. In Marco et al (2019) one can see an exhaustive set of coefficients of developments for each set Ω . There, it can be observed that the values of the obtained parameters and their evolution (in the distance) depend on both magnitudes and spectral types, so that the corrections must be more specific than what is usually considered. This step, in itself, was qualitatively and quantitatively finer and more precise than other more usual procedures.

4. STEP 4: USING VECTOR FIELDS TO OBTAIN QUALITATIVE DATA

Before applying any correction (which is in J2000), we study stars where (or very close where) the residual field is singular and, in addition, the rotational component of the field is irrelevant. These points have the particularity of being maximum or minimum of the function of magnitude VT of Tycho, used in the reduction of the 2MASS. Note that from Helmholtz decomposition, a vector field is split into two components (rotational and irrotational) by means of $\vec{X} = \nabla \phi + \vec{\nabla} \times \vec{u}$ where X is an spherical vector field. Taking divergence operator, we deduce the relation $div \vec{X} = \Delta \phi$ and assuming $\phi(\alpha, \delta) = \sum_{n,m} a_{nm} Y_{nm}(\alpha, \delta)$, from the application of properties of the Laplace-Beltrami operator we deduce:

$$\Delta \phi = \sum_{n,m} a_{nm} \Delta Y_{nm} = \sum_{n,m} [-n(n+1) a_{nm}] Y_{nm} \quad (5)$$

where

$$a_{nm} = -\frac{1}{n(n+1)} \frac{\langle \Delta \phi, Y_{nm} \rangle}{\langle Y_{nm}, Y_{nm} \rangle} \quad (6)$$

We show here only two examples of singular points of the vector field near singular points of the potential (see Figures 1 and 2). For more examples, see the above mentioned paper.

5. CONCLUSION

Returning to the text of the Abstract, after the correction process, we obtain the possibility of exploring the aforementioned "second advantage". On the other hand, regarding the "first advantage: both "ground based" catalogs will be improved using Hipparcos2 so that by comparing two improved catalogs with each other, we can launch the hypothesis that the Hipparcos effect has only affected the improvement and not the residual component related to the "Earth-observed"

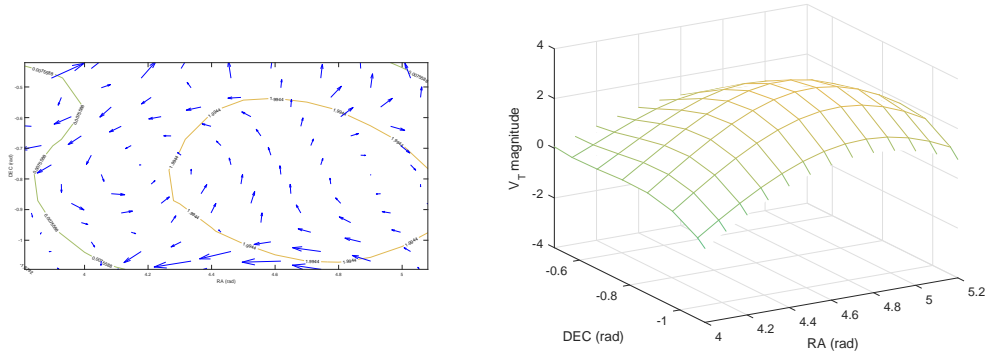


Figure 1: Slice 25-200. Area III, $KM - m_5$, Shrink (1.6,1); On the left, the potential vector field. On the right, the corresponding V_T surfaces.

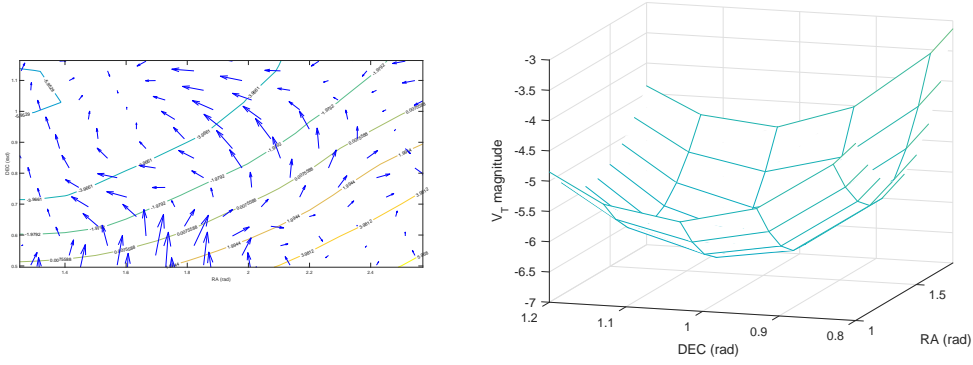


Figure 2: Slice 25-200. Up, Area I, $KM - m_4$, Source (4.9,-0.8); On the left, the potential vector field. On the right, the corresponding V_T surfaces.

Table 1: Comparison between the proper motions from DR1, PMA and our obtained results for some stars in the neighborhood of some singular points of their vector field. Hip stands for the number of the star in the Hipparcos catalogue, DR1 for the DR1 identifier. Subindex (1) means *DR1* and (2) means *PMA*. The proper motions are given in *mas*, being the last two columns $\Delta\mu_\alpha^*$ & $\Delta\mu_\delta$ our obtained results.

Hip	DR1	$\alpha_{(1)}$	$\delta_{(1)}$	$\Delta\mu_{\alpha(1)}^*$	$\Delta\mu_{\delta(1)}$	$\Delta\mu_{\alpha(2)}^*$	$\Delta\mu_{\delta(2)}$	$\Delta\mu_\alpha^*$	$\Delta\mu_\delta$
28951	1008018207212849024	91.6628127275	63.4538738263	-35.558	8.594	-34.73	21.84	-36.35	21.33
30031	998050069154382592	94.7912065760	56.5264619828	-37.640	-31.332	-	-	-39.10	-31.05
24771	188796557490084480	79.6695937289	-32.3228506874	4.963	-13.891	3.08	-20.75	4.47	-23.68
27047	4756115082715073920	86.0379453784	-65.1018594755	-2.259	21.541	-4.01	26.0	-2.24	27.01
23865	279443525899748352	76.9426318743	55.7590984639	26.115	-14.343	22.01	-16.58	29.28	-21.70
89345	6721441368029854976	273.4528707722	-43.2043919512	-9.007	-13.989	-8.55	-17.27	-9.91	-18.69
44931	3841861165533628672	137.2857737710	-1.5880525106	-27.981	-35.349	-28.80	-45.08	-23.34	-43.16
23863	279443525899748352	76.9426318743	55.7590984639	26.115	-14.3434	22.01	-16.58	28.47	-22.17

character of both catalogs that may remain. Extension to Tycho-2 stars must be performed preserving the Hipparcos-2 corrections.

4. REFERENCES

The 2MASS All-Sky Catalog of Point Sources: <http://cdsarc.u-strasbg.fr/viz-bin/cat/II/246>.

Astraatmadja, Tri I. and Bailer-Jones, A.L., 2016."Estimating distances from parallaxes. III. Distances of two million stars in the Gaia DR1 Catalogue". The Astrophysical Journal 833(1), p. 119.

Gaia Data Release 1: <https://www.cosmos.esa.int/web/Gaia/dr1>.

Hipparcos-2 Catalogue: <https://www.cosmos.esa.int/web/Hipparcos/Hipparcos-2>.

F.J. Marco Castillo, M.J. Martínez Usó, J.A. López Ortí, 2019, "Global and Local Three-dimensional Studies of The Residual Vector Field from 2MASS and Hipparcos-2 Catalog", Publications of the Astronomical Society of the Pacific.

PMA Catalogue : I/341 : <http://cdsarc.u-strasbg.fr/viz-bin/cat/I/341>.

Session II

EARTH ROTATION AND GEODYNAMICS

1. OBSERVATIONS AND ANALYSIS

THE IAU COMMISSION “EARTH ROTATION” AND THE IAU DEFINITION OF THE POLE AND UT1

N. CAPITAIN^{1,2}

¹ SYRTE, Observatoire de Paris- Université PSL, CNRS, Sorbonne Université - France

² Bureau des longitudes - France - nicole.capitaine@obspm.fr

ABSTRACT. During the period 1964-2019, a number of IAU/IUGG resolutions on reference systems have introduced improved definitions and concepts concerning the Earth’s rotation. The aim of this presentation is to report on the successive improvements of the IAU definition of the pole and UT1 and on the role of IAU Commission 19 and the IERS in this evolution. This presentation is part of the session on “The 100-year history of the IAU Commission 19/A2”.

INTRODUCTION

The Earth’s orientation in space is traditionally represented by five Earth orientation parameters (EOP), which provide the direction of the pole in the International terrestrial reference system (ITRS) due to polar motion, the direction of the pole in the Geocentric celestial reference system (GCRS) due to precession-nutation, and the variations in the Earths diurnal rotation based on Universal Time, UT1. At the occasion of the centenary of IAU Commission 19 “Earth Rotation”, this presentation recalls the evolution during the latest fifty five years regarding 1. the definition of the pole and 2. the definition of UT1, which have been regularly discussed and updated within several IAU Working Groups, meetings and resolutions during that period.

1. THE DEFINITION OF THE POLE

1.1 Relationships between various reference axes: Poincot representation

Different axes (and the corresponding poles) are considered in the Earth’s precession-nutation theory: the axis of figure, \vec{C} , the axis of angular momentum, \vec{H} , the instantaneous axis of rotation, $\vec{\Omega}$, and the axis of the ecliptic, \vec{Z} , ϵ being the obliquity of the ecliptic. In the case of a rigid Earth, according to Poincot’s representation, $\vec{\Omega}$ undergoes the following motions:

(a) The free *Eulerian motion* within the Earth (around \vec{C}), known as *polar motion* (PM) and its corresponding diurnal motion (i.e. the *sway*) in space around \vec{H} ,

(b) The forced precession-nutation (PN) in space around \vec{Z} and its corresponding retrograde nearly diurnal motion within the Earth, known as *diurnal nutation* or *forced diurnal polar motion*.

The differences between the forced motions of \vec{C} and \vec{H} (or $\vec{\Omega}$), are called *Oppolzer terms* (see Fig. 1, Woolard 1953); they are responsible for corresponding (dynamical) *variations of latitude* in the astronomically observed values (see Fig. 2, Fedorov 1963).

Referring to $\vec{\Omega}$ or \vec{H} separates the forced motion in the GCRS into two parts: the celestial part (PN) and the terrestrial part (diurnal nutation), corresponding to Oppolzer terms in space.

1.2 IAU discussion/recommendations on the reference pole: 1964-1979

- The instantaneous pole of rotation (IRP) (of the axis of rotation) was the pole of reference of the IAU 1964 nutation based on Woolard (1953) theory of nutation for a rigid Earth (providing nutation for various axes). The corresponding forced diurnal polar motion of the IRP was considered separately.

$\delta\psi = +AC\gamma_0\sin\theta\cos(\varphi + \Gamma_0)$					
sig	l	l'	F	D	Ω
+0.01615"	0	0	+2	0	+2
- 338	0	0	0	0	+1
+ 334	0	0	+2	0	+1
+ 309	+1	0	+2	0	+2
+ 753	0	0	+2	-2	+2

$\delta\theta = +AC\gamma_0\sin\theta\cos(\varphi + \Gamma_0) - 0.00868''$					
cos	l	l'	F	D	Ω
+0.00590"	0	0	+2	0	+2
+ 113	+1	0	+2	0	+2
- 100	0	0	0	0	+1
+ 99	0	0	+2	0	+1
- 97	+1	0	0	0	0
+ 275	0	0	+2	-2	+2

Figure 1: Free motion and Oppolzer terms (with Delaunay variables $\ell, \ell', F, D, \Omega$) in ecliptic longitude ($\delta\psi$) and obliquity ($\delta\theta$) for a rigid Earth: terms larger than 1 mas (Woolard 1953).

$$\Delta\varphi = +0.0066''\sin(S) - 0.0051''\sin(S - 2l) - 0.0022''\sin(S - 2L) - 0.0010''\sin(S - 2(l - \Omega)) - 0.0010''\sin(S - 3(l + \Gamma')) + 0.0009''\sin(S - \Omega).$$

Figure 2: Fedorov's expression (1963) for the *variation of latitude* for an elastic Earth, S being the local sidereal time.

- Fedorov (1963), Jeffreys (1963) and Atkinson (1973) questioned the choice of the axis of rotation and recommended to use instead the axis of figure (geophysical concept) or the axis of angular momentum (kinematical concept).
- Atkinson (1975) showed that optical astrometric observations "do no ever involve the axis of rotation but do give directly the instantaneous position on the celestial sphere of the pole of figure".
- Recommendation 4 to the IAU 1976 General Assembly (GA), associated with the adoption of the IAU 1976 System of astronomical constants and of the new fundamental reference system (FK5), was to refer the tabular nutation to the axis of figure in place of the axis of rotation.
- The discussion on a new theory of nutation for a non-rigid Earth began at the IAU Symposium 78 "Nutation and the Earth's rotation", held in Kiev in 1977 and sponsored by Commission 19 (see Fedorov et al. 1977 and Yatskiv & Korsun 2008). It recommended that the theory refers to the instantaneous axis of rotation of the mantle.
- Following a long and detailed discussion within the IAU Working Group (WG) on nutation formed after Symposium 78, the final IAU 1979 recommendation was to refer the new nutation model to a pole called the *Celestial Ephemeris Pole*, which was defined as including the forced diurnal polar motion into the celestial nutation (cf. Atkinson's proposal).

1.3 The Celestial Ephemeris Pole (1980-2000)

- The IAU-1980 theory of nutation (Seidelmann et al. 1982), adopted the Celestial Ephemeris Pole (CEP) to which the numerical values of the conventional model were referred.
- These numerical values have been computed so as to include the forced diurnal polar motion, consequently this latter has no more to be considered separately in PM.

- A tentative conceptual definition of the CEP has been given as the “pole that has no nearly-diurnal motion with respect to a space-fixed coordinate system or an Earth-fixed coordinate system”, or “the center of the quasi-circular paths of the stars in the sky”.
- The following improvements have been progressively achieved in the PN and PM models as well as in processing EOP observations: the semi-diurnal and diurnal prograde nutations, which were considered to be negligible, have been considered in the nutation theory for a rigid Earth at a microsecond level (1997); models for the daily and subdaily tidal variations in polar motion have been developed and included in the IERS models for polar motion; the “celestial pole offsets” (i.e. estimated corrections to the IAU PN) are published on a regular basis by the IERS since 1980; “intensive” EOP series are available since 1994.
- An improved definition of the CEP appeared to be necessary in order to be in agreement with modern models and observations and to take into account the overlapping between the GCRS and ITRS pole motions in the high frequency domain.
- Several options for an extended definition of the CEP were considered (1998-2000) by the IAU WG T5 “Computational Consequences” of the IAU Working Group ICRS: see <https://syrtel.obspm.fr/iau/iauWGT5>.
- These proposals were discussed at the IAU Colloquia 178 (Cagliari, 1999) “Polar Motion: Historical and Scientific Problems” (see Capitaine 2000) and 180 (Washington, 2000) “Towards Models and Constants for Sub Microsecond Astrometry” and during the JD2 Discussion “Models and constants for sub-microarcsecond astrometry” (see Capitaine 2002) at the IAU 2000 GA in Manchester..
- A Resolution proposal on the CIP was submitted to the IAU 2000 GA.

1.4 The Celestial Intermediate Pole, IAU 2000

The Celestial Intermediate Pole (CIP) was adopted by IAU 2000 Resolution B1.7 together with Resolution B1.6 adopting the IAU 2000 IAU precession-nutation. The relevant definitions were specified by the IAU Div 1 WG “Nomenclature for Fundamental Astronomy”: NFA WG: 2003-2006 (Capitaine et al. 2007); see the NFA Glossary at <https://syrtel.obspm.fr/iauWGnfa>.

- The CIP is the geocentric equatorial pole defined by IAU 2000 Resolution B1.7 as being the intermediate pole, in the transformation from the GCRS to the ITRS, separating nutation from polar motion. It replaced the CEP on 1 January 2003.
- Its GCRS position results from (i) the part of precession-nutation with periods greater than 2 days, and (ii) the retrograde diurnal part of polar motion (including the free core nutation, FCN) and (iii) the frame bias.
- Its ITRS position results from (i) the part of polar motion which is outside the retrograde diurnal band in the ITRS and (ii) the motion in the ITRS corresponding to nutations with periods less than 2 days.
- The motion of the CIP is realized by the IAU precession-nutation plus time-dependent corrections provided by the IERS.

It is important to note that the CIP definition is not a conceptual definition, but that the CIP is defined by a convention in the frequency domain. This new definition of the pole, extending the

CEP definition to the high frequency domain in both the GCRS and ITRS, has been implemented in the IERS Conventions 2003 (and then 2010) as well as in the astronomical almanacs.

2. THE DEFINITION OF UT1

2.1 IAU procedures to define UT1 (1964-2000)

- Universal time, UT1, was defined by an expression relating it to Greenwich mean sidereal time, GMST, which was directly obtained from the apparent right ascensions of transiting stars. The formula was based on Newcomb's (1895) expression for the right ascension of the "fictitious mean Sun".
- The IAU procedure for deriving Apparent Greenwich sidereal time, GST, was (i) to use the relationship between GMST and UT1, giving GMST at date t , (ii) to take into account the interval of GMST from 0h UT1 to the hour of observation and (iii) to use the expression for the difference between GST and GMST, called the *equation of the equinoxes*.
- IAU 1976 Rec 4 recommended that, in certain applications, it may be convenient to remove the effects of the periodic variations by subtracting the equation of the equinoxes, while the origin of apparent right ascension should continue to be the true equinox of date.
- A new expression relating UT1 and GMST developed by Aoki et al. (1982) was adopted in order to be consistent with the IAU 1976 System of astronomical constants, the IAU 1976 precession, the IAU 1980 nutation and the FK5 equinox and to maintain the continuity of UT1 both in value and rate at the epoch of the change.

2.2 Towards a new definition of UT1 (1997-2000)

- IAU 1997 Resolution B2 adopted, in replacement of the FK5, the International celestial reference system (ICRS) and the international celestial reference frame (ICRF), which has no global rotation and is no longer dependent on the Earth's motion (as the FK5 was).
- There has been a significant improvement during the period 1980-2000 in both the precision and the temporal resolution of ER measurements as well as in the theory.
- These required that the PN parameters and GST, which were defined in the FK5 System, be replaced by more basic parameters referred to the ICRS and be based on clarified concepts.
- The important defect of the angle GST, which refers to the equinox of date, for representing the Earth Rotation (ER), is that it mixes ER and PN, while the *non-rotating origin* (NRO) proposed by Guinot (1979) in place of the equinox as the origin on the CIP equator, clearly separates ER and PN.
- Such a proposal for a new equatorial origin extended a proposal from Atkinson & Sadler's (1951) for a new origin both for GST and right ascension (RA) obtained with subtracting nutation, in order to simplify a number of routine calculations.
- The difference GST–GMST was provided, since the 1st January 1997, by the "complete equation of the equinoxes", i.e. the accumulated precession and nutation in right ascension (Aoki & Kinoshita, 1983), which involved the NRO concept.
- The IERS Conventions 1996 considered the NRO as one possible option for the equatorial origin in the ITRS-to-GCRS transformation.

- The proposals for the EOP in the ICRS, including the choice of a new origin on the celestial equator in place of the equinox, have been under consideration by the IAU WG T5 (1998-2000) and several possibilities have been compared.
- Proposals have been discussed at the IAU Colloquium 180 and then at the IAU JD2 at the IAU 2000 GA (see Capitaine 2002).
- A Resolution proposal on the choice of the equatorial origin and its consequence on the definition of the Earth's angle of rotation and UT1 was submitted to the IAU 2000 GA.

2.3 The IAU 2000 Resolution on the Earth rotation angle and UT1

- New celestial and terrestrial origins have been adopted (IAU 2000 Resolution B1.8) and afterwards renamed (IAU 2006 Resolution B2) "Celestial and Terrestrial Intermediate Origins" (CIO and TIO), defined as being the NRO (w.r.t. the GCRS and the ITRS, respectively) on the equator of the Celestial Intermediate Pole (CIP).
- The *Earth Rotation Angle* (ERA) is the angle from the Celestial Intermediate Origin (CIO) to the Terrestrial Intermediate Origin (TIO) on the CIP equator (see Capitaine et al. 2003).
- ERA is such that $d\text{ERA}/dt = \omega_3$, i.e. the component of the instantaneous rotation vector along the CIP axis.
- IAU 2000 Resolution B1.8 adopted the definition of the ERA and the corresponding new definition of UT1.

2.4 The IAU 2000 definition of Universal Time (UT1)

- According to IAU 2000 B1.8 Resolution (see also the NFA Glossary), UT1 is the angle of the Earth's rotation about the CIP axis defined by its conventional linear relation to the ERA:

$$\text{ERA}(T_u) = 2\pi(0.779\,057\,273\,264\,0 + 1.002\,737\,811\,911\,354\,48\,T_u), \quad (1)$$

where $T_u = (\text{Julian UT1 date} - 2\,451\,545.0)$.

- The numerical coefficients in (1) ensured continuity in UT1 with the previous (1982) definition both in value and rate at the epoch of the change (Capitaine et al. 2000).
- UT1 can be related to GST through the ERA: $\text{GST} = \text{ERA}(\text{UT1}) - \text{EO}$, EO being the *equation of the origins*, i.e the distance between the CIO and the equinox along the CIP equator.
- UT1 is determined by observations (currently from VLBI observations of the diurnal motions of distant radio sources).
- UT1 can also be obtained from the uniform time scale UTC by using the quantity $\text{UT1} - \text{UTC}$, which is provided by the IERS.

These new definitions of the ERA and UT1 and their relationships with other parameters, have been implemented in the IERS Conventions 2003 (and then 2010) as well as in the astronomical almanacs.

3. REFERENCES

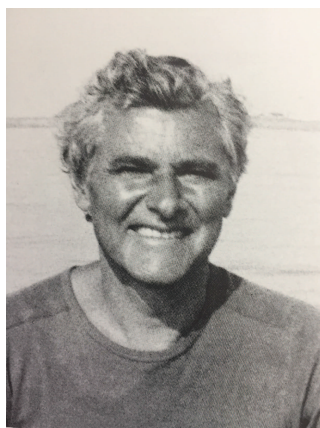
- Aoki, S., Kinoshita, H., Guinot, B., Kaplan, G. et al., 1982, "The new definition of universal time", *Celest. Mech.* 105(2), pp. 359–361.
- Aoki, S. and Kinoshita, H., 1983, "Note on the relation between the equinox and Guinot's non-rotating origin", *Celest. Mech.* 29, pp. 335–360.
- Atkinson R. d'E., 1973, "On the Dynamical Variations of latitude and time, *AJ* 78, 147.
- Atkinson R. d'E., 1975, "On the Earth's axes of rotation and figure", *MNRAS* 171(1), pp. 381–386.
- Atkinson, R.d'E. and Sadler, D.H., 1951, "On the use of mean sidereal time", *MNRAS* 111, 619.
- Capitaine, N., 2000, "Overview and proposition for a modern definition of the CEP" in *Polar Motion: Historical and Scientific Problems*, ASP Conference Series, Vol. 208, IAU Coll. 178. S. Dick, D.D. McCarthy, and B. Luzum (eds), ISBN: 1-58381-039-0, 2000, pp. 573–584
- Capitaine, N., 2002, "New definition for the celestial pole and the celestial origin in the ICRS", in *Highlights of Astronomy*, Vol. 12, H. Rickmann (ed), CA: Astronomical Society of the Pacific, ISBN 1-58381-086-2, pp. 102–106.
- Capitaine, N., Guinot, B. and McCarthy, D.D., 2000, "Definition of the Celestial Ephemeris Origin and of UT1 in the International Celestial Reference Frame", *A&A* 335, pp. 398–405.
- Capitaine, N., Wallace, P.T, McCarthy, D.D., 2003, "Expressions to implement the IAU 2000 definition of UT1", *A&A* 406, pp. 1135–1149.
- Capitaine, N., Andrei A.H., Calabretta M.R., Dehant, V. et al., 2007, "Proposed terminology in fundamental astronomy based on IAU 2000 resolutions", *Highlights of Astronomy*, 2, Vol 14, pp. 474–475.
- Fedorov, E. P., 1963, "Nutation and Forced Motion of the Earth's Pole", The MacMillan Co, New York.
- Fedorov, E. P., Smith, M. L., Bender, P. L. (eds), 1977, "Nutation and the Earth's rotation", *Proc. IAU Symp. 78 (Kiev 1977)*, Dordrecht, Holland: Reidel Publ. Comp.
- Guinot, B., 1979, "Basic Problems in the Kinematics of the Rotation of the Earth" in *Time and the Earth's Rotation*, D.D. McCarthy and J.D. Pilkington (eds.), D. Reidel Publishing Company, pp. 7–18.
- IERS Conventions 1996, D. McCarthy (ed.), (IERS Technical Note 21), Observatoire de Paris.
- IERS Conventions 2003, D.D. McCarthy and G. Petit (eds.), (IERS Technical Note 32).
- IERS Conventions 2010, G. Petit and B. Luzum (eds.) (IERS Technical Note 36).
- Jeffreys H., 1963, Foreword to "Nutation and Forced Motion of the Earth's Pole" by E.P. Fedorov, Pergamon Press.
- Newcomb, S., 1895, in *Astronomical Papers for the American Ephemeris and Nautical Almanac*, AP, Vol. 5, Part IV-3.
- Seidelmann, P. K., 1982, "1980 IAU theory of nutation - The final report of the IAU Working Group on Nutation", *Celest. Mech.* 27, 79–106.
- Woolard, E., "Theory of the Rotation of the Earth Around its Center of Mass", *Astron.Pap.Amer.Ephem.* XV, Part, I., 165, Washington, D.C., 1953.
- Yatskiv, Y. S., Korsun, A., 2008, "IAU Symp. 78 as the first step in the consideration of the non-rigid Earth nutation theory" in *Proc. of the Journées 2007 Systèmes de référence spatio-temporels*, pp. 88–90, N. Capitaine (ed.), Observatoire de Paris, ISBN 978-2-901057-59-8.

TRIBUTE TO BERNARD GUINOT (1925-2017)

N. CAPITAIN^{1,2}, F. ARIAS^{1,2}, C. BOUCHER²

¹ Observatoire de Paris / SYRTE - Université PSL, CNRS, Sorbonne Université - France

² Bureau des longitudes - France - nicole.capitaine@obspm.fr



Bernard Guinot, honorary astronomer of the Observatoire de Paris, died on March 6, 2017, aged 91. He was Correspondent of the French Académie des sciences, Honorary Member of the Bureau des longitudes and Member of the Academia Europaea. He has been a faithful and active participant in the Journées in Paris since their beginning.

Being at first an officer in the shipping department, he became an astronomer at Paris Observatory in 1952, where André Danjon, then Director, associated him with his research on the astrolabe, named after him. B. Guinot was actively involved in the further development of this instrument and of its scientific applications, especially for polar motion and Earth rotation determination. In 1958, he obtained his doctoral thesis on this subject.

In 1965, he became Director of the Bureau International de l'Heure (BIH), a position he held until 1985 at Paris Observatory, in the Department of Fundamental Astronomy (now SYRTE). In this context, he was one of the most active authors of the transition from the astronomical measurement of time to its quantum measurement and one of the major players in the organization of world time metrology. In parallel, he devised new algorithms for the calculation of Universal Time UT1 and pole coordinates; he developed methods for the transition from optical measurements to space geodesy techniques and created a rapid service for the needs of space research. In 1979, he proposed the use of a new equatorial origin, the "non-rotating origin" (NRO), which was adopted at the international level in 2000 for defining the Earth rotation angle (ERA) as a basis for the modern definition of UT1.

In 1980, Bernard Guinot proposed, within the framework of a co-operation with the IGN, the use of space geodesy observatories contributing to the measurement of the Earth's rotation for the maintenance of the global geodetic reference system. He is thus the instigator of the geodetic reference system used worldwide, which gave birth to the current International Terrestrial Reference System (ITRS), which plays a major role for geodesy, geodynamics, oceanography, climate and relativity. The first realization of this system was in 1985, and later in 1988 with the creation of the International Earth Rotation and Reference System Service (IERS).

In 1985, he joined the International Bureau of Weights and Measures (BIPM) as a principal physicist. He officially transferred the BIH activity on TAI to the BIPM in 1988 at the creation

of the IERS, which replaced the IPMS and the Earth rotation section of the BIH. In addition to his activities on time scales, Bernard Guinot devoted himself to the problem of the relativistic definitions of space-time references of which he assured the recognition by the IAU in 2000.

During his career, B. Guinot has been given many responsibilities in which his competence, rigor and scientific authority have always been unanimously recognized.

At the national level, he was :

in charge of the Astrolabe Service and then the Service de l'Heure at Paris Observatory, director of the Primary Time and Frequency Laboratory (LPTF), a member of the board of directors of the Bureau national de métrologie (BNM), the Executive director of the Groupe de recherche de géodésie spatiale (GRGS) and President of the Bureau des longitudes.

At the international level, he was President of :

IAU Commission 19 (Rotation of the Earth; 1961-1967), the Scientific Council of the International Polar Motion Service (IPMS), the Federation of the Astronomical and Geophysical data analysis Services (FAGS), the CIPM Consultative Committee for the Definition of the Second (CCDS) and he was a Member of the International Committee of Weights and Measures (CIPM).

B. Guinot wrote a large number of authoritative publications on space and time references and had an extraordinary clarity for presenting his ideas. He co-authored two reference books (see below) and strongly emphasized the book "Les références de temps et d'espace", edited by the Bureau des longitudes (May 2017), which has been dedicated to his memory.

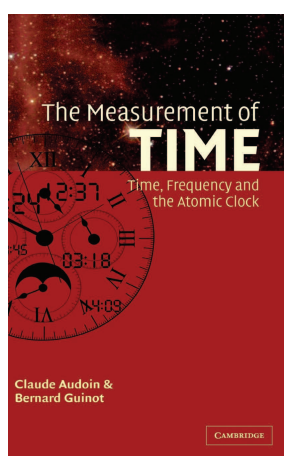
During his sixty years of scientific activity B. Guinot made outstanding contributions to space and time metrology. His great scientific rigor and innovative concepts have allowed him to make astronomy and time measurements best benefit from the gain of precision brought by space geodesy and atomic clocks.

We have lost with him a very prominent personality, a great scientist and a very good friend. He is sorely missed.

REFERENCES

Débarbat, S. & Guinot, B., 1970, "La méthode des hauteurs égales en astronomie", Gordon & Breach, 150 p.

Audoin, C. & Guinot, B., 1998, "Les fondements de la mesure du temps", Masson, France, 300 p., ISBN 2-225-83261-7, English translation "The Measurement of Time - Time, Frequency and the Atomic Clock", Cambridge University Press 2001, Russian translation 2002



TRIBUTE TO PROFESSOR BARBARA KOŁACZEK (19312017)

J. NASTULA¹, A. BRZEZIŃSKI², J. KRYŃSKI³

¹ Space Research Centre, Polish Academy of Sciences - Poland - nastula@cbk.waw.pl

² Warsaw University of Technology - Poland - aleksander.brzezinski@pw.edu.pl

³ Institute of Geodesy and Cartography - Poland - jan.krynski@igik.edu.pl

Obituary

Barbara Kołaczek, age 86, passed away on 19 February 2017, after a serious illness. She was one of the outstanding researchers of her generation in geodynamics, geodesy and astronomy, with the wide international reputation in the international scientific community.

Barbara Kołaczek received the degree of Master of Science in physics, specialization of astronomy at the Jagiellonian University in Krakow. She started her professional carrier as a staff member of the Chair of Geodetic Astronomy at the Warsaw University of Technology (WUT). Conducting an advanced research Barbara Kołaczek substantially contributed to the development of astrometry successfully affecting students and collaborators with her enthusiasm and dedication to research. She was one of the major developers and organizers of the Astro-Geodetic Observatory of WUT in Jozefoslaw, near Warsaw. Among other accomplishments, she was responsible for setting up and running of the astronomic latitude observation program with the zenith telescope in Jozefoslaw in the framework of the International Latitude Service. At the Warsaw University of Technology she received her PhD, while the habilitation (degree of Doctor of Science) was given to her at her alma mater the Jagiellonian University in Krakow.

An important step in her professional life was in 1977 when she joined the team of just getting established Space Research Centre (SRC) of the Polish Academy of Sciences where within a number of years she created a Polish school of research in the field of the Earth's rotation. Her scientific accomplishments were acknowledged. She was awarded a title of a professor by the President of Poland and then a title of full professor. In SRC she was acting as a head of the Earth Rotation Department, a long-standing member of the Scientific Council and a Deputy Director for scientific affairs from 1990 to 1994.

Professor Barbara Kołaczek served many important functions in international scientific organizations, in particular the International Association of Geodesy (IAG) and the International Astronomical Union (IAU). In the period 1987-1991 she was a president of the Section II of IAG and in the period 1991-94 a president of the Commission 19 of IAU. In 1991 she was honored with a fellowship of the IAG.

She also actively participated in the work of numerous national organizations and scientific societies. She was, among others, an active member of the Polish Astronomical Society (since 1953), and the Warsaw Society of Sciences (since 1983). She was a member of the Committee on Geodesy of the Polish Academy of Sciences, and for almost two decades she was a chair of the Section of Geodynamics in that Committee. After her retirement, she was elected an honorary member of that Committee.

In 1974 Barbara Kołaczek organized the first colloquium devoted to the Fundamental References Systems for Geodynamics in Torun, Poland, which was a milestone in communication of research in this topic. In 1981 she organized the second IAU colloquium on Reference Systemes for Earth Dynamics in Warsaw. She established close relations with French astronomical community, and initiated long-term collaborations with other groups in the international community. Barbara was very involved and associated with the organization of numerous Journees.

On the initiative of Professor Barbara Kołaczek, the first Journees Conference outside Paris was held in Warsaw in 1995. She was the organizer of the next meeting in Poland Journees 2005.

Professor Barbara Kołaczek supervised the scientific development of numerous young researchers. Among them there are four doctors (PhD) and two doctors of science.

She was awarded the Knights of the Order of Polonia Restituta and the Medal of Merit for Geodesy and Cartography.

She was the author of many recognized scientific publications.

Professor Barbara Kołaczek had carried on investigations of the following problems of the Earths rotation::

- Seasonal, sub-seasonal, short-term periodic oscillations of the Earths rotation variations,
- Geophysical interpretation of the Earths rotation variations,
- Chandler wobble of polar motion,
- Methods of spectral analyses and filtration of short periodic oscillations in noisy stochastic processes,
- Prediction of the Earths rotation variations,
- Optimisation of the Conventional Terrestrial Reference Frame.

Professor Barbara Kołaczek was recognized as a respected scientist, involved in international scientific cooperation, always supporting interdisciplinary cooperation in research. She was an unquestionable authority. She was also a wonderful, kind and generous person, respected and extremely popular among her collaborators, students and alumni. She will be missed very much by many of her friends and collaborators. She will be remembered in the academic community as unattainable model, outstanding scientist, honorable person and a true friend.



Figure 1: Professor Barbara Kołaczek



Figure 2: Professor Barbara Kołaczek, Journees 2005, Warsaw



Figure 3: Journees 2005, Warsaw

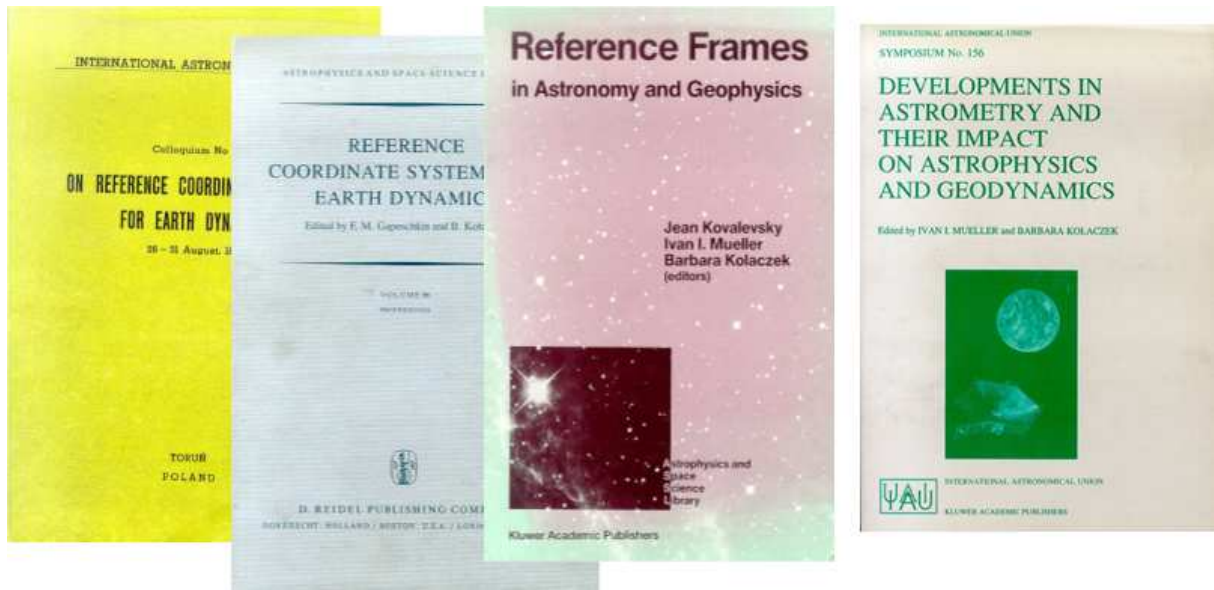


Figure 4: Some of the books co-authored or co-edited by Professor Barbara Kołaczek



Figure 5: 80th birthday of Professor Barbara Kołaczek

IMPACT OF THE PARAMETERIZATION OF THE SOURCE POSITIONS ON THE FREE CORE NUTATION

M. Karbon , S. Lambert, C. Bizouard, J.Y. Richard

SYRTE, Observatoire de Paris, Université PSL, CNRS, Sorbonne Université, LNE
France - maria.karbon@obspm.fr

ABSTRACT. The positions of the radio sources in the ICRF3 catalog, representing the newest realization of the Celestial Reference Frame (CRF), are given as time invariant coordinate pairs. Failing to acknowledge systematics within the source positions leads to a deterioration in the quality of the frame, and thus in all derived variables, such as the Earth orientation parameters (EOP). A proven approach to overcome these shortcomings is to extend the parameterization of source positions using the multivariate adaptive regression splines (MARS). They allow a great deal of automation, by combining recursive partitioning and spline fitting in an optimal way. Here we present first results on the impact of the parameterization of the source positions on the EOP and the estimation of the free core nutation.

1. INTRODUCTION

The Earth's Free Core Nutation (FCN) is one of the free rotational modes of the Earth. It describes the retrograde motion due to the misalignment between the rotation axes of the mantle and the liquid core (Smith 1977, Wahr 1981). It has a retrograde period of about 430 days, with an average amplitude of about $100 \mu\text{as}$ (Mathews 2002, Vondrak 2005, Lambert & Dehant 2007) relative to a space-fixed reference frame. A comprehensive description of the precession and nutation theory detailing also the FCN can be found in Dehant and Mathews (2015).

However, until this day no models can predict this free motion, as its excitation mechanism is not fully understood. Thus it is not included in the precession-nutation model IAU2000/2006 (Mathews et al. 2002, Capitaine et al. 2003) recommended by the IERS (International Earth Rotation Service) Conventions (Petit and Luzum, 2010). However, the IERS Conventions propose an empirical model based on the IERS EOP C04 series (that can be found at <http://ivsopar.obspm.fr/fcn/>) that provides one reference value for yearly amplitudes.

Geodetic VLBI is the only space geodetic technique that is capable of accurately observing the variation of the Earth's rotation axis in space in terms of celestial pole offsets (CPO), and thus the therein contained FCN signal. It is based on the observation of extra-galactic radio sources, which realize the inertial International Celestial Reference System (ICRS). The accuracies in positions of these radio sources depend on their individual intrinsic structural variations (Charlot, 2002), however in ICRF3 (Charlot et al, in prep.) the sources are considered as time-invariant and point-like. Neglecting any deviation from this definition can lead to a deterioration of the nutation estimates as shown for instance by Feissel-Vernier et al. (2005). Extending the parameterization of the source coordinates as proposed in Karbon et al. (2016a,b) can mitigate such effects, mainly by eliminating systematics in the sources defining the datum, and thus stabilizing the frame. Further, the modeling of the systematics in the source positions, allows the introduction of sources into the datum definition, which were until then classified as too unstable.

This work follows up on these results and gives a first impression on the impact of the parameterization of the source positions on the FCN signal.

2. PARAMETERIZATION OF THE SOURCES

The MARS algorithm (Friedman, 1991) is a method for flexible regression modeling, and delivering continuous linear splines. As it can be fully automated, the large number of source coordinate time-series to be parameterized does not pose a problem. The model consists of a weighted sum of spline basis functions. The number of basis functions as well as the associated parameters (e.g. degree and knot locations) are determined automatically by the data using recursive partitioning. Here only an example of the results shall be given. For further information refer to the original publication by Friedman and to Karbon et al. (2016a,b).

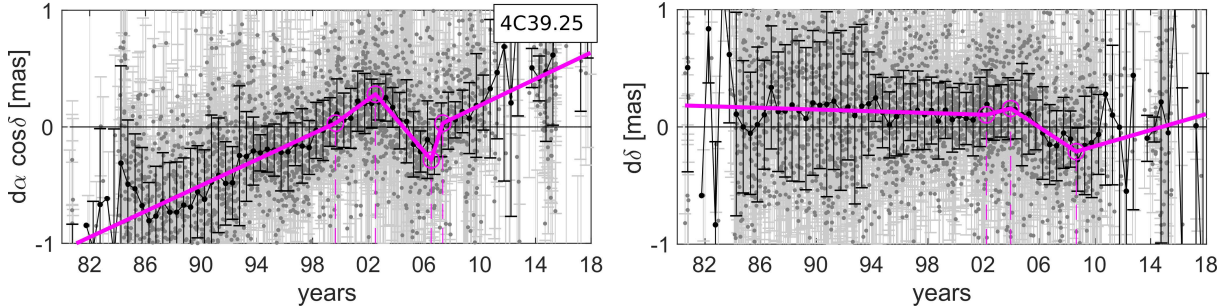


Figure 1: The estimates for former special handling source 4C39.25 with their error bars in gray and the semi-annual mean values in black. The estimated MARS spline is given in magenta.

Figure 1 shows the estimates of the source positions of the ICRF2 special handling source 4C39.25 in gray, overlaid with the magenta spline determined by MARS. It is an exceptionally well observed source, however, due to its instability it cannot contribute to the datum definition of the reference frame. As one can see, the spline follows to great extent the semi-annual mean values (black). Only where the estimates show larger uncertainties, the algorithm down-weights the positions considerably, thus the segmentation of the spline remains unaffected.

For all sources which are observed in more than 10 sessions, we estimated such splines. These splines are then introduced in the VLBI analysis software as corrections for the a-priori source positions taken from the ICRF3 catalog. Hence, where the instability of some sources prevented their inclusion in the datum definition, the extension of the coordinate model of these sources makes this now possible.

3. DATA AND PROCESSING

For our study we used more than 4500 sessions within 1980 and 2018, with station networks that encompass more than 10^{15}m^3 to ensure a stable geometry, and hence a reliable estimation of the EOP. The geodetic data analysis is performed using the VLBI software package VieVS (Böhm et al., 2018), and following the conventions of the IERS. The modeling settings are chosen with respect to the routine single-session data analysis strategies of the International VLBI Service for Geodesy and Astrometry (IVS, Nothnagel et al., 2015). For the stacking of the normal equations we used our own stand-alone software.

As reference serves the solution (0) using the 303 ICRF3-defining sources for the datum definition (i.e. sets of sources which enter the no-net-rotation condition), and without additional parameterization for the sources. For the solutions applying the parameterization to the source positions, we defined 3 different datums. A map of the distribution of the used datum sources is shown on the left in Figure 2:

- (I) all ICRF3 defining sources: 303,

- (II) all ICRF3 defining sources except the 32 least observed ones, plus the 32 most observed special handling sources: 303,
- (III) the 152 most observed sources in the northern and southern hemisphere, independent of classification: 304.

As can be seen on the left in Figure 2 the distribution of the ICRF3 defining sources (gray) improved significantly compared to ICRF2. However, the alternative datum definitions (magenta and black) still show larger numbers in the far south. Yet, the number of defining sources per sessions has not increased with ICRF3, especially the first decade of observations is still lacking. The alternative datum definitions can increase these numbers dramatically by 100% for (II) and almost 150% for (III). Over the entire time-span the increase w.r.t. ICRF3 is 30% and 50%, respectively.

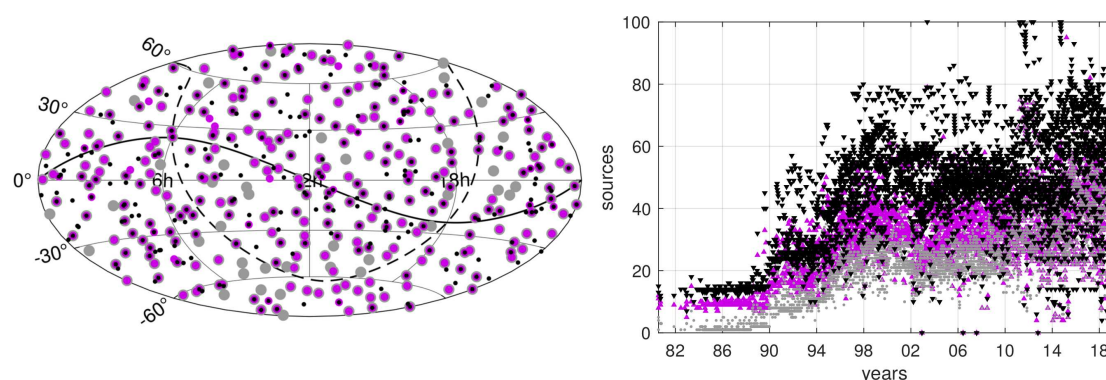


Figure 2: **left:** Datum definitions: ICRF3 in gray (I), (II) in magenta and (III) in black. **right:** number of datum sources per session.

4. QUICK-LOOK: CELESTIAL POLE OFFSETS

Using each datum definition, four sets of normal equations were generated, which were then stacked to generate four homogeneous time series of the CPO. Although the ICRF3 defining sources are much better distributed than they were in ICRF2, the increased number of them within the alternative datum definition has still a significant positive impact on the CPO. Figure 3 shows on the left exemplarily the estimates for dX and dY for the reference solution (0) in gray and solution (II) in magenta, to the a-priori the values given by IERS 14 C04. On the right we show the difference. (II) reduces the weighted RMS about 30%, and about 10% when neglecting the early data until 1995; same for solution (III).

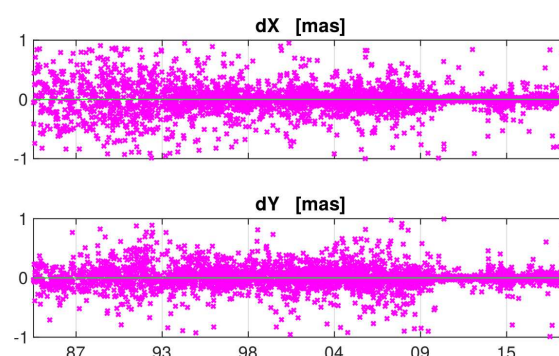


Figure 3: **Difference** between the CPO residuals using (0) and (II).

5. EMPIRICAL MODEL OF FCN

Using the processing scheme presented in Chap. 3, we determined CPO time-series omitting the IERS-FCN model. Then we used the model described in Eq. 1 to generate our empirical FCN models.

$$\begin{aligned} X_{FCN} &= A_C \cos(\sigma_{FCN} \cdot t) - A_S \sin(\sigma_{FCN} \cdot t), \\ Y_{FCN} &= A_S \cos(\sigma_{FCN} \cdot t) + A_C \sin(\sigma_{FCN} \cdot t). \end{aligned} \quad (1)$$

Based on the work of Belda et al, (2017) we chose as a-priori period 430 days and an averaging window of 400 days. The left plot in Figure 4 shows the various input time-series with the clear FCN-signature, and exemplarily one of the estimated FCN models. The right plot shows the residuals of the individual time series w.r.t. the respective model: (0) in grey, (I) in purple, (II) in magenta and (III) in black. In green we show the solution including the IERS FCN-model a-priori in the analysis. Although slight differences exist, none of the models outperforms any of the others. Looking at the statistics of the residuals, the solutions applying the source parameterization show slightly smaller values for the weighted RMS, whereas the IERS-model gives the smallest standard deviations.

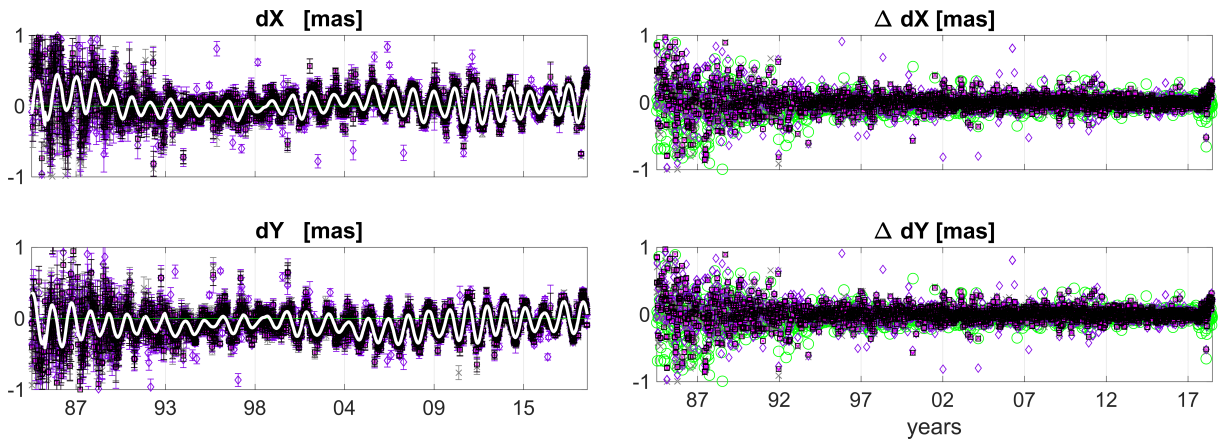


Figure 4: **left:** CPO time-series omitting FCN modeling and one model in white. **right:** Residuals w.r.t. models. **Color code:** (0) in gray, (I) in violet, (II) in magenta and (III) in black. The green solution applies the Lambert model a-priori.

We further compared our models with other established ones, i.e. the models by Lambert & Dehant (2007), Malkin (2013) and Belda et al. (2016). For this we restricted the time-span to 01.01.1990-31.12.2015 where all three models are available.

The left plot in Figure 5 shows the amplitudes and phases of the individual models. The smoothest curve is given by the Lambert-model (solid light-orange line) which uses the smallest number of constituents. The Malkin- (dashed light orange) and Belda-model (dashed dark orange) show more variability and better agreement with our models given in gray, violet, magenta and black (0-I-II-III). All our models are very close together in both amplitude and phase, (II) and (III) are practically identical. Only in the 90s the models diverge. These are the years where the parameterization and alternative datum definitions show the largest impact.

The right plot in Figure 5 shows the residual CPO w.r.t. the models. Besides a clear yearly signal remaining in all time-series, no clear differences in performance can be made out. Also looking at the statistics of these residuals shows again no clear differences. Our models perform overall better, however that is mostly due to the higher variability of the models. Again (II) and (III) show the smallest wRMS, whereas (0) gives the the smallest standard deviation.

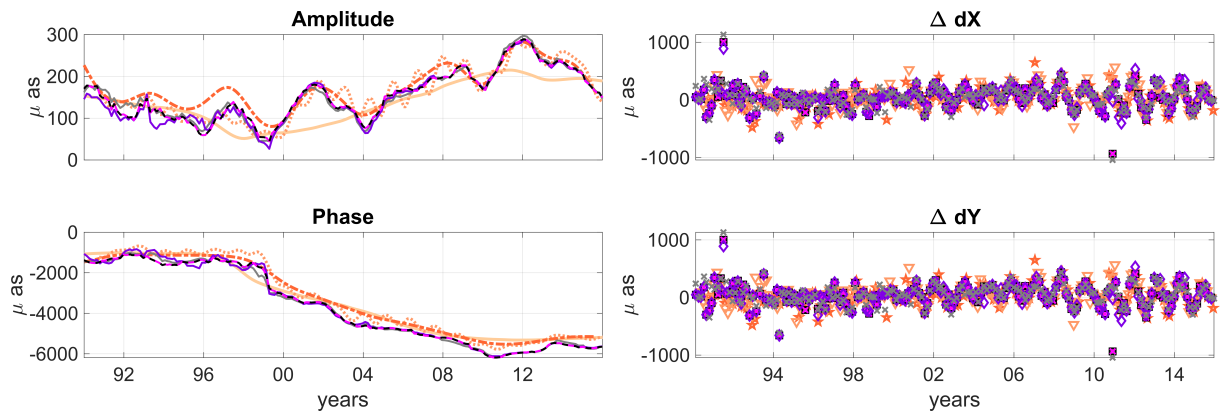


Figure 5: **left:** Amplitudes and phases of the FCN models. **right:** Residuals w.r.t. models. **Color code:** light upward triangle: Lambert, light downward triangle: Malkin, orange star: Belda, (I): violet, (II): magenta, (III): black.

6. CONCLUSIONS

The parameterization of source coordinates reduces the wRMS of CPO by 10–30%, also in view of the improved geometrical distribution of the ICRF3 defining sources. Our estimated FCN empirical models agree with established ones, however comparisons prove to be difficult, as no VLBI-independent solutions available. Further investigations need to be carried out.

7. REFERENCES

- S. Belda, R. Heinkelmann, J.M. Ferrndiz, M. Karbon, T. Nilsson, and H. Schuh, 2017, "An improved empirical harmonic model of the celestial intermediate pole offsets from a global VLBI solution", *AJ* 154(4), p. 166.
- Böhm, J., Böhm, S., Boisits, J., et al., 2018, "Vienna VLBI and satellite software (VieVS) for geodesy and astrometry", *Publications of the Astronomical Society of the Pacific*, 130(986), p. 044503.
- N. Capitaine, P. T. Wallace, and J. Chapront, 2003, "Expressions for IAU 2000 precession quantities", *A&A*, 412, pp. 567–586,
- P. Charlot, 2002, "Modeling radio source structure for improved VLBI data analysis", in N. R. Vandenberg and K. D. Baver, editors, *International VLBI service for geodesy and astrometry 2002 general meeting proceedings*, pp. 233–242. NASA/CP-2, pp. 233–24.
- P. Charlot, C.S. Jacobs, D. Gordon, S. Lambert, A. de Witt, J. Böhm, A. Fey, R. Heinkelmann, E. Skurikhina, O. Titov, E. Arias, S. Bolotin, G. Bourda, C. Ma, Z. Malkin, A. Nothnagel, D. Mayer, D.S. MacMillan, T. Nilsson, R. Gaume, 2020, "The Third Realization of the International Celestial Reference Frame by Very Long Baseline Interferometry", *A&A*, doi: 10.1051/0004-6361/202038368.
- V. Dehant and P.M. Mathews., 2015, "Precession, Nutation and Wobble of the Earth", CAMBRIDGE UNIVERSITY PRESS, Cambridge, United Kingdom.
- M. Feissel-Vernier, C. Ma, A. M. Gontier, and C. Barache, 2005, "Sidereal orientation of the Earth and stability of the VLBI celestial reference fram, *A&A*, 438, pp. 1141–1148
- J. H. Friedman, 1991, "Multivariate Adaptive Regression Splines", *The Annals of Statistics*, 19(1), pp. 1–141.
- M. Karbon, R. Heinkelmann, J. A. Mora-Diaz, M. Xu, T. Nilsson, and H. Schuh, 2016a, "The modeling of radio source time series as linear splines", In D. Behrend, editor, *Proceedings of the Ninth IVS General Meeting: New Horizons with VGOS*, Science Press, Johannesburg, South

Africa.

- M. Karbon, R. Heinkelmann, J. A. Mora-Diaz, M. Xu, T. Nilsson, and H. Schuh, 2016b, "About the extension of the parametrization of the radio source coordinates in geodetic VLBI and its impact on the time series analysis", *J. Geodesy* .
- S. B. Lambert and V. Dehant, 2007, "The Earth's core parameters as seen by the VLBI", *A&A*, 469, pp. 777–781.
- Z. Malkin, 2013, "Free core nutation and geomagnetic jerks", *Journal of Geodynamics* 72, pp. 53–58.
- P. M. Mathews, T. A. Herring, and B. A. Buffett, 2002, "Modeling of nutation and precession: New nutation series for nonrigid Earth and insights into the Earth's interior", *J. Geophys. Res. (Solid Earth)* 107(B4), ETG 31ETG 326.
- Nothnagel, A., Alef, W., Amagai, J., et al., 2015, "The IVS data input to ITRF2014", GFZ Data Services, Helmholtz Centre, Potsdam, Germany
- G. Petit and B. Luzum, editors, 2010, *IERS Conventions (2010)*.
- M.L. Smith, 1977, "Wobble and Nutation of the Earth", *Geophysical Journal of the Royal Astronomical Society*, 50(1), pp. 103–140.
- J. Vondrák, R. Weber, and C. Ron, 2005, "Free Core Nutation: direct observations and resonance effects", *A&A* 444, pp. 297–303.
- J.M. Wahr, 1981, "The forced nutations of an elliptical, rotating, elastic and oceanless Earth", *Geophysical Journal of the Royal Astronomical Society*, 64(3), pp. 705–727.

ON THE MUTUAL INTERRELATION BETWEEN EARTH ROTATION AND EARTHQUAKE ACTIVITY

CS. FODOR^{1,2,3}, R. HEINKELMANN³, S. MODIRI^{3,4}, S. RAUT^{3,4},
H. SCHUH^{3,4}, P. VARGA²

¹ Eötvös Loránd University - Hungary - fodor.csilla92@gmail.com

² Research Centre for Astronomy and Earth Sciences, Geodetic and Geophysical Institute - Hungary

³ Helmholtz-Centre Potsdam - GFZ German Research Centre for Geosciences, Germany

⁴ Technische Universität Berlin, Germany

ABSTRACT. In this paper, we analyse the mutual interrelation between earthquake activity and Earth rotation. The influence of earthquakes on the Earth rotation has been the subject of several studies before (Varga et al., 2005; Bizouard, 2005; Gross et al., 2006; Xu et al., 2014). Based on our investigations we concluded that the relationship between these two phenomena could be detected in the reverse direction too: changes in the speed of Earth's rotation (that is, changes in the Length-of-Day (LOD)) may affect earthquake activity.

1. INTRODUCTION

The study of short periodic variations of Earth Rotation Parameters (ERP) became possible using atomic clocks in the 1950s (Essen and Parry, 1955), with the appearance of Very Long Baseline Interferometry and methods of space geodesy (Satellite and Lunar Laser Ranging and Global Positioning System) (Eubanks et al., 1988; Dickey et al., 1994; Gross 1993; Hide and Dickey, 1991). Precise Length-of-Day (LOD) and Polar Motion (PM) measurements have shown variations down to days and even subdaily frequencies. The formal error of PM data are less than 50 microseconds of arc (μas) and 10 microseconds (μs) in case of LOD. This development made it possible to examine the relationship between ERP variations and hydro-meteorological/geodynamic processes. Our present research is focused on the relationship between earthquake activity and ERP. In this respect, the momentum magnitudes (M_w) introduced by Hanks and Kanamori (1979) in earthquake research is of great importance, as it allows a reliable determination of the magnitude of major (≥ 8) seismic events. It is evident that the temporal distribution of earthquakes and the release of seismic energy are primarily determined by tectonic conditions. Despite the fact that the annual rate of earthquake energy (9.5×10^{18} J/a) is slightly lower than that of Earth's rotation (1.6×10^{19} J/a) (Varga, 2006), it is important to examine the possible relationship between earthquakes and ERP. On one hand, it helps to better understand the processes that trigger earthquakes. On the other hand, it is an interesting problem how the greatest earthquakes can affect the Earth's rotation.

2. DATA DESCRIPTION

For the earthquake parameters, the version 6.0 of the ISC-GEM Global Instrumental Earthquake Catalogue provided by the International Seismological Centre was chosen (Storchak et al., 2013; 2015; Di Giacomo et al., 2018). This catalogue contains M_w values that were re-computed such a way that the resulting catalogue is consistent for the whole period starting from 1904 until the end of 2015 (Di Giacomo et al., 2015). It is important for this work because the released seismic energy can only be accurately determined from M_w , especially for high ($M_w \geq 8$) values, where

Mw does not saturate (Kanamori, 2004).

Furthermore, in order to obtain the 1D (radial) physical parameters of the Earth, the Preliminary Reference Earth Model (PREM) was used (Dziewonski and Anderson, 1981). The subduction zone lengths determined for 15° wide latitude zones were calculated for us by Dr. Friedhelm Krumm (University of Stuttgart, Institute of Geodesy). The ERP data were taken from the products of the International Earth Rotation and Reference Systems Service (IERS). The C04 time series was used as observations time series, and Bulletin A was used for the Earth rotation predictions (Bizouard et al., 2019).

3. BASIC INFORMATION ON EARTH'S SEISMICITY

The radiated energy by an earthquake can be calculated using the Gutenberg and Richter relation (Hanks and Kanamori, 1979; Kanamori, 2004):

$$\log E_R = 4.8 + 1.5M_W. \quad (1)$$

The annual seismic energy varies significantly in time, as only a few earthquakes occur with very high moment magnitude (and thus, energy). This phenomenon can be seen on Figure 1, where the seismic events that cause the largest peaks (with energies above 10^{18} J) are identified.

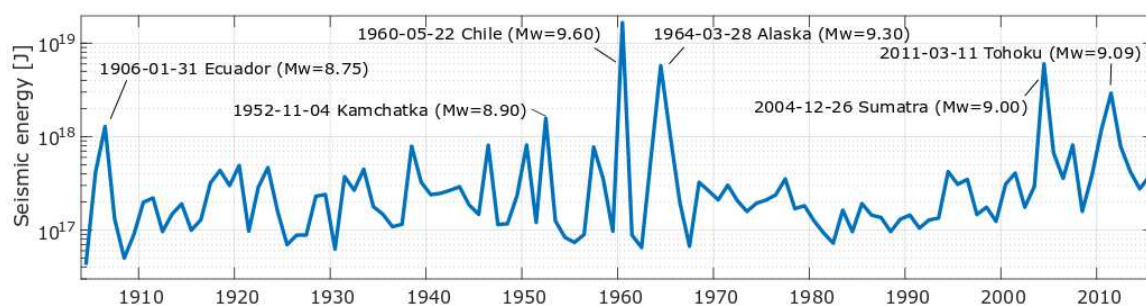


Figure 1: The released seismic energy from 1904 until the end of 2015, calculated from the Mw values of the ISC-GEM Catalogue. Events that cause the peaks of energy above 10^{18} J are identified.

4. THE EFFECT OF EARTH ROTATION ON GLOBAL SEISMICITY

The seismic energy distribution with respect to latitude was calculated from all events contained in the ISC-GEM Catalogue from 1904 until the end of 2015 (35 712 events). We aimed to determine the so-called 'effectiveness' of each latitude zone by dividing the radiated seismic energy with the subduction zone length. The result of this calculation is presented in Figure 2, which also contains the 'effectiveness' of the earthquakes in line with the depth zones.

The overall 'effectiveness' of the Earth's seismicity is determined by the shallow focus earthquakes, due to the fact that they produce most of the radiated elastic energy. The 'effectiveness' in this brittle outer part of the Earth (focal depth ≤ 70 km) has two sharp maxima at mid-latitudes which shows that the radiated energy is likely to be influenced by the stress built up by the despinning of Earth rotation. This means that the seismic activity of our planet in addition to the tectonic processes is affected by an external component too, through variations of the hydrostatic figure of the Earth. Comparison of the 'effectiveness' in different depth zones show the same tendencies (two large peaks) around mid-latitudes. As we look in deeper zones, the peaks of 'effectiveness' tend to move towards the equator. This difference of 'effectiveness' suggests that shallow and deep earthquakes have different tectonic origin. Another feature that can be observed is that the point of symmetry of the peaks is not precisely at the equator, but around $\phi = 15^\circ\text{N}$. The cause of this asymmetry is still unknown. The presence of the two large peaks on Figure 2 are the result

of the constant change in the geometrical flattening of the Earth due to the secular despinning. Based on Melosh (1977), Amalvict and Legros (1996), Denis and Varga (1990) have derived the stress tensor components that would be caused by this variation. Denis and Varga (1990) have shown how changes in geometrical flattening cause variations in the stress tensor components. They found that at the so-called critical latitude ($\phi = \pm 48.2^\circ$) the stress derivatives have their maxima, thus generating the greatest stress along the latitude.

Earth experiences a constant loss of rotational speed because of tidal friction. Due to this, the secular despinning of the Earth amounts to $\Delta\text{LOD} = (2.31 \pm 0.1) \text{ ms/century}$ (Stacey, 1992). Changes in the rotational speed result in flattening variations. The results shown in Figure 2 hint that the two processes are related to each other through seismicity: tidal friction influences the seismic energy release at mid-latitudes significantly - variations of the rotational speed (the constant despinning of the Earth) highly affect the global seismicity.

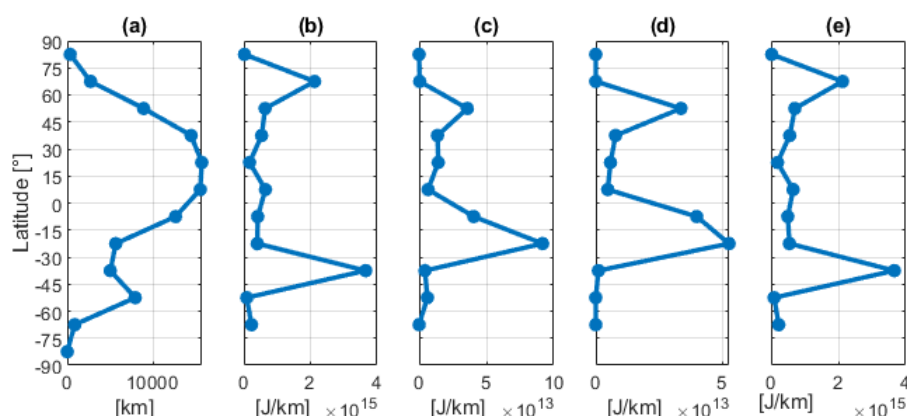


Figure 2: The latitudinal distribution of the subduction zone lengths (a), the 'effectiveness' of the shallow (0 - 70 km) (b), intermediate (70 - 300 km) (c) and the deep focus (300 - 700 km) earthquakes (d). The cumulative 'effectiveness' of seismic energy w.r.t. latitude (e).

5. IMPACT OF LARGE EARTHQUAKES ON THE ROTATION OF EARTH

5.1 Applied formulation

There have been two main approaches to calculate the co-seismic effect on Earth rotation: dislocation theory and normal mode method. Both are based on the fact that mass re-distributions caused by earthquakes cause changes in the Earth's inertia tensor, which affects the vector of rotation of the Earth (both its speed and direction) in the light of the angular momentum conservation. In this paper, the calculation of the co-seismic changes in Earth rotation was performed based on the formulation presented by Xu et al. (2014). One should note that the PM excitation is about 300 times more efficient than the excitation of ΔLOD (Xu et al., 2014). Using this method, one can determine the co-seismic ΔLOD and ΔPM from the parameters of an earthquake: source parameters (strike, dip, slip), M_w and location (geographical latitude, longitude and focal depth). The paper by Xu et al. (2013) contains a detailed description how these parameters can change the results.

5.2 Result of the modelled co-seismic changes in Earth Rotation

With the procedure described in the previous section, using the earthquake parameters from the ISC-GEM Catalogue, the co-seismic changes in ΔLOD and ΔPM (displacement of the figure axis) were calculated from 2000 until the end of 2015 (Figure 3). This period was chosen because of the availability of the Earth rotation predictions provided by IERS Bulletin A. From Figure 3 one can see that the co-seismic changes both in ΔLOD and ΔPM are highly correlated with the

released seismic energy of an earthquake. It is evident, that only a few large earthquakes can produce observable effects in PM, and co-seismic Δ LOD cannot be detected at the current level of data precision. Figure 3d illustrates more clearly the generated PM in 2D for case of four seismic events (Sumatra 2004 M=9.3, Chile 2010 M=8.9, Tohoku-Oki 2011 M=9.1, and Sumatra 2012 M=8.6). Details and exact co-seismic values of these four events are presented in Table 1.

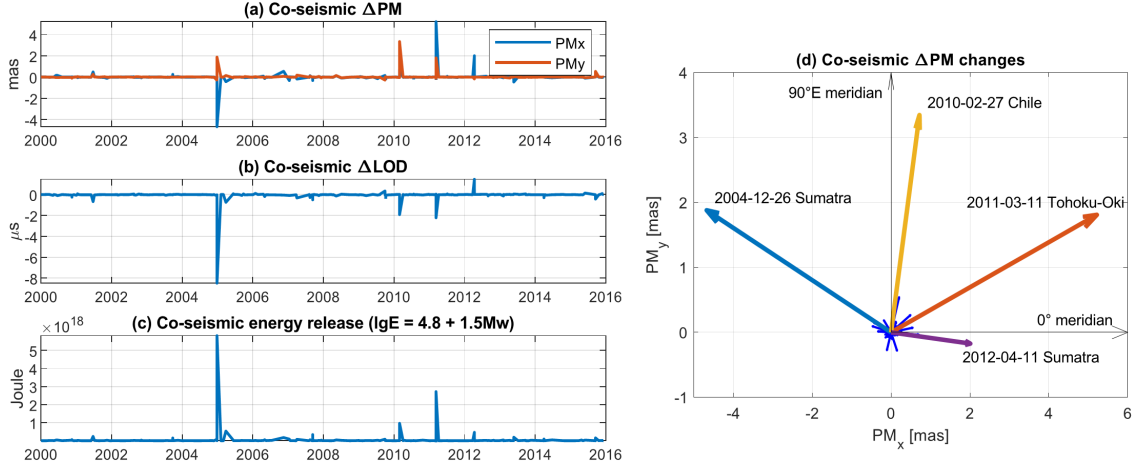


Figure 3: Coseismic changes in ERP (a-b, d) and released seismic energy (c) of $M_w \geq 7$ earthquakes (235 events).

	2004. 12. 26. Sumatra	2010. 02. 27. Chile	2011. 03. 11. Tohoku-Oki	2012. 04. 11. Sumatra
M_w [ISC]	9.3	8.9	9.1	8.6
Depth [ISC]	30 km	20 km	25 km	20 km
ΔLOD [μs]	-8.473	-1.916	-2.217	1.469
ΔPM_x [mas]	-4.675	0.720	5.217	2.009
ΔPM_y [mas]	1.880	3.346	1.810	-0.173

Table 1: Parameters and co-seismic changes of the largest co-seismic effects (2000-2016).

5.3 First results in the detection of co-seismic ERP changes

Using the modelled values of the co-seismic Earth rotation changes, our aim was to prove that this signal is present in the Earth rotation observations. However, this is a complicated task. Earth rotation is measured continuously and its variations are uniformly sampled. In contrast, earthquakes occur in a stochastic way, which means that special tools have to be applied when trying to determine their temporal characteristics. The second reason is that the signal to be proven has a magnitude in the vicinity of the current precision of ERP measurements. Lastly, the co-seismic signal is orders of magnitude smaller than the observed one. This means that one should remove each modelled signal from the observations, but doing this more errors are added to the resulting residual, and that is unfortunate given the fact that the co-seismic signal is already near the precision of the measurements.

In order to bypass the above mentioned difficulties, our first approach was to look into the prediction errors of Earth rotation. Because of the their hazardous occurrence the earthquakes cannot be accounted anyhow in ERP prediction. In this respect, the co-seismic excitation could impact the prediction error of ERP at the prediction dates when an powerful Earthquake occurs. The prediction error is estimated by removing from the ERP predictions (IERS Bulletin A) the

corresponding observed values (IERS C04). Since Bulletin A is published every 7 days and each release contains 365 days of prediction, we always used the most recent predicted values in our analysis. The result of these calculations for 10 weeks before and after the four events listed in Table 1 is presented in Figure 4, where the vertical axis shows the days into the prediction and the horizontal axis the week of the prediction (with a total of 20 weeks centered around the seismic event).

There is a promising signal in the PM_x component at the 2004 Sumatra event as high as the expected (modelled) co-seismic Δ PM_x value. However, if we look further, there are no such promising results, in some cases, the large prediction errors are present a few weeks after or even before the earthquake. This suggests that this method is either unable to prove the existence of the co-seismic signal or that our hypothesis was somewhere wrong, in the worst case, that the model was wrong.

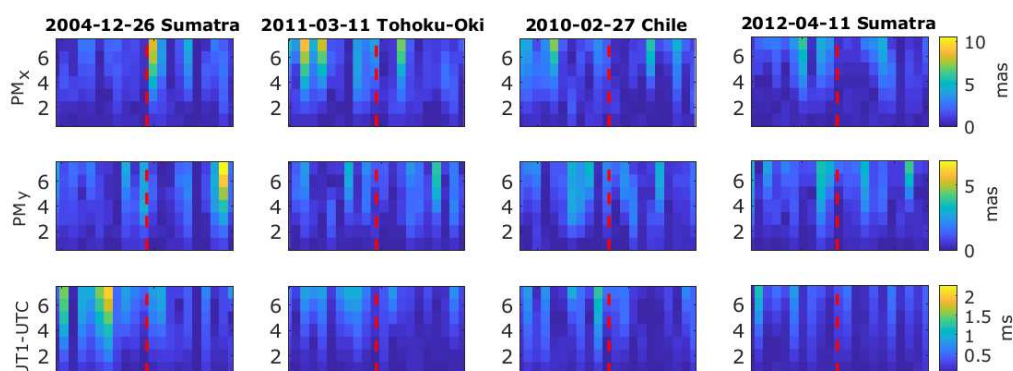


Figure 4: The prediction errors 10 weeks before and after the events listed in Table 1.

6. DISCUSSION AND CONCLUSIONS

In this paper, the interrelation of Earth rotation and seismicity is studied.

The seismic 'effectiveness' in line with the latitude shows two significant peaks at mid-latitudes. This is likely to be a result of the despinning of the Earth due to tidal friction. It was also seen that different depth zones show similar patterns but as we look into deeper zones, the energy peaks move towards the equator. This suggests that they have different tectonic origin. Also, the peaks present a symmetry with respect to $\phi = 15^\circ\text{N}$, of which the reason is still unknown.

In the second part of this paper, we studied how individual earthquakes can affect Earth rotation. We have modelled co-seismic changes in the ERP and we presented the result of a preliminary approach in order to prove that the modelled signal is present in the observations. To this aim we have calculated the prediction errors and so far our results do not confirm the expectations. Further studies will be performed in order to draw a more sound conclusion in this topic.

Acknowledgement. The first author would like to express her gratitude to the GFZ, Dr. Changyi Xu and Dr. Friedhelm Krumm for their contribution and the Journées Local Organizing Committee for their generosity.

7. REFERENCES

- Amalvict, M., Legros, H., 1993, "Stresses in the lithosphere induced by geophysical processes of degree two", *Manuscripta Geodaetica* 16, pp. 332–352.
 Bizouard C., 2005, "Influence of the earthquakes on the polar motion with emphasis on the Sumatra

- event", *Journées Systèmes de Référence Spatio-Temporels, Proceedings*, pp. 229–232.
- Bizouard, C., Lambert, S., Gattano, C., Becker, O., Richard, J. Y., 2019, "The IERS EOP 14C04 solution for Earth orientation parameters consistent with ITRF 2014", *J. Geodesy* 93(5), pp. 621–633.
- Denis, C., Varga, P., 1990, "Tectonic consequences of the Earth's variable rotation", In: *Earth rotation from eons to days*, (Eds.: Brosche P., Sündermann J.) Springer, pp. 146–162.
- Dickey, J.O., Marcus, S.L., Hide, R., Eubanks, T.M., Boggs, D.H., 1994, "Angular momentum exchange among the solid Earth, atmosphere, and oceans: A case study of the 1982-1983 El Niño event", *J. Geophys. Res. (Solid Earth)* 99(B12), pp. 23921–23937.
- Di Giacomo, D., Bondár, I., Storchak, D.A., Engdahl, E.R., Bormann, P., Harris, J., 2015, "ISC-GEM: Global Instrumental Earthquake Catalogue (1900-2009): III. Re-computed MS and mb, proxy MW, final magnitude composition and completeness assessment", *Physics of the Earth and Planetary Interiors* 239, pp. 33–47.
- Di Giacomo, D., Engdahl, E.R., Storchak, D.A., 2018, "The ISC-GEM Earthquake Catalogue (1904-2014): status after the Extension Project", *Earth System Science Data* 10, pp. 1877–1899.
- Dziewonski, A.M.; Anderson, D.L., 1981, "Preliminary reference Earth model", *Physics of the Earth and Planetary Interiors* 25(4), pp. 297–356.
- Essen, L., Parry, J.V., 1955, "An atomic standard of frequency and time interval: a caesium resonator", *Nature* 176(4476), pp. 280–282.
- Eubanks, T.M., Steppe, J.A., Dickey, J.O., Rosen, R.D., Salstein, D.A., 1988, "Causes of rapid motions of the Earth's pole", *Nature* 334(6178), p. 115.
- Gross, R.S., 1993, "The effect of ocean tides on the Earth's rotation as predicted by the results of an ocean tide model", *Geophys. Res. Lett.* 20(4), pp. 293–296.
- Gross, R.S., Chao, B.F., 2006, "The rotational and gravitational signature of the December 26, 2004 Sumatran earthquake", *Surveys in Geophysics*, 27(6), pp. 615–632.
- Hanks, T.C., Kanamori, H., 1979, "A moment magnitude scale", *J. Geophys. Res. (Solid Earth)* 84(B5), pp. 2348–2350.
- Hide, R., Dickey, J.O., 1991, "Earth's variable rotation", *Science* 253(5020), pp. 629–637.
- Kanamori, H., 2004, "The diversity of the physics of earthquakes", *Proceedings of the Japan Academy, Series B*, 80(7), pp. 297–316.
- Melosh, H.J., 1977, "Global tectonics of a despun planet", *Icarus* 31(2), pp. 221–243.
- Stacey, F.D., 1992, "Physics of the Earth", Brookfield Press, Australia, ISBN 0-646-09091-7.
- Storchak, D.A., Di Giacomo, D., Bondár, I., Engdahl, E.R., Harris, J., Lee, W.H.K., Villaseñor, A., Bormann, P., 2013, "Public Release of the ISC-GEM Global Instrumental Earthquake Catalogue (1900-2009)", *Seismological Research Letters* 84(5), pp. 810–815.
- Storchak, D.A., Di Giacomo, D., Engdahl, E.R., Harris, J., Bondár, I., Lee, W.H.K., Bormann, P., Villaseñor, A., 2015, "The ISC-GEM Global Instrumental Earthquake Catalogue (1900-2009): Introduction" *Physics of the Earth and Planetary Interiors*, 239, pp. 48–63.
- Varga, P., 2006, "Temporal variation of geodynamical properties due to tidal friction", *Journal of Geodynamics* 41(1-3), pp. 140–146.
- Varga, P., Gambis, D., Bus, Z., Bizouard, C., 2005, "The Relation Between the Global Seismicity and the Rotation of the Earth", *Observatoire de Paris, Systèmes de référence temps-espace UMR8630/CNRS*, pp. 115–121.
- Xu, C., Sun, W., Zhou, X., 2013, "Effects of huge earthquakes on Earth rotation and the length of day", *Terrestrial, Atmospheric and Oceanic Sciences* 24(4), 649.
- Xu, C., Sun, W., Chao, B.F., 2014, "Formulation of coseismic changes in Earth rotation and low-degree gravity field based on the spherical Earth dislocation theory", *J. Geophys. Res. (Solid Earth)* 119(12), pp. 9031–9041.

ON THE POSSIBLE SOURCES TO INTERANNUAL DEFORMATIONS AT THE EARTH'S SURFACE

S. ROSAT¹, N. GILLET², J.-P. BOY¹

¹ Université de Strasbourg, CNRS, EOST, IPGS UMR 7516,
Strasbourg, France - severine.rosat@unistra.fr

² Univ. Grenoble Alpes, Univ. Savoie Mont Blanc, CNRS, IRD, IFSTTAR,
ISTerre, 38000 Grenoble, France

ABSTRACT. Signals of period around 6 years were recently observed in GNSS observations, and tentatively attributed to the dynamics of the fluid core. Fluid core motions may indeed induce changes in the fluid pressure acting at the core boundaries, and thus in the Earth's surface topography when considering an elastic mantle. However, we find unlikely the possibility for an interannual deformation of some mm at the Earth's surface due to core flows. We perform a spectral as well as a spherical harmonic analysis of more than 18 years of GNSS observations and confirm the existence of the 6-year signal previously detected. We also find a significant amplitude of hydrological loading effects at such periods. These should be considered when interpreting interannual deformations.

1. INTRODUCTION

Accessing the Earth's deep interior from surface observations is challenging. Constraining fluid flows acting in the Earth's core is possible using geomagnetic data (in particular through the rate of change of the core field). However, core flow models obtained this way suffer of non-unicity and are limited to large length-scales (e.g. Holme, 2015) and periods longer than a couple of years, due to ambiguities between core and external magnetic fields towards higher frequencies (see Gillet et al. 2015). Fluid core motions possibly induce global elastic deformations through changes in the non-hydrostatic pressure acting on the core-mantle boundary (CMB) (see Dumberry 2010).

Flows near the core boundaries may result in torques acting on the mantle and inner-core (e.g. Roberts & Aurnou, 2012). If we apply a torque at the CMB, the angular momentum conservation between the fluid core and the mantle will result in perturbations of the Earth's rotation (Jault et al., 1988; Jault & Finlay, 2015). Decadal variations in the length-of-day (LOD) have been observed and attributed to the core fluid motions (e.g. Gillet et al., 2019). On interannual time-scales, a 6-year periodic oscillation in LOD has been isolated (Abarca del Rio et al., 2000; Chao et al., 2014), which is not attributed to external fluid envelopes (Gross et al., 2004). This interannual signal was later on confirmed by Holme & De Viron (2013), who proposed a correlation with geomagnetic jerks.

Fluctuations of period about 6 yr were also detected in GNSS data (GPS data only), and related to magnetic field changes by Ding & Chao (2018), who postulate that a non-zonal (degree-2 and order-2) pressure wave travels within the core. A potential link between this 6-year GPS signal and axisymmetric core flows was proposed by Watkins et al. (2018). A possible interpretation involves the libration of the solid inner core under its gravitational coupling with the mantle (Mound & Buffett, 2003, 2006; Davies et al., 2014). Axi-symmetric motions at the core surface, imaged from independent magnetic observations, explain the above subdecadal LOD oscillations if interpreted as the signature of geostrophic (i.e. axially invariant) motions, as are torsional Alfvén waves (Gillet et al., 2010, 2015). Their excitation mechanism remains an open issue. Aubert & Finlay (2019),

analysing high resolution geodynamo simulations, put forward the possibility of jerks triggered by localized (non axisymmetric) quasi-geostrophic Alfvén waves, also associated with Lorentz torques and thus to inflections into LOD series.

In this paper we recall the equations relating surface deformation and pressure changes at the CMB. We then present our analysis of GNSS data in the search for subdecadal oscillation, confronted with surface hydrological mass processes. Finally, we discuss our results.

2. CORE FLOW AND SURFACE DEFORMATION

Core flow velocities at the CMB can be reconstructed from geomagnetic observations. However, to access the non-hydrostatic pressure field p acting at the CMB, we need to know the forces at stake. This can be done under some hypothesis, like the tangentially geostrophic approximation (Gire & Le Mouél, 1990). Under this assumption, any horizontal gradient in pressure is compensated by the horizontal component of the Coriolis force

$$2\rho_c \left(\vec{\Omega} \wedge \vec{U} \right)_H = -\vec{\nabla}_H p, \quad (1)$$

with ρ_c the outer core density, $\vec{\Omega}$ the Earth's rotation vector, \vec{U} the fluid core velocity in the rotating frame, and where $\vec{\nabla}_H$ stands for the horizontal gradient. The pressure at the CMB can be decomposed by means of spherical harmonics of degree n and order m as

$$p(\theta, \phi) = \sum_{n=0}^{\infty} \sum_{m=0}^n p_{nm} Y_n^m(\theta, \phi),$$

where we have introduced the spherical harmonic functions Y_n^m at colatitude θ and longitude ϕ .

Using the Love number formalism (Love, 1909), the radial displacement at the Earth's surface induced by a pressure field acting at the CMB is given by

$$u_r(\theta, \phi) = \sum_{n=2}^{\infty} \sum_{m=0}^n \bar{h}_n \frac{\rho_{nm}}{\rho g_0} Y_n^m(\theta, \phi), \quad (2)$$

where ρ is the averaged density of the Earth, g_0 is the mean surface gravity value. \bar{h}_n is the degree- n Love number. We refer e.g. to Crossley (1975) for the elasto-gravitational equations permitting to compute these Love numbers in the case of an isotropic Earth. We adopt below the value $\bar{h}_2 = 0.2302$ (Dumberry & Bloxham, 2004). Fang et al. (1996) and Greff-Lefftz et al. (2004), using the constraint from (1), estimated to a couple of mm the decadal changes in the Earth's surface topography, induced by the fluid pressure at the top of the core (some 100 Pa). For the degree-2 zonal components, Dumberry & Bloxham (2004) have introduced a correction (perturbation of the mantle and inner core rotation rates by the zonal flow, due to centrifugal effects) that reduces by a factor ≈ 2 the amplitude of the surface deformation. This leads to decadal changes in the zonal harmonic coefficient of the radial displacement of the order of only a fraction of mm. Given the red temporal spectrum of core motions (longer periods display larger fluctuations, see Gillet et al., 2015), we then expect significantly less deformation on interannual time-scales due to dynamical fluid pressure at the CMB.

3. GNSS DISPLACEMENT OBSERVATIONS AND ANALYSIS

Ding & Chao (2018) have used GPS data from the JPL website release¹. Among all these datasets, they have selected 38 records of timespan longer than 18 years (between 1995/01/01 and

¹<https://sideshow.jpl.nasa.gov/post/series.html>.

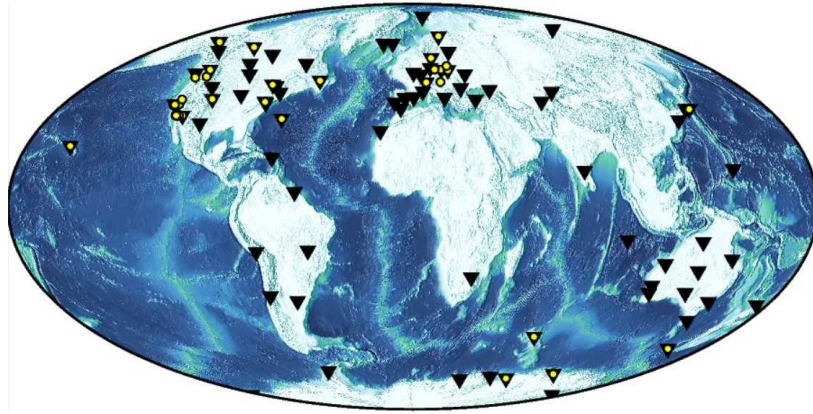


Figure 1: Map of the selected 83 GPS stations with time duration 19.8 years (Network 1, black triangles), and of the 38 GPS stations used by Ding & Chao (2018) (Network 2, yellow circles).

2015/04/02) for the vertical component. The JPL-released solutions are already corrected for the solid and ocean tidal signals. They further removed spikes and prominent steps in the timeseries as well as pole tide effect. However, they have not corrected for hydrological loading effects. Using the Optimal Sequence Estimation (OSE), which is an array-processing method based on the spherical harmonic decomposition in complex form (see Ding & Shen, 2013), they have extracted a degree-2 order-2 periodic oscillation at a period of 5.9 year. They obtained a vertical surface displacement of 1.7 ± 0.7 mm. Ding & Chao (2018) mention instead 4.3 ± 1.7 mm, but this was once normalized by the Y_2^2 value at $(\theta, \phi) = (90^\circ, 0^\circ)$ (Greenwich equator), so the actual amplitude at the surface is obtained by multiplying by 0.386 (Ben Chao, personal communication).

Watkins et al. (2018) also used JPL residual time-series spanning 2002-2014 (12 years). They considered 523 stacked GPS radial time series and found a ~ 6 -year deformation signal that they compared with hydrological loading data from the GFZ (Dill & Dobslaw, 2013). They claim that the surface loading does not account for the ~ 6 -year deformation signal. However, in the amplitude spectra of their Figure 1, a strong spectral peak exists at sub-decadal time scales in loading data.

In the following we analyze ~ 20 years of GPS vertical displacement time series and hydrological loading data in the search for such ~ 6 -year deformation signal.

3.1 Stacked GPS vertical time-series

From the JPL solutions reprocessed for the 2018 International GNSS Service campaign (IGS Repro2018a), we select stations with duration longer than 18 years (that is about three periods of 6 yr). We finally keep 83 time-records of duration 19.8 years with a homogeneous geographical distribution ('Network 1'). We also consider for a 'Network 2' the same 38 stations as in Ding & Chao (2018), with time duration of 21 years. The two networks are shown in Figure 1.

We perform two kinds of stacking on these residual time-series: a sum of the Fourier transform amplitude spectra and an Optimal Sequence Estimation (OSE) as in Ding & Chao (2018) for extracting degree-2 spherical harmonic components. The resulting amplitude spectra are respectively plotted in Figure 2 for the stacked FFTs, Figure 3 for OSE applied on Network 1 and Network 2.

3.2 Hydrological loading effect

We compare GPS vertical displacements to deformation models due to continental hydrology loading estimated at each individual station of the two networks (Figure 1) provided by the EOST loading service²; more details regarding the loading computation can be found in Petrov & Boy (2004) and Gegout et al. (2010). Loading estimates (in millimeters) are provided in the Center-

²<http://loading.u-strasbg.fr/>.

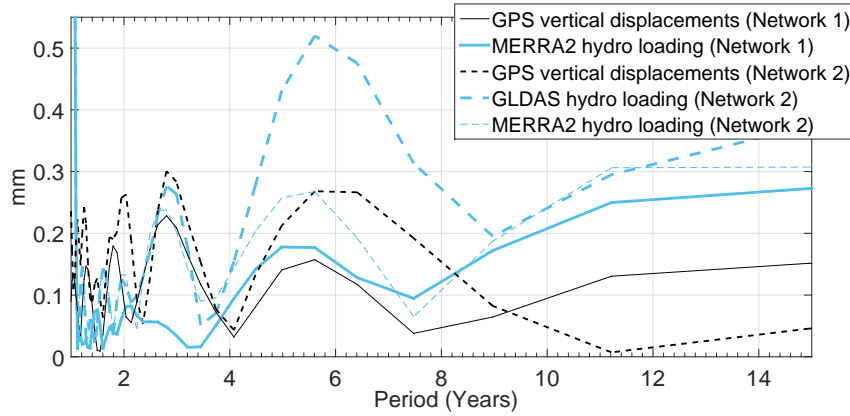


Figure 2: Stacked amplitude spectra of 83 (solid lines) and 38 (dashed lines) vertical GPS displacements of ~ 20 -year duration from JPL residuals. Hydrological loading for MERRA2 and GLDAS models from EOST loading service are also shown in blue.

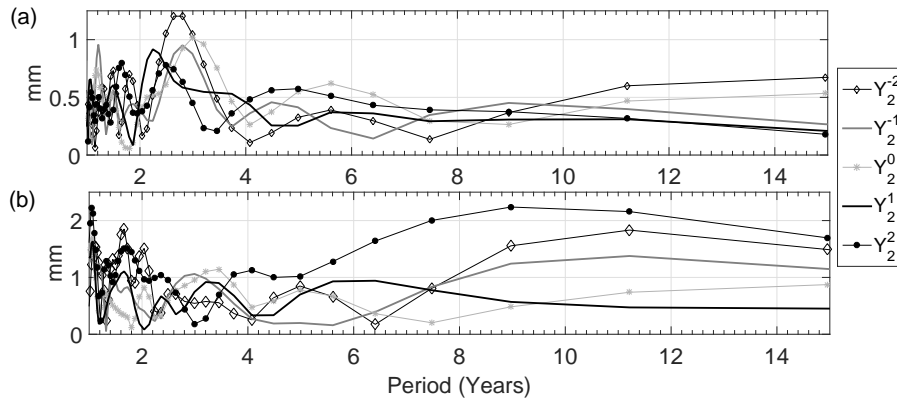


Figure 3: Optimal Sequence Estimation on (a) 83 vertical displacements of ~ 20 -year duration (Network 1) and (b) 38 vertical displacements of ~ 20 -year duration (Network 2) from JPL residuals. The Y_n^m denote the degree- n order- m components retrieved from the OSE.

of-Figure reference frame. We have tested two different hydrological models: soil moisture, snow and canopy water from GLDAS/Noah v1.0 model (Rodell et al., 2004, 3 hours, 0.25 degree) ; soil moisture and snow from MERRA2 (Modern Era-Retrospective Analysis) reanalysis (Gelaro et al., 2017, 1 hour, 0.50x0.625 degree). In both cases, permanent ice-covered regions have been masked out.

Resulting stacked FFT spectra are plotted on Figure 2, showing 3-year and 6-year spectral peaks for both hydrological models (larger for GLDAS than for MERRA2). We have also applied the OSE on the hydrological loading predictions. Results for the stations of Network 2 are shown in Figure 4. We recover a broad peak around 6 years on the components of degree-2 and order-2.

4. DISCUSSION AND CONCLUSION

Both FFT stacking method and OSE show a spectral peak around ~ 6 years with an amplitude less than 1.5 mm on GPS time-series spanning ~ 20 years of continuous measurements. Radial deformation due to hydrological loading also exhibits a spectral peak around ~ 6 years with an am-

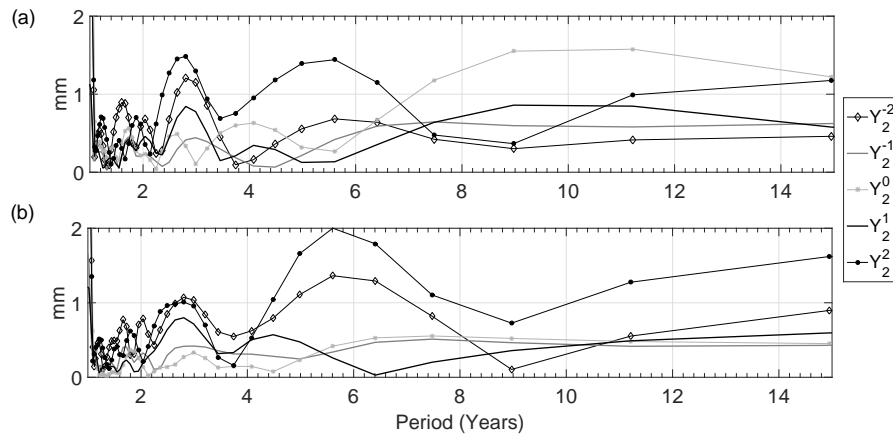


Figure 4: OSE on ~ 20 years of hydrological loading predictions for (a) MERRA2 and (b) GLDAS model at stations of Network 2. The Y_n^m denote the degree- n order- m components retrieved from the OSE.

plitude larger than (for GLDAS) or equal to (for MERRA2) the GPS-derived vertical displacement. When comparing the OSE method on two station networks (Figure 3), the retrieved degree-2 spherical harmonic components are however clearly different. A bias due to the network geometry is inherent to any spherical harmonic method and was noticed for example in the application of OSE with noisy data by Majstorović et al. (2018). As known in signal processing, spectral aliasing of higher spherical degrees on the retrieved degree-2 components is another difficulty, particularly when the distribution of stations is sparse. Indeed, Network 2 (Figure 1) exhibits a non-uniform geometrical pattern for which spherical harmonic functions cannot be orthogonal.

Previous estimates using zonal pressure flows (Dumberry & Bloxham, 2004) show that the expected radial deformation at the Earth's surface will hardly reach the millimeter level on sub-decadal periods. If accounting for non-axisymmetric motions may help reach larger surface deformation, we may still miss one order of magnitude. Alternatively, hydrological decadal fluctuations are large and have already proven to be responsible for polar motion (Adhikari & Lvins, 2016). Hydrological models exhibit a strong degree-2 and order-2 component at ~ 6 years (Figure 4) that may partially explain the interannual observed signal in GPS observations. Note that alternative mechanisms, like crystallization and dissolution processes at the CMB (Mandea et al., 2015), might also result in interannual deformation signals of similar pattern.

As a conclusion, if a signal from the outer core cannot be entirely discarded, our preliminary analysis render more probable a hydrological source to interannual surface deformation of degree-2. Further analyses using longer GNSS time-series corrected from hydrological loading will be required. However, sources of errors in vertical GPS solutions are numerous (Teferle et al., 2008) and separating the several geophysical contributions still remains a challenge.

5. REFERENCES

- Abarca del Rio, R., Gambis, D., & Salstein, D., 2000, "Interannual signals in length of day and atmospheric angular momentum", in *Annales Geophysicae* 18, pp. 347–364, Springer.
- Adhikari, S. & Ivins, E. R., 2016, "Climate-driven polar motion: 2003-2015", *Science advances*, 2(4), e1501693.
- Aubert, J. & Finlay, C. C., 2019, "Geomagnetic jerks and rapid hydromagnetic waves focusing at Earth's core surface", *Nature Geoscience*, 12(5), p. 393.

- Chao, B. F., Chung, W., Shih, Z., & Hsieh, Y., 2014, "Earth's rotation variations: a wavelet analysis", *Terra Nova*, 26, pp. 260–264.
- Crossley, D., 1975, "The free-oscillation equations at the centre of the Earth", *Geophys. J. Int.*, 41(2), pp. 153–163.
- Davies, C. J., Stegman, D. R., & Dumberry, M., 2014, "The strength of gravitational core-mantle coupling", *Geophys. Res. Lett.* 41(11), pp. 3786–3792.
- Dill, R. & Dobslaw, H., 2013, "Numerical simulations of global-scale high-resolution hydrological crustal deformations", *J. Geophys. Res. (Solid Earth)* 118(9), pp. 5008–5017.
- Ding, H. & Chao, B. F., 2018, "A 6-year westward rotary motion in the Earth: Detection and possible MICG coupling mechanism", *Earth Planet. Sc. Lett.*, 495, pp. 50–55.
- Ding, H. & Shen, W.-B., 2013, "Search for the Slichter modes based on a new method: Optimal sequence estimation", *J. Geophys. Res. (Solid Earth)* 118(9), pp. 5018–5029.
- Dumberry, M., 2010, "Gravity variations induced by core flows", *Geophys. J. Int.* 180(2), pp. 635–650.
- Dumberry, M. & Bloxham, J., 2004, "Variations in the Earth's gravity field caused by torsional oscillations in the core", *Geophys. J. Int.* 159(2), pp. 417–434.
- Fang, M., Hager, B. H., & Herring, T. A., 1996, "Surface deformation caused by pressure changes in the fluid core", *Geophys. Res. Lett.* 23(12), pp. 1493–1496.
- Gegout, P., Boy, J.-P., Hinderer, J., & Ferhat, G., 2010, "Modeling and observation of loading contribution to time-variable GPS sites positions, in *Gravity, geoid and Earth observation*", pp. 651–659, Springer.
- Gelaro, R., McCarty, W., Suárez, M. J., Todling, R., Molod, A., Takacs, L., Randles, C. A., Darmenov, A., Bosilovich, M. G., Reichle, R., et al., 2017, "The modern-era retrospective analysis for research and applications, version 2 (MERRA-2)", *Journal of Climate*, 30(14), pp. 5419–5454.
- Gillet, N., Jault, D., Canet, E., & Fournier, A., 2010, "Fast torsional waves and strong magnetic field within the Earth's core", *Nature*, 465(7294), pp. 74–77.
- Gillet, N., Jault, D., & Finlay, C., 2015, "Planetary gyre, time-dependent eddies, torsional waves, and equatorial jets at the Earth's core surface", *J. Geophys. Res. (Solid Earth)* 120(6), pp. 3991–4013.
- Gillet, N., Huder, L., & Aubert, J., 2019, "A reduced stochastic model of core surface dynamics based on geodynamo simulations", *Geophys. J. Int.*, 219(1), pp. 522–539.
- Gire, C. & Le Mouél, J.-L., 1990, "Tangentially geostrophic flow at the core-mantle boundary compatible with the observed geomagnetic secular variation: the large-scale component of the flow", *Physics Earth Planet. Int.*, 59(4), pp. 259–287.
- Greff-Lefftz, M., Pais, M., & Le Mouél, J.-L., 2004, "Surface gravitational field and topography changes induced by the Earth's fluid core motions", *J. Geodesy* 78(6), pp. 386–392.
- Gross, R. S., Fukumori, I., Menemenlis, D., & Gegout, P., 2004, "Atmospheric and oceanic excitation of length-of-day variations during 1980-2000", *J. Geophys. Res.* 109, B01406.
- Holme, R., 2015, "Large scale flow in the core, in *Treatise in Geophysics*", Core Dynamics, vol. 8, chap. 4, pp. 91–113, eds Olson, P. & Schubert, G., Elsevier.
- Holme, R. & De Viron, O., 2013, "Characterization and implications of intradecadal variations in length of day", *Nature* 499, pp. 202–204.
- Jault, D. & Finlay, C. C., 2015, "Waves in the core and mechanical core-mantle interactions", in *Treatise on Geophysics, Core Dynamics*, 2nd edition, vol. 8, chap. 8.09, pp. 225–244, eds Schubert, G. & Olson, P., Elsevier, Oxford.
- Jault, D., Gire, C., & Le Mouél, J., 1988, "Westward drift, core motions and exchanges of angular momentum between core and mantle", *Nature* 333, pp. 353–356.
- Love, A. E. H., 1909, "The yielding of the Earth to disturbing forces", *Proceedings R. Soc. London A, Containing Papers of a Mathematical and Physical Character*, 82(551), pp. 73–88.

- Majstorović, J., Rosat, S., Lambotte, S., & Rogister, Y., 2018, "Testing performances of the optimal sequence estimation and autoregressive method in the frequency domain for estimating eigenfrequencies and zonal structure coefficients of low-frequency normal modes", *Geophys. J. Int.* 216(2), pp. 1157-1176.
- Mandea, M., Narteau, C., Panet, I., & Le Mouél, J.-L., 2015, "Gravimetric and magnetic anomalies produced by dissolution-crystallization at the core-mantle boundary", *J. Geophys. Res. (Solid Earth)* 120(9), pp. 5983-6000.
- Mound, J. E. & Buffett, B. A., 2003, "Interannual oscillations in length of day: implications for the structure of the mantle and core", *J. Geophys. Res.* 108(B7), p. 2334.
- Mound, J. E. & Buffett, B. A., 2006, "Detection of a gravitational oscillation in length-of-day", *Earth Planet. Sci. Lett.* 243, pp. 383-389.
- Petrov, L. & Boy, J., 2004, "Study of the atmospheric pressure loading signal in VLBI observations", *J. Geophys. Res.* 109(B03405).
- Roberts, P. H. & Aurnou, J. M., 2012, "On the theory of core-mantle coupling", *Geophys. Astrophys. Fluid Dyn.* 106(2), pp. 157-230.
- Rodell, M., Houser, P., Jambor, U., Gottschalck, J., Mitchell, K., Meng, C.-J., Arsenault, K., Cosgrove, B., Radakovich, J., Bosilovich, M., et al., 2004. "The global land data assimilation system", *Bulletin of the American Meteorological Society* 85(3), pp. 381-394.
- Teferle, F. N., Williams, S. D., Kierulf, H. P., Bingley, R. M., & Plag, H.-P., 2008. "A continuous GPS coordinate time series analysis strategy for high-accuracy vertical land movements", *Physics and Chemistry of the Earth, Parts A/B/C*, 33(3), pp. 205-216.
- Watkins, A., Fu, Y., & Gross, R., 2018. "Earth's subdecadal angular momentum balance from deformation and rotation data", *Scientific reports* 8(1), 13761.

IERS RAPID SERVICE / PREDICTION CENTER PRODUCTS AND SERVICES: IMPROVEMENTS, CHANGES, AND CHALLENGES, 2017 TO 2019.

N. STAMATAKOS, M. DAVIS, N. SHUMATE

U.S. Naval Observatory, Washington D.C. - USA - nick.stamatakos@navy.mil

ABSTRACT. The International Earth Rotation and Reference Systems Service (IERS) Rapid Service/Prediction Centre (RS/PC) has continued to make improvements to its products throughout the time period from 2017 to 2019. Several noteworthy improvements are as follows: a) the method of computing Celestial Pole Offsets (CPO) was updated; b) the Navy Global Environment Model (NAVGEN) atmospheric angular momentum (AAM) input was updated from version 1.4 to 1.4.3eop; c) a new version of the Earth Orientation (EO) matrix calculator using the IERS Conventions 2010 (v1.2.0) was made available; and d) updated VLBI 24-hour and intensive series solutions were incorporated.

In order to improve accuracy and increase robustness of the EO parameter (EOP) results, development work for future enhancements is being performed in the following areas: a) investigating the use of a new combination of Very Long Baseline Array (VLBA) and Very Long Baseline Interferometry (VLBI) intensives, named the w-series using a combination of Mauna Kea (Mk), Wettzell (Wz), and Wettzell-North (Wn) radio telescopes; b) improving polar motion and possibly UT1-UTC accuracy and robustness through the use of AAM and oceanic angular momentum (OAM) inputs; c) investigating the use of improved optimal estimation techniques to improve the accuracy and robustness of the EOP combination results; and d) investigating improving EOP prediction techniques.

A few anomalous EOP results that were reported, but not fully explained in the IERS RS/PC contribution to the IERS Annual Report 2018 (Stamatakos *et. al*, 2020), are further discussed. These are the larger than expected residuals in the Nxdaily/off-hours EOP solutions and the USNO versus IGS polar motion products reported in the weekly statistics (contained in the gpsspol.asc file).

Between the time of the Journées 2019 conference¹ and the writing of this document, the U.S. Naval Observatory's IERS RS/PC web and FTP sites (maia.usno.navy.mil and toshi.nofs.navy) were ordered to be taken offline to undergo modernization, starting on 24 October 2019. The expected completion of work and return to service are estimated to be no earlier than June, 2020. The implications of this change are that a) the EO matrix calculator will not be available until the return-to-service work is completed and b) the RS/PC EOP results and the IERS Conventions will also be unavailable at <https://maia.usno.navy.mil> and <https://toshi.nofs.navy.mil>. However, both EOPs and Conventions are hosted at other servers – as discussed later in this report.

1. OVERVIEW OF RS/PC SOLUTION.

The operational, daily EOP combination and prediction (CP) solution (which includes finals.daily) is produced at approximately 17:00 UTC each day; the weekly version (Bulletin A) is produced on Thursdays just after 17:30 UTC. Both provide EOP values that include polar motion, UT1-UTC, and CPOs used to relate the terrestrial to celestial reference systems. Observations from VLBI, the Global Positioning System (GPS), Satellite Laser Ranging (SLR), and AAM are used to generate these solutions. Further details about inputs, processes, numbers of users, and

¹Journées 2019, "Astronomy, Earth Rotation, and Reference Systems in the Gaia Era," Paris, France, 7-9 October 2019.

results are provided in Stamatakos *et al.*, (2011) and in Section 3.5.2 of the IERS Annual Report 2018 (Stamatakos *et al.*, 2020).

In addition to the operational, daily EOP CP solution, there are three additional EOP solutions (referred to as the *Nxdaily* solutions) that have been produced each day since 16 December 2011. The automated processes that generate the *Nxdaily* solutions begin at 03:10, 09:10, and 21:10 UTC and should be completed within 20 minutes after the initial start time. The only solution that is currently actively monitored by EOP RS/PC personnel is the operational, daily EOP solution that begins processing at 17:00 UTC. A discussion of the advantages, increased accuracy of results, and additional observations available at the 03:10, 09:10, and 21:10 EOP solution update times is provided in the Prediction Techniques and Results subsection within Section 3.5.2 of the IERS Annual Report 2018 (Stamatakos *et al.*, 2020).

Until 24 October 2019, all EOP results were located at <http://maia.usno.navy.mil/ser7> (*maia*) and <http://toshi.nofs.navy.mil/ser7> (*toshi*) and several other backup locations as listed in Table 8 of Section 3.5.2 of the IERS Annual Report 2018 (Stamatakos *et al.*, 2020). Until the restoration of *maia*, planned for June 2020, the 17:00 UTC, *operational daily*, EOP solutions are available only at Crustal Dynamics Data Information System (CDDIS)² and IERS³ servers, with USNO uploading directly to each of those sites on a daily basis. As of the writing of this report, the *Nxdaily* solutions are only available at the CDDIS site. (Lastly, CDDIS does host RS/PC EOP results at an https site; contact CDDIS for details on how to access this site.)

2. IERS RS/PC IMPROVEMENTS AND CHANGES, 2017 TO 2019.

Beginning on 29 March 2018, an updated method for computing CPOs was integrated into the RS/PC EOP products. Prior to this date, some of the CPO inputs used in the combination were based on $(d\psi / d\epsilon)_{(1976/1980)}$ (based on the 1976 precession and 1980 nutation theory) and some inputs were based on $(dX / dY)_{2006/2000}$ (the 2006 precession and 2000 nutation theory, Wallace *et al.*, (2006)). With the updated software, all CPO inputs are based on $(dX / dY)_{2006/2000}$, thus making the combination algorithm much simpler to implement and making systematic correction adjustments more straightforward.

The algorithm to predict CPOs after the last combination value has also been updated and is illustrated in the flowchart in Figure 1. First, empirical fits are performed on two years of combination values to obtain offsets, rates, and annual, semi-annual, free-core, 9.1 year, and 27.55 day periodic signals, and then residuals are created by subtracting the empirical fits from the combination data. An auto-regressive model of order 4, AR(4), is fit to the residuals and then used to predict that portion of the signal forward 1 to 90 days. In addition, the empirical fit coefficients are used to project forward the same 1 to 90 day period and then added to the AR(4) signal; the results are dX and dY prediction values from 1 to 90 days into the future from the last observation day.

Following the implementation of the updated CPO methodology, there has been an improvement in accuracy in the 0-day and 1-day CPO predictions. A chart is shown in Figure 2 that compares the CPOs obtained during the period 29 March 2018 to 31 July 2019 (Period 2) with the period from 1 January 2016 to 28 March 2018 (Period 1). When compared to the C04 observational data, the Period 2 dX RMS 0-day prediction residuals were reduced by 11% when compared to Period 1 and 0-day dY prediction residuals were reduced by 23%. Similarly, the 1-day dX prediction residuals were reduced by 5% and the 1-day dY were reduced by 14%.

Several times between 2017 and 2019, the USNO and NASA Goddard (GSFC) VLBI input series were updated; USNO VLBI updated on 27 September 2017, 23 August 2018, and 01 August

²<ftp://cddis.gsfc.nasa.gov/pub/products/iers>

³<https://www.iers.org/IERS/EN/DataProducts/EarthOrientationData/eop.html>

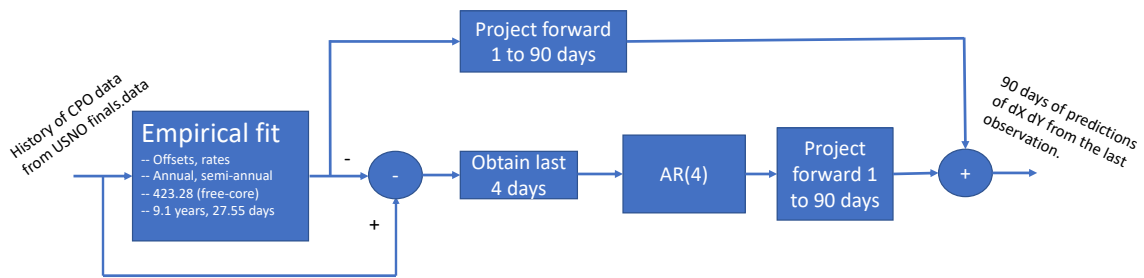


Figure 1: CPO Prediction Algorithm Flow Chart Used in RS/PC Software Since 29-March-2018.

Prediction Day	Period 1: dX RMS (milliarcsec)	Period 2: dX RMS (milliarcsec)	% decrease	Prediction Day	Period 1: dY RMS (milliarcsec)	Period 2: dY RMS (milliarcsec)	% decrease
0-day	0.110	0.099	11	0-day	0.106	0.086	23
1-day	0.111	0.106	5	1-day	0.099	0.087	14

Figure 2: CPO Prediction Statistics Before (Period 1) and After (Period 2) the Upgrade in Processing.

2019, while GSFC updated on 29 August 2019. Each time an update was included in the RS/PC combination, systematic adjustments for UT1-UTC, polar motion, and CPOs were re-computed and applied to each series to maintain a minimal residual between each new series and the IERS reference series (the C04).

Starting on 17 May 2019, the upgraded AAM model input, named the Navy Fleet Numerical Meteorology and Oceanography Center (FNMOC) Navy Global Environmental Model (NAVEM) AAM version 1.4.3eop, was incorporated into the RS/PC combination and prediction software. This new model incorporated the following upgraded features: a) approximately 31 km grid spacing, b) an atmosphere up to a height of approximately 60 km, c) hybrid 4-D data assimilation, d) ozone assimilation, and e) an engineering fit to better model upper atmospheric (zonal) winds.

Using the NOAA AAM forecast results as a benchmark, one can see the improvement of the NAVEM version 1.4.3eop to version 1.4. The top two plots are the mean and RMS errors of the NOAA and NAVEM version 1.4 forecast results compared to the NOAA analysis data from 01 January 2016 through 15 May 2018; the bottom two plots are comparisons of the NOAA and NAVEM version 1.4.3eop forecasts from 01 June 2018 through 15 September 2019. The x-axis in each plot is the prediction hour from the current day midnight hour, and the y-axis is the dimensionless effective angular momentum coefficients, χ_i . The top plots show the NAVEM v1.4 mean and RMS residuals have higher residuals than the NOAA results; whereas, the v1.4.3eop has lower mean and comparable RMS residuals to NOAA.

A new on-line EO matrix calculator providing the direction cosine matrix (DCM) between the terrestrial (ITRF) and celestial (GCRS) reference frames was developed and made available to users in August 2018. It is based on the the Celestial Intermediate Pole and Origin (CIP and CIO, respectively) and Terrestrial Intermediate Origin (TIO), non-equinox algorithms presented in Chapter 5, IERS Conventions (2010, Tech Note 36.) However, as was stated in the Overview section, the U.S. Naval Observatory's IERS RS/PC web and FTP sites (maia.usno.navy.mil and toshi.nofs.navy) were taken offline to undergo modernization, starting on 24 October 2019; the

expected completion of work and return to service are estimated to be no earlier than mid-June 2020, at which time it is anticipated that the EO matrix calculator will be made available to users again.

The matrix code is written in FORTRAN with HTML and web interface codes, and relies heavily on code from the IERS Conventions 2010 software and the Standards of Fundamental of Astronomy (SOFA) libraries. The observable quantities are from a version of finals2000A.data or finals2000A.daily, and, if necessary, the polar motion, UT1-UTC, and celestial pole observables are interpolated. Long period tidal terms are removed and then, long period tidal, diurnal, and sub-diurnal tidal terms are added back to these observables after interpolation. Sub-diurnal/diurnal tides, CPOs, and librations are used by default, but can be turned off. Outputs include the ITRF to GCRS direction cosine matrix at each requested epoch and several intermediate transformations. The EO matrix calculator user-interface is shown in Figure 4. In Figure 5, a comparison table of the Equinox-based and CIP/CIO/TIO-based calculators is provided.

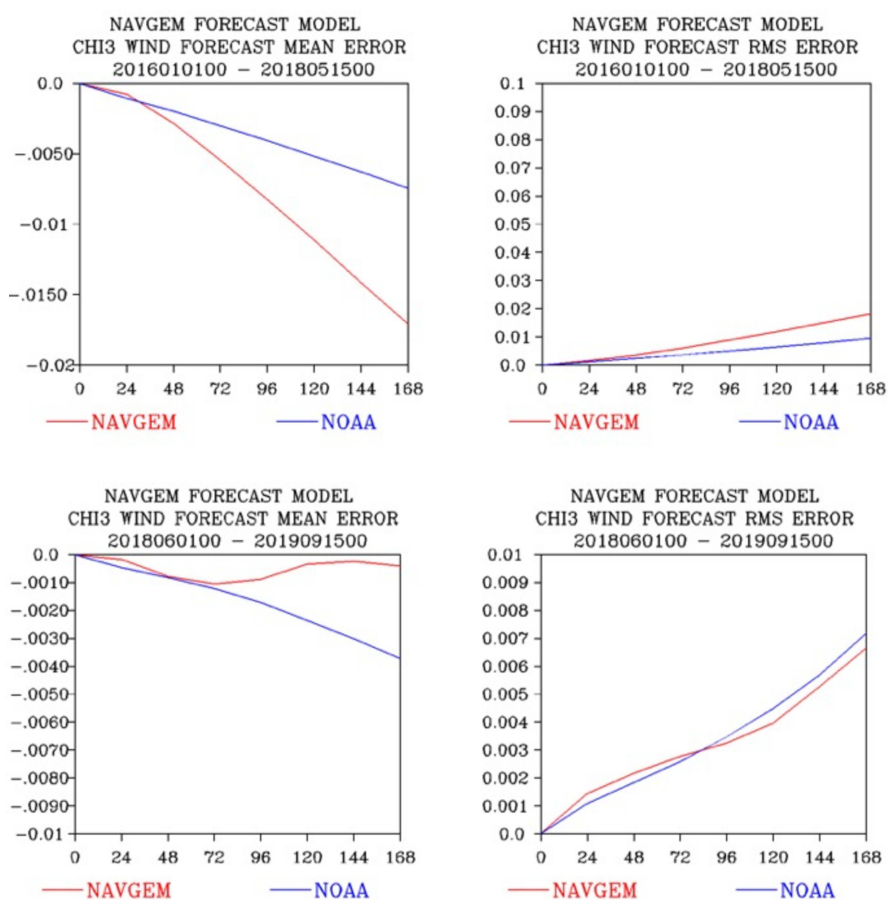


Figure 3: NAVGEM v1.4, NAVGEM v1.4.3eop, and NOAA CHI3 (χ_3) Wind Forecast Coefficient residuals versus NOAA analysis data. (Plots provided by Dr. Tim Hogan of NRL Monterey.) The X-axis of each plot has units of Days, and the Y-axis is the dimensionless effective angular momentum coefficient (χ_3).

As discussed in the IERS Annual Report 2018 (Stamatakos *et. al*, 2020), as more observational data becomes available, there should be an improvement in the polar motion predictions. The last IGS Ultra observation available for the operational solution made at 17:00 UTC is at 00:00 UTC of the current day (MJD); a prediction of the polar motion solution for 00:00 UTC of MJD+1 is created based on that last observation. At each of the later EOP Nxdaily solution updates begun

Figure 4: CIP/CIO/TIO-based EO matrix calculator user interface.

<u>Equinox-based</u>	<u>CIP/CIO/TIO-based</u>
<ul style="list-style-type: none"> • Observations ($x, y, UT1-UTC, dX, dY$) from <i>finals2000A</i> • Equinox-based (Bias-Precession-Nutation): <i>iau_c2teq</i> (IAU) <ul style="list-style-type: none"> • IAU 2006 precession & IAU2000A nutation: <i>iau_pnm06a, iau_bpr2xy, iau_s06</i> (IAU) • Polar Motion: <i>iau_pom00</i> (IAU) <ul style="list-style-type: none"> • Earth Tides: <i>RG_ZONT2</i> (IERS Conventions 2010) • Diurnal & Sub-diurnal Tides: <i>ORTHO_EOP & CNMTX</i> (IERS) • "Sub-diurnal Nutation" quasi-diurnal terms: <i>PMSDNUT2</i> (IERS) • TIO Locator (s') <i>iau_sp00</i> (IERS) • Sidereal Time: <i>iau_gst06</i> (IAU) <ul style="list-style-type: none"> • Earth Tides: <i>RG_ZONT2</i> (IERS Conventions 2010) • Diurnal & Sub-diurnal Tides: <i>ORTHO_EOP & CNMTX</i> (IERS) 	<ul style="list-style-type: none"> • Observations ($x, y, UT1-UTC, dX, dY$) from <i>finals2000A</i> • Celestial Intermediate Origin & Pole based: Matrix (USNO) • Bias-Precession-Nutation: <i>iau_c2IXYS</i> (IAU) <ul style="list-style-type: none"> • IAU 2006 precession & IAU2000A nutation (X, Y): <i>iau_xy06</i> (IAU); (CIO locator (s)) <i>iau_s06</i> (IAU) • Polar Motion: <i>iau_pom00</i> (IAU) <ul style="list-style-type: none"> • Earth Tides: <i>RG_ZONT2</i> (IERS Conventions 2010) • Diurnal & Sub-diurnal Tides: <i>ORTHO_EOP & CNMTX</i> (IERS) <ul style="list-style-type: none"> • "Sub-diurnal Nutation" quasi-diurnal terms: <i>PMSDNUT2</i> (IERS) • TIO Locator (s') <i>iau_sp00</i> (IERS) • Earth Rotation Angle: <i>iau_era00</i> (IAU) <ul style="list-style-type: none"> • Earth Tides: <i>RG_ZONT2</i> (IERS Conventions 2010) • Diurnal & Sub-diurnal Tides: <i>ORTHO_EOP & CNMTX</i> (IERS) • Sub-diurnal Libration: <i>UTILIBR</i> (IERS)

Figure 5: Comparison of CIP/CIO/TIO-based and Equinox-based EO matrix calculator algorithms.

at 21:10 UTC (4 hours after the 17:00 UTC update time), and at 03:10 UTC and 09:10 UTC of the following day, updated IGS Ultra observations are made available, and in theory, these later EOP solution updates should have improved predictions of polar motion at 00:00 UTC of MJD+1. As shown in Figure 7, the Nxdaily / off-hour 2016 and 2017 statistics show agreement with this theory – the RMS of the residual decreases from column 1 (17:00 UTC) to column 4 (09:10 UTC).

Unfortunately, as one can see in the last rows of the tables in Figure 7, for 2018, there was no such significant improvement as more observational data became available at 21:10, 03:10, and 09:10 UTC. After the 2018 Annual Report was published, the RS/PC performed an investigation and an improperly implemented code change was identified, namely, the updated IGS Ultra inputs were not being used. As of 15 Sept 2019, a code fix was implemented and final EOP results with updated IGS Ultra inputs are being generated. The forthcoming 2019 IERS Annual Report should demonstrate an improved polar motion as additional observational inputs become available throughout the day.

Another potential issue affecting the RS/PC results was identified in the 2018 Annual Report, namely, the polar motion residual statistics of the RS/PC versus the IGS finals reported in the Annual Report and that published weekly by the RS/PC (at the beginning of the file, *gpspol.asc*), both appear to be lower than that published in the weekly statistics at the end of the same file. After some analysis, the RS/PC determined that the method of interpolation used to compute the residuals was different among the cases. The IGS finals are produced for each noon epoch and the RS/PC results are produced for the midnight epoch. The IERS report and the beginning of the *gpspol.asc* use an interpolation method based on smoothing, weighted cubic spline (SWCS) coefficients; whereas, the reported statistics at the end of the *gpspol.asc* file use a simple cubic spline for interpolation. Since using the SWCS more accurately reflects the residuals between the contributor and the combination, as of July 11, 2019, the SWCS was chosen to replace the weekly statistics reported at the end of the *gpspol.asc* file – thus, more accurately reporting the accuracy of the RS/PC polar motion solution compared to the IGS finals.

3. FUTURE DEVELOPMENTS

Improvements in polar motion near-term prediction accuracies may be possible using combined AAM and OAM model data; AAM inputs used in these studies are based on the NAVGEM and the OAM based on the U.S. Navy Hybrid Coordinate Ocean Model (HYCOM). At the 2019 European Geophysical Union (EGU) meeting, a poster (Stamatakos *et al.*, 2019) was presented that explained the work in detail. As shown in the flowchart contained in that poster, excitation functions are derived from existing USNO EOP data and are differenced with combined and adjusted analysis AAM and OAM excitation functions to form residuals, from which a predictive AR model

is determined. This AR model predicts the non-angular momentum part of the polar motion and is combined with the predicted (forecast) AAM and OAM data to form the polar motion near-term predictions.

As backup to the INT1, INT2, and INT3 intensives, USNO and the IVS have been developing new baselines combining VLBI and VLBA radio telescopes. One baseline that is being used is the Mauna-Kea (Mk) to Wettzell (Wz) pair, partly because of its similarity to the existing and well-characterized Kokee Park (Kk) Wz baseline. As shown in Figure 8, the two stations would share similar visibility to desired radio sources, yet they are far enough apart (>500 km) that adverse weather conditions may not affect both stations simultaneously. After USNO personnel had re-characterized the station position, which was significantly affected by seismic activity in mid-2018, the Mk-Wz baseline has been used in the operational RS/PC combination since December 2019, and continues to be a backup to the Ishioka (Is) to Wz baseline when Is is unable to observe. Another baseline being rapidly characterized is the Mk to Wettzell-North (Wn).

The RS/PC is conducting a research and development project to investigate using improved optimal estimate techniques to better combine EOP inputs. First, code that uses an improved smoothing, weighted cubic spline (SWCS) that allows for state and derivative state inputs (such as UT1-UTC and length-of-day (LOD)) is being developed. Using this new spline should increase robustness and possibly accuracy of EOP solutions. Then, a development to broaden the improved SWCS to allow for covariance based inputs (such as from SINEX files) will be implemented. The use of a Kalman Filter or other type of filtering technique might also be investigated to determine if improvements in accuracy and robustness can be improved further. In addition, improved prediction techniques will be investigated in the later years of the project.

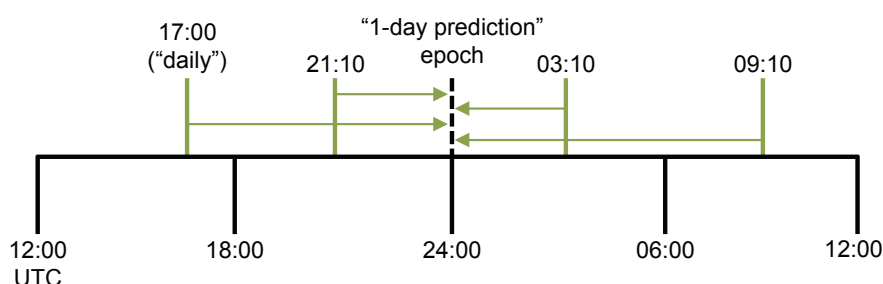


Figure 6: Timeline of Nxdaily EOP 1-day prediction solutions in relation to the EOP operational solution produced at 17:00 UTC. The 21:00 UTC solution is updated on the present day (MJD), while the 03:10 UTC and 09:10 UTC Nxdaily EOP solutions are updated at MJD+1.

PMx	Time of solution in UTC. Results in milliarseconds			
Year	17:00 UTC	21:10	03:10	09:10
2016	0.34	0.29	0.16	0.08
2017	0.35	0.29	0.13	0.08
2018	0.31	0.29	0.29	0.27

PMy	Time of solution in UTC. Results in milliarseconds			
Year	17:00 UTC	21:10	03:10	09:10
2016	0.25	0.22	0.08	0.09
2017	0.26	0.20	0.09	0.09
2018	0.23	0.21	0.28	0.21

Figure 7: Nxdaily EOP Solution Results. The 2016 and 2017 polar motion results are as expected; whereas, the 2018 results were anomalous.

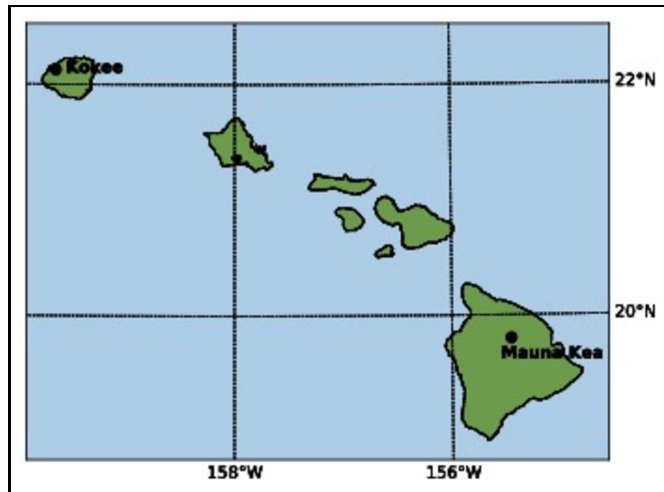


Figure 8: Proximity of Kokee Park and Mauna-Kea radio telescope locations.

Acknowledgements. The authors would like to thank Dr. Christine Hackman (Head, EO Department), Merri Sue Carter, and Dr. Dennis McCarthy in helping to edit this paper.

4. REFERENCES.

- Petit, G., Luzum B., (eds.), 2010, IERS Conventions 2010, IERS Technical Note No. 36., Frankfurt, Germany.
- Stamatakos N., Luzum B., Stetzler B., Shumate, N., Carter, M. S., 2011, "Recent improvements in the IERS Rapid Service/Prediction Center Products", *Journées Systèmes de Référence Spatio-Temporels* 2010, pp. 184–187.
- Stamatakos, N., McCarthy, D., Salstein, D., 2019, "Investigating Possible Combinations of Atmospheric, Ocean, and other Geophysical Angular Momentum Data to Improve Operational Earth Orientation Information", EGU2019-3164 POSTER at the European Geophysical Union Meeting, Vienna, Austria, April 2019.
- Stamatakos, N., Hackman, C., Davis, M., Carter, M. S., Shumate, N., 2020, *IERS Annual Report 2018*, retrieved from the International Earth Rotation and Reference Systems Service website: <https://www.iers.org/IERS/EN/Publications/AnnualReports/AnnualReport2018.html>.
- Wallace, P.T., Capitaine, N., 2006, "Precession-nutation procedures consistent with IAU 2006 resolutions", *A&A* 459, pp. 981–985, <https://www.aanda.org/articles/aa/pdf/2006/45/aa5897-06.pdf>.

ANALYSES OF CELESTIAL POLE OFFSETS WITH VLBI, LLR, AND OPTICAL OBSERVATIONS

Y.-T. Cheng, J.-C. Liu, Zi Zhu

School of Astronomy and Space Science, Key Laboratory of Modern Astronomy and Astrophysics, Nanjing University - China - jcliu@nju.edu.cn

ABSTRACT.

Aim. This work aims to explore the possibilities of determining the long-periodic part of the Earth's precession-nutation with techniques besides VLBI. Lunar laser ranging (LLR) is chosen for its relatively high accuracy and long period. Results of previous studies could be updated using latest data with generally higher quality, as well as adding ten years to the total time span. Historical optical data are also analyzed for its rather long time coverage to look into its possibility to improve the current Earth's precession-nutation model.

Methods. Celestial pole offsets (CPO) series are obtained from LLR and optical observations, and analyzed separately by weighted least square fits of three empirical models. A joint analysis of VLBI and LLR data is also presented for further discussion.

Results. Determination of the nutation terms with both VLBI and LLR data have been improved. LLR shows its potential to determine celestial pole offsets with a comparably high accuracy with VLBI in the future and to serve as an independent check for the VLBI results. CPO series from historic optical observations have a typical standard error of about two hundred times larger than that of the VLBI series, hence is hardly able to make any contribution to the contemporary precession-nutation theory.

1. INTRODUCTION

The Earth's precession-nutation models describe the long-term and long-periodic changes of the Celestial Intermediate Pole (CIP) direction in the Geocentric celestial reference system (GCRS). In this work, we focus on the Celestial Pole Offsets (CPO), representing the differences between observations and theoretical predictions of the CIP locations (i.e. dX , dY).

By far, VLBI has been playing the most crucial role in this domain given its micro-arcsecond level accuracy. However, the relatively short time span of VLBI observations can be a disadvantage in revealing effects with long periods such as the deficiencies in the Earth's precession model with a period of about 26 000 years.

Lunar Laser Ranging (LLR), being operated since 1969, is the only space-geodetic technique now capable to realize a stable dynamical reference system, with sufficient accuracy of determinations of the lunar orbit (Zerhouni & Capitaine 2009, denoted as ZC09 hereafter). ZC09 provided a basic method of determining CPO from LLR observations using data in the interval of 1969-2008. Hofmann et al. (2018) (denoted as H18 hereafter) have estimated of reflector coordinates, station coordinates and velocities and EOP at the same time, with LLR data during 1969-2016.

The history of optical observations is much longer than that of both VLBI and LLR observations. Vondrák & Štefka (2010) have constructed a series of Earth Orientation Catalogs (EOC) based on a combination of Hipparcos/Tycho Catalogs and long lasting ground-based astrometric observations. These catalogs have been used to derive the CPO during time interval 1899.7-1992.0, referred to the Hipparcos Celestial Reference Frame (HCRF), which can be regarded as the optical realization of the ICRS.

In this work, we aim to improve the determination of precession-nutation corrections based on analyses of VLBI observations solely, and also a joint analysis of VLBI and LLR data. We follow the basic method of ZC09 for the analyses of LLR and the joint analysis of LLR and VLBI, and make a comparison with the results of H18. Further discussions and the future potential of LLR are presented. The time distribution of CPO series derived from LLR, VLBI (opa2018a) and optical observations are plotted in Figure 1 to show the differences in both the number of observations and in time span.

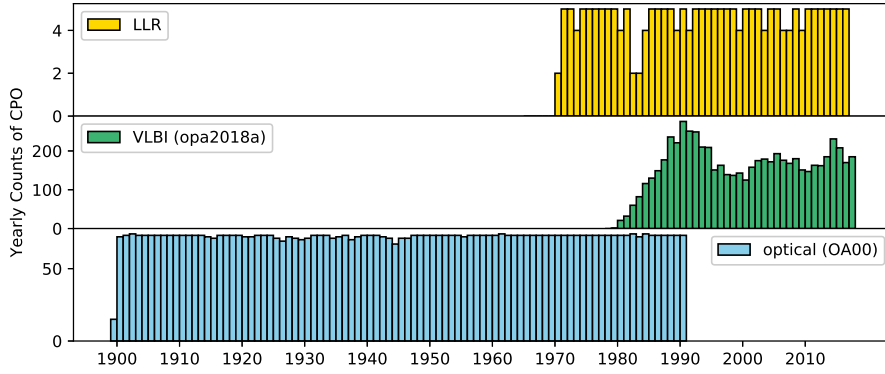


Figure 1: Time distributions of LLR, VLBI (opa2018a) and optical CPO series. Time span of every CPO series: LLR 1970.6-2017.7; VLBI (opa2018a) 1979.9-2018.5; optical (OA00) 1899.7-1991.9.

2. MODELS USED IN CPO ANALYSES

Three empirical models are fitted to the CPO series in the following analysis:

1. A parabola, namely a quadratic function of t .
2. A linear term and 18.6-year nutation term.
3. A linear term, 18.6-year and 9.3-year nutation terms.

All models are functions of t (centuries from the basic epoch). The basic epoch was set to be J2000.0 for VLBI and LLR series, but J1956.0 for optical series, which is almost the central epoch of the time coverage of optical observations.

3. CPO RESIDUALS WITH VLBI OBSERVATIONS

We use CPO series from 1979 to 2018 derived by the Calc/Solve software at the Paris Observatory analysis center (OPA) and also the series derived by the Goddard Space Flight Center (GSF) in the framework of the International VLBI Service for geodesy and astronomy (IVS, Nothnagel et al. 2017). The quasi-periodic free core nutation (FCN), with a period of 430.23 days, is removed before analyzing the residuals. We remove this effect according to the model recommended by the IERS conventions 2010 (Petit & Luzum 2010).

We fit all of the three models mentioned to the residuals, and show the results in Table 1, with both sources of data presented for comparison. The fitted coefficients of the secular terms show an underestimation in the IAU model of the precession rate in X about 0.3 mas cy^{-1} . Capitaine et al. (2009) have pointed out that the 18.6-year nutation term is the most sensitive to the error in the precession-nutation model, with VLBI data up to 2008. With the accumulated high-precision data, we here obtain more consistent results of the corrections of the 18.6-year nutation term. All fit

Table 1: Weighted fits of three models to VLBI residuals (1979.6-2018.6), corresponding to IAU 2006/2000 model.

Term		t^0	t^1	t^2	$\sin(18.6 \text{ yr})$	$\cos(18.6 \text{ yr})$	$\sin(9.3 \text{ yr})$	$\cos(9.3 \text{ yr})$	WRMS _{pre}	WRMS _{post}
Unit		as	as/cy	as/cy^2	as	as	as	as	as	as
opa2018a	dX	18 ± 1	266 ± 21	-4338 ± 143					126	119
	dY	-86 ± 1	-519 ± 22	5325 ± 145					147	130
gsf2016a	dX	49 ± 1	215 ± 19	540 ± 120					134	104
	dY	-101 ± 1	-477 ± 20	5492 ± 122					131	109
opa2018a	dX	13 ± 1	381 ± 12		36 ± 1	-18 ± 1			126	116
	dY	-71 ± 1	-34 ± 12		-35 ± 1	40 ± 1			147	128
gsf2016a	dX	49 ± 1	441 ± 10		43 ± 1	-11 ± 1			134	101
	dY	-87 ± 1	61 ± 10		-34 ± 1	47 ± 1			131	107
opa2018a	dX	13 ± 1	334 ± 12		34 ± 1	-24 ± 1	-19 ± 1	-3 ± 1	126	116
	dY	-70 ± 1	4 ± 12		-38 ± 1	46 ± 1	22 ± 1	23 ± 1	147	126
gsf2016a	dX	49 ± 1	413 ± 11		41 ± 1	-14 ± 1	-13 ± 1	3 ± 1	134	101
	dY	-84 ± 1	40 ± 11		-43 ± 1	48 ± 1	20 ± 1	23 ± 1	131	105

coefficients of the 18.6-year nutation term reveal that the amplitude is underestimated by about 35 as . However, the formal errors of the CPO derived from VLBI data are probably underestimated by about a factor 2 according to Herring et al. (2002).

4. ANALYSES OF LLR RESIDUALS

LLR observations are presented as so-called normal points. They refer to lines of data containing the emission time of the laser, observed round trip time in UTC, telescope and reflector ID, and some atmospheric parameters of each observation. These data can be used to calculate the round-trip times, then the residuals of the round-trip time [observation minus calculation (O–C)], which can be converted to residuals in one-way distance in centimeters. Finally we obtain CPO series based on these residuals.

We used the residuals spanning 1970-2017 (O–C of the one-way distance in centimeters) provided by Pavlov et al. (2016)¹. The rejection procedure is taken in advance to exclude data with relatively poor quality. The rejection criterion is such that O–C values that are higher than three times the respective formal error and the total WRMS of all normal points of the same station are excluded.

ZC09 offered a method of calculating the CPO from LLR observations. We generally follow their method in converting LLR residuals into CPO. The method of getting LLR residuals from the observational data (also known as “normal points”) in ZC09 (Chapront et al. 1999) and Pavlov et al. (2016) are basically the same. Among all the effects which have to be considered in the process of deriving dX and dY from LLR observations, only the transformation matrix for precession and nutation is related to X and Y. In the calculation of partial derivatives $\frac{\partial \Delta t}{\partial X}$ and $\frac{\partial \Delta t}{\partial Y}$, we ignored minor effects such as solid tide deformations of the Earth and the Moon, since we do not need an accuracy of the moment of time as high as that in the calculation residuals of one-way distance. The relativistic transformations between terrestrial and selenocentric reference systems to the BCRS Petit & Luzum (2010) are applied. The relativistic gravitational delay (Kopeikin 1990) and the tropospheric delay (Mendes & Pavlis 2004, Mendes et al. 2002) are also taken into account.

We use JPL (Jet Propulsion Laboratory) planetary ephemerides DE430 (Folkner et al. 2014) for the geocentric and barycentric positions of the Sun, Earth, Moon and major planets, and also for the lunar libration angles and TT–TDB transformations.

Uncertainties are presented as two times and three times the formal error, in ZC09 and H18 respectively, after fitting the CPO series to the models to account for unmodeled effects and

¹<http://iaaras.ru/en/dept/ephemeris/llr-oc/>

Table 2: Weighted fits of model 2 and 3 to LLR residuals.

Term		t^0	t^1	$\sin(18.6 \text{ yr})$	$\cos(18.6 \text{ yr})$	$\sin(9.3 \text{ yr})$	$\cos(9.3 \text{ yr})$	WRMS _{pre}	WRMS _{post}
Unit		mas	mas/cy	mas	mas	mas	mas	mas	mas
This work	dX	-0.38 ± 0.02	1.43 ± 0.18	-0.26 ± 0.02	-0.37 ± 0.01			0.526	0.463
	dY	-0.36 ± 0.03	-0.54 ± 0.19	-0.81 ± 0.02	-0.30 ± 0.01			0.672	0.581
ZC09	dX	0.27 ± 0.13	5.77 ± 3.25	0.00 ± 0.22	0.01 ± 0.13				
	dY	-0.17 ± 0.13	1.07 ± 3.11	-0.02 ± 0.21	-0.22 ± 0.12				
This work	dX	-0.28 ± 0.03	1.77 ± 0.19	-0.14 ± 0.04	-0.26 ± 0.02	0.20 ± 0.02	0.01 ± 0.02	0.526	0.458
	dY	-0.12 ± 0.04	0.02 ± 0.19	-0.25 ± 0.05	-0.24 ± 0.02	-0.05 ± 0.02	-0.40 ± 0.03	0.672	0.562
ZC09	dX	0.16 ± 0.15	3.52 ± 3.84	0.17 ± 0.27	0.12 ± 0.14	0.12 ± 0.16	0.32 ± 0.14		
	dY	-0.22 ± 0.14	-0.16 ± 3.67	0.08 ± 0.26	-0.24 ± 0.14	0.10 ± 0.15	-0.01 ± 0.14		
H18	$d\psi \sin \epsilon$			0.58 ± 0.18	-0.09 ± 0.13	0.04 ± 0.12	-0.01 ± 0.12		
	$d\epsilon$			-0.12 ± 0.17	-0.36 ± 0.16	-0.49 ± 0.12	0.17 ± 0.13		

further model deficiencies. The factor three was checked by analyses of sub-sets of used LLR normal points.

Here we estimate several possible sources of uncertainty:

1. Signal propagation through the troposphere and stratosphere (for 523 nm): 0.82 cm (Mendes & Pavlis 2003)
2. Differences in ephemerides (DE430–INPOP17a): 0.11 cm

The sum of the two estimations above is approximately two times the formal error of LLR observations (0.61 cm). Therefore we multiply the formal errors of residuals in one-way distance with a factor three before obtaining CPO with weighted least square fits. In this way, the weighted average uncertainty of CPO determined from LLR observations are 0.061 mas, but it is necessary to stress that the quality of the CPO series also depends on the resolution (70 days for LLR instead of 1 day for VLBI).

We present estimations using empirical models 2 and 3 for the long period components of nutation after removing the FCN. In our results, the fitted coefficients of the 18.6-year nutation term with and without the 9.3-year term are not consistent. This feature is different from the results obtained by VLBI analyses. Meanwhile, the correlation coefficients between two nutation terms are over 0.7, revealing the incapability of LLR data to separate the components effectively. This is probably because that LLR observations are directly related with the motions of the Moon, which is also the most important excitation of the 18.6-year and 9.3-year nutations. Nevertheless, the correlation coefficients between the secular term and the nutation terms are generally smaller than those of VLBI, probably benefiting from the longer time span of ten years. Furthermore, the correlation coefficient between the secular term and the sine term of 18.6yr nutation remains larger than its counterparts (0.4), which may reveal a common problem shared by VLBI and LLR technique.

Further discussion of obtaining more CPO from LLR data and a joint analysis of VLBI and LLR can be seen in the published paper (Cheng et al. 2019).

5. FUTURE IMPROVEMENTS OF LLR OBSERVATIONS FOR A BETTER DETERMINATION OF CPO

Accuracy of CPO determined from LLR observations can be affected by many aspects. Of all, the observational error and frequency are most directly related to the observation itself. The observational accuracy, though suffering from instability, is improving. Comparing number of normal points and corresponding observation errors (see Figure 2), especially between 2000 and 2010, we can draw a conclusion that the dispersion and larger uncertainties of CPO in this period are the consequences of the lower frequency of observations. Therefore, making LLR observations

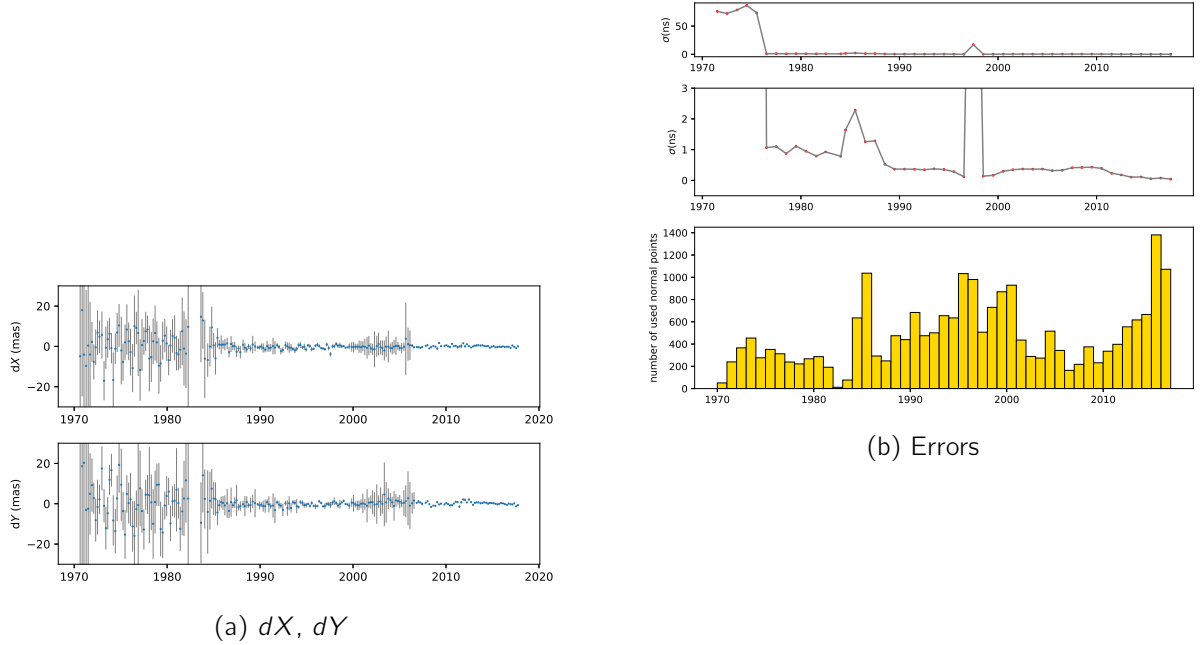


Figure 2: (a) dX and dY residuals of LLR observations in mas, using separated windows of 70 days. (b) Time series of observational errors and number of used normal points, the second figure being details of the first one. Each point/bin represents the weighted average/total within a year.

regular and sufficiently frequent to achieve a more uniform time distribution of normal points is quite essential in the future, before other necessary developments of related theories becoming conceivable.

6. ANALYSES OF THE OPTICAL RESIDUALS

The OA00 series provides time series of nutation offsets $d\psi$ and $d\epsilon$ with respect to the IAU 1976/1980 precession-nutation models (Lieske et al. 1977; Wahr 1981; Seidelmann 1982) between 1899 and 1972. Therefore, we followed the method described by Capitaine & Wallace (2006) to transform them into the same system of VLBI series, i.e. dX and dY with respect to IAU 2006/2000 precession-nutation models.

Models 1 and 2 are fitted to the transformed celestial pole offsets (CPO) to estimate the possible long term corrections. In both models t refers to the number of centuries from a reference epoch J1956.0, which is almost the central epoch of the time coverage of optical observations. Contrary to the VLBI results, there are no significant difference between the constant and secular terms in fitting results of the two models, and the correlation coefficients between secular term and nutation terms are negligible. These indicate that a time span long enough (over ninety years) may be sufficient to separate the quadratic term and the 18.6-year nutation term, whereas optical data cannot help in improving the precession-nutation model nowadays due to the poor accuracy.

Acknowledgement. This research is funded by the National Natural Science Foundation of China (NSFC) No. 11473013 and No. 11833004.

7. REFERENCES

Capitaine, N., Mathews, P. M., Dehant, V. Wallace, P.T., and Lambert, S.B., 2009, "On the IAU2000/2006 precession nutation and comparison with other models and VLBI observations",

- Celest. Mech. 103, pp. 179–190.
- Capitaine, N. and Wallace, P. T., 2006, “High precision methods for locating the celestial intermediate pole and origin”, *A&A* 450, pp. 855–872.
- Chapront, J., Chapront-Touzé, M., and Francou, G., 1999, “Determination of the lunar orbital and rotational parameters and of the ecliptic reference system orientation from LLR measurements and IERS data”, *A&A* 343, pp. 624–633.
- Cheng, Y. T., Liu, J. C., and Zhu, Z., 2019, “Analyses of celestial pole offsets with VLBI, LLR, and optical observations”, *A&A* 627, A81.
- Folkner, W. M., Williams, J. G., Boggs, D. H., Park, R. S., and Kuchynka, P., 2014, “The Planetary and Lunar Ephemerides DE430 and DE431”, *Interplanetary Network Progress Report* 196, pp. 1–81.
- Herring, T. A., Mathews, P. M., and Buffett, B. A., 2002, “Modeling of nutation-precession: Very long baseline interferometry results”, *J. Geophys. Res. (Solid Earth)* 107, pp. 2069.
- Hofmann, F., Biskupek, L., and Müller, J., 2018, “Contributions to reference systems from Lunar Laser Ranging using the lFE analysis model”, *J. Geodesy* 92, pp. 975–987.
- Kopeikin, S. M., 1990, “Theory of Relativity in Observational Radio Astronomy”, *Soviet Ast.* 34, p. 5.
- Lieske, J. H., Lederle, T., Fricke, W., and Morando, B., 1977, “Expressions for the precession quantities based upon the IAU /1976/ system of astronomical constants”, *A&A* 58, pp. 1–16.
- Mendes, V. B. and Pavlis, E. C., 2003, “Atmospheric refraction at optical wavelengths: problems and solutions” in *Proceedings of the 13th International Laser Ranging Workshop*, Washington D.C., Noomen, R., Klosko, S., Noll, C., and Pearlman, M. (eds.), NASA/CP-2003- 212248.
- Mendes, V. B. and Pavlis, E. C., 2004, “High-accuracy zenith delay prediction at optical wavelengths”, *Geophys. Res. Lett.* 31, L14602.
- Mendes, V. B., Prates, G., Pavlis, E. C., Pavlis, D. E., and Langley, R. B., 2002, “Improved mapping functions for atmospheric refraction correction in SLR”, *Geophys. Res. Lett.* 29, pp. 1414.
- Nothnagel, A., Artz, T., Behrend, D., and Malkin, Z., 2017, “International VLBI Service for Geodesy and Astrometry. Delivering high-quality products and embarking on observations of the next generation”, *J. Geodesy* 91, pp. 711–721.
- Pavlov, D. A., Williams, J. G., and Suvorkin, V. V., 2016, “Determining parameters of Moon’s orbital and rotational motion from LLR observations using GRAIL and IERS-recommended models” *Celest. Mech.* 126, pp. 61–88.
- Petit, G. and Luzum, B., 2010, *IERS Conventions (2010)*, IERS Technical Note, 36.
- Seidelmann, P. K., 1982, “1980 IAU theory of nutation - The final report of the IAU Working Group on Nutation”, *Celest. Mech.* 27, pp. 79–106.
- Vondrák, J. and Štefka, V., 2010, “The Earth Orientation Catalog 4 . An optical reference frame for monitoring Earth’s orientation in the 20th century”, *A&A* 509, pp. A3.
- Wahr, J. M., 1981, “The forced nutations of an elliptical, rotating, elastic and oceanless earth”, *Geophys. J.* 64, pp. 705–727.
- Zerhouni, W. and Capitaine, N., 2009, “Celestial pole offsets from lunar laser ranging and comparison with VLBI”, *A&A* 507, pp. 1687–1695.

OUTSTANDING PULKOVO LATITUDE OBSERVERS LIDIA KOSTINA AND NATALIA PERSIYANINOVA

Z. MALKIN, N. MILLER, T. SOBOLEVA
Pulkovo Observatory - Russia - malkin@gaoran.ru

ABSTRACT. Lidia Dmitrievna Kostina and Natalia Romanovna Persiyaninova left a bright mark in the history of the Pulkovo Observatory, as well as in the history of the domestic and international latitude services. In the first place, they were absolute leaders in the latitude observations with the famous zenith telescope ZTF-135. In 1954-2001, they obtained together more than 66 000 highly accurate latitudes, which make about 2/3 of all the observations made by 23 observers with the ZTF-135 after the WW2. They also provided a large contribution to investigation of the instrumental errors, methods of the data analysis, developing of the observing programs. Their results in studies of the latitude variations and polar motion were also highly recognized by the community.

1. INTRODUCTION

Pulkovo astrometrists Lidia Dmitrievna Kostina (Dec 8, 1926 – Jun 4, 2010) and Natalia Romanovna Persiyaninova (Aug 26, 1929 – Jan 16, 2003) left a bright mark in the history of the Pulkovo Observatory, as well as in the Russian and international latitude services.

First, Lidia Kostina and Natalia Persiyaninova have been known as outstanding observers at the famous zenith telescope ZTF-135 (originally called Large Pulkovo Zenith Telescope with the lens diameter of 135 mm constructed in 1899–1904 in the mechanical workshop of the Pulkovo Observatory by Heinrich Andreevich Freiberg). It is known that ZTF-135 was recognized as the best zenith telescope in the world. However, the glory of this instrument was deserved not only by the art of its creator, but also by the highly qualified work of the observers. The Pleiades of the remarkable observers of the ZTF-135, the brightest representatives of which were Natalia Persiyaninova and Lidia Kostina. Together they obtained 39% of all observations on this instrument in its more than a century history, including 59% of all post-WW2 observations. They were the absolute leaders among Pulkovo (and most likely all domestic) observers in the number of observing nights, as well as ZTF-135 was the leader among Pulkovo instruments. They were repeatedly awarded with the first and other prizes in the “Best Pulkovo observer of the year” competition.

Lidia Kostina and Natalia Persiyaninova also made a very large contribution to the research of the instrument, to the theory and practice of observation processing, interpreting changes in latitude and studying the motion of the Earth's pole, determining astronomical constants. In these fields, they deserved great prestige among their colleagues too.

2. LIDIA KOSTINA

In the year of graduation of Lidia Kostina from the Leningrad University (1950), the Pulkovo Observatory was still being restored. She joined the Northwest Airborne Surveying Enterprise, but soon became a graduate student at the Pulkovo Observatory. After completing the course in 1955, she became an employee of the Department of Astronomical Constants and the Earth's Pole Movement, ZTF-135 group, where she worked for the rest of her scientific life. In 1959, she defended a dissertation on the topic “Determination of Right Ascension of FK3 Near-Polar Stars”.

Although the restored Observatory was officially opened in May of 1954, regular observations



Figure 1: L.D.Kostina, 1956.



Figure 2: L.D.Kostina at the ZTF-135, 1956.

with ZTF-135 started in September 1948. Lidia Kostina joined the latitude observers group and immediately became involved in processing of the observations. Since April 1956, she was also included in the observing schedule. It is worth recalling that in those years there were no computers in the Observatory (the first one appeared in 1967), and the processing was carried out by observers and calculators. The processing was carried out, as it was called, “in two hands”: first by observer, then by calculator. Only computation of apparent places of the stars could be made in the Leningrad city computer center. Lidia Kostina thoroughly understood the astronomical and computational aspects of this problem and created a new more accurate and computationally efficient algorithm of routine computation. Using this algorithm, she analyzed the second post-WW2 ZTF-135 series (1955.0–1961.3). Later this technique was applied at all Russian latitudinal stations.

Lidia Kostina was also involved in such a complicated task as the compilation of long-term observing programs for zenith telescopes, which should be observed for at least 20 years and ensure maximum uniformity of the series by observing the same stars. She compiled a special program for the new Ulan-Bator latitude station in Mongolia, designed for observations over 50 years. Subsequently, she composed sixth and seventh programs for ZTF-135, which was observed until the end of 2006, that is, until the end of the active life of the telescope.

The scientific interest of Lidia Kostina covered many aspects of the Earth's rotation problem. Among them, was improvement in the accuracy of computation of the latitudes, and the definition of astronomical constants, which she worked with her colleagues. In particular, a new definition of the aberration constant was made in 1969, and a new estimation of the principal nutation term was obtained in 1988. However, she was interested, in the first place, in studying of the long-term changes in the pole motion, such as secular, Chandler, and annual terms.

Lidia Kostina, a truly zealous observer, was a living reproach for an observer who was careless or negligent. Some observers sometimes called the unstable weather with rapidly changing clouds “the weather of Lidia Kostina”. For its long observing life at ZTF-135 (20.05.1956-28.08.2001), Lidia Kostina obtained 32075 instant latitudes during 2279 nights.



Figure 3: N.R.Persiyaninova, the 1970s.



Figure 4: N.R.Persiyaninova at ZTF-135.

Despite being very busy, along with the scientific activities Lidia Kostina has a lot of historical research. Their main theme was women of science, women astronomers. And no wonder, it was a vivid example of Sophia Vasilievna Romanskaya, the most active observer and scientists working in the ZTF-135 group in 1918–1962. It was to her that Lidia Kostina's first biographical article was devoted. Among about 70 her publications, 12 papers were on the history of astronomy. As a specialist and a person, Lidia Kostina enjoyed great respect among colleagues. She was very sociable and open, always ready to answer a question, share experiences, interesting information. She was an active traveller and often put her notes about an interesting tourist or business trip in the hand-made wall newspaper, which was issued at the Observatory in that time.

3. NATALIA PERSIYANINOVA

Natalia Persiyaninova graduated from the astronomical department of the Faculty of mathematics and mechanics of the Leningrad State University in 1953 and came to work to the same department of the Pulkovo Observatory. Just at that time, preparations for the International Geophysical Year began at the observatory and a new zenith telescope ZTL-180 (Zenith Telescope Leningradsky with a lens diameter of 180 mm), manufactured by the Leningrad enterprise GOMZ was installed at Pulkovo. The first work of Natalia Persiyaninova was devoted to the study of the new instrument. She started as a calculator, then, since 1955, she participated in observations at both Pulkovo zenith telescopes, but, in the end, she connected her further scientific life with ZTF-135.

The variety of scientific interests of Natalia Persiyaninova is demonstrated by the list of topics of her publications. They include the connection of latitude variations with meteorological factors, non-polar latitude (z -term), impact of errors in star positions, the determination of the principal term of nutation, investigations of the main components in the polar movement, inter-technique



Figure 5: In Pulkovo at ZTF-135.



Figure 6: At Kitab ILS stations.

comparison of latitude variations. In particular, she studied the distribution of clear weather depending on the moon phases.

Everything new that appeared in the mathematical processing of observations, she immediately considered and put into practice. As soon as the first computer appeared in the observatory in 1967, Natalia Persiyaninova mastered it and provided both zenith telescopes with programs for processing of the observations. One of the main topics in her work was the application of spectral analysis to the study of variations of latitudes. Her dissertation defended in 1969 and devoted on investigation of non-polar variations was one of the first study in which correlation and spectral analysis was used for astrometric problems.

Natalia Persiyaninova, as well as Lidia Kostina, always had a high sense of responsibility. This was especially true for observations. During the period from 08.01.1955 till 16.11.2001 she obtained 33996 instantaneous latitudes during 2414 nights (the record for ZTF-135!). Numerous observations aimed at the determination of instrument constants, near-pole stars in elongations, scale pairs and time series for determining the screw revolution should be added to this value. She also took part on latitude observations in Blagoveshchensk (ZTL-180) and Kitab (ZTL-180 and Bamberg ZT).

The scientific authority of Natalia Persiyaninova was very high. The same was her public authority. She not only taught students and trainees astrometric wisdom, but also became an adviser in worldly affairs. Contacts established during common work continued to exist in correspondence. When a scientific conference was held at Pulkovo, discussions in her cozy house were sometimes more active than in and around the conference room.

4. PUBLICATIONS

Although Lidia Kostina and Natalia Persiyaninova each had their own research topics of interest to them, being members of the same Pulkovo latitudinal group, they naturally had many general

publications and reports at conferences (and in those years astrometric and specialized latitudinal conferences took place in our much more often than now), based primarily on observations with ZTF-135. Almost two-thirds of the group's publications were written together. These are articles on the studies of the of the Pulkovo latitude variations, the instrumental studies, the determination of nutation coefficients, the analysis of non-polar variations in latitude observations, and the improvement of the catalog of coordinates of latitudinal stars.

Very productive was long-term cooperation of Lidia Kostina and Vladimir Ivanovich Sakharov, many-year head of the ZTF-135 group. They published 17 articles devoted to study of the Chandler, annual and secular components of the pole motion. In 1977, they first investigated the relationship between the pole motion and solar activity. The presence of common cycles in the variations of the main components of the pole motion and Wolf numbers led them to conclude that some of them are generated by solar processes such as 11-yr cycle (Kostina and Sakharov, 1989). Studying the Chandler oscillation, the authors were among the first to study the phase changes of this oscillation, in particular, around 1925 and drew attention to the fact that neglecting the phase variations can lead to constructing of a wrong model of the polar motion. The value of the Chandler period of 1.189 ± 0.002 yr obtained by them corresponds to the theoretical estimation for the second model of the Earth's structure developed by Michael Molodensky (elastic mantle, liquid core with a solid inner core). The authors proposed the theory of extreme cycles in the variation of the amplitude of the Chandler wobble. Analyzing the maximum amplitudes, they estimated the main low-frequency period in the variations of the Chandler wobble of 43.8 yr. Their assumption is that the maximum of the third extreme cycle will fall on 1989, turned out to be close to the truth (the maximum was observed in the early 1990s).

Very interesting was also the joint work of Natalia Persiyaninova with Niklen Petrovich Godisov. In this study of the main components of the pole motion, the method of sequential separation of components was used with parabolic interpolation in the region of the maximum spectral function, which was then used by many authors. In the spectrum of amplitudes of the Chandler pole motion, a component with a period of 44 yr was found, which corresponds to the conclusions of Sakharov and Kostina.

Over their nearly half-century scientific and, in particular, observing lives, Lidia Kostina and Natalia Persiyaninova observed 66071 high-precision latitudes, distributed approximately equally between them. A simple estimate (four latitudes per hour in a typical observing program) shows that to obtain such a result, each of them spent about 8300 hours with the instrument or about 345 days, i.e. about a whole year! If one takes into account also auxiliary, but necessary observations, this will be even more than a year.

For preparation of this paper, materials of the archive of the Pulkovo Observatory were used (Pulkovo Observatory archives 1–5).

5. REFERENCES

- Kostina L.D., Sakharov V.I., 1989, "Investigations of the Earth pole motion in the Pulkovo Observatory", in: 150 years of Pulkovo Observatory, Leningrad, Nauka 1989, pp. 137–152.
- Pulkovo Observatory archive 1, f. 1, op. 2, d. 105, ll. 112-141 (Personal file of postgraduate student L.D. Kostina).
- Pulkovo Observatory archive 2, f. 1, op. 2, d. 863, ll. 34-97 (Personal file of L.D.Kostina).
- Pulkovo Observatory archive 3, f, 1, op. 2, d. 385, ll. 163-194 (Personal file of postgraduate student N.R. Persiyaninova).
- Pulkovo Observatory archive 4, f. 1, op., 2, d. 905, ll. 178-235 (Personal file of N.R. Persiyaninova).
- Pulkovo Observatory archive 5, f. 4, op. 1, d. 106, l. 26 (Photo album "150 years of Pulkovo Observatory").

A REVISION OF ΔT VALUES FOR THE V, VI AND VIIITH CENTURIES

M.J. MARTÍNEZ¹, F.J. MARCO²

¹ Universidad Politécnica de Valencia, IUMPA, Dept. Matemàtica Aplicada - Spain
mjmartin@mat.upv.es

² Universidad Jaume I. IMAC. Dept. Matemàtiques, Castellón - Spain - marco@mat.uji.es

ABSTRACT. Studies of pretelescopic values of ΔT have been arranged by many authors. Ancient observational records of total and annular solar eclipses and in a lesser extend also lunar eclipses and occultation have been used to calculate limits to the value of ΔT (Soma and Tanikawa, 2016; Stephenson et al., 2016; Tanikawa and Soma, 2004) among others. We provide a first approximation for computed values of ΔT from the 5th to the 7th centuries considering all the available ancient astronomical records, paying special attention to those from Western Europe for which new analysis and reductions have been carried out. We present two examples of ancient observations with their associated discussions that lead to new values of some astronomical parameters. Similar studies have been carried out for more than a hundred of ancient registers. The results obtained in the first instance corroborate those obtained by Soma and Tanikawa in the sense that the ΔT for these centuries seems to be significantly lower than that obtained by Morrison and Stephenson (Morrison and Stephenson, 2014; Stephenson, 2010) and Stephenson et al. (2016).

1. EXAMPLE 1: TOTAL SOLAR ECLIPSE. AD 418, July 19

This eclipse was collected in numerous no contemporary European chronicles from Austria, Denmark, Germany, France; in many cases only reference is made to the darkening of the sun in broad daylight with or without mentioning the date. Other more complete records include the time of day the event took place. For these records, we must bear in mid a classical problem that usually appears when we deal with Medieval sources: non-contemporary authors were limited to copying records of other authors prior to them, for mainly prestige reasons. See (Newton, 1972; Soma and Tanikawa, 2016) for a further study. Anyway, some contemporary authors such as Hidatius, from Northern Spain and Philostorgius from somewhere near Istambul, provide valuable and more detailed data (http://www.tertullian.org/fathers/philostorgius_fn.htm#218):

When Theodosius had entered the years of boyhood, on the 19th of July, a little after noon-day, the sun was so completely eclipsed that the stars appeared; and so great a drought followed on this eclipse that a sudden mortality carried off great multitudes both of men and of beasts in all parts. Moreover, at the time that the sun was eclipsed, a bright meteor appeared in the sky, in shape like a cone, which some persons in their ignorance called a comet (. . .) For it arose first in the east, just where the sun rises at the equinox, and then passing across the lowest star in the constellation of the Bear, crossed gradually over to the west (. . .) it at length disappeared, after it had continued its course for more than four months. Its apex, moreover, at one time was carried up to a high and narrow point, so that the meteor exceeded the length and shape of a cone, while at another time it returned to that particular form. (. . .) At the same time with the earthquakes, fire came down from the skies, which seemed to banish all hope of escape; however, it caused no destruction of life, for the mercy of God sent a violent wind which scattered the fire in every direction, and at length drove it into

In his time, we saw grapes grow on the tree we call saucum [= elder tree] without having any vine on it, and the blossoms of the same trees (. . .) Then a star coming from the opposite direction was seen to enter the disk of the fifth Moon. I suppose these signs announced the death of the king.

The data provided lead us to accept the date of October 9, 554 as the most likely for the occultation, involving Venus and the Moon. Gregory of Tours (538-594) could have witnessed it in his youth, perhaps this explains the error in the appreciation "the fifth Moon" since the Moon would have been, in fact, on his 26th day. The capital of these Merovingian kings was Metz, which we assume as the place of observation. That day sunrise was at 5h50m. The first contact of Venus with the limb of the Moon occurred at 5h15m and the end of the occultation at 6h30m. A $\Delta T < 3000$ s would have meant that the occultation occurred after sunrise, while a ΔT greater than 5500 s would have led to seeing the Venus emersion. Therefore, the values obtained are consistent with those of Espenak and Meeus and with those of Stephenson et al. Soma and Tanikawa (Stephenson, 1997) obtained a ΔT between 2893 and 5246 s. The result that we have obtained is a refinement for the lower limit of this interval.

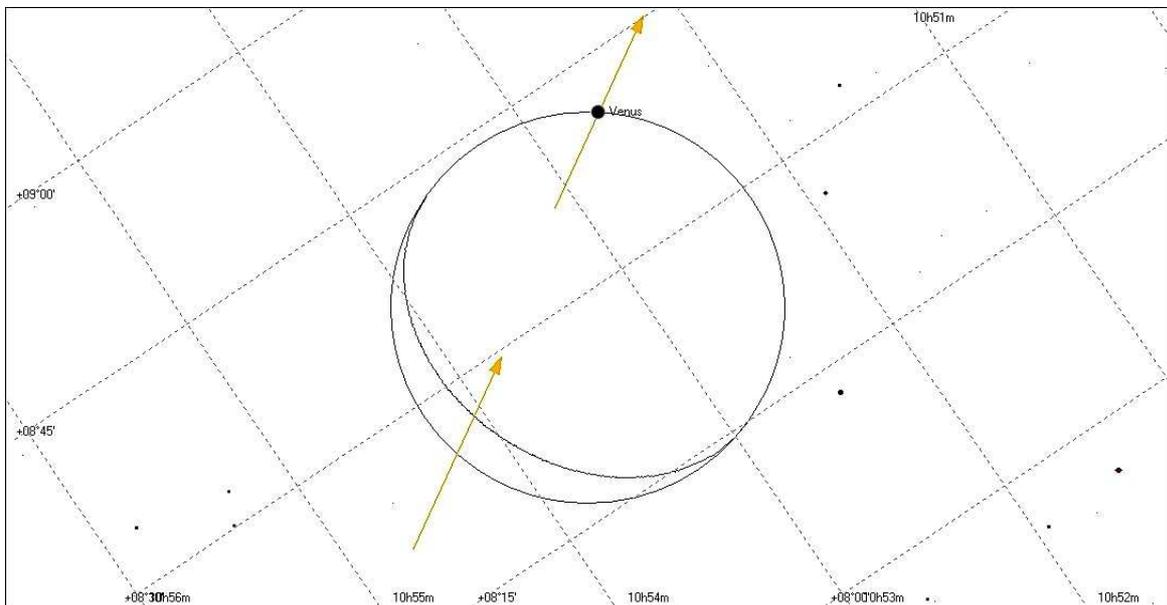


Figure 2: Occultation of Venus by the Moon. AD 554 October 9.

3. CONCLUSION

To obtain preliminary results we have worked with a total of 43 observations included in the AD418-AD693 period and coming from both Asia and Europe and North Africa. Among them are eclipses of the Sun, Moon and occultations of planets by the Moon. Each observation has been examined separately, calculating a new interval of ΔT for which the characteristics of the phenomenon have been taken into account, if it was observed in a single place or in multiple places, the time interval in which it could be observed, in the event that it occurs near sunrise or sunset, etc.

The result obtained can be seen in Figure 3. The solid red and blue lines correspond to the splines obtained Morrison and Stephenson (Morrison and Stephenson, 2014) and Stephenson et al. (2016), respectively. The black line is the spline obtained using our results showing a significantly lower ΔT is than the one provided by other authors for the time considered.

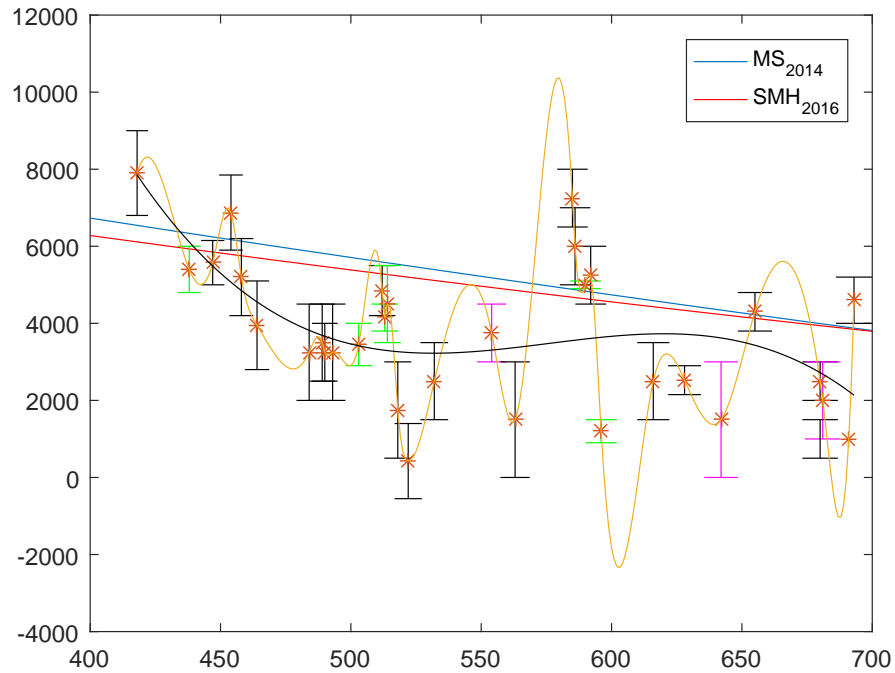


Figure 3: ΔT (s) from AD 418 to AD 693. The asterisks represent the values considered for each observation, for which the error bar is also provided. The black color corresponds to a solar eclipse, the green with a lunar eclipse and the magenta with an occultation of a planet by the Moon.

4. REFERENCES

- Martínez M.J., Marco F.J., 2019, "Occultation Of Planets By The Moon In European Narrative Medieval Sources", *Journal for the History of Astronomy* 50, pp. 192–220.
- Morrison L.V., Stephenson F.R., 2014, "Historical values of the Earth's clock error ΔT and the calculation of eclipses", *Journal for the History of Astronomy* 35, pp. 327–336.
- Newton R.R., 1972, "Medieval Chronicles and the rotation of the Earth", Johns Hopkins University Press. Baltimore and London.
- Pingré A. G., 1783, "Cométographie; ou Traité historique et théorique des comètes"
- Stephenson F.R., 1997, "Historical Eclipses and Earth rotation", Cambridge University Press.
- Soma M., Tanikawa K., 2016, "Earth rotation derived from occultation records", *Publ. Astron. Soc. Japan.* 68(2), 29, pp. 1–8.
- Stephenson F.R., 2010, "Investigation of medieval European records of solar eclipses", *Journal for the History of Astronomy*, 41, pp 95–104.
- Stephenson F.R., Morrison L.V., Hohenkerk C.Y., 2016, "Measurement of the Earth's rotation: 700 BC to AD 2015", *Proc. R. Soc. Lond. A.* 472.
- Tanikawa K., Soma M., 2004, " ΔT and the Tidal acceleration of the Lunar motion from eclipses observed at plural sites", *Publ. Astron. Soc. Japan.* 56, pp. 879–885.

ESTIMATION OF EARTH ROTATION RESONANCE PARAMETERS THROUGH VLBI ANALYSIS

I. NURUL HUDA, C. BIZOUARD, S. LAMBERT, AND Y. ZIEGLER

Paris Observatory / SYRTE, PSL - ibnu.nurulhuda@obspm.fr

ABSTRACT. The VLBI observations enable the investigation of the Earth rotation resonances, associated with Free Core Nutation, Free Inner Core Nutation, and Polar Motion Resonance, in the retrograde diurnal band with respect to a terrestrial frame. The resonance parameters (period and quality factor) are estimated by confronting the theoretical rigid Earth nutation terms to the corresponding nutation terms observed by VLBI. We revisit this problem by considering 40 years of VLBI observations and more complete atmospheric + oceanic non-tidal perturbations, that have to be removed from the observed nutation terms before the estimation. The inclusion of complete atmosphere and ocean correction produce a significant change in the period and quality factor of Free Core Nutation and Free Inner Core Nutation. On the other hand, the nutation analysis allows us to investigate the frequency dependence of Polar Motion Resonance in the diurnal retrograde band. We analyzed the frequency sensitivity of Polar Motion resonance and found that this resonance is mostly determined by the prograde nutation terms of period smaller than 386 days.

1. INTRODUCTION

Since the beginning of the 20th century, the observation of the Earth rotation variations through astro-geodetic techniques enables to investigate the global rheological properties of the Earth, in particular, the resonance parameters of the free rotation modes, i.e. Polar Motion Resonance (PMR), Free Core Nutation (FCN), and Free Inner Core Nutation (FICN). In this study, we focus on the adjustment of resonance parameters in the diurnal retrograde band, so called nutation band, which can be done through a comparison of the observed nutation, determined from VLBI analysis, with the corresponding rigid nutation terms that reflects the luni-solar forcing. Furthermore, we study the effect of atmosphere and ocean to the Earth resonance parameters estimation. The nutation contribution caused by diurnal circulation in the hydro-atmospheric layer perturbs the estimates of the resonance parameters and has to be removed from total nutation before inversion. Finally, we investigate the sensitivity of polar motion resonance parameters to the frequency band of the selected set of nutation terms.

2. METHOD AND DATA

Following the procedure of Mathews et al. 2002, the Earth resonance parameters are estimated through a relation between the observed nutation $\tilde{\eta} = X + iY$ and corresponding rigid Earth nutation $\tilde{\eta}_R$ in the frequency domain as follows

$$\tilde{\eta}(\sigma') = \tilde{T}(\sigma'; \tilde{\sigma}'_j) \tilde{\eta}_R(\sigma') \quad (1)$$

where the transfer function $\tilde{T}(\sigma'; \tilde{\sigma}'_j)$ is represented by

$$\tilde{T}(\sigma'; \tilde{\sigma}'_j) = \frac{e - \sigma'}{e + 1} \left(1 + (1 + \sigma') \sum_{j=1}^3 \frac{\tilde{N}_j}{\sigma' - \tilde{\sigma}'_j} \right). \quad (2)$$

Here σ' is the frequency in cpd as seen from a celestial frame, e is the dynamical ellipticity of the Earth, \tilde{N}_j and $\tilde{\sigma}'_j = 2\pi/P'_j(1 + n(i/2Q'_j))$ are the coefficient and frequency specifying the resonance modes in celestial frame, n is '+1' for prograde and '-1' for retrograde, P'_j and Q'_j are the space-referred period and quality factor of the resonance terms respectively. The celestial frequencies $\tilde{\sigma}'_j$ are mapped into terrestrial frequencies $\tilde{\sigma}_j = \tilde{\sigma}'_j - \Omega$ with corresponding period and quality factor P_j and Q_j , where Ω is the mean angular velocity of the Earth. The index 1 until 3 is for representing the resonances associated with PMR, FCN, and FICN respectively. We estimate \tilde{N}_j and $\tilde{\sigma}'_j$ from 42 observed nutation terms (see Table 1) and the corresponding set of rigid Earth terms by performing a weight least square inversion. The observed nutation terms are estimated through VLBI observation from 1979 to 2017. Before the inversion is performed, some corrections have to be applied. First, the nutation terms have to be referred to a dynamical celestial reference frame by removing the geodetic nutation and then non-linear effects are suppressed (see Table 7 of Mathews et al. 2002). Finally, we eventually get rid of the atmospheric + oceanic contribution, which cannot be related to rigid Earth nutation caused by luni-solar tides.

Table 1: In-phase and out-phase coefficients of 42 observed nutation terms.

Period (days)	X (mas)	Y (mas)	Period (days)	X (mas)	Y (mas)
-6798.38	-8024.74	1.41	31.81	3.18	0.00
6798.38	-1180.44	-0.14	-27.55	-13.82	-0.04
-3399.19	86.14	-0.04	27.55	14.48	-0.00
3399.19	3.63	-0.01	-23.94	0.05	-0.00
-1615.75	-0.01	-0.01	23.94	1.18	-0.00
1615.75	-0.12	-0.01	-14.77	-1.20	-0.00
-1305.48	0.30	0.01	14.77	1.32	-0.00
1305.48	2.12	0.00	-13.78	-0.55	-0.00
-1095.18	0.22	0.00	13.78	0.61	-0.00
1095.18	-0.23	0.00	-13.66	-3.66	-0.02
-386.00	-0.16	-0.00	13.66	-94.20	0.13
386.00	-0.71	-0.00	-9.56	-0.09	-0.00
-365.26	-33.01	0.34	9.56	-2.46	0.01
365.26	25.65	0.14	-9.13	-0.46	-0.00
-346.64	-0.59	0.00	9.13	-12.45	0.04
346.64	-0.07	-0.00	-9.12	-0.29	0.00
-182.62	-24.58	-0.04	9.12	-2.34	0.00
182.62	-548.46	-0.51	-7.10	-0.06	0.00
-121.75	-0.94	0.00	7.10	-1.59	0.01
121.75	-21.49	-0.02	-6.86	-0.04	-0.00
-31.81	-3.06	-0.01	6.86	-1.28	0.01

3. ATMOSPHERIC AND OCEANIC CONTRIBUTION

The analysis done in Mathews et al. 2002 was restricted to the atmospheric effect on the annual prograde nutation. Actually, a more complete treatment of the fluid layer perturbations has to include other nutation components (-365 d, +182.6 d, +121.75 d, +13.66 d) and consider the contribution of the non-tidal circulation in the ocean. The corresponding effects were evaluated by using the non-inverted barometer version of atmospheric angular momentum time series from TU Vienna (based upon ECMWF model) (Schindelegger et al. 2011) and oceanic angular momentum series from ERA40 and ERA operational (based upon OMCT model) (Dobslaw & Thomas 2007) from 1984 until 2017. This calculation is done through Celestial Angular Momentum Functions, and their effects on the nutation are estimated by using the formula reported in Brzezinski 1994. The results are shown in Figure 4.

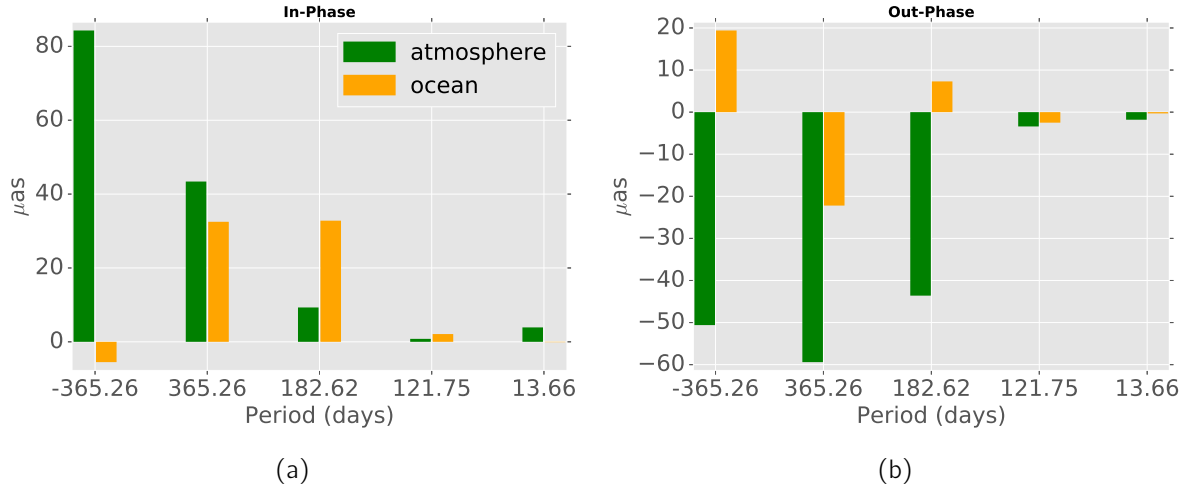


Figure 4: The contribution of atmosphere and non-tidal ocean to the nutation terms. Here (a) is for in-phase and (b) is for out-phase components.

4. RESULTS

The results of Earth resonances estimation is displayed in Figure 5. The excitation of atmosphere and ocean has no impact in the polar motion resonance. However, the inclusion of these correction could make a significant change in the FCN and FICN parameters. We found that the inclusion of atmospheric + oceanic correction would increase the value of FCN quality factor for about 500 and decrease the period in half days. For FICN, the inclusion of complete excitation correction has diminished the quality factor by about 100 and the period for about 10 days. For the purpose of comparison, Table 2 shows the result of ours and Mathews et al. 2002. It shows that our results have a good agreement with Mathews et al 2002 except for the quality factor of FCN and FICN.

Table 2: Resonance parameters of PMR, FCN, and FICN. The FICN and FCN periods are given in CRF and other is in TRF. Periods are in mean solar days.

Parameter	Mathews et al. 2002	This study
P_{PMR}	(381.9, 385.0)	(380.7, 383.4)
Q_{PMR}	-10.4	(-11.0, -9.9)
P'_{FCN}	(-429.9, -430.5)	(-430.3, -430.0)
Q_{FCN}	20000	(16946, 17736)
P'_{FICN}	(930, 1140)	(735.6, 1143.5)
Q_{FICN}	677	(304, 380)

5. ANALYSIS OF POLAR MOTION RESONANCE

The estimated parameters of the PMR ($P_{PMR} = 382$ d, $Q_{PMR} = -10$) are at discrepancy with the ones corresponding to the common polar motion ($P_{PMR} = 433$ d, $Q_{PMR} = 100$). This modification results from the dynamical oceanic response in the diurnal band (more insight about this topic is given in Bizouard et al. 2020). Mathews et al. 2002 assumed that the estimated values ($P_{PMR} = 383$ d, $Q_{PMR} = -10$) are mostly constrained by the 18.6 year ($\sigma = -1.00288$

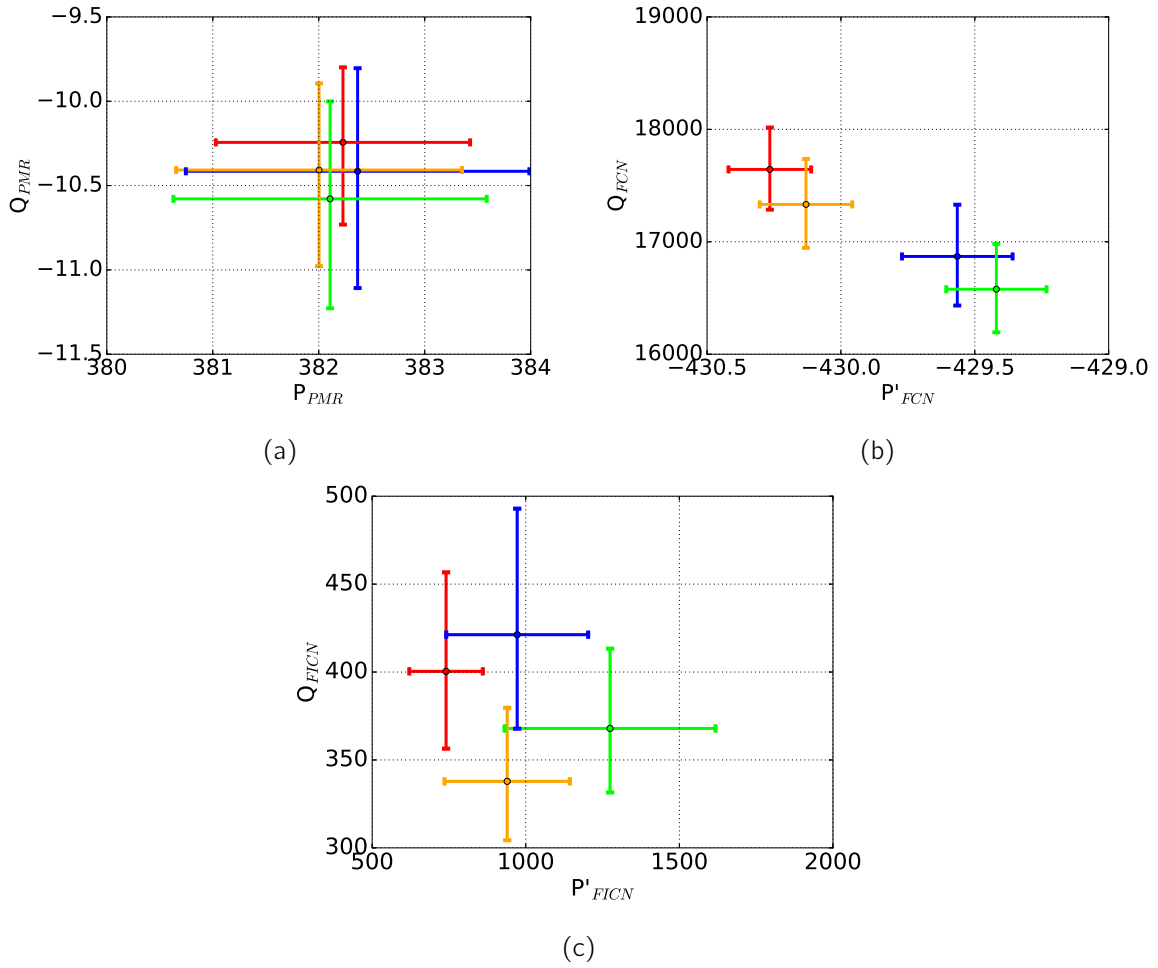


Figure 5: The comparison of atmospheric and oceanic contribution to the Earth resonance parameters. Here (a) is PMR, (b) is FCN, and (c) is FICN. The period of PMR is in TRF and the others are in CRF. Here ●: no atmospheric and oceanic correction, ●: atmospheric correction, ●: oceanic correction, and ●: atmospheric + oceanic correction.

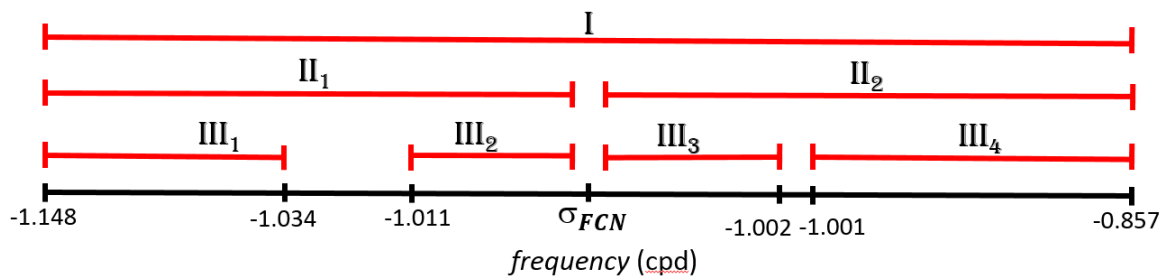


Figure 6: Selected frequency band in the terrestrial frame for least-square adjustment of the PMR parameters. 18.6 year nutation term is belong to the Band III₃. Their limits are precisely reported in Table 3.

Table 3: The period and quality factor of PMR determined over certain band of frequencies.

Band	frequency (cpd)	P_{PMR}	Q_{PMR}
I	$(-\Omega - 1/6.86 \leq \sigma \leq -\Omega + 1/6.86)$	382.0 ± 1.3	-10.4 ± 0.5
II ₁	$(-\Omega - 1/6.86 \leq \sigma \leq -\Omega - 1/386)$	418.5 ± 7.2	-8.24 ± 1.7
II ₂	$(-\Omega - 1/1095.18 \leq \sigma \leq -\Omega + 1/6.86)$	381.8 ± 1.2	-10.4 ± 0.5
III ₁	$(-\Omega - 1/6.86 \leq \sigma \leq -\Omega - 1/31.81)$	415.1 ± 3.3	-7.7 ± 0.7
III ₂	$(-\Omega - 1/121.75 \leq \sigma \leq -\Omega - 1/386)$	486.8 ± 58.4	$+13.4 \pm 30.7$
III ₃	$(-\Omega - 1/1095.18 \leq \sigma \leq -\Omega + 1/1095.18)$	381.7 ± 7.6	-10.2 ± 2.9
III ₄	$(-\Omega + 1/386 \leq \sigma \leq -\Omega + 1/6.86)$	381.8 ± 1.3	-10.4 ± 0.5

cpd) nutation term. To check this assumption, $\tilde{\sigma}_1$ is re-estimated over restricted sets of nutation terms sweeping frequency band -1.15 cpd, -0.85 cpd of the polar motion (see Figure 6). It turns out that the estimates $\bar{P}_{PMR} = 382$, $\bar{Q}_{PMR} = -10$ over the whole set (band I) are at discrepancy with the ones obtained over restricted bands, as shown by Table 3. In particular, for frequencies smaller than σ_{FCN} (Band II₁, III₁, III₂) we get P_{PMR} significantly larger than 415 days. Although the 18.6 year retrograde nutation prevails, the estimates of PMR parameters are quite loose in the K_1 band (band III₃) ($P_{PMR} = 382 \pm 8$, $Q_{PMR} = -10 \pm 3$) and better constrained by the prograde short period terms (band III₄) ($P_{PMR} = 382 \pm 1$, $Q_{PMR} = -10 \pm 1$).

6. CONCLUSIONS

In this study, we perform the adjustment of Earth resonance parameters, in the diurnal retrograde band, through VLBI analysis. The inclusion of the complete atmospheric and ocean non-tidal corrections has increased the FCN quality factor in terrestrial frame for about 500 and decreased the period in celestial frame in half days. The FICN parameters have decreased by 10 days and 100 for its period and quality factor respectively. More importantly, the PM resonance parameters are mostly determined by the prograde nutation terms of period smaller than 386 days. The PM period and quality factor seem to be frequency dependent in the diurnal band in reason of the FCN resonance (explored in more details in Bizouard et al. 2020).

7. REFERENCES

- Bizouard, C., Nurul Huda, I., Ziegler, Y., & Lambert, S., 2020, "Frequency dependence of the polar motion resonance", *Geophys. J. Int.* 220(2), pp. 753–758.
- Brzezinski, A., 1994, "Polar motion excitation by variations of the effective angular momentum function, II: extended model", *Manuscripta Geodaetica* 19, 157.
- Dobslaw, H. & Thomas, M., 2007, "Simulation and observation of global ocean mass anomalies", *J. Geophys. Res. (Oceans)* 112.
- Mathews, P. M., Herring, T. A., & Buffett, B. A., 2002, "Modeling of nutation and precession: New nutation series for nonrigid Earth and insights into the Earth's interior", *J. Geophys. Res. (Solid Earth)* 107.
- Schindelegger, M., Bohm, J., Salstein, D., & Schuh, H., 2011, "High-resolution atmospheric angular momentum functions related to Earth rotation parameters during CONT08", *J. Geodesy* 85, 425.

THE DEVELOPMENT OF THE GNSS-BASED PRODUCTS SERVICE SYSTEM

H.-E. Park, K. M. Roh, S.-M. Yoo, J. Cho

Korea Astronomy and Space Science Institute - South Korea - hpark@kasi.re.kr

ABSTRACT. The Korea Astronomy and Space Science Institute (KASI) is developing a GNSS-based products service system, which regularly generates station positions, GNSS satellite orbits, earth rotation parameters (ERP), and the analysis results, in order to utilize it in the Earth system research and the development of the Korean Positioning System (KPS). The service system consists largely of a Data Processing Server (DPS) and a Data Archive and Service Server (DAS). The DPS collects data necessary for processing data, such as RINEX files, and carries out data processing and data analysis with the Position and Navigation Data Analyst (PANDA) software or Bernese GNSS software 5.2, where various GNSS products are generated. The DAS stores the GNSS products generated by the DPS and serves them to user. In this poster, the architecture of the GNSS-based products service system is introduced and several analysis results for the GNSS products are explained.

1. INTRODUCTION

The Korea Astronomy and Space Science Institute (KASI) is developing a GNSS-based products service system to secure technology for determining GNSS products and to support research on the Earth system and the development of Korean Positioning System (KPS), a Korean navigation satellite system. Our goal is to develop a system that can routinely produce and service GNSS products such as a Terrestrial Reference Frame (TRF), GNSS satellite Ephemerides and Earth rotation by means of automating data collection and data processing. In this poster, the architecture of the GNSS-based products service system and the data processing methods used are briefly introduced, and the GPS satellite orbit and Earth rotation parameters (ERP) obtained from this system are explained.

2. GNSS-BASED PRODUCTS SERVICE SYSTEM

The system consists of two high-performance servers, Data Processing Server (DPS) and Data Archive and Service Server (DAS). Detailed hardware specifications for this system can be found in Table 1. Figure 1 shows the overall structure and function of the system, the flow of data, and the installed software. The DPS collects data from IGS global data center and CODE FTP server and carries out data processing for GNSS products using the Bernese GNSS software 5.2 or the Position and Navigation Data Analysis (PANDA). It also monitors the data processing process and notifies the administrator when a problem occurs. The DAS stores the GNSS products produced by the DPS and services them via the Web and FTP. However, in practice, GNSS products are stored on a Network Access Server (NAS) that is physically away from the DAS for security reasons.

3. GLOBAL GNSS NETWORK

A global network of 134 GNSS stations was used to estimate GPS satellite orbit and ERP. The global network was selected based on IGS14 core sites, taking into account its distribution and observation quality during data processing. Figure 2 shows the distribution of the ground stations

Sever name	DPS: Data Processing Server DAS: Data Archive and Service Server
The specification of the server	Model: HP ProLiant DL360p Gen8 - 2 Intel Xeon E5-2640 (2.0GHz, 8-core) - 512GB SSD 4EA - 2TB HDD 4EA (DAS)
O/S	LINUX
Software	Bernese GNSS software v5.2 PANDA

Table 1: Hardware specifications and installed software of the GNSS-based products service system

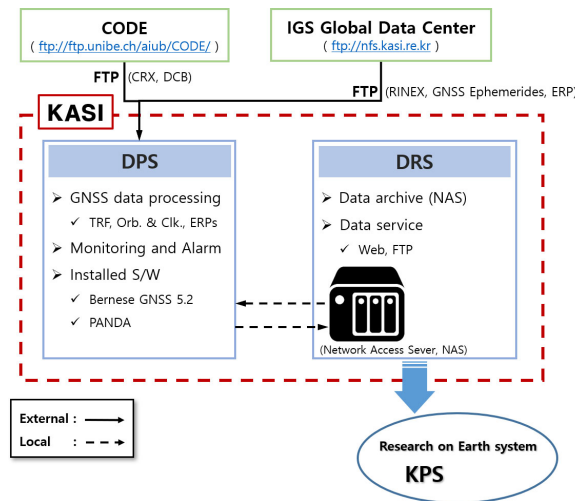


Figure 1: The architecture of the GNSS-based products service system

currently selected. The global network requires continuous optimization.

4. DATA PROCESSING

The GNSS-based products service system is currently under development and the data processing tool to be mounted on the system has yet to be determined. In the current study, GPS satellite orbit was determined using PANDA and ERP was determined using Bernese GNSS v5.2. Table 2 lists the key strategies for each data processing and the models used.

GPS precise orbit determination (POD) was performed by using the PANDA software developed at Wuhan University, China. Undifferenced observation data were used in the data processing for the POD, and the GPS orbit calculated from a broadcast navigation file was used as a priori orbit. Detailed data processing methods and models used for the GPS POD are shown in Table 2. Earth rotation parameters (ERP) was estimated using Bernese GNSS v5.2 developed by the University of Bern in Switzerland. IGS final products were used for GNSS satellite ephemerides for data processing, and IGS ultra-rapid products were used for a priori ERP. The basic strategy of data processing is double difference, and Berneses SNGDIF and MKCLUS modules were used for baselines generation and clustering. In other words, a single differential baseline was created using SNGDIF to maximize the common observation (OBS-MAX option), and clusters of several baseline were constructed using the MKCLUS module. The reason for performing data processing with clusters is because of the large number of baselines to be processed. If data processing is carried out for all stations at once, it may cause time and memory problems. Finally, out of the 134 stations, 62 were used to tie the solution to the IGS14 datum with a No-Net-Rotation (NNR)

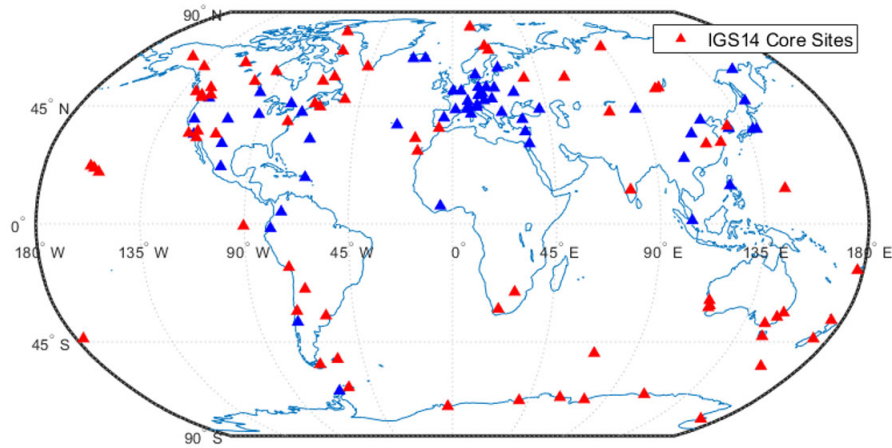


Figure 2: Global GNSS network used in the GNSS-based products service system

condition. Additional information on the data processing can be found in Table 2.

4.1 GPS satellite orbit

The GPS satellite orbit determination product was generated on Jan. 1, 2019. To validate the orbit product, we compared with the IGS final orbit product. Figure 3 shows the 3-D rms position error of the all GPS satellites as a function of time. Most position errors did not exceed 6 cm. In Table 3, the mean position error of GPS satellites from G01 to G10 can be found. Figure 4 graphically shows the position error of all GPS satellites.

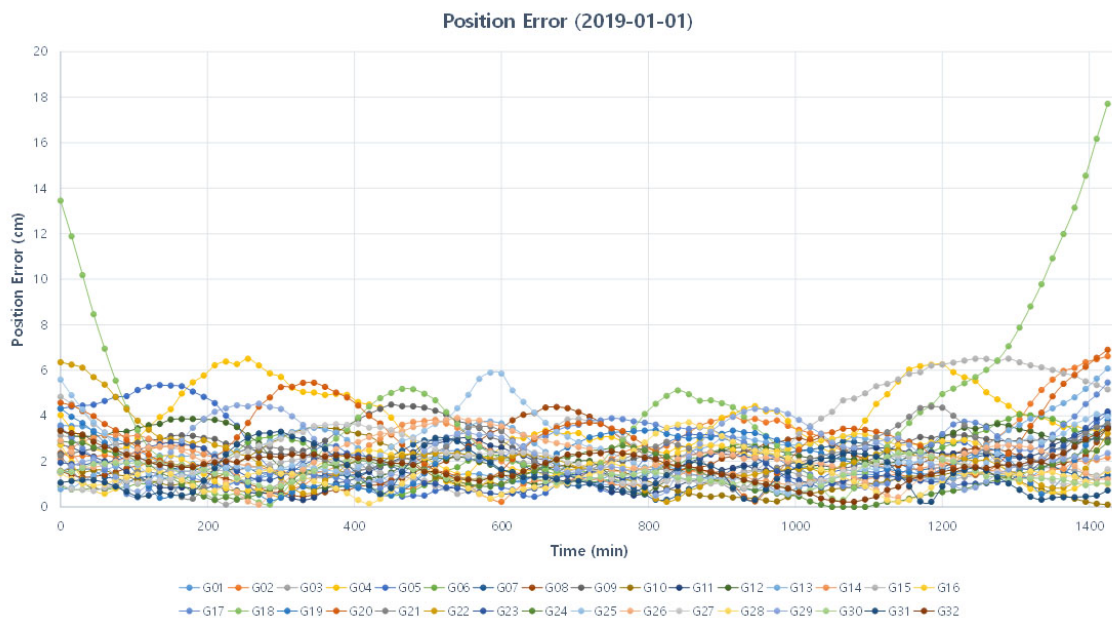


Figure 3: POD results: time series of position errors of all GPS satellites [2019-01-01]

4.2 Earth rotation parameters

The ERPs were estimated from 1 January 2019 to 29 June 2019 (180 days). The values of the estimated ERPs were compared with the IERS C04 and the results are shown in Figure 5 and

Products	GPS Satellite Orbit	Earth Rotation Parameters
Software	PANDA	Bernese GNSS S/W 5.2
Processing Period	2019.1.1	2019.1.1 – 2019.6.28
Type of Solution	1-Day solution	1-Day solution
Observation	GPS	GPS, GLONASS
A priori Orbit	Broadcast navigation	IGS final products
A priori ERP	IERS final products	IGS ultra-rapid products
Station position & velocity	IGS 2014	IGS 2014
Absolute antenna model	IGS14	IGS14
GNSS network	134	134
Processing Mode	Undifference	Double Difference
Ambiguity resolution	Round	QIF & WL/NL
Earth's Gravity	EGM 12	EGM 2008_SMALL
Subdaily pole model	IERS2010	IERS2010XY
Nutation model	IAU2000R06	IAU2000R06
Solid Earth Tide Model	IERS2010	TIDE2000
Ocean Tides	FES2004	FES2004
Planetary Ephemerides	DE405	DE405

Table 2: Data processing strategies and models used for GPS satellite orbit and ERP

PRN	G01	G02	G03	G04	G05	G06	G07	G08	G09	G10
Radial (cm)	0.779	1.455	0.944	1.334	0.976	1.086	1.110	1.121	1.913	0.597
Along (cm)	1.169	1.634	0.883	3.133	1.953	1.860	1.095	1.863	0.993	1.376
Cross (cm)	0.965	1.655	1.059	2.284	1.614	0.489	1.018	0.850	1.821	0.608
3D RMS (cm)	1.705	2.743	1.671	4.100	2.715	2.209	1.862	2.335	2.822	1.619

Table 3: POD results: the mean position error of G01 and G10 satellites [2019-01-01]

7. Figure 5 shows the changes of the estimated polar motion (blue dash line) and one of IERS C04 (red line). The X and Y axes of the horizontal plane are X_p and Y_p , respectively, and the vertical axis is the date. Although we could not see the polar motion changing as it was drawn in a circle due to its short data processing period, we could see that the values of the estimated polar motion matched IERS C04. Figure 6 shows the differences from IERS C04 over time for polar motion and UT1-UTC. Most of the X_p and Y_p errors did not exceed 0.2 mas and UT1-UTC had a error within 0.2 millisecond. Table 4 shows the difference values between the IERS C04 and the estimated ERP over 180 days. Figure 7 shows the histograms for the differences of ERP.

	X_p (mas)	Y_p (mas)	UT1-UTC (ms)
Min	-0.202	-0.255	-0.085
Max	0.304	0.338	0.171
Mean	0.041	-0.002	0.024
Std.	0.100	0.116	0.047
RMS	0.108	0.116	0.053

Table 4: The difference between the estimated ERPs and IERS C04

5. SUMMARY

- GNSS-based products service system is developed to secure technology and to support related research.
- GPS satellite orbit and ERP were determined using PANDA and Bernese GNSS v5.2 respectively.

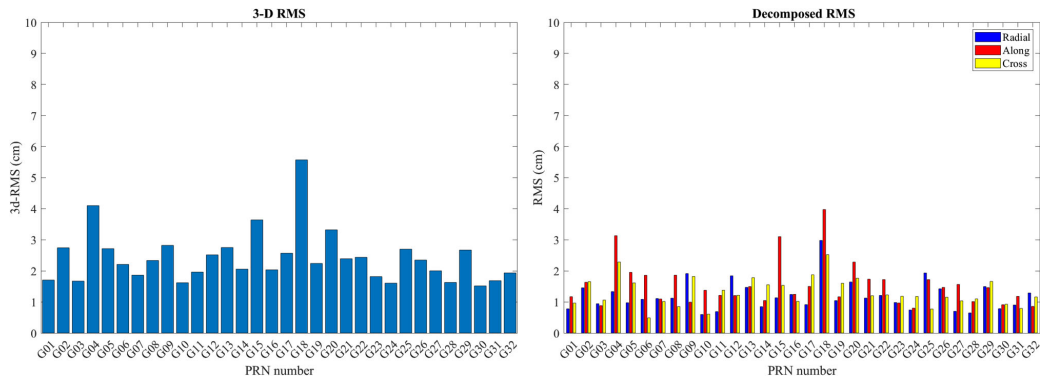


Figure 4: POD results: the mean position errors (3-D RMS: left, decomposed RMS: right) of all GPS satellites [2019-01-01]

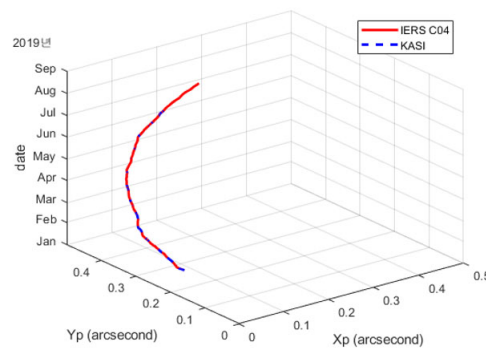


Figure 5: ERP results: a comparison of polar motions in KASI and IERS C04

- Most position errors of GPS orbit were within 6 cm compared to IGS final products.
- The estimated ERP had a difference of about 100 microarcsec in polar motion and about 50 microsec in UT1-UTC compared to IERS C04.

6. REFERENCES

- Zhao, Q., Guo, J., Li, M., Qu, L., Hu, Z., Shi, C., Liu, J., 2013, "Initial results of precise orbit and clock determination for COMPASS navigation satellite system", *J. Geodesy* 87(5), pp. 475-486.
- Dach, R., Hugentobler, U., Fridez, P., Meindl, M., 2007, "Bernese GPS Software Version 5.0. User manual", (Bern: Stampfli publications)

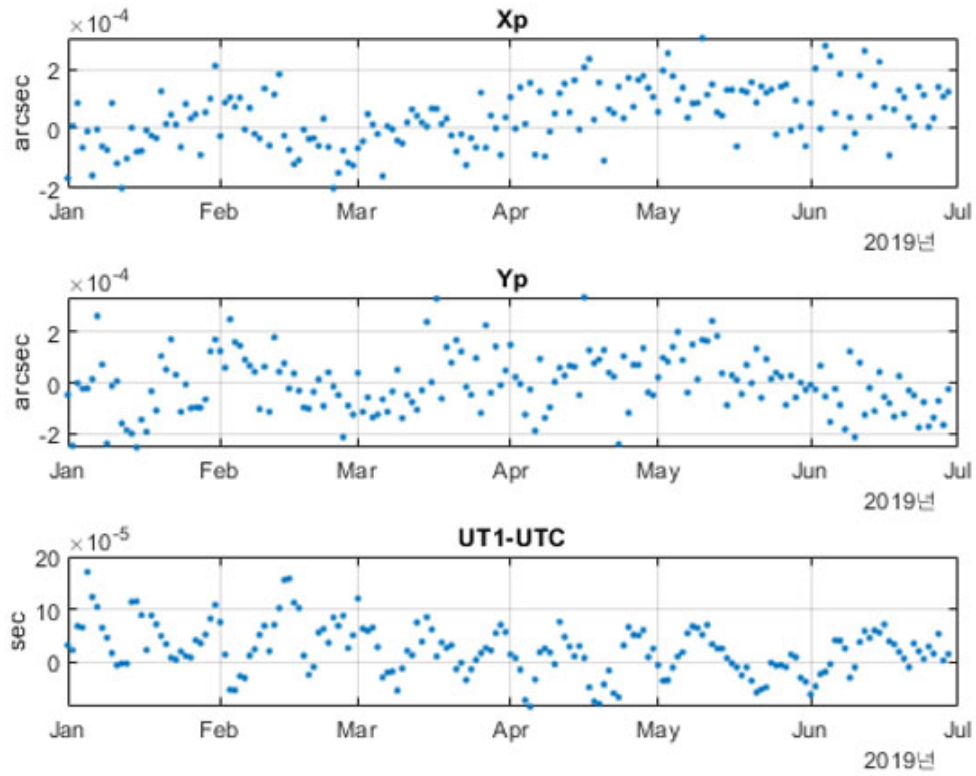


Figure 6: ERP results: time series of the ERP differences between KASI and IERS C04

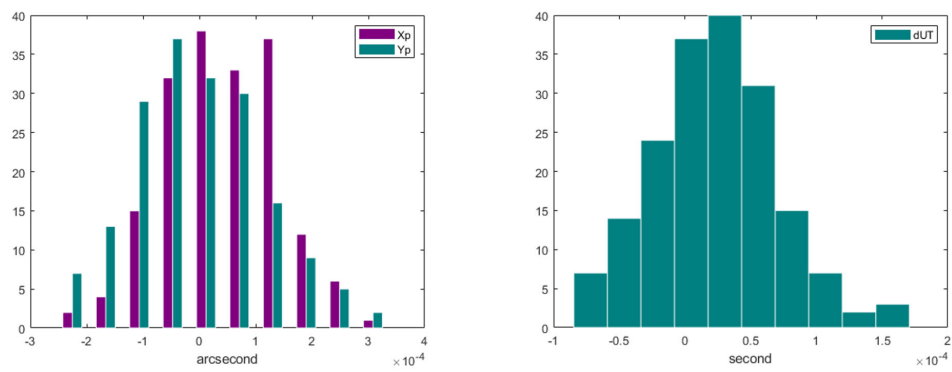


Figure 7: ERP results: histograms of polar motion (left) and UT1-UTC (right) differences between KASI and IERS C04

OPERATIVE EOP ACTIVITIES AT VNIIFTRI

S. PASYNOK¹, I. BEZMENOV¹, I. IGNATENKO¹, E. TCYBA¹, V. ZHAROV²

¹ National Research Institute for Physical-Technical and Radio Engineering Measurements (VNIIFTRI) - Russia - pasynok@vniiftri.ru, bezmenov@vniiftri.ru, igig@vniiftri.ru, tsyba@vniiftri.ru

² VNIIFTRI and SAI of the Moscow State University - Russia - zharov@sai.msu.ru

ABSTRACT. VNIIFTRI as the Russian Main Metrological Center of Time, Frequencies and Earth Rotation Service has carried out rapid EOP processing based on GNSS, VLBI and SLR observations for many years. VNIIFTRI also participates in GNSS and SLR observations of IGS and ILRS respectively.

The EOP activities at VNIIFTRI can be grouped in five basic topics:

- 1) Processing of VLBI, GNSS, SLR and LLR observation data for EOP evaluation;
- 2) Evaluation of combined EOP values based on EOP series and SINEX combination;
- 3) Evaluation and combination of GLONASS satellites orbit/clock;
- 4) Satellite altimetry data processing;
- 5) Providing GNSS and SLR observations at five metrological sites acting under the auspices of VNIIFTRI.

These fields of activity are considered shortly.

1. INTRODUCTION

VNIIFTRI participates in Earth's orientation parameters (EOP) activity as:

- 1) Russian Main Metrological Center of State Service for Time, Frequencies and Earth orientation parameters evaluation (MMC SSTF);
- 2) Analysis Center (AC) and regional Data Center for five measurement sites of metrological control of ROSSTANDART.

2. SITES OF METROLOGICAL CONTROL

2.1 Metrological control sites

GNSS observations on the five metrological control sites of Rosstandard (Mendeleevo (MDVJ), Novosibirsk (NOVM), Irkutsk (IRKJ), Khabarovsk and Petropavlovsk-Kamchatsky) are carried out permanently and hourly files are formed. SLR observations are carried out at Mendeleevo and Irkutsk using satellite laser range finders "Sazen-TM". So, Mendeleevo and Irkutsk are sites with collocation of GNSS and SLR (Ignatenko et al, 2016). MDVJ, NOVM, IRKJ are sites of the International GNSS Service (GNSS). MDVJ and IRKJ are sites of the International Laser Ranging Service (ILRS). MDVJ is included in EUREF GNSS Permanent Network (EPN). The results of GNSS observations are accumulated at VNIIFTRI in hourly mode and, as well as SLR data, they are used for rapid EOP evaluation. The direct results of SLR observations are transferred to the Information and Analysis Center (IAC) monitoring GLONASS observations and to ILRS.

2.2 Moving to sites of new generation

The two new laser range finders "Tochka" which meet the requirements SLR2000 were built in Mendeleevo (VNIIVTRI) and Irkutsk (North-Eastern branch of VNIIFTRI). These laser range finders have instrumental errors not exceeding a few millimeters for a single measurement and their

declared characteristics were confirmed through preliminary tests (Baryshnikov et al, 2019).

3. GNSS ORBITS AND CLOCK DETERMINATION

By now, GPS and GLONASS satellites orbits and clock corrections are determined at VNIIFTRI. Data processing is performed in three regimes:

- 1) Final: orbits and clock combination obtained by several Russian and IGS AC (Bezmenov and Pasynok, 2015);
- 2) Rapid: data processing of about 500 IGS and Russian sites for determination of own MMC SSTF orbits and clock corrections (Bezmenov and Pasynok, 2017);
- 3) Ultra rapid: processing hourly RINEX d/n/g data received from about 500 IGS and Russian sites and determination of own MMC SSTF orbits and clock corrections (Bezmenov, 2018);

Software for orbit /clock calculation in the first regime was entirely developed at VNIIFTRI. It is based on a well-known algorithm (Beutler et al,1996).

The softwares for orbit/clock calculation in the other regimes are based on BERNESE GNSS Software 5.2 developed at Astronomical Institute of the University of Bern (AIUB, Switzerland). Additional program modules were developed at MMC SSTF. The BERNESE GNSS Software 5.2 shell is used to input parameters for all programs. Some additional program units and associated panels were created. Test results obtained at VNIIFTRI for GLONASS satellites clock corrections (ultra-rapid mode) in comparison with other AC are shown in Figure 1.

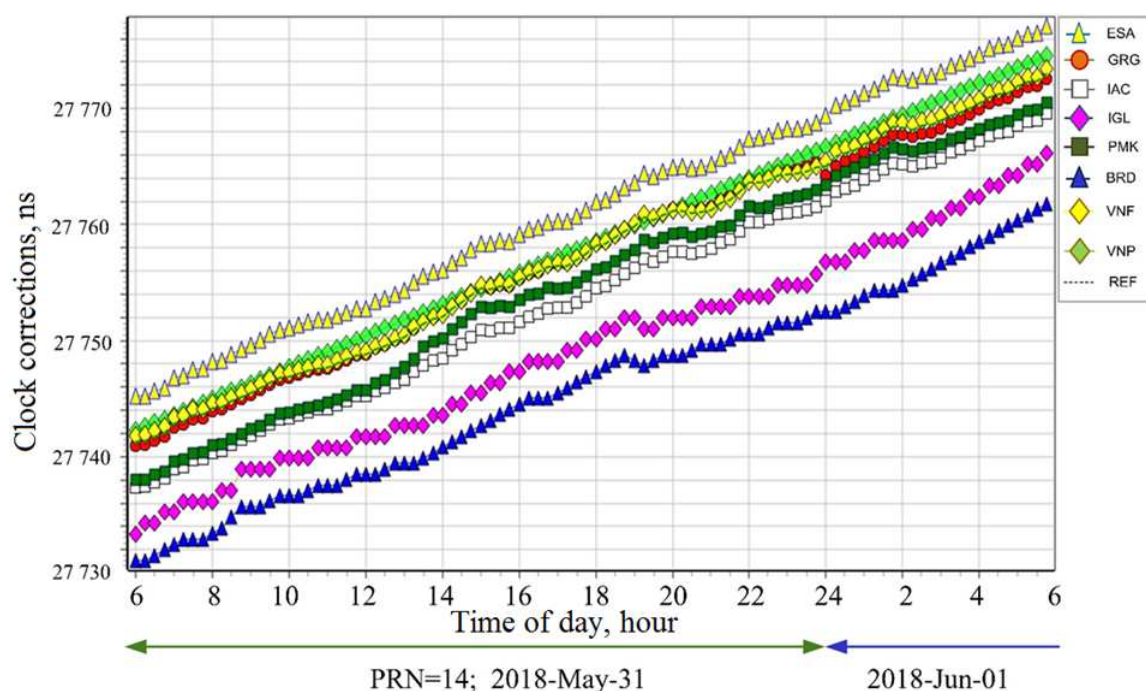


Figure 1: GLONASS Satellite clock corrections (PRN=R03) estimated at MMC SSTF in ultra rapid mode: VNF estimated part, VNP prediction part derived from the previous day. Comparison of estimated values of clock corrections with similar aposteriori values of other ACs and reference values (REF). The reference values were formed as weighted average data of other ACs. The inter daily jumps in ESA data were removed.

4. SATILLITE ALTIMETRY PROCESSING

The software for determination deflection of vertical (DOV), geoid heights (GH) and gravity anomalies (GA) has been also developed at VNIIFTRI. More informations can be found in (Tcyba, 2019).

5. EARTH ORIENTATION PARAMETERS EVALUATION

5.1 SLR and LLR processing for Earth orientation parameters evaluation

The daily processing of SLR Lageos-1 and Lageos 2 observations has been undertaken at MMC SSTF. The results can be seen in Figure 2. The STD of pole coordinates x_p and y_p evaluation with respect oto EOP C04 values are 0.08 and 0.1 mas respectively.

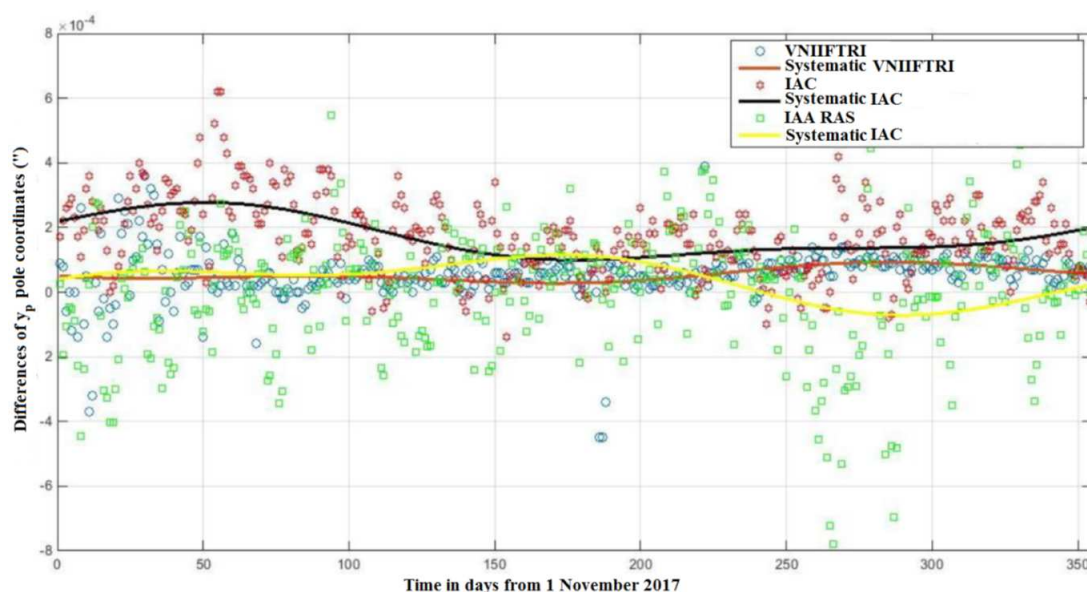


Figure 2: Comparison of SLR pole coordinates with EOPC04 values.

The modern program of UT1 evaluation based on Lunar Laser Ranging measurements was created in the MATLAB environment (Tcyba and Volkova, 2019).

Whereas only ILRS LLR data are processed, program for processing the Altay LLR station measurements has been set up. The main window interface of this software is shown in Figure 3.

5.2 VLBI processing for Earth orientation parameters evaluation

For VLBI data analysis VNIIFTRI uses the ARIADNA software package developed by V. Zharov (2011). The version 4.11 of this software was finished and tested at the end of 2018 in the framework of the VLBI AC operating both at SAI (Sternberg Astronomical Institute of the Moscow State University) and VNIIFTRI. This version allows to read observation data in vgosDB format and to create SINEX files for hourly sessions. The daily processing IVS VLBI data for EOP evaluation are performed at VNIIFTRI now.

The comparison with other AC is showed in Figure 4.

5.3 GNSS processing for Earth's orientation parameters evaluation

The GNSS processing of measurements and EOP evaluations are carried out using the BERNESE GNSS software developed in Astronomical Institute of the University of Bern (AIUB, Switzerland).

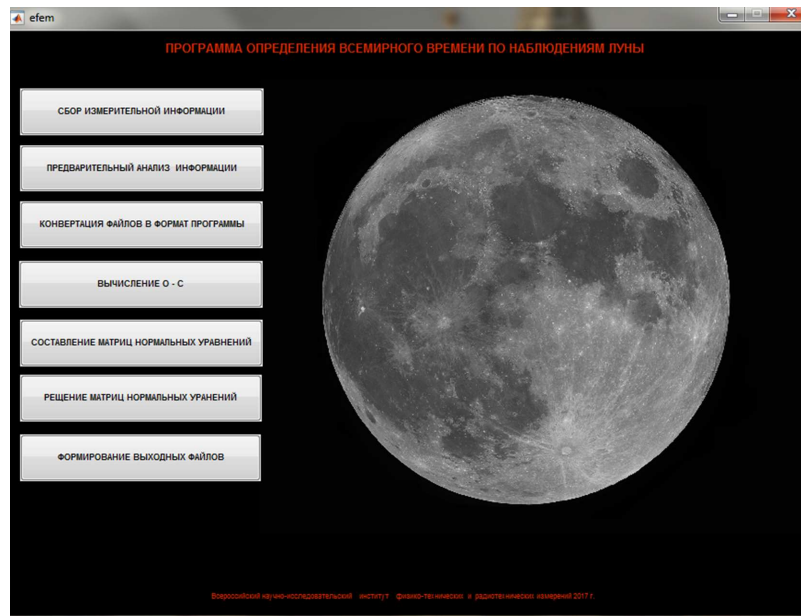


Figure 3: Main window of LLR UT1 software.

The actual algorithm was set up in 2006 with some changes (Kaufman, M., Pasynok S., 2010). It is based on the so-called method of Precise Point Positioning (PPP) using phase measurements with a-priori knowledge of precise satellites coordinates and onboard clocks biases for navigation tasks. Then the values of UT1 and pole coordinates are calculated using the calculated instantaneous coordinates of stations and their catalogue values. Processing is carried out separately for each daily session of measurements.

6. EARTH ORIENTATION PARAMETERS COMBINATION

Combination for operative EOP evaluation has been done at VNIIFTRI since 1955. Now two types of EOP combination are maintained: combination at time raw level and combination at normal equation level (see Figure 5).

6.1 Combination on EOP time raws level

Combination EOP at time raw level are calculated at VNIIFTRI by combining nine independent individual EOP series provided by the following Russian analysis centers: VNF (VNIIFTRI), IAA (Institute of Applied Astronomy), IAC (Information-Analytical Center of Russian Space Agency) and SVOEVP (Russian Space Agency).

6.2 Combination on normal equation level

Combination EOP at normal equation level are calculated at VNIIFTRI by combining the SINEX files, mostly provided by international services.

The core of SINEX combination program - SINCom software package - has been developed at Institute of Applied Astronomy. The Perl scripts for automatization of data preparation, realisation of calculation strategy, prediction and forming results were developed at VNIIFTRI.

7. CONCLUSION

We have presented an overview of EOP production and its main developments at VNIIFTRI in the frame of the Russian Main Metrological Center of Time, Frequencies and Earth Rotation

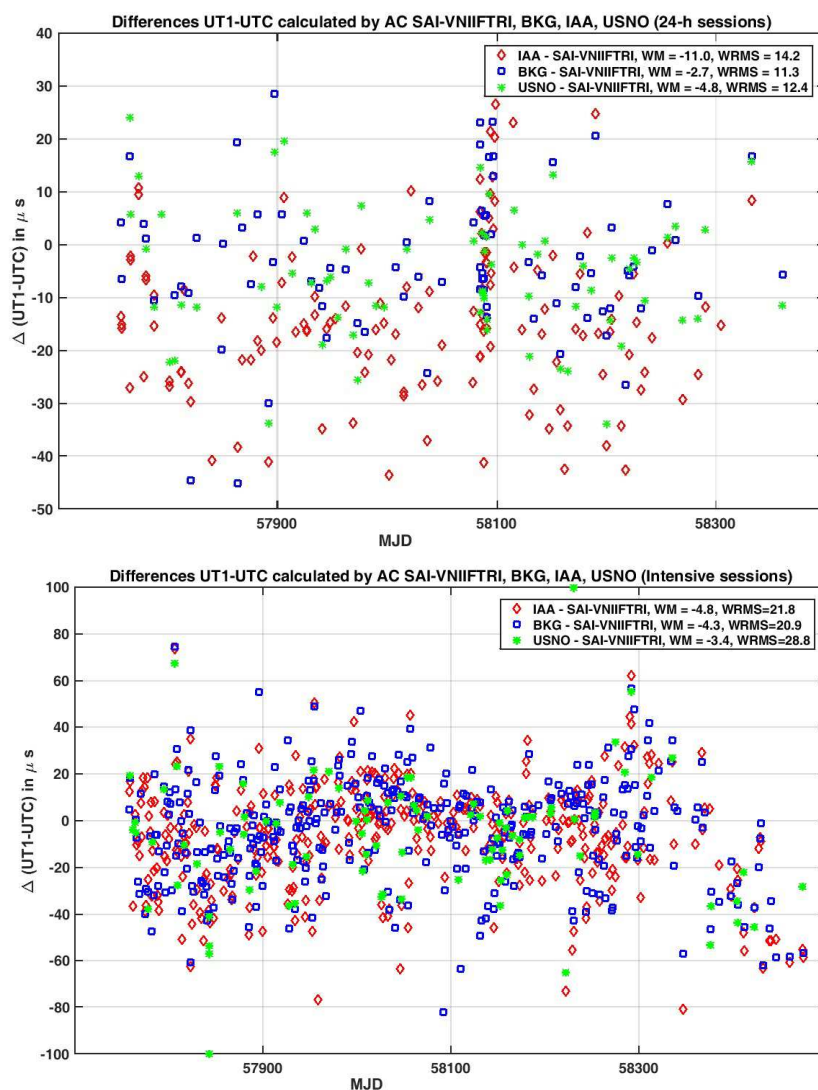


Figure 4: AC BKG, IAA, USNO - AC SAI-VNIIFTRI UT1 differences.

Service. More information and data are in open anonymous access through www.vniiftri.ru and <ftp.vniiftri.ru>.

8. REFERENCES

- Ignatenko I.Yu., Zhestkov A.G., Shlegel V.R., Emelyanov V.A., 2016, "Metrologicheskie aspekty lazerno-lokacionnykh izmerenij", Metrologiya vremeni i prostranstva. Materialy VIII Mezhdunarodnogo simpoziuma, Abstracts book, ISBN 978-5-903232-63-5, 14-16 September 2016, S. Peterburg - Mendeleevo: FSUE VNIIFTRI, p. 192 (in russian).
- Baryshnikov M.V., Blinov I.Yu., Bondarev N.N., Borisov B.A., Donchenko S.I., Kolychev A.M., Nekrasov Y.V., Martynov S.V., Sadovnikov M.A., Shargorodsky V.D., 2019, "Rezul'taty ispytaniy rossijskoj lazernoj stancii novogo pokoleniya Tochka", Book of abstarcts of 8-th All-Russian conference Fundamentalnoye i prikladnoye koordinatno-vremennoye i navigatsionnoye obespecheniye (KVNO-2019), St. Petersburg, IAA RAS 15-19, p. 18 (in russian).
- Bezmenov I.V., Pasynok S.L., 2015, "GLONASS orbit clock combination in VNIIFTRI", Proceedings of the Journées 2014 Systèmes de reference spatio-temporels, Z. Malkin and N. Capitaine

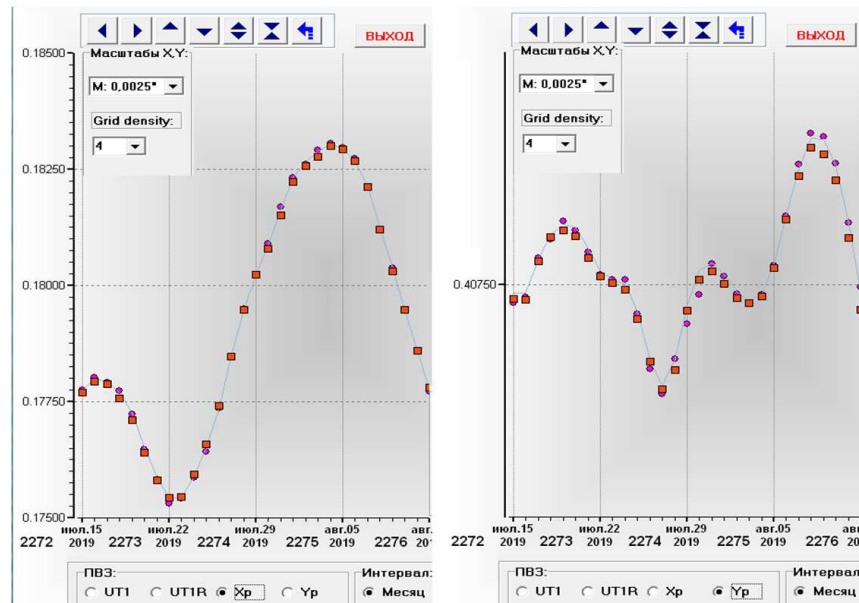


Figure 5: The Earth pole coordinates (trend removed). Solid line – USNO combination, squares – VNIIFTRI time raw combination, circles – VNIIFTRI SINEX combination results

- (eds), Pulkovo observatory, ISBN 978-5-9651-0873-2 ISBN 978-2-901057-70-3, pp. 215–216.
- Bezmenov I.V., Pasyok S.L., 2017, “Ephemeris-time Calculation for GNSS satellites in rapid regime based on measurement data”, *Almanac of Modern Metrology* 11, pp. 104–120.
- Bezmenov I.V., 2018, “Estimation in MMC SSTF orbits and clock corrections of GNSS navigation satellites in ultra-rapid regime based on observation data”, *Proceedings of IX International Symposium Metrologiya vremeni i prostranstva, Mendeleevo 2018, FSUE VNIIFTRI*, pp. 107–117. (in russian).
- Beutler G., Brockmann E., Hugentobler U. et al., 1996, “Combining consecutive short arcs into long arcs for precise and efficient GPS Orbit Determination”, *J. Geodesy* 70, pp. 287–299, doi: 10.1007/BF00867349
- Тсыба Е.Н., 2019, “Предварительные результаты построения модели геоида акватории Мирового океана по данным спутниковой альтиметрии в GMC GSVCh”, *Book of abstracts of 8-th All-Russian conference Fundamentalnoye i prikladnoye koordinatno-vremennoye i navigatsionnoye obespecheniye (KVNO-2019)*, St. Petersburg, IAA RAS 15-19, p. 191 (in russian).
- ТСЫБА Е., Volkova O., 2019, “Determination of Earth Orientation Parameters by SLR in MMC SSTF FSUE VNIIFTRI”, *Journées 2019 proceeding, poster session*.
- Zharov V.E., 2011, “Osnovy radioastrometrii”, *Fizicheskiy fakultet MGU im. M. V. Lomonosova. Moscow*, pp. 208–224 (in russian).
- Kaufman M., Pasyok S., 2010, “Russian state time and Earth rotation service: observation, EOP series, prediction”, *Artificial Satellites* 45(2), pp. 81–86.

EFFECT OF VLBI INTENSIVE SESSIONS ON DAILY AND SUB-DAILY ERP DETERMINED FROM CONT17 IVS DATA

S. Raut^{1,2}, R. Heinkelmann², S. Modiri^{2,3}, H. Schuh^{2,3}

¹ TU Berlin, Chair of Space Engineering, Institute für Luft- und Raumfahrt - Germany
shrishail.raut@campus.tu-berlin.de

² GFZ German Research Centre for Geosciences, Potsdam - Germany
rob@gfz-potsdam.de, sadegh.modiri@gfz-potsdam.de, schuh@gfz-potsdam.de

³ TU Berlin, Institute for Geodesy and Geoinformation Science - Germany

ABSTRACT. This work deals with validating the established approach of analyzing VLBI intensive sessions to determine dUT1. VLBI sessions from the CONT17 campaign are chosen as they provide continuous VLBI observations over two weeks (28th Nov - 12th Dec 2017) of the currently highest quality. For the standard 24-hour sessions in this campaign, two different legacy networks were involved, the legacy-1 network, which was entirely based on IVS network stations with global distribution, and legacy-2 network involving VLBA and a few IVS network stations for the global extension. In addition to these 24-hour sessions, two different IVS and one Russian intensive sessions were observed every day during CONT17. The dUT1 determined from the intensive sessions are compared with daily and hourly dUT1 from 24-hour sessions during this 15-day time-frame. The results show that the dUT1 determined from intensive sessions do not show good agreement with daily dUT1 from 24-hour sessions; however, it shows better agreement with hourly dUT1.

1. INTRODUCTION

Very long baseline interferometry (VLBI) is a microwave-based space geodetic technique that measures the difference in arrival time of signals from extra-galactic radio source (e.g., the Quasars) received simultaneously at two or more radio telescopes. VLBI is one of the high precision space geodetic techniques which can provide the full set of the Earth orientation parameters (EOP). The EOP represent the link between the Terrestrial reference frame (TRF) and the Celestial reference frame (CRF). The EOP consist of five angles, namely x_p and y_p the pole coordinates describing the polar motion, UT1–UTC correcting the phase of the rotation angle Ω UT1(Ω is the nominal Earth angular velocity), and celestial pole offsets (CPO) (dX,dY).

The International VLBI Service for Geodesy and Astrometry (IVS) normally conducts two types of VLBI network sessions, 24-hour sessions, which are carried out about three days per week, and the hour-long one-baseline intensives which are carried out daily. The intensives are used to determine UT1-UTC on a daily basis, whereas the 24-hour sessions give the complete set of EOP several times per week. The so-called dUT1 value is determined from the one-hour intensive VLBI daily session carried out on one baseline. During the analysis of intensive session, parameters like dUT1, single clock offset, and zenith wet delay are estimated whereas other parameters such as polar motion (PM), celestial pole offsets (CPO), station and source coordinates and tropospheric gradients are fixed to their a priori values respectively. Such kind of parameterization is chosen as there are not enough observations per parameter. Besides, the station coordinates cannot be estimated as one baseline is insufficient to fix the degree of freedom of the terrestrial basis. As intensive sessions contain observations during one hour, they give rise to correlations between CPO and terrestrial pole coordinates. The dUT1, which is estimated from this approach, may contain inaccuracies.

Whereas analyzing 24-hour VLBI sessions, the parameters which were fixed to their respective a priori values in the approach mentioned above, are estimated in this approach. This is possible as the 24-hour sessions contain multiple baselines and enough observations per parameter. This can be validated by comparing dUT1 values derived from intensive sessions and 24-hour VLBI sessions considering their different observation intervals through sub-daily parameterization. This gives an idea of how different parameterization can affect dUT1 determination. For this work, we chose the continuous VLBI campaign CONT17. Such campaign, that take place every three years intend to have continuous VLBI observations over two weeks. The CONT17 campain differed from the previous ones, as the observations were carried out by three independent networks: two legacy networks observed at S/X band, one VGOS network performed broadband observing. During these 15 days, 24-hour sessions took place daily, along with two intensive sessions.

2. CONT17 campaign

The campaign began on Tuesday, 28th November 2017, at 00:00:00 UT, and it concluded on Tuesday, 12th December 2017, at 23:59:59 UT. The geographical positions of the stations that participate in this CONT17 campaign can be seen in Figure 1.

The number of observations during the CONT17 period are shown in Figure 2. The observations in a single session in the legacy-1 network are around 10,000, and legacy-2 has around 15,000 observations. Besides, we have 5 VGOS sessions from 4th December to 8th December, and every session has around 3000 - 4000 observations. The Badary-Zelenchk (Russian) intensives have approximately 25 observations in a single session, and the Kokee-Wettzell (IVS) intensives have around 18 observations except for four days where it has approximately 30 observations.

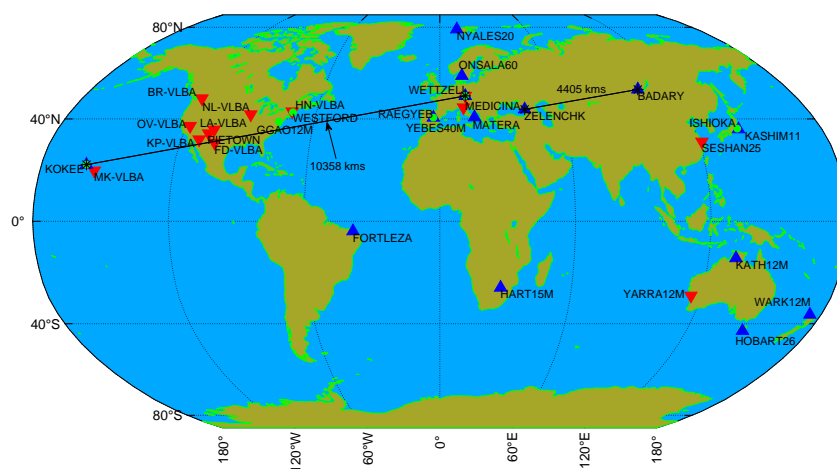


Figure 1: Geographical representation of the stations of the various network. Legacy (S/X) stations in VLBA network (marked as the red triangle), IVS network (marked as the blue triangle); VGOS stations are represented by a Green circle; stations which participate in intensives are indicated by a black cross and their baselines are represented by a black solid line.

3. METHODOLOGY

We will validate the credibility of the two methods, which estimate dUT1 from intensive and 24-hour sessions, respectively. The dUT1 is estimated using VieVs@GFZ software. The dUT1 estimated from intensive sessions are compared with daily dUT1 and hourly dUT1 values derived

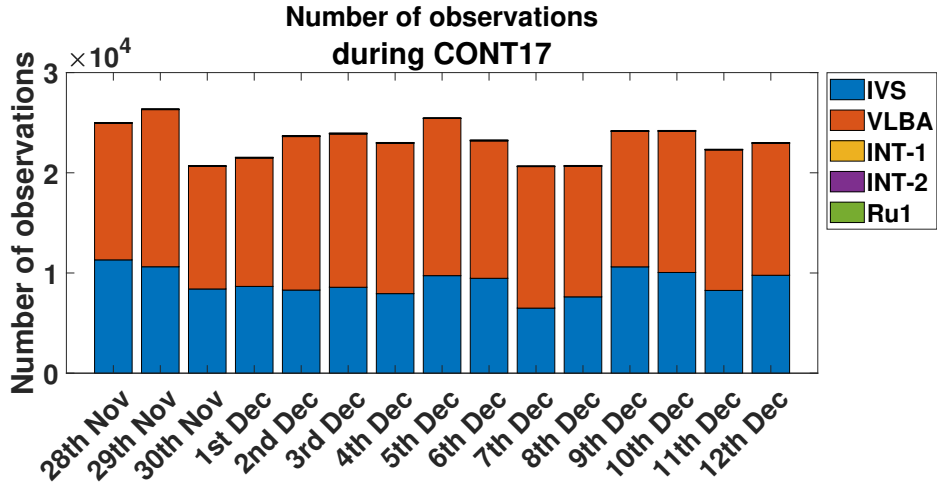


Figure 2: Number of VLBI observations during CONT17 campaign. (observations from VGOS are not included)

from 24-hour sessions, respectively.

4. RESULTS

The Figure 3 shows a comparison of dUT1 estimated from two intensive baselines, i.e., Kokee-Wettzell (IVS), and Badary-Zelenchik (Russian) during the 15 days. We can observe that dUT1 estimated from Russian intensives have higher formal errors as compared to IVS intensives. The main reason for this is due to the different baseline length, and dUT1 is sensitive to a more extended east-west baseline. Since Russian intensive (4405 km) has a shorter baseline than IVS intensive (10358 km), resulting in higher formal errors in dUT1. Now, the dUT1 from the intensives are

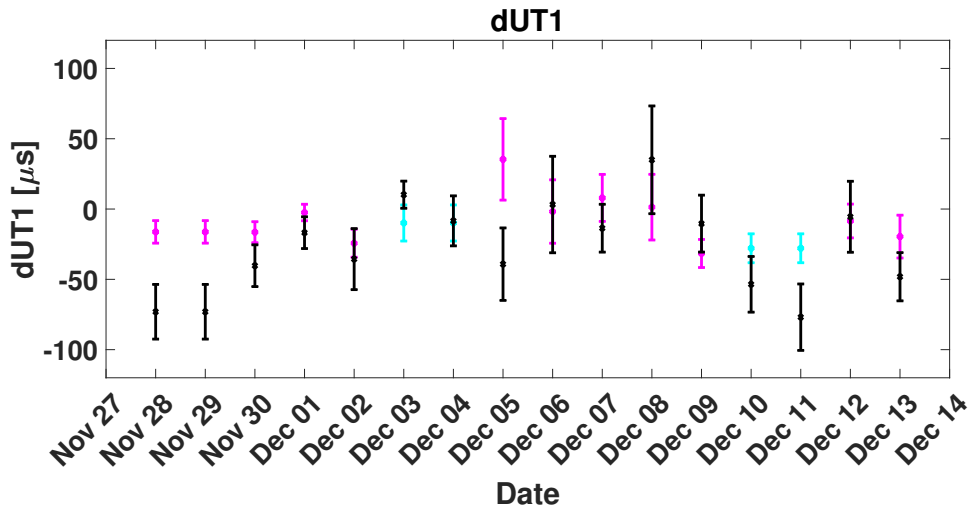


Figure 3: dUT1 from IVS and Russian intensives sessions; Magenta, cyan and black points represents dUT1 from IVS(INT-1), IVS(INT-2), and Russian intensives respectively.

plotted against daily dUT1 values from 24-hour sessions in the Figure 4. It can be observed that the dUT1 values from intensives do not show good agreement with daily dUT1 values from 24-hour sessions. The reason can be explained as most parameters are not estimated, i.e., fixed to a priori

values when estimating dUT1 from intensives. The inaccuracies present in the a priori values of fixed parameters, it will propagate in dUT1 determination.

As can be seen in Figure 5, the dUT1 estimated from the intensives are plotted against hourly dUT1 estimated from 24-hour sessions. Even in this case, the dUT1 from intensives does not show a good agreement with dUT1 from 24-hour sessions. For further investigation, the root mean square of the difference between dUT1 from intensives and 24-hour session were taken. It was found that dUT1 from intensives (IVS and Russian) show slightly better agreement (7 percent) with hourly dUT1 than daily dUT1 from the 24-hour sessions. This can be because the sub-daily variations are accounted in hourly dUT1 values from the 24-hour sessions.

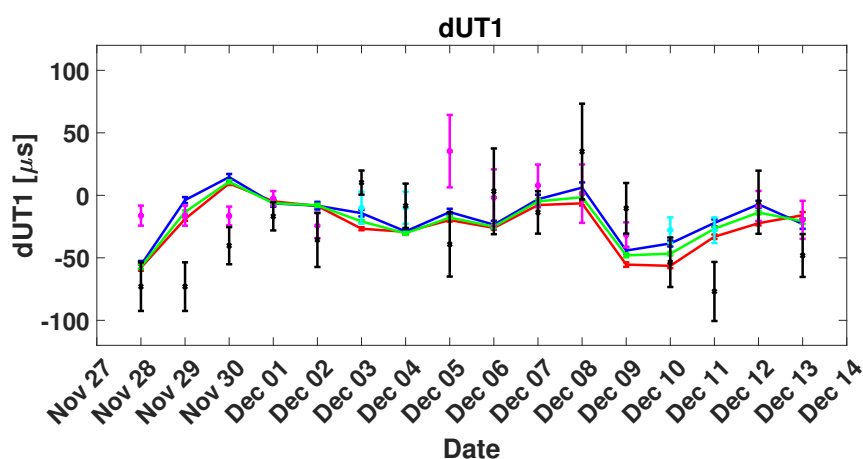


Figure 4: dUT1 from intensives and 24-hour sessions (daily). Blue, red and green lines represent daily dUT1 derived from IVS, VLBA and combined network respectively. Magenta, cyan and black points represent dUT1 from IVS(INT-1), IVS(INT-2), and Russian intensives respectively.

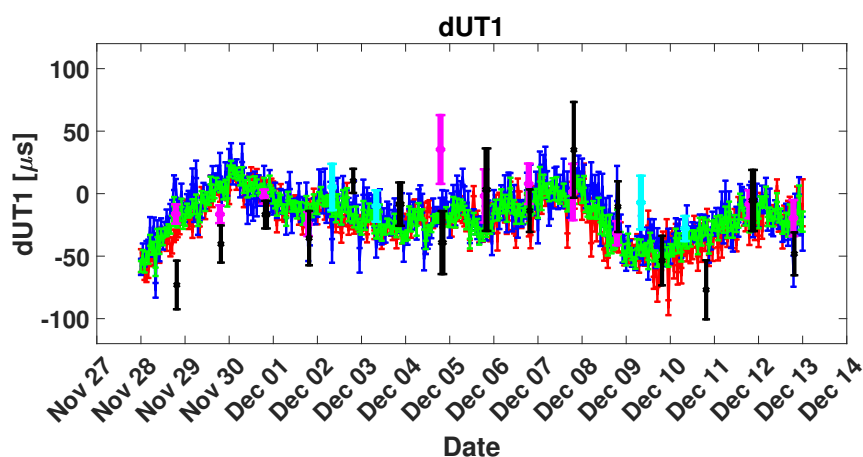


Figure 5: dUT1 from intensives and 24-hour sessions (hourly); Blue, red and green line represents hourly dUT1 derived from IVS, VLBA and combined network respectively. Magenta, cyan and black points represents dUT1 from IVS(INT-1), IVS(INT-2), and Russian intensives respectively.

5. CONCLUSIONS

The dUT1 values derived from intensives and 24-hour sessions show differences that can exceed the formal errors. The dUT1 obtained from intensive sessions show approximately 7 percent better agreement with hourly dUT1 of the CONT17 campaign as compared to daily dUT1 from 24-hour sessions.

6. REFERENCES

- Petit, G. and Luzum, B., 2010, IERS conventions (2010) (No. IERS-TN-36), BUREAU INTERNATIONAL DES POIDS ET MESURES SEVRES (FRANCE).
- Schuh, H. and Behrend, D., 2012, "VLBI: a fascinating technique for geodesy and astrometry", *Journal of Geodynamics* 61, pp. 68–80.
- Behrend, D., Thomas, C., Gipson, J. and Himwich, E., 2017, "Planning of the Continuous VLBI Campaign 2017 (CONT17)", In 23rd European VLBI Group for Geodesy and Astrometry Working Meeting, pp. 132–135.
- Nilsson, T., Soja, B., Karbon, M., Heinkelmann, R. and Schuh, H., 2015, "Application of Kalman filtering in VLBI data analysis", *Earth, Planets and Space* 67(1), p.136.

NEW EARTH ORIENTATION PARAMETERS BY COMBINATION OF GNSS AND VLBI

J-Y. RICHARD, C. BIZOUARD, S. LAMBERT, O. BECKER, M. KARBON

Observatoire de PARIS - FRANCE - jean-yves.richard@obspm.fr

ABSTRACT. We present the combined processing of GNSS and VLBI normal equations produced at the IERS technique centers. The DYNAMO software allows to obtain the combined solution for EOP and station coordinates, along with the corresponding intra-technique VLBI and GNSS solutions. The combined GNSS/VLBI solution seems to be more robust than the intratechnique ones. First the EOP are better decorrelated, second sub-monthly nutation and UT1 have a better stability.

INTRODUCTION. At SYRTE, thanks to the IERS COL Working Group (Polet, 2011), we have developed a combined treatment of normal equations produced respectively by the International GNSS Service (IGS) and International VLBI Service (IVS). This approach allows to determine the EOP on a daily basis, pole coordinates (x,y) and associated rates (x_r,y_r) , Universal Time UT1 and length of day offset LOD, and nutation offset with respect to IAU2000A/2006 precession-nutation model (dX,dY) , simultaneously with station coordinates constituting the terrestrial frame (TRF) and possibly the quasar coordinates constituting the celestial frame (CRF). The process of such a combination is presented and results over the period 2000-2019 are analyzed.

1. STRATEGY

1.1 Pre-processing Before the combination, we apply a pre-processing to the GNSS and VLBI Sinex files - containing the normal equations - according to the top of Figure 1. This step rebuilds the GNSS and VLBI normal equations using IGS/IVS combination solution Sinex files. The normal equations are stacked on a weekly basis. For estimating the systematic effects of the GNSS/VLBI networks with respect to the International Terrestrial Reference Frame (ITRF), we introduced the *systematic Helmert parameters*: translation and scale factor for GNSS networks, scale factor for VLBI (Polet, 2011).

1.2 Processing

The weekly normal equations generated by the afore-mentioned pre-processing with the systematics parameters (magenta square for GNSS et green square for VLBI in Figure 1) are stacked using the Helmert weighting algorithm (Sahin, 1992). The common parameters are the pole coordinates, pole rate and LOD. Moreover minimal constraints are applied on GNSS network: No Net Translation (NNT), Scale (Sc), No Net Rotation (NNR). For VLBI network we apply local ties for colocalized GNSS stations. A least square inversion is performed on the system composed of the normal equations and of the constrain relations on a weekly bases to determine the EOP, the GNSS and VLBI station positions, the Helmert parameters, and the geocenter coordinates. We also perform the mono-technique inversion (without local ties for VLBI) for evaluating the performances of the GNSS/VLBI combination.

Bottom part of the Figure 1 synthesizes this combination strategy

2. DATA AND PARAMETERS

The interval of twenty years covers the period from January 2000 until July 2019. The daily GNSS Sinex in the *covariance matrix format* are uploaded from <ftp://igs.ign.fr> (5513 daily

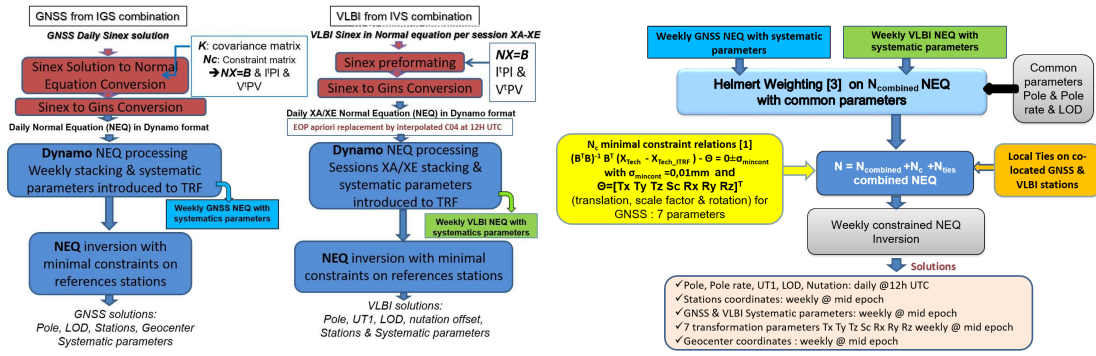


Figure 1: GNSS and VLBI intra and inter technique processing

files). The VLBI Sinex in *normal matrix format* are uploaded from <ftp://cddis.gsfc.nasa.gov> (2585 sessions XA and XE).

In Figure 2 we report the common Earth Orientation Parameters that can be estimated from VLBI and GNSS observations: pole coordinates (XPO, YPO), polar rates (XPOR, YPOR), length of day offset LOD.

Parameters	GNSS daily		VLBI R1/R4 sessions	
	Sinex parameters	Initial values	Sinex parameters	Initial values
Polar coordinates	XPO, YPO @12h	IERS EOP 08-C04	XPO, YPO @~04-06h	IERS EOP 14-C04
Polar motion rate	XPOR, YPOR @12h	IERS EOP 08-C04	XPOR, YPOR @~04-06h	0.0
Delta time UT1-UTC	-		UT @~04-06h	IERS EOP 14-C04
Length of Day LOD	LOD @12h	IERS EOP 08-C04	LOD @~04-06h	IERS EOP 14-C04
Nutation offset dX, dY IAU2000/2006 model	-		NUT_X, NUT_Y @~05-07h	0.0
Station coordinates	STAX, STAY, STAZ ~500 stations @12h	IGb08 & IGS14 from February 2017	STAX, STAY, STAZ ~5 stations /session @~04-06h	ITRF14
Geo-centre	XGC, YGC, ZGC @12h	Set to 0.0	-	

Figure 2: GNSS and VLBI common EOP parameters and their a-priori in the GNSS/VLBI Sinex files

3. EOP SOLUTIONS

All EOP are determined at midday. The EOP intra-technique solutions (GNSS and VLBI) and corresponding GNSS/VLBI combined solution (COMB) are compared with the IERS EOP series 14C04 interpolated at midday. Table 1 reports the mean and standard deviations of the paired differences with respect to the 14C04 time series over the period 2000-2019. The nutation

Table 1: EOP Solution Comparison wrt C04

	xp (μ as)	yp (μ as)	lod (μ s)	dX (μ as)	dY (μ as)	UT1 (μ s)
VLBI	-133±126	-15±117	2±18	-3±45	-1±68	8.6±19.3
GNSS	-10±32	16±35	0±20	-	-	-
COMB	-13±32	18±35	0±17	1±60	-6±73	8.9±19.3

offsets (with respect to the IAU 2000 model) of the GNSS/VLBI combined solution are plotted

in Figure 3 along with the reference series C04 for the period 2000-2019. COMB shows larger discrepancies than the intra-technique VLBI solution. It could be due to the limitation of VLBI observations to the XA and XE VLBI sessions. The stability of the nutation offsets for GNSS,

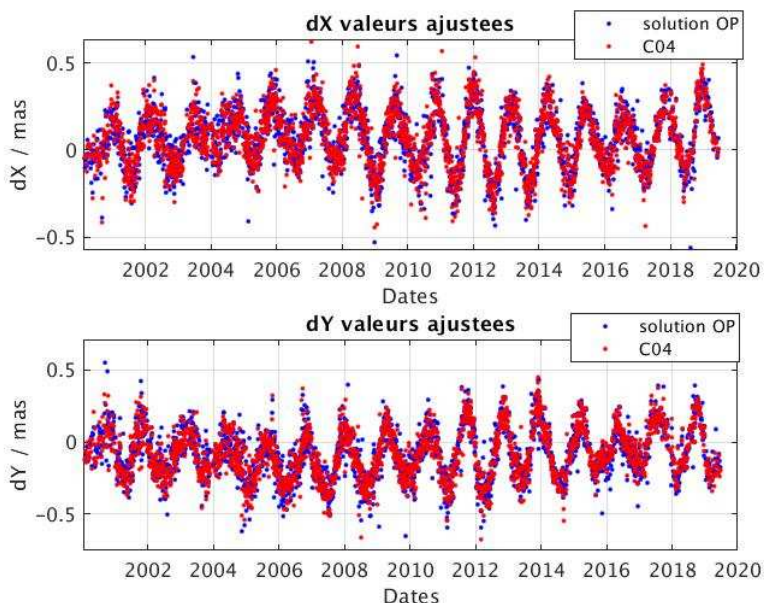


Figure 3: Nutation offsets with respect to IAU2000 model: combined GNSS/VLBI solution (COMB) and reference solution (C04)

VLBI and GNSS/VLBI combination is investigated in light of the overlapping Allan deviation. This one is plotted in the left part of Figure 4. It shows that the combination nutation corrections have a stronger stability at sub-monthly periods, but this one is downgraded beyond 3 years. For the residuals UT1 wrt C04, the right part of Figure 4 shows that the combination significantly reinforces the stability in regard to the pure VLBI solution. This could results from a stabilization of the VLBI network through local ties. The EOP correlations between EOP are extracted from

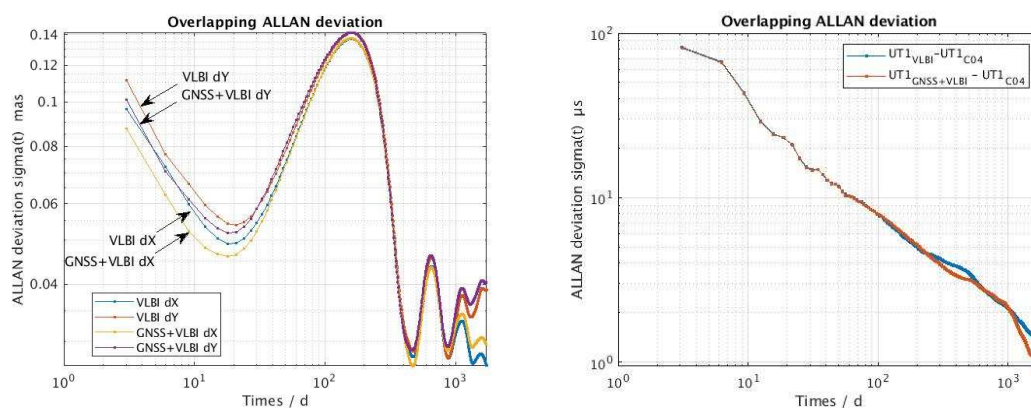


Figure 4: Nutation offsets stability for the VLBI and combined solution (left plot) / UT1 wrt C04 residuals for VLBI and combined solution (right plot)

the covariance matrix of the solutions. For all parameters a significant diminution of correlation is

noticed for COMB compared to the VLBI solution. The Figure 5 shows that the correlations of nutation offsets dX and dY with the others EOP decrease for COMB EOP solution.

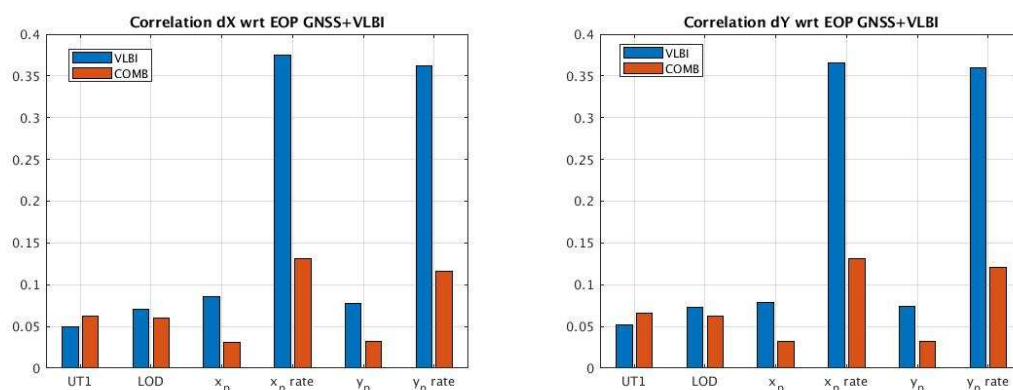


Figure 5: Correlations between nutation offsets dX and dY with the others EOP, VLBI only and combined solution (COMB)

4. STATION SOLUTIONS

The station coordinates are estimated simultaneously with EOP. As an example, the X, Y, Z displacements of the collocated GPS and VLBI stations of TIGO and WESTFORD are shown in Figure 6 and the RMS of the displacement for 6 stations are reported in Table 2. The positions are estimated at midday on Wednesday for the period 2000-2019.

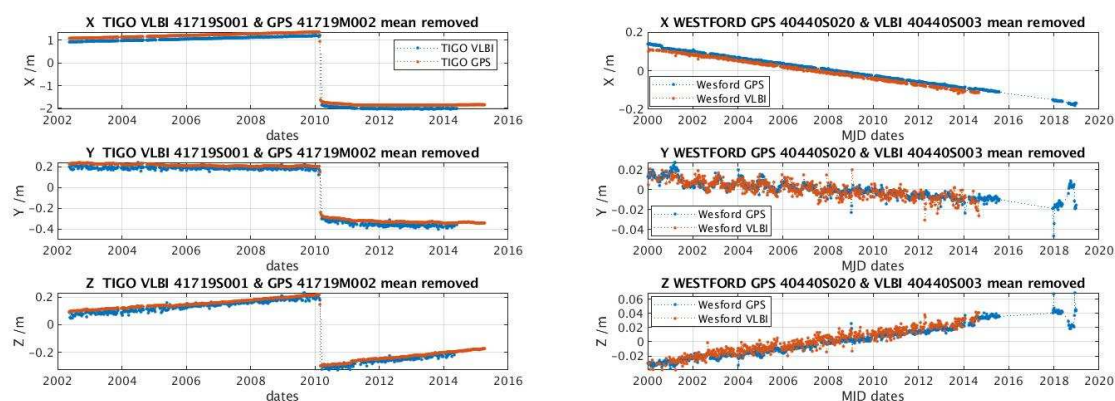


Figure 6: X, Y, Z displacements of GPS/VLBI collocated stations of TIGO and Westford

Table 2: RMS (mm) of the 3D displacment for 6 VLBI/GPS collocated stations, period 2000-2019

Station	TSUKUBA	FAIRBANKS	TIGO	WETTZELL	WESTFORD	HOBART
VLBI	11.4	7.5	18.2	6.0	8.0	18.0
GPS	-	-	4.7	2.8	2.9	6.0

Over the period 2000-2019, the systematic effects of GNSS and VLBI station network are estimated on Wednesday. The Figure 7 shows weekly estimation of these parameters for the GPS (magenta) and VLBI (blue) station networks respectively.

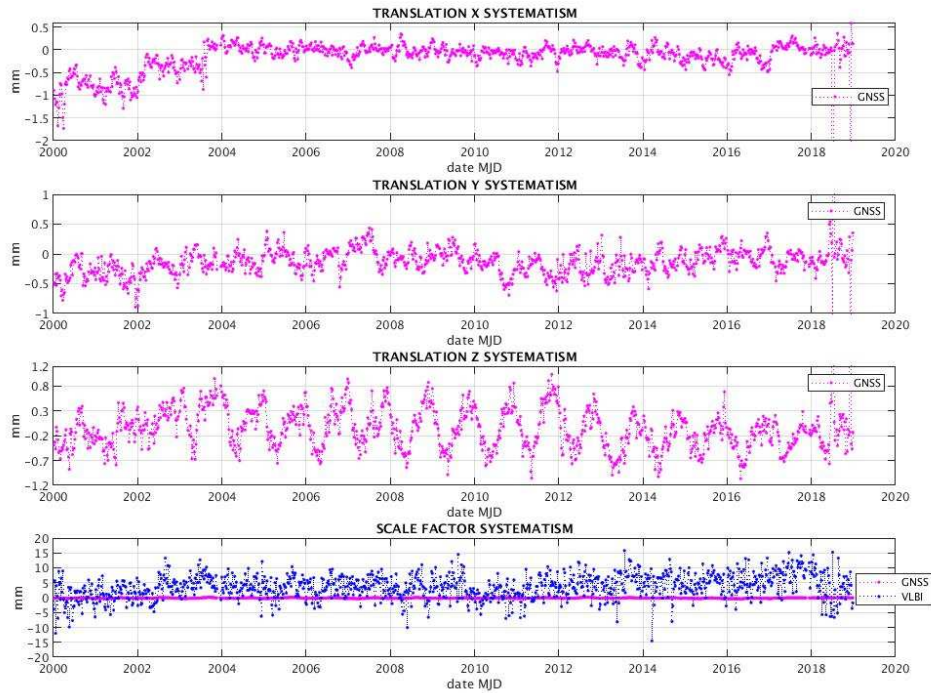


Figure 7: Systematic effects for GPS and VLBI station networks

The Table 3 brings together the means and rates of these weekly systematic parameters, translation and scale for GPS station network and scale factor for VLBI station network.

Table 3: Systematic effects for GPS and VLBI station networks, means and rates wrt ITRF for the period 2000-2019

	T_x (mm)	T_y (mm)	T_z (mm)	Sc (mm)
GNSS	-0.185 ± 0.709	-0.136 ± 0.376	-0.028 ± 1.021	-0.979 ± 0.689
rate (mm/y)	+0.031	-0.0006	-0.010	-0.767
VLBI				$+3.624 \pm 4.205$
rate (mm/y)				-1.558

5. CONCLUSION

At SYRTE, an operational chain, based on the CNES/GRGS DYNAMO software, allows to combine GNSS and VLBI observations at the normal equation level (SINEX files from IERS technique centers). The results show a good consistency with ITRF14 and could be useful to control the consistency of the IERS C04 series with respect to the ITRF. Nutation offsets stability is improved for sub-monthly periods and UT1 stability is slightly better than C04 beyond a few year. Correlations between EOP are significantly reduced, suggesting that such a combined treatment is more robust. Obtained EOP are consistency with the ITRF, and freed of network effects. For densifying the EOP, all VLBI sessions have to be included. In the near future, this process will be extended to the SLR technique, and the quasars coordinates (CRF) will be simultaneously estimated with the

EOP and station coordinates.

6. REFERENCES

- Pollet, A., 2011, "Combinaison des techniques de geodesie spatiale", Thèse de doctorat en Astronomie et astrophysique.
- Ray, J., Kouba, J., Altamimi, Z., 2005, "Is there utility in rigorous combination of VLBI and GPS Earth orientation parameters", *J. Geodesy* 79, pp. 505–511, doi: 10.1007/s00190-005-0007.
- Sahin, M., 1992, "Variance component estimation applied to satellite laser ranging", *Bulletin Geodesique Springer-Verlag* 1992, pp. 284–295.

ESTIMATION OF THE ACCURACY OF PREDICTION OF THE EARTH ORIENTATION PARAMETERS AT THE IAA DATA ANALYSIS CENTER

E. SKURIKHINA

IAA RAS - Russia - sea@iaaras.ru

ABSTRACT. The prediction of the Earth's orientation (EOP) parameters is especially important in the tasks of operational determination of the ERP. The Data Analysis Center of IAA RAS uses its own ERP forecast, which was developed and tested for the IAA EOP service in 1996. Since then, only minor changes regarding the nutation forecast (and the coordinates of the celestial pole) were applied. The algorithm is distinguished by high reliability and acceptable forecast quality. The accuracy of the prediction has not been evaluated since its introduction into the ERP service. In this regard, in the light of the increasing requirements for the accuracy of determining the EOP, it has become necessary to estimate the real accuracy of the forecast used. In the work, the accuracy of the prediction of the ERP used in the IAA is estimated.

1. ERP FORECASTING TECHNIQUE AT THE IAA RAS

The Data Analysis Center of IAA RAS (IAA AC) uses its own EOP forecast, which was implemented in the IAA EOP service in 1996. Since then, only minor changes have been made regarding the nutation forecast (and the coordinates of the celestial pole). The algorithm is distinguished by high reliability and acceptable forecast quality. The algorithm is rather reliable and has an acceptable forecast quality. The forecasting method is based on a combination of the deterministic and stochastic component of the EOP series (Malkin and Skurikhina, 1996). The deterministic component consists of polynomial and seasonal parts. To predict the stochastic component, the method of autoregression of the integrated moving average (ARIMA) is used. For each parameter (coordinates of the Earth's Pole, Universal Time, Nutation Parameters), its own order of autoregression and moving average is used, as well as its own length of the reference interval, on which the parameters for further forecasting are determined. The accuracy of the forecast has not been evaluated since its implementation in the EOP Service. In this regard, in the light of increasing requirements for the accuracy of the determination of EOP, it became necessary to evaluate the accuracy of the forecast of EOP. This is the purpose of this work.

2. DATA USED AND COMPARISON WITH IERS RESULTS

Since the IAA AC did not continuously archive the EOP series generated using their own forecasts, it was decided to use the data from the weekly IAA RAS EOP Bulletins, which have been published at the IAA RAS web page since 2005 year (<http://iaaras.ru/dept/lsgcr/eop>), to evaluate the quality of the prediction. The IAA RAS EOP Bulletins calculates once a week by Thursday.

The bulletin contains one month long EOP time series calculated from VLBI, SLR and GNSS observations and provides a one year long EOP prediction for the rs.dat time series based on SLR data.

It turned out that the forecast step in some of bulletins is different, in most cases the forecast for up to 10 days is given in steps of 1 day, for a number of EOP rs.dat, then up to 75 days the step is 5 days, up to 200 days – 10 days, then – 15 days, in some Bulletins a failure of this order is observed, therefore the number of points for the forecast of one length may differ (Table 1). The

forecast accuracy was determined as the RMS of the differences of the forecast and the real series.

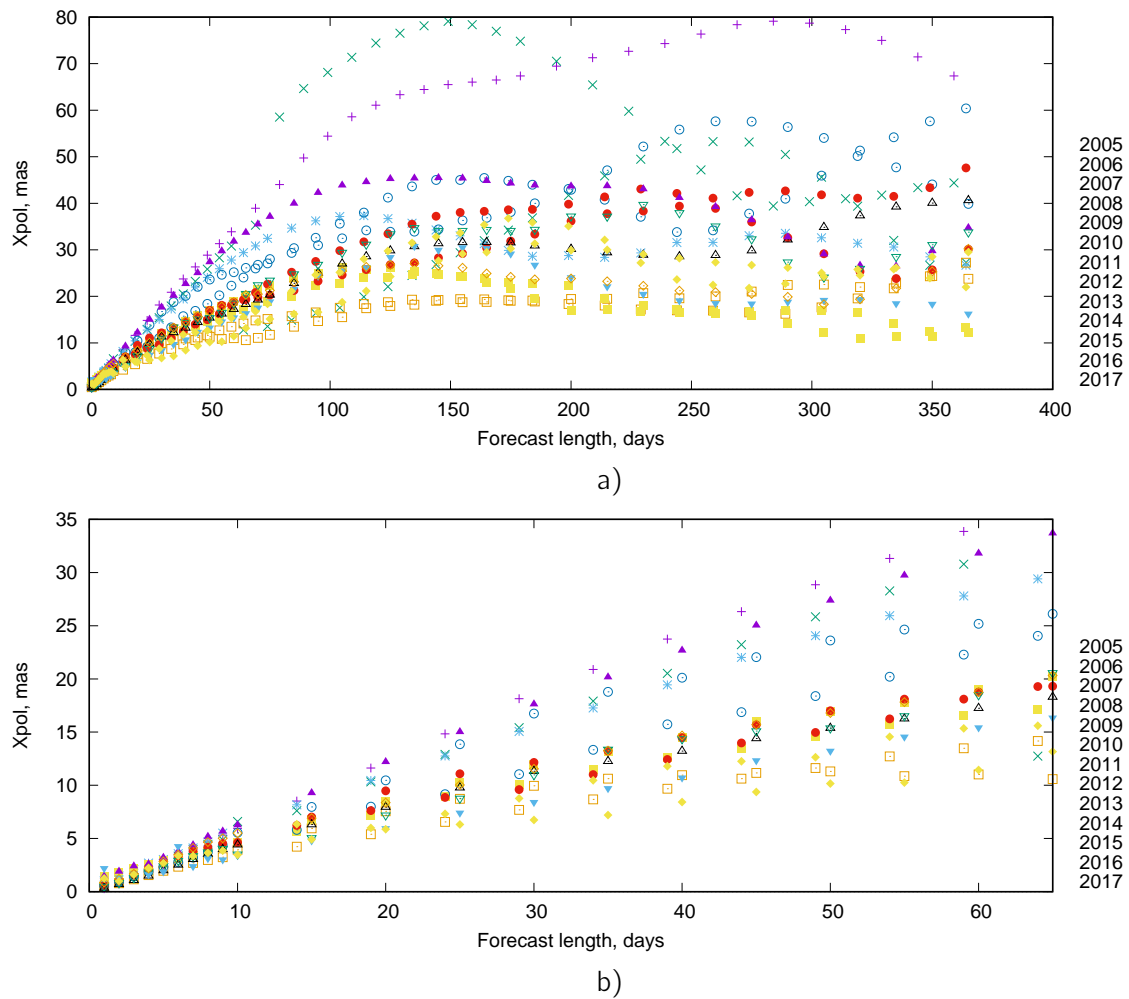
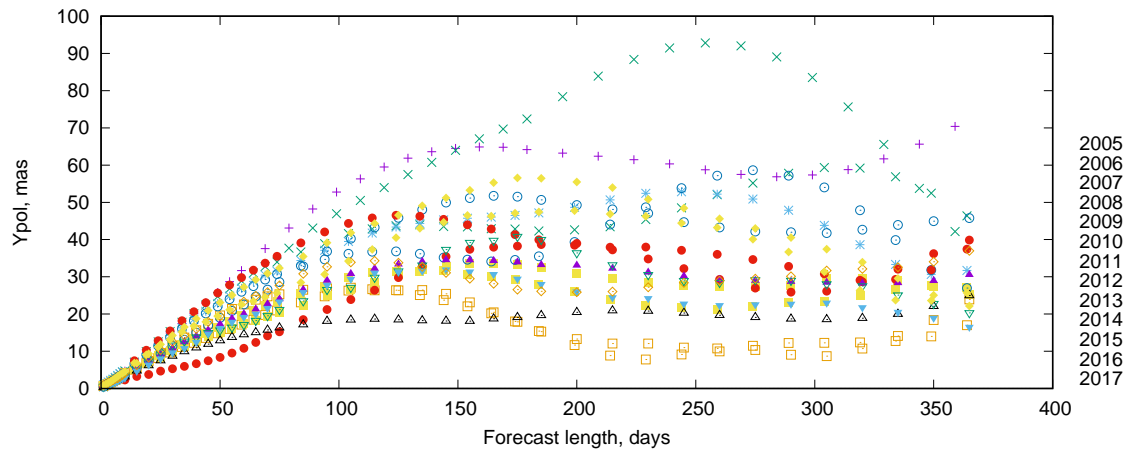


Figure 1: x_p forecast accuracy of the rs.dat series up to 60 days (left) and up to 1 year (right)

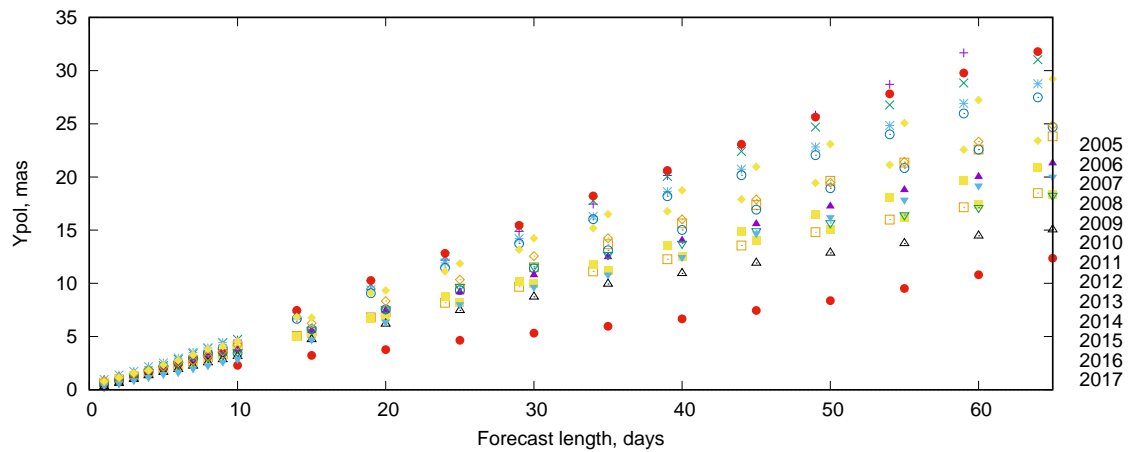
Figures 1–3 shows the estimates of the accuracy of the EOP forecast obtained from the IAA EOP Bulletins based on a comparison with the real series. The figure shows the accuracy estimates by year for all available Bulletins from the 2005 till 2017 year. The figures divided at two parts in agreement with time scale: the estimates of forecast accuracy up to 1 year are presented at the right parts and the estimates of forecast accuracy up to 60 days are presented at the left parts of the Figures. It should be emphasized that the EOP rs.dat series is based on the analysis of SLR observations and its accuracy differs from the accuracy of the IERS EOP series; therefore, this comparison is not entirely correct, but gives some insight about the accuracy of the prediction. It is necessary to evaluate the accuracy of the forecast of IERS EOP time series by another method.

Tables 1, 2, 3 compares our estimates of the accuracy of the ERP prediction (for rs.dat EOP time series) and estimates of the ERP forecast of the IERS Rapid Service Prediction Centre (data from annual IERS reports for the years 2005–2018¹) for x pole position x_p , y Pole position y_p and Universal Time $UT1 - UTC$ respectively. The Length of Prediction is designed as LP .

¹<https://www.iers.org/IERS/EN/Publications/AnnualReports/AnnualReports.html>.



a)

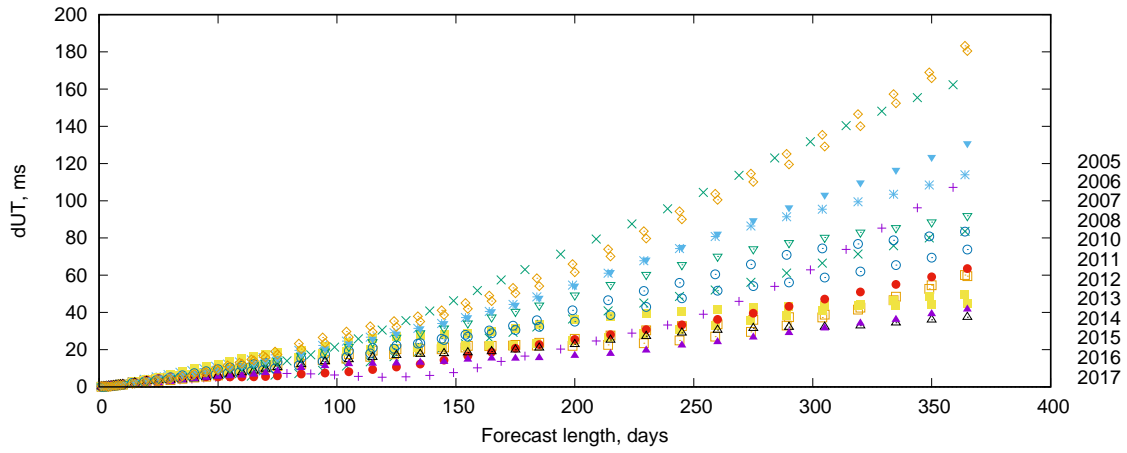


b)

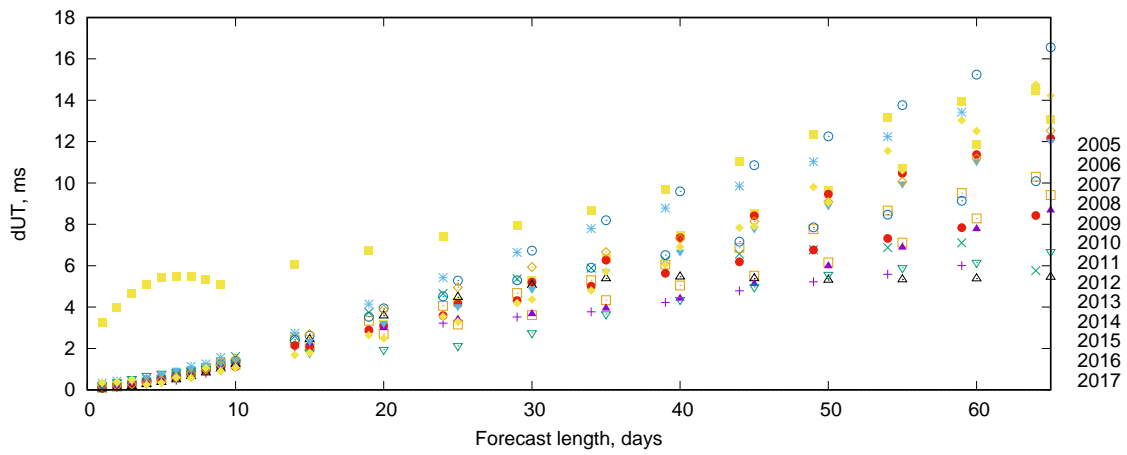
Figure 2: y_p forecast accuracy of the rs.dat series up to 60 days (left) and up to 1 year (right)

3. REFERENCES

Malkin, Z.; Skurikhina, E., 1996, "On Prediction of EOP", Communications of the Institute of Applied Astronomy RAS 93.



a)



b)

Figure 3: UT1-UTC forecast accuracy of the rs.dat series up to 60 days (left) and up to 1 year (right)

LP	1 day		5 days		10 days		20 days		40 days		90 days	
	IERS	IAA	IERS	IAA	IERS	IAA	IERS	IAA	IERS	IAA	IERS	IAA
2016	0.34	0.85	2.09	2.84	3.52	5.50	6.85	8.36	7.52	14.67	7.94	24.63
2015	0.34	2.19	2.02	1.88	3.42	3.34	5.50	5.94	9.34	10.71	N/A	24.36
2014	0.31	0.49	1.68	2.40	3.14	3.51	5.50	7.19	10.1	14.36	21.7	26.83
2013	0.33	1.43	1.81	3.19	3.46	6.26	6.75	12.20	12.9	22.68	23.8	42.26
2012	0.35	0.35	2.01	1.98	3.92	4.40	7.52	7.94	13.7	13.22	22.1	25.06
2011	0.39	0.54	2.22	2.85	4.01	4.62	6.72	9.48	11.9	14.48	26.6	27.48
2010	0.46	0.53	2.20	2.33	4.49	5.54	8.33	10.46	14.7	20.10	21.0	32.58
2009	0.43	1.41	2.04	2.91	3.49	4.59	5.85	8.43	10.2	14.49	17.6	22.25
2008	0.38	0.48	1.86	1.97	3.38	3.93	5.70	7.56	10.6	10.94	23.4	16.54
2007	0.42	1.01	2.06	3.01	3.75	5.50	6.92	10.45	12.1	19.44	15.3	36.22
2006	0.42	0.42	2.33	2.65	4.44	6.59	8.25	10.32	16.3	20.51	33.5	64.66
2005	0.44	0.28	2.44	2.53	4.13	5.95	6.82	11.64	11.9	23.75	25.2	49.74

Table 1: x_p forecast accuracy (mas)

LP	1 day		5 days		10 days		20 days		40 days		90 days	
	IERS	IAA	IERS	IAA	IERS	IAA	IERS	IAA	IERS	IAA	IERS	IAA
2016	0.25	0.83	1.38	2.16	2.49	4.18	4.50	8.33	8.16	16.02	15.2	24.42
2015	0.24	0.41	1.18	1.46	2.01	2.88	3.09	6.48	4.69	12.44	N/A	27.78
2014	0.23	0.54	1.18	2.00	2.00	3.53	3.34	7.58	5.32	13.74	12.1	26.54
2013	0.23	0.91	1.22	2.10	1.94	3.77	2.66	7.44	4.12	14.03	16.5	29.00
2012	0.25	0.29	1.35	1.65	2.76	3.16	5.66	6.19	11.3	10.93	24.4	18.07
2011	0.28	0.55	1.37	1.99	2.49	2.28	4.71	3.75	9.13	16.65	17.7	42.04
2010	0.29	0.47	1.35	2.18	2.33	3.44	4.26	7.56	9.11	15.02	23.3	34.57
2009	0.29	0.72	1.26	2.02	2.34	3.76	4.16	6.83	7.00	12.51	13.9	27.41
2008	0.31	0.66	1.38	1.91	2.42	4.09	4.27	7.30	6.94	15.64	7.81	24.74
2007	0.33	0.96	1.33	2.51	2.27	4.42	4.26	9.39	8.47	18.62	17.7	37.10
2006	0.36	0.43	1.51	2.26	2.55	4.71	4.72	9.89	9.14	20.05	18.7	43.10
2005	0.37	0.23	1.70	2.04	2.77	4.65	4.56	9.43	8.32	20.14	18.9	48.23

Table 2: y_p forecast accuracy (mas)

LP	1 day		5 days		10 days		20 days		40 days		90 days	
	IERS	IAA	IERS	IAA	IERS	IAA	IERS	IAA	IERS	IAA	IERS	IAA
2016	0.131	0.171	0.223	0.463	0.663	1.508	2.00	3.88	4.52	7.30	9.13	20.63
2015	0.073	0.317	0.207	0.745	0.567	1.147	2.32	3.21	5.90	6.67	17.25	19.19
2014	0.058	0.234	0.204	0.792	0.481	1.342	1.61	1.94	4.51	4.36	14.3	11.29
2013	0.058	0.132	0.214	0.628	0.525	1.350	1.88	2.99	2.82	4.42	8.49	13.68
2012	0.063	0.060	0.256	0.368	0.662	1.235	2.22	3.38	5.77	5.46	10.8	7.48
2011	0.054	0.077	0.305	0.484	0.776	1.120	1.99	3.09	3.62	7.35	13.6	13.7
2010	0.075	0.094	0.308	0.548	0.718	1.391	2.17	3.94	5.09	9.59	7.90	18.00
2009	0.112	0.327	0.366	0.541	0.757	1.172	1.72	3.15	5.61	7.47	17.4	17.57
2008	0.126	0.110	0.375	0.501	0.718	1.216	2.08	2.70	5.63	5.04	N/A	14.36
2007	0.141	0.312	0.452	0.642	0.921	1.556	3.29	4.14	7.77	8.78	13.4	22.27
2006	0.147	0.083	0.518	0.480	1.060	1.603	3.11	3.74	6.88	6.27	22.1	17.21
2005	0.127	0.064	0.380	0.337	0.935	1.222	3.30	2.80	5.98	4.22	7.61	7.02

Table 3: $UT1 - UTC$ forecast accuracy (ms)

DETERMINATION OF EARTH ROTATION PARAMETERS BY SLR AT MMC SSTF / FSUE VNIIFTRI

E. N. TCYBA ¹, O. A. VOLKOVA ²

¹ National Research Institute for Physical-Technical and Radio Engineering Measurements
141570, Mendeleevo, Moscow Reg. - RUSSIA - tsyba@vniiftri.ru

² Mosengineering Group LLC, 125502, Moscow - RUSSIA

ABSTRACT. At the end of 2014, the MMC SSTF completed the development of a program for determining the Earth Rotation Parameters (ERP) by SLR. Since 2017 a new software based upon neural network models permits to perform regular operational ERP determinations with an accuracy matching the modern requirements. The paper presents the results obtained for pole coordinates.

1. INTRODUCTION

The Federal State Unitary Enterprise (FSUE) "All-Russian Research Institute of physico-technical and radio-technical measurements" (VNIIFTRI) is one of the leading national institutes of metrology in Russia. One of the main divisions of the Institute is the Main Metrological Centre of State Service for Time, Frequency and Earth Rotation Parameters (ERP) evaluation (MMC SSTF). Now the East-Siberian Branch of VNIIFTRI in the city of Irkutsk operates 2 SLR stations, namely "Mendeleevo 1874" and "Irkutsk 1891", displayed in Figure 1, with the followings characteristics:

- Operating wavelength 0.532 micron;
- Frequency 300 Hz;
- Pulse duration of 250 ps;
- Pulse energy 2.5/2.7 mJ;
- Beam divergence 712 arcsec;
- The diameter of the receiving aperture and TV Guide 25 cm. SLR stations produced in Russia in 2011. VNIIFTRI use SLR stations together with:
 - Time and frequency state standards in Mendeleevo UTC(SU);
 - State standard of length in Mendeleevo;
 - Secondary time and frequency standard in Irkutsk city.

Additional equipment:

- Mobile laboratory with mobile TWSTFT station and active H-maser;
- Fixed TWSTFT station in Mendeleevo;
- Standard of comparison: Leica TDA 5005.

The main purposes of operating laser ranging at VNIIFTRI are Time and frequency transfer and ERP determination.

2. DETERMINATION OF THE PARAMETERS OF THE EARTH'S ROTATION

The Main Metrological Centre of State Service for Time, Frequency and ERP evaluation was founded based on the Head office of the unified time service and has been actively estimated the ERP based on the combination of the entire measurement data since 1955.

The ERP activities at VNIIFTRI can be grouped in four basic topics:



Figure 1: Stations "Mendeleevo 1874" (left) and SLR station "Irkutsk 1891" (right)

- processing GNSS, SLR, LLR [1,2] and VLBI observation data for ERP evaluation;
- combination of ERP series for evaluation of reference ERP values (on the ERP level and observation level);
- combination of GLONASS/GPS satellites orbit/clock;
- providing GNSS and SLR observations at five metrological sites acting under the auspices of Federal Agency on Technical Regulating of Metrology (ROSSTANDART).

The regular computing of ERP from the Satellite Laser Ranging (SLR) measurements started in the MMC SSTF in 1995. In 2010 the processing of SLR measurements had to be suspended due to technical reasons. The processing of laser measurements in VNIIFTRI has been resumed in 2015.

At this time ILRS Network includes about 40 stations. Thirty of them, listed in Table 1, are dedicated to ERP estimation.

Table 1 List of ILRS station which measurements were used for ERP calculation

Monument	Location Name, Country	Monument	Location Name, Country
1873	Simeiz, Russia	7328	Koganei, Japan
1874	Mendeleevo, Russia	7405	Concepcion, Chile
1879	Altay, Russia	7406	San Juan, Argentina
1884	Riga, Latvia	7501	Hartebeesthoek, South Africa
1891	Irkutsk, Russia	7810	Zimmerwald, Switzerland
1893	Katzively, Ukraine	7821	Shanghai, China
7080	McDonald Observatory, Texas	7824	San Fernando, Spain
7090	Yarragadee, Australia	7825	Mt Stromlo, Australia
7105	Greenbelt, Maryland	7838	Simosato, Japan
7110	Monument Peak, California	7839	Graz, Austria
7119	Haleakala, Hawaii	7840	Herstmonceux, United Kingdom
7124	Tahiti, French Polynesia	7841	Potsdam, Germany
7237	Changchun, China	7845	Grasse, France
7249	Beijing, China	7941	Matera, Italy
7308	Koganei, Japan(CRL)	8834	Wetzell, Germany

3. RESULTS

The pole coordinates x_p and y_p are estimated from the combination of Lageos 1 and Lageos 2 SLR data over the year 2019. Their offsets with respect to the C04 series provided by the International Earth Rotation and Reference System Service (IERS) and presented in Figure 2 (x_p) and Figure 3 (y_p) show standard deviations at 0.08 mas level.

In 2017, the development of a new software module for determining ERP from SLR, LLR as well as GNSS measurements by using neural network models has been completed. This software module made it possible to increase the accuracy of ERP determination from SLR and GNSS data by 12-20%. Tests were carried out in the frame of the VNIIFTRI, IAA (Institute of Applied Astronomy) and IAC (Information and Analytical Center of the Russian Space Agency). In order to integrate the programme into the service activity the only thing left to do is to overcome a series of technical issues.

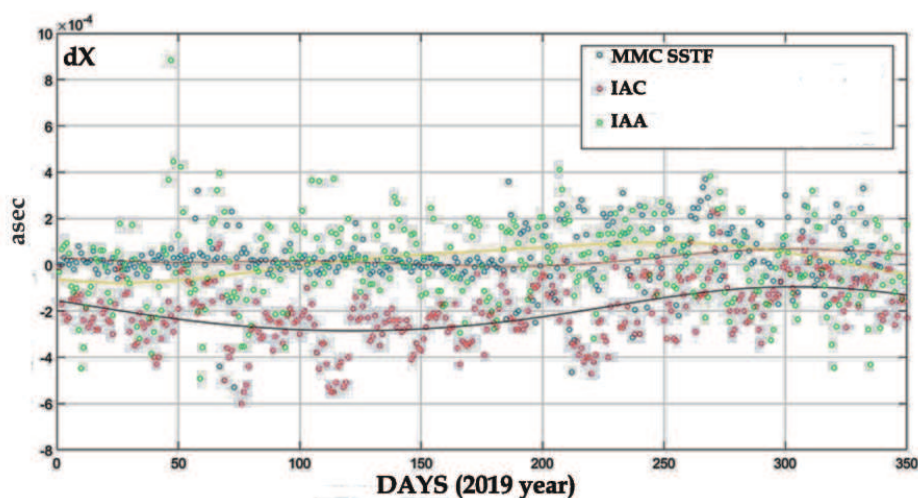


Figure 2: Offsets between calculated x_p pole coordinates and IERS C04 values.

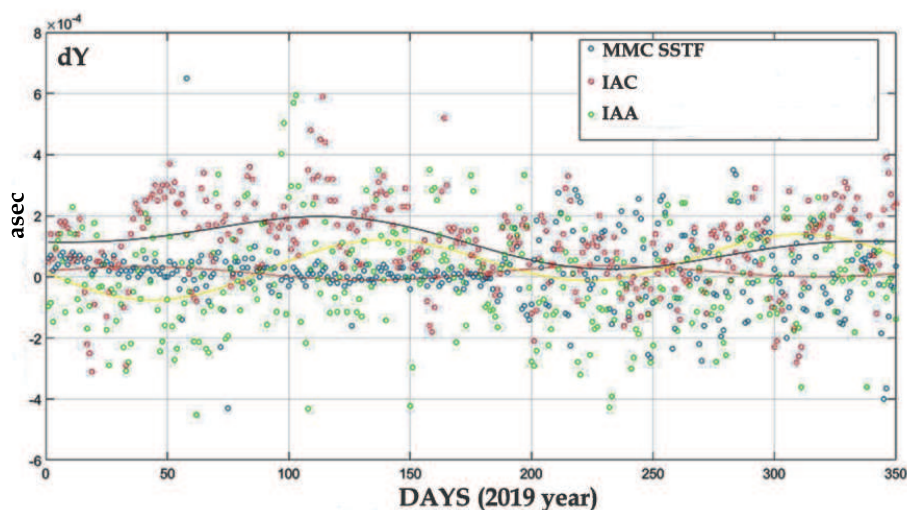


Figure 3: Offsets between calculated y_p pole coordinates and IERS C04 values.

4. CONCLUSIONS

A new programme for determining the Earth Rotation Parameters (ERP) from SLR, LLR and GNSS measurements has been developed. Neural network models can increase the accuracy of ERP by an average of 12-20%. Now, the pole coordinates obtained fromh SLR data have an accuracy approaching the one of the reference series of the IERS.

5. REFERENCES

- Tcyba E.N., Vostrukhov N.A., 2018, "Improvement of means for processing data of measurements of SLR and LLR in MMC SSTF", Proceedings of the Institute of Applied Astronomy RAS 45, pp. 120–123
- Tcyba E.N., 2016, "Calculation of the Earth rotation parameters by the results of the SLR of the International ILRS network", Proceedings of the Institute of Applied Astronomy RAS 38, pp. 66–70.

Session III

ICRF AND ASTROGEODESY

THE FUNDAMENTAL REFERENCE AGN MONITORING EXPERIMENT (FRAMEX)

B. DORLAND¹, N. SECREST¹, M. JOHNSON¹, T. FISCHER², N. ZACHARIAS¹,
J. SOUCHAY³, S. LAMBERT³, C. BARACHE³, F. TARIS³

¹ U.S. Naval Observatory, Washington, DC - USA

bryan.dorland@navy.mil, nathan.secrest@navy.mil, megan.johnson@navy.mil,
norbert.zacharias@navy.mil

² Space Telescope Science Institute, Baltimore, MD - USA - tfischer@stsci.edu

³ Observatoire de Paris, PSL Research University, UMR8630 CNRS - France

jean.souchay@obspm.fr, sebastien.lambert@obspm.fr, christophe.barache@obspm.fr,
francois.taris@obspm.fr

ABSTRACT. The U.S. Naval Observatory (USNO), in collaboration with Paris Observatory (OP), is conducting the Fundamental Reference AGN Monitoring Experiment, or FRAMEX. FRAMEX will use USNO's and OP's in-house observing assets in the radio, infrared (IR) and visible, as well as other ground- and space-based telescopes (e.g., in the X-ray) that we can access for these purposes, to observe and monitor current and candidate Reference Frame Objects (RFOs)—consisting of Active Galactic Nuclei (AGN)—as well as representative AGN, in order to better understand astrometric and photometric variability at multiple timescales. FRAMEX will improve the selection of RFOs as well as provide significant new data to the AGN research community. This paper describes the FRAMEX objectives, specific areas of investigation, and the initial data collection campaigns.

1. INTRODUCTION AND BACKGROUND

The International Celestial Reference System (ICRS) is the standard reference system for defining position and motion of celestial objects. It is currently realized by the International Celestial Reference Frame 3 (ICRF3), which consists of Very Long Baseline Interferometry (VLBI) measurements of a total of 4536 extragalactic radio sources (Charlot, et al. 2020). These are primarily Active Galactic Nuclei (AGN), which are Supermassive Black Holes (SMBH) at the centers of galaxies, with a typical redshift of $z = 1.0$. (Fey & Charlot 2000, Charlot, et al. 2020, Souchay, et al. 2019)

ICRF3 was adopted as the international standard by the International Astronomical Union (IAU) on 1 January 2019 (Lago 2019). It is the first multi-wavelength reference frame to be adopted by the IAU, with observations in S/X (4536 sources), K (824 sources), and X/Ka (674 sources). Of these sources, 303 are considered “defining sources,” which are distributed quasi-isotropically over the entire sky, and set the rotation of the reference frame. The remaining sources are used to densify the resultant reference frame. ICRF3 is assessed to have a mean defining source position uncertainty of $30 \mu\text{as}$ in DEC and $3 \mu\text{as}$ in RA, with a per-source positional noise floor of $30 \mu\text{as}$ (Charlot, et al. 2020).

Nearly simultaneous with the release of ICRF3, the European Space Agency (ESA) Gaia mission, using AGN previously identified in the IR from NASA's Wide-field Infrared Survey Explorer (WISE) mission (Secrest, et al. 2015), produced an optical catalog of over 500k AGN (including ICRF3 sources) accurate to the 1 mas level or better (Mignard, et al. 2018). Ultimately, Gaia aims to produce an optical reference frame at the few tens of μas accuracy per source, comparable to the ICRF3.

With realizations of the ICRS now effectively in four different wavelengths, it will be the respon-

sibility over the next decade, as new data are taken, of the Celestial Reference Frame community—including the IAU and the International Earth Rotation and Reference Systems Service (IERS)—to ensure that the integrated reference frame is both accurate and aligned properly across wavelengths. As new and improved instrumentation becomes available for observing reference frame objects, these new capabilities should be deployed to identify the most stable and accurate candidate objects across wavelengths, and to deselect objects that are unstable or otherwise problematic. In doing so, a much better understanding of the underlying astrophysics of AGN will be enabled.

2. REFERENCE FRAME OBJECTS: ISSUES AND QUESTIONS

As described in section 1, the underlying reference frame is realized by over four thousand reference frame objects (RFOs) (i.e., AGN) in the radio observed at three different frequencies, and half a million observed in the visible. How accurate are these observations? How do positions measured in one wavelength compare to positions measured in a different one? These positions were measured in different epochs using different classes of instruments: how do the positions change in time due to physical changes of the sources, differences at the measurement instrument, or differences in observing epochs?

A significant amount of work has already gone into exploring issues associated with apparent offsets of astrometric positions measured in different wavelengths. These include Zacharias & Zacharias (2015), which observed a number of positional offsets between radio and optical positions that significantly exceeded ($> 3\sigma$) offsets expected due to measurement errors; Makarov et al. (2019) found that 20%, rather than the expected 1%, of RFOs exceeded a normalized radio-optical offset of 3; Roland, et al. (2019) argued for the effects of binary black holes on the apparent radio position “noise” of RFOs; and Petrov, et al. (2019) found a significant correlation between radio-optical offsets and the direction of the ostensible AGN jet as observed in the radio. These all point to aspects of the problem of variability in position between wavelengths and in time, and to possible “clutter” causing offsets in the measured positions of AGN in one or more wavelengths.

The goal of the Fundamental Reference Frame AGN Monitoring Experiment (FRAMEx) is to observe and constrain the astrometric position of RFOs by monitoring both the astrometry and photometry of RFOs and other, representative AGN across multiple wavelengths, spanning extended time periods, and at a variety of different temporal frequencies. FRAMEx will probe possible correlations between photometric variability across the spectrum and astrometric position variability. Specific areas of issues and questions to be probed include:

- **Source of RFO/AGN emissions.** What physical processes are responsible for the emissions observed at different wavelengths? What are the magnitudes of the offsets measured in different bands or frequencies? What are the dependencies of these positions and offset considerations such as the resolving power or sensitivity of the instrument? What are contributions from possible sources of offset such as:
 - Confused foreground or background sources of emission and *in situ* sources of offset such as off-nuclear AGN, host galaxy structure and brightness
 - Confusion or blending of discrete sources
 - Different sources of emission as a function of wavelength
 - Narrow Line Region (NLR) emission and AGN outflows
 - Wavelength-dependent line-of-sight AGN obscuration
 - Emission from extended radio jets.

- **Photometric and astrometric variability.** What is the time-dependent astrometric and photometric behavior of the sources of AGN emission defined previously? What timescales are relevant for variability? What are the correlations between astrometric and photometric variability, and what does this tell us about what is going on at the AGN, in the host galaxy environment, the intervening intergalactic medium, or even our local observing conditions?
- **Binary/Multiple SMBH population, orbital characteristics, and resultant phenomenology.** What is the population of binary (or multiple) SMBHs? For binary or multiple SMBHs, what critical phenomenologies reveal their presence or allow us to determine their physical parameters? What are the range of parameters (e.g., orbital periods and distances) observed? Are there binary systems in which the VLBI counterpart is one AGN while the Gaia counterpart is the other?
- **Possible RFO proper motion.** What is the explanation of the (apparent) large proper motion of AGN as observed in Gaia DR2?

3. FRAMEX AGN AND HOST GALAXY DISTANCE SCALES

In order to understand what can and can't be observed (and, therefore, what astrophysics can be probed by FRAMEX), we first consider the spatial scales associated with the observations. As noted in section 1, the “typical” AGN used as an RFO is at $z = 1.0$. This translates to an angular size distance $D_A \approx 5 \times 10^9$ light years (see various cosmological calculators, such as <http://www.astro.ucla.edu/~wright/CosmoCalc.html> and associated references). Typical distances for a “Milky Way”-type galaxy are shown in Figure 1, along with the angles subtended for an angular size distance $D_A \approx 5 \times 10^9$ light years corresponding to $z = 1.0$. The inset in the upper center shows the neighborhood around the AGN with the major features of the AGN noted. Distances for the features are taken from Ricci (2020). To put this configuration in scale, the event horizon is solar-system sized; the accretion disk is the size of the Sun's Oort cloud, and the torus is on the scale of stellar distances in our local region of the Galaxy. The Narrow Line Region is much more extended, going out to as far as ≈ 300 pc from the central AGN. Different radiative processes (both emission and absorption) are associated with each of these features, and all of them will contribute or affect the measured position of the AGN as a function of both wavelength and time.

Beyond the AGN features, the scale of the host galaxy is shown. The central bulge is about 2 kpc, the disk diameter is 20 kpc, and the halo is 30 kpc. Satellite galaxies are approximately 50 kpc from the core of the host galaxy of the AGN, and nearby galaxies of comparable size are 800 kpc distant. Each one of these regions may contain sources of emission or absorption that affect the measured position of the central AGN as a function of both wavelength and time.

Table 1 captures this information for each of the AGN and host galaxy features. Because these features span nine orders of magnitude in distance, different “natural units” are associated with the different features. These are included in the table where they are considered useful. Also included is the subtended angle, calculated using D_A . The final two columns on the right indicate what instruments, if any, are capable of measuring either the astrometric position of the AGN or resolving the relevant feature. Photometric accuracy is driven primarily by the sensitivity of the instrument and integration time of the observation, but is also affected by blending of sources that only high resolution may be able to resolve.

Figure 2 displays the orbital periods for three binary AGN configurations as a function of apparent angular separation for $z = 1.0$. The three configurations consist of 10^6 , 10^9 and $10^{10} M_\odot$ pairs of SMBHs, respectively. The relevant features from Figure 1 and Table 1 are shown along the top, and representative instrument capabilities for astrometric measurements and resolved images. This figure clarifies a few key concepts: first, orbital motion will only be detectable over

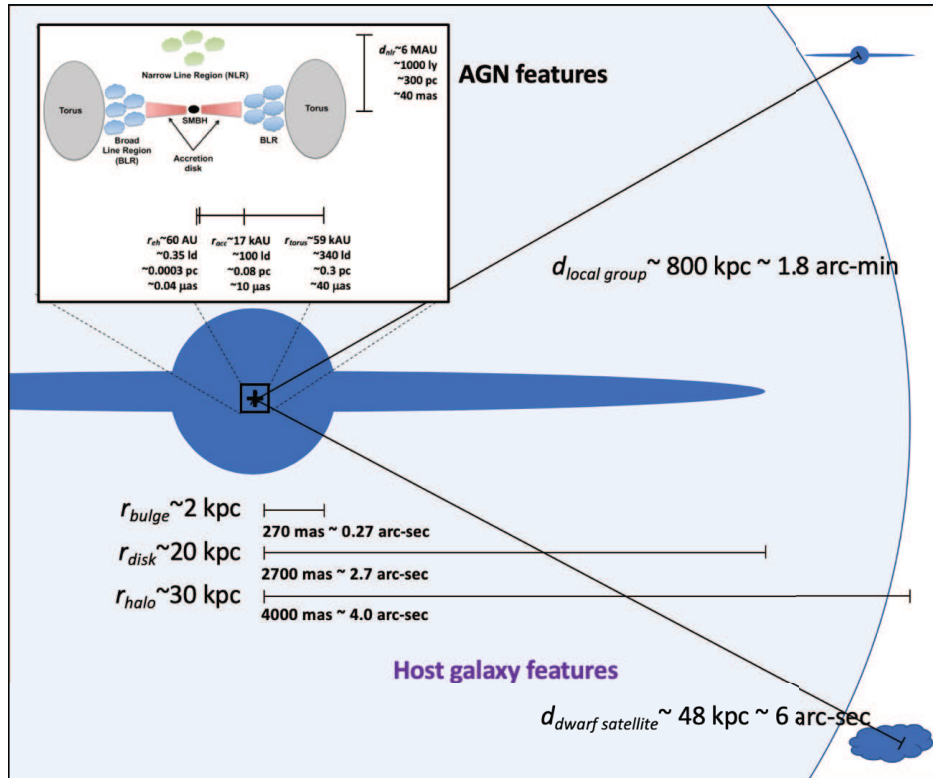


Figure 1: Relevant distances scales for “typical” ($z = 1.0$) RFO AGN. Angular equivalents assume a distance of 5×10^9 light years. Host galaxy similar to Milky Way is shown, with central box indicating the AGN core region. Figure not to scale. Inset taken from C. Ricci’s website, http://www.isdc.unige.ch/~ricci/Website/Active_Galactic_Nuclei.html.

the timescales accessible to FRAMEx for the largest and closest pairs of binary AGN. Second, the array of instruments available to us for probing scales down to the NLR is limited; spatial scales for the AGN (e.g., torus, accretion disk, event horizon), will require new, more precise instrumentation to be developed. VLBI in general and the VLBA specifically are critical to probing spatial scales smaller than the bulge, and are able to resolve components that would be blended in other types of observations. VLBI, because of the much narrower resolution element, also offers the highest astrometric resolution for single measurements, being sensitive to measurements at scales that probe the narrow line region.

4. INITIAL AREAS OF INVESTIGATION

FRAMEx will utilize the instrumentation available to the U.S. Naval Observatory and the Paris Observatory, as part of the collaboration activity. This includes 1 and 2-m class optical and near infrared (NIR) telescopes operated by both USNO and OP in a variety of locations, as well as both the UK Infrared Telescope (UKIRT) and the Very Long Baseline Array (VLBA). Additional observations will be conducted using instruments that are accessed on a case-by-case basis, including both ground- and space-based telescopes requiring proposals.

The initial areas of investigation will focus on the following:

- **Volume-limited sample of AGN** The “volume limited AGN sample” will concentrate on

Table 1: Typical distances for AGN-related and host galaxy features for a Milky Way-type galaxy in a “Local Group”-like cluster, from Figure 1. Features are show in column 1, with (r) indicating a radius, and (s) a separation. Distances are shown in columns 2–6, with the equivalent angular plane-of-sky separation shown in column 6. Columns 3 and 4 refer to “light days” and “light years”. Columns 7 and 8 indicate the class of astronomical telescope/array needed to make the observation. Column 7 is for single-epoch astrometric position measurement, and column 8 is to resolve the RFO feature. 1 indicates VLBA, 2 is VLA, 3 is space-based optical, and 4 is ground-based optical. A subscript “AO” indicates where adaptive optics is required to reach the indicated resolution from the ground. The asterisk indicates the specialized “Event Horizon Telescope” (EVT), a world-wide Very Long Baseline Interferometric demonstration array that was able to image the accretion disk of the M87 SMBH in 2019 (Event Horizon Telescope Collaboration, et al., 2019).

Feature (parameter)	Distance					Instrumentation	
	AU	light days	light years	parsecs	angle subtend.	to measure position	to resolve
Event hor. (r)	60	0.35		3×10^{-4}	$0.04 \mu\text{as}$		
Acc. disk (r)	1.7×10^4	100	0.3	8×10^{-2}	$10 \mu\text{as}$		(*)
Torus (r)	5.9×10^4	300	0.8	2.4×10^{-1}	$40 \mu\text{as}$	1	
NLR (s)			10^3	3×10^2	40mas	1, 2, 3, 4	1
Bulge (r)			6.5×10^3	2×10^3	270mas	1, 2, 3, 4	1, 2, 3, 4 _{AO}
Disk (r)			6.5×10^4	2×10^4	2.7"	1, 2, 3, 4	2, 3, 4
Halo (r)			9.8×10^4	3×10^4	4"	1, 2, 3, 4	2, 3, 4
Sat. dwarf (s)			1.6×10^5	4.8×10^4	6"	1, 2, 3, 4	2, 3, 4
Local grp. (s)			2.6×10^6	8×10^5	1.8'	1, 2, 3, 4	3, 4

≈ 25 of the nearest AGN that are visible from the Northern Hemisphere. Observations will characterize these AGN at spatial resolutions that are not available for more distant AGN, on the assumption that the results will be extensible. The volume-limited approach significantly reduces biases that result from selection effects. The goal will be to observe this limited sample in visible, IR, radio and x-ray. These multi-wavelength observations that are conducted at the same epoch for this set of targets will be a unique set of data for AGN and RFO research.

- **Problematic ICRF Defining Sources** We will identify approximately three dozen “problematic” ICRF defining sources that display statistically significant offsets between S/X and either K or X/Ka positions or with Gaia optical positions. We will also identify a comparable number of non-problematic sources. We will monitor both of these groups in the radio, visible and IR for astrometric or photometric variability, and use these observations to identify possible astrophysical explanations of the offsets.

In addition to these areas of investigation, we plan to complement FRAMEx with the following activities:

- **Redshift survey for all RFOs and candidate RFOs.** Approximately half of RFOs have traceable spectroscopic redshifts, mostly from the Sloan Digital Sky Survey. Observing priority will be on ICRF3 defining sources, but the goal is to survey all ICRF3 RFOs for which we do not currently have a measured redshift.
- **ICRF Source Structure Imaging Database.** Associated with FRAMEx, and in support of USNO agreements with the International VLBI Service for Geodesy and Astrometry (IVS) and IERS agreements, we are in the process of developing a data archive of VLBA and VLBI

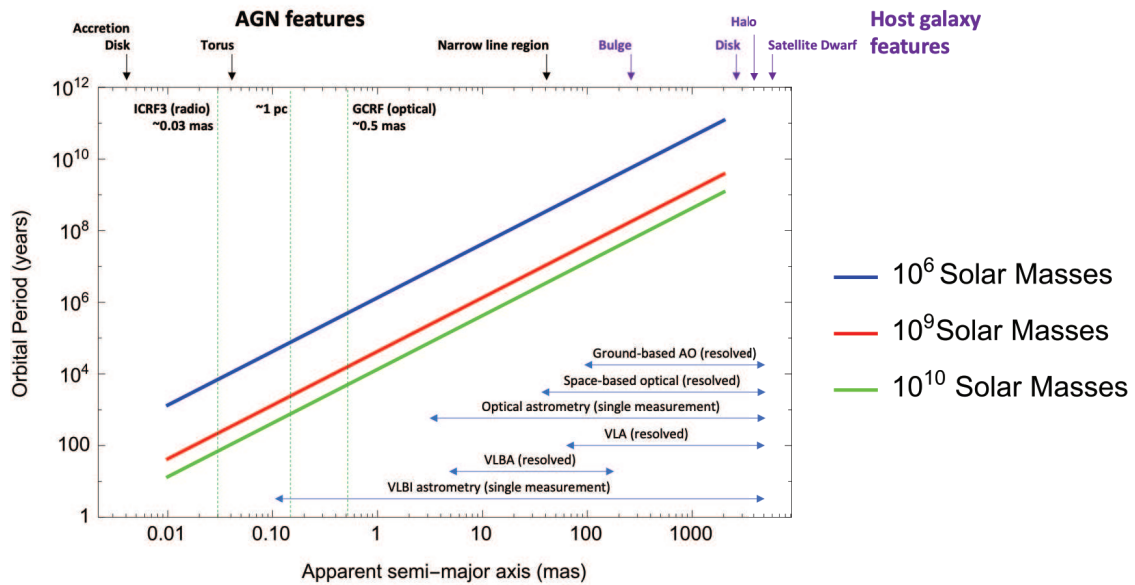


Figure 2: Apparent angular separation vs. orbital period, shown for three binary SMBH configurations: 10^6 , 10^9 , and 10^{10} solar mass components. Relevant AGN (black) and Host galaxy features (purple) (see Figure 1 and Table 1) are shown along the top of the plot. Also shown, in lower right, are approximate equivalent observing capabilities of radio and visible telescopes and arrays. ICRF3 and Gaia Celestial Reference Frame (GCRF) accuracies are shown as dashed green lines. Also shown is the equivalent 1 pc plane-of-the-sky distance at $z = 1.0$.

images of AGN (the Fundamental Reference Image Data Archive, or FRIDA (Hunt 2019, 2020)). These high-resolution images will be made available to the public, and will eventually be supplemented by other data products (including any visible, IR, or x-ray observations) associated with the relevant RFOs.

- **Southern Hemisphere 1-m Monitoring Survey.** USNO's 1-m visible and NIR Deep South Telescope (DST) is being dedicated primarily to observing RFOs. Target lists concentrate on astrometric and photometric variability across this spectral regime for RFOs. These data will not only support FRAMEx work, but be used to populate the FRIDA to support general AGN and RFO research and development activities.
- **Multi-wavelength, highly stable RFO selection** One by-product of the FRAMEx work to identify AGN variability will be an identification of those AGN that are either not, or minimally, variable across wavelengths (assuming there are such AGN). These AGN can then be used as “pre-screened candidates”, with well-characterized offsets and well-understood stability parameters for use in the development of future reference frames.

5. CONCLUSION

USNO, in collaboration with Paris Observatory and other partners, is moving forward with a dedicated investigation of reference frame objects (RFOs) using both in-house and external observing assets. The multi-year collaboration, called FRAMEx, will concentrate on ICRF3 sources, but also seek to observe other AGN and quasar sources so as to better understand the underlying astrophysics and improve the reference frame across the spectrum going forward.

6. REFERENCES

- Charlot, P., et al., 2020, “The third realization of the International Celestial Reference Frame by VLBI”, *A&A*, doi: 10.1051/0004-6361/202038368.
- Event Horizon Telescope Collaboration, Akiyama, K., Alberdi, A., et al., 2019, “First M87 Event Horizon Telescope Results. I. The Shadow of the Supermassive Black Hole”, *ApJL* 875, L1.
- Fey, A. L., & Charlot, P., 2000, “VLBA Observations of Radio Reference Frame Sources. III. Astrometric Suitability of an Additional 225 Sources”, *ApJS* 128(17).
- Hunt, L., Johnson, M., Fey, A. L., Gordon, D., Spitzak, 2019, “VLBA Imaging of ICRF3 Sources”, these proceedings.
- Hunt, L., Fey, A. L., Gordon, D., Spitzak, J., 2020, “Imaging over 3,000 Quasars that are a part of the International Celestial Reference Frame”, *American Astronomical Society Meeting Abstracts #235*.
- Lago, T. (ed.), 2019, “RESOLUTION B2 on The Third Realization of the International Celestial Reference Frame”, *Proc. XXX IAU General Assembly, Volume XXXB*.
- Makarov, V. V., Berghea, C. T., Frouard, J., et al., 2019, “The Precious Set of Radio-optical Reference Frame Objects in the Light of Gaia DR2 Data”, *ApJ* 873(132).
- Mignard, F., Klioner, S. A., et al., 2018, “Gaia Data Release 2. The celestial reference frame (Gaia-CRF2)”, *A&A* 616(A14).
- Petrov, L., Kovalev, Y. Y., & Plavin, A. V., 2019, “A quantitative analysis of systematic differences in the positions and proper motions of Gaia DR2 with respect to VLBI”, *MNRAS* 482(3), pp. 3023–3031.
- Ricci, C., 2020, “Active Galactic Nuclei”, http://www.isdc.unige.ch/~ricci/Website/Active_Galactic_Nuclei.html.
- Roland, J., Gattano, C., Lambert, S., & Taris, F., 2019, “Structure and variability of quasars”, <https://syrtel.obspm.fr/astro/journees2019/FILES/>.
- Secrest, N., Dudik, R., Dorland, B. N., et al., 2015, “Identification of 1.4 Million Active Galactic Nuclei in the Mid-Infrared using WISE Data”, *ApJ Supplement* 221, 12S.
- Souchay, J., Gattano, C., Andrei, A., et al., 2019, “LQAC-5: The fifth release of the Large Quasar Astrometric Catalogue”, *A&A* 624(A145).
- Zacharias, N., & Zacharias, M. I., 2014, “Radio-Optical Reference Frame Link Using the U.S. Naval Observatory Astrograph and Deep CCD Imaging”, *AJ* 147, 95

OBSERVATIONS OF RADIO STARS IN GEODETIC VLBI EXPERIMENTS

O. TITOV¹, F. SHU², W. CHEN³

¹ Geoscience Australia - Australia - oleg.titov@ga.gov.au

² Shanghai Astronomical Observatory - China - sfc@shao.ac.cn

³ Yunnan Observatories - China - chenwen@yao.ac.cn

ABSTRACT. Proper motion and parallaxes of radio stars will enable us to align the latest International Celestial Reference Frame (ICRF3) based on VLBI observations with the optical astrometric catalogue obtained by the Gaia mission. The Gaia mission has observed approximately 500,000 extragalactic objects in optical with a competitive precision, and produced an independent astrometric catalogue of 2820 objects common to the ICRF2 (Gaia Collaboration et al. 2018) and contains astrometric solutions of parallaxes and proper motions for significant amount of stars. This provides a rare opportunity for independent verification of the VLBI astrometric catalogues. However, due to an average parallax zero-point of $-29 \mu\text{as}$ of the Gaia catalogue (Lindgren et al. 2018), independent assessment of the Gaia parallaxes is required. Unfortunately, very few optically bright radio stars were observed with VLBI, therefore it is important to identify more Galactic stars that could be observed by both VLBI and optical mission for the parallax verification. Here we show the astrometric results for five radio stars (HR1099, UX Ari, HR132742, HR5907 and LSI+61 303) in several VLBI experiments between 2015 and 2019.

1. ASTROMETRIC OBSERVATIONS OF RADIO STARS IN THE PAST

Radio stars were observed since 1970s during some astrophysical projects (e.g. Lestrade et al. 1984). The brightest radio stars (optical magnitude brighter than 11 mag) could serve as transfer objects for the link between the optical and radio reference frames in the time of Hipparcos (Lestrade et al. 1986). Dedicated VLBI experiments in phase-reference mode were organised between 1983 and 1995 using VLBI facilities in USA and Europe (Lestrade et al. 1999). Van Leeuwen (2007) presented final results of the link of the Hipparcos and VLBI reference frames using 11 radio stars those final positional uncertainties were measured at the level from 0.12 to 5 mas. The solution also comprises the proper motions and trigonometric parallaxes of the objects. Ten stars were found to be in close binaries, and few of them are members of wide visual binaries. One star, UX Ari showed a statistically significant accelerated motion, probably, caused by a hidden companion.

Boboltz et al (2003, 2007) run new experiments using the Very Large Array and Pie Town VLBA antenna between 2000 and 2004 to determine astrometric positions of 59 radio stars in the International Celestial Reference Frame (ICRF). The new positions were estimated with position errors from 3 to 25 mas with a mean value about 10 mas. Combination of all available astrometric results over 1978-2004 resulted in estimation of the proper motion of all stars with formal uncertainties of about 1 mas/year.

2. NEW VLBI OBSERVATIONS

Since phase-reference VLBI observations demand at least one calibrator radio source, the estimated positions and proper motion of a radio star could be affected by either poor astrometric positions or intrinsic structure effect of the selected calibrators. Therefore, we tried to run a few VLBI experiments in the absolute astrometric mode, observing the radio stars at S and X bands

simultaneously to calibrate the ionosphere effects. No calibrator radio sources are necessary in this mode. For the ‘pilot project’ four radio stars (HR1099, UX Ari, HR132742 and HR5907) were selected. They are all located near the equatorial zone, suitable for joint observations using Asian and Oceanian VLBI stations. In the observing sessions dedicated to absolute astrometry and geodesy, we inserted some scans of radio stars with a goal to detect them and obtain their positions estimation. Tianma65 or Parkes radio telescope was used as an anchor station in the observing network to improve the detection rate of the weak radio stars. The experiments are summarized in Table 1.

Table 1: Summary of VLBI experiments with observations of radio stars.

Code	Date	Dur. (hr)	Data rate (Mbps)	Stations ^a
AOV003	17-May-2015	24	256	HbHolsKeKmT6TsWwYg
AUA011	12-Jul-2016	24	1024	HoKbPaT6Ur
AOV010	27-Jul-2016	24	1024	HolsK1KeKgKmPaShT6TsUrWwYg
V515C	19-Jul-2018	24	1024	BdHhHoKmShSvZc
AUA020	01-May-2017	24	1024	BdHhHoKvShSvZc
AOV019	23-Jan-2018	24	1024	HolsKbKeKmShT6UrWwYg
AOV033	20-Mar-2019	24	1024	HolsKeKmT6UrWwYg
AOV034	03-Apr-2019	24	1024	HolsKbKeKmKvT6UrWwYg

^a Bd: Badary; Hb: Hobart12; Hh: HartRAO; Ho: Hobart26; Is: Ishioka; K1: Kashim11; Kb: Kashim34; Ke: Kath12m; Kg: Koganei; Km: Kunming; Kv: Sejong; Pa: Parkes; Sh: Seshan25; Sv: Svetloe; T6: Tianma65; Ts: Tsukub32; Ur: Urumqi; Ww: Wark12m; Yg: Yarra12m; Zc: Zelench.

For the first experiment AOV003 in 2015, we used standard S/X dual band geodetic mode with a data rate of 256 Mbps. The radio stars were scheduled in the same way as geodetic sources. We set a priori flux densities of those stars to a fix value of 40 mJy, and required that all baselines in one scan met the minimum SNR requirement. Thus, only four stations (Tianma65, Parkes, Kunming and Tsukuba32) were scheduled to observe the stars. The results show only HR1099 was detected on a few baselines, which indicate the other two stars were much weaker than their a priori flux densities.

We conducted two experiments in July 2016. In order to reach higher baseline sensitivity, both sessions were performed at a data rate of 1 Gbps. The session AUA011 was almost scheduled in the same way as AOV003, but the radio stars were expected to be as weak as 20 mJy. Unfortunately, we still only detected HR1099. The session AOV010 was a great success. We inserted manually scans of radio stars into geodetic blocks. For each radio star scan, all visible stations were used to form as many baselines as possible. HR1099 and UX Ari were observed in a few scans of 480 s length. For HD132742, we tested a piggy-back phase referencing mode. A radio source 1454-060, with a separation angle of 2.47°, was selected as a calibrator source. We observed both HD132742 and 1454-060 in a set of scans of 120 s length. Those scans were divided into three blocks with each block spanning approximately 40 minutes. The gap between two blocks is at least one hour in order to produce better UV coverage. The total on-source time of HD132742 is 36 minutes.

One experiment (V515C) was organized in 2018 as a part of the Long Baseline Array radio astrometric program V515 supported by the ATNF, CSIRO. As Tianma65 was unavailable, we conducted a similar piggy-back phase referencing observations of HR1099, using a strong radio source CTA26 as the calibrator. The angular distance between the target and CTA26 is 2.46°. The scan length is 180 s for HR1099 and 60 s for CTA26 respectively. The observational network is very large with participation of the Russian stations operated by Institute of Applied Astronomy and 26-m HartRAO antenna in South Africa. The total on-source time of HR1099 is 75 minutes,

but there were fewer participating stations and only middle size antennas available compared to AOV010.

The fourth radio star HR5907 was observed in the absolute astrometric mode in four experiments in 2017-2019. This is one of the most rapidly rotating magnetic B-type stars with a rotation period 0.508276 day (Grunhut et al. 2012). Its radio emission detected in a range of GHz frequencies with flux density from 46 to 104 mJy (Murphy et al. 2010) is supposed to be generated by a strong magnetic field induced by the rapid rotation. Independently, Healey et al (2007) detected a strong emission at 8.4 GHz at the VLA array. Therefore, in spite of a greater distance from the Solar system (annual parallax of 7.64 ± 0.37 mas) with respect to other three stars, it has a stronger signal and was detected in all four experiments.

3. RESULTS

We processed each experiment in the same way as used in regular geodetic observing sessions. After data correlation and fringe fitting, group delay observables for radio stars and geodetic sources were extracted. Then data analysis was performed to derive the positions of radio stars. We also estimated flux densities of radio stars based on fringe SNRs at X and S band respectively. Table 2 shows the statistics on solutions of absolute astrometric data.

There is a different approach for the piggy-back phase referencing observations. We need to convert the correlator output into FITS-IDI data format and then generate images of radio stars with the AIPS. Figure 1 shows the X-band images of HD132742 and HR1099. The HD132742 image made from AOV010 data and the HR1099 image made from V515C data. Each image was performed with natural weighting. We plotted contours that start at three times the noise level of images. It is interesting that HR1099 shows a binary structure. Therefore additional phase reference observations of this radio star are important.

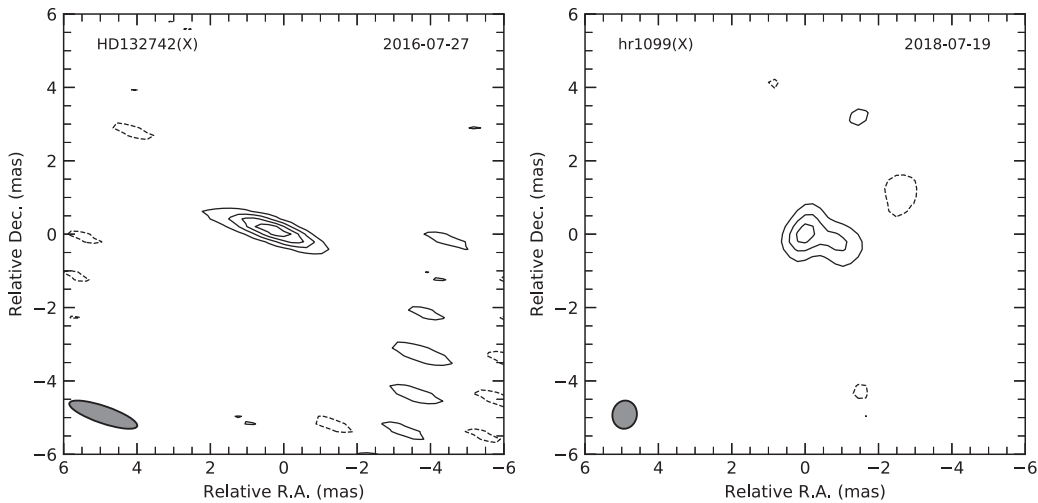


Figure 1: The images of HD132742 (left panel) and HR1099 (right panel) made from X band (8.39 and 8.60 GHz) data using natural weighting. The peak has been shifted to the image center. The SNR (the ratio of the flux density of peak to the rms) are 15.24 and 11.80 respectively. The synthesized beam is represented by the black ellipse in the bottom left corner of each panel.

Based on the imaging results, we could determine the relative position between a target star and a calibrator source. Since the position estimates from a single session are not so accurate, we used the positions of calibrator sources in the ICRF3 as reference. Finally we obtained the position of target stars as shown in the last two rows of Table 2.

Table 2: Astrometric positions of all radio stars between 2015 and 2019

Code	Star	α (J2000.0) (h m sec)	δ (J2000.0) ($^{\circ}$ ' ")	σ_{α} (ms)	σ_{δ} (mas)	#Obs	F_X (Jy)	F_S (Jy)
AOV003	HR1099	03 36 47.2573	+00 35 13.470	0.8	4	6	0.02	0.03
AUA011	HR1099	03 36 47.2562	+00 35 13.308	0.34	2	10	0.01	0.02
AOV010	HR1099	03 36 47.2569	+00 35 13.269	0.03	0.3	56	0.02	0.03
AOV010	UX Ari	03 26 35.4353	+28 42 52.596	0.1	1	6	0.01	0.01
AUA020	HR5907	15 53 55.84739	-23 58 41.5622	0.02	0.4	4	0.05	0.05
AOV019	HR5907	15 53 55.84654	-23 58 41.5783	0.06	0.3	16	0.09	0.07
AOV033	HR5907	15 53 55.84558	-23 58 41.6062	0.04	0.6	12	0.10	0.05
AOV034	HR5907	15 53 55.84533	-23 58 41.6081	0.04	0.4	16	0.05	0.03
UF001I	LSI+61 303	02 40 31.66387	+61 13 45.5905	0.37	4.3	/	/	/
AOV010	HD132742	15 00 58.27745	-08 31 08.3003	0.013	0.12	/	0.003	/
V515C	HR1099	03 36 47.25259	+00 35 12.9481	0.006	0.08	/	0.004	/

Note. Besides the solutions of absolute astrometric data, the phase referencing results are listed in last two rows.

We plotted the time series of the HR1099 positions (Figure 2) based on the previous optical and radio observations (Boboltz et al. 2003). Our analysis of the time series with assumption on the linear motion yields the proper motion of $\mu_{\alpha}\cos\delta = -2.09 \pm 0.02$ mas/y in right ascension and $\mu_{\delta} = -160.9 \pm 0.3$ mas/y in declination. These estimates are consistent with the Boboltz et al (2003) numbers ($\mu_{\alpha}\cos\delta = -2.12 \pm 0.02$ mas/y and $\mu_{\delta} = -161.7 \pm 0.25$ mas/y).

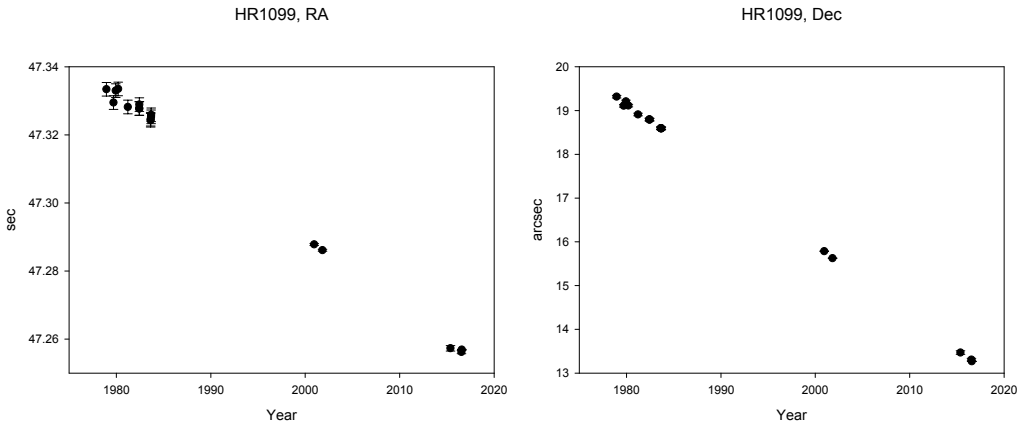


Figure 2: Time series of HR1099 astrometric positions

The radio star UX Ari is a very special object for astrometric research. This is an active binary star (type RS CVn) with period 6.44 days. Additionally, in contrast to most other radio stars, UX Ari exposes a significant non-linear proper motion. Lestarde et al. (1999) reported that the found acceleration term (-0.54 ± 0.07 mas/y² in right ascension and -0.29 ± 0.07 mas/y² in declination) may be induced by the gravitational attraction of a hidden counterpart with a long period. Boboltz et al. confirmed this effect with new estimates (-0.60 ± 0.03 mas/y² in right ascension and -0.31 ± 0.07 mas/y² in declination). Duemmler and Aarum (2001) measured systematic variations of the center of mass velocity with spectroscopic data and proposed a third star with periods of 10.7 and 21.5 years for circular and elliptical orbits. Peterson et al (2011) concluded a presence of the third component with orbital period about 111 years.

In spite of the fact that only one epoch positions were measured in our experiments (Figure 3), it favours a shorter orbital motion of the third component than was suggested by Peterson et al (2011). As the discussion on the systematic factors is beyond of the scope of this paper, we

conservatively estimate the orbital period of the third component to be between 20 and 30 years, i.e. closer to the Duemmler and Aarum (2001) elliptical motion hypothesis. More observations are required to solve the UX Ari system problem.

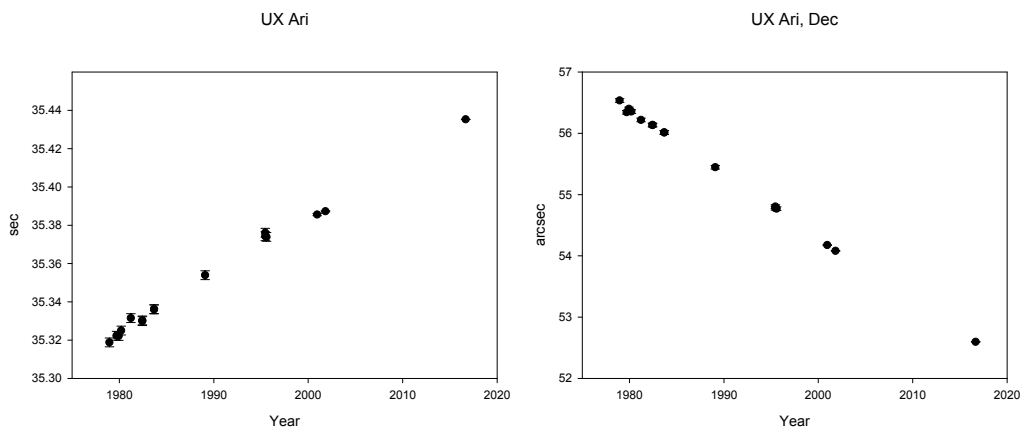


Figure 3: Time series of UX Ari astrometric positions

Also we found a set of legacy geodetic experiments including a radio star LSI+61 303 in 1990s organised by Marshall Eubanks (private communication). However, the daily positions of the radio star are not precise due to a weak flux density of the source. This radio star was also detected at a recent VLBA experiment (UF0011) on 27 May 2017 and the positions are presented in Table 2. Unfortunately, this set of data is not able to produce accurate proper motion (Figure 4).

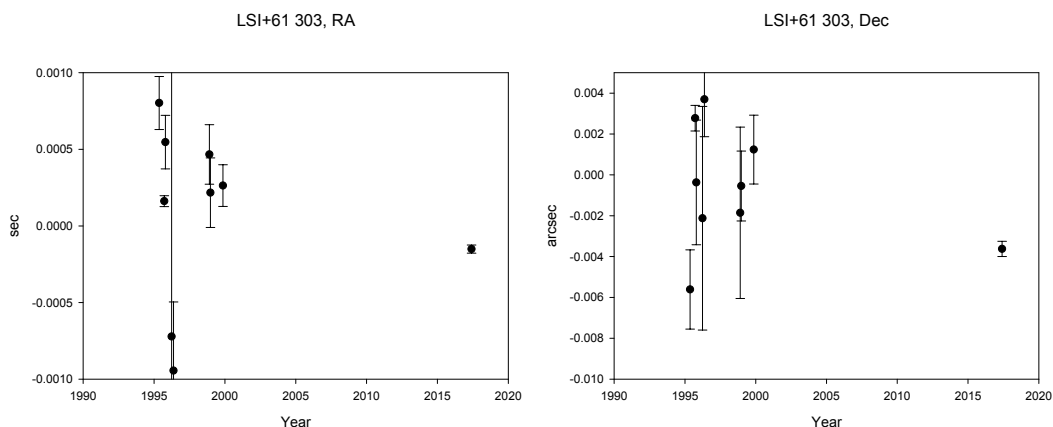


Figure 4: Time series of LSI+61 303 astrometric positions

4. CONCLUSION

We are aiming to detect some radio emitting stars in the absolute astrometric mode using S/X VLBI observations. Four radio stars (HR1099, UX Ari, HR5907 and LSI+61 303) have been detected in a few experiments. The minimum flux density of detection could reach as weak as 10 mJy. The success of detections benefits to the improved baseline sensitivity in term of participation of large radio telescopes and increased data rate. However, it can be challenging to obtain good quality data of weak stars at both S and X bands due to limited frequency coverage and more serious radio frequency interferences at S band. Moreover, two radio stars (HD132742 and HR1099) with flux densities below 10 mJy were detected in phase-reference mode.

Acknowledgement. We acknowledge the use of two large radio telescopes: Tianma65 and Parkes. The Parkes radio telescope is part of the Australia Telescope National Facility which is funded by the Australian Government for operation as a National Facility managed by CSIRO. The observations of radio stars were coordinated within the framework of the Asia-Oceania VLBI Group for Geodesy and Astrometry (AOV). The scheduling and data correlation were supported by three AOV member institutes which include Shanghai Astronomical Observatory of Chinese Academy of Sciences, University of Tasmania in Australia and Geospatial Information Authority of Japan. Experiments of V515C and AUA020 were done with participation of the radio astronomical VLBI network "Quasar" of the Institute of Applied Astronomy of the Russian Academy of Science (IAA RAS). This paper is published with the permission of the Geoscience Australia, CEO.

5. REFERENCES

- Boboltz, D. A.; Fey, A. L., Johnston, K. J., et al., 2003, "Astrometric Positions and Proper Motions of 19 Radio Stars", *AJ* 126, pp. 484–493, doi: 10.1086/375462.
- Boboltz, D. A., Fey, A. L., Puatua, W. K., et al., 2007, "Very Large Array Plus Pie Town Astrometry of 46 Radio Stars", *AJ* 133, pp. 906–916, doi: 10.1086/510154.
- Duemmler, R., Aarum, V., 2001, "The radial velocities of the RS CVn star UX Ari. A triple system with a binary on the same line of sight", *A&A* 370, pp. 974–981, doi: 10.1051/0004-6361:20010275.
- Gaia Collaboration, Brown, A. G. A., et al., 2018, "Gaia Data Release 2. Summary of the contents and survey properties", *A&A* 616, doi: 10.1051/0004-6361/201833051.
- Grunhut, J. H., the MiMeS Collaboration, 2012, "HR5907: Discovery of the most rapidly rotating magnetic early B-type star by the MiMeS Collaboration", *MNRAS* 419, pp. 1610–1627, doi: 10.1111/j.1365-2966.2011.19824.x.
- Healey, S. E., Romani, R. W., Gregory, B., et al., 2007, "CRATES: An All-Sky Survey of Flat-Spectrum Radio Sources", *ApJS* 171, pp. 61–71, doi: 10.1086/513742.
- Lestrade, J. F., Mutel, R. L., Phillips, R. B., et al., 1984, "Detection of a sub-milliarcsecond radio component in the RS CVn system HR 1099", *AJ* 282, doi: 10.1086/184296.
- Lestrade, J. -F., Preston, R. A., Niell, A. E., 1986, "Astrometric precisions in very long baseline interferometry observations of radio stars", *Processing of scientific data from the E.S.A. astrometry satellite HIPPARCOS*, pp. 383–389.
- Lestrade, J. -F., Preston, R. A., Jones, D. L., et al., 1999, "High-precision VLBI astrometry of radio-emitting stars", *A&A* 344, pp. 1014–1026.
- Lindgren, L., Hernández, J., Bombrun, A., et al., 2018, "Gaia Data Release 2 - The astrometric solution", *A&A* 616, doi: 10.1051/0004-6361/201832727.
- Murphy, T., Sadler, E. M., Ekers, R. D., et al., 2010, "The Australia Telescope 20 GHz Survey: the source catalogue", *MNRAS* 402, pp. 2403–2423, doi: 10.1111/j.1365-2966.2009.15961.x.
- Peterson, W. M., Mutel, R. L., Lestrade, J. -F., et al., 2011, "Radio Astrometry Of The Triple Systems Algol And UX Arietis", *ApJ* 737, doi: 10.1088/0004-637X/737/2/104.
- Van Leeuwen, F., 2007, "Validation of the new Hipparcos reduction", *A&A* 474, pp. 653–664, doi:10.1051/0004-6361:20078357.

DEEP SOUTH TELESCOPE

N. ZACHARIAS, C. FINCH, B. DORLAND, N. SECREST, M. JOHNSON

U.S. Naval Observatory - USA - nziauc8@gmail.com, charliefinch@gmail.com

ABSTRACT. The US Naval Observatory acquired a 1-meter telescope, the Deep South Telescope (DST). It was deployed at Cerro Tololo Interamerican Observatory (CTIO), Chile in March 2019. A 4k CCD camera will be used to image selected optical counterparts of ICRF sources which display significant radio-optical position offsets. This high cadence observing program is a joint effort between USNO and Paris Observatory. DST will also be used for other programs in the future, including near infra-red (IR) observations with a camera mounted at the 2nd Nasmyth focus.

1. HISTORY OF THE DST PROJECT

Around 2015, the era of ground-based, astrometric, all-sky surveys (e.g. Zacharias et al. 2013) came to an end due to the success of the Gaia space mission (Gaia collaboration, 2016). The U.S. Naval Observatory shifted focus toward going deeper on selected fields of interest in its southern hemisphere operations. In 2018 a 1-meter telescope (PW1000) was purchased from PlaneWave Instruments together with a 4k CCD camera (Sophia) from Princeton Instruments. Construction of the telescope was completed in December 2018 with on-sky testing in the factory backyard near Los Angeles.

2. DEPLOYMENT OF INSTRUMENT AT CTIO

In March 2019, the telescope was deployed at Cerro Tololo Interamerican Observatory (CTIO) (Figure 1). Delivery of the camera was delayed due to ongoing repairs after a shipping accident. Waiting for the 4k camera, system integration and testing took about 5 months. Routine operations began in August 2019. This telescope is particularly suited for astrometry due to the optical design with a fixed, spherical secondary mirror and a 3-lens corrector system. Using an elaborate pointing model, blind tracking is performed without a guider in the focal plane. A summary of the telescope and camera specifications is given in Table 1, while Figure 2 shows the focal plane layout.



Figure 1: The Deep South Telescope at CTIO.

telescope aperture	1.00	m
focal length	6.00	m
optical field of view	1.00	deg diameter
mount	alt-az	2 foci
number of pixels	4k by 4k	
pixel scale	0.515	arcsec/pixel
field of view	35 by 35	arcmin

Table 1: Specifications of DST and camera.

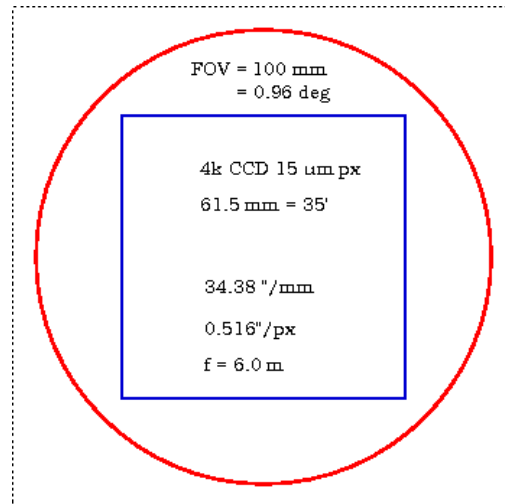


Figure 2: DST focal plane layout.

3. SCIENCE PROGRAM

The first observing program to be conducted with DST is monitoring selected ICRF sources with high cadence with the goal to obtain a better understanding of why about 10% of reference frame sources (Makarov, Frouard & Berhea 2016) display a significant position offset between the radio (VLBI) and optical (Gaia) centers of emission. Indications for such outliers were noticed even before the first Gaia data release (e.g. Zacharias & Zacharias 2014). Each source on our list is observed through B, V, R, I filters every other night during visibility season of about 6 months. A total of about 200 sources are being monitored as part of the FRAMEX collaboration between USNO and Paris Observatory.

Sources were selected from 4 groups: nearby AGN (Secrest, priv. comm.), large optical-radio offset sources from ICRF3 (Makarov, priv. comm.), those from the Radio Fundamental Catalog (Petrov 2018), and about a dozen sources where radio and optical positions agree as control sample. All sources are brighter than about $R = 18.5$ mag, resulting in high S/N observations of 3 to 4 minute exposures with the DST. All sources are south of $\text{Dec} = +25^\circ$ and about evenly distributed along RA to allow observing near the meridian at all times. The distribution of radio-optical position offsets of our sources is given in Table 2.

4. STATUS OF OPERATIONS

During commissioning, it was discovered that the focus curve is not symmetric (Figure 3). Stellar image size as a function of out-of-focus distance changed differently for intra- and extra-

no info or ≤ 0.1 mas	23
> 0.1 to 2.9 mas	50
> 2.9 to 5.0 mas	14
> 5.0 to 10.0 mas	32
> 10.0 to 30.0 mas	38
> 30.0 to 100.0 mas	15
>100.0 to 300.0 mas	8
>300.0 mas	12

Table 2: Number of sources by radio-optical position difference.

focal positions. The focus does correlate very well with temperature, in particular that of the primary mirror, however, not well enough for an accurate prediction of the focus. Best focus is currently obtained by observing focus sequences with many exposures and small step size several times during the night.

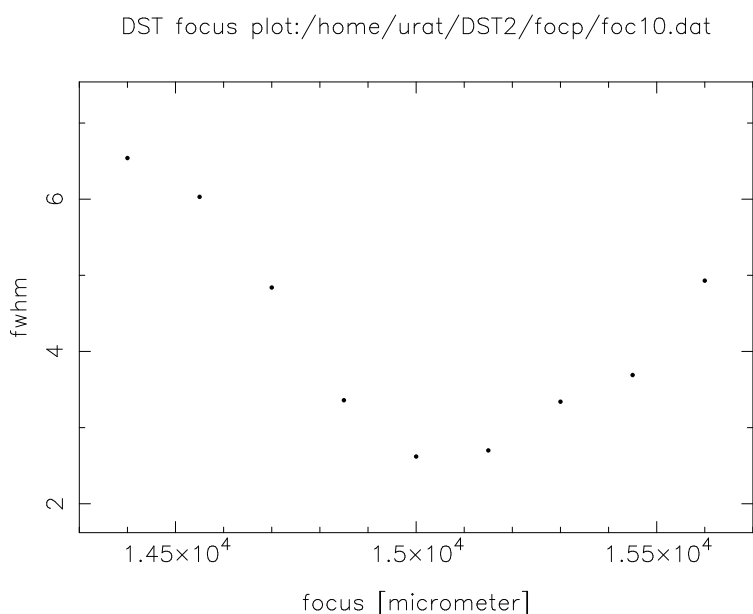


Figure 3: Example focus curve of DST.

The dynamic range of the instrument is very large, about 8 magnitudes, due to the relatively large pixels, sampling and low noise properties of the detector running at -80°C cooled by TEC with glycol (no liquid nitrogen, no dewar). Properties of stellar images as a function of magnitude of a single exposure are shown in Figure 4. The top left graph (image fit radius) shows that saturation is near instrumental magnitude 5. The lower left graph (position error) gives the limiting magnitude (here defined as position error reaches 0.1 pixel) near instrumental magnitude 13.

Table 3 provides the observing statistics for the first month of observing. Several issues remain to be solved for improved performance. A relatively large fraction of exposures (about 30%) display image elongation above our stringent threshold. More frequently this is the case for long exposures than short exposures. However, some exposures up to 10 min have been obtained with acceptable quality.

Occasionally, telescope mount drives become disabled or communication to the telescope is lost. The reduction software is still in its early steps. First science results are not expected until mid 2020.

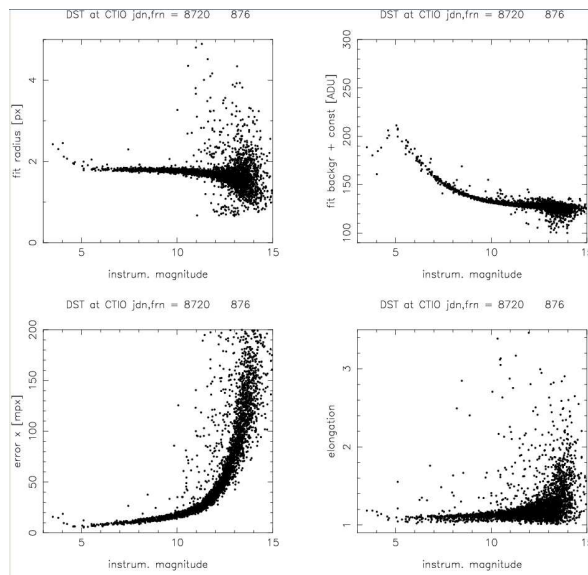


Figure 4: Stellar image properties as function of magnitude.

total number of nights	38
lost due to weather	4
lost due to instrument	4
nights with observing	30
total number of exposures	2797
total number of sources	≈ 100

Table 3: DST observing from Aug 24 to Sep 30, 2019

Acknowledgement. A program like this would not be possible without a large, diverse team of dedicated experts. This paper is based on observations obtained at Cerro Tololo Inter-American Observatory, a division of the National Optical Astronomy Observatories, which is operated by the Association of Universities for Research in Astronomy, Inc. under cooperative agreement with the National Science Foundation. We like to thank the entire staff of CTIO, Greg Bredthauer (STA), Marion Zacharias, the teams from PlaneWave and Princeton Instruments for their contributions to this program. We thank the USNO Instrument shop (Gary Wieder, Chris Kilian and Phil Eakens) for outstanding support, and Valeri Makarov and Jean Souchay for the FRAMEX collaboration.

5. REFERENCES

- Gaia Collaboration, Brown, A. et al., 2016, "Gaia Data Release 1", A&A 595(A2).
- Makarov, V., Frouard, J., Berghea, C. et al., 2017, "Astrometric evidence for a population of dislodged AGNs", ApJ 835(30).
- Petrov, L. 2018, "Radio Fundamental Catalog (RFC) vers. 2018d", <http://astrogeo.org/rfc>.
- Zacharias, N., Finch, C.T., Girard, T.M. et al., 2013, "The fourth US Naval Observatory CCD Astrograph Catalog (UCAC4)", AJ 145(44).
- Zacharias, N. & Zacharias, M.I. 2014, "Radio-optical reference frame link using the US Naval Observatory astrograph and deep CCD imaging", AJ 147(95).

VLBA IMAGING OF ICRF3 SOURCES

M. JOHNSON¹, L. HUNT^{1,2}, A. FEY¹, D. GORDON³, & J. SPITZAK^{1,4}

¹ United States Naval Observatory - USA - megan.johnson@navy.mil

² George Mason University - USA - lucas.hunt.ctr@navy.mil

³ NVI Inc., NASA Goddard Space Flight Center - USA - david.gordon-1@nasa.gov

⁴ Computational Physics, Inc. - USA - jspitzak@cpi.com

ABSTRACT

We present images created from the first year of an ongoing campaign to monitor sources used for the third iteration of the International Celestial Reference Frame (ICRF) with the Very Long Baseline Array (VLBA). Imaging these sources allows us to determine spectral index, peak flux density, compactness and source structure index. This information is crucial to understanding source structure and variability which better allows us to determine if a source is suitable for inclusion in the ICRF and suitability as a phase reference calibrator. We also present the current status and future of the Fundamental Reference Image Data Archive which is a new data archive to include not only images of the sources in this observing campaign, but a suite of ancillary data related to the ICRF sources.

1. INTRODUCTION

The International Celestial Reference Frame is the realization of the International Celestial Reference System and is comprised of positions of compact quasars calculated from Very Long Baseline Interferometry (VLBI) observations at 2.3 GHz and 8.4 GHz. It has now been through three full realizations (Hereafter ICRF1, ICRF2, and ICRF3) ((Ma et al, 1998; Fey et al, 2015; Charlot et al., 2020, respectively). The third realization (ICRF3; Charlot et al. in progress) was adopted by the International Astronomical Union on 1 January 2019.

The sources that make up the ICRF are compact radio quasars believed to be so distant that they have no measurable proper motions or parallax. Therefore, any observable changes in position would need to be derived from intrinsic properties of the source itself such as, outflows, hot spots within jets, shocks, or unresolved binary supermassive black holes. Understanding the physical source of positional changes and offsets for the ICRF quasars is an active area of current research. It is in this area of research that we focus our talk.

In January 2017, the United States Naval Observatory (USNO) entered an agreement with the Long Baseline Observatory to contribute 50% of the operations cost in exchange for 50% of the time on the VLBA. Because of the USNO partnership with the VLBA, the Long Baseline Observatory was disbanded and the management for the VLBA was restored to the NRAO. The USNO has since begun an imaging campaign designed to study and monitor the source structure, flux density, and positional properties of more than 3500 quasars from the ICRF.

This conference proceeding will provide an update to the imaging of the aforementioned monitoring campaign, and describe how the data will be accessible in the future.

2. USNO VLBA IMAGING CAMPAIGN

We present an update to the imaging campaign and some of the initial analysis. For more information on the details of the image calibration, processing, and methodologies, please see Hunt et al. (2019).

We observed 3,628 sources over the 20 sessions during the course of 2017. The left panel of

Figure 1 shows nearly 3,000 sources were observed only once during the year and only one source was included in every observation. The right panel of Figure 1 shows a histogram of the peak flux distribution for all of the observed sources. The peak of the distribution is ~ 75 mJy/bm.

The imaging success rate for our data was $\sim 93\%$ at 8.7 GHz and $\sim 96\%$ at 2.3 GHz. Due to limitations in some of the data, however, about 3% of the images from each observing session did not have enough uv coverage to form a high fidelity image and we therefore, flagged these images out of our final queue.

We are exploring new capabilities of NRAO's Common Astronomical Software Application (CASA) for moving toward an automated calibration and imaging pipeline. We have been successful in implementing a calibration script including the new CASA task *fringefit*, which solves for antenna-based phase, delay, and rate. We have also been successful in implementing CASA's *tclean* task for producing images, which have comparable rms noise to those images produced in AIPS and DifMAP. Progress is currently ongoing in this area.

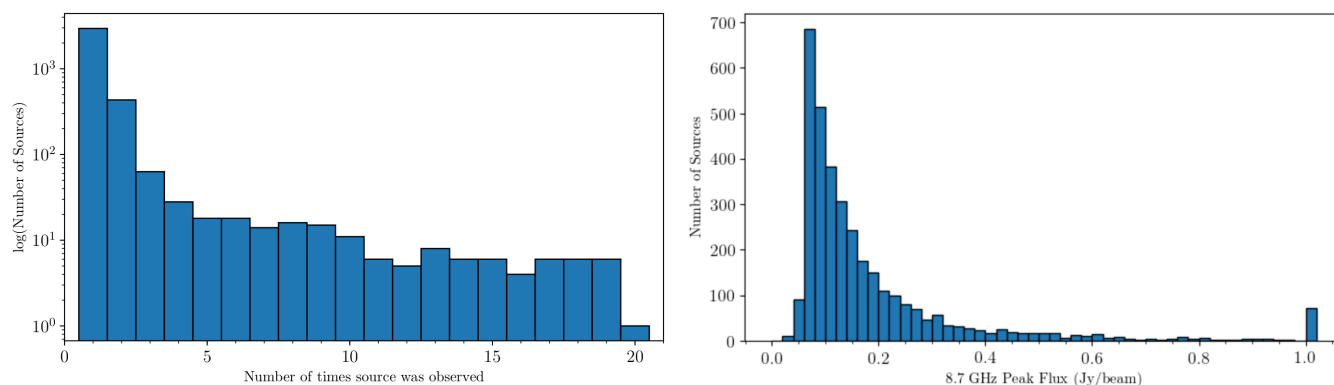


Figure 1: Left: Histogram showing how often sources were visited over 20 sessions. Right: Histogram showing peak flux distribution measured at 8.7 GHz. The bin at 1.0 includes all sources brighter than 1 Jy.

3. FUNDAMENTAL REFERENCE IMAGE DATA ARCHIVE

USNO is responsible for preparing images of sources included in the ICRF. Traditionally we have made those images publicly available to the astronomical and geodetic communities through the Radio Reference Frame Image Database. We are upgrading that website and changing the name to the Fundamental Reference Image Data Archive (FRIDA). The upgraded FRIDA website will include data from additional observations that span wavelengths from across the electromagnetic spectrum including, radio, near-infrared, optical, and X-ray. The available radio VLBI images will go back to data included in ICRF1 and include images of sources from S-band through Ka-band. The upgraded website will include data on each source including radio contour plots of the source, the calibrated data sets, and log files to show how the imaging was processed. The site will allow users to find sources based on specific search criteria, and download the data that might be useful to their research.

4. REFERENCES

- Charlot, P., et al., 2020, "The third realization of the International Celestial Reference Frame by VLBI", *A&A*, doi: 10.1051/0004-6361/202038368.
- Fey, A., Gordon, D., Jacobs, C. S., et al., 2015, *AJ*, 150, 58
- Hunt, L., Johnson, M. J., Fey, A., Spitzak, J., & Gordon, D., 2019, "VLBA Imaging of ICRF3 Sources", *Proceedings of the 24th European VLBI Group for Geodesy and Astrometry Working Meeting*, Eds. Haas, R. and Garcia-Espada, S. and López Fernández, J. A., pp. 214-218
- Ma, C., Arias, E. F., Eubanks, T. M., et al., 1998, *AJ*, 116, 516

GEODESY AT K-BAND WITH THE EUROPEAN VLBI NETWORK

M.E. Gomez¹, P. Charlot¹, R. Campbell², M. Kettenis², A. Keimpema²

¹ Laboratoire d'Astrophysique de Bordeaux, Pessac - France - maria.gomez@u-bordeaux.fr

² Joint institute for VLBI-ERIC, Dwingeloo - The Netherlands

ABSTRACT. The paper presents the current status of adding geodetic capabilities to the European VLBI Network (EVN) software correlator at JIVE (SFXC), which is accomplished as part of the JUMPING JIVE project. Even though the EVN is not a geodetic array, there are many reasons why accurate radio telescope positions are desirable, including frequent observations using the phase-referencing technique to detect weak radio sources. Several changes were made at the SFXC so that the correlator can successfully correlate geodetic experiments. Detailed testing using data from the International VLBI Service for geodesy and astrometry (IVS) was performed to check the implementation. Additionally, a non-standard geodetic VLBI experiment was carried out at K-band (22 GHz) in June 2018 using 14 radio telescopes from the EVN. The purpose of this experiment was to determine accurate geodetic positions for those EVN telescopes that do not possess S/X receivers and hence do not participate in regular experiments organized by the IVS. The experiment was fully correlated with SFXC and exported into Mk4 format so that it can be further processed with standard geodesy software packages. That experiment is used as another means to demonstrate the full geodetic capabilities of the JIVE correlator.

1. INTRODUCTION

The EVN software correlator at JIVE (SFXC) has recently been upgraded with a new capability permitting to correlate and to export VLBI data acquired in geodetic mode. Thanks to this upgrade, the correlator is now able to handle sessions conducted with sub-netting (as is usually the case in geodesy) and export the data in a suitable format for post-processing and analysis in a geodetic way. The validation of this new capability was achieved in two ways, (i) by reprocessing completely an IVS-R1 session from beginning to end, and (ii) by processing a dedicated EVN geodetic experiment at K-band aimed to measure the positions of non-geodetic EVN telescopes. This paper describes the methodology used for this validation and presents initial analysis results of the acquired K-band data.

2. A NEW GEODETIC CAPABILITY FOR THE JIVE CORRELATOR

The SFXC correlator at JIVE was upgraded in order to handle geodetic sessions scheduled with sub-netting and to attach the correlator model and phase-calibration information to the correlator output. As HOPS is the standard software package for fringe-fitting geodetic data, a new path was added so that the correlator data can be exported into Mk4 format which is the proper format to be used with HOPS.

In order to test the pipeline implemented at JIVE, a 24-hour IVS session, IVS-R1872, originally correlated with the DiFX Bonn correlator, was selected. This experiment involved eight IVS stations and comprised 1069 scans. The Bonn correlator group provided us with the correlated data along with the fringe-fitted data and the vgos data base files (vgosDB), which is the new geodetic format to store VLBI data. The same processing was done at JIVE, i.e., the observed sampled data were independently correlated with SFXC, post-processed and exported into vgosDB format. For the post-processing and data export we used the same version of HOPS as that used in Bonn to avoid

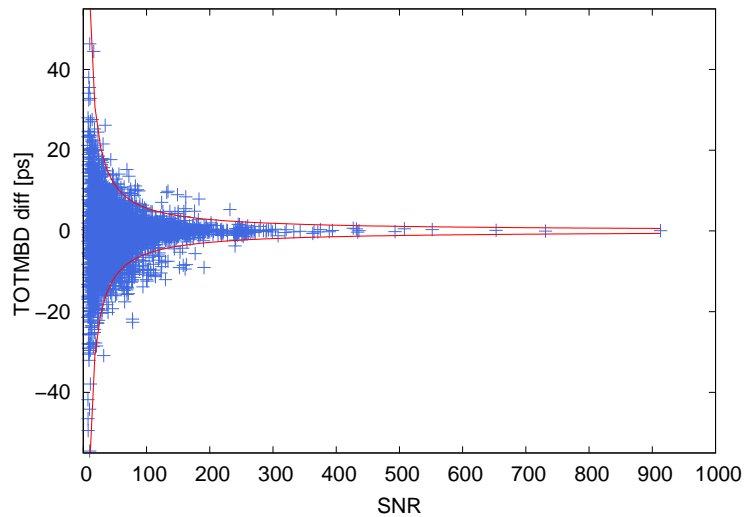


Figure 1: TOTMBD differences vs. SNR for X-band. The red curves represent $\pm 1\sigma$; 95 % of the differences are below this standard error.

potential differences due to software changes. In terms of models, it must be noted that SFXC uses a delay model based on CALC 10 whereas the delay model used with DiFX is CALC 11.

To validate the procedure, we compared our results with those from Bonn at the level of the vgosDB data set. This was not straightforward because of differences in the correlation process and correlator architecture. The time of each observation is tagged according to what is called the Fourfit Reference Time (FRT) which may differ from one correlator to the other due to differences in how the correlators search for the first valid input data for each scan. For the present case, there was a difference of 0.5 s between FRTs for some observations which caused discrepancies when comparing the Total Multiband Delay (TOTMBD) just because this quantity was being evaluated at different FRTs. To remove that effect, we shifted the FRTs of the TOTMBDs of JIVE to the Bonn FRTs and we corrected the TOTMBD derived at JIVE with the delay rate estimated during the fringe-fitting done with HOPS.

For the comparison, we divided the data into two subsets: one that includes the data that have the same FRTs (3462 out of 5826 observations) and one that includes the data that have different FRTs. When the FRT is the same, 80 % of the TOTMBD differences are below 5 ps. The ensemble has a mean of -0.09 ps and a wRMS of 5.5 ps. In the case of those observations that had different time tags (2364 observations), the ensemble of TOTMBD differences, after correction, has a mean of -1.0 ps and a wRMS of 8.5 ps. The wRMS is thus similar, although slightly larger, to that derived for those observations without time tag discrepancies. The level of the differences is consistent with the expected size of second-order residuals arising from the use of a linear correction to the TOTMBDs of JIVE, based on propagating the delay-rate over the 0.5 s FRT difference. As a further check, we inspected the relationship between the standard error of the TOTMBD (σ_{MBD}) and the SNR. According to Rogers et al. (1993),

$$\sigma_{\text{MBD}} \propto \text{SNR}^{-1} \quad (1)$$

For the IVS session R1872, with a spanned bandwidth of 720 MHz and an RMS bandwidth of 280.4 MHz, this equation can be written as $\sigma_{\text{MBD}}[\text{ps}] = 567/\text{SNR}$. Figure 1 show the results of this check for all observations. As expected, the TOTMBD differences decrease as the SNR increases and 95 % of them are below the 1σ standard error value. Further details on the validation process

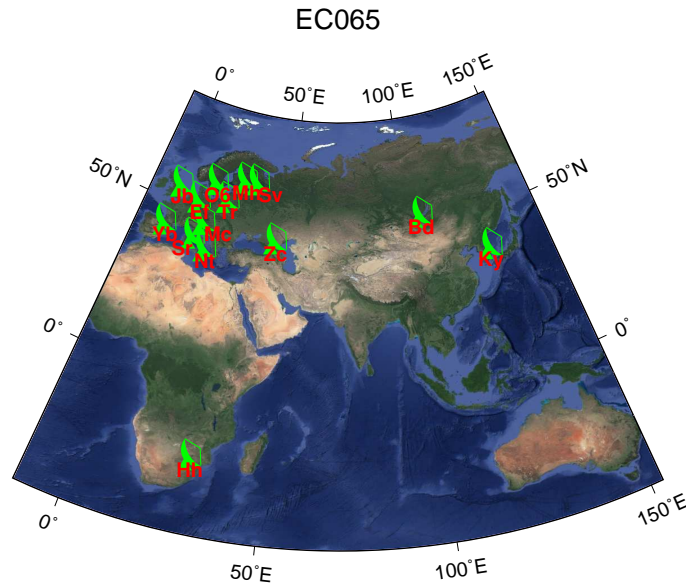


Figure 2: Stations that have participated in the EC065 experiment.

can be found in Gomez et al. (2019).

3. PRELIMINARY ANALYSIS OF EVN GEODETIC DATA ACQUIRED AT K-BAND

A non-standard EVN geodetic experiment at K-band, coded EC065, was carried out on June 13, 2018. Data from 14 EVN telescopes, including Sardinia, Jodrell2, KVN-Yonsei and Torun which are non-geodetic, were acquired (Fig. 2). A total of 478 scans spread over the 24-hour duration of the experiment were observed. The data were correlated with SXFC and post-processed with HOPS following the established path.

The geodetic analysis was conducted with VieVS (Böhm et al., 2018) in a standard way with models and apriori data as in Table 1.

Data/Models	Comments
Ephemeris	JPL421
Earth Orientation Parameters	IERS C04
Terrestrial Reference Frame	ITRF2014
Celestial Reference Frame	ICRF3(K)
Ocean Tide Loading	FES2004
Ionospheric correction	CODE
Galactic Acceleration	YES
Tropospheric hydrostatic model	Saastamoinen
Tidal atmospheric loading	Vienna
Non-tidal atmospheric loading	Vienna
Tropospheric Mapping function	VMF3

Table 1: Models (non-exhaustive) used for the analysis of the EC065 experiment.

As only a single frequency was observed, correction of ionospheric effects was necessary. For this purpose we used total electron content maps produced by the Center for Orbit Determination in Europe (CODE) based on data from the Global Navigation Satellite Systems. A trial using

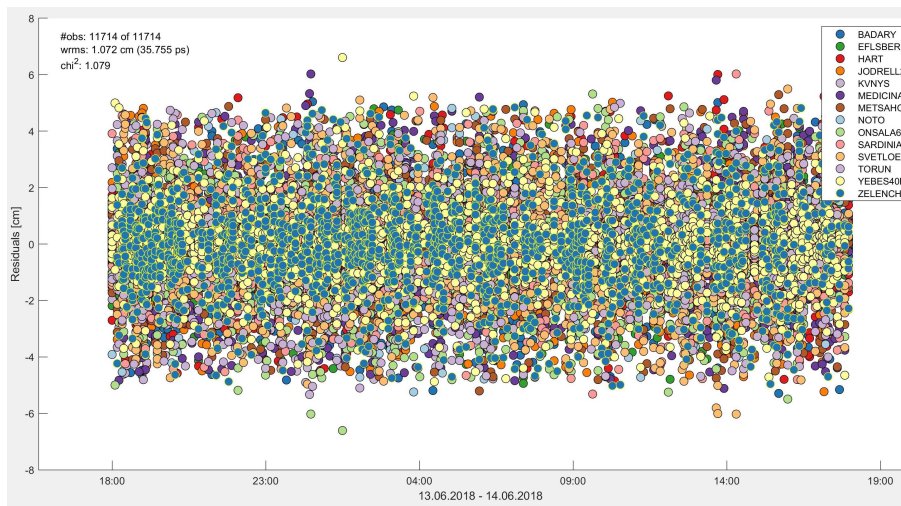


Figure 3: Post-fit delay residuals resulting from the VieVS analysis.

ionospheric maps from the Jet Propulsion Laboratory (JPL) showed insignificant differences in the results as previously noted by Langi et al. (2010).

The post-fit residuals are plotted in Figure 3. These have an wRMS of about 1 cm which brings a promising perspective for the estimation of station positions with these data.

4. CONCLUSION

We have shown that a typical 24-hour IVS session can be fully processed with the EVN software correlator at JIVE (SFXC), post-processed and analyzed with standard geodetic tools. Comparison of the correlator output with that from the DiFX correlator at the Bonn correlation center indicates an agreement at the 5 ps level in total multiband delay, which is the level of consistency expected. We have further demonstrated that the pipeline from correlation to session analysis works also for a non-standard geodetic session like EC065. These two end-to-end tests show that the SFXC correlator is now technically capable to process and export geodetic data.

Acknowledgement. This work was carried out as part of the JUMPING JIVE project which received funding from the European Union's Horizon 2020 Research and Innovation Programme, under grant agreement No. 730884. We also thanks to RadioNet for its support.

5. REFERENCES

- Böhm, J., Böhm, S., Boisits, J., Girdiuk, A., Gruber, J., Hellerschmied, A., Krásná, H., Landskron, D., Madzak, M., Mayer, D., McCallum, J., McCallum, L., Schartner, M., Teke, K., 2018, "Vienna VLBI and Satellite Software (VieVS) for Geodesy and Astrometry", Publications of the Astronomical Society of the Pacific 130(986), 044503.
- Gomez, M.E., Kettenis, M., Charlot, P., Campbell, R.M., Keimpema, A., 2019, "Implentation of a geodetic path at the JIVE correlator", Proceedings of the 24th European VLBI Group for Geodesy and Astrometry Working Meeting (CNIG-Madrid, Spain), pp. 112–115.
- Lanyi G. E. et al., 2010, AJ 139, 1695.
- Rogers, A.E.E. et al., 1993, "Improvements in the Accuracy of Geodetic VLBI". Smith D. E. and Turcotte D. L. Eds., Geodynamics Series.

PARAMETRIZATION OF THE SOURCE COORDINATES AND ITS ASTROPHYSICAL INTERPRETATION

C. GATTANO¹, M. KARBON²

¹ Laboratoire d'astrophysique de Bordeaux, CNRS - France - cesar.gattano@u-bordeaux.fr

² SYRTE, Observatoire de Paris, PSL, CNRS - France - maria.karbon@obspm.fr

ABSTRACT. In the ICRF3 catalog, the positions of the radio-sources are given as invariant with time. New evidences argued recently on the generalization of systematic variation of the position to all reference sources, albeit at different levels and time scales. By neglecting these systematics in the realization of the celestial reference frame (CRF), its quality may be deteriorated, and it may affect the quality of derived parameters. One solution is to extend the parametrization of the source positions in VLBI data analysis. We use the multivariate adaptive regression splines (MARS) which combines recursive partitioning and spline fitting on position time series. Then, we investigate the source coordinate residual time series after application of the found parameterization. We aim to identify their noise level and content through the computation of the Allan standard deviation functions.

1. MOTIVATION

The International Celestial Reference Frame ICRF3 [Charlot et al., 2020, in press] was released in August 2018 after approval by the International Astronomical Union during its XXXth general assembly in Vienna. It is the newest realization of the International Celestial Reference System [ICRS, Arias et al., 1995]. In the ICRF3 catalog, the positions of the radio-sources are given as time invariant coordinate pairs. Nevertheless, systematic variation within the astrometric positions are known, which led, in the past, to the alienation of a small number of sources in the ICRF2 catalog [Fey et al., 2015]. Recently new evidences were presented for a generalization of such systematics, showing that a majority of the sources is subjected to positional variations [Karbon et al., 2016, Gattano et al., 2018], albeit at different levels and time scales. Such systematics, if neglected, may affect the quality of the CRF, and consequently impair depending parameters such as the Earth orientation parameters (EOP). A proven approach to overcome these shortcomings is to extend the parameterization of the source positions within the VLBI data analysis [Karbon et al., 2016] : the multivariate adaptive regression splines (MARS) allow a complete automation by combining recursive partitioning and spline fitting in an optimal way.

In this paper, we present our initial investigation based on the combination of the MARS parametrization of source coordinate time series with the Allan standard deviation analysis of the residuals after the application of said parameterization. With this methodology, we aim to identify the effect of the parameterization on the noise content and level within the residual source position time series. We illustrate the principle with three examples on the sources 0048–097, 4C39.25 and 2234+282.

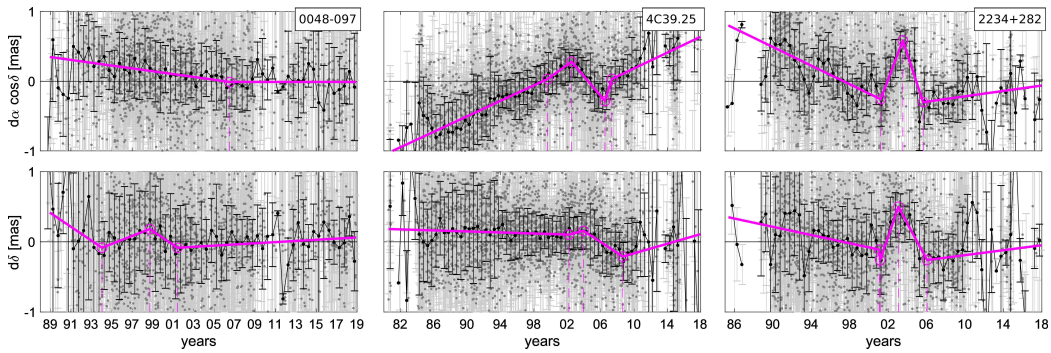


Figure 1: Position time series with respect to the a-priori coordinates given in the ICRF3 catalog of the ICRF3 defining source 0048–097 and the ICRF2 special handling sources 4C39.25 and 2234+282. The individual session-wise results are represented in gray, the half-year mean values in black, both with the corresponding error bars. In magenta, the splines are represented as determined by the MARS algorithm.

2. METHOD

Our study is based on more than 4 500 sessions with global station networks spanning the time frame 1980–2018. The geodetic data analysis is performed using the VLBI software package VieVS [Böhm et al., 2018], and following the conventions of the International Earth Rotation and Reference Systems Service [IERS, Petit et al., 2010]. The modeling settings are chosen with respect to the routine single-session data analysis strategies of the International VLBI Service for Geodesy and Astrometry [IVS, Nothnagel et al., 2015].

2.1 Multivariate adaptive regression splines (MARS)

The resulting source position time-series are processed using the MARS algorithm to determine the splines. The methodology is discussed in Karbon et al [2016]. In Figure 1, we present exemplarily the results of the spline determination for the ICRF3 defining source 0048–097 and the ICRF2 special handling sources 4C39.25 and 2234+282. The resulting splines can then be used to correct the a-priori source positions, i.e. the position in the ICRF3 catalog, which enter the VLBI analysis. Such time-dependent corrections improve the determination of correlated parameters, such as the EOP. By subtracting the splines to the initial source position time series, we get the source coordinate residual time series.

2.2 Allan standard deviation

To assess the noise content of the source position time series, we used the Allan standard deviation function [Allan, 1966] that enables to identify in a data time series the different colors of the noise dominating at different time scales by the slope of the function represented in a log-log scale. The principle is illustrated by the scheme in Figure 2. The details of the method in practical and in the context of VLBI source position time series are presented and discussed in Gattano et al. [2018]. On the astrometric point of view, a perfect source as fiducial mark on the sky would have its two coordinate offset time series with respect to the a priori position, given in the ICRF3 catalog, that return a dominating white noise at all time scales. On the opposite, a source affected by any position perturbation would present a dominating colored noise at some time scales from one or both coordinates.

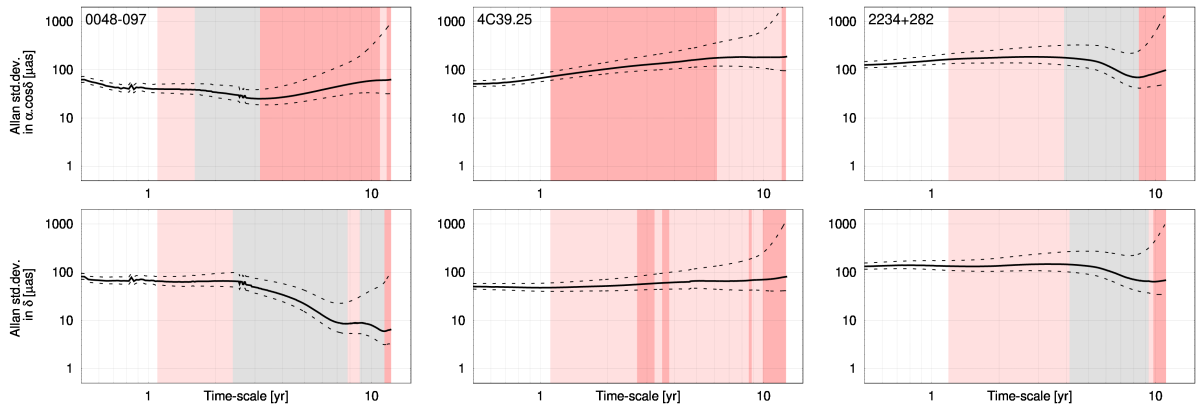
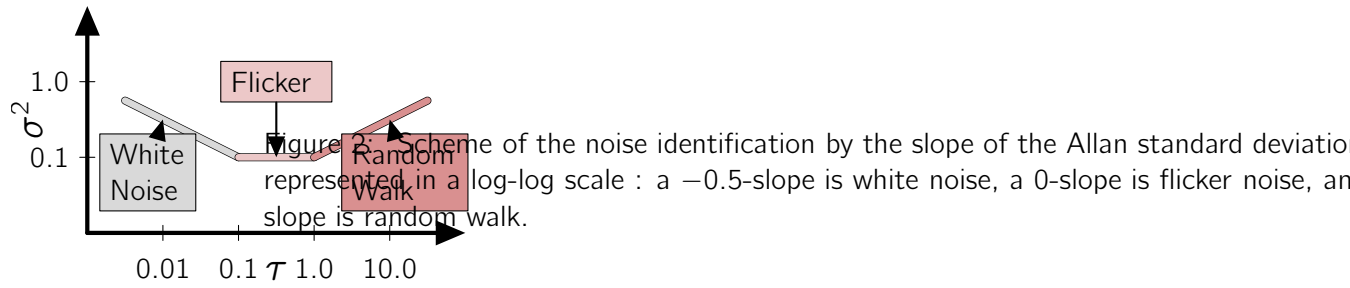


Figure 3: Allan standard deviation functions of the original position offset time series with respect to the ICRF3 a-priori coordinates of 0048–097, 4C39.25 and 2234+282. The background colors indicate the noise color identified at the corresponding time scale following the color scheme of Figure 2.

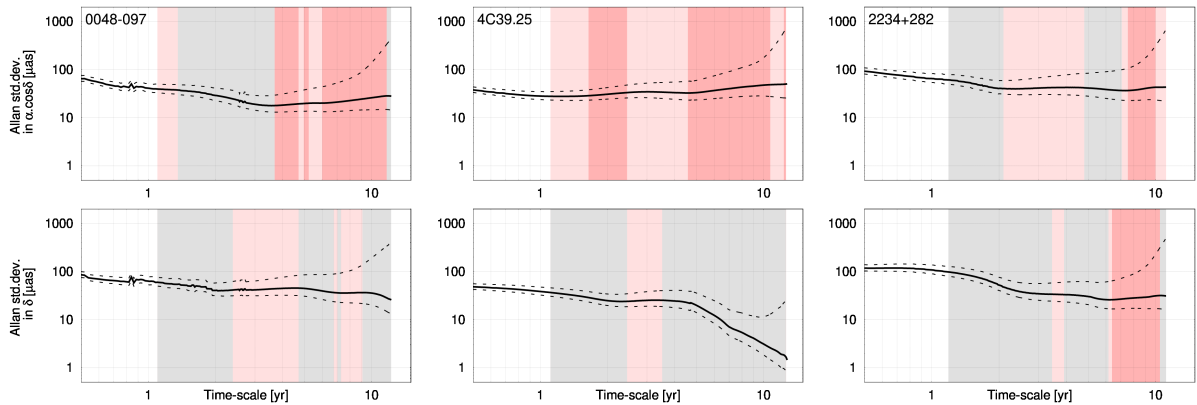


Figure 4: Allan standard deviation functions of the position residual time series after applying the correction using the MARS splines for 0048–097, 4C39.25 and 2234+282. The respective splines are represented in magenta in Figure 1. The background colors indicates the noise color identified at the corresponding time scale following the color scheme of Figure 2.

3. RESULTS

Despite its ICRF3 defining status, we observed systematics for the source 0048–097, revealed by the MARS algorithm (Figure 1) and the Allan standard deviation functions of its two coordinates (Figure 3). The right ascension is dominated by a random walk at time scales longer than 3 years. The declination is affected by a flicker noise at time scales shorter than 3 years and by a white noise at longer time scales. The effect of the correction from the splines mitigates the noise level on the right ascension but does not change the noise content (Figure 4). The flicker noise on declination is removed at shorter time scales. The source 4C39.25 is known to present exceptionally large systematics in its astrometric position as seen in Figure 1. Its right ascension systematic is recognized as random walk, whereas its declination systematic is recognized as flicker noise like (Figure 3). The effect of the spline corrections change the dominating noise content at most of the time scales. The right ascension becomes mostly dominated by flicker noise whereas the right ascension is in majority dominated by white noise. The two coordinates of the source 2234+282 are both dominated by flicker noise at time scales shorter than 4 years and by white noise in majority at longer time scales. The linear spline corrections evince in majority the flicker noise and the noise level is diminished at all time scales even if the final residuals are not purely dominated by white noise.

4. INTERPRETATION

Taking into account the linear splines to correct the source coordinates from systematics mitigate the noise level of the residual position time series, and sometimes changes the noise content. Colored noises (e.g. flicker noise, random walk) may be associated with source-dependent perturbation that affect the position estimates from VLBI. The most probable perturbation is a change of the source structure. For example, starting from a compact structure, the appearance of an extension may drift the position estimates in a peculiar direction on the plane of the sky. Such a noisy drift would appear as a random walk domination. Then, if the extent disappears, the position will drift in the opposite way. A succession of jumps in the position estimates is characterized by a flicker noise. Therefore, only the white noise process is an evidence of source stability in term of behavior.

5. CONCLUSIONS AND OUTLOOK

We present a new approach to model the astrometric position variations of radio sources selected to define the CRF from VLBI data analysis. We assess the quality of the models in terms of noise content in the residuals after subtraction of the models. The method benefits from two statistical tools: the MARS algorithm enables to extract an empirical model of the source position variation in time, and the Allan standard deviation analysis enables to characterize the noise content of data time series. Their combination allows the tuning of the parametrization in order to retrieve purely white noise source position residuals. This method will be applied to the most observed sources within VLBI sessions. The primer aim is to find a parameterization for the position of each source so that their remaining noise is white. For the determination of the MARS splines, we will investigate different methods, allowing more nodes between the splines, or using cubic splines. Also, the effect of irregular data coverage from VLBI observation will be evaluated. Last but not least, further work will be done to interpret the physical nature of the splines models. The final goal is to pin down the astrophysical processes driving the source.

6. REFERENCES

- Charlot, P., Jacobs, C. S., Gordon, D., et al., 2020, "The third realization of the International Celestial Reference Frame by very long baseline interferometry", *A&A* , doi: 10.1051/0004-6361/202038368.
- Arias, E. F., Charlot, P., Feissel, M., et al., 1995, "The extragalactic reference system of the International Earth Rotation Service, ICRS", *A&A* 303, pp. 604–608.
- Fey, A. L., Gordon, D., Jacobs, C. S., et al., 2015, "The Second Realization of the International Celestial Reference Frame by Very Long Baseline Interferometry", *AJ* 150, p. 58.
- Karbon, M., Heinkelmann, R., Mora-Diaz, J., et al., 2016, "The extension of the parametrization of the radio source coordinates in geodetic VLBI and its impact on the time series analysis", *Journal of Geodesy*.
- Gattano, C., Lambert, S. B., Le Bail, K., 2018, "Extragalactic radio source stability and VLBI celestial reference frame: insights from the Allan standard deviation", *A&A* 618, A80.
- Böhm, J., Böhm, S., Boisits, J., et al., 2018, "Vienna VLBI and satellite software (VieVS) for geodesy and astrometry", *Publications of the Astronomical Society of the Pacific*, 130(986), p. 044503.
- Petit, G., Luzum, B., et al., 2010, "IERS Conventions", *IERS Technical Note* 36.
- Nothnagel, A., Aef, W., Amagai, J., et al., 2015, "The IVS data input to ITRF2014", *GFZ Data Services*, Helmholtz Centre, Potsdam, Germany.
- Allan, D. W., 1966, "Statistics of atomic frequency standards", *IEEE Proceedings* 54, pp. 221–230.

TOTAL ELECTRON CONTENT OVER VOSTOK ANTARCTIC STATION

D. TROFIMOV¹, S. PETROV¹, S. SMIRNOV¹, K. ZHELTOVA¹, I. CHEKUNOV²,
YU. SEROV³, O. TROSHICHEV³

¹ Saint Petersburg State University - Russia - d.trofimov@spbu.ru

² Bauman Moscow State Technical University - Russia

³ Arctic and Antarctic Research Institute - Russia

ABSTRACT. Total Electron Content (TEC) is one of the most important parameters of the ionosphere for propagation of radio waves. TEC is now being routinely monitored by global GNSS networks almost everywhere on Earth except geomagnetic poles. In order to study TEC evolution near the southern magnetic pole, two series of GNSS observations were carried out at the Vostok Antarctic station. Every of the two series lasted about one year each, 2016 and 2018. The collected GNSS observations were processed with RTKLIB and GeNeSiS software packages. TEC was estimated both from code and phase observables. The resulting TEC time series were analysed and compared to the global TEC map. These results may potentially augment our knowledge about ionosphere structure and evolution near the geomagnetic poles. As a continuation of this study a permanent GNSS receiver is considered to be installed at the Vostok Antarctic station.

1. INTRODUCTION

The ionosphere is a layer of the Earth's atmosphere that is highly ionized due to exposure to the Sun. The Earth's ionosphere consists of a mixture of neutral gases and a quasi-neutral plasma. The ionosphere starts at about 60 km. One of the main characteristics of the state of the ionosphere is the total electron content - the number of free electrons located in a cylinder with a cross section of 1 square meter and oriented along the line of sight. This value is measured in TECU (Total Electron Content Unit), $1 \text{ TECU} = 1 \times 10^{16} m^{-2}$. TEC is determined by the delay of the radio signal passing through the ionosphere. Signal transmission at two frequencies allows you to fully take into account this effect, which is used in VLBI and GNSS. At present, GNSS is the most convenient technology for determining the TEC, since the receiving equipment is the cheapest among analogues, and the constellations of the existing GNSS systems (GPS, GLONASS, Galileo and Baidou) provide a fairly dense coverage of the celestial sphere for the observer. For GNSS, TEC can be obtained based on the technique described in Alizadeh et al., 2013. In the case of code measurements, the TEC is determined from the ratio:

$$P_2 - P_1 = \frac{40.4 \cdot (f_1^2 - f_2^2)}{f_1^2 \cdot f_2^2} TEC + B^s + B_r + \epsilon,$$

where P_2 , P_1 are pseudo-range at frequencies f_2 and f_1 , B^s and B_r are delays in the satellite and receiver equipment. Thus, GNSS is a good and inexpensive method for determining the state of the ionosphere. Radio communication depends on the state of the ionosphere, thus determining the parameters of the ionosphere is an important task. Of interest is the determination of ionosphere parameters at high latitudes of the northern and southern hemispheres.

Now, quite a lot of work (Correia et al., 2013, Purohit et al., 2011, Sulaiman et al., 2007) has been completed on the definition of TEC over Antarctica. As a rule, all work was performed on the basis of GNSS observations, or based on measurements of the signal from satellite altimetry

missions. At the same time, it is necessary to note the following disadvantages of these works, organically arising from the conditions of their implementation. Almost all observation points where GNSS receivers are installed are located on the coast of Antarctica, that is, in the zone of latitudes from 63° to 78° south latitude. Given the fact that the orbital inclination of GPS satellites is 55° , and GLONASS satellites 64.8° , it becomes clear that it is difficult to determine the total electron content directly above the observation points. Only GLONASS satellites can pass directly above the receiver, for GPS satellites the minimum zenith distance z is about 15° . Thus, from GNSS observations performed on the coast, it is impossible to construct a map of the ionosphere covering the Antarctic coast itself and a strip of southern territory about 400 km deep. In order to determine the total electron content over these territories, the observations should be performed substantially farther south. One of the most convenient places for installing the receiver for this purpose is the Russian Antarctic station Vostok. Vostok station is located at $78^{\circ}27'51''$ south latitude and $106^{\circ}50'14''$ east longitude near the south geomagnetic pole. Regular geomagnetic observations are made at the station, the corresponding series of geomagnetic indices are displayed, which will make it possible, if necessary, to compare our TEC series with the series of geomagnetic indices. The climate at the station is extremely severe, which leads to the need to protect equipment from external conditions.



Figure 1: Receiver installation at Vostok station

2. OBSERVATIONS

The observations were carried out jointly by Saint-Petersburg State University and Arctic and Antarctic Research Institute. To carry out observations, the Department of Astronomy of St.Petersburg State University provided the JAVAD TRIUMPH-1 geodetic GNSS receiver. During the first expedition of 2016-2017, a GNSS observation point was laid at Vostok station. A beam was frozen in the firn, and a platform with a heating cable and a screw mark was installed on top of the beam, where the receiver was fixed. Before the receiver was delivered to the Vostok station, a 24-day series of observations was made at Progress station on the coast of Antarctica. The observations at Vostok station were carried out from February 7, 2016 and ended on January

31, 2017. In 2017, the receiver returned to the department. Based on these observations were obtained coordinates and velocity of point Trofimov et al., 2017. The obtained velocity are in good agreement with the results of measurements of the radar satellite missions. A year later, a new expedition was organized, where observations were made at the same receiver and observation post from February 4, 2018 to February 10, 2019. In all series, observations were carried out at two frequencies with the possibility of phase and code measurements. The interval between measurements is 30 seconds.

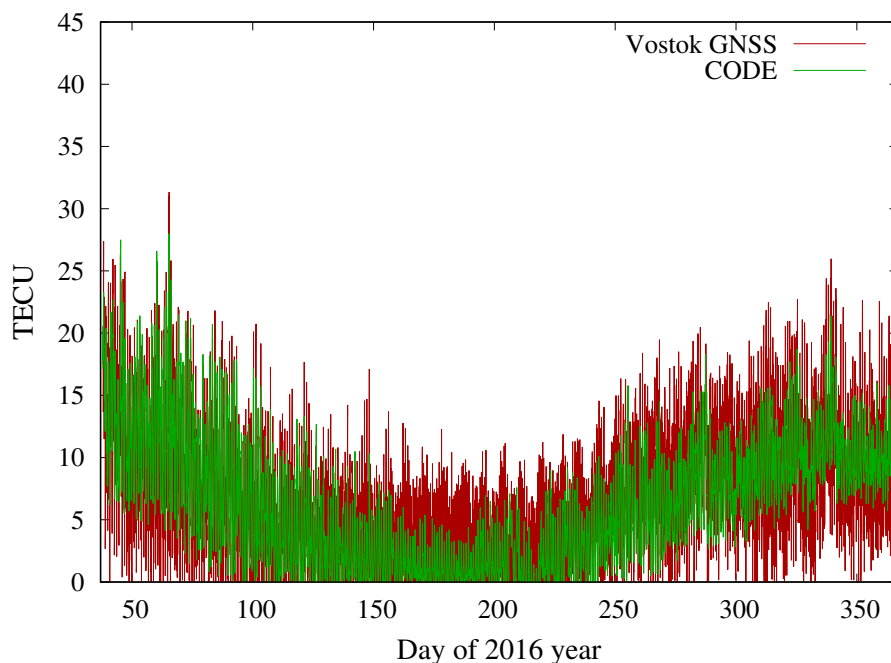


Figure 2: TEC from GNSS observations and from CODE

3. DATA PROCESSING AND RESULTS

The TEC shown in the figures below was calculated on the basis of code measurements, from a linear combination of the pseudo-range obtained at two frequencies (used frequencies L1 and L2) for each satellite, the slant electron content in the ionosphere (along the line of sight) was calculated, after which the vertical electron content was determined based on the mapping function described in Alizadeh et al., 2013 for each satellite.

$$VTEC = \frac{1}{F(z)} STEC,$$

$$F(z) = \frac{1}{\sqrt{1 - \sin^2 z'}},$$

$$\sin z' = \frac{R}{R + H} \sin z,$$

where R is the mean Earth radius and H is the height of the single layer, z - zenith angle on the ground station and z' - zenith angle on the point, where signal transmitted from satellite to receiver crosses ionospheric shell, $STEC$ - slant TEC and $VTEC$ - vertical TEC. The height of the conductive layer was taken equal to 350 km. The final result was obtained by simple averaging over the hourly interval. Thus, the share of obtaining one value was averaged by the results of 120 measurements. The program that calculates TEC values includes the filtering of knowingly

false TEC values (too large and too small), vertical TEC from satellites that do not meet these conditions do not participate in the derivation of the final TEC value. The software calculated TEC based on all GNSS measurements, and only on the basis of GPS and GLONASS observations.

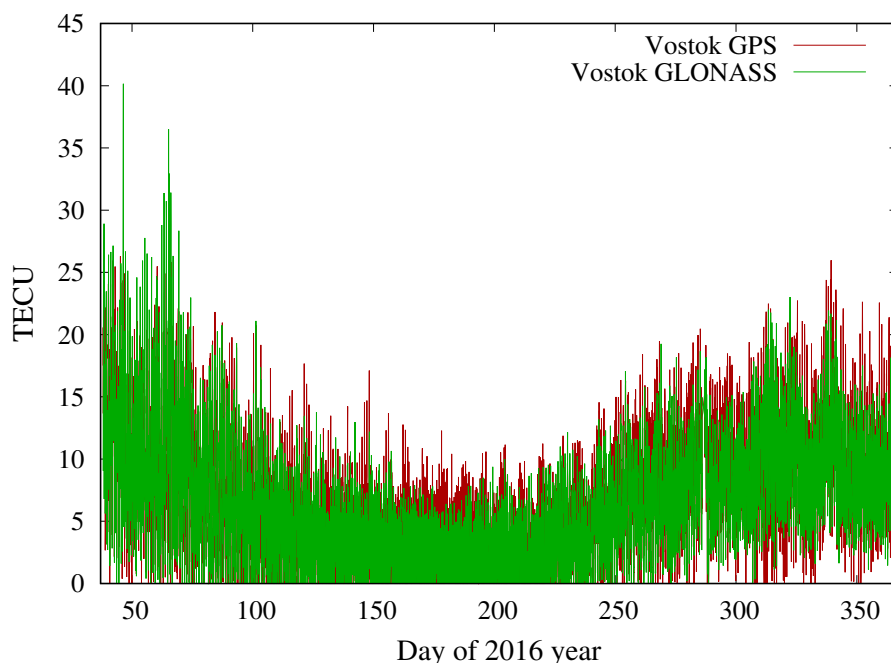


Figure 3: TEC from GPS and GLONASS observations on the Vostok station

The result of the first observation series of 2016 was compared with the global ionospheric maps of CODE. Due to the fact that the observations were carried out at very high latitudes, it was interesting to compare the results of GPS and GLONASS observations. GLONASS satellites have a higher inclination of the orbit, which was done in order to improve positioning accuracy at high latitudes. As can be seen from the graphs, the TEC received from the GLONASS satellites is in good agreement with the data obtained by GPS and the data provided by CODE. As an advantage of GLONASS, it can be noted that during processing the number of filtered false values was less, in comparison with GPS.

It seems interesting to compare the series of the total electron content of the ionosphere of different years, since ionization of the ionosphere is caused by solar radiation. It can be seen that the characteristic seasonal features are repeated: a decrease in the TEC during the polar night. However, there is some difference. The figures shows the series for 2016 and 2018.

4. CONCLUSION

As a result of the work done a seasonal GNSS station was established at the Vostok Antarctic base. Observations in 2016 and 2018 were performed and processed. A comparison of the data shows that the characteristic seasonal features of the TEC change are repeated. In 2018, the changes were less drastic than in 2016. Comparison of data with independent sources shows the high reliability of our TEC values. The observations will be continued.

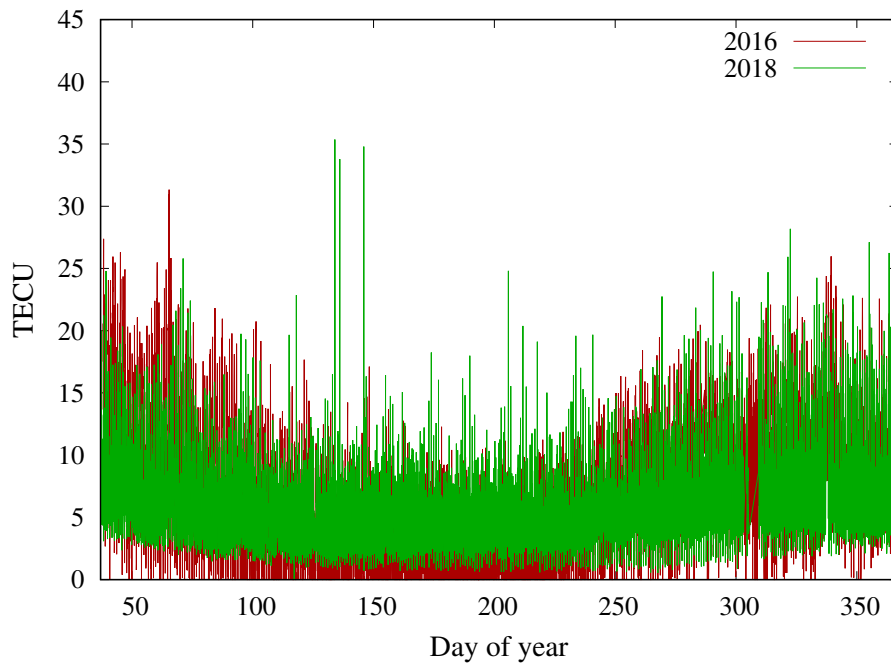


Figure 4: TEC depending on the time of year for 2016 and 2018

5. REFERENCES

- Mahdi M. Alizadeh, Dudy D. Wijaya, Thomas Hobiger, Robert Weber, and Harald Schuh, 2013, "Ionospheric Effects on Microwave Signals", Springer Berlin Heidelberg, Berlin, Heidelberg, pp. 35–71.
- Emlia Correia, Amanda Junqueira Paz, Mauricio A. Gende, 2013, "Characterization of GPS total electron content (GPS-TEC) in Antarctica from 2004 to 2011", *Annals of Geophysics* 56(2), doi:10.4401/ag-6223
- Pramod Purohit, Dr. Purushottam Bhawre, Azad Mansoori, Parvaiz Khan, and A. Gwal, 2011, "GPS derived Total Electron Content (TEC) variations over Indinan Antarctica station, Maitri", *World Academy of Science, Engineering and Technology* 59 pp. 597–599.
- Sulaiman, S., Ali, M.S., and Yatim, B. 2007, "Ionospheric GPS-TEC observations at Scott Base Antarctica during 2004". 2007 Asia-Pacific Conference on Applied Electromagnetics, pp. 1–3.
- D. Trofimov, Y. Serov, S. Petrov, I. Chekunov, L. Shombina, 2017, "GNSS-observations on the Vostok station", II International Conference on Applied Science "Geodesy, cartography, geoinformatics and cadastre. From idea to application", pp. 74–80 (in russian).

ON THE CONSISTENCY BETWEEN LOCAL TIES AND SPACE GEODESY ESTIMATES IN THE SIMEIZ–KATZIVELY CO-LOCATION SITE

Ya.S. YATSKIV, O. KHODA

Main Astronomical Observatory of the National Academy of Sciences of Ukraine,
Kiev - Ukraine - yatskiv@mao.kiev.ua

ABSTRACT. The agreement between local ties of measuring points of the stations in the Simeiz–Katzively co-location site and space geodesy estimates of coordinates of these stations was quantified. There are large discrepancies (up to 120 mm) between these data, the reason for which needs a further study.

1. INTRODUCTION

The ITRF2014 construction depends on the availability of co-location sites where several instruments of different space geodesy techniques are operated and local surveys between instrument measuring points are available (Altamimi et al., 2017).

One of those co-locations sites is the Simeiz–Katzively site (Figure 1) that is situated on the south coast of the Crimea, Ukraine (Yatskiv et al., 2014). There are five stations of space geodesy techniques located on the site: RT–22 radio telescope (IVS name: CRIMEA, IVS code: Sm, CDP number 7332), two SLR stations — Simeiz (ILRS code: SIML, CDP Number 1873) and Katzively (ILRS code: KTZL, CDP number 1893), two GNSS stations — CRAO (IGS station) and KTVL (EPN station). On early 1990s observations with a mobile SLR station was carried out on the ground marker SIME (CDP number 7561) that is situated not far from the Simeiz SLR station. At present, coordinates and velocities of these stations are available in the ITRF2014 reference frame (Altamimi et al., 2016) at epoch 2010.0.

The Main Astronomical Observatory of the National Academy of Sciences of Ukraine (MAO NASU) performed on the Simeiz–Katzively site local survey geodetic campaigns in 1994 (Samoilenko, 1996), 2004 (Samoilenko et al., 2007), 2008 and 2011 (Odynets et al., 2013) as well as GNSS campaigns in 1994 (Bolotin et al., 1995), 2001 (Khoda, 2004), 2004 (Khoda, 2006), 2009 (Khoda, 2011). As the results corresponding local ties for measurement points of SLR and GNSS stations with respect to the position of the VLBI station (RT–22) at the epoch 2004.6 were estimated (Odynets et al., 2013) and has been provided the IERS Central Bureau.

2. PRELIMINARY ANALYSIS OF DATA

The ITRF2014 coordinates of the space geodesy stations on the Simeiz–Katzively site were propagated to the epoch 2004.6. Differences between coordinates of the SLR and GNSS stations with respect to the coordinates of the VLBI station (RT–22 radio telescope) will set the so-called “catalogue values” of local ties on the site.

Variations of the distances ΔR , defined as $(\Delta R)^2 = (\Delta X)^2 + (\Delta Y)^2 + (\Delta Z)^2$, where ΔX , ΔY and ΔZ are survey geodetic local-tie values, are shown in Figure 2 as differences between values ΔR and their mean values. The types of lines are the same for the stations or markers located on the same areas of the site (the first is around the RT–22 radio telescope, the second is around the Katzively SLR station and the third is around the Simeiz SLR station).

The maximum variation of distances for markers around the RT–22 radio telescope (KTRT,

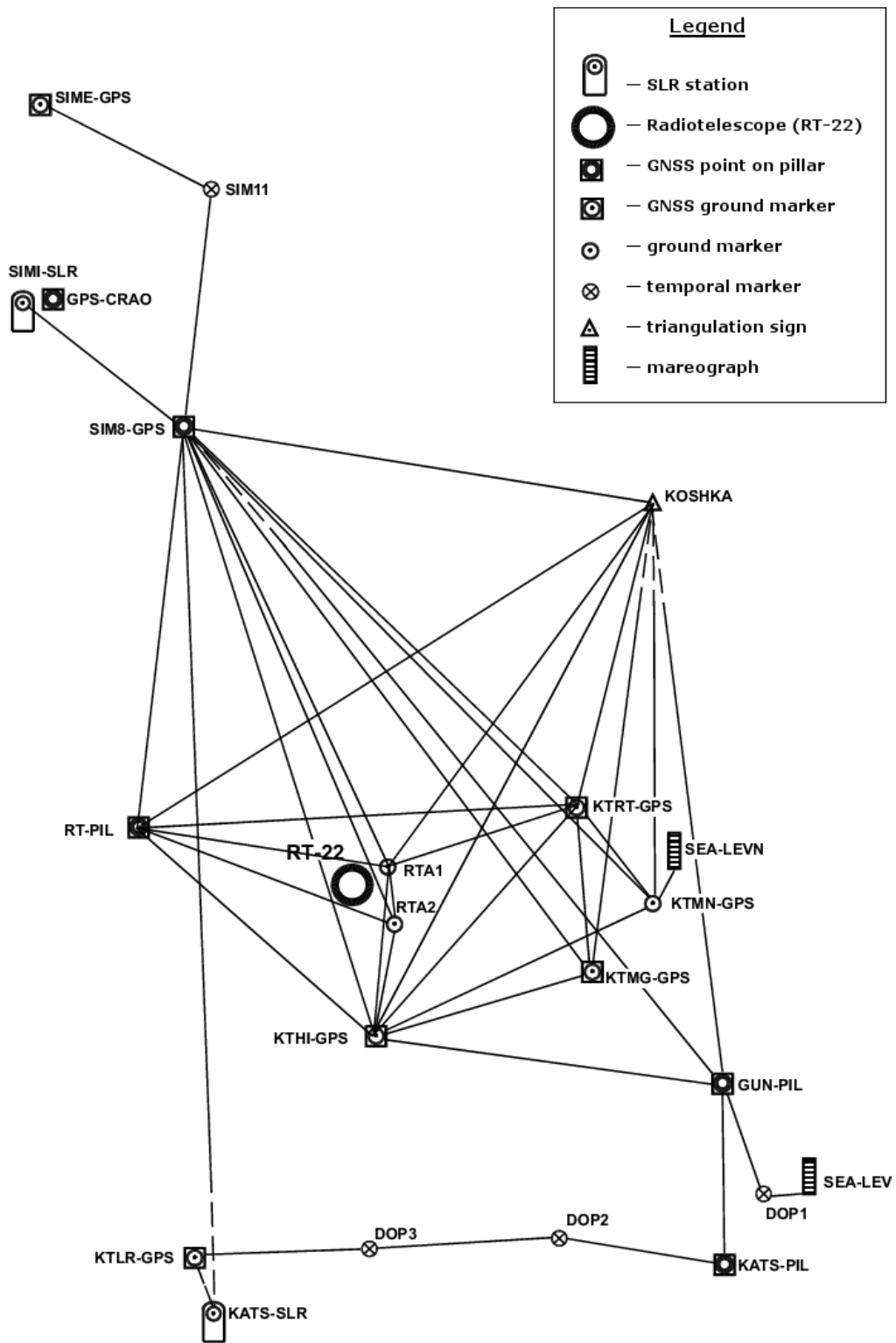


Figure 1: The Simeiz–Katzively site

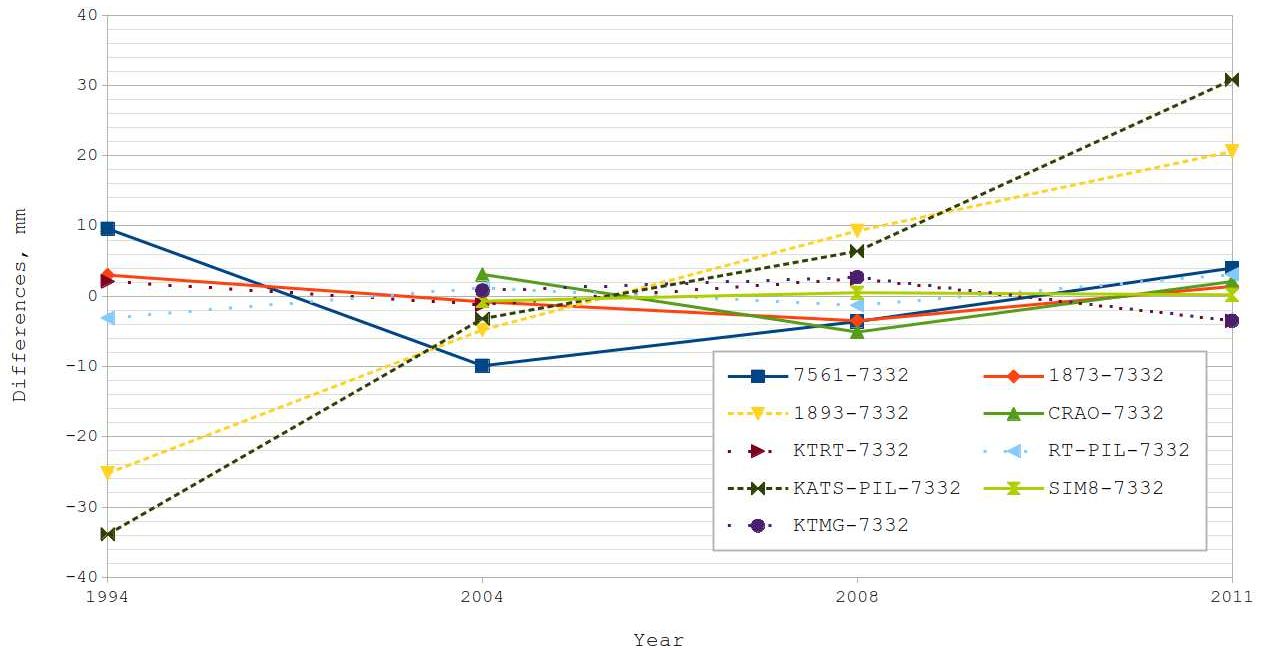


Figure 2: Differences between estimated distances ΔR on the Simeiz–Katzively site and their mean values

KTMG, RT–PIL) is 3.5 mm. Approximately the same values are for both stations and the SIM8 marker located around the Simeiz SLR station: from 0.7 mm for SIM8 to 3.5 mm for 1873 and 5.1 mm for CRAO. The differences between the distances for the mobile SLR station (7561) and their mean value are in the range from -9.9 mm to 9.6 mm. Before campaigns in 1994 the centre of the marker 7561 was destroyed that may be one of a cause of possible errors of centring and determining the heights of the devices above the marker during measurements. Another possible source of this large variation is excavation works around the 7561 marker between campaigns.

The Katzively SLR station (1893) and the KATS–PIL marker have significant offsets relative to the RT–22 radio telescope. They are situated on the area that moves towards the sea in the south direction with non-negligible velocity.

3. CONSISTENCY BETWEEN LOCAL TIES AND SPACE GEODESY ESTIMATES

As pointed out by Altamimi et al. (2017), quantifying the level of agreement between survey geodetic local ties and space geodesy estimates of relative positions of the stations is very critical for further investigation of the ITRF. Therefore the station position residuals (or tie discrepancies) for the Simeiz–Katzively co-location site were computed. The obtained differences $d(\Delta R)$ between survey geodetic local tie distances and space geodesy catalogue distances on the site are shown in Figure 3.

It is easy to see that line for 1893–7332 differences (for distances between the Katzively SLR station and the RT–22 radio telescope) exhibits peculiar behaviour. We know that the velocities for both the SLR stations on the Simeiz–Katzively site have the same values in the ITRF2014 catalogue. But as mentioned above the area around the Katzively SLR station has significant local movements. One can compare velocities values in the catalogue for the Katzively SLR station

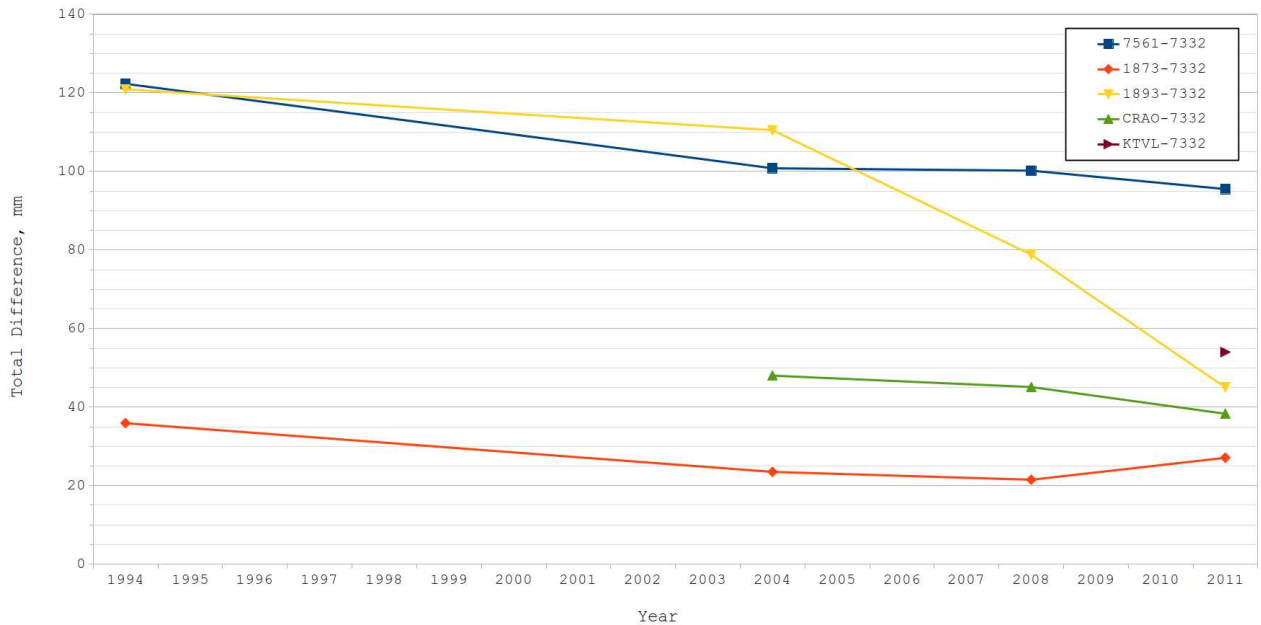


Figure 3: Differences $d(\Delta R)$ between estimated and catalogue distances on the Simeiz–Katzively site

(1893) and the GNSS station KTVL that located near it, especially for Z component.

$$\begin{aligned}
 V_X(1893) &= -0.01742 \text{ m/y}, & V_X(KTVL) &= -0.01967 \text{ m/y}, \\
 V_Y(1893) &= 0.01914 \text{ m/y}, & V_Y(KTVL) &= 0.01766 \text{ m/y}, \\
 V_Z(1893) &= 0.00819 \text{ m/y}, & V_Z(KTVL) &= -0.00106 \text{ m/y}.
 \end{aligned}$$

The residuals which are shown in Figure 3 are very large (up to 120 mm). Reasons for these discrepancies could be both namely due to errors in survey geodetic local ties and in the ITRF2014 estimates of space geodesy coordinates for the Simeiz–Katzively site. Identifying the error sources needs further study.

At first glance, it is obvious that during the construction of the ITRF2014 local tie vectors between reference points on the Simeiz–Katzively site were not taking into account. Velocities of the SLR stations 1873 and 1893 in the ITRF2014 are the same that contradicts the data shown in Figure 2. Taking into account the significant local movements of the area around the Katzively SLR station, for future ITRS realizations this area should be considered as a separate site.

4. REFERENCES

- Altamimi, Z., Rebischung, P., Métivier, L., Collilieux, X., 2016, “ITRF2014: A new release of the International Terrestrial Reference Frame modeling nonlinear station motions”, *J. Geophys. Res. (Solid Earth)* 121(8), pp. 6109–6131, doi:10.1002/2016jb013098.
- Altamimi, Z., Rebischung, P., Métivier, L., Collilieux, X., 2017, “Analysis and results of ITRF2014 (IERS Technical Note; 38)”, Frankfurt am Main: Verlag des Bundesamts für Kartographie und Geodäsie, 76 pp.
- Bolotin, S., Gaiovitch, I., Khoda, O., Samoilenko, A., Yatskiv, Ya., 1995, “GPS observational campaign in the geodynamics test area “Simeiz–Katsiveli”: Data Processing and Results”, *Space Science and Technology Supp.* 1(2), pp. 1–16.
- Khoda, O., 2004, “GPS Campaign in Crimean Test Area “Simeiz–Katsiveli” in 2001: Data Processing” *Kinematics Phys. Celest. Bodies* 20(6), pp. 360–367.

- Khoda, O., 2006, "GPS-campaign in Crimean Test Area "Simeiz–Katsively" in 2004", Proc. International Science-Practical Conference "New Achievements of Geodesy Geoinformatics and Land Information System — European Experiences", Chernihiv, pp. 29–32 (In Ukrainian).
- Khoda, O., 2011, "GNSS campaign in the local test area Simeiz–Katzively in 2009", Proc. International Science-Practical Conference "New Achievements of Geodesy Geoinformatics and Land Information System — European Experiences", Chernihiv, pp. 21–24 (In Ukrainian).
- Odynets, P., Samoilenko, O., Yatskiv, Ya., 2013, "Study of the Earth surface deformations and local ties of astronomy-geodetic instruments at the Crimean geodynamics test area Simeiz–Katzively", Bull. Ukrainian Centre of Determination of the Earth Orientation Parameters, 8, pp. 15–34 (In Russian).
- Samoilenko, A., 1996, "Local geodetic network at Simeiz geodynamics test area", Preprint of the MAO NASU, GAO–96–1R, 36 pp (In Russian).
- Samoilenko, O., Khoda, O., Zayets, V., 2007, "Some results of geodetic reffering of the radio telescope and SLR stations to GPS markers in Crimean Geodynamical Test Area Simeiz–Katsyveli", Kinematics Phys. Celest. Bodies 23(1), pp. 1–6, doi:10.3103/S0884591307010011.
- Yatskiv, Ya., Odynets, P., Volvach, O., 2014, "The "Simeiz–Katzively" co-location site of space geodesy techniques: Current state and future activity, Proc. Journées 2013 "Systèmes de référence spatio-temporels": Scientific developments from highly accurate space-time reference systems, Paris, pp. 216–219.

Session IV

EARTH ROTATION AND GEODYNAMICS

2. MODELS

ATMOSPHERIC ANGULAR MOMENTUM RELATED TO EARTH ROTATION STUDIES: HISTORY AND MODERN DEVELOPMENTS

D. SALSTEIN

Atmospheric and Environmental Research - USA - dsalstei@aer.com

ABSTRACT. It was noted some time ago that the angular momentum of the atmosphere varies, both regionally as well as in total. Given the conservation of angular momentum in the Earth system, except for known external torques, such variability implies transfer of the angular momentum across the atmosphere's lower boundary. As nearly all is absorbed by the Earth below, the solid Earth changes its overall rotation from this impact. Due to the large difference between in the moments of inertia of the atmosphere and Earth, relatively big differences in the atmosphere are translated as relatively very small differences in the Earth, measurable as changes in Earth rotation rate, and polar motion. The atmospheric angular momentum (AAM) is that due to the motion of the winds and to the changes in mass distribution, closely related to the atmosphere pressure patterns; its variability in the atmosphere is mirrored in the Earth rotation rate and polar motion. This connection between the global solid Earth properties and the global and regional atmosphere on a number of time scales, especially seasonal and interannual, was much appreciated by Barbara Kolaczek, with Jolanta Nastula, at the Space Research Center in Warsaw, and this was a subject of our collaborative studies. Many calculations were made of atmospheric angular momentum, leading to a service under the Global Geophysical Fluids Center of the IERS based on calculations using both operational meteorological series, determined for weather forecasting purposes, and retrospective analyses of the atmosphere. Theoretical development of the connection between the AAM, Earth rotation/polar motion, and also the angular momentum of the other geophysical fluids occurred at the same time that space-based observations and enhanced computer power were allowing improved skills for both weather analysis and forecasting. Hence better determination of the AAM became possible, which could be used as a measure for forecasting Earth rotation. Today we are looking at the atmosphere in combination with the ocean and other fluids, and also assessing the implications of climate variability on Earth rotation through climate model research. According to models of the Earth system, significant changes in winds appear to be a possible result of climate change, with implications for the Earth rotation parameters.

1. INTRODUCTION

Variations in the angular momentum of the atmosphere have been shown to be strongly related to changes in the Earth orientation parameters due to the conservation of angular momentum in the Earth system. The atmosphere (and the ocean) can be modeled based on physical equations. We discuss how atmospheric angular momentum is measured and calculated and its relationship to climate signals. Angular momentum of the atmosphere varies on a number of important timescales, including seasonal, sub season, and inter annual, and all of these manifest in the related Earth orientation signal.

Dynamically, angular momentum in a system changes by means of torques upon the system, and this is true in the exchange of angular momentum between the atmosphere and the solid Earth. Specifically, the main mechanisms causing these torques are normal torques against topography by varying atmospheric pressure, and tangential torques from the lowest level of the winds upon the Earth's surface.

Long-period models of the atmosphere and ocean show what has happened and might happen in the future to angular momentum. The Coupled Model Intercomparison Project (CMIP) is an effort to run multiple climate models, and determine the physical parameters in the future. Potential global change in the winds and pressures point to changes in Atmospheric Angular Momentum throughout the past and present centuries.

This presentation is dedicated to the memory of Prof. Barbara Kolaczek of the Space Research Institute, Warsaw, Poland, with whom I collaborated with for many years. I was inspired by her scientific insight and curiosity, determination, and genuine kindness.

2. METHODS TO DETERMINE ATMOSPHERIC ANGULAR MOMENTUM

Concerning the atmosphere, we need to have observations from the surface, upper air, and from space. In order to use all of these observations, there are a number of methods of combining them with each other and with modeled information. The model itself is based on physical principles. The backbone of the meteorological data is the radiosonde network of instruments that are launched at a network of weather stations around the globe. In addition data from microwave instruments in polar or oblique orbits, and infrared observations from geostationary satellites are needed used as well. Information from GPS receivers yields temperature and moisture data. Data from the nosecones of aircraft flying through their scheduled routes are also brought into the mix. Additionally ocean measurements such as those from buoys, and expendable bathythermographs are used.

To put the information together, the observations are merged into an analysis whose basic state is the short-term (typically 6-hour) forecast of a meteorological model. Geodetic functions are calculated from the raw parameters of the new fields. Also, these fields become the base of new forecasts both to carry on until the next assimilation time 6-hours later, or for more extended weather forecasts, often out to 10 days or so.

Atmospheric models are expressed from physical principles. The equations of motion about an axis in the rotating frame form the most important part of the framework. In this case the torques which cause changes in angular momentum are products of the moment of inertia and the angular acceleration. A second important equation is the equation of thermodynamics, in which heat imposed on a system is the increase in temperature multiplied by the specific heat, plus the work done by expansion. A third physical law is conservation of mass in which inflows of mass are balanced by divergence in the absence of changes in local density. Conservation of mass applies to both dry air and water vapor.

3. HISTORICAL CONTEXT OF VARIABLE EARTH ROTATION CONNECTION TO ATMOSPHERIC ANGULAR MOMENTUM

The earliest observations of changes in length of day were made at Paris Observatory by Stoyko and Stoyko (1936), who observed the annual variation of length of day. In 1948, Victor Starr of the Massachusetts Institute of Technology (MIT) noted that the atmosphere need not conserve angular momentum, and could share it with the Earth below. Starr started the *General Circulation Project* at MIT, and one of its features was calculations of fluxes and changes in atmospheric angular momentum. Walter Munk and his collaborators calculated atmospheric angular momentum and wrote about connections to Earth rotation variations (Munk and MacDonald, 1960). Lambeck and Cazenave (1973) of Paris Observatory made use of the MIT data to determine the excitations of Earth rotation. Subsequently this connection was continued: Feissel and Gambis (1980) analyzed intraseasonal oscillations in geodetic study, followed by Langley et al. (1981) of the same timescales in the atmosphere.

Raymond Hide was instrumental in codifying the theory of the relationship of length of day and polar motion from atmospheric models in Barnes et al. (1980). This formalism was used for

calculations by the Sub-bureau for Atmospheric Angular Momentum, an agency of the International Earth Rotation and Reference System Service (IERS). Salstein et al. (1993) organized the service based on operational weather analyses from four meteorological centers: US National Centers for Environmental Prediction, the European Centre for Medium-Range Weather Forecasts, the United Kingdom Meteorological Agency, and the Japan Meteorological Agency. The Sub-bureau was later renamed the Special Bureau for the Atmosphere of the Global Geophysical Fluids Center (GGFC/IERS). Later, the procedures were later updated in Zhou et al. (2006) using more accurate integration techniques and updated geophysical parameters. Besides calculations from operational meteorological series, during the period of operation of the special bureau, Reanalyses of the atmosphere became available and were routinely produced as well. Such series go back to use all raw observational meteorological data and in order to reconstruct the fields of the atmosphere. From the reanalyses, we were able to calculate the angular momentum parameters to produce a more consistent result. The best known of these series have been the NCEP-NCAR reanalysis (U.S. National Centers for Environmental Prediction-National Center for Atmospheric Research), the ERA (European Centre Reanalyses), the the MERRA analysis from the US National Aeronautics and Space Administration.

Efforts to use analysis and forecasts of AAM as a proxy for Length-of-day were used by Rosen et al. (1987) and at the US Naval Observatory by Johnson et al. (2005) and with later improvements by Stamatakos et al. (2018), including the use of the NAVGEM (U.S. Navy Global Environmental Model and HYCOM (Hybrid Coordinate Ocean Model). At the GeoforschungsZentrum (GFZ), Dill et al (2019) used ECMWF models, with ocean, land hydrology and sea-level models. At Vienna University of Technology, an archive was established of atmospheric information for many geodetic purposes (see Böhm and Schuh, 2013). Quite a bit of research was done on the connections between AAM and Earth rotation parameters on time scales from seasonal (e.g. Höpfner et al., 2001) and inter annual, including signals of the 2.2 year quasi-biennial oscillation and El Niño/Southern Oscillation (especially J. Dickey at the Jet Propulsion Laboratory). Exhaustive survey of these agreements was made by N. Sidorenkov in many publications and books.

4. METHODS TO DETERMINE ATMOSPHERIC ANGULAR MOMENTUM AND CURRENT THEMES

AAM has three components. The axial component is to be compared with variations in the rotation rate of the Earth, reckoned in changes in the length of day. The two components about the equatorial axes may be related with change in the motion of the Earth's pole.

In discussing length of day, it is noted that the excess length of day has had variations on many time scales, from the century to decadal to the very high frequency. The C04 series of Earth rotation, from Paris Observatory maintains the long term stability of this series. Variations on sub-decadal scales down to a few days have been noted to be related to AAM. Formulas relating the atmospheric series (Barnes et al., 1983) include volume integrals through the atmosphere for the wind terms (known as u , the axial, or eastward or westerly, wind, and v , the meridional, or northward or southerly, winds). Integrals on the surface of the Earth relating to the surface pressure (or p_s), approximate the mass term, because the total mass above a point on the surface, per area, multiplied by the gravitation field, is approximately equivalent to the surface pressure, given an assumption of hydrostatic equilibrium. Lastly, the so-called inverted barometer approximation has generally been invoked to estimate the effect of a modified mass term in the ocean that counteracts the changes in atmospheric mass over each point in the ocean. However, the equilibrium time for the inverted barometer to hold is generally a few days or more.

The axial AAM is determined from different geographical regions in the manner as noted above. In the annual mean, most of the atmosphere is positively oriented, which is to say that the mean winds are from the west to the east. This movement of the air has positive angular momentum

by convention. These mean westerlies exist throughout the subtropics, middle latitudes, and peak in the 30-40 degree latitude zone in both hemispheres, near the 200 hPa level due to jets at these areas. In contrast, negative values of the angular momentum occurs in the mean between the subtropics of each hemisphere and the tropics in the lower part of the atmosphere. These winds flow predominantly from east to west, and are often known as the trade winds.

An important interannual signature is known as the El Niño/Southern Oscillation, whose basic characteristics are warm ocean surface temperatures in the upper levels of the Pacific off the coast of South America (El Niño) accompanied by a vacillation of atmospheric mass across the breadth of the Pacific Ocean (Southern Oscillation). The oscillation period is approximately 4 years. Some El Niño events are stronger than others, but in recent decades particularly important ones occurred in 1982-83, 1997-98, and 2014-16.

Whereas angular momentum is exchanged between the solid Earth and the geophysical fluids, leading to the equivalence of AAM and LOD variations, there must be a dynamic mechanism to effect such changes. Torques do exist to foment the changes in angular momentum. Typically two principal torque mechanisms occur either as normal or as tangential forces over the Earth surface. The so-called mountain or topographic torque occurs when differential pressure on opposite side of topographic features yield a force and interpreted as a torque at the distance to the Earth's axis. These occur largely on the time scales when weather phenomena are changing, on the order of several days to a week. A second type of torque is a result of winds blowing across the surface, where tangential friction is a drag force between the atmospheric fluid and the solid Earth. It has time scales from the highest frequency of days, to sub-seasonal. A third torque is derived as gravity-wave drag that simulates the forces on spatial scales smaller than the grid points of models in use.

On long time scales, from decadal to century, the angular momentum of the Earth, and hence the Length-of-Day, have varied in part due to tidal exchanges from the moon, and exchanges of angular momentum with the Earth's liquid core. However, the atmosphere also has variability on the decade-to-century scales. A dedicated project known as the Climate of the 20th Century, is based only on atmospheric surface pressures back to approximately 1870; this is the only consistent observational data set back that far.

Currently, an important theme of research is running experiments with climate models to determine what the future might be under certain scenarios. The Climate Model Intercomparison Project (CMIP) uses atmosphere and ocean models coupled to each other, and in cases, land-surface models as well to examine the state of the atmosphere based on possible changes in the composition of the atmosphere for sociological and economic reasons, mostly due to the imposition of new greenhouse gases. We have taken the mass and motion fields from the atmospheric portion of the CMIP project to determine that under increased carbon dioxide in the atmosphere, the composition of the winds in the atmosphere may change (Salstein et al., 2012). In particular, increases in the westerly winds, especially at the high altitude levels will be accompanied by increased axial angular momentum. Such increases may occur up to about 10% of the current relative angular momentum of the atmosphere by the end of the 21st century. Further explanations and results are given in the proceedings of this meeting in the paper of Böhm and Salstein.

Variations in polar motion have also been driven by the geophysical fluids, the atmosphere and the ocean. There were many efforts to determine the origins of atmosphere-driven polar motion variations. Links especially were found to areas over Eurasia and North America where weather systems bring strong variations of mass in the form of fluctuations of weather systems (Nastula et al., 2005). In addition, mass changes from land-based hydrology, have been noted as being important to excitations of polar motion. Such information has been determined from atmospheric analyses, land hydrology models, and fields from the Gravity Recovery and Climate Experiment (GRACE) (Nastula et al., 2007).

In conclusion, the atmosphere is a mobile and variable component of the Earth system. Even

though it is so much less massive than the solid Earth, the changes are visible in the angular momentum of the solid Earth, and hence the Earth rotation parameters itself.

5. REFERENCES

- Barnes R.T.H., Hide, R., White, A.A., Wilson, C.A., 1983, "Atmospheric angular momentum fluctuations, length-of-day changes, and polar motion", *Proceedings Royal Society A*, 387, pp. 31–73.
- Böhm, J., and Schuh, editors, 2013, "Atmospheric Effects in Space Geodesy", Springer.
- Dill, R., Dobsław, H., Thomas, M., 2019, "Improved 90-day Earth orientation predictions from angular momentum forecasts of atmosphere, ocean, and terrestrial hydrosphere", *J. Geodesy* 93, pp. 287–295.
- Feissel, M., Gambis, D., 1980, "La mise en évidence des variations rapides de la durée du jour", *Comptes Rendus Acad. des Sciences de Paris, B* 291, pp. 271–273.
- Höpfner, J., 2001, "Atmospheric, oceanic and hydrological contributions to seasonal variations in length of day", *J. Geodesy* 75, pp. 137-150.
- Johnson, T., Luzum, B., Ray, J., 2005, "Improved near-term Earth rotation predictions using atmospheric angular momentum analysis and forecasts", *J. Geodynamics* 38, pp. 209–221.
- Lambeck, K. and Cazenave, A., 1973, "The Earth's Rotation and Atmospheric Circulation" I Seasonal Variations", *Geophys. J. Int.* 32, pp. 79–93.
- Langley, R. B., King, R. W., Shapiro, I.I., Rosen, R. D., Salstein, D. A., 1981, "Angular momentum and the length of day: a common fluctuation with a period near 50 days", *Nature* 294, pp. 730–732.
- Munk, W. and MacDonald, G., 1960, "The Rotation of the Earth: a Geophysical Discussion".
- Nastula, J., Salstein, D., Kolaczek, B., 2005, "Patterns of atmospheric functions of polar motion from high-resolution regional sectors", *J. Geodynamics* 39, pp. 209–221.
- Nastula, J., Ponte, R.M., Salstein, D., 2007, "Comparison of polar motion excitation series derived from GRACE and from analyses of geophysical fluids", *Geophysical Research Letters*, 114, B04407, doi:10.1029/2008JB005605.
- Rosen, R.D., Salstein, D.A., Nehrkorn, T., McCalla, M.R.P., Miller, A.J., Dickey, J.O., Eubanks, T.M., Steppe, J.A., 1987, "Medium-range numerical forecasts of atmospheric angular momentum", *Monthly Weather Review* 115, pp. 2170–2175.
- Salstein, D., Kann, D.M., Miller, A.J. and Rosen, R.D., 1993, "The Sub-bureau for Atmospheric Angular Momentum of the International Earth Rotation Service: A Meteorological Data Center with Geodetic Applications", *Bulletin American Meteorological Society* 74, pp. 67–80.
- Salstein, D., Quinn, K. J., and Abarca del Rio, R., 2012, "Using Coupled Climate Models for Predictions of Angular Momentum", presentation at the 92nd American Meteorological Society Annual Meeting, New Orleans.
- Stamatakis, N., McCarthy, D., and Salstein, D., 2018, "Updates on the use of Atmospheric and Ocean Angular Momentum for Earth Orientation within the IERS Rapid Service/Prediction Center", *American Geophysical Union Fall Meeting*.
- Starr, V., 1948, "An essay on the general circulation of the Earth's atmosphere", *J. Meteorology* 5, pp. 39–43.
- Stoyko N., and Stoyko, A., 1936, "Sur l'irrégularité de la rotation de la Terre", *Comptes Rendus Acad. Ici. Paris.* 203, pp. 39–40.
- Zhou, Y.H., Salstein, D.A., and Chen, J.L., 2006, "Revised atmospheric excitation function series related to Earth's variable rotation under consolidations of surface topography", *J. Geophys. Res.* 111, D12108, doi:10.1029/2005JD006608.

PROGRADE AND RETROGRADE TERMS OF GRAVIMETRIC POLAR MOTION EXCITATION ESTIMATES FROM THE NEWEST GRACE GRAVITY FIELD MODELS

J. ŚLIWIŃSKA, J. NASTULA

Space Research Centre, Polish Academy of Sciences - Poland

jsliwinska@cbk.waw.pl, nastula@cbk.waw.pl

ABSTRACT. In this study, we computed hydrological polar motion excitation functions (Hydrological Angular Momentum, HAM) from two recent releases of GRACE (Gravity Recovery and Climate Experiment) monthly gravity field models, RL05 and RL06. In contrast to the previous works, here, the equatorial components of polar motion excitation functions (χ_1 and χ_2) were decomposed into prograde (χ_P) and retrograde (χ_R) time series by applying Complex Fourier Transform (CFT). The computed series were evaluated by comparison with the hydrological signal in observed polar motion excitation (geodetic residuals, GAO). We examined temporal variations of HAM series in seasonal and non-seasonal spectral bands. We showed that both χ_P and χ_R terms of HAM can be determined by GRACE satellites with congruous levels of accuracy. We also demonstrated that the new GRACE RL06 data increased the consistency between solutions from different data centres and improved the agreement between GRACE-based HAM and GAO.

1. INTRODUCTION

It is commonly known that for time scales of a few years or shorter, the main contributors to polar motion (PM) excitation are variations in global mass distribution of atmosphere, ocean and continental hydrosphere. The atmospheric and oceanic contributions have been well-established (Gross et al. 2003; Nastula et al. 2007; 2009) but HAM is believed to be the main source of uncertainties in PM excitation. It was shown in recent researches that compared to Hydrological Angular Momentum (HAM) estimations obtained from either hydrological or climate models, GRACE-based HAM functions were in better agreement with hydrological signal in observed PM excitation (Nastula et al. 2019; Seoane et al. 2011; Śliwińska et al. 2019).

Recently, the official GRACE data centres have been released new GRACE RL06 solutions and the first efforts to evaluate these data have been made in the work of (Göttl et al. 2018). That paper showed that both the consistency between particular solutions and the agreement between HAM and GAO have increased when applying the newly processed GRACE data.

A common method to describe PM excitation is the use of two equatorial components of this function, χ_1 and χ_2 . However, the polar motion excitation exhibits two circular terms: retrograde (clockwise) and prograde (counter-clockwise). In previous works, the PM excitation was generally decomposed into prograde and retrograde terms but at one fixed frequency. In this study, we considered the total prograde (χ_P) and retrograde (χ_R) parts of PM excitation function. We reconstructed these terms in time domain from χ_1 and χ_2 with the use of Complex Fourier Transform (CFT) (Bizouard 2016). The circular terms of investigated series were then separated into seasonal and non-seasonal oscillations.

The objective of this study was to consider what the new GRACE RL06 solutions might contribute to the understanding of residual PM excitations as observed by space geodesy techniques. Here, we validated HAM series from the new GRACE RL06 and from previous GRACE RL05 data, using observed hydrological signal in PM excitation, derived from precise measurements of pole

coordinates (geodetic residuals, GAO). The GRACE estimations of HAM were also compared with the HAM from Land Surface Discharge Model (LSDM).

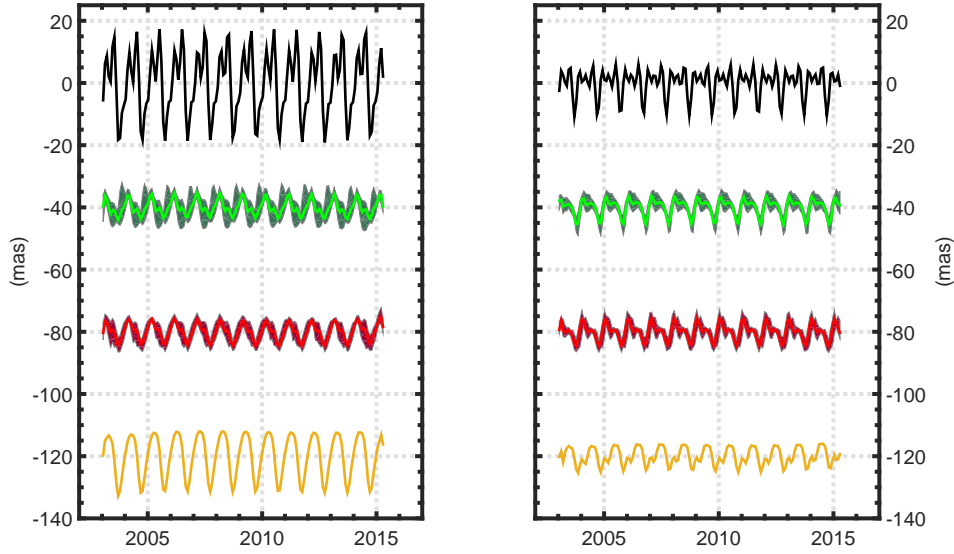


Figure 1: Retrograde (left) and prograde (right) parts of the seasonal HAM variation. Black line: GAO. Green and red lines: old and new averaged GRACE solutions respectively with the range between minimum and maximum values of the 5 individual solutions. Yellow line: LSDM model.

2. DATA SETS

2.1 Geodetic residuals (GAO)

The χ_1 and χ_2 components of the observed geodetic PM excitation function (Geodetic Angular Momentum, GAM) can be computed from observed coordinates (x , y) of the Earth pole which are routinely delivered as daily C04 series of Earth Orientation Parameters (EOP). In order to separate hydrology-related effects from GAM, the atmosphere and ocean angular momentum should be removed (AAM and OAM functions, respectively). The resulting residual series are denoted as geodetic residuals (GAO). In this study, GAM, obtained from the EOP 14 C04 series, were taken from the International Earth Rotation and Reference Systems Service (IERS) website (<https://www.iers.org/>). For mass terms of atmosphere and ocean, we used GAC JPL RL06 time series of ΔC_{21} , ΔS_{21} coefficients of the GRACE non-tidal atmosphere and ocean de-aliasing data, available from <https://podaac-tools.jpl.nasa.gov/drive/files/allData/grace/L2/JPL/RL06>. Motion terms of AAM were computed by the GFZ from the European Centre for Medium-range Weather Forecasts (ECMWF) model and accessed from <ftp://esmdata.gfz-potsdam.de/./EAM/>. For motion terms of OAM, we used the series provided by GFZ and computed from Max Planck Institute Ocean Model (MPIOM).

2.2 HAM functions from GRACE

Here, we evaluated monthly GRACE satellite-only models (GSM), also denoted as GRACE Level-2 data. In order to compute HAM, we converted ΔC_{21} , ΔS_{21} coefficients of the geopotential into χ_1 and χ_2 equatorial components of mass-related PM excitation function, based on formulas given in (Gross 2015). In this paper, we used the GRACE GSM fields provided by five different pro-

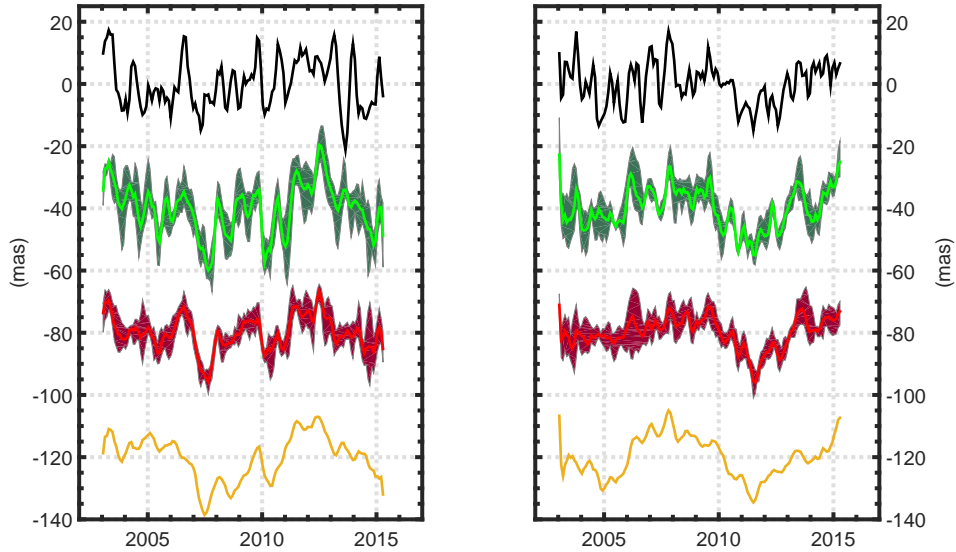


Figure 2: Retrograde (left) and prograde (right) parts of the non-seasonal HAM variation. Black line: GAO. Green and red lines: old and new averaged GRACE solutions respectively with the range between minimum and maximum values of the 5 individual solutions. Yellow line: LSDM model.

processing centres: Center for Space Research (CSR RL05 and CSR RL06 solutions), Jet Propulsion Laboratory (JPL RL05 and JPL RL06 solutions), GeoForschungsZentrum (GFZ RL05 and GFZ RL06 solutions), Centre National d'Études Spatiales (CNES RL03 and CNES RL04 solutions), Institute of Theoretical Geodesy and Satellite Geodesy of the Graz University of Technology (ITSG 2016 and ITSG 2018 solutions).

2.3 HAM and SLAM functions processed by GFZ

We also considered HAM computed from the Land Surface Discharge Model (LSDM) and provided by GFZ (<ftp://esmdata.gfz-potsdam.de/./EAM/>). It should be kept in mind that both GRACE and GAO include barystatic sea level changes due to inflow of water from lands into the oceans (sea-level angular momentum, SLAM) but SLAM is not included in hydrological models. Therefore, to make LSDM-based HAM more comparable with GAO and GRACE estimates, we added SLAM to it. These SLAM series are also provided by the GFZ.

3. RESULTS

Figure 1 compares the prograde and retrograde values of seasonal HAM for the GRACE RL05 and RL06 averaged solutions. For each averaged values, we display the range between minimum and maximum values of the 5 GRACE individual solutions, mentioned above. Time series of GAO and HAM from the LSDM model (with SLAM added) are provided for comparison. It is clear that updating some background models and processing algorithms in the GRACE RL06 data resulted in increased compatibility of HAM between solutions from different data centres (indicated by reduced range), especially for the χ_R term. Notably, the χ_R part for the GRACE-based mean HAM data underestimated seasonal variations of both GAO and LSDM-based HAM. Figure 2 replicates Figure 1 but for the non-seasonal variations. It showed that non-seasonal variations were characterized by bigger amplitudes than seasonal ones, which was especially visible for GRACE data. With the new GRACE RL06 solutions, different estimations of HAM were more similar to each other but

visible discrepancies were still present. Nevertheless, the HAM from the mean of all new GRACE solutions revealed to be more consistent with GAO and LSDM-based HAM than the HAM from any single GRACE solution. In order to assess the variability of analysed time series, we computed their standard deviation (STD), shown in Table 1. For seasonal variations, the χ_P and χ_R parts reveal rather similar STD within each GRACE solution. Notably, almost all GRACE solutions underestimate the STD of HAM (except χ_R for JPL RL05), and this was more evident for the χ_R term. In terms of non-seasonal changes, the χ_R circular term variation appeared to be stronger than the χ_P term for most of the HAM series from old GRACE RL05 series (CSR RL05, JPL RL05, ITSG 2016, CNES RL03, except GFZ RL05), as indicated by the STD values (Table 1). For new GRACE RL06 data, χ_R is stronger than χ_P for HAM from CSR RL06, JPL RL06 and CNES RL04. GAO and HAM computed using LSDM are also characterized by biggest STD values for χ_R . In order to analyse the agreement between different HAM series and GAO, we computed correlation coefficients (Table 2) and relative explained variances (Table 3). The relative explained variances were computed using formulae shown in Śliwińska et al. 2020. Table 2 showed that for seasonal oscillations, the CSR RL06 solution provided the highest correlation of HAM with GAO (0.87) for the χ_R term, while the best result for the χ_P part was obtained for CNES RL03 and CNES RL04 (0.74 and 0.73 respectively). The highest relative explained variance was obtained for CSR RL06 in χ_R (51%) and for CNES RL03 and CNES RL04 in χ_P (49% and 52%, respectively). Notably, the HAM function obtained from LSDM revealed a very good agreement with the GAO series but only pertaining to the retrograde part (correlation coefficient of 0.74 and relative explained variance of 54%).

Table 1: Standard deviation of retrograde and prograde terms of GAO and HAM time series for seasonal and non-seasonal variation. The values are given in mas

Series	Seasonal		Non-seasonal	
	χ_R	χ_P	χ_R	χ_P
GAO	10.24	4.35	8.00	6.83
CSR RL05	3.29	3.08	8.20	7.37
CSR RL06	3.82	3.80	6.43	5.80
JPL RL05	4.95	4.69	11.83	6.49
JPL RL06	3.14	3.00	6.35	5.69
GFZ RL05	3.31	2.77	8.68	8.76
GFZ RL06	2.36	2.42	5.96	6.05
CNES RL03	2.73	2.22	8.12	7.71
CNES RL04	2.86	2.64	7.15	6.13
ITSG 2016	2.48	1.94	9.02	6.94
ITSG 2018	2.95	3.14	5.65	5.84
LSDM	6.75	2.72	7.20	6.61

In terms of non-seasonal HAM changes, the best correlation agreement with GAO for both χ_P and χ_R terms was observed for CSR RL06 (0.66 and 0.68 for χ_R and χ_P , respectively) and ITSG 2018 data (0.64 and 0.59 for χ_R and χ_P , respectively), and the highest relative explained variance was obtained for CSR RL06 (42% and 44% for χ_R and χ_P , respectively) and ITSG 2018 solutions (40% and 28% for χ_R and χ_P , respectively). For χ_P , LSDM-based HAM provided results comparable with those obtained for CSR RL06 and ITSG 2018.

4. CONCLUSIONS

In this study, we decomposed equatorial components of HAM (χ_1 and χ_2) into prograde and retrograde circular terms (χ_P and χ_R), using CFT. We evaluated χ_P and χ_R components of HAM

Table 2: Correlation coefficients of retrograde and prograde parts of seasonal and non-seasonal variation between GAO and different HAM. The critical value of the correlation coefficient for 25 independent points and a confidence level of 0.95 was 0.34. The standard error of the difference between two correlation coefficients for 25 independent points was 0.30

Series	Seasonal		Non-seasonal	
	χ_R	χ_P	χ_R	χ_P
CSR RL05	0.84	0.48	0.50	0.51
CSR RL06	0.87	0.62	0.66	0.68
JPL RL05	-0.57	0.31	0.45	0.56
JPL RL06	-0.07	0.08	0.50	0.35
GFZ RL05	0.67	0.40	0.42	0.67
GFZ RL06	0.84	0.58	0.30	0.48
CNES RL03	0.63	0.74	0.49	0.53
CNES RL04	0.60	0.73	0.48	0.56
ITSG 2016	0.80	0.28	0.49	0.57
ITSG 2018	0.68	0.64	0.64	0.59
LSDM	0.74	0.11	0.35	0.64

Table 3: Percentage of variance in GAO explained by HAM functions for retrograde and prograde parts of seasonal and non-seasonal variation. The values are given in %

Series	Seasonal		Non-seasonal	
	χ_R	χ_P	χ_R	χ_P
CSR RL05	43	18	-3	-6
CSR RL06	51	32	42	44
JPL RL05	-78	-50	-87	16
JPL RL06	-13	-37	16	-12
GFZ RL05	33	11	-26	8
GFZ RL06	34	34	-11	7
CNES RL03	27	49	-4	-8
CNES RL04	26	52	6	21
ITSG 2016	33	5	-15	13
ITSG 2018	31	41	40	28
LSDM	54	-25	-19	29

obtained from GRACE RL05 and RL06 series and from LSDM hydrological model by comparing them with hydrological signal confused with PM excitation residual (GAO). In contrast to χ_1 and χ_2 representation, where we observed significantly better results for χ_2 than for χ_1 component (see e.g. Nastula et al 2019, Śliwińska et al. 2019, 2020), the consistency with GAO was at the similar level for both χ_R and χ_P . The new GRACE solutions leads to an better consistency between χ_R and χ_P .

Despite different methods of representation, our general conclusions are similar to those drawn in works dedicated to χ_1 and χ_2 analyses. With the new GRACE data, the consistency between different solutions has been increased. HAM from the new RL06 GRACE data were more smoothed (smaller amplitudes and standard deviation) compared to HAM from RL05. The new GRACE solutions provide better correlation and variance agreement with observed PM excitation than the previous GRACE data. Despite improved correlation agreement with reference data, there is still no satisfactory amplitude and variance compatibility. For most of the oscillations considered, the highest agreement with reference data was obtained for CSR RL06 and ITSG 2018 solutions. The highest results improvement was detected for JPL.

We also noted that the HAM obtained from LSDM model is significantly correlated with GAO for the non-seasonal prograde and seasonal retrograde parts.

Acknowledgements. This research was funded by National Science Centre, Poland (NCN), grant number 2018/31/N/ST10/00209.

5. REFERENCES

- Bizouard, C., 2016, "Elliptic polarisation of the polar motion excitation", *J. Geodesy* 90(2), pp. 179–188, doi:10.1007/s00190-015-0864-7.
- Göttl, F., Schmidt, M., Seitz, F., 2018, "Mass related excitation of polar motion: an assessment of the new RL06 GRACE gravity field models", *Earth Planets Space* 70(1), doi:10.1186/s40623-018-0968-4.
- Gross, R., 2015. "Theory of earth rotation variations". Sneeuw, N., Novak, P., Crespi, M., Sanso, F. (Eds.), VIII Hotine-Marussi Symposium on Mathematical Geodesy, doi:10.1007/1345_2015_13S.
- Gross, R.S., Fukumori, I., Menemenlis, D., 2003, "Atmospheric and oceanic excitation of the Earth's wobbles during 1980-2000", *J. Geophys. Res. (Solid Earth)*, 108(B8), 2370, doi:10.1029/2002JB00214.
- Nastula, J., Wińska, M., Śliwińska, J., Salstein, D., 2019, "Hydrological signals in polar motion excitation - Evidence after fifteen years of the GRACE mission", *J. Geodyn.* 124, pp. 119–132, doi:10.1016/j.jog.2019.01.014
- Nastula, J., Ponte, R.M., Salstein, D.A., 2007, "Comparison of polar motion excitation series derived from GRACE and from analyses of geophysical fluids", *Geophys. Res. Lett.* 34(11), 2-7, doi:10.1029/2006GL028983.
- Nastula, J., Salstein, D.A., Kolaczek, B., 2009, "Patterns of atmospheric excitation functions of polar motion from high-resolution regional sectors", *J. Geophys. Res.* 114(B4), B04407, doi:10.1029/2008JB005605.
- Seoane, L., Nastula, J., Bizouard, C., Gambis, D., 2011, "Hydrological excitation of polar motion derived from GRACE gravity field solutions", *International Journal of Geophysics*, doi:10.1155/2011/174396.
- Śliwińska, J., Nastula, J., Dobslaw, H., Dill, R., 2020, "Evaluating gravimetric polar motion excitation estimates from the RL06 GRACE monthly-mean gravity field models", *Remote Sensing* 12(6), doi:10.3390/rs12060930.
- Śliwińska, J., Wińska, M., Nastula, J., 2019, "Terrestrial water storage variations and their effect on polar motion", *Acta Geophys.* 67(1), pp. 17–39, doi:10.1007/s11600-018-0227-x.

SECOND ORDER EFFECTS IN IAU2000 NUTATION MODEL

A. ESCAPA^{1,2}, J. GETINO³, J. M. FERRÁNDIZ², T. BAENAS⁴

¹ Universidad de León, Dept. Ingeniería Aeroespacial, León - Spain - alberto.escapa@ua.es

² Universidad de Alicante, Dept. Matemática Aplicada, Alicante - Spain

³ Universidad de Valladolid, Dept. Matemática Aplicada, Valladolid - Spain

⁴ Centro Universitario de la Defensa, Dept. Ciencias e Informática, Murcia - Spain

ABSTRACT. Second order effects, in the sense of perturbation theories, of IAU2000 nutation model (Mathews et al. 2002) are inherited from the Hamiltonian rigid Earth nutations REN2000 (Souchay et al. 1999). The transformation to IAU2000 non-rigid Earth model is made by applying the same frequency-dependent transfer function as in the case of first order nutations.

We analyze the nature of the second order effects considered in REN2000 and the used way to derive their corresponding non-rigid contributions. In addition, we discuss the existence of some additional second order terms that, in contrast to the rigid model, might play a role for the non-rigid Earth. The situation is exemplified for a Poincaré non-rigid Earth model, obtaining the second order nutations of the angular momentum axis (Poisson terms) by means of a Hamiltonian approach.

1. INTRODUCTION

Current accuracy demands in the Earth rotation modeling require the incorporation of terms previously neglected (e.g., Ferrándiz et al. 2020). Among them, one of the most important group is that referred to as second order terms. In fact, some of those terms were considered in the first works of the modern Earth rotation theories (e.g., Kinoshita 1977 or Kinoshita & Souchay 1990).

The nature of second order effects, however, is not uniform. We can distinguish between physical and mathematical second order terms. The first ones are due to interactions, Earth model features, etc. that have a small magnitude with respect to a reference value associated to the Earth rotational dynamics—typically the kinetic energy in the free rotational motion. Some representatives are higher order terms of the geopotential, direct effects of the inner core, etc. Once modeled, they can be incorporated into the theory following a standard first order, or linear, procedure.

The second ones are related to our (un)skill to solve the differential equations of the rotational motion. They emerge as a consequence of developing a more approximate solution to those equations. Their determination is cumbersome, specially if one is interested in obtaining analytical solutions, and many techniques have been historically developed to tackle with those terms (e.g., Ferraz-Mello 2007). Within our context the names second order effects in the sense of perturbation theories, nutation-nutation coupling, crossed-nutation effect, etc. belong to this kind of contributions and are equivalent.

In this article, we aim at sketching how these mathematical second order terms are currently incorporated in IAU2000 nutation model and why their treatment is neither consistent nor complete.

2. SECOND ORDER TERMS IN IAU2000

IAU2000 nutation model (Mathews et al. 2002) is based on a transfer function—or normalized amplitude—characterizing the features of the Earth model under consideration (three layers, anelastic mantle, etc.) which is applied to the rigid Earth Hamiltonian nutation series REN2000 (Souchay et al. 1999).

By doing so, the non-rigid nutations due to the lunisolar torque are obtained from the rigid

nutations of the Earth figure axis¹ described by the rigid amplitude nutation $\tilde{\eta}_R(t)$. This is accomplished by the product of $\tilde{\eta}_R(\sigma)$ with the transfer function $T(\sigma)$ in the frequency domain, where σ denotes the frequency of any spectral component of the gravitational potential relative to the rotating Earth and stemming from the orbital motion of the Moon and the Sun —see Mathews et al. (1991) for further details.

This way of obtaining the nutations is very useful, since it uses the rigid model as a proxy, avoiding the direct manipulation of the geopotential. In its derivation, however, it is implicitly assumed a first order theory of the rigid Earth (e.g., Mathews et al. 1991) what represents a limitation for its general application to higher orders of perturbation.

Indeed, the procedure of construction of the transfer function considers a relationship between the polar motion of the rigid Earth $\tilde{m}_R(\sigma)$ and the tesseral part of the second degree of the gravitational potential of the Earth $\tilde{\phi}(\sigma)$ given by

$$\tilde{m}_R(\sigma) = \frac{e}{e - \sigma} \tilde{\phi}(\sigma). \quad (1)$$

Here, $e = (C - A)/A$ is the ellipticity of the Earth with A the principal moment of inertia about any axis contained in the equatorial plane —passing through the Earth's center of mass— and C about the axis perpendicular to it.

Equation (1) is similar to the first order theory developed in Eqs. (6.22) and (6.23) by Kinoshita (1977), as it can be shown by a proper identification of the notations. In this regard, the Hamiltonian framework employs customarily the dynamical ellipticity $H_d = (C - A)/C$ instead of e . That dynamical ellipticity is included in the parameter k — k_M and k_S — related to the perturbers and considered in those theories. Specifically, we have

$$k_{M,S} = 3 \frac{GM_{M,S}}{a_{M,S}^3 \omega_E} H_d. \quad (2)$$

The linear e dependence in the numerator of Eq. (1) —alternatively, the H_d dependence— is due to the linear response of the polar motion to the geopotential, valid for a first order theory. The functional form of the denominator is associated with the proper modes of the Earth model. Hence, in the case of a rigid Earth it just involves the Eulerian frequency.

When moving to non-rigid Earth models the number of proper modes increases and Eq. (1) is substituted by

$$\tilde{m}(\sigma) = [M^{-1}(\sigma)y(\sigma)]_1 \tilde{\phi}(\sigma). \quad (3)$$

In this way, the transfer function is given by (Mathews et al. 1991)

$$T(\sigma) = \frac{\tilde{\eta}(\sigma)}{\tilde{\eta}_R(\sigma)} = \frac{\tilde{m}(\sigma)}{\tilde{m}_R(\sigma)} = \frac{e - \sigma}{e} [M^{-1}(\sigma)y(\sigma)]_1, \quad (4)$$

which keeps the linear dependence with e in the denominator as derived from Eq. (1). It allows the computation of the non-rigid amplitude by

$$\tilde{\eta}(\sigma) = T(\sigma) \tilde{\eta}_R(\sigma). \quad (5)$$

The current standard of the Earth nutation IAU2000 (Mathews et al. 2002) applies the former procedure (Eqs. 4 & 5) to the total rigid nutation amplitudes of the figure axis due to the lunisolar perturbation (Souchay et al. 1999). However, those amplitudes result from different effects.

In particular, one part of the rigid terms is due to second order effects in the sense considered in this work (Souchay et al. 1999, Table 1). They take into account two main contributions:

¹The situation is different for the nutations of planetary origin as it has been recently shown in Ferrándiz et al. (2018).

- Crossed-nutations: characterized by the influence of the nutation itself on the torque exerted by the Moon and the Sun. This is the most important part and it is intrinsically associated to the rotation —rotation on rotation effects.
- Spin-orbit coupling: it is due to the interaction between the orbital motion of the Moon and the J_2 component of the geopotential. This effect is mainly related to the way in which the Moon ephemeris (ELP-2000, Chapront-Touzé & Chapront 1983) are used when constructing the rotation theory of the Earth.

Since the second order nutations are expected to be small, REN2000 (Souchay et al. 1999) performs different simplifications that make easier the computations. One of the most important is the identification of the amplitudes of the figure axis with those of the angular momentum axis (Poisson terms), i.e., it neglects contributions related to the Oppolzer terms. Those approximations are right from a numerical point of view —at the $2 \mu\text{as}$ level— as it was shown in the comprehensive second order theory constructed in Getino et al. (2010), where the main part of those simplifications are removed.

As a consequence, the amplitudes in longitude and obliquity of the angular momentum axis provided in REN2000 (Souchay et al. 1999; sections 2 and 3) depend mainly on the orbital characteristics of the perturbers, which are known functions of time provided by the corresponding orbital ephemeris, but not on the Earth model.

The only way in which the Earth structure enters into these expressions is through a linear dependence with the parameter H_d^2 , not H_d . There is no dependence of those formulae on the proper mode of the rigid model which would be introduced through the Eulerian frequency as it is the case in the first order expressions (e.g., Kinoshita 1977, Eqs. 6.22 and 6.23 through N_g).

The application of the transfer function approach, as done in IAU2000, under these circumstances gives raise, at least, to the main following problems:

- The transfer function given in Eq. (4) cannot be applied to second order terms, since the second order contributions to the polar motion are proportional to e^2 (Getino et al. 2010, Eqs. 69) and not to e like in Eq. (1)
- Even if it were correct, it cannot be applied to REN 2000 (Souchay et al. 1999) second order terms, because they do not depend on Earth structure (not consistent). They just require a scaling of the form H_d^2/H_{Rd}^2 to take into account the change in the dynamical ellipticity value when passing from the rigid to the non-rigid Earth model

Those facts, although numerically small, represent inconsistencies in IAU2000 that must be avoided.

In addition, IAU2000 totally lacks from the effect of Earth's structure on the second order terms, simply because it is the case of REN2000 (Souchay et al. 1999). Hence, all the second order contributions to the Oppolzer terms are absent. It is also the case of the part of the second order amplitudes of Poisson that depends on the Earth model.

Due to the fluid core resonance those terms can be amplified, contributing in a non-negligible way in view of current accuracies as it has been shown in the case of precession (Baenas et al. 2017). This situation is summarized in Table 1.

3. POINCARÉ EARTH MODEL: POISSON TERMS

To solve the former difficulties concerning the construction of a second order theory of the non-rigid Earth two main steps are required. First, it is necessary to develop a framework where the second order terms can be derived in a consistent way, since the current transfer function procedure

is not valid at the second order. Second, we have to compute the second order amplitudes for different Earth models, evaluating the real contribution of the non rigidity to the nutations through the normal modes of the considered non-rigid Earth.

Second order terms	REN2000	IAU2000
Poisson Model independent (but H_d^2)	Present	Incorrect modeled (not consistent)
Poisson Model dependent	Absent	Absent (incomplete)
Oppolzer Model dependent	Absent	Absent (incomplete)

Table 1: Second order terms considered in IAU2000.

Both can be accomplished following a Hamiltonian approach, since this formalism is naturally fitted to construct analytical approximate solutions of the second order by means of perturbation theories. Indeed, the same approach was used for the rigid Earth in REN2000 (Souhay et al. 1999) and later extended by Getino et al. (2010).

The procedure, even with the use of symbolic software, is quite cumbersome due to the intrinsic complexity of second order theories and to the number of degrees of freedom of the non-rigid models. Hence, we have started this study considering the second order nutations for the Poisson terms of a Poincaré Earth model —rigid mantle and fluid core. The developments are out of the scope of this contribution and are presented in detail in Getino et al. (2020).

They are based on considering an specific Non Singular Complex Canonical Variables (NSCCV) set combined with a perturbation theory based on canonical transformations (Hori 1966). The use of the NSCCV set allows obtaining an Hori kernel that simplifies the application of the perturbation algorithm up to the second order.

That procedure leads to the determination of second order analytical expressions for the nutations of the angular momentum axis. The most important conclusion is that, in contrast to first order results, Poisson terms do depend on the Earth interior structure. In our case, that dependence arises from the normal modes of the Poincaré model, i.e., the Chandler Wobble (CW) and the Free Core Nutation (FCN).

The general structure of those nutations are

$$\begin{aligned}\Delta_2\lambda &= H_d^2 \sum_{p,q} c_p c_q \left[\sum_{\substack{i_p \neq 0, j_q \neq 0 \\ \tau, \rho = \pm 1}} \mathcal{L}_{i_p, j_q, \tau, \rho}^a + \sum_{\substack{i_p, j_q \\ \tau, \rho = \pm 1}} \mathcal{L}_{i_p, j_q, \tau, \rho}^b \right] \sin(\tau\Theta_{i_p} - \rho\Theta_{j_q}), \\ \Delta_2 l &= H_d^2 \sum_{p,q} c_p c_q \left[\sum_{\substack{i_p \neq 0, j_q \neq 0 \\ \tau, \rho = \pm 1}} \mathcal{O}_{i_p, j_q, \tau, \rho}^a + \sum_{\substack{i_p, j_q \\ \tau, \rho = \pm 1}} \mathcal{O}_{i_p, j_q, \tau, \rho}^b \right] \cos(\tau\Theta_{i_p} - \rho\Theta_{j_q}),\end{aligned}\tag{6}$$

where the amplitudes with superscript a are independent of the Earth model—but H_d^2 , and those with superscript b do depend on it. For example, one of the contributions of $\mathcal{L}_{i_p, j_q, \tau, \rho}^a$ and $\mathcal{O}_{i_p, j_q, \tau, \rho}^a$ —model independent— given by

$$\frac{1}{8} \frac{\tau m_{5i}}{\tau n_i - \rho n_j} \left(\frac{1}{\tau n_i} + \frac{1}{\rho n_j} \right) (\tau m_{5i} B_i B_j' + \rho m_{5j} B_i' B_j).\tag{7}$$

And for $\mathcal{L}_{i_p, j_q, \tau, \rho}^b$ and $\mathcal{O}_{i_p, j_q, \tau, \rho}^b$ —model dependent— by

$$\frac{\sin I}{2} \frac{1}{(\tau n_i - \rho n_j)} \frac{\omega_E - \tau n_i - r_3}{\prod_{k=1,2} (\omega_E - \tau n_i - \sigma_k)} (C'_{i,\tau} C_{j,\rho} + C_{i,\tau} C'_{j,\rho}). \quad (8)$$

In the former expressions, Θ_k denotes a combination of the Delaunay variables for the Moon and the Sun and n_k represent its time derivative. The orbital functions B and C were introduced in Kinoshita (1977) — see Getino et al. (2020) for a full explanation of the notations.

Equation (7) provides basically the same contributions as those given in REN2000 (Souchay et al. 1999), since they are model independent. However, the terms of the form of Eq. (8) depend on the Earth model through r_3 and the parameters $\sigma_{1,2}$ that are related to CW and FCN.

For a particular parameter set of a Poincaré model derived from Getino & Ferrándiz (2001), we have evaluated the former formulas, recovering as a limiting case the rigid values. We have also reproduced (not displayed) the second order contribution to the precession rate (Baenas et al. 2017). As it can be seen in Table 2, the numerical differences, i.e., the second order contributions of the non-rigidity, are relevant for some frequencies at the tens μas level even for the Poisson terms.

Argument		Period	Poincaré Earth		Rigid Earth		Difference				
l_M	l_S	F	D	Ω	(days)	Lon.	Obl.	Lon.	Obl.	Lon.	Obl.
0	0	0	0	1	-6798.36	-27.2	72.0	-30.1	30.0	2.9	42.0
0	0	0	0	2	-3399.18	-1209.0	234.5	-1212.6	236.4	3.6	-1.9
0	1	0	0	0	365.26	0.4	-0.9	1.1	-0.1	-0.7	-0.8
0	0	2	-2	2	182.62	-7.4	3.7	-0.3	0.1	-7.2	3.9
0	0	2	-2	1	177.84	91.9	-72.5	92.6	-73.0	-0.8	0.6
0	0	2	0	2	13.66	-5.7	1.4	-4.9	1.0	-0.9	0.6

Table 2: Second order Poisson terms: In-phase, Poincaré model (Units: μas).

4. CONCLUSIONS

Second order terms in the sense of perturbation theories are not consistently considered by current IAU2000 (Mathews et al. 2002) nutation model. That incorrect modeling might lead to some differences of a few μas —to be determined. It can be corrected by transforming second order rigid amplitudes of REN2000 (Souchay et al. 1999) through a re-scaling of H_d^2 . In addition, IAU2000 (Mathews et al. 2002) lacks the influence of the Earth structure (normal modes) in Poisson terms and Opolzer terms, simply because it was not considered in REN2000 (Souchay et al. 1999).

Even having the complete amplitudes of the second order rigid part (Getino et al. 2010), obtaining the non-rigid contributions with the current approach is not direct, because the used transfer function assumes linearity what is not valid for second order terms.

The Hamiltonian approach provides a suitable framework to derived the second order nutations of a non-rigid Earth. For Poincaré model, we have shown that at the second order Poisson terms are affected by the Earth structure with non-negligible amplitudes (Getino et al. 2020). This approach must be extended to compute Opolzer terms and incorporated in the standard models of the rotation of the Earth.

Acknowledgement. This work has been partially supported by the Spanish project AYA2016-79775-P (AEI/FEDER, UE) and Junta de Castilla y León project GIR VA141G18.

5. REFERENCES

- Baenas, T., Ferrándiz, J.M., Escapa, A., Getino, J., & Navarro, J.F., 2017, *AJ* 153, 79.
- Chapront-Touzé, M. & Chapront, J., 1983, *A&A* 124, 50.
- Ferrándiz, J. M., Navarro, J. F., Martínez-Belda, M. C., Escapa, A., & Getino, J., 2018, *A&A* 618, A69.
- Ferrándiz, J. M., Gross, R. S., Escapa, A., Getino, J., Brzeziński, A., & Heinkelmann, R., 2020, Report of the IAU/IAG Joint Working Group on Theory of Earth rotation and validation, International Association of Geodesy Symposia, Springer, Berlin, Heidelberg, doi: 10.1007/1345_2020_103.
- Ferraz-Mello, S., 2007, "Canonical Perturbation Theories: Degenerate Systems and Resonance" (Springer, New York).
- Getino, J. & Ferrándiz, J.M., 2001, *MNRAS* 322, 785.
- Getino, J., Escapa, A., & Miguel, D., 2010, *AJ* 139, 1916.
- Getino, J., Escapa, A., Ferrándiz, J. M., & Baenas, T., 2020, "Second order nutations of a Poincaré model: general framework and Poisson terms" (in preparation).
- Kinoshita, H., 1977, *Celest. Mech.* 15, 277.
- Kinoshita, H. & Souchay, J., 1990, *Celest. Mech. Dyn. Astr.* 48, 187.
- Hori, G. I., 1966, *Publ. Astron. Soc. Jpn* 18, 287.
- Mathews, P. M., B. A. Buffett, T. A. Herring, & I. I. Shapiro, 1991, *J. Geophys. Res.* 96, 8219.
- Mathews, P.M., Herring, T.A., & Buffet, B.A., 2002, *J. Geophys. Res.* 107(B4), 2068.
- Souchay, J., Losley, B., Kinoshita, H., & Folgueira, M., 1999, *A&AS* 135 111.

TESTING THE IMPROVEMENT OF THE IAU PRECESSION USING DIFFERENT J_2 VARIATION WITH TIME

J.-C. LIU¹, N. CAPITAINE², Y.-T. CHENG¹

¹ School of Astronomy and Space Science, Nanjing University - China - jcliu@nju.edu.cn

² Observatoire de Paris-Université PSL, CNRS, Sorbonne Université, LNE - France

ABSTRACT. At its 2006 General Assembly, the International Astronomical Union (IAU) has adopted a new precession theory, called the "IAU 2006 precession", that is dynamically consistent and compliant with the IAU 2000 nutation. The time variation of the Earth's dynamical flattening J_2 is one of the contributions to the IAU 2006 model for the precession rate in longitude. However, the uncertainty in the J_2 model is one of the greatest sources of uncertainty in this precession theory. In this paper, we use the latest observational data from the satellite laser ranging to investigate the effect of different J_2 long time variations in solving the precession of the equator. The polynomial expressions for precession quantities are developed with a method similar to the IAU 2006 approach and are checked using the latest VLBI series of celestial pole offsets. However, a longer time span of VLBI data is required to reveal which J_2 model is more realistic. A serious study should be carried out before introducing a new J_2 variation in the IAU precession model.

1. INTRODUCTION

The current precession model recommended by the IAU and IERS is named the IAU 2006 precession (Capitaine et al. 2003). It is compatible with the IAU 2000 nutation and provides polynomial formulas for a number of quantities for the CRS-to-TRS transformation paradigms.

As one part of the IAU 2006 model, the precession of the ecliptic was derived by fitting the analytical ephemerides VSOP87 to the long term numerical ephemerides DE406 over the time span J1000.0 to J3000.0. For the precession of the equator, the basic quantities ψ_A and ω_A were derived by solving the dynamical differential equations using the improved ecliptic precession, updated integration constants provided by the IAU 2000 model, and the best non-rigid Earth model available at that time (Capitaine et al. 2003). One important feature of the IAU 2006 precession of the equator is the inclusion of a negative J_2 rate (J_2 is known as the Earth's form factor or the second-degree zonal harmonic of the Earth's gravitational field) that is generally attributed to the postglacial rebound of the Earth's mantle. The value for the J_2 rate adopted in the IAU 2006 model, according to Williams (1994), is such that

$$\dot{J}_2 = -3.001 \times 10^{-9} \text{ cy}^{-1}. \quad (1)$$

However the relative uncertainty of the J_2 rate reaches about 20% (Williams 1994), which is therefore one of the main limiting factors of the accuracy of the precession in longitude.

More recently, Liu & Capitaine (2017, denoted LC17) tried to construct an improved precession model by taking into account various progresses in Earth rotation theories, solar system ephemerides, as well as the best available celestial pole offsets monitored by the very long baseline interferometry (VLBI). In the LC17 work, new ephemerides INPOP10, DE406, and VSOP2013 were used to build the precession of the ecliptic. Several progresses in theoretical precession rates including contributions from revised non-linear terms, tidal Poisson terms, second-order torque, Galactic aberration, and more importantly, new determinations of the J_2 variation, were applied to

Table 1: Theoretical contributions of J_2 to precession rates in X component. Unit: mas cy^{-2} and mas cy^{-3} .

		t^2	t^3
IAU 2006	$r_\psi(J_2)$	-14.0 ± 3.0	0
LC17	$r_\psi(J_2)$	-2.5 ± 1.2	$+50.6 \pm 9.2$
LC19	$r_\psi(J_2)$	-1.4 ± 1.1	$+87.0 \pm 9.1$
J_2 data (2002-2019)	$r_\psi(J_2)$	$+17.7 \pm 1.0$	0
No J_2	$r_\psi(J_2)$	0	0

integrate the dynamical differential equations for the precession of the equator:

$$\sin \omega_A \frac{d\psi_A}{dt} = (r_\psi \sin \epsilon_A) \cos \chi_A - r_\epsilon \sin \chi_A, \quad \frac{d\omega_A}{dt} = r_\epsilon \cos \chi_A + (r_\psi \sin \epsilon_A) \sin \chi_A. \quad (2)$$

The solution in Liu & Capitaine (2017) has significant difference for the quadratic and cubic term in the polynomials of ψ_A . It shows certain improvement with respect to the IAU 2006 precession as indicated by VLBI residuals. However, due to large uncertainty in the J_2 empirical models and limited time span of the VLBI observations, the authors recommended to retain the current IAU model. In this short paper (denoted LC19), we report our new effort of improving the IAU precession model. The main updates of the present study are consideration of new J_2 data provided by NASA GSFC SLR observations and the use of a longer VLBI series of celestial pole offsets.

2. LONG TERM VARIATION OF THE EARTH'S J_2

Generally the long-term trend in J_2 has been approximated by a negative linear drift attributed to postglacial rebound of the Earth's mantle or the ongoing global isostatic adjustment, therefore a constant J_2 rate was adopted in the IAU 2006 precession. The observations from SLR data used in LC17 (up to 2011, denoted by gray dots in Figure 1) demonstrates that the deceleration in J_2 variation is significant. One important conclusion is that the long-term variation of the Earth's dynamical form-factor J_2 appears, from SLR observations up to 2011, to be more quadratic than linear in nature (Cheng et al. 2013).

According to newly added SLR data from 2002 to 2018 plotted as green dots in Figure 1, the J_2 rate seems positive in recent years (Loomis et al. 2019), which is opposite to the value adopted by the IAU model. This fact gives us adequate reason to believe that J_2 variation adopted in LC17 is still appropriate and motivates us to study more carefully this effect on the Earth's precession. In all, we have 43-year data from 1976 to 2019 as illustrated in Figure 1, and they are fitted to a parabola again in the whole interval. Based on the theoretical contribution of the Earth's oblateness to the precession rate in longitude (Capitaine et al. 2003), we calculated the numerical values of r_ψ corresponding to different J_2 empirical models. In Table 1 the first and second lines give the theoretical contribution of J_2 used in the IAU 2006 and the LC17 paper. The third line corresponds to the updated coefficients when new SLR data are added in the present analysis, which have been brought into the integration of the precession equation. We call the new solution L19 in this work. The last line has been obtained from only new data between 2002 and 2018 such that the trend of J_2 is positive.

3. UPDATED SOLUTION

The upgraded precession of the equator is obtained by solving the differential Eq. 2 with using (i) as in LC17, the updated ecliptic precession expressions derived from VSOP2013 and DE422 as given in LC17, (ii) the theoretical contributions to the precession rates including the J_2 as listed in

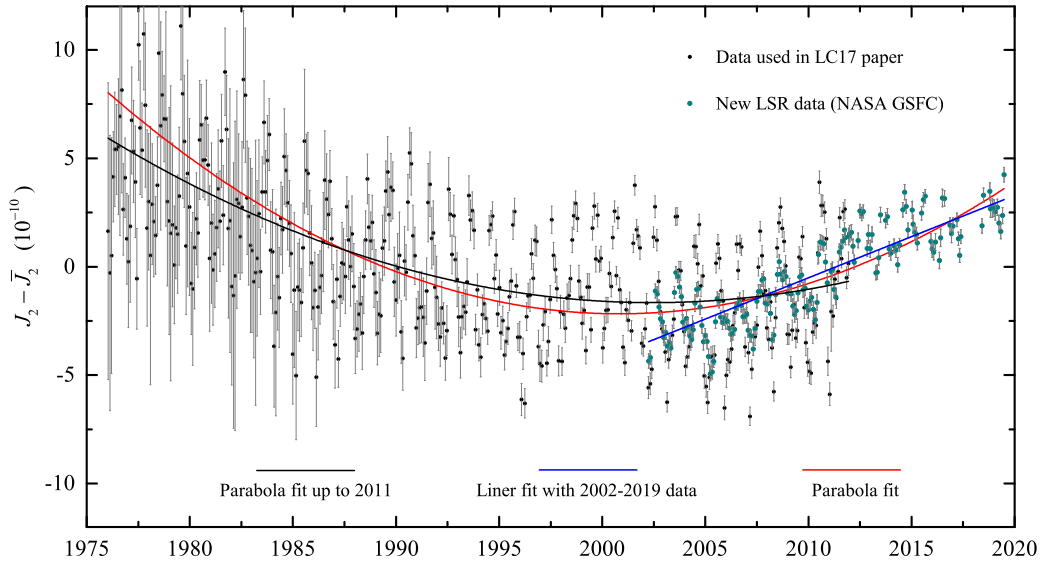


Figure 1: The Earth's J_2 values evaluated from SLR and its long term variation. The constant \bar{J}_2 is the mean value for J_2 , which equals 0.0010826359797. The original data are provided by Cheng et al. (2013) and Loomis et al. (2019). The error bars are shown in grey on the plot.

Table 2: Difference to IAU 2006 of the coefficients of the polynomial expressions up to the third degree for the quantity ψ_A from various precession solutions. Unit: $\mu\text{as cy}^{-1}$, $\mu\text{as cy}^{-2}$, $\mu\text{as cy}^{-3}$.

$\Delta\psi_A$	t^1	t^2	t^3
IAU 2006	0	0	0
LC17	532	5 767	16 847
LC19	534	6320	28 995
Positive J_2 rate	534	15 862	-5
No J_2	534	7 012	-2

line 3 (LC19) of Table 1. The expressions corresponding to the updated solution for the primary precession quantities of the equator, ψ_A and ω_A , are such that

$$\begin{aligned}\psi_A &= 5\,038''.482\,041\,t - 1''.072\,687\,t^2 + 0''.0278\,555\,t^3 + 0''.000\,123\,42\,t^4 - 0''.000\,000\,109\,6\,t^5 \\ \omega_A &= \epsilon_0 - 0''.025\,754\,t + 0''.0512\,626\,t^2 - 0''.0077\,249\,t^3 - 0''.000\,000\,086\,t^4 + 0''.000\,000\,221\,t^5\end{aligned}$$

with $\epsilon_0 = 84\,381''.406$ being the obliquity of epoch. The secondary precession quantities (ρ_A , ϵ_A , and χ_A) are not listed here.

The comparison of the different solutions for ψ_A (mainly different in J_2 contributions) by taking the IAU 2006 as a reference is shown in Table 2. The largest differences in the quadratic and cubic terms for ψ_A and ρ_A are attributed to the use of updated empirical model for J_2 variation. The signs for the t^3 terms of ψ_A are now positive while it was negative in IAU 2006. The precession in obliquity ω_A is identical to the IAU 2006 value because the integration constant for both cases are the same: the only difference for ω_A , which is at an order smaller than $1\,\mu\text{as cy}^{-1}$, originates from the ϵ -dependence of these new theoretical contributions. The largest uncertainties in our solution for the precession in longitude are still attributed to the imperfection modeling of J_2 variation. Based on the numerical values in Table 1, the relative error in t^2 and t^3 terms in r_ψ are as high as 48% and 18% for the LC17 solution, but they are even higher for the new solution (78% for the quadratic term).

4. COMPARISON OF PRECESSION EXPRESSIONS WITH VLBI CELESTIAL POLE OFFSETS

The geodetic/astrometric VLBI technique plays a crucial role in understanding the Earth's rotation. It monitors the celestial coordinates of the CIP and the Universal Time (UT1), which are known as the Earth orientation parameters (EOP). The current accuracy of VLBI observation is unprecedented high, namely at microarcsecond level, thus it provides the best observational material for studying the behavior of the precession-nutation models. The VLBI observations have shown that there are deficiencies in the IAU 2006/2000 model of the order of 0.2 mas, mainly due to the fact that the free core nutation (FCN) is not part of the model. The differences between the CIP positions estimated by VLBI observations and the CIP positions predicted with the IAU 2000/2006 model are reported as "celestial pole offsets" (CPO) dX_{IAU} and dY_{IAU} :

$$dX_{IAU} = X_{obs} - X_{IAU}, \quad dY_{IAU} = Y_{obs} - Y_{IAU}, \quad (4)$$

the subscript "IAU" meaning that the reference model is the standard IAU 2006/2000 A_{R06} precession-nutation model.

To interpret more deeply the residuals between the observations and different precession solutions, we have used (i) straight line plus 18.6-year nutation, and (ii) a parabola plus the 18.6-year nutation as in Capitaine et al. (2009) for the least squares fit. The 18.6-year nutation is the largest nutation term and is expected to be sensitive to the errors of the secular precession model. The equations used for the fit of celestial pole offsets are such that:

$$dX = \begin{cases} A_0 + A_1 t + A_s \sin \Omega + A_c \cos \Omega & \text{(i)} \\ A_0 + A_1 t + A_2 t^2 + A_s \sin \Omega + A_c \cos \Omega & \text{(ii)} \end{cases}, \quad (5)$$

where Ω (polynomial function of t) is the mean longitude of the ascending node of the Moon with a period of 6798.38 days (approximately equals 18.6 years).

The coefficients (A_0 , A_1 , A_2 , A_s , A_c) in the two functions of Eq. (5), as well as the pre- and post-fit weighted root means squares of the residuals are estimated (see Table 3). Note that only the results for the dX component is presented in this report.

Table 3: Weighted fits of the CIP coordinates X to VLBI residuals for different precession models. Unit: Unit: $\mu\text{as cy}^{-1}$, $\mu\text{as cy}^{-2}$, $\mu\text{as cy}^{-3}$.

Model	A_0	A_1	A_2	A_s	A_c	WRMS _{pre}	WRMS _{post}
IAU 2006	13 ± 1	382 ± 12	--	36 ± 1	-18 ± 1	126	116
	2 ± 1	-90 ± 23	4436 ± 184	54 ± 1	-31 ± 1	126	115
LC17	9 ± 1	-210 ± 12	--	48 ± 1	-31 ± 1	128	115
	6 ± 1	-353 ± 23	1355 ± 184	54 ± 1	-35 ± 1	128	115
LC19	9 ± 1	-330 ± 12	--	52 ± 1	-36 ± 1	135	115
	8 ± 1	-391 ± 23	579 ± 184	54 ± 1	-38 ± 1	135	115
Positive J_2 rate	-2 ± 1	-503 ± 12	--	61 ± 1	-37 ± 1	152	115
	3 ± 1	-301 ± 23	-1884 ± 184	54 ± 1	-31 ± 1	152	115
No J_2	6 ± 1	82 ± 12	--	47 ± 1	-26 ± 1	152	115
	3 ± 1	-92 ± 23	1635 ± 184	54 ± 1	-31 ± 1	152	115

From Table 3, one can see that the pre-fit WRMS for the first three precession expressions, i.e. IAU 2006, LC17, and LC19, are of the same level, but that for forth and fifth experiments with positive and no- J_2 effects, respectively, the pre-fit WRMS are higher by about 20% with respect to the previous solutions. Note that the pre-fit WRMS can be used to indicate the global consistency

between the observed CIP location and the theoretical CIP positions predicted by the corresponding precession-nutation models, one can conclude that a positive or zero value for J_2 rate are flawed, although the post-fit WRMS are of the same level as the others.

From this table, we found that the coefficient of t^2 term decreased significantly when the empirical model adopted for J_2 includes a quadratic term. Since the most important changes in the LC17 or LC19 precession is the introduction of an updated J_2 variation, which mainly modified the quadratic term and cubic terms of the precession in longitude, we have shown that the use of J_2 quadratic variation eliminated most of the residual quadratic curvature in the celestial pole offsets. Furthermore, the smallest coefficient A_2 appears in the LC19 precession model which is constructed using the whole SLR observational data. This indicates that the updated model for the J_2 variation derived from longest time span is appropriate even though the duration of SLR observations is not long enough.

Table 4: Correlation coefficients of the VLBI fitting results with two empirical models. The precession model is LC19.

Term	A_0	A_1	A_2	$\sin \Omega$
A_1	-0.7			
A_s	+0.0	+0.4		
A_c	+0.2	-0.3		-0.0
A_1	-0.1			
A_2	-0.3	-0.8		
A_s	-0.2	-0.3	+0.5	
A_c	+0.2	+0.3	-0.4	-0.2

Table 4 presents the correlation matrix of the coefficients in different empirical models for the precession solution LC19. In the model comprising of a linear plus a 18.6 year periodic term, the correlation coefficients ρ_{A_0, A_1} and ρ_{A_1, A_s} are significant. For the parabola plus a 18.6-yr model, the correlation coefficients ρ_{A_1, A_2} are also unexpectedly high. This should be attributed to the relative short time interval of the VLBI CPO series, which may be not sufficient to separate the secular and periodic signal in the residuals.

5. CONCLUSION

In this study, we have investigated the possibility of improving the IAU 2006 precession model with updating our work in 2017. We have introduced an empirical expression for J_2 based on the most recent and accurate determination by the SLR observations over 43 years before integrating the precession equations for the equator. The quadratic and cubic terms in the precession quantity ψ_A have difference at the order of 6 mas cy^{-2} and 29 mas cy^{-3} with respect to the IAU 2006 (see Table 2). With the help of additional two years of VLBI data, we tried to check the precession models against observations. The newly developed precession have shown some advantages with respect to the IAU 2006 model, but due to the limited time span of VLBI data and relatively large uncertainties in the J_2 variation, this effect should be studied more carefully in the future before introducing such a different Earth model in precession-nutation. Moreover the model for the J_2 variations should be consistent with a dynamical model. Therefore it is still preferable to retain the IAU 2006 as the standard model before the corrections such as J_2 variation are significant and robust enough.

Acknowledgement. This work is funded by the National Natural Science Foundation of China (NSFC) under grant No. 11833004.

6. REFERENCES

- Capitaine, N., Wallace, P. T., Chapront, J., 2003, "Expressions for the IAU 2000 precession quantities", *A&A* 412, pp. 567–586, doi: 10.1051/0004-6361:20031539.
- Capitaine, N., Mathews, P. M., Dehant, V., Wallace, P. T., Lambert, S. B., 2009, "On the IAU 2000/20006 precession-nutation and comparison with other models and VLBI observations", *Celest. Mech. Dyn. Astr.* 103, pp. 179–190, doi: 10.1007/s10569-008-9179-9.
- Cheng, M., Tapley, B. D., Ries, J. C., 2013, "Deceleration of the Earth's oblateness", *J. Geophys. Res. (Solid Earth)* 118, 740-747, doi: 10.1002/jgrb.50058.
- Liu, J.-C., Capitaine, N., 2017, "Evaluation of a possible upgrade of the IAU 2006 precession", *A&A* 597, A83, doi: 10.1051/0004-6361/201628717.
- Loomis, D. B., Rachlin, K. E., Luthcke, S. B., 2019, "Improved Earth oblateness rate reveals increased ice sheet losses and mass-driven sea level rise", *Geophys. Res. Lett.* 46, doi: 10.1029/2019GL082929.
- Williams, J. G., 1994, "Contribution to the Earth's Obliquity Rate, Precession, and Nutation", *AJ* 108, 711, doi: 10.1086/117108.

PROGRESS IN UNDERSTANDING NUTATIONS

V. DEHANT^{1, 2}, S.A. TRIANA¹, J. REKIER¹, A. TRINH¹, P. ZHU¹, R. LAGUERRE¹,
A. HOULIEZ¹, T. VAN HOOLST¹

¹ Royal Observatory of Belgium - Belgium - v.dehant@oma.be

² Université Catholique de Louvain - Belgium

ABSTRACT. We present an overview of the recent activities within the project RotaNut (Rotation and Nutation of a Wobbly Earth), an ERC Advanced Grant funding from the European Research Council. We have recomputed the Basic Earth Parameters (BEP) from recent VLBI series and we interpret them in terms of physics of the Earth's deep interior. This includes updates of the nutational constraints on Earth's internal magnetic field as well as of the coupling constants at the core-mantle boundary (CMB) and inner core boundary (ICB). We have explored on simplified Earth models the interactions between rotational and inertial modes. With the help of numerical simulations, we have also addressed the coupling between the global rotation and the inertial waves in the fluid core, including ohmic and viscous dissipation effects. Special interests have been given to the influence of the magnetic field onto the large scale flow in the liquid core and its influence on the different dissipation mechanisms. The role of precession and nutation forcing for the liquid core is characterized as well as the interaction between the Free Core Nutation (known as the spin-over mode in the fluid core community) and inertial waves.

1. VLBI OBSERVATION

We first analyzed the VLBI observation for obtaining the nutations. We used several nutation series among which, the C04 IERS nutation series. The Basic Earth Parameters (see Mathews et al., 2002, Koot et al., 2010, Zhu et al., 2017) are shown in Table 1.

BEPs	Mathews et al 2002	Koot et al 2010	Zhu et al 2017
$10^3 (e_f + \Re K_{CMB})$	2.6681 ± 20	2.6752 ± 15	2.6760 ± 8
$10^3 \Im K_{CMB}$	-0.0185 ± 14	-0.0186 ± 5	-0.0188 ± 5
$10^3 \Re K_{ICB}$	1.11 ± 10	0.98 ± 6	1.01 ± 4
$10^3 \Im K_{ICB}$	-0.78 ± 13	-0.87 ± 22	-1.11 ± 4

Table 1: Values of some of the Basic Earth Parameters (BEPs) for different nutation series.

The coefficient $(e_f + \Re K_{CMB})$ is in the range $[2.674 \cdot 10^{-3}, 2.677 \cdot 10^{-3}]$ and $\Im K_{CMB}$ in the range $[-0.019 \cdot 10^{-3}, -0.018 \cdot 10^{-3}]$ in the last two studies. They did not change too much. So it remains to interpret these values as previously. Concerning the ICB parameters, their ranges differ quite a lot between the studies. For the last studies of Zhu et al. (2017) and Koot et al. (2010), $\Re K_{ICB}$ is in the range $[0.92 \cdot 10^{-3}, 1.05 \cdot 10^{-3}]$ and $\Im K_{ICB}$ in the range $[-1.15 \cdot 10^{-3}, -0.65 \cdot 10^{-3}]$ respectively.

2. INTERPRETATION OF THE CMB BEPS

Buffett et al. (2002) have interpreted the CMB BEP by considering that the differences with respect to the hydrostatic value of the Free Core Nutation (FCN) are due to an increase of the flattening of the core and the presence of a dipolar and uniform magnetic field at the CMB.

However, the value of the uniform field that is necessary to explain the data is at the level of 0.6 mT, twice the value of the observed field (e.g. Olsen et al., 2009).

We consider that it is indeed necessary to include the existence of a magnetic field inside the core to explain the observed nutations but that, while previously thought to have a very minor influence, it is also necessary to incorporate the presence of viscosity within the core as well as its influence on the core flow to explain the value of the BEP K_{CMB} .

3. INTERPRETATION OF THE ICB BEPS

The values of the ICB coupling constants have tentatively be explained by Koot and Dumberry (2011) by considering the inner core viscosity. They computed the effects on the K_{ICB} as a function of the inner core viscosity. The observed values of the real and imaginary parts provide lower bound on the inner core viscosity but as seen by the observed values, there is too much energy dissipated to be explained by the inner core viscosity only.

Just as for the case for the CMB, we consider as well that it is necessary to include viscosity in the outer core as well as the existence of a magnetic field to explain the observed K_{ICB} .

4. FLUID CORE BEHAVIOUR FOR EXPLAINING THE BEPS

Usually, the scientists studying the core in the frame of geodynamo ignore variations of the mantle's spin axis. Scientists studying the nutations usually consider that the core motion is prescribed as a uniform vorticity (or Poincaré) flow. Within the RotaNut project, Requier et al. (2019) propose a numerical method to compute the inertial modes of a container with near spherical geometry based on the fully spectral discretization of the angular and radial directions using spherical harmonics and Gegenbauer polynomial expansion, respectively. This permits to solve simultaneously the Poincaré equation and the no penetration condition as an algebraic polynomial eigenvalue problem. This allows them to recover the inertial modes of an exact oblate spheroid undergoing uniform rotation.

On the other hand, no core flow motion beyond the simple Poincaré flow model is considered in traditional geodetic studies. In reality, in a viscous rotating fluid, there are Coriolis-restored (or inertial) oscillations, and, in a flattened core, there are rotational modes (related to nutations). These motions interact. In the vicinity of the FCN, as parameters such as the mantle's moment of inertia vary, the FCN frequency can increase at the same time that it becomes more damped. Under certain conditions, the FCN can interact with nearby inertial modes and can even exchange personality with them. In this situation, the FCN ceases to be the least damped mode. This has been shown in the paper of Triana et al. (2019). It shows the importance of considering the inertial modes in the core.

For the Earth, we are not in the parameter range where the FCN interacts with other modes, at least not through viscous interactions. However, the presence of other inertial modes have consequences on the FCN itself. For a viscosity value in the core that is close to the real Earth, Triana et al. (2020, in preparation) have considered the presence of a magnetic field, which complicates the matter.

Buffett (2010) has studied the core flow and ohmic dissipation associated with the FICN by 'mimicking' the radial flow that the FICN mode would produce at the inner core surface. Thus the model is based on a boundary flow forcing at the inner core at the theoretical FICN frequency ($\omega = 0.9975 \text{ day}^{-1}$). Assuming a uniform background magnetic field, he showed that the ohmic dissipation \mathcal{D}_{ohm} increased as the viscosity decreased, following a $\mathcal{D}_{\text{ohm}} \propto E^{-2/3}$ scaling law. However, he only reached an Ekman number near $E \sim 10^{-7}$ while the low viscosity for the real Earth's fluid core corresponds to an Ekman number $E \sim 10^{-15}$.

Triana et al. (2020, in preparation) are able to go further down in the Ekman number at the level

of 10^{-10} . Surprisingly, the behaviour of the viscous and ohmic dissipations are not as expected by Buffett (2010). Instead of a continuous increase of the ohmic dissipation and a continuous decrease of the viscous dissipation, the Ohmic dissipation saturates! And the viscous dissipation can even start increasing in some cases. What we are seeing is that, at that particular forcing frequency, we are hitting a resonance of the inertial modes, which completely perturb the smooth behaviour shown by Buffett (2010). This behaviour is found to be different for different magnetic field amplitudes. At a moderate field like in the Earth's core (corresponding to a Lehnert number $Le \sim 10^{-4}$), inertial mode resonances still persist in the curve showing the ohmic dissipation as a function of the frequencies around the FICN (see figure below) and the total energy dissipation will depend on how close the forcing frequency is to an inertial mode resonance. We emphasize that, in this model, the FICN is represented as a forced boundary flow coming radially from the inner core surface. This effectively 'mimicks' a wobbling inner core but with the notable exception that no torques or any back-reaction from the fluid core on the solid inner core are allowed. In other words, the FICN eigenmode itself is missing in the eigenmode spectrum. This indicates that a more suitable model is needed, i.e. a model including a spheroidal inner core responding dynamically to torques (pressure, viscous and magnetic) exerted by the fluid core and gravitational torques by the mantle, thus incorporating the FICN eigenmode along with the rest of inertial modes.

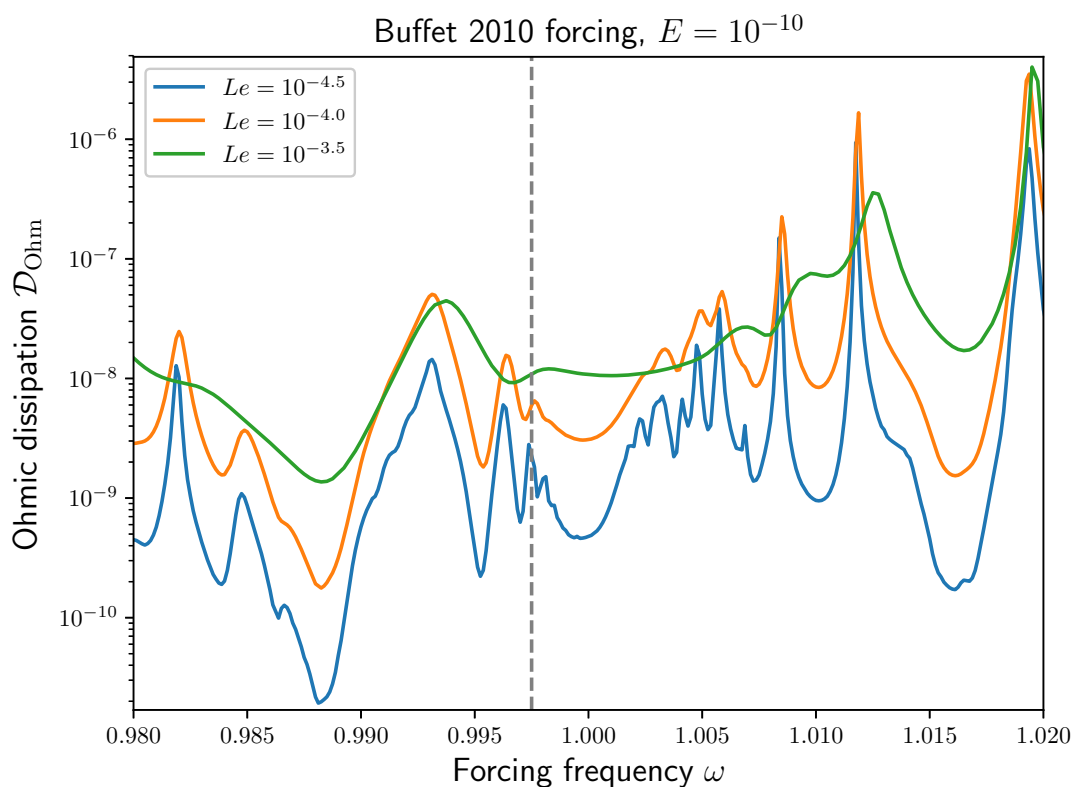


Figure 1: The ohmic dissipation in the model proposed by Buffett (2010) depends on the frequency used for the forcing. At the Ekman number in this figure ($E = 10^{-10}$), a small change in the frequency can lead to a more than an order of magnitude change in the dissipation, or even more if the Ekman number is smaller (note that $E \sim 10^{-15}$ for the Earth's fluid core). Increasing the background magnetic field (here represented adimensionally by the Lehnert number Le) reduces the resonances' quality factor.

5. CONCLUSION

After having presenting the Basic Earth Parameters (BEPs) that are fitted on VLBI observations of the nutation, we have discussed how to explain them. We have considered a fully coupled system of fluid flow obeying the classical Navier-Stokes equation in the core and the mantle rotational excitation (tidal excitation). In such a system, inertial waves and global nutation in the fluid core interact. The frequencies and damping of the inertial modes and global rotation mode change with the core flattening, the viscosity, and the mantle moment of inertia. The FCN in particular can be very much influenced. Both ohmic and viscous dissipations are important to consider. While a simple model as the one from Buffett (2010) provided Ekman number scalings for the ohmic and viscous dissipations, the real Earth case seems to be much more complicated due to the likely interaction between the inertial modes and global rotation inside the fluid core. We are in the process of deducing effects on nutation of this mechanism.

Acknowledgement. The research leading to these results has received funding from the European Research Council under ERC advanced grant 670874.

6. REFERENCES

- Buffett B.A., Mathews P.M., and Herring T.A., 2002, "Modelling of nutation and precession: Effects of electromagnetic coupling", *J. Geophys. Res.*, 107(B4), CI: 2070, doi: 10.1029/2000JB000056.
- Buffett B.A., 2010, "Chemical stratification at the top of Earth's core: Constraints from observations of nutations", *Earth Planet. Science Letters*, 296(3-4), pp. 367–372, doi: 10.1016/j.epsl.-2010.05.020.
- Koot L., Dumberry M., Rivoldini A., de Viron O., and Dehant V., 2010, "Constraints on the coupling at the core-mantle and inner core boundaries inferred from nutation observations", *Geophys. J. Int.*, doi: 10.1111/j.1365-246X.2010.04711.x.
- Koot L., and Dumberry M., 2011, "Viscosity of the Earth's inner core: constraints from nutation observations", *Earth and Planetary Science Letters* 308, pp. 343–349, doi: 10.1016/j.epsl.-2011.06.004.
- Mathews P.M., Herring T.A., and Buffett B.A., 2002, "Modeling of nutation and precession: new nutation series for nonrigid Earth and insights into the Earth's interior", *J. Geophys. Res. (Solid Earth)* 107(B4), doi:10.1029/2001JB000390.
- Olsen N., Manda M., Sabaka T.J., Toffner-Clausen L., 2009, "CHAOS-2-a geomagnetic field model derived from one decade of continuous satellite data", *Geophysical Journal* 179(3), pp. 1477–1487, doi: 10.1111/j.1365-246X.2009.04386.x.
- Rekier J., Trinh A., Triana S.A., Dehant V., 2019, "Inertial modes in near-spherical geometries", *Geophys. J. Int.* 216(2), pp. 777–793, DOI: 10.1093/gji/ggy465.
- Triana S.A., Rekier J., Trinh A., Dehant V., 2019, "The coupling between inertial and rotational eigenmodes in 2 planets with liquid cores", *Geophys. J. Int.* 218(2), pp. 1071–1086, doi: 10.1093/gji/ggz212.
- Zhu P., Rivoldini A., Koot L., and Dehant V., 2017, "Basic Earth's Parameters as estimated from VLBI observations", *Geodesy and Geodynamics*, doi: 10.1016/j.geog.2017.04.007.

EXCITATION OF THE EARTH'S CHANDLER WOBBLE BY THE NORTH ATLANTIC DOUBLE-GYRE

S. E. NAGHIBI¹, S. A. KARABASOV²

¹ Department of Aeronautics, Imperial College London - UK - e.naghibi@imperial.ac.uk

² School of Engineering and Materials Science Queen Mary, University of London - UK
s.karabasov@qmul.ac.uk

ABSTRACT. We investigate the effect of North Atlantic double-gyre on Chandler wobble excitation. To this end, we calculate the motion term of the Chandler wobble excitation for the North Atlantic region using two different ocean models: i) a quasi-geostrophic double-gyre model in an idealized quadrangle domain with steady wind forcing and ii) HYCOM (HYbrid Coordinate Ocean Model) simulations with realistic continent boundaries and time dependent wind forcing. We analyze the discrepancies between the resulting excitation of the two models and discuss how the differences in the models' assumptions can result in different predictions of Chandler wobble excitation.

1. BACKGROUND

Chandler wobble, the main component of polar motion, is a 14-month free motion, the period of which is determined by elliptic geometry and the rigidity of the Earth (Dickman 1985, Munk and MacDonald 1975). Being damped by imperfections in the Earth's elasticity and non-equilibrium ocean response, the Chandler wobble requires an unceasing injection of energy to persist in time. Several geophysical phenomena such as earthquakes (Dahlen, 1971; Xu et al., 2014), atmospheric processes and oceanic flows (Gross et al., 2003; Adhikari & Ivins, 2016) have been investigated as possible sources of the excitation of the Chandler wobble while the exact role of each phenomenon is still a matter of debate. Recent GRACE (Gravity Recovery and Climate Experiment) and SLR (Satellite Laser Ranging) observations have revealed that the mass redistribution of geophysical fluids is the dominant source of excitation for the Chandler wobble (Brzezinski et al., 2012). The motion terms of Chandler wobble excitation, defined by motion of the fluid particles relative to the terrestrial reference system, are currently calculated based on general circulation models for oceans and atmosphere. Due to variety the assumptions, different geophysical models for ocean dynamics report different contributions of oceanic currents in Earth rotation excitation (Yu et al., 2018). Hence, high-resolution ocean modeling, which is the main focus of this paper, can provide a better understanding of the exact role of oceanic currents in Chandler wobble excitation.

Ocean gyres are large wind driven systems of circulating currents developed by Coriolis effect and horizontal and vertical frictions. The North Atlantic subtropical gyre together with its smaller subpolar counterpart constitute a double-gyre which is mainly characterised by its eastward jet, Gulf Stream. The isolated double-gyre dynamics has been attracting scientists' attention since 1950s (Munk 1950, Holland 1978; Shen et al., 1999) and has further been investigated using a range of methods from high-resolution techniques (Berloff, 2005; Karabasov et al., 2009; Maddison et al., 2015) to semi-analytical solutions (Jamal 2018; Naghibi et al., 2019). The double-gyre problem has also been studied as a part of general circulation ocean models such as MITgcm (Adcroft et al., 2008) and HYCOM (Wallcraft et al., 2009).

The North Atlantic double-gyre has been reported to have a small contribution in Chandler wobble excitation (Ma et al.2009; Nastula et al., 2012; Naghibi et al., 2017). We calculate the

Chandler wobble excitation for the North Atlantic region using two different ocean models: a quasi-geostrophic double-gyre model and the general circulation model, HYCOM. The goal of this study is to analyze the discrepancies between the predicted Chandler wobble excitation resulting from the two double-gyre models.

2. METHODS

2.1 Chandler wobble equation

Chandler wobble dynamics is described as

$$\frac{i}{(\sigma_0 + i/2Q)} \frac{d\mathbf{m}}{dt} + \mathbf{m} = \boldsymbol{\Psi} = \left[1 - \frac{i}{\Omega} \frac{d}{dt} \right] \{ \alpha \mathbf{c} + \beta \mathbf{h} \}, \quad (1)$$

where $\mathbf{m} = m_1 + im_2$ are Chandler wobble components, $\boldsymbol{\Psi} = \psi_1 + i\psi_2$ are excitation function components, $\mathbf{h} = h_1 + ih_2$ is the relative angular momentum vector and $\mathbf{c} = c_{13} + ic_{23}$ is perturbation of inertia tensor. σ_0 is the Chandler wobble frequency with the period $T_0 = 2\pi/\sigma_0 \approx 433$ days, and Q is the quality factor. The constants α and β are considered for the case of complete decoupling between the Earth's core and mantle. Equation 1 is related to the velocity and acceleration fields of the oceans through \mathbf{h} vector.

2.2 Double-gyre equations

Quasi-geostrophic Model: The quasi-geostrophic model represents wind-driven double-gyre dynamics in a mid-latitude flat basin bounded by north-south and east-west solid walls. The governing equations are stratified three-layer, quasi-geostrophic potential vorticity equations (Holland 1978) and the source terms consist of the meridional gradient of the Coriolis parameter, the lateral viscosity, bottom friction, and the steady wind forcing

$$\partial_t q_i + J(\psi_i, q_i + \beta y) = \delta_{1i} F_w - \delta_{i3} \frac{a_v}{H_3^2} \Delta \psi_i + a_h \Delta^2 \psi_i, \quad i = 1, 2, 3, \quad (2)$$

where F_w , a_v and a_h are the wind curl forcing, bottom friction and lateral viscosity coefficients respectively, $J(f, g) = f_x g_y - f_y g_x$, δ_{ij} is the Kronecker symbol and β is the planetary vorticity gradient equal to $2 \times 10^{-11} \text{m}^{-1} \text{s}^{-1}$. q_i is the layer-wise potential vorticity defined as

$$q_i = \Delta \psi_i - (1 - \delta_{i1}) S_{i1} (\psi_i - \psi_{i-1}) - (1 - \delta_{i3}) S_{i2} (\psi_i - \psi_{i+1}). \quad (3)$$

Here S_{i1} and S_{i2} are stratification parameters linked to the first and second Rossby deformation radii $Rd_1 = 40$ km and $Rd_2 = 23$ km, respectively. The three ocean layers have the depths of $H_1 = 250$, $H_2 = 750$ and $H_3 = 3000$ meters. The governing quasi-geostrophic equations (2) are solved using the high-resolution CABARET method (Karabasov and Goloviznin 2009).

HYCOM (HYbrid Coordinate Ocean Model): HYCOM governing equations are composed of the conservation laws for momentum, temperature, salinity and mass, as well as the equation of state:

$$\begin{aligned} \frac{\partial \mathbf{v}}{\partial t} + (\mathbf{v} \cdot \nabla) \mathbf{v} + 2\boldsymbol{\Omega} \times \mathbf{v} &= -\frac{\nabla M}{\rho} + \frac{\nabla \cdot \boldsymbol{\theta}}{\rho}, \\ \frac{\partial (\Delta h T)}{\partial t} + \nabla \cdot (\Delta h T \mathbf{v}) &= \nabla \cdot (\kappa \Delta h \nabla T) + F^T, \\ \frac{\partial (\Delta h S)}{\partial t} + \nabla \cdot (\Delta h S \mathbf{v}) &= \nabla \cdot (\kappa \Delta h \nabla S) + F^S, \\ \frac{\partial}{\partial t} (\Delta h) + \nabla \cdot (\mathbf{v} \Delta h) &= 0, \\ \rho &= \rho(T, S, P), \end{aligned} \quad (4)$$

where \mathbf{v} is the velocity vector, $\boldsymbol{\Omega}$ is the Earth's angular velocity, M is the Montgomery potential, Δh is the depth of the ocean layer and $\boldsymbol{\sigma}$ is a stress tensor (which includes viscosity). T and S are temperature and salinity with F^T and F^S being the corresponding source terms in their conservation equations, κ is diffusivity tensor and ρ is the density. HYCOM runs over 1/12 degree horizontal resolution in the longitude and latitude and 41 isopycnal layers. The hybrid coordinate is isopycnal in the open, stratified ocean. However, it smoothly returns to a terrain-following coordinates in shallow coastal regions and to z-level coordinates in the mixed layer and unstratified seas. The atmospheric wind forcing in HYCOM is time-dependent and is generated by general atmospheric circulation models (Wallcraft et al., 2009).

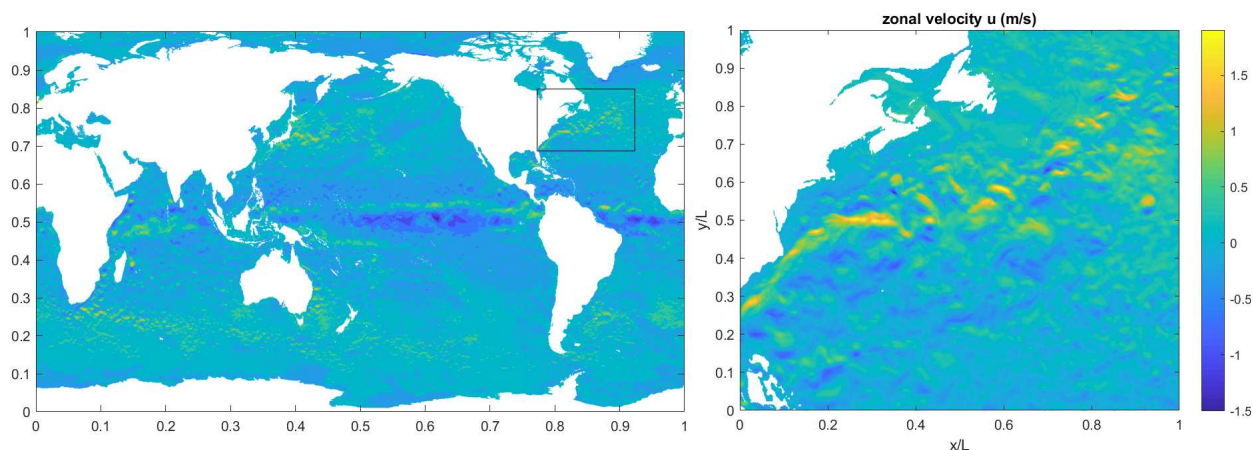


Figure 1: Top layer zonal velocity distribution in HYCOM outputs. Left panel shows global oceans and right panel shows the North Atlantic region

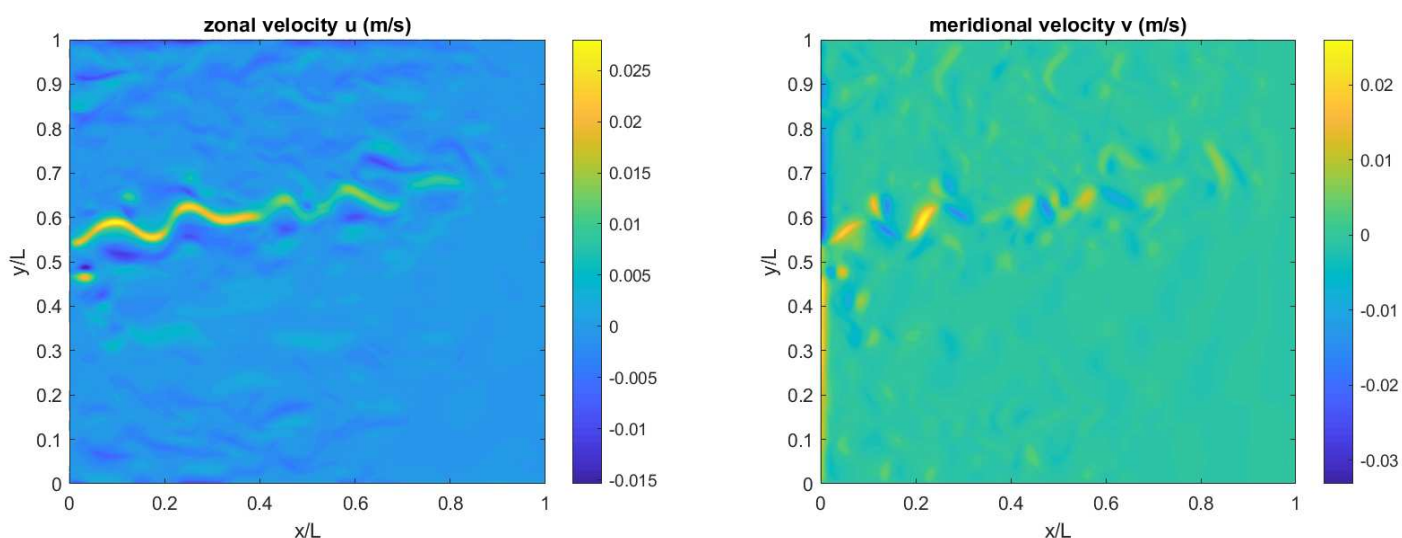


Figure 2: Top layer zonal (left) and meridional (right) velocity distributions in the quasi-geostrophic model

4. RESULTS

We first present the instantaneous velocity outputs of the two double-gyre models. Figure 1 depicts top layer zonal velocity distribution in HYCOM outputs for global oceans as well as the

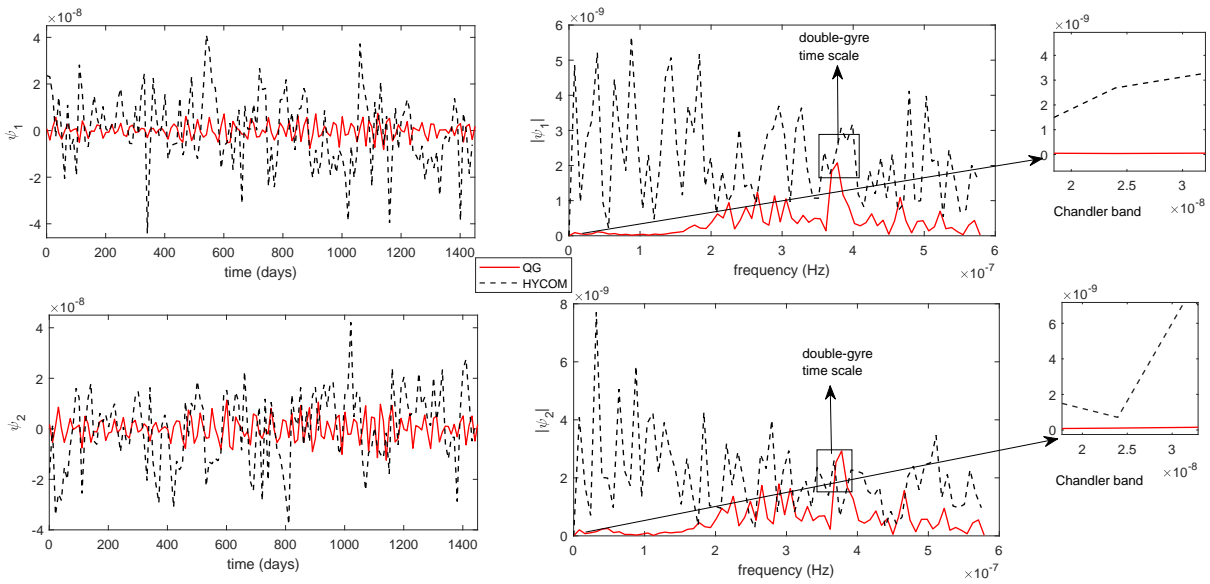


Figure 3: Comparison of Chandler wobble excitation functions using HYCOM and quasi-geostrophic (QG) model velocity fields for the North Atlantic region. Left panels are in time domain and right panels are in frequency domain.

North Atlantic region, which is a basin of the size $3840 \text{ km} \times 3840 \text{ km}$ in both models. Figure 2 illustrates top layer meridional and zonal velocity distributions in the quasi-geostrophic model.

Figure 3 compares Chandler wobble excitation functions using HYCOM and quasi-geostrophic model velocity fields for the North Atlantic region both in time and frequency space. The outputs of both models are analysed in a four-year period and sampled every 10 days. The mean values of the Chandler wobble excitation functions are filtered in all graphs. As observed in Figure 3, the two models behave differently specially in the frequency spectra. The only frequency line both models agree in corresponds to the time scale of one month which is approximately equal to the time required for the jet to travel the diagonal of the quadrangle region. This implies that, as an idealized model, the quasi-geostrophic model is only calibrated to mimic the jet dynamics in high fidelity models such as HYCOM. Figure 4 compares the meanflow and RMS profiles for zonal velocity in HYCOM and quasi-geostrophic model. As it can be seen in this Figure, the meanflow and RMS profiles reasonably agree in both models which again confirms that the parameters in the quasi-geostrophic model are calibrated to capture the mean jet correctly.

Finally, Figure 5 compares the Chandler wobble excitation functions for global oceans vs. the North Atlantic region in HYCOM. In agreement with similar works [21, 20] on regional excitation of the Chandler wobble, North Atlantic is not the dominant contributor in the excitations.

3. CONCLUSION

This paper compares the Chandler wobble excitation for the North Atlantic region using two different ocean models: an idealized quasi-geostrophic double-gyre model and the general circulation model, HYCOM. The resulting excitation functions are significantly different in the two models. Our analysis of the frequency domains show that the quasi-geostrophic model is only calibrated to capture mesoscale dynamics of the double-gyre and its eastward jet and does not produce the same excitation for the Chandler wobble as HYCOM. Different predictions of the two models can

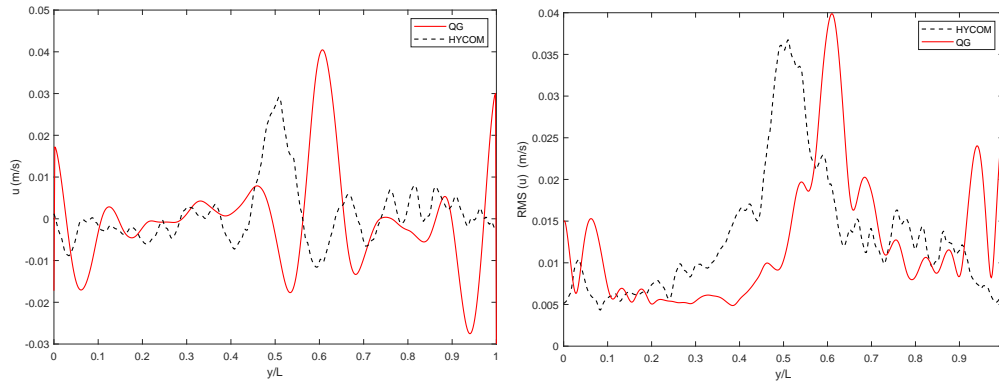


Figure 4: Comparison of the meanflow (left) and RMS (right) profiles for zonal velocity in HYCOM and quasi-geostrophic (QG) model

also be related to differences in the time variations of the wind forcing.

4. REFERENCES

- Dickman, S.R., 1985, "Comments on Normal Modes of the Coupled Earth and Ocean System by John M. Wahr", *J. Geophys. Res.* 90(B13), pp. 11553–11556.
- Munk, W.H. & MacDonald, G.J.F. (1975), "The Rotation of the Earth: A Geophysical Discussion", Cambridge University Press.
- Dahlen, F.A., 1971, "The Excitation of the Chandler Wobble by Earthquakes", *Geophys. J. Int.* 25(13), p. 15720.
- Xu, C., Sun, W. & Chao, B.F., 2014, "Formulation of Coseismic Changes in Earth Rotation and Low-Degree Gravity Field Based on the Spherical Earth Dislocation Theory", *J. Geophys. Res.* 119(12), pp. 9031–9041.
- Gross, R.S., Fukumori, I. & Menemenlis, D., 2003, "Atmospheric and Oceanic Excitation of the Earth's Wobbles during 1980–2000", *J. Geophys. Res.* 108(B8), pp. 2370–2385.
- Adhikari, S. & Ivins, E.R., 2016, "Climate-Driven Polar Motion: 2003–2015", *Sci Ad*, 2(4), e1501693.
- Brzezinski, A., Dobslaw, H., Dill, R. & Thomas, M., 2012, "Geophysical Excitation of the Chandler Wobble Revisited", *Geodesy for Planet Earth*, Springer, pp. 499–505.
- Yu, N., Li, J., Ray, J., & Chen, W., 2018, "Improved geophysical excitation of length-of-day constrained by Earth orientation parameters and satellite gravimetry products", *Geophys. J. Int.* 214(3), pp. 1633–1651.
- Munk, W. H., 1950, "On the wind-driven ocean circulation", *Journal of meteorology* 7(2), pp. 80–93.
- Holland, W. R., 1978, "The role of mesoscale eddies in the general circulation of the ocean. Numerical experiments using a wind-driven quasi-geostrophic model", *Journal of Physical Oceanography* 8(3), pp. 363–392.
- Shen, J., Medjo, T. T., & Wang, S., 1999, "On a wind-driven, double-gyre, quasi-geostrophic ocean model: numerical simulations and structural analysis", *Journal of Computational Physics* 155(2), pp. 387–409.
- Berloff, P. S., 2005, "Random-forcing model of the mesoscale oceanic eddies", *Journal of Fluid Mechanics* 529, pp. 71–95.

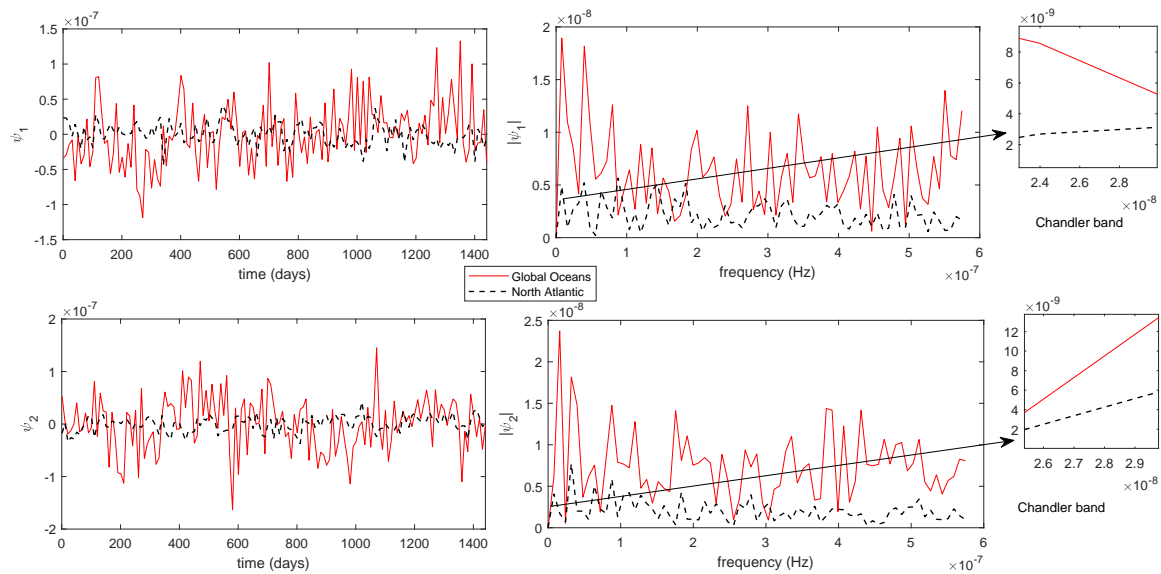


Figure 5: Chandler wobble excitation functions: Global oceans vs. the North Atlantic (motion term). Left panels are in time domain and right panels are in frequency domain

Karabasov, S. A., Berloff, P. S., & Goloviznin, V. M., 2009, "CABARET in the ocean gyres", *Ocean Modelling* 30(2-3), pp. 155–168.

Maddison, J. R., Marshall, D. P., & Shipton, J., 2015, "On the dynamical influence of ocean eddy potential vorticity fluxes", *Ocean Modelling* 92, pp. 169–182.

Jamal, S. (2018), "Solutions of quasi-geostrophic turbulence in multi-layered configurations", *Quaestiones Mathematicae* 41(3), pp. 409–421.

Naghibi, S. E., Karabasov, S. A., Jalali, M. A., & Sadati, S. H., 2019, "Fast spectral solutions of the double-gyre problem in a turbulent flow regime", *Applied Mathematical Modelling* 66, pp. 745–767.

Adcroft, A., Campin, J. M., Dutkiewicz, S., Evangelinos, C., Ferreira, D., Forget, G., ... & Hill, H., 2008, "17 user manual", Massachusetts Institute of Technology. Wallcraft et al.2009

Wallcraft, A. J., Metzger, E. J., & Carroll, S. N., 2009, "Software design description for the hybrid coordinate ocean model (18)", Version 2.2.

Ma, J., Zhou, Y. H., Liao, D. C., & Chen, J. L., 2009, "Excitation of Chandler wobble by Pacific, Indian and Atlantic Oceans from 1980 to 2005", *Chinese Astronomy and Astrophysics* 33(4), pp. 410–420.

Nastula, J., Gross, R., & Salstein, D. A. (2012), "Oceanic excitation of polar motion: Identification of specific oceanic areas important for polar motion excitation", *Journal of Geodynamics* 62, pp. 16–23.

Naghibi, S. E., Jalali, M. A., Karabasov, S. A., & Alam, M. R., 2017, "Excitation of the Earth's Chandler wobble by a turbulent oceanic double-gyre", *Geophys. J. Int.* 209(1), pp. 509–516.

Karabasov, S. A., & Goloviznin, V. M., 2009, "Compact accurately boundary-adjusting high-resolution technique for fluid dynamics", *Journal of Computational Physics* 228(19), pp. 7426–7451.

DECADAL FLUCTUATIONS IN EARTH'S ROTATION AS EVIDENCES OF LITHOSPHERIC DRIFT OVER THE ASTHENOSPHERE

N. SIDORENKOV¹, E. DIONIS², C. BIZOUARD², L. ZOTOV³

¹ Hydrometcentre of Russia, Moscow - Russia - sidorenkov@mecom.ru

² SYRTE, Observatoire de Paris, CNRS/UPMC - France

³ Sternberg Astronomical Institute of Moscow State University - Russia

ABSTRACT. The decadal instabilities in Earth's rotation (DIER) are thought to be caused by the interactions between the Earth's core and its mantle. This hypothesis successfully explains why there is a close correlation between DIER and the variations in the rate of the westward drift of the geomagnetic eccentric dipole, since it is successfully reproduced by modeling of the redistribution of the angular momentum between the fluid core and the mantle of the Earth. However, the hypothesis can not explain the close correlations of DIER: with the observable variations in the masses of the Antarctic and Greenland ice sheets; with the decade oscillations of the types of synoptic processes (i.e. the epochs of the atmospheric circulation); with the anomalies of the global temperature; and with regional anomalies of the cloudiness, precipitations, and other climatic characteristics. An alternative to the core-mantle interaction hypothesis is presented here. This alternative hypothesis claims that the DIER are actually caused by fluctuations in the angular velocity of lithospheric drift over the asthenosphere. The sliding of the lithosphere over the asthenosphere is possible due to of the vibrational displacement mechanism produced by tidal forces. The lithospheric plates exhibit vibrational displacements over the asthenosphere in the horizontal direction by shear stresses caused by friction, wind, and ocean currents. There is abundant evidence supporting this lithospheric drift model.

1. INTRODUCTION

Nontidal instabilities of Earth's rotation, i.e., variations in the daily rotation rate and polar motion are caused basically by the atmospheric and oceanic circulations. Exchange of angular momentum between the solid Earth and the moving shells occurs due to the friction forces of wind and currents on the lithosphere surface and due to the pressure exerted by the air and water on the mountain ridges. However, the lithosphere is not monolithic, but is split into plates, some of which carry continents. The atmosphere and the ocean affect the lithospheric plates, which then transmit this action to the Earth. What are the consequences of the action experienced by the lithospheric plates? Recall that the lithosphere is underlain by a layer of lower viscosity-the asthenosphere- in which the lithospheric plates are capable of floating. The continents are frozen into the oceanic plates and can also passively move with them (Trubitsyn and Rykov, 1998). Therefore, it is natural to expect that the plates move under the friction force and pressure produced by the atmosphere and the ocean on the plates' outer surfaces. The movement of the plates is impeded by the viscous cohesive force between the asthenosphere and their bases and edges, but the external forces can overcome this resistance, since they are able to accelerate or slow down the Earth's rotation. So why cannot they move relatively thin plates floating on the asthenosphere? It is natural to look for indirect evidence of this phenomenon.

2. INDIRECT EVIDENCES

An illustrative example of what was said above is a situation occurring near the Drake Passage (Sidorenkov, 2009). The westerly winds prevailing in the Roaring Forties (area between latitudes 40° - 50° th in the Southern Hemisphere) form the powerful Antarctic Circumpolar Current in the ocean (≈ 1 m/s). South America, the Antarctic Peninsula, and the underwater lithosphere represent a barrier to these atmospheric and oceanic flows. They have broken through the lithospheric connection that existed sometime in the past between South America and Antarctica and moved it 1500 km to the east. As a result, the East Scotia Basin was formed, which extends in the streamwise direction and is surrounded by the remains of the connection in the form of the Scotia Arc and numerous islands. The main of the latter is the arc of the South Sandwich Islands, which crushed the oceanic lithosphere in its eastward drift and formed the deep South Sandwich Trench.

Another piece of evidence to support our hypothesis is as follows. The atmospheric circulation has a remarkable feature: at latitudes of 35° N and 35° S, the wind direction reverses, i.e., easterlies (trade winds) prevail in the tropical zones between these latitudes, while westerlies dominate in moderate and high latitudes. Accordingly, the shear stresses on the lithosphere surface are oppositely directed. Therefore, maximum shear stresses in the latitudinal direction must concentrate in the lithosphere near latitudes of . These zones must exhibit higher seismic and tectonic activities. Indeed, within this zone in the Northern Hemisphere, there is a continuous chain of mountain systems running through the Mediterranean Sea, Anatolia, Iran, Pamir, Tibet, Japan, and the USA, where earthquakes and volcanic eruptions are observed most frequently. In the Southern Hemisphere, the zone of wind direction reversion passes through the ocean, due to which, possibly, seismic and tectonic processes are not evident.

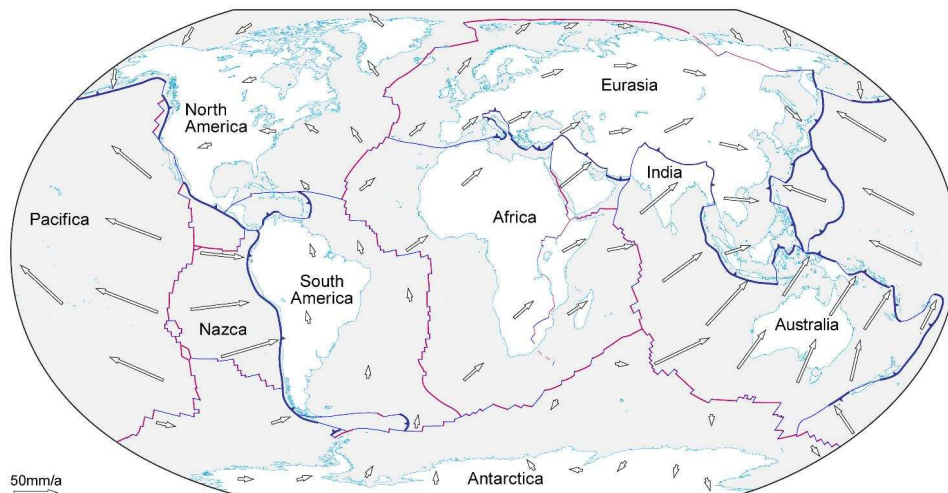


Figure 1: Map of annual mean displacements of GPS receivers over the globe from the data at <http://www.files.ethz.ch/structuralgeology/JPB/files/English/1Introtecto.pdf> (The arrows show the direction and velocity of the receivers' displacements per year)

3. GPS OBSERVATIONS

Now Global Positioning System is used to study moving of the Earth's tectonic plates (Figure 1). Here we can see that plates Europe, Asia, Africa, Australia and Nazca drifts from the West on the East. Only America is moving a little from the East on the West. Plates move as slow as a few centimeters in a year. Here, in subduction zones of "Ring of Fire", the plates collide with each other and sink into the mantle, where they melt. The total effect of the movement of all

lithospheric plates is interpreted by geophysicists as the decadal fluctuations of the Earth's rotation.

4. ANTARCTIC ICE MASS DYNAMICS

In (Sidorenkov, 1982) I derived equations relating the Earth's rotation rate and the polar wobble coordinates to variations in the World Ocean water mass and the ice mass in Antarctica, Greenland, and the other Continents. We was found that the variations observed in the Antarctic ice sheet mass qualitative agreed with theoretical mass's variations. As to the quantitative agreement, I believed that the variations observed in the ice masses proved to be 28 times less than the required variations.

Etienne Dionis and Christian Bzouard refined the coefficients in my equations and recalculated specific mass series for the Ocean, Antarctica, Greenland, and Continents. In contrast to my calculations, which relied on the polar wobble series derived by the Ukrainian team of Evgeny Fedorov and Yaroslav Yatskiv (1972), Dionis used series of IERS pole coordinates. The numerical results for Antarctica are shown in the Figure 2. It can be seen that both theoretical curves agree well with each other. By comparing the theoretical curve with Petrov's empirical results, Dionis found an error in my calculations. It turned out that the observation values are less than the theoretical ones roughly by a factor of 100, rather than 28, as I believed. I have corrected this error. The error affected only the scale of the empirical curve, but not its configuration. Therefore, the high correlation coefficient of 0.84 between the theoretical and empirical curves remained unchanged (Figure 2). If the scale of the empirical curve is less than the theoretical one by a factor of 100, then the moment of inertia of the drifting Earth crust layer has to be less than the moment of inertia of the entire Earth by a factor of 100. It is easy to calculate that in this case the thickness of the drifting crust layer is about 20 km.

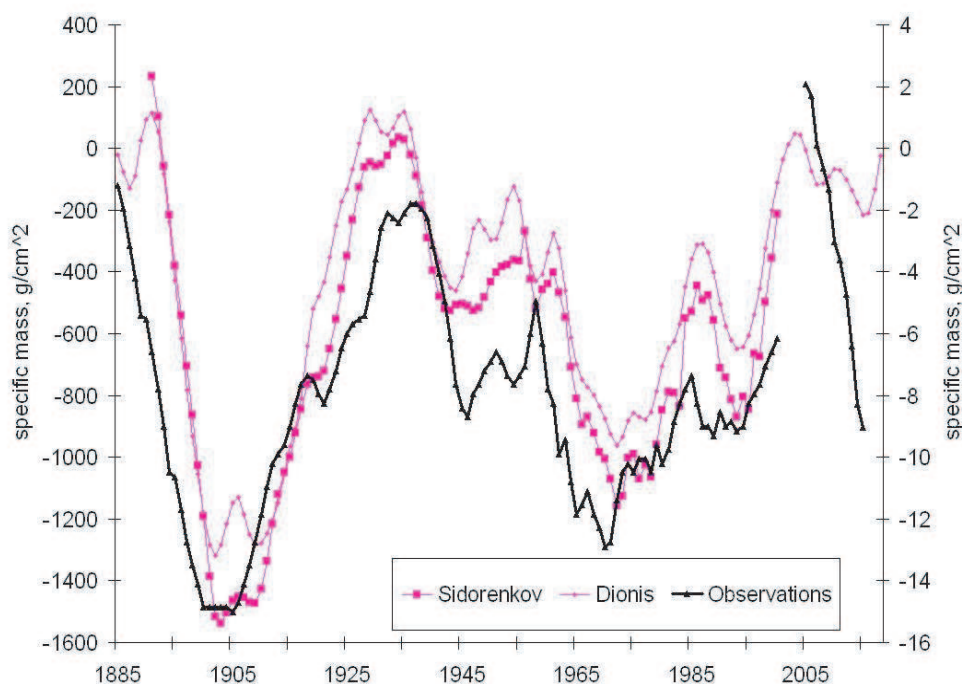


Figure 2: Temporal variations the specific mass of ice in Antarctica obtained from theoretical calculations and observations ($r=0,84$)

Relying on GRACE satellite data, Dionis computed series of specific mass variations in Antarctica (from 2005 to 2015) and Greenland (from 1993 to 2016). The scale of the series of specific mass variations in Antarctica is less than the theoretical value by a factor of 28. In this case, the thickness of the drifting crust layer has to be about 70 km.

The scale of the series of specific mass variation in Greenland as inferred from GRACE satellite data is less than the theoretical scale by a factor of 4.

These contradictory results also indicate that the observed decadal-long fluctuations in the Earth's rotation rate are not due to the rotation and polar motion of the whole Earth but rather to changes in the speed of drift of the lithosphere over the asthenosphere. The Earth's layers that are deeper than the asthenosphere don't take part in the formation of the observed decadal fluctuations.

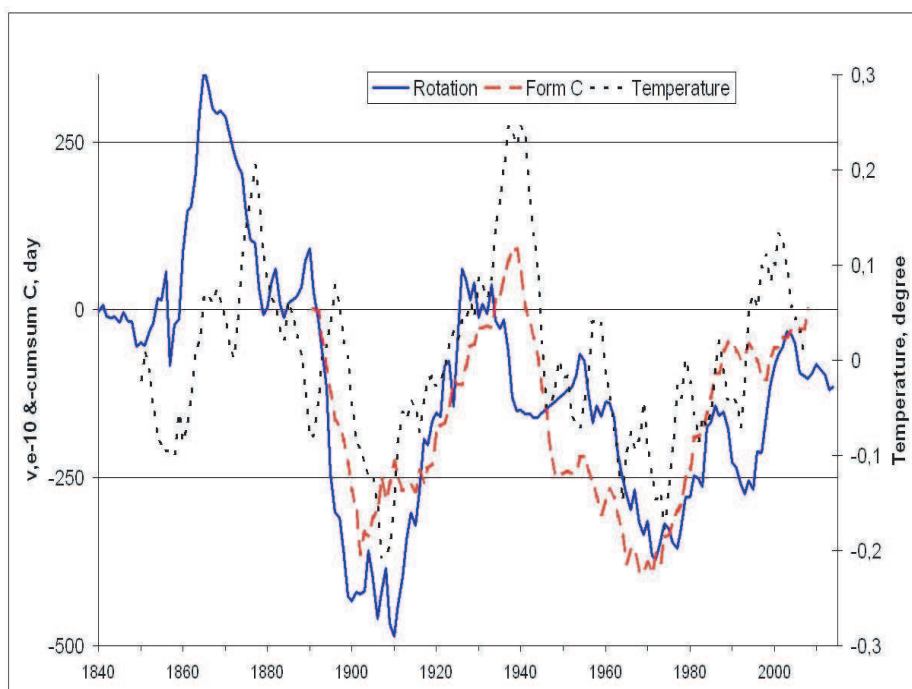


Figure 3: Synchronous changes in the Earth's rotation angular velocity v (blue line), atmospheric circulation forms C (red line) and of five year running anomalies of the Northern Hemisphere's air temperature

5. ESTIMATIONS

According to a classical estimate, the lithosphere can slide over the asthenosphere if the forcing period T is much longer than the stress relaxation time τ in the asthenosphere. As is well known, the relaxation time τ is determined by the ratio of the viscosity η to the shear modulus μ . According to a variety of estimates, the viscosity of the asthenospheric substance lies in the range 10^{18} - 10^{23} P (Poise). The shear modulus μ is 10^{12} dyn/cm². Then we have $\tau = \eta/\mu \approx 10^6$ - 10^{11} s or 0.03 - 3000 years. Thus, for the lower limit of η , our hypothesis is acceptable. For the upper limit of viscosity, lithospheric drift is unlikely.

However, this classical estimate does not take into account the effects of lithospheric vibrational displacements. Indeed, the lithospheric plates constantly vibrate in the vertical direction (roughly

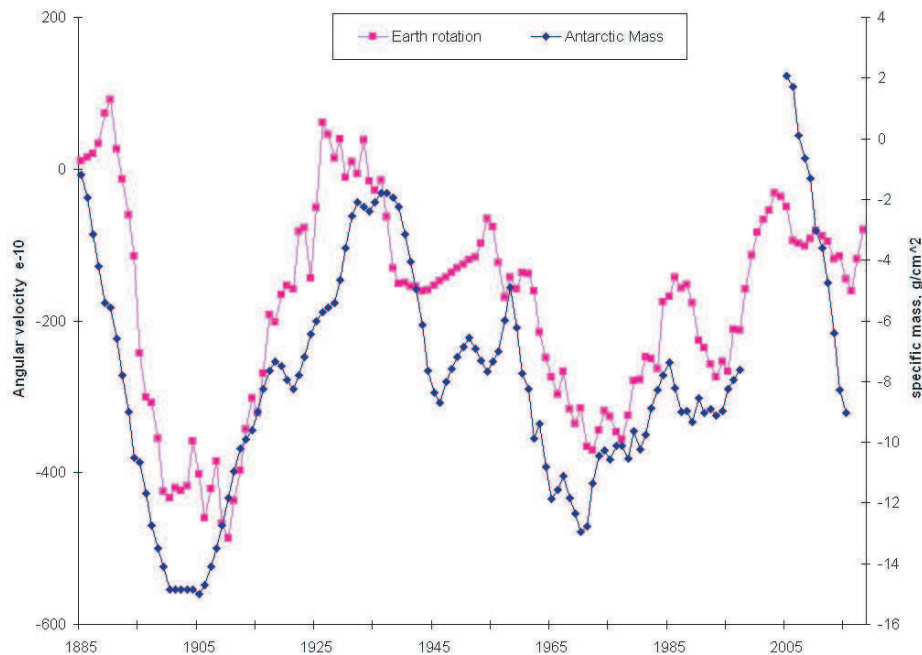


Figure 4: Variations in the specific mass of ice in Antarctica and in the Earth's rotation angular velocity (red line). Correlation's coefficient $r=0,85$.

by 50 cm) under the action of lunisolar tides. On the other hand, the lithospheric plates are permanently affected in the horizontal direction by shear stresses caused by wind and ocean currents. As a result, the lithospheric plates must exhibit vibrational displacements over the asthenosphere in the direction of the acting tangential forces. Vibrational motions dominate in nature (especially, in biosphere)!

6. CLIMATE VARIATIONS

The state of the ice sheets in the Antarctic and Greenland depends on the climatic variations. Therefore, the decadal fluctuations in the Earth's rotation may also correlate with the fluctuations in the climatic characteristics and indices. This relationship has been found in many papers. There is a close correlation between the Earth's rotation fluctuations and the frequencies of the atmospheric circulation forms, the anomalies of the global and hemisphere-averaged air temperature (Figure 3), accumulation ice mass in Antarctica (Figure 4), and many another climate characteristics. These relationships are explained given the assumption that the lithosphere drifts along the asthenosphere.

7. REFERENCES

- Fedorov, E. P., Korsun, A.A., Mayor, S.P., Panchenko, N. I., Taradiy, V. K., Yatskiv, Ya., 1972, "Motion of the Earth's pole from 1890.0 to 1969.0", Kiev: Naukova dumka. 264 [in Russian.]
- Trubitsyn, V.P., Rykov, V.V., 1998, "Global tectonics of the floating continents and oceanic lithosphere plates", *Doklady Rossiyskoy Akademii Nauk.* 359(1), pp. 109–111.
- Sidorenkov, N.S., 1982, "Estimation of some parameters of the global water exchange based on data on the secular polar motion and nonuniformity of the Earth's rotation", *Vodnye Resursy* 1982(3), pp. 39–46. [in Russian.]
- Sidorenkov N.S., 2009, "The interaction between Earth's rotation and geophysical processes", Weinheim WILEY-VCH Verlag GmbH and Co. KGaA., 317 p.

ON THE VARIABILITY OF THE CHANDLER WOBBLE

L. ZOTOV^{1,4,5}, C. BIZOUARD², N. SIDORENKOV³, WB. SHEN⁴, ZL. GUO⁴

¹ Sternberg Astronomical Institute of Moscow State University - Russia - wolftempus@gmail.com

² SYRTE, Observatoire de Paris, PSL - France - christian.bizouard@obspm.fr

³ Hydrometcentre of Russia, Moscow - Russia

⁴ School of Geodesy and Geomatics, Wuhan University - China

⁵ National Research University Higher School of Economics - Russia

ABSTRACT. The works that we carried out during the last ten years lead to significant progress in the knowledge of the Chandler wobble (CW) of the Earth polar motion (PM). In Zotov and Bizouard (2012) we reconstructed the excitation of this resonant mode by using Panteleev's corrective filtering. Now we are sure, that this filtering is a regularizing algorithm as far as its parameters are consistently selected with the uncertainty affecting the resonance parameters and the observations. The excitation demonstrated a quasi 20-year amplitude modulation. In the framework of the first order differential linear equation describing the polar motion, it is easy to show that this modulation accounts for the 40-year change of the CW amplitude as well as the splitting of the CW spectra. A simple model of the CW, composed of 80 and 40-year harmonics, accounts for the present minimum in Chandler wobble amplitude, like in 1930s, and also predicts that its amplitude will start to increase in the nearest future with a phase shift of π . On the other hand, geodetic excitation of the CW well matches the ocean-atmospheric excitation (Bizouard, 2020) over recent 50 years with a dominant role of the ocean, producing the 20-year modulation. Thus, the physical cause of it could stem from climatic or tidal process influencing the oceanic circulation.

1. INTRODUCTION

What is the Chandler wobble? For answering this questions two centuries of theoretical and observational studies should be matched. Euler published equations of the rigid body precession in 1765. Given the polar flattening of the Earth, the period of its free precession if it is assumed rigid would be 305 days. Chandler published his discovery in 1891, succeeding the series of attempts of the XIX-century astronomers to find the motion of latitudes. The two main wobbles found by Chandler had periods around 435 and 365 days. Nobody considered the annual component as the free Euler wobble, because it was attributed to mass redistribution in the Earth system, that are prominent at seasonal time scale. Therefore the Euler free motion was linked with the unexpected 435 day wobble, now known as a Chandler wobble. The mismatch of $435-305=135$ days had to be explained. Earlier works of Liouville (1858) allowed to write the homogeneous Euler equations for the Earth, whose tensor of inertia undergoes small changes. That allowed to incorporate small changes of the Earth inertia tensor and, after linearisation to move them to the right-hand side of equations as the so-called excitations. In the commonly-used form of Euler-Liouville equations:

$$\frac{i}{\sigma_c} \frac{dp(t)}{dt} + p(t) = \chi(t) \quad (1)$$

complex polar motion $p = p_1 + ip_2 \approx x_p - iy_p$ can be obtained from the observed pole coordinates x_p, y_p . Input χ is the excitation. By σ_c we denote the frequency of resonance.

The equations were still required to be adjusted to the observed frequency. The works of Newcomb (1892), helped to bring it closer to the observed one, 435 (more precise 433) days, by introduction of the elastic response of the Earth and oceans, trying to adapt their shape to the changed rotational axis position. The corresponding polar tide, raised by the additional centrifugal

potential, as a kind of back-propagation effect, formalised by Love (1909) numbers, allows to adjust the theoretical period of the free mode to about 482 days, as we can calculate now (Bizouard, 2020, Bizouard C., Zotov L., 2013). To reduce it closer to 433 days the theory should take into account the Earth's core.

The rotation theory of the Earth modelled as a solid ellipsoidal shell containing a fluid core was treated by Poincare (1910), and some results were obtained by Zhukovsky (1904). This theory was further developed by Molodensky (1961), Sasao et al. (1980), Mathews et al. (1991). Contemporary theory includes outer core stratification and inner solid core, see Dehant and Mathews (2015) book. Accounting for the electro-magnetic coupling, triaxiality and other second-order effects is also possible, but it does not change the Chandler period by more than several days (Guo and Shen, 2020), though it helps to build precise theory of precession and nutation.

Here we should briefly remind the reader, that the precession and nutation, as the solution of non-homogeneous Euler equations originate from the astronomical tides causing an external momentum of force on the Earth. On the contrary, the polar motion (PM), including the free wobble, is commonly treated as the homogeneous solution of eq. (1) resulting of geophysical excitations only. But it is quite difficult to separate astronomical and geophysical causes. For example, Earth geophysical properties define the eigen-frequencies of the transfer function, by which the amplitudes of solid-Earth nutations are multiplied. PM is also not free from the astronomically-induced changes. To make notions more distinctive, the precession-nutation was conventionally separated from the polar motion by a frequency criterium. So the first one is inside the band $[-0.5, 0.5]$ cycles per day in celestial reference frame (CRF), while the PM is outside it.

Going back to the main question – why the Chandler wobble, theoretically the eigen mode, adjusted to the observational 433 days by implementation of nonrigid effects, is quite enigmatic, – we face the problem of its changing amplitude and phase at decadal time scale. It is well seen in Figure 1 up, where CW is shown, extracted from EOP C01 PM time series, covering 1846-2020 interval with 0.05 year sampling (the 0.1 year original sampling before 1900 required an interpolation) by Panteleev's filtering locating resonance at 0.843 cycles per year.

It was already proposed by Kant (1754) that the Earth decelerates because of tidal energy dissipation. Dissipative properties were also introduced through the imaginary parts of rheological coefficients into the Chandler wobble frequency. The complex Chandler frequency $\sigma_c = 2\pi f_c(1 + i/2Q)$ in eq. (1) now incorporates real frequency f_c and quality factor Q . The characteristic time of dissipation, estimated from observations themselves, is about 50-100 years. Not going into details the Q value estimates vary from tenth to hundreds. Some authors suppose, that the intervals where CW decreases rapidly, correspond to its free decay, while other scientists, estimating the input excitations χ from geophysical data, try to adjust the parameters of the eq. (1), given the observed output p . All the methods have their drawbacks and are based on the idea, posed already by Jeffreys (1916), that the energy is somehow supplied to maintain CW. Thus, the "free" mode, thanks to dissipation, becomes actually not free. And not only the adjustment of the observable frequency and quality factor, but also the search of the energy source is required.

R. Gross, A. Brzezinsky and their followers found the source of CW excitation in the ocean and atmosphere. It is done by means of cross-correlation and cross-coherence analysis of the so-called geophysical excitation with the geodetic excitation, computed from polar motion. To do this, much efforts were undertaken to collect geophysical data over the ocean and atmosphere and run global circulation models, assimilating observation. The angular momentum functions χ , representing geophysical excitations, obtained from such reanalysis, are used, assuming that the ocean-atmosphere-solid Earth system is closed and no external momentum is supplied. In result, the excitation budget at Chandler frequency was closed by the ocean and, atmosphere, whereas the hydrological input seems to be negligible for now. The amplitude and phase of excitations found to be in good agreement, explaining the energy supply for the Chandler wobble. But the reliable geophysical excitations are available only since 1950s for atmosphere and since the 1990s for the

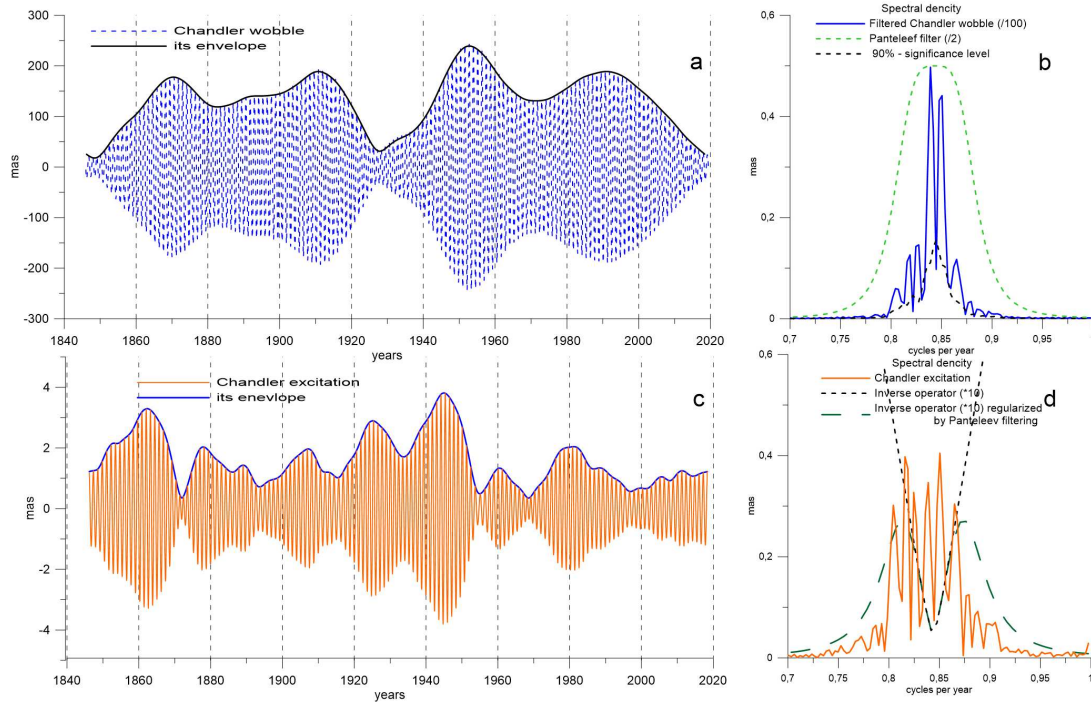


Figure 1: a) Chandler wobble extracted by the Pantelev filter, b) its spectra, c) Chandler excitation, and d) its spectra with superimposed inverse operator (black) and its regularized version (green) (Zotov, Bizouard, 2015).

ocean. The major amplitude changes of the CW, observed over more than a century, including decay happened in the 1930s, were not covered. To overcome this difficulty, B. Chao (2012) run modelling covering several hundreds of years pointing out, that the amplitude changes of CW can result from the integration of random white noises and occur occasionally over centuries. Still what we observe for the CW today was not predicted by any model. And we cannot be fully satisfied with a general statistical hypothesis, saying that noises in the atmospheric and oceanic excitations are responsible for modulations of the Chandler wobble observed in Figure 1a.

2. VARIATIONS OF CW AND ITS EXCITATION

Looking at the Chandler wobble spectrum, Figure 1b, obtained through the Fourier transform of the auto-covariance function for the EOP C01 time interval, we see, that Chandler wobble pike is splitted and has multiple side-harmonics. This reflects the to CW amplitude modulations. We consider here only the prograde Chandler band, not accounting for ellipticity and effects of triaxiality and not discussing different ways of filtering, developed by Gross, Malkin, Wang, Chao and others. We just use Pantelev's narrow-band filter (Zotov, Bizouard, 2012). The amplitude changes of the Chandler wobble, emphasised in Figure 1a by the solid-line envelope, reveal some regularities, which can be reduced to 80- and 40-year quasi-periodical changes. Many sceptical scientists pose question – to what extent can we trust observations of the 19-th and early 20-th century? Taking into account drastic change of precision starting from 0.1 arcsec and reaching tenth of microseconds today, the question is reasonable. But similar increase of observational precision happens in many fields of science. Does it mean we should through away old observations? Of cause not!. In least squares procedure the weights, inversely proportional to squared standard error and changed by 1000 times, would make recent observations million times more influential, what would pull the adjustment to the recent 30 years. But the simple regularisation of weights while estimating

amplitudes and phases of 80 and 40-year harmonics in envelope gives results not very different from the unweighed non-linear least squares. Based on these results we predicted the increase of the CW amplitude in the decade 2020-2030 after the present decrease with possible phase jump by π , as in the 1930s.

A simple simulation, with CW harmonic modelled by 150 mas, annual harmonic by 100 mas amplitude oscillation, and white noises of $a_n = 10, 30, 60, 90, 120$ mas variance, result in standard errors of CW extraction by Panteleev's filter $\sigma = 2.4, 2.6, 4.5, 6.4, 8.0$ mas, correspondingly. That means that the difference between simulated CW and that, extracted from the mix of signals, is less than 8% of the total CW amplitude.

So the obtained results, Figure 1a and b can be accepted as a matter of fact. An investigation comparing the geodetic and geophysical excitations on the left and right hand sides of Euler-Liouville equation (1) requires the estimation of the geodetic excitation, which is an inverse problem. Differentiation of observations p can amplify the noises and real cause of CW will be lost in errors. To regularize inverse problem we should get rid of annual oscillation and noises, what actually is done by implementation of the Panteleev filter. The fact, that its frequency transfer band is very narrow, requires the filter-window to be long in time and causes border effects of 20 years. To compare geodetic and geophysical excitations we can use only time interval of mutual data availability, let's say since 1940th for ECCO oceanic (OAM) and NCEP atmospheric angular momentum (AAM) χ . Cutting out 20 years from the edges, or developing the techniques of edge-effects reduction, we would have only about four decades for intercomparison, 1960-2000. Comparison made in Zotov, Bizouard (2016) revealed that the ocean and atmosphere together can explain more than 90% of CW excitation almost on equal share, in agreement with other published results.

But can the ocean and atmosphere be responsible for 80 and 40-year quasi-regular variations in the CW amplitude? The preliminarily analysis made in Zotov, Bizouard (2016), over 1960-2000 interval showed, that the ocean could be responsible.

We did reconstruction of geodetic excitation χ for CW in Zotov et al. (2016) and obtained results shown in Figure 1c. Initially our attention was attracted by quasy 20-year regular envelope, more or less in phase with 18-year lunar nodes precession. As further study revealed, the observed 20-year excitation amplitude changes can be explained by the 40-year CW amplitude changes (Zotov, 2019) superimposed on the mean amplitude of CW, assuming constant parameters of equation (1). Their cause can be interpreted as an alternation of 20-years periods of CW amplitude increase and 20-years periods of amplitude decrease. A 80-year variations also present in excitation amplitude, but they are less prominent and appears only if more narrow-band filter is applied. A frequency-dependent phase shift between excitation's and CW's envelopes occurs, since the first one depends on the derivative of the letter, eq. (1).

The excitation of 2-3 mas, provides Chandler wobble of almost 200-mas. It agrees with the resonant amplification of input, but makes the inverse reconstruction and research of the Chandler excitation very complicated. Can we estimate the error in geodetic excitation, introduced by noises, narrow-band filtering and operator inversion? Theory of inverse problems solutions states that such an error can not be accessed. It depends on our a-priory knowledge: errors of observations and operator, eq. (1), stability of its parameters f_c, Q . The only way to give an approximate error of inverse solutions is to estimate the diameter of the set, they are selected from. Shortly speaking, if a-priory knowledge was wrong and our filter was improperly designed, the solution could be wrong. But if we put some reasonable constraints on the noises and operator errors, we can estimate the error in the solution through the spread of the worst scenarios. From such simulations we testified our Panteleev's filter, finding its width 0.04 years^{-1} optimal, for the CW excitation error the upper limit obtained is 1 mas.

3. POSSIBLE CAUSES OF VARIABILITY

Since we still want to find the cause of CW amplitude changes and its spectral line split, we allow ourselves to speculate, trying to choose the most probable pathway for further research. So we assume, that quasi 80 and 40-years variations of CW amplitude really exist in 19-20 cnt., and at the stage of CW filtering the noises in observations were treated properly.

It seems that our contemporary knowledge of resonant period is correct since the theoretical CW eigenfrequency is now consistent with observations, Love numbers, precession and nutation model, etc. But what if we still miss-interpret 433-day wobble? Could it result from input at another frequency interplay with resonance at not yet quite known frequency? Linear theory says, that input and output should be at the same frequency, and it is the simplest assumption. The hypothesis of double Chandler resonance, which could split the pike, drifting parameters, and so on, make the model too complicated and contradicts the Occam razor principle. In fact, there is no notable spectral pike in OAM and AAM at Chandler frequency. We do not know any other geophysical process at 433-day frequency. The only planetary process, whose frequency is close to 433 days, was mentioned by Yu. Avsyuk (1996): it is a 412-day period of the full moon in perigee. This important periodic event, called "Big Moon" has astronomical origin, it modulates the tides, but we do not have evident spectral line in geophysical processes at this frequency. It might be in result of improper selection of reference system for the consideration of modulations. But since we deal with PM, related to geophysical causes, CW in particular, we try to look for small excitations hidden in noises of oceanic and atmospheric variability and suppose, that they are sufficient. So, low-frequency astronomical processes become out of scope. But can the processes on Earth be really so radically isolated?

Let us think about the problem in the framework of mechanics of several oscillators, where, if they are coupled together and synchronized, the changes of amplitude of particular oscillator is often observed in result of energy transfer from one pendulum to another. We can treat multiple Chandler wobble spectral pikes and side-lobes as an effect of such multiple oscillators, providing modulations. In Fig 1d we can observe spectral lines not only at $1/433$, but also at $1/450$, $1/440$, $1/410$ cycles per day, altogether responsible for 80-year, 40-year and 20-year modulations of excitation amplitude. The blue dashed line of 90% confidence level shows in Figure 1b, that the majority of these spectral lines are quite real. What if some of them appears at one interval of time, others – at another, then Fourier analysis would not be a proper technique. Wavelet and time-frequency analysis in a moving window do not alter the observed peaks. The average CW period seems to be stable. The only phase jump by π happened in 1930s during the amplitude minima can be modelled by a simple decay of the wobble amplitude with the envelope sign changing from "positive decrease" to "negative increase". If we would try to imagine, that the input excitation frequency crosses the eigen-frequency, let's say from left to right, then the phase jump would happen in result of phase response at resonance, but at the same time, the amplitude of response should increase, what is not observed. Thus, this phase-shift even remains unexplained.

Going back to mutual oscillators and synchronisation hypothesis, we need to identify them. Probably the correct way is to look for processes, which could interact and synchronise each other in the Earth shells and surrounding space not at the periods close to the CW carrying 433-day frequency or its side-lobes, but at the periods of CW envelopes.

In this framework all the variations, including climatic modes, like El Niño, 35-year meteorological period, related with the beating between lunar (355 days) and solar year, 412-day period of the 'Big Moon' should not be ignored.

We expect critics, saying that the old "astrological" methods has nothing in common with contemporary physics. But we would only mention, that the properly chosen "reference system" has been always the crucial point in astronomy and mechanics. We also know many examples, when physical models and eigenfrequencies of multi-dimensional systems of differential equations

were adjusted, to satisfy evident synchronisations and to explain what we observe in reality. On this way of combination of intuition, precise observations, new evidences uncovered from noises, and novel mathematical modelling, we sooner or later, will solve the detective story of Chandler wobble variability.

4. CONCLUSIONS

Despite the great progress of precession/nutation theory and its agreement with observations up to the 0.1 milliseconds order, the modelling of polar motion and its prediction remain unsatisfactory. Complex system of ocean, atmosphere, mantle and Earth interior shells, involving a great diversity of long and short-term geophysical processes, makes this field of scientific research comprehensive and less developed. Though PM parameters are needed for matrix transformations from celestial to terrestrial system as well as nutation parameters, being precisely estimated from GPS, VLBI and laser observations, they are hardly predictable. Chandler wobble, changing its amplitude from tens to hundreds of mas, introduces the major uncertainty into the polar motion predictions for horizons larger than one year. Explanation of its changes are crucial for geophysics and applications, including navigation, but requires a deep understanding of meteorological, oceanographic, climatological processes and global planetary geophysics.

Acknowledgement. This work is supported by Chinese Discipline Innovative Engineering Plan of Modern Geodesy and Geodynamics, NSFC grant N B17033, NSFC grants N 41721003, 41804012, 41874023, and NRU HSE grant N 20-04-033.

5. REFERENCES

- Bizouard C., Zotov L., 2013, "Asymmetric effects on polar motion", *Celest. Mech. Dyn. Astr.* 116(2), pp. 195–212.
- Bizouard C., 2020, "Geophysical modelling of the polar motion", Paris Observatory, 366 p., De Gruyter.
- Zotov L., Bizouard C., 2012, "On modulations of the Chandler wobble excitation", *Journal of Geodynamics*, special issue "Earth rotation" 62, pp. 30–34, DOI: 10.1016/j.jog.2012.03.010.
- Zotov L., Bizouard C., 2016, "Reconstruction of prograde and retrograde Chandler excitation", *Journal of Inverse and Ill-posed problems*, Vol. 24, Iss. 1, pp. 99–105, doi: 10.1515/jiip-2013-0085.
- Zotov L., Bizouard C., Shum C.K., 2016, "A possible interrelation between Earth rotation and climatic variability at decadal time-scale", *Geodesy and Geodynamics* 7(3), pp. 216-222, KeAi, China, doi:10.1016/j.geog.2016.05.005.
- Zotov L., 2019, "Study of the links between the Earth rotation and geophysical processes", Doctoral thesis, Lomonosov Moscow State University (in Russian),

DETERMINATION OF FCN PARAMETERS FROM DIFFERENT VLBI SOLUTIONS, CONSIDERING GEOPHYSICAL EXCITATIONS

J. VONDRÁK, C. RON

Astronomical Institute CAS - Czech Republic - vondrak@ig.cas.cz, ron@asu.cas.cz

ABSTRACT. Different VLBI solutions of celestial pole offsets (CPO) are used to determine parameters (period T and Q -factor) of Free Core Nutation (FCN). To this end, Brzeziński's broad-band Liouville equations are numerically integrated to account for geophysical excitations. Effects of the atmosphere, oceans and geomagnetic jerks (GMJ) are considered. Best-fitting values of FCN parameters are found by least-squares fit to observed CPO, corrected for the difference between the FCN parameters used in IAU 2000 model of nutation and newly estimated ones; MHB transfer function is used to compute these corrections. Out of all 42 solutions that we made the best fit is obtained for CPO from IERS C04, with only GMJ excitations considered. Estimated values of FCN parameters from this solution are $T = 430.23 \pm 0.03$, $Q = 19600 \pm 130$. Very probably, excitations of FCN by GMJ are more important than those by the atmosphere and oceans.

1. INTRODUCTION, MOTIVATION

Dominant part of nutation is caused by external torques, exerted by the Moon, Sun, and planets. Excitations by geophysical fluids (atmosphere, oceans) play much smaller role, but they are now detectable by VLBI. Rapid changes of amplitude and phase of the free term (FCN) occur near the epochs of geomagnetic jerks (rapid changes of the second time derivatives of intensity of geomagnetic field), as recently shown by Malkin (2013). We developed a method of determining FCN parameters (period T , Q -factor), considering all these effects (Vondrák & Ron, 2017). Here we apply this method to several VLBI solutions and models of geophysical excitations, and compare the results. The motivation is to demonstrate how much the solution is influenced by different VLBI solutions of CPO and different models of geophysical excitations.

2. SHORT DESCRIPTION OF THE METOD

The method is described in detail elsewhere (Vondrák & Ron, 2017), so only a very short description is given below.

We use Brzeziński's (1994) broad band Liouville equations to integrate numerically the influence of geophysical excitations, and compare the results with observed CPO. To this end, we use standard atmospheric and oceanic excitations from different sources, transformed from terrestrial to celestial reference frame (details see below). The effect of geomagnetic jerks is modeled by impulse-like excitation functions whose amplitudes are determined to yield the best agreement with observations.

Brzeziński's equations in celestial frame read, in complex form,

$$\begin{aligned} \ddot{P} &= i(\sigma'_C + \sigma'_f)\dot{P} - \sigma'_C\sigma'_f P = \\ &= \sigma'_C \{ \sigma'_f(\chi'_p + \chi'_w) + \sigma'_C(a_p\chi'_p + a_w\chi'_w) + i[(1 + a_p)\chi'_p + (1 + a_w)\chi'_w] \}, \end{aligned} \quad (1)$$

in which $P = dX + idY$ denotes the part of CPO, caused by geophysical excitation, σ_C is the prograde Chandler frequency in terrestrial frame. σ'_C , σ'_f are the Chandler and retrograde FCN

frequencies, and χ'_p, χ'_w are the effective angular momentum functions (pressure and wind terms, respectively), all in celestial frame. All complex frequencies σ are expressed in radians per day. Numerical constants $a_p = 9.200 \times 10^{-2}$, $a_w = 2.628 \times 10^{-4}$ express different reaction on pressure and wind terms. The complex effective angular momentum functions $\chi = \chi_1 + i\chi_2$ in terrestrial frame are transformed into celestial frame, using a simple formula $\chi' = -\chi e^{i\phi}$, where ϕ is the Greenwich sidereal time; retrograde quasi-diurnal signal in terrestrial frame thus becomes long-periodic in celestial frame.

Prior to comparison, the observed CPO are corrected for the difference between the FCN parameters as used in standard IAU model of nutation and the estimated ones, to account for resonance effects. To this end, we use the Mathews-Herring-Bufferet transfer function (Mathews et al., 2002):

$$T_{MHB}(\sigma) = \frac{e_R - \sigma}{e_R + 1} N_o \left[1 + (1 + \sigma) \left(Q_o + \sum_{j=1}^4 \frac{Q_j}{\sigma - s_j} \right) \right], \quad (2)$$

where σ is the frequency of nutation, e_R is the dynamical ellipticity of the rigid Earth, N, Q are complex constants, and s_j are complex resonance frequencies, corresponding to:

1. Chandler wobble CW;
2. Retrograde Free Core Nutation RFCN;
3. Prograde Free Core Nutation PFCN;
4. Inner Core Wobble ICW.

All frequencies of Eq.(2) are given in terrestrial frame and expressed in cycles per sidereal day. The most important is the resonance near RFCN, whose frequency is related to σ'_f of Eq. (1) by a simple relation $s_2 = \sigma'_f / \Omega - 1$, where $\Omega = 6.30038$ rad/day is the mean speed of Earth's rotation. When the estimated FCN parameters differ from the ones used in IAU model of nutation ($T=430.21$ d, $Q=20000$), transfer function for each nutation term changes, and so do its amplitude and phase as well as CPO. We then find the FCN parameters that yield the best fit between integrated and corrected CPO values, using standard least-squares estimation.

3. DATA USED

All data used in this study cover the same interval 1986.0–2018.5. They are as follows:

3.1 Celestial pole offsets

Celestial pole offsets (in 1-day steps), all referred to IAU2000, solutions by the following IVS analysis centers are used:

1. combined IERS C04, solution eopc04_IAU2000.dat;
2. combined IVS, solution ivs18q2X.eops;
3. Bundesamt für Kartografie und Geodäsie (BKG), solution bkg00014.eoxy;
4. Goddard Space Flight Center (GSF), solution gsf2016a.eoxy;
5. Institute for Applied Astronomy (IAA), solution iaa2017a.eops;
6. Observatoire de Paris (OPA), solution opa2019a.eops;
7. U.S. Naval Observatory (USN), solution usn2019c.eoxy.

All these data were filtered (Vondrák, 1977) to contain periods between 10 and 6000 days and centered. For FCN parameters different from the values used in IAU2000 model of nutation, these were further corrected by using MHB transfer function, as outlined above.

3.2 Atmospheric and oceanic excitations

Three different variants of excitations are used:

1. No atmospheric and oceanic excitations;

2. NCEP/NCAR atmosphere with IB correction (representing a simple oceanic model), in 6-hour steps (Zhou et al., 2006);

3. ESM GFZ atmosphere + ocean, in 3-hour steps (Dobslaw & Dill, 2018).

All excitations, originally given in terrestrial frame, were re-calculated into celestial frame, centered and smoothed to contain only periods longer than 10 days.

3.3 Excitations by geomagnetic jerks (GMJ)

Eight epochs of GMJ, found in literature are used, namely 1991.0, 1994.0, 1999.0, 2003.5, 2004.7, 2007.5, 2011.0, and 2014.0. References to corresponding papers can be found in (Vondrák & Ron, 2017). The complex amplitudes a of bell-shaped excitations, centered around these epochs and lasting 200 days, are estimated to yield the best fit to observations. The excitations have the form

$$\chi'_{\text{GMJ}} = \frac{a}{2} \left[1 + \cos \frac{2\pi(t - t_0)}{\Delta} \right], \quad (3)$$

in which t_0 is equal to GMJ epochs and $\Delta = 200$ days.

4. RESULTS

We used the above described procedure, both without and with GMJ excitations, leading to 42 different solutions of period T and Q -factor. All of them are represented below graphically in Figs. 1 through 3.

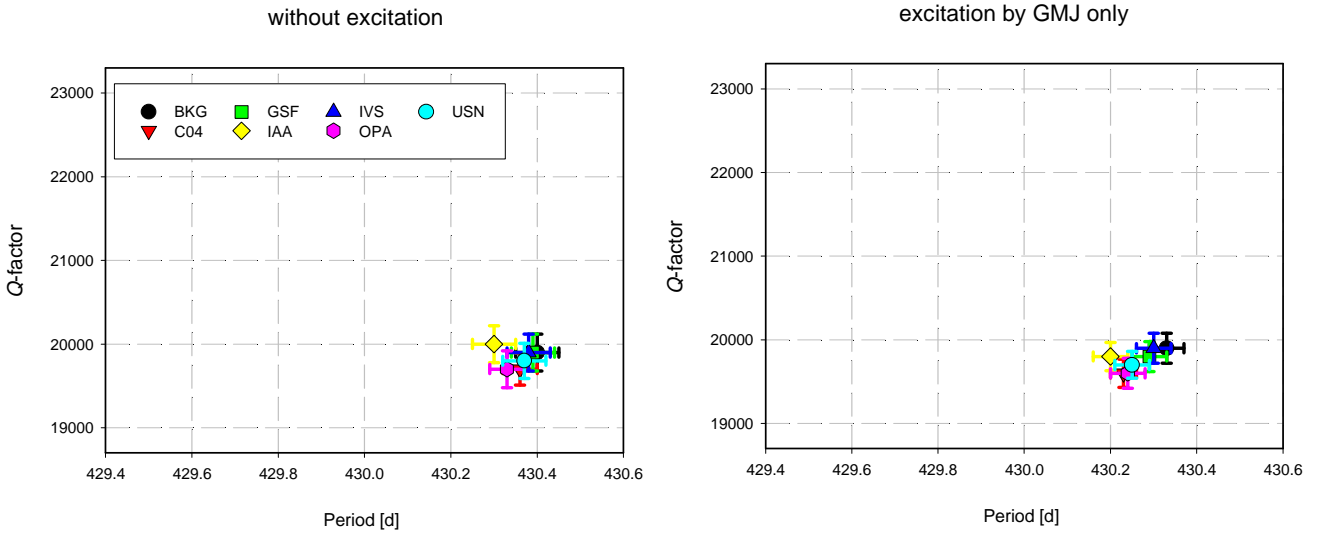


Figure 1: Solutions without atmospheric and oceanic excitations; left - no excitations at all, right - excitations by GMJ only.

Figure 1 (no atmospheric and oceanic excitations) shows clearly that all VLBI solutions yield very similar T and Q values; they agree within their formal uncertainties. The rms fit between integrated and observed CPO range from 0.232 to 0.280 mas, the best fit corresponds to IERS C04 solution. Inclusion of GMJ excitations does not change the Q -factor, and it shortens the period by less than 0.1d. It also improves the fits substantially to 0.166-0.227 mas, with the lowest value again for C04 CPO.

Figure 2 (excitations by NCEP IB atmosphere) offers a similar pattern as the preceding one; all solutions agree within their uncertainties, rms fits are slightly worse (0.246-0.351 mas for atmospheric excitation, 0.188-0.243 mas for GMJ effect added). The best fit is achieved again for

IERS C04 CPO. Difference between left and right plot is however different – Q -factor diminishes by about 1000, and period remains practically the same.

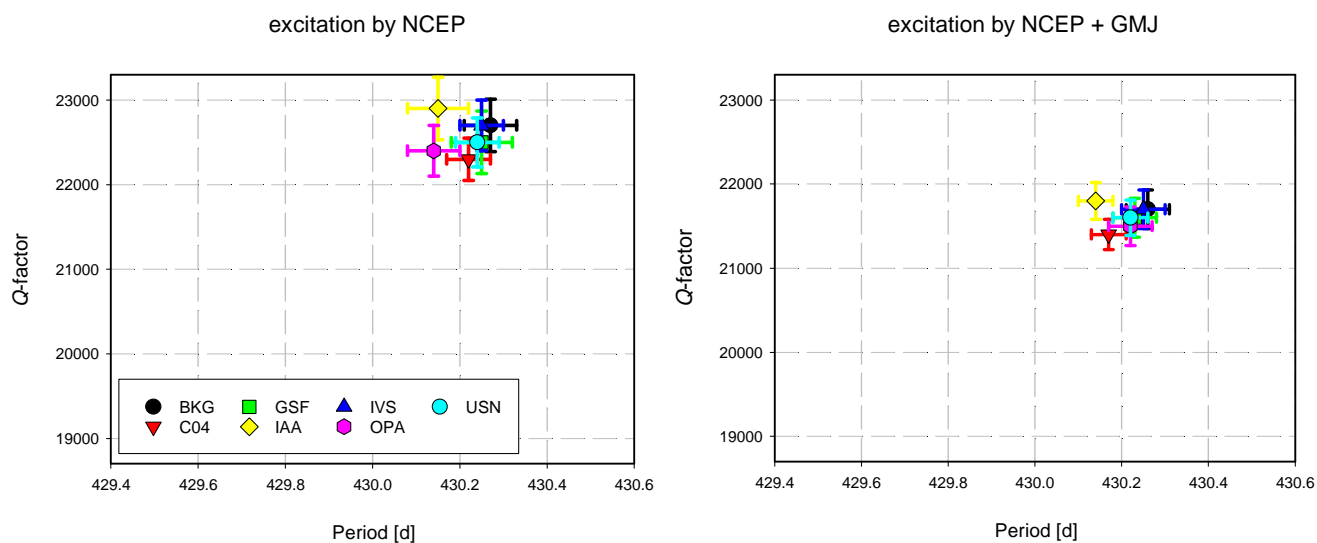


Figure 2: Solutions with atmospheric excitations NCEP IB; left - without GMJ excitations, right - with GMJ excitations.

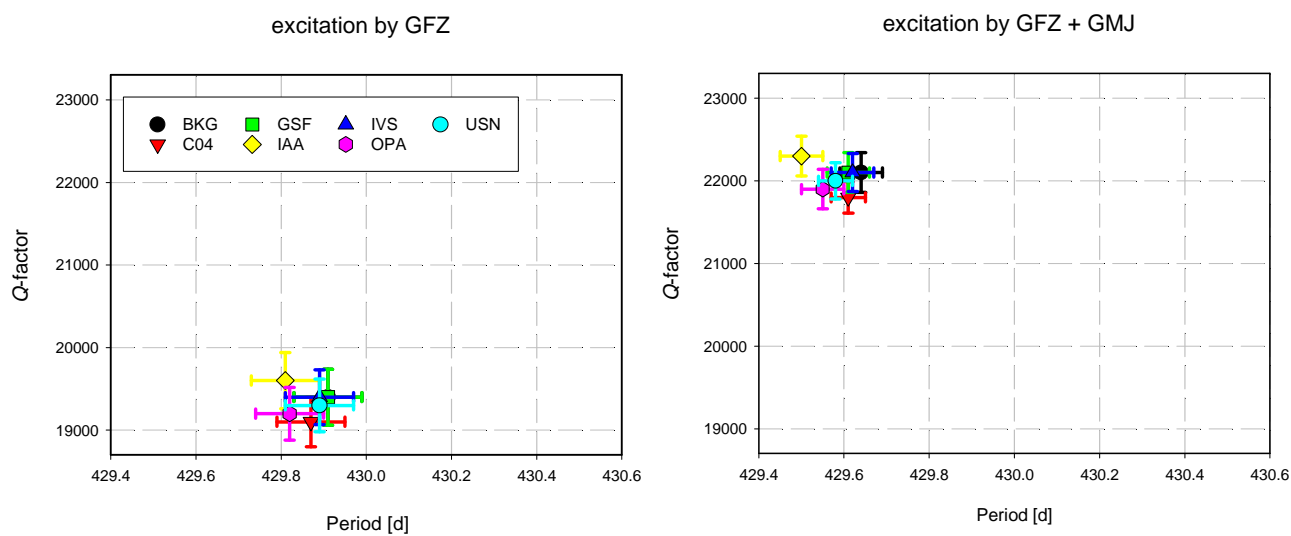


Figure 3: Solutions with atmospheric and oceanic excitations GFZ; left - without GMJ excitations, right - with GMJ excitations.

Results depicted in Figure 3 (excitations by EMS GFZ atmosphere and oceans) yield the highest values of rms fits (0.414–0.445 mas without GMJ, significantly reduced by including GMJ effect to only 0.197–0.251 mas). Similarly to Figs. 1 and 2, different CPO solutions lead to almost identical results. FCN parameters are rather different from the preceding two cases; period is shorter by about 0.3d, with GMJ excitations even more, Q -factor grows by almost 3000 if GMJ effect is added.

5. CONCLUSIONS

All results based on different VLBI solutions agree at the level of their formal uncertainties, if the same excitation model is used. The best rms fit to observations is always obtained with IERS C04 solution. Different models of excitation yield values of FCN parameters whose differences often exceed their formal errors. Quite surprisingly, the best fit is obtained when atmospheric and oceanic excitations are neglected. Inclusion of GMJ effect always improves the fit, the most significant improvement occurs in case of EMS GFZ excitations, but in some cases it brings about relatively large changes of FCN parameters, exceeding their formal errors. Out of our 42 solutions the best fitting one is based on CPO from IERS C04, when only GMJ excitations are considered: $T = 430.23 \pm 0.03$, $Q = 19600 \pm 130$, with rms fit to observations 0.166 mas. Thus it seems that the excitations by GMJ are probably more important than the ones by atmosphere and oceans.

6. REFERENCES

- Breziński, A., 1994, "Polar motion excitation by variations of the effective angular momentum function: II. Extended Model", *Manuscripta geodaetica* 19, pp. 157–171.
- Dobslaw, H., Dill, R., 2018, "Predicting Earth orientation changes from global forecasts of atmosphere-hydrosphere dynamics", *Adv. Space Res.* 61, 4, pp. 1047–1054, doi: 10.1016/j.asr.2017.11.044.
- Malkin, Z., 2013, "Free core nutation and geomagnetic jerks", *J. Geodyn.* 72, pp. 53–58, doi: 10.1016/j.jog.2013.06.001.
- Mathews, P.M., Herring, T.A., Buffet, B.A., 2002, "Modeling of nutation-precession for nonrigid Earth, and insights into the Earth's interior", *J. Geophys. Res.* 107, B4, doi: 10.1029/2001JB000390
- Vondrák, J., 1977, "Problem of smoothing observational data II", *Bull. Astron. Inst. Czechosl.* 28, pp. 84–89.
- Vondrák, J., Ron, C., 2017, "New method for determining free core nutation parameters, considering geophysical effects", *A&A* 604, A56, doi: 10.1051/004-6361/201730635.
- Zhou, Y.H., Salstein, D.A., Chen, J.L., 2006, "Revised atmospheric excitation function series related to Earth variable rotation under consideration of surface topography", *J. Geophys. Res.* 111, D12108, doi:10.1029/2005JD006608.

POLAR MOTION RESONANCE IN THE RETROGRADE DIURNAL BAND

C. BIZOUARD, I. NURUL HUDA, Y. ZIEGLER, S. LAMBERT

Paris Observatory / SYRTE, PSL - France - christian.bizouard@obspm.fr

ABSTRACT. The period of the polar motion resonance as estimated from luni-solar nutation terms is not equal to 433 days, namely the Chandler wobble period, but about 380 days. This puzzling estimate, first obtained by Mathews et al (2002), is caused by the dynamical response of the ocean in the nutation band, corresponding to the retrograde diurnal polar motion with respect a crust-fixed frame. The complex part of the resonance frequency is also strongly modified, and mostly results from the phase shift introduced by the ocean response to the pole tide potential. These conclusions are based upon our knowledge of the diurnal ocean tides, from which we can deduce the ocean pole tide in the same frequency band. Moreover, it seems that we have detected the effect of the free core nutation on the polar resonance parameter in the vicinity of the free core nutation frequency at -1.005 cycle/day.

1. INTRODUCTION

The resonance parameters (T_{PM} , Q_{PM}) of the polar motion (PM) are generally considered as the Chandler wobble period $T_c = 430 - 432$ days and its quality factor $Q_c = 56 - 255$ respectively (Nastula and Gross, 2015). But this coincidence is only insured in the broad frequency band surrounding the Chandler wobble, including annual period. Actually, in the retrograde diurnal band of the polar motion, that is the nutation band in a non-rotating frame, these resonance parameters become $T_{PM} \approx 383$ d, $Q_{PM} \approx -11$ (Nurul Huda et al, 2019). We propose a modelling of this phenomenon by accounting the response of a dynamical ocean and anelastic solid Earth to the pole tide potential.

2. RESONANT PERIOD OF THE COMMON POLAR MOTION

Let C be the Earth axial principal moment of inertia, A and A_m the equatorial principal moments of inertia of the Earth and of the mantle respectively, $e = (C - A)/A \approx 1/304.5$ the Earth dynamical flattening, and $\sigma_e = e\Omega$ the frequency of the Euler free wobble. The resonant angular frequency of the polar motion is given by (see e.g. Dehant and Mathews, 2015)

$$\sigma_{PM} = \sigma_e \frac{A}{A_m} \left(1 - \frac{\tilde{k}}{k_s} + O(e^2)\right) = \frac{A}{A_m} \Omega(e - \kappa + O(e)), \quad (1)$$

where $k_s = 0.938$ is the secular Love number, \tilde{k} is the coefficient accounting for Earth response to the pole tide potential, and $\kappa = e\tilde{k}/k_s$ is the compliance. Actually \tilde{k} is composed of two parts:

$$\tilde{k} = \tilde{k}_2 + \tilde{k}_o. \quad (2)$$

Here \tilde{k}_2 means the body Love number of degree 2 accounting for the solid Earth response to the pole tide tesseral potential, and \tilde{k}_o the oceanic Love number describing the ocean response to the same potential. For the common polar motion (beyond 2 days) the ocean response is considered at equilibrium. This leads to $\tilde{k}_o = 0.0477$. The solid Earth response is assumed as quasi-elastic, described by the body Love number $\tilde{k}_2 = 0.307 - i0.0035$ (Petit and Luzum, 2010). These

Q ₁	-0.037 + i0.039	O ₁	-0.030 + i0.038		
P ₁	-0.023 + i0.042	K ₁	-0.023 + i0.042	J ₁	-0.022 + i0.047

Table 1: Oceanic Love number for some prominent waves of the retrograde diurnal band.

values determine the resonance parameters ($T_{PM} = 433.6$, $Q_{PM} = 85$) in conformity with the observations.

3. CONTRIBUTION OF THE DYNAMICAL OCEAN RESPONSE

Below 10 days the ocean response is no more hydrostatic, and k_o changes accordingly. In the diurnal band, this issue can be solved in light of the diurnal ocean tides. For, as the pole tide potential has the same form than the luni-solar tesseral potential and concerns the same frequency band, the Earth response should be formally the same. The tidal height variation produces an equatorial component $H(t)$ of the ocean angular momentum. The observed diurnal ocean tide height is smaller than the theoretical equilibrium tide ξ , and strongly out-of-phased with respect to the tidal potential. Meanwhile, dynamical processes produce currents, in turn a relative angular momentum $h(t)$. At a location of colatitude θ and longitude λ the tesseral tidal potential is

$$W = -\frac{\Omega^2 r^2}{3} \operatorname{Re} [\tilde{\phi}(t) \mathcal{Y}_2^{-1}] \quad , \quad \mathcal{Y}_2^{-1} = 3 \sin \theta \cos \theta e^{-i\lambda} \quad , \quad (3)$$

where

$$\tilde{\phi}(t) = \frac{3gN_2^1}{\Omega^2 R_e^2} \sum_{\sigma \geq 0} \xi_\sigma e^{-i(\theta_\sigma(t) - \pi/2)} \quad , \quad N_2^1 = \sqrt{\frac{5}{24\pi}} \quad . \quad (4)$$

is formally equivalent to $m(t)$ in pole tide potential. So, in Liouville equation, the tidal excitation $\chi_o(t)$ is proportional to $\tilde{\phi}(t)$, as the rotational excitation is proportional to $m(t)$:

$$\chi_o = \tilde{k}_o / k_s \tilde{\phi} \quad . \quad (5)$$

The components of χ_o are computed from FES 2012 reported in (Madzak, 2016). For tesseral tides J₁, K₁, P₁, O₁, Q₁, we extract the retrograde diurnal components H^- and h^- . Then, accounting for loading effect through the loading Love number k'_2 , for a tidal constituent at frequency σ we have

$$\chi_o(t) = \frac{H_\sigma^-(t)(1 + k'_2) + h_\sigma^-(t)}{(C - A)\Omega} = \frac{H_\sigma^-(1 + k'_2) + h_\sigma^-}{(C - A)\Omega} e^{-i(\theta + \chi)} \quad , \quad (6)$$

where θ is the tidal argument. It results

$$\tilde{k}_o = k_s \frac{H_\sigma^-(t)(1 + k'_2) + h_\sigma^-(t)}{(C - A)\Omega \tilde{\phi}_\sigma} = -k_s \frac{H_\sigma^-(1 + k'_2) + h_\sigma^-}{C - A} \frac{\Omega R_e^2}{3gN_2^1 \xi_\sigma} \quad . \quad (7)$$

We estimate \tilde{k}_o for each tidal components H_σ^- , h_σ^- and corresponding tidal height ξ_σ . The resonance of the loading love number k'_2 at FCN frequency does not impact significantly \tilde{k}_o in retrograde the diurnal band. For $k'_2 = -0.3075$, the obtained values differ strikingly from the oceanic Love number $k_o = 0.0477$ estimated for an equilibrium pole tide: at K₁ $k_o = -0.023 + i0.042$ or compliance $\tilde{k}_o = \tilde{k}_o e / k_s = (-7.9 + i14.6) 10^{-5}$ in agreement with $(-6.9 + i11.5) 10^{-5}$ proposed by Mathews et al (2002). The values of Table 1 allow to model $k_o(\sigma)$ through a degree 2 polynomial of the frequency in the the diurnal retrograde band:

$$k_o(f) = (-0.716 + i0.721)f^2 + (-1.483 + i1.337)f + (-0.791 + i0.658) \quad , \quad (8)$$

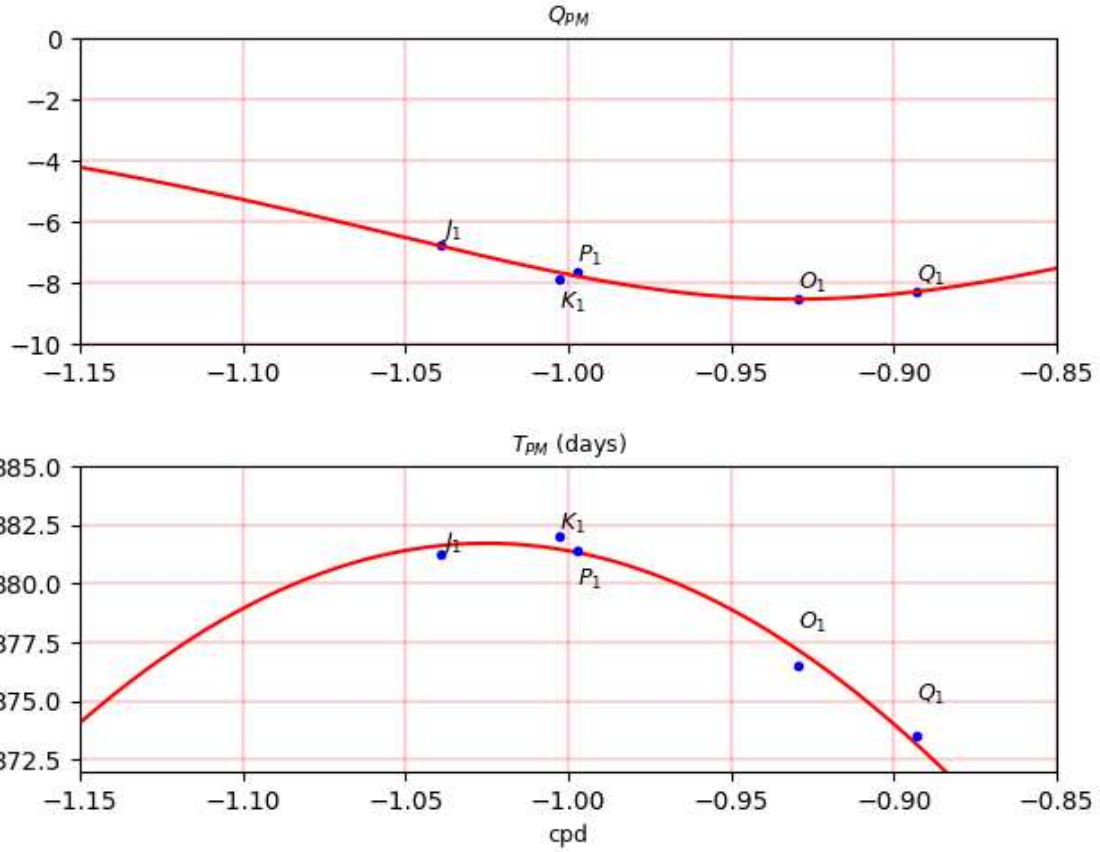


Figure 1: PM Resonance parameters in the diurnal retrograde band for an anelastic solid Earth covered by oceans.

where f is in cpd. Then we see that the resonance frequency (1) becomes frequency dependent:

$$\sigma_{PM}(\sigma) = \sigma_e \frac{A}{A_m} \frac{\tilde{k}_2 + \tilde{k}_o(\sigma)}{k_s} , \quad (9)$$

where \tilde{k}_2 is taken as the Love number of an anelastic Earth, slightly varying with frequency. In the diurnal domain we have $\tilde{k}_2 = 0.299 - i 0.00144$ (Petit and Luzum, 2010). The corresponding period and quality factor, namely $T_{PM}(\sigma) = 2\pi/\text{Re}(\sigma_{PM})$ and $Q_{PM}(\sigma) = \text{Re}(\sigma_{PM})/(2\text{Im}(\sigma_{PM}))$ are displayed in Figure 1. So, in the frequency band $[-1.15 \text{ cpd}, -0.85 \text{ cpd}]$, the dynamical ocean response leads to the resonance parameters lying in the intervals $374 \text{ d} < T_{PM} \leq 382.5 \text{ d}$ and $-4 \leq Q_{PM} \leq -10$, confirmed by $T_{PM} = 382.0 \pm 1.3 \text{ days}$ and $Q_{PM} = -10.4 \pm 0.5$ obtained from nutation analysis in (Nurul Huda et al, 2019).

4. INFLUENCE OF THE FLUID CORE

Close to the retrograde diurnal frequency $\sigma_{FCN} = -1.00506 \text{ cycle/day (cpd)}$ of the free core nutation, the solid Earth tide departs from the one of a quasi-elastic Earth. Other perturbations, of much lesser amplitude (100 times less), occur because of the free inner core nutation (FICN) mode at $\sigma_{FICN} \sim 1.0017 \text{ cpd}$ in the TRF, and because of the Polar motion resonance appearing at the period $\sim 380 \text{ days}$, as justified in the former section. From IERS Conventions 2010 (IERS, 2010), Table 6.4, Eq. 6.9 and 6.10, the "diurnal" body Love number has the form

$$k_2(\sigma) = 0.29954 - i 0.1412 \cdot 10^{-2} - \frac{L_{PM}}{\sigma - \tilde{\sigma}_{PM}} - \frac{L_{FCN}}{\sigma - \tilde{\sigma}_{FCN}} - \frac{L_{FICN}}{\sigma - \tilde{\sigma}_{FICN}} , \quad (10)$$

with the dominant term $L_{FCN} = (0.91 \cdot 10^{-4} - i 0.30 \cdot 10^{-5})$ cpd. Here $\sigma_{PM} \approx 1/383$ cpd. Replacing in (9) the pure anelastic value of k_2 by its resonant version (10), we get

$$\sigma_{PM}(\sigma) = \sigma_e \frac{A}{A_m} \frac{\tilde{k}_2(\sigma) + \tilde{k}_0(\sigma)}{k_s} . \quad (11)$$

The resonance parameters deduced from (11) are plotted in Figure 2 over the band $[-1.15 \text{ cpd}, -0.85 \text{ cpd}]$ (denoted band I). This theoretical curve is compared with the estimated values from different sets of dominant luni-solar nutation terms, as reported in (Nurul Huda et al, 2019). In average, far from the resonance at σ_{FCN} , the theoretical curve corresponds grossly to the estimated value obtained for the whole band I ($T_{PM} = 382 \pm 1.3 \text{ d}$, $Q_{PM} = -10.4 \pm 0.5$).

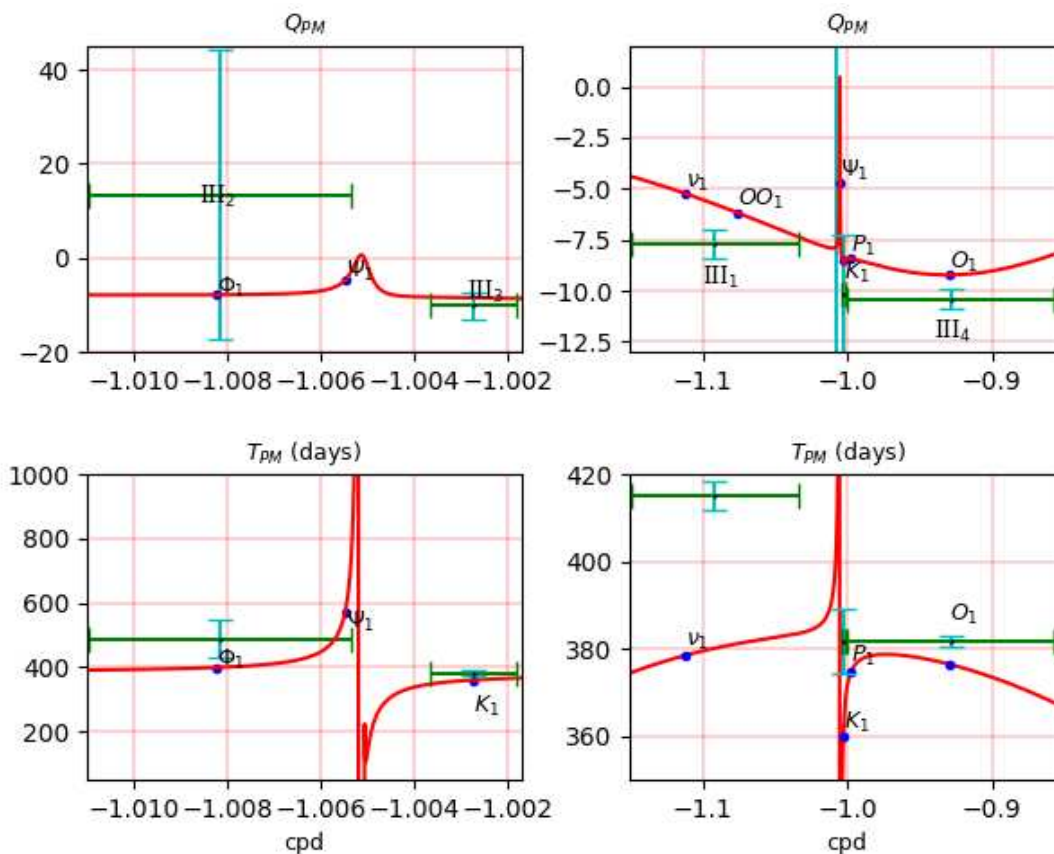


Figure 2: Resonance parameters of the polar motion in the diurnal retrograde band for an anelastic Earth covered by oceans and containing a fluid core. Green crosses specify the values obtained from nutation inversion over the restricted frequency bands III₁ (ν_1, OO_1), III₂ (Φ_1, Ψ_1), III₃ (K_1), III₄ (S_1, P_1, O_1, Q_1): the horizontal bar extension gives the frequency band, and the vertical bar the uncertainty of the estimated value.

The resonance produced by the free core nutation strongly is partly confirmed by nutation inversion for restricted bands:

- K_1 - precession and long period nutation terms (6798 d, 1095 d, 3399 d) in the CRF (band III₃). Modeled values ($T_{PM} = 360 \text{ d}$, $Q_{PM} = -10$) at K_1 quite well predict the estimated value ($382 \pm 8 \text{ d}$, -8.5).
- Ψ_1 - retrograde nutation terms in 365.25 d, 386 d in the CRF (band III₂). Enhancement of T_{PM} up to 470 d at Ψ_1 , matching $T_{PM}^{observed} = 487 \pm 58 \text{ d}$. The value $Q_{PM}^{observed} = 13 \pm 31$ too uncertain for confirming the modeled value -5 at Ψ_1 .

- far from K_1 and Ψ_1 , the resonance parameters rejoin the curves obtained for an anelastic Earth covered by oceans. At the right part of the spectrum corresponding to band III₄, covering tidal lines S_1 and O_1 , the estimates ($T_{PM} = 381.8 \pm 1.3$ d, $Q_{PM} = -10.4 \pm 0.5$) are close to the modeled parameters. For the opposite band (III₁), the estimated period is longer (418 days), as expected from the asymmetry of the resonance.

5. CONCLUSION

The dynamical response of the oceans to the pole tide potential is the main factor reducing the polar motion resonance period to about 380 days in the retrograde diurnal band. The associated quality factor ~ -10 reflects the strong phase-shift of the this response with respect to the pole tide. In reason of the free core nutation resonance, the body Love number strongly deviates from its mean value of 0.3 in vicinity of the FCN frequency ($\sigma_{FCN} = -1.0050$ cpd). In turn, in the band $[-1.15$ cpd, -0.85 cpd] as observed from the Earth, the resonance period of the polar motion increases above 400 days for frequencies smaller than σ_{FCN} , and remains below this threshold for the band above σ_{FCN} .

In contrast to common polar motion, the excitation at stake, namely the diurnal tidal torque through rigid Earth nutation terms, is almost perfectly known. Despite the remoteness of the polar resonance period from the retrograde diurnal nutation terms in the terrestrial frame, the confrontation of observed nutation terms to those of a rigid Earth, as carried out in (Nurul Huda et al, 2019), amazingly confirms the modeled frequency dependence. So, the luni-solar nutation determined by VLBI reflect the dynamical behavior of the ocean and influence of the fluid core on solid Earth deformation in the retrograde diurnal band.

6. REFERENCE

- Bizouard, C., Nurul Huda, I., Ziegler, Y., Lambert, S.B., 2020, "Frequency dependence of the polar motion resonance", *Geophys. J. Int.* , 220(2), pp. 753–758
- Dehant, V. and Mathews, P. M., 2015, "Precession, Nutation and Wobble of the Earth", Cambridge University Press, 554 p.
- Mathews, P., Herring, T. and Buffett, B., 2002, "Modeling of nutation and precession: New nutation series from non rigid Earth and insights into the Earth interior", *J. Geophys. Res.* 107(B4).
- Nurul Huda, I., Ziegler, Y., Bizouard, C., Lambert, S.B., 2020, "Nutation terms adjustment and implication for the Earth rotation resonance parameters", *Geophys. J. Int.* 220, 759 and *Journées Poster II-6*.
- Petit, Gérard and Luzum, Brian, 2010, *IERS Conventions 2010 (IERS Technical Note 36)*, Frankfurt am Main: Verlag des Bundesamts für Kartographie und Geodäsie.
- Madzak, M., 2016, "Short period ocean tidal variations in Earth rotation", Ph-D Thesis report, TU Wien.
- Nastula, J. and Gross, R., 2015, "Chandler wobble parameters from SLR and GRACE", *J. Geophys. Res. : Solid Earth* 120, pp. 4474-4483.

THE IMPORTANCE OF SEASONAL SEA-LEVEL VARIATIONS FROM GEOPHYSICAL MODELS AND SATELLITE GRAVIMETRY FOR EXCITATION OF LENGTH-OF-DAY

R. DILL, H. DOBSLAW

GFZ, Sec. 1.3 Earth System Modelling, Dep. 1 - Germany

dill@gfz-potsdam.de, dobslaw@gfz-potsdam.de

ABSTRACT. In addition to atmospheric, oceanic, and hydrological contributions, the seasonal length-of-day variation is significantly affected by global mass redistribution between the Earth subsystems. This study uses the new ESMGFZ barystatic sea-level product SLAM as well as estimates of the barystatic ocean bottom pressure anomalies from the GRACE Level 3 GravIS products to quantify the global mass balance. For the annual cycle the global mass balance effect overcompensates the contributions from terrestrial hydrology. Considering the global mass balance, model based mass induced excitation on seasonal length-of-day variations coincide well with estimates from satellite gravimetry. Moreover, the mass terms can be determined accurate enough to attribute the remaining gap in the length-of-day excitation budget between models and observation clearly to an underestimation of atmospheric wind speeds in the global European weather forecast model by -7%.

1. INTRODUCTION

On seasonal time-scales changes in length-of-day (ΔLOD) are mainly caused by external gravitational forces, the redistribution of water masses within Earth's fluid layers atmosphere, ocean, and terrestrial hydrosphere, and the exchange of water masses between these components. Models of the hydrosphere dynamics, i.e., numerical weather prediction models, ocean general circulation models, and terrestrial water storage models can be used to calculate effective angular momentum functions (EAM) describing the excitation of Earth rotation. Atmospheric angular momentum (AAM) consisting of wind and surface pressure changes account for almost 90 % of observed ΔLOD . To a smaller extent ΔLOD is excited by terrestrial hydrology (HAM) and the exchange of water masses between the continents and the ocean responsible for the seasonal sea-level changes (SLAM). The global mass balance, expressed as sea-level variation including effects of loading and self-attraction is generally not included in the available EAM data sets.

2. BARYSTATIC SEA-LEVEL CHANGES

Barystatic sea-level changes are induced by the net-inflow of water from the continents or the atmosphere into the oceans and by a spatially variable deformation of an equipotential surface of the Earth's gravity field that coincides with the sea-surface on a global average. Ocean mass variations can be directly extracted from gravity variations from the Gravity Recovery and Climate Experiment GRACE (2002 - 2017) and GRACE-FO (launched on May 22nd, 2018), e.g. latest GRACE reprocessing release 06 performed at GFZ (Dahle et al., 2018), publicly available from the GravIS portal (gravis.gfz-potsdam.de).

Alternatively, barystatic sea-level changes can be calculated from global water balance assuming that the total mass of water on the globe is constant in time. Gravitationally consistent spatially heterogeneous sea-level variations can be deduced by solving the so-called sea-level equation. Based on daily estimates of the ESMGFZ models of the atmosphere (i.e., global ECMWF analysis and re-analysis data) and the continental hydrosphere (i.e., Land Surface Discharge Model LSDM),

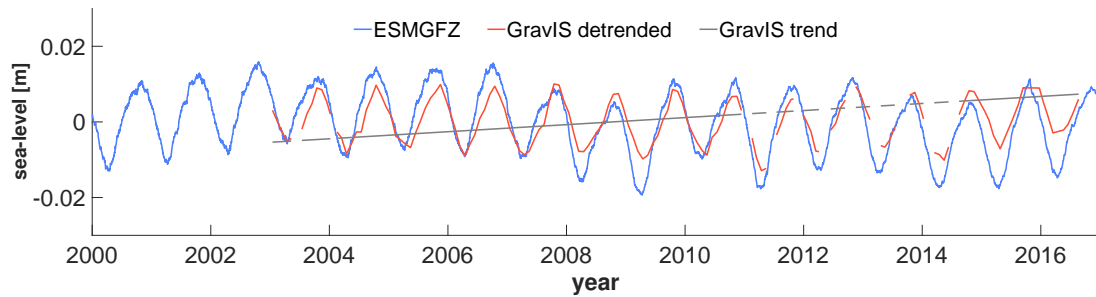


Figure 1: Barystatic sea-level variations for the years 2000 - 2016 in [m]. Blue: 24-hourly sea-level calculated from atmospheric and hydrological mass changes in the ESGMFZ models ECMWF and LSDM by solving the sea-level equation. Red: Monthly GRACE based sea-level variation from GravIS Barystatic Pressure Anomalies, detrended. Gray: Removed trend of GravIS Barystatic Pressure Anomalies.

we note that, apart from the trend, both signals agree very well even on interannual time-scales (Figure 1). The annual amplitude of the barystatic sea-level changes inferred from the ESGMFZ models is about 5% higher than the most recent GRACE estimate from GFZ, and the phase difference is about 7 days. ESGMFZ does not account for post-glacial rebound.

3. EFFECTIVE ANGULAR MOMENTUM FUNCTIONS

Effective Angular Momentum (EAM) functions (χ_1 , χ_2 , χ_3) summarize the geophysical excitation of Earth rotation. Each EAM function consists of so-called mass terms induced by mass redistributions, and motion terms caused by mass transports associated with atmospheric winds and ocean currents. The axial component χ_3 quantifies ΔLOD . Global numerical models allow for the separate quantification of atmospheric angular momentum changes AAM, oceanic angular momentum OAM, and hydrological angular momentum HAM. Alternatively, satellite geodesy allows for the quantification of the total excitation from the inversion of the Earth Orientation Parameters as available from in particular geometric techniques, and additionally also for the estimation of the total mass term from the analysis of gravimetric observations.

3.1 Model-based AAM, OAM, HAM, and SLAM

Since more than 10 years, the Earth System Modelling group at GFZ Potsdam (ESMGFZ) provides daily updated EAM functions as calculated from numerical model data. Since the beginning of 2017 ESGMFZ provides in addition so-called barystatic Sea-Level Angular Momentum functions (SLAM) that account for the GMB consistent to their models used for the calculation of AAM, OAM, and HAM. SLAM is calculated from the global distributions of modeled atmospheric and terrestrial water storage masses by means of the sea-level equation (Tamisiea et al., 2010). SLAM thus balances the global mass in the model system in a way that the sum of the total mass in all four different EAM components is constant at any time. SLAM represents mainly the hydrological and atmospheric excess mass distributed globally into the ocean but includes also the gravimetric effect of loading and self-attraction acting on the ocean sea-level.

Alternative model-based EAM time-series for this study were taken from the Global Geophysical Fluids Center (GGFC) of the International Earth Rotation and Reference Systems Service (IERS). AAM from Atmospheric and Environmental Research (AER) based on the Reanalysis-2 of the National Center for Environmental Prediction and OAM from the Jet Propulsion Laboratory (JPL) using the ocean model ECCO version kf080h.

3.2 Mass Terms from SLR and GRACE

Mass terms of the total excitation χ_3 are directly related to time-variations of the second degree zonal coefficient ΔC_{20} of the Earth's gravity field via the MacCullag's formula. We utilize ΔC_{20} from a multi-satellite Satellite Laser Ranging (SLR) solution (SLR_Multi) as provided by the Center for Space Research (Cheng et al., 2011). We further consider the annual amplitudes and phases obtained from a comparable SLR analysis setting reported by Zhang (2017) noted as SLR_Zhang. Thirdly, we use a SLR series that has been specifically calculated to replace ΔC_{20} in the GRACE RL06 series as published in the GRACE TN11 (SLR_TN11; Cheng et al., 2013). Fourthly, we test an SLR-series processed at GFZ that considers in total six different satellites (SLR_GFZ; Koenig et al., 2018).

In addition, the Gravity Information Service website <http://gravis.gfz-potsdam.de/> (GravIS) provides a preliminary separation of the ocean gravity signal observed by GRACE into the part induced by general circulation pressure anomalies and the GMB part induced by barostatic pressure anomalies. From the latter mass distribution we can derive a SLAM products that relies almost purely on observations from GRACE.

3.3 GAM from IERS C04

The geodetic angular momentum function (GAM) is inverted from the geodetically observed Earth's rotation time series IERS EOP 14 C04 by means of the Liouville equation. Effects of long-period tides were removed from the GAM ΔLOD component.

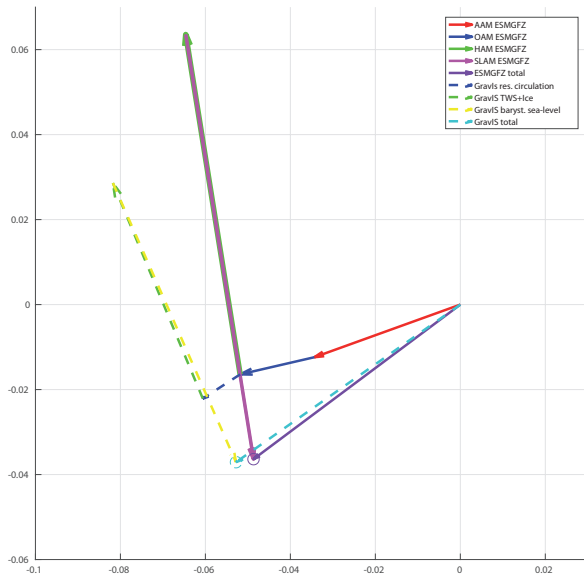
4. ANNUAL MASS TERM VARIABILITY

We initially focus on the effects of the quasi-static mass distribution on the annual and semi-annual harmonic in ΔLOD excitation. We estimated a least squares harmonic fit to the angular momentum time series with bias, trend, annual, semi-annual, and ter-annual harmonics.

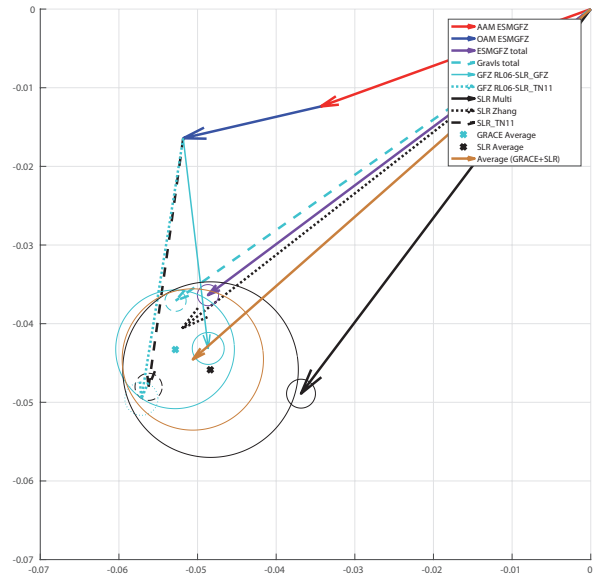
The sum of all model-based ESMGFZ EAM coincides quite well with the total GRACE-based contribution as given by GravIS (Figs. 2a). Annual OAM mass term contributions are well in phase with the atmospheric mass excitations. Residual ocean bottom pressure variability observed by GRACE indicates that MPIOM is still missing a considerable fraction (35%) of the excitation.

For both, ESMGFZ and GravIS, HAM is overcompensated by SLAM with a 24% larger magnitude. SLAM arises by 82% from the hydrological balance, 16% from the atmospheric balance, and 2% from the gravitational effects of atmospheric and continental water masses on the sea-level topography.

The comparison of SLR_TN11 with the GRACE solution GFZ RL06-SLR_TN11 including a replaced C_{20} estimate from SLR_TN11 confirms that numerical integration of EAM from global mass grids obtained with GRACE is sufficiently accurate and do not affect the results (Figs. 2b). In contrast, the choice of an particular SLR solution for the C_{20} replacement in the GRACE level 2 processing significantly impacts the results, see differences between GFZ RL06-SLR_TN11 and GFZ RL06-SLR_GFZ. Considering all three GRACE based solutions, the annual mass term is determined with an accuracy of $\pm 0.9 \cdot 10^{-10}$ in amplitude and $\pm 3.7^\circ$ in phase. The SLR solutions reveal a somewhat larger deviation from each other, $\pm 1.3 \cdot 10^{-10}$ in amplitude and $\pm 8.1^\circ$ in phase. The unweighted mean of the three SLR solutions leads to almost the same annual mass term signal as the GRACE average estimate. Moreover, the result from the ESMGFZ model fit also quite well within the distribution of all considered geodetic estimates. We thus conclude that the mass terms of annual ΔLOD excitations is fairly well understood from a combination of satellite gravimetry and numerical models.



(a) Phasor plot of annual mass term contribution χ_3 mass, part 1. Individual contributions from atmosphere (red), ocean (blue), terrestrial hydrology (green), and barystatic sea-level (pink ESMGFZ, yellow GravIS) as well as the sums (purple ESMGFZ, turquoise GravIS) are given for the model ESMGFZ (solid lines) and GRACE L3 product GravIS (dashed lines). Circles represent the uncertainties in estimating the annual harmonic signal. Amplitudes are in milliseconds, phases are defined as φ in $\sin(\omega(t - t_0) + \varphi)$, where t_0 refers to 0 UTC on January 1 and $\omega = 1/365.25d$.



(b) Phasor plot of annual mass term contribution χ_3 mass, part 2. Individual GRACE based estimates (turquoise) for GravIS (dashed), GFZ RL06-SLR_TN11 (dotted) using the $\Delta C20$ replacement SLR_TN11 and GFZ RL06-SLR_GFZ (solid) using SLR_GFZ, like in GravIS. Orange X and circle defines the unweighted average incl. spread of all three GRACE based estimates. Individual SLR estimates (black) based on $\Delta C20$ from a multi-satellite solution (solid), the low degree replacement for GRACE GSM (dashed), and results published by Zhang (2017) (dotted). Black X and circle defines the unweighted average incl. spread of all three SLR estimates. The average and spread of all satellite (GRACE and SLR) estimates together leads to the mean mass term estimate (brown). For comparison the ESMGFZ model estimate is given in purple. Amplitudes are in milliseconds, phases are defined as φ in $\sin(\omega(t - t_0) + \varphi)$, where t_0 refers to 0 UTC on January 1 and $\omega = 1/365.25d$.

5. ANNUAL MOTION TERM VARIABILITY

On seasonal-to-interannual time-scales, the motion term contributions to ΔLOD are clearly dominated by tropospheric winds (Figure 3). OAM current contributions as simulated by MPIOM are almost two magnitudes smaller. AAM motion terms of ESMGFZ and AER agree very well in their annual phase, ± 2 days. Annual amplitudes of ECMWF-based estimates are lower by about 7% than NCEP results. In addition the annual amplitude – but not the semi-annual amplitude – of NCEP $\chi_{3,motion}$ depends considerably on the analysis period. NCEP gradually converges from $49.11 \cdot 10^{-10}$ (for the years 2000 - 2016) down to $47.01 \cdot 10^{-10}$ (for the years 1990 - 2000), towards the ECMWF level.

As AAM motion terms are two magnitudes larger than the second largest contribution from OAM, an alternative access to AAM $\chi_{3,motion}$ is given by subtracting the total mass contribution $\chi_{3,mass}$ discussed in the previous section from the geodetically observed excitation of ΔLOD .

We calculate two pseudo-observed $\chi_{3,motion}$ terms: (i) by using $\chi_{3,mass}$ terms from the sum of ESMGFZ EAMs; and (ii) by using the unweighted average of all GRACE and SLR estimates

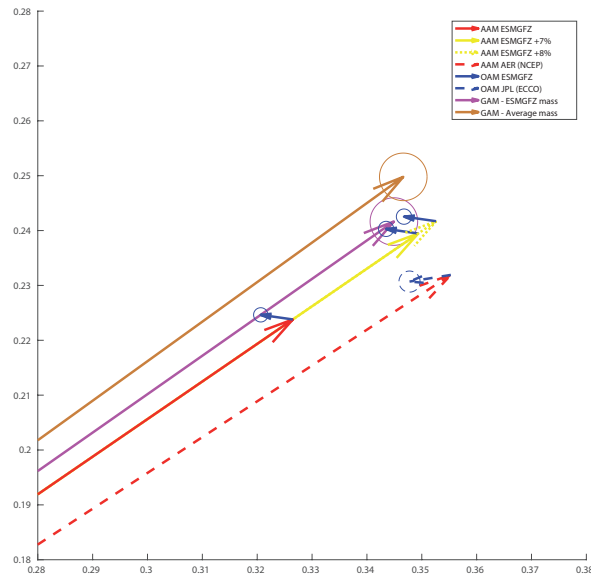


Figure 3: Phasor plot of annual motion term contribution χ_3 motion. Contributions of atmospheric winds (red) from ESMGFZ ECMWF (solid) and AER NCEP (dashed). Contributions of ocean currents (blue) from ESMGFZ MPIOM (solid) and JPL ECCO (dashed). Contributions of enhanced atmospheric winds (yellow) from ESMGFZ ECMWF + 7% (solid) and from ESMGFZ ECMWF + 8% (dotted). Pseudo-observation using GAM (IERS C04) reduced by the ESMGFZ mass term (purple) and the average mass term from GRACE/SLR satellite solutions (brown). Amplitudes are in milliseconds, phases are defined as φ in $\sin(\omega(t - t_0) + \varphi)$, where t_0 refers to 0 UTC on January 1 and $\omega = 1/365.25d$. Circles represent the uncertainties in estimating the annual harmonic signal.

discussed above. The uncertainties arising from the differences of those two mass term estimates account only for 2% in the annual amplitude of $\chi_{3,motion}$ and almost no uncertainty in the annual phase. Hence, the match between pseudo-observed and modeled $\chi_{3,motion}$ terms represents to a large extent the ability of the numerical weather models to capture the seasonal wind variations. By introducing a scaling factor that linearly increases the ECMWF wind terms by +7% we are able to obtain a remarkable closure of the IERS C04 Δ LOD excitation budget for the ESMGFZ mass term combination. When using the mass term estimates from GRACE/SLR, the ECMWF wind terms appear to be underestimated by even 8% or more, and also the NCEP wind terms are some 2% too low.

6. CONCLUSION

In order to validate the atmospheric motion excitation as calculated from predicted winds of numerical weather models against geodetic observation of Earth rotation, we first assess all other contributions coming from mass redistributions within the Earth system components atmosphere, ocean, and continental hydrosphere. Especially, the interactions between this subsystems via the global hydrological cycle cause substantial mass redistributions among atmosphere, ocean and continents.

Alternatively to the sum off all mass induced geophysical fluid excitation functions AAM, OAM, HAM, and SLAM, we used estimates of the Δ LOD mass term derived from satellite missions GRACE and SLR. GRACE based solution are very sensitive to the applied Δ C20 replacement derived from two different SLR solutions. This considerable diversity in SLR Δ C20 estimates is further supported by three more SLR solutions considered in this study. Nevertheless, the mass terms can be determined accurate enough from the ESMGFZ model combination as well as from

an average of all satellite based $\Delta C20$ solutions to attribute the mismatch between modeled and observed seasonal ΔLOD excitation clearly to the modeled motion terms. Especially ECMWF tends to underestimate strong atmospheric winds by -7%.

The conclusion of underestimated atmospheric winds is also supported by several studies comparing upper air wind predictions from numerical weather models with commercial aviation data. Applying a constant multiplier (presently set at 1.04) to the wind speeds forecasted by the Met Office the flight time errors are best minimized. Likely, assimilation systems used at the major weather operational centers (e.g. ECMWF, NCEP) tend to smooth sharp gradients, especially near the strong jets, resulting in too weak jet streaks by -5% to -9% (Cardinali et al., 2004).

7. REFERENCES

- Cardinali, C., Rukhovets, L. & Tenenbaum, J., 2004, "Jet Stream Analysis and Forecast Errors Using Aircraft Observations in the DAO, ECMWF, and NCEP Models", *Monthly Weather Review* 132, American Meteorological Society, pp. 764–779.
- Cheng, M. K., Tapley, B. D. & Ries, J. C., 2013, "Deceleration in the Earth's oblateness", *J. Geophys. Res. (Solid Earth)*, V118, pp. 1–8, doi:10.1002/jgrb.50058.
- Cheng, M., Ries, J. C. & Tapley, B. D., 2011, "Variations of the Earth's Figure Axis from Satellite Laser Ranging and GRACE", *J. Geophys. Res. (Solid Earth)* 116, B01409, doi: 10.1029/2010JB000850.
- Dahle, C., Flechtner, F., Murböck, M., Michalak, G., Neumayer, K., Abrykosov, O., Reinhold, A. & König, R., 2018, "GRACE 327-743 (Gravity Recovery and Climate Experiment): GFZ Level-2 Processing Standards Document for Level-2 Product Release 06 (Rev. 1.0, October 26, 2018)", *Scientific Technical Report STR - Data, 18/04*, Potsdam : GFZ German Research Centre for Geosciences, 20 p., doi: 10.2312/GFZ.b103-18048.
- König, R., Fagiolini, E., Raimondo, J. & Veil, M., 2018, "A Non-tidal Atmospheric Loading Model: On Its Quality and Impacts on Orbit Determination and C20 from SLR", – In: Freymueller, J. T., Sánchez, L.(Eds.), *International Symposium on Earth and Environmental Sciences for Future Generations : Proceedings of the IAG General Assembly, Prague, Czech Republic, June 22- July 2, 2015*, (International Association of Geodesy Symposia ; 147), Springer, pp. 189–194. doi:10.1007/1345_2016_257.
- Tamisiea, M. E., Hill, E. M., Ponte, R. M., Davis, J. L., Velicogna, I. & Vinogradova, N. T., 2010, "Impact of self-attraction and loading on the annual cycle in sea level", *J. Geophys. Res. (Oceans)* 115(C7), pp. 1–15., doi:10.1029/2009JC005687.
- Zhang, X., Jin, S., & Lu, X., 2017, "Global surface mass variations from continuous GPS observations and satellite altimetry data", *Remote Sensing* 9(10), doi:10.3390/rs9101000.

INFLUENCE OF THE 2015-2016 ENSO EVENT ON LENGTH-OF-DAY VARIATIONS

L.I. FERNÁNDEZ^{1,2}, S. BÖHM³

¹ MAGGIA Lab. FCAG. UNLP - Argentina - lauraf@fcaglp.unlp.edu.ar

² CONICET - Argentina

³ TU Wien - Austria - sigrid.boehm@tuwien.ac.at

ABSTRACT. Since the 1980's it is very well known that the El Niño Southern Oscillation (ENSO) event involves a large atmospheric excitation that induces changes of the Earth rotation rate at inter annual scales. In return, ENSO is the trigger of atmospheric teleconnections affecting the global atmospheric circulation. In this work we analyze the regional behavior of the anomalies in the motion terms of the axial component of the Atmospheric Angular Momentum (AAM) taking into account the teleconnections between the ENSO 2015-16 event and other expected regional phenomena. In this way we attempt to confirm previous results that classify this ENSO episode as mixed behavior (i.e. EP and CP type of El Nio).

1. INTRODUCTION.

The austral summer 2015-2016 was unusual and particularly active for the Pacific ocean and the tropical Pacific atmosphere. An El Niño event took place and it has been recorded as one of the most intense (Lambert et al., 2017). Moreover, almost simultaneously, there was an anomaly in the stratospheric Quasi Biennial Oscillation (QBO) (Newman et al. 2016).

ENSO is defined as the most conspicuous interannual variability of the Earths climate system (Yeh et al., 2018). During the canonical El Niño (EN) conditions the easterly trade winds are weakened and the westerly winds increases and as a result the surface of the tropical Pacific ocean gets warmer than usual. Consequently, this effect is linked with the raise in the wind terms (also called motion terms) of the AAM causing that the rotation of the Earth becomes slower and the length-of-day (LOD) increases (Chao, 1989, Dickey et al, 2007). On the opposite, during La Niña (LN) the easterly winds blow stronger than normal in the tropical Pacific resulting in a lower than normal Sea Surface Temperature (SST) over the area (Yeh et al., 2018). This event is then related with an acceleration in the speed of the Earth's rotation, i. e. a shortening of LOD (de Viron and Dickey, 2014).

Since 2005 several studies (see Ren and Jin, 2011 for a brief) addressed the existence of two types of EN that can be classified according to the resultant interaction with the tropical Pacific ocean: the Eastern Pacific (EP) and the Central Pacific (CP) type.

During an EP type El Niño the atmospheric pressure gradient is caused by the high pressure system present over the eastern Pacific Ocean and a low pressure system over Indonesia. This causes that the tropical Pacific ocean interacts with the atmospheric Walker circulation. The EP events were the first characterized and therefore named "canonical El Niño".

In a Central Pacific type event the Pacific Ocean interacts with the Hadley circulation. As a result the air rising near the Equator, flows poleward at a height of 10-15 kilometers and descends about 30° latitude, returning then equatorwards near the surface. This CP type of EN event is also named a El Niño Modoki or Dateline El Niño.

On the other hand, the QBO is an event in the tropical lower stratosphere (about 18-30 km in altitude) that controls the zonal mean wind variability and changes the downward descending

easterly and westerly zonal winds with an approximate period of 28 months (Baldwin et al., 2001).

Since the 80s (see Gross, 2007 and references therein) it is very well known that ENSO excites noticeable interannual variations on LOD and these are caused by changes in the AM of the zonal winds. Besides that, Dickey et al. (1994) studied the ENSO 1982-83 and analyzed a stratospheric AAM time series obtained by integrating (100-50 mbar) data from numerical weather models. The authors asseverate that the wind terms of the stratospheric AAM account for about 20 % of the LOD variance relative to the atmosphere below 100 mbar. More recently Zhou et al. (2008) not only confirmed that the wind terms dominate the intraseasonal variation of the Earth rotation but also confirmed that the stratospheric wind contribution is just about 20 % of the tropospheric AAM wind term.

Recently some authors had linked the stratospheric QBO with ENSO although these links are neither direct nor linear. In 2017, Barton and McCormack linked the abnormal QBO 2015-16 with the ENSO phenomenon 2015-2016, that turned out to be one of the strongest events registered. One year before Newman et al. (2016) reported the anomalous feature in the QBO during the Northern Hemisphere winter of 2015-2016. The expected downward propagation of the westerly phase of the stratospheric winds was modified and there was an anomalous upward displacement from 30 hPa to 15 hPa. This happened in QBO for the first time since 1980.

In view of the above, we recently investigated the influence of the QBO anomaly detected during the El Niño event 2015-2016 on the observed Earth rotation rate and the associated AAM (Fernandez and Bhm, 2019). The results indicated that, even taking into account this anomaly, the stratospheric contribution remains not powerful enough to justify the LOD anomalies but the tropospheric contribution of the combined ENSO effect does, as expected.

On the other hand, De Viron and Dickey (2014) studied the different types of ENSO (EP and CP) and their influence on LOD variations. They conclude that the EP kind of ENSO is more than twice as large as CP and that explains the different impact of the ENSO events on Earth rotation. Lambert et al, (2017) asseverated that although the three extreme ENSO events (1982-83, 1997-98 and 2015-16) produced comparable answers in LOD excitations (near 1 ms.), the ENSO 2015-16 is a mix kind EP-CP.

In this study we seek to regionally characterize the contributions of the anomalies in the atmospheric angular momentum and its relationship with the teleconnections triggered by the ENSO 2015-16 event, taking into account that these connections are different depending on whether it is an EP or a CP event.

2. DATA AND METHOD.

In order to characterize the ENSO 2015-16 event we used the indexes ONI, N3 and N4. They are provided by the Earth System Research Laboratory of the NOAA Climate Prediction Center (<https://www.cpc.ncep.noaa.gov/data/indices/>).

Table 1: The Oceanic Niño Index (ONI) provided by the Climate Prediction Center (CPC), National Weather Service, USA. Values are computed as a 3-month running mean of SST anomalies in the Niño 3.4 region.

Year	DJF	JFM	FMA	MAM	AMJ	MJJ	JJA	JAS	ASO	SON	OND	NDJ
2015	0.6	0.6	0.6	0.8	1.0	1.2	1.5	1.8	2.1	2.4	2.5	2.6
2016	2.5	2.2	1.7	1.0	0.5	0.0	-0.3	-0.6	-0.7	-0.7	-0.7	-0.6

The Oceanic Niño Index (ONI) is used to identify and distinguish El Niño (warm) and La Niña (cool) events in the tropical Pacific. It is the running 3-month mean Sea Surface Temperature anomaly for the Niño 3.4 region (5°N-5°S, 170°-120°W) (Kousky and Higgins, 2007). In general,

El Niño is characterized by a positive ONI greater than or equal to $+0.5^{\circ}\text{C}$ while La Niña events have a negative ONI less than or equal to -0.5°C .

El Niño 3 (N3) and El Niño 4 (N4) indexes correspond to the values of the SST at the Nio 3 (5°N - 5°S , 150° - 90°W) and Nio 4 (5°N - 5°S , 160°E - 150°W) areas respectively. By using N3 and N4, one could built NCP and NEP (Ren and Jin, 2011) from which we can discern if it is an EP or CP El Niño event.

$$\begin{aligned} NEP &= N3 - \alpha N4 \\ NCP &= N4 - \alpha N3 \end{aligned} \quad (1)$$

where

$$\alpha = \begin{cases} 2/5 \\ 0 \end{cases} \quad \text{if } N3.N4 < 0$$

In this study we used the Atmospheric Angular Momentum approach, it means that if considering that the angular momentum of the system Earth is conserved, we estimated the Earth rotation change. In this case: the change in the angular velocity of the Earth with respect to an inertial frame (the variation to the length-of-day, LOD).

The AAM employed for this study was computed by using data from the operational analysis of the European Centre for Medium-Range Weather Forecasts (ECMWF). Mass and motion terms were calculated as volume integrals over pressure increments as described in Schindelegger et al. (2011).

The axial components of the AAM can be written as:

$$AAM_z^{motion} = \int_0^{P_{surf}} \int_{-\pi/2}^{\pi/2} \int_0^{2\pi} \frac{r(\theta, \lambda)^3}{g} u(P, \theta, \lambda) \cos^2(\theta) d\lambda d\theta dP \quad (2)$$

$$AAM_z^{mass} = \int_0^{P_{surf}} \int_{-\pi/2}^{\pi/2} \int_0^{2\pi} \frac{r(\theta, \lambda)^4}{g} \cos^3(\theta) d\lambda d\theta dP \quad (3)$$

Let's call $Z(i, j, t)$ to the elements of AAM_z^{motion} after performing the vertical integration from surface till ∞ . Then,

$$\overline{Z(i, j)}^A = \sum_{t_A} \frac{Z(i, j)}{N_A} \quad (4)$$

where A = EN (El Niño), LN (La Niña) or N (Neutral); t_A and N_A refer to time and number of values, respectively. Moreover, g is the mean gravity acceleration, θ and λ refers to latitude and longitude; P is the atmospheric pressure and u are the zonal wind velocities.

Thus, the elements of the mean AAM_z^{motion} anomalies are

$$\begin{aligned} \Delta Z^{EN}(i, j) &= \overline{Z}^{EN}(i, j) - \overline{Z}^N(i, j) \\ \Delta Z^{LN}(i, j) &= \overline{Z}^{LN}(i, j) - \overline{Z}^N(i, j) \end{aligned} \quad (5)$$

LOD series were taken from the International Earth Rotation and Reference System Service (IERS) Earth Orientation Parameters (EOP) 14 C04 series. This multi-technique combined series is publicly available at the IERS Earth Orientation Center web site (<https://datacenter.iers.org/eop.php>).

LOD data (2010-2019) was evenly spaced, taking one sample every 7 days. Then, the time series was processed to remove the effects of zonal tides, secular tidal breaking, post-glacial rebound

and variations in the fluid core angular momentum (Lambert et al., 2017), as well as seasonal variations (annual and semi-annual). Finally, a 5.9-year periodic function was estimated from a longer LOD time series (1962-2019) and removed. The resultant LOD time series is named as LOD ENSO.

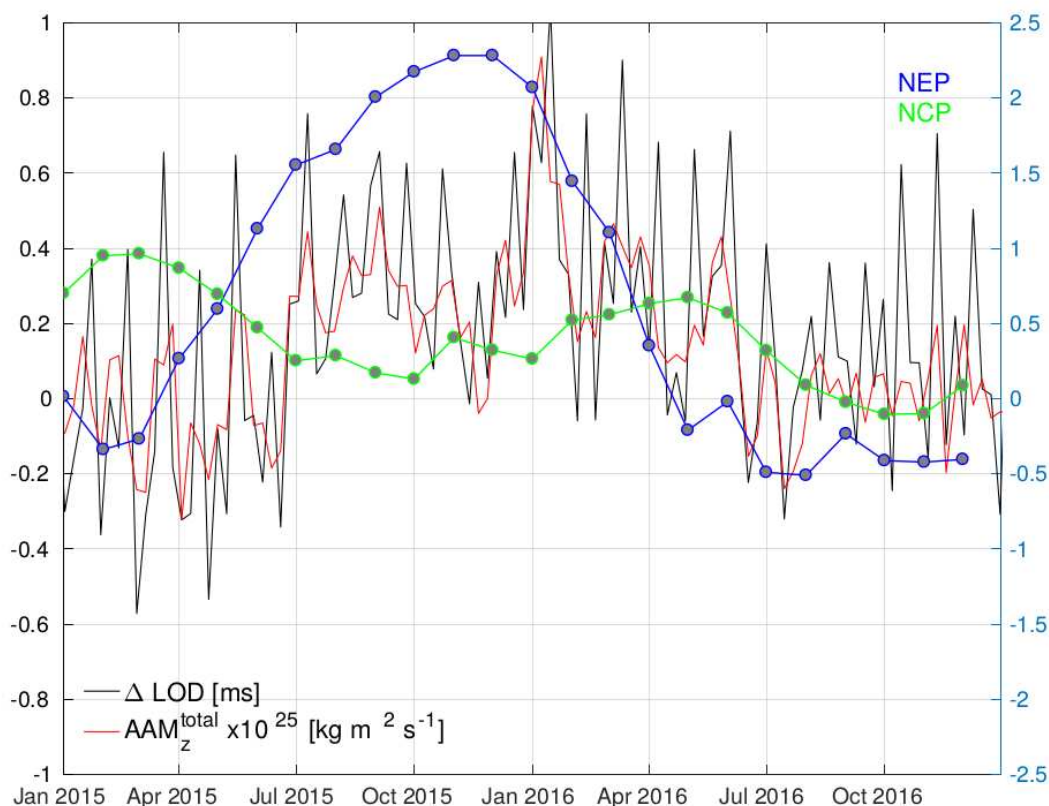


Figure 1: LOD ENSO along with AAMz, the NEP and NCP anomalies.

3. RESULTS

Figure 1 shows the detrended length-of-day time series (LOD ENSO) along with AAMz, and the EP and CP anomalies as defined by Ren and Jin (2011) for the period 2015-2016. Notice that a value of NEP is almost 5 times larger than NCP during austral summer (maximum of ENSO 2015-16). We can also see that NEP is the biggest and NCP values are less than 0.5 during the austral summer 15-16. Notice that, from Ren and Jin (2011), during a CP event $NEP < 0.5$. These results emphasize the behavior of an El Niño canonical event.

Figure 2 shows the AAM_z^{motion} anomalies computed from Eq. (5) for the period $t_{EN} = \text{Jan 1, 2015- May 1, 2016}$ (top) along with the AAM_z^{motion} anomalies for the period $t_{LN} = \text{Aug 2, 2016- Dec 31, 2016}$ (bottom). The correspondent periods for El Niño and La Niña were considered in agreement to the values of ONI (see Table 1). May 2, 2016- Aug 1, 2016 is the neutral period.

From Figure 2 (top) the time averages of the axial AAM wind anomalies during El Niño shows intense activity in Indonesia, North and South Atlantic ocean at mid latitudes and at the North Pacific ocean including North Eurasia and partially North America. Most of these events are expected as ENSO teleconnections without distinguishing between EP or CP El Niño (Yeh et al., 2018). Focusing in the North Pacific this could be the result of the ENSO-like atmosphere-ocean interactions linked to SST anomalies. Although such SST variabilities have a decadal timescale (Pacific Decadal Oscillation, PDO; Interdecadal Pacific Oscillation, IPO), both effects (ENSO and

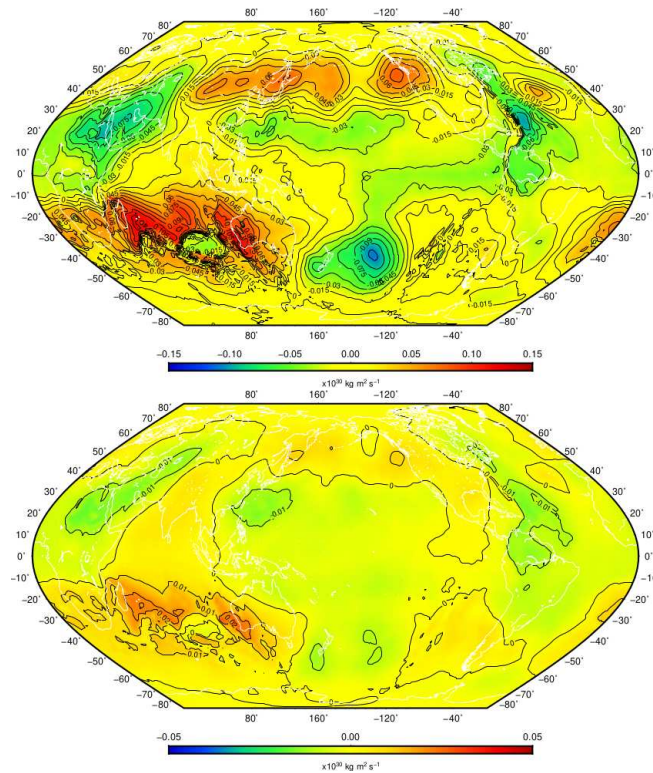


Figure 2: AAM z^{motion} anomalies during El Niño (top) and La Niña (bottom).

PDO/IPO) can be in phase or out of phase in association with the connection between atmospheric effects around the Pacific basin (Yeh et al., 2018). At last, the results in the Atlantic and Indian oceans also come from variabilities in the SST although they have another explanation. In figure 2 (bottom) we can see the axial AAM wind anomalies during La Niña. Notice that the scale is 1/3 smaller than the previous one. Here we can corroborate that there is not significant activity in AAM from the winds during La Niña.

The secondary effects of the teleconnections are in precipitation and temperature changes recorded in different parts of the planet. Because such effects are different depending on whether it is a EP or CP type of El Niño, we emphasize that our conclusions are preliminary and much work still needs to be done.

4. DISCUSSION

ENSO 2015-16 has been recorded as one of the three extreme events (Lambert et al., 2017), but the literature does not converge when classifying it as clearly defined as EP type (e.g. see Palmiero et al., 2017). Effectively, the recent work of Lambert et al., (2017) specifically studied the influence of the atmospheric torques on Earth rotation for the ENSO 15-16 concluding that it contradicts the expected behavior of the mountain torque for an intense EP type El Niño. ENSO has been shown to have a strong impact on different parts of the planet through atmospheric teleconnections. Such teleconnections are sensitive to the longitudes and different according to the type of EN (Yeh et al., 2018). According to the same authors, such connections involve changes in the regional pattern of surface temperature, precipitation and atmospheric circulation outside the tropical Pacific, more specifically, on the North Pacific, the Indian and the Atlantic Ocean.

Provided that we are analyzing the axial component of the motion terms of the AAM, we should carefully study and characterize the resultant effect of such teleconnections on the atmospheric

winds (atmospheric circulation, tropical cyclone activity, etc.) for well-known EP and CP El Niño events.

Because these preliminary results are not conclusive some more work has to be done. Our next steps will include an analysis of the differences between the teleconnections for some other EP and CP events from global meteorological parameters, understanding their impact on the conservation of the Earth's total angular momentum.

5. REFERENCES

- Baldwin, M.P., Gray, L.J., Dunkerton, T.J., Hamilton, K., Haynes, P. H., Randel, W. J., Holton, J. R., Alexander, M. J., Hirota, I., Horinouchi, T., Jones, D.B.A., Kinnersley, J. S., Marquardt, C., Sato, K., Takahasi, M., 2001, "The Quasi-Biennial Oscillation", *Reviews of Geophys.* 39(2), pp. 179–229.
- Barton, C. A., McCormack, J. P., 2017, "Origin of the 2016 QBO disruption and its relationship to extreme El Niño events", *Geophys. Res. Lett.* 44, pp. 11150–11157, doi: 10.1002/2017GL075576.
- Chao, B. F., 1989, "Length-of-day variations caused by El Niño-Southern Oscillation and quasi-biennial oscillation", *Science* 243(4893), pp. 923–925.
- de Viron, O., Dickey, J. O., 2014, "The two types of El Niño and their impacts on the length of day", *Geophys. Res. Lett.* 41, pp. 3407–3412, doi: 10.1002/2014GL059948.
- Dickey, J. O., Marcus, S. L., Hide, R., Eubanks, T. M., Boggs, D. H., 1994, "Angular momentum exchange among the solid Earth, atmosphere, and oceans: A case study of the 1982-1983 El Niño event", *J. Geophys. Res. (Solid Earth)* 99(B12), pp. 23921–23937.
- Dickey, J. O., Marcus, S. L., Chin, T. M., 2007, "Thermal wind forcing and atmospheric angular momentum: Origin of the Earth's delayed response to ENSO", *Geophys. Res. Lett.* 34, L17803, doi: 10.1029/2007GL030846.
- Fernandez, L.I., Böhm, S., 2019, "Influence of the abnormal QBO feature during 2015-2016 on the Earth rotation rate", *Geophys. Res. Abstracts* 21, EGU2019-5493.
- Gross, R.S., 2007, "Earth rotation variations - long period". In Herring, T.A. ed., *Geodesy*, Vol. 3 of *Treatise on Geophysics*, pp. 239–294, Elsevier, Amsterdam.
- Kousky V.E., Higgins, R. W., 2007, "An Alert Classification System for Monitoring and Assessing the ENSO Cycle", *Weather and Forecasting* 22(2), pp. 353–371, doi: 10.1175/WAF987.1.
- Lambert, S.B., Marcus, S.L., de Viron, O., 2017, "Atmospheric torques and Earth's rotation: what drove the millisecond-level length-of-day response to the 2015-2016 El Niño?", *Earth Syst. Dynam.* 8, pp. 1009–1017, doi: 10.5194/esd-8-1009-2017.
- Newman, P. A., Coy L., Pawson S., Lait L. R., 2016, "The anomalous change in the QBO in 2015-2016", *Geophys. Res. Lett.* 43, pp. 8791–8797, doi: 10.1002/2016GL070373.
- Palmeiro, F. M., Iza, M., Barriopedro, D., Calvo, N., Garca-Herrera, R., 2017, "The complex behavior of El Niño winter 2015-2016", *Geophys. Res. Lett.* 44(6), pp. 2902–2910.
- Ren, H.L., Jin, F.F., 2011, "Niño indices for two types of ENSO", *Geophys. Res. Lett.* 38(4), doi:10.1029/2010GL046031.
- Schindelegger, M., Böhm, J., Salstein, D., Schuh, H., 2011, "High-resolution atmospheric angular momentum functions related to Earth rotation parameters during CONT08", *J. Geodesy*, doi: 10.1007/s00190-011-0458-y.
- Yeh, S.W., Cai, W., Min, S.K., McPhaden, M.J., Dommenges, D., Dewitte, B., ... Kug, J. S., 2018, "ENSO atmospheric teleconnections and their response to greenhouse gas forcing", *Reviews of Geophysics* 56(1), pp. 185–206.
- Zhou, Y.H., Chen, J.L., Salstein D.A., 2008, "Tropospheric and stratospheric wind contributions to Earth's variable rotation from NCEP/NCAR reanalysis (2000-2005)", *Geophys. J. Int.* 174, pp. 453–463, doi: 10.1111/j.1365-246X.2008.03843.x.

ATMOSPHERIC EXCITATION OF THE CHANDLER WOBBLE ALONG THE 20TH CENTURY: INSIGHTS FROM ECMWF ERA-20C REANALYSIS

S. LAMBERT

Observatoire de Paris, Université PSL, CNRS - France - sebastien.lambert@obspm.fr

ABSTRACT. We used the grids of the ECMWF ERA-20C atmospheric global circulation model to compute the atmospheric excitation and torques in the Chandler frequency band over 1900-2010. We showed that (i) the atmosphere acts dominantly over Eurasia (via a mountain torque on the Tibetan plateau and a large variability of the angular momentum over Western Siberia) with strong bursts in the AAM around 1910, 1940 and the 1970s, and (ii) the mountain torque appears to be correlated with North Atlantic modes (AMO, NAO, AO). The study suggests that the variability of the Chandler wobble at decadal/multidecadal time scales is controlled by the North Atlantic/Arctic system that acts mainly on the Tibetan mountains.

1. INTRODUCTION

The Earth's Chandler wobble is a free rotational mode of the mantle associated with the Earth's ellipticity whose period is close to fourteen months in the rotating frame and amplitude is about 0.2 arcsecond, strongly variable. Its excitation mechanism has remained quite mysterious long after its discovery at the end of the 19th century, until the development of atmospheric and oceanic circulation models shed new lights. It is now admitted that the Chandler wobble is fueled through continuous atmospheric and oceanic mass redistribution (Gross 2000; Brzeziński and Nastula 2002; Bizouard et al. 2011). Most of the studies rely on the recent period covered by the standard global circulation reanalyses released by the main climate center like the National Center for Environmental Prediction/National Center for Atmospheric Research (NCEP/NCAR) or the European Center for Medium-range Weather Forecast (ECMWF). However, the recent development of century reanalyses, at least for the atmosphere, opens new perspectives on assessing the excitation of the Chandler wobble, measured since 1860, by the Earth's external fluid layers.

This work uses the ECMWF ERA-20C reanalysis data to assess the atmospheric contribution to the Chandler wobble over the entire 20th century. Although we miss the oceanic contribution, we nevertheless reveal the regional interactions between the atmosphere and the solid Earth as well as possible impact of global climate oscillations.

2. DATA AND METHODS

We used grids of surface pressure, instantaneous north/eastward turbulent stress, zonal and meridional wind speeds at 17 pressure levels between 10 and 1000 mBar as provided by the ECMWF ERA-20C reanalysis (Poli et al. 2015) covering 1900-2010. Gridded values are directly monthly means of 6-hourly model output. The spatial resolution was set to $2^\circ \times 2^\circ$. From local values of the variables, we obtained local values of the pressure and wind terms of the atmospheric angular momentum (AAM) as well as mountain and friction torques following standard formulations (Barnes et al. 1983; Huang et al. 1999). The mountain torque was computed using the orography of the model. Then, to obtain the AAM and torques contained only in the Chandler frequency band, we filtered AAM and torques in time domain by applying a Panteleev filter (Panteleev and Chesnokova

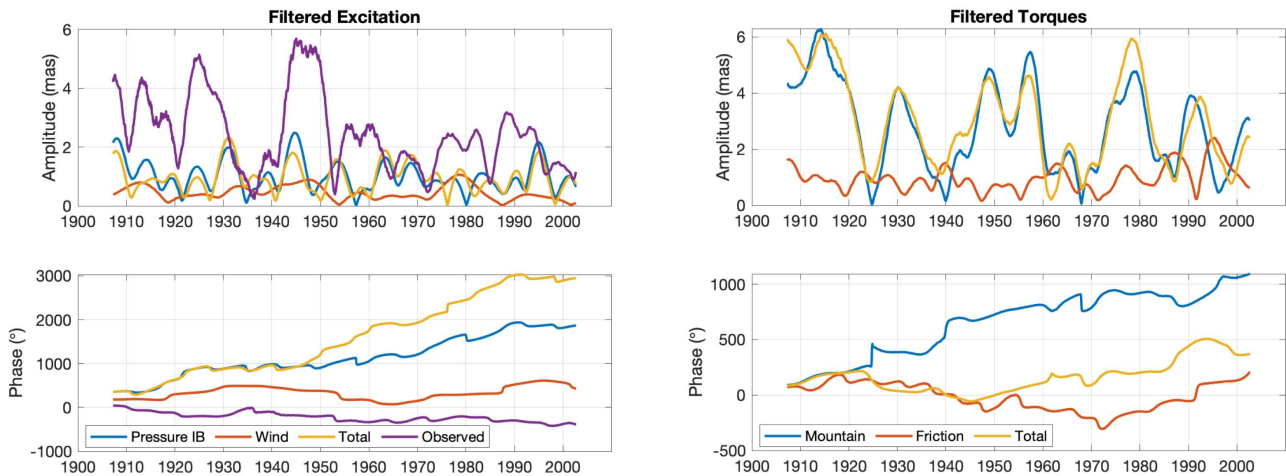


Figure 1: Amplitudes and phases of the complex excitation and torques in the Chandler frequency band.

2011) of bandwidth 35 days and central period 430.3 days. We removed 7 years of data at the beginning and the end of the filtered series in order to account for edge filtering effects, thus letting an effective period covering 1907-2003. The choice of the central frequency and the bandwidth is debatable: we rely on previous studies using similar values (e.g., Zotov and Bizouard 2012; 2015) and on the fact that the window should not be too large to avoid catching the premises of the annual wobble.

The observed excitation was derived from the observed polar motion series taken at the International Earth rotation and Reference systems Service (IERS) EOP C01 provided by the IERS Earth Orientation Center (Bizouard et al. 2019). The excitation was derived following Wilson (1985) and then filtered to keep only the signal in the Chandler frequency band.

Regarding climate indices, we searched for long datasets, resulting in some inhomogeneity since the different series were generally based on different datasets. We retrieved the Atlantic Multidecadal Oscillation (AMO) index from the Earth System Research Laboratory (ESRL) of the National Oceanic and Atmospheric Administration (NOAA). It is derived from the Kaplan extended sea surface temperature (SST) data set (Kaplan et al. 1998) and starts in 1856. The Pacific Decadal Oscillation (PDO) was derived from the UKMO Historical SST data set for 1900-81 and made available by the Joint Institute for the Study of Atmosphere and Ocean (JISAO), University of Washington. We also considered the Southern Oscillation Index (SOI), the North Atlantic Oscillation (NAO), the Arctic Oscillation (AO), and the Antarctic Oscillation (AAO), all derived from the NOAA 20C reanalysis (Compo et al. 2011).

All time series were made consistent by resampling geodetic data and climate indices at the epochs of the final AAM and torque series.

3. DISCUSSION AND CONCLUSION

The filtered time domain globally integrated quantities are shown in Figure 1. The atmospheric excitation is dominated by the surface pressure with prominent activity in 1930, 1940, and 1995. It is far insufficient to explain the observed geodetic excitation that shows large peaks in 1925 and 1945, letting a possible important contribution from the oceans but also for a deficiency of the current atmosphere reanalysis. The mountain torques strongly dominates the total torque.

The Figure 2 represents the regression of the local excitation and torques onto their globally integrated values (allowing to locate the regions that are the most representative of the global

activity) and the Hovmoeller (time-latitude and time-longitude) diagrams (that allow to get a time-domain view of the activity). The charts reveal the existence of 'hot spots' concentrating the interaction between the atmosphere and the solid Earth. The surface pressure excitation is thus dominated by Eurasia, consistently with a mountain torque essentially acting over the Himalaya and the Tibetan plateau, fueled by meridional pressure gradients between Siberia and Southern Eurasia. Strong bursts in this Eurasian excitation are observed circa 1910, 1940, and 1970. A relatively important mountain torque is seen around the Antarctic plateau with an interannual variability. Note that a strong mountain torque does not necessarily correspond to a high AAM, the latter being the time integration of the former, a persistently (even moderately) high mountain torque is relevant to lead to a high AAM. The wind AAM and friction torque pictures are consistent with what one can expect from pressure patterns (e.g., strong surface wind and friction torque acting at the west entry of the surface pressure pattern, i.e., over Western Europe) and are not shown here.

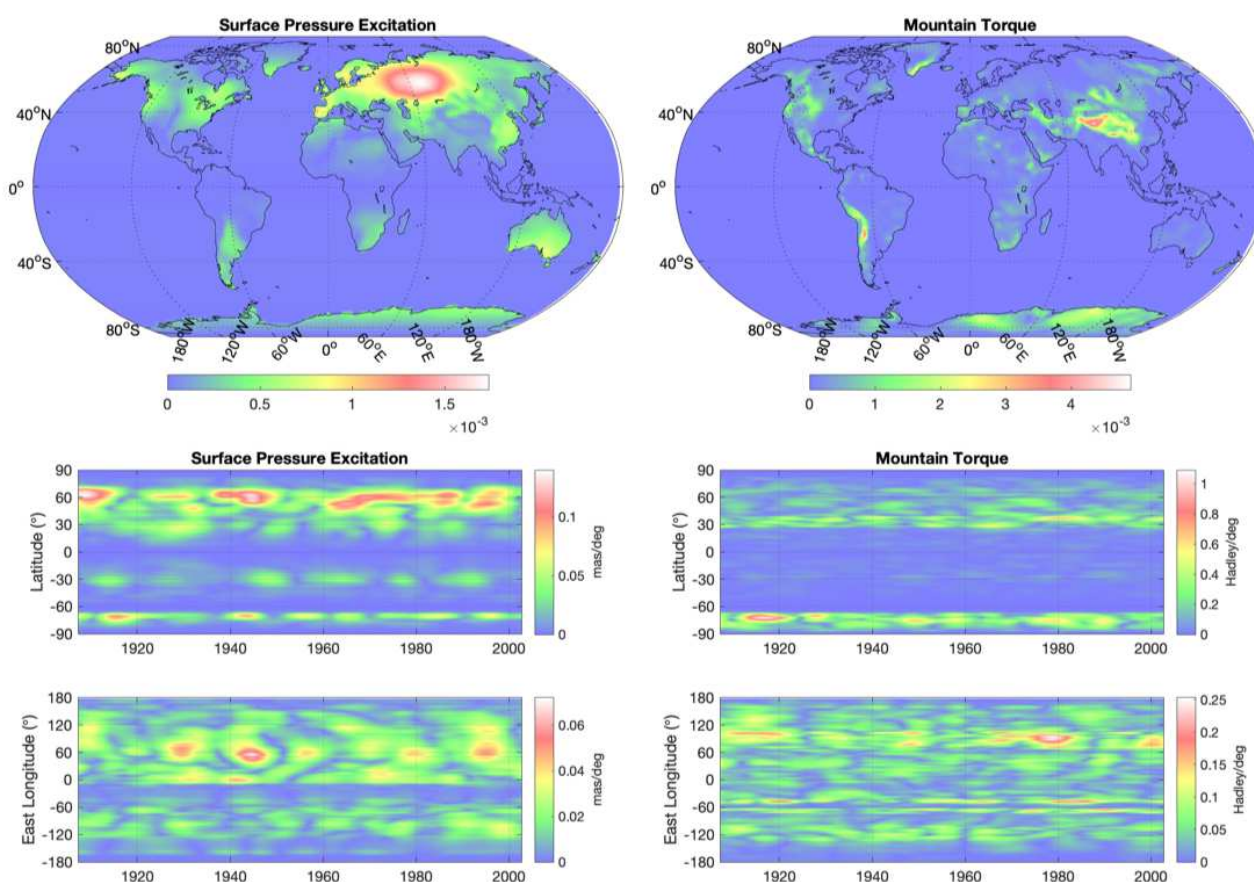


Figure 2: (Top) Regression of the local pressure AAM and mountain torque onto the global pressure AAM and mountain torque. (Bottom) Time-latitude and time-longitude (Hovmoeller) diagrams of the surface pressure excitation and mountain torque.

The activity of the surface pressure and mountain torque being strongly localized, one could ask whether their time variations are connected to local climate modes like, e.g., the various climate modes inherent to the North-Atlantic/Eurasia system (NAO, AO, AMO). To test this hypothesis, we computed the Pearson correlation coefficients r between various climate indices with global surface pressure excitation and the mountain torque for several time lags (Table 1). One has

to note that short time lag (say less than 10 years) might be understood as ‘no lag’ since the Panteleev filtering acts as a smoothing window of about 7 years. The significance of the correlation was evaluated using the null hypothesis that detrended series are independent AR1 processes (e.g., Anderson 1958) under which the sample value of the Fisher z-transformation of the correlation is expected to differ from zero by a number $s = z\sqrt{\text{DOF} - 3}$ of standard deviations. Here, DOF is the number of degrees of freedom and can be estimated as the ratio of the length of the series to the length of the segment corresponding to the decorrelation time (itself deduced as the lag for which the autocorrelation function decreases to $1/e$). We highlight below the correlations with small lags (here given in years) and Fisher s coefficient larger than 2, i.e., providing a probability of rejection of the null hypothesis larger than 95%. Thus, we detected a possible connection of the surface pressure excitation with the AAO and of the mountain torque with the NAO, the AO and the AMO. These results are consistent with the finding of a mountain torque detected on the edge of the Antarctic plateau and the surface pressure pattern found over Eurasia on the regression map varying at interannual and multidecadal time scales, producing a strong mountain torque on the Himalayan and Tibetan mountains. Note that the inconsistency between the climate indices (some of them being dependent on another circulation model) and ERA-20C grids may lead to miss some correlations or misestimate their statistical significance: ideally, the indices should be derived from the ERA-20C data.

		X			Y		
		r	Lag (yr)	s	r	Lag (yr)	s
Global Pressure Excitation	AAO	0.599	0.2	3.0	-0.365	-37.3	2.3
	AMO	-0.469	10.8	1.5	-0.380	9.4	1.1
	AO	-0.357	-15.4	1.7	-0.419	-25.3	2.0
	NAO	0.235	-13.3	1.2	-0.387	2.3	2.0
	PDO	0.489	26.8	2.2	0.415	17.9	1.5
	SOI	-0.320	26.6	1.7	-0.422	16.7	2.2
Global Mountain Torque	AAO	-0.416	-4.3	2.0	-0.448	15.9	2.4
	AMO	0.760	0.0	2.5	-0.420	15.8	1.2
	AO	-0.593	9.2	3.3	0.321	-37.2	1.3
	NAO	-0.469	8.9	2.6	-0.541	7.5	3.1
	PDO	-0.562	20.6	2.4	0.479	29.5	2.3
	SOI	-0.608	-19.5	4.2	-0.286	-24.4	1.3

Table 1: Pearson correlation coefficient r and optimal lag between the globally integrated surface pressure excitation and mountain torque and various climate indices. The coefficient s represents the Fisher z-score interpreted as a measurement of the significance of the correlation estimates.

In conclusion, our study suggests that the variability of the Chandler wobble at decadal and multidecadal time scales is controlled by the North Atlantic/Arctic system that produces surface pressure variations over Siberia and, as a consequence, a mountain torque on the Tibetan mountains. Although never done over such a long period, this study remains partial since (i) no ocean data were used and (ii) only one atmospheric circulation model was tested. It can be continued in two directions. The first one is completing the atmospheric study with ERA-20C ensemble members in order to evaluate a model error and introduce at least one other reanalysis, possibly from an independent meteorological center (e.g., the NOAA-CIRES-DOE Twentieth Century Reanalysis project; Compo et al. 2011). The second direction is to explore the recently released ocean reanalyses (e.g., SODA, Carton and Giese 2008; ORA 20C, de Boisseson and Alonso-Balmaseda 2016) to test the closure of the AAM budget over an entire century. The comparison of the most

consistent models with the observed polar motion excitation could lead to understanding the causes of the historical minimum of the Chandler wobble in the 1920s (Guinot 1978) and assess whether the current minimum (likely reached mid-2018) is due to the same reasons.

4. REFERENCES

- Anderson, T. W., 1958, "An Introduction to Multivariate Statistical Analysis", Wiley.
- Barnes, R. T. H., R. Hide, A. A. White, and C. A. Wilson, 1983, "Atmospheric angular momentum fluctuations, length-of-day changes and polar motion", *Proceedings of the Royal Society of London Series A* 387, pp. 31-73.
- Bizouard, C., S. Lambert, C. Gattano, J.-Y. Richard, and O. Becker, 2019, "The IERS EOP 14C04 solution for Earth orientation parameters consistent with ITRF 2014", *J. Geodesy* 1, pp. 1–13.
- Bizouard, C., F. Remus, S. Lambert, L. Seoane, and D. Gambis, 2011, "The Earth's variable Chandler wobble", *Astronomy & Astrophysics*, 526:A106.
- de Boisseson, E. and M. Alonso-Balmaseda, 2016, "An ensemble of 20th century ocean reanalyses for providing ocean initial conditions for CERA-20C coupled streams", Technical Report 24, ECMWF.
- Brzeziński A., and J. Nastula, 2002, "Oceanic excitation of the Chandler wobble", *Advances in Space Research*, 30(2), pp. 195-200.
- Carton, J. A. and B. S. Giese, 2008, "A reanalysis of ocean climate using simple ocean data assimilation (SODA)", *Monthly Weather Review* 136(8), pp. 2999–3017, 2019/12/05.
- Compo, G. P., J. S. Whitaker, P. D. Sardeshmukh, et al., 2011, "The twentieth century reanalysis project", *Quarterly Journal of the Royal Meteorological Society* 137(654), pp. 1–28.
- Gross, R. S., 2000, "The excitation of the Chandler wobble", *Geophys. Res. Lett.* 27, pp. 2329–2332.
- Guinot, B., 1972, "The Chandlerian Wobble from 1900 to 1970, *A&A* 19, p. 207.
- Huang, H.-P., P. D. Sardeshmukh, and K. M. Weickmann, 1999, "The balance of global angular momentum in a long-term atmospheric data set", *J. Geophys. Res.* 104, pp. 2031–2040
- Kaplan, A., M. A. Cane, Y. Kushnir, A. C. Clement, M. B. Blumenthal, and B. Rajagopalan, 1998, "Analyses of global sea surface temperature", pp. 1856-1991. *J. Geophys. Res. (Oceans)* 103(C9), pp. 18567–18589.
- Panteleev, V., and T. Chesnokova. 2011, "Deconvolution problem in inertial gravimetry", *Moscow University Physics Bulletin* 66(1), pp. 78–82.
- Poli, P., H. Hersbach, P. Berrisford, et al., 2015, "ERA-20C deterministic", Technical Report 20, ECMWF, Shinfield Park, Reading.
- Wilson, C. R., 1985, "Discrete polar motion equations", *Geophysical Journal* 80, pp. 551–554.
- Zotov, L. and C. Bizouard, 2012, "On modulations of the Chandler wobble excitation", *Journal of Geodynamics* 62, pp. 30–34.
- Zotov, L. and C. Bizouard., 2015, "Regional atmospheric influence on the Chandler wobble", *Advances in Space Research* 55(5), pp. 1300–1306.

DYNAMIC EFFECTS OF THE SPATIAL MOVEMENT OF THE EARTH-MOON SYSTEM IN THE EARTH'S POLE OSCILLATION

V. PEREPELKIN¹, A. FILIPPOVA², S. KRYLOV³

¹ Moscow aviation institute - Russia - vadimkin1@yandex.ru

² Moscow aviation institute - Russia - filippova.alex@gmail.com

³ Moscow aviation institute - Russia - krylov@mai.ru

ABSTRACT. On the basis of a numerical-analytical approach, the irregular effects of the oscillatory process of the Earth's pole, associated with changes in the Chandler and annual component, are investigated. An approach to the study of oscillatory processes in the motion of the Earth's pole is proposed on the basis of joint consideration of the Chandler and annual components of its motion. Within the framework of this approach, a transformation to a new coordinate system has been found, in which the in-phase motion of the pole and the precession of the lunar orbit are shown.

1. INTRODUCTION

The trajectory of the motion of the pole at the Earth's surface forms a spiral curve that is traced out as the pole moves around its mean position. The drift of the mean pole has a long-period and secular character represented by the coordinates (c_x, c_y) . The time dependence of the pole coordinates can be represented by the superposition of the trend, the 433 day Chandler wobble (amplitude a_{ch} , angular frequency \dot{w}_{ch}), the annual term (amplitude a_h , angular frequency \dot{w}_h), and small-scale oscillations, as a rule, having an irregular or quasi-regular character. As a consequence of the superposition of the Chandler and annual components, the radius of the trajectory varies, on average, from 70 to 230 milliarcseconds (mas) with a period of approximately 6.45 years.

The irregular behavior of the main components, namely of the Chandler and annual oscillations, is poorly understood. Of a significant interest are studies aimed at establishing the geophysical and celestial-mechanical reasons for such behavior, and the construction of refined prediction models for the EOP required for solving high-precision satellite navigation problems.

2. THE OSCILLATORY PROCESS OF THE EARTH POLE AT THE FREQUENCY OF THE MOON'S ORBIT PRECESSION

We analyzed the variations of the main components of the polar oscillations by carrying out a transformation of the coordinates of the pole in several steps. This transformation of the coordinate system can be written in matrix form (Perepelkin et al, 2019) :

$$\begin{pmatrix} \xi_p \\ \eta_p \end{pmatrix} = \Pi(w_{ch/h} - w_1) \left[\Pi(w_1) \begin{pmatrix} x_p - c_x \\ y_p - c_y \end{pmatrix} - \begin{pmatrix} a_0 \\ 0 \end{pmatrix} \right], \quad (1)$$

where $w_{ch/h}$ and w_1 are uniformly increasing angles at the frequencies $\dot{w}_{ch/h}$ and \dot{w}_1 determined by the set of relations

$$\dot{w}_{ch/h} = \begin{cases} \dot{w}_h, & \text{if } a_h < a_{ch}, \\ \dot{w}_{ch}, & \text{if } a_h > a_{ch}, \end{cases}$$
$$\dot{w}_1 = \begin{cases} \dot{w}_{ch}, & \text{if } a_h < a_{ch}, \\ \dot{w}_h, & \text{if } a_h > a_{ch}, \end{cases}$$

$$\dot{\omega}_{ch} = 2\pi(0.84 \div 0.85)\omega_*, \quad \dot{\omega}_h = 2\pi\omega_*$$

Here ω_* is the yearly frequency.

In (1) Π is a planar rotation matrix, a_0 the mean amplitude of the oscillations of the pole about its mean position (i.e., without the trend), c_x and c_y represent the mean position of the pole and contain constants, secular terms, and variations with periods exceeding six years, and $\dot{\omega}_{ch/h} - \dot{\omega}_1 = \pm\nu\tau$ is the frequency of the six-year cyclic motion of the pole.

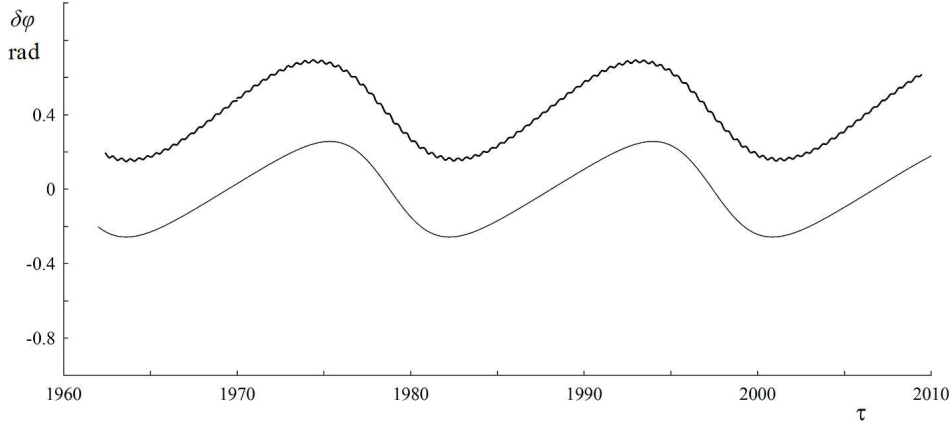


Figure 1: Comparison of the polar angle variations $\delta\varphi$ (bottom line) with the oscillations along the equator of the point of intersection of the lunar orbit and the equator (upper line), constructed using the lunar ephemeris.

We can illustrate oscillations of the Earth's pole synchronous with the precessional motion of the lunar orbit in the new coordinate system (ξ_p, η_p) , and determine the regular component of the phase variations $\delta\varphi$.

In Figure 1 the polar angle $\delta\varphi$ is compared with the oscillations of the intersection point between the equator and the lunar orbit. The units of the oscillation amplitudes are radians, and τ is time in standard years. In the new coordinate system, it is possible to illustrate synchronous oscillations of the Earth pole with the precessional motion of the Moon orbit and to determine the regular component of the $\delta\varphi$ phase variation, which makes it possible to use lunar ephemeris when predicting additional terms in the model of Earth pole motion.

3. CONCLUSION

Based on the results of our numerical simulations and model verification on various time intervals, we conclude that, when the stability of the oscillations of the Earth's pole with a frequency close to the precessional frequency of the lunar orbit is preserved, the terms added to the model enable an enhancement of the precision with which the position of the Earth's pole can be predicted by, on average, 30 cm at horizon intervals from two to eight years within a single oscillatory regime for the pole (before the change in the oscillation frequency of the additional harmonics).

4. REFERENCES

Perepelkin V.V., Rykhlova L.V., Filippova A.S., 2019, "Long-Period Variations in Oscillations of the Earth's Pole due to Lunar Perturbations", *Astronomy reports* 63(3), pp. 238–247, doi: 10.1134/S1063772919020070.

NEXT GENERATION OF COUPLED CLIMATE MODELS AND THE PREDICTED ATMOSPHERIC EXCITATION OF LENGTH OF DAY

S. BÖHM¹, D. SALSTEIN²

¹ Department of Geodesy and Geoinformation, TU Wien - Austria - sigrid.boehm@tuwien.ac.at

² Atmospheric and Environmental Research, Inc. - USA - dsalstei@aer.com

ABSTRACT. The Earth's climate, past, present, and future, is one of the most important topics of our time. The Coupled Model Intercomparison Project (CMIP) is a global effort to gather outputs of climate models from numerous institutions worldwide, built on common experimental design with standardized target quantities. We investigate the historical and predicted evolution of two such variables, namely the eastward zonal wind velocity and the surface temperature, with the aim of deriving connections between global warming (under different scenarios) and long-term variations in the Earth rotation speed. Axial atmospheric angular momentum functions and trends thereof were calculated from one model of CMIP phase 6 and compared to results from a previous work that used a CMIP5 model. Both studies reveal an increase in axial atmospheric angular momentum (with the magnitude depending on the assumed scenario), which would result in a corresponding slowing of Earth rotation.

1. INTRODUCTION

The Coupled Model Intercomparison Project (CMIP) is an initiative of the World Climate Research Programme with the aim of understanding past and future climate changes due to natural variability or in response to changing radiative forcing. A variety of different groups and Earth system models from research groups all over the world are contributing to the ongoing CMIP phase 6 (Eyring et al., 2016). Such models relate to physical variables of the atmosphere, ocean, and other climate elements.

In this paper we identify models and experimental designs (as available) common to the previous version (CMIP5) and to CMIP6 and show the differences between the project phases. Both CMIP phases use the so-called Representative Concentration Pathways (RCP) to simulate future greenhouse gas concentration trajectories in terms of a possible rate of radiative forcing values leading up to the year 2100, and may be related to socioeconomic factors. Our main focus is on the comparison of trends in zonal winds and axial angular momentum functions derived from global wind fields associated with different model runs from historical times to the future centuries.

2. CMIP phase 6

The current phase CMIP6 differs from the predecessor CMIP5 in several points. First, a new generation of climate models has come into operation. Second, since time has advanced, the starting year for the future simulations is 2015 instead of 2006. Third, a new set of scenarios of concentrations, emissions, and land use was defined. And finally, a more federated structure was adopted, building on an ensemble of CMIP-Endorsed MIPs.

For this work we employed data produced in the frame of the so-called ScenarioMIP, which is one of the CMIP6-Endorsed MIPs with the mission to provide multi-model climate projections based on alternative scenarios of future emissions and land use changes produced with integrated assessment models (O'Neill et al., 2016). In CMIP5 the RCPs were used as a basis for the climate projections. Within CMIP6 the climate projections are driven by a new set of emissions and land

use scenarios evolving from a combination of revised future pathways of societal development, the Shared Socioeconomic Pathways (SSPs) and the RCPs (RCPs are identified by radiative forcing levels of X.X W/m² in 2100).

The most important scenarios of CMIP6 are briefly described in the following with the corresponding scenarios from CMIP5 given in braces, if applicable:

- SSP1-2.6 (RCP26) Sustainability Taking the Green Road: multi-model mean of less than 2 degrees Celsius warming by 2100 expected, substantial land use change (increased global forest cover), low forcing.
- SSP2-4.5 (RCP45) Middle of the Road: combines intermediate societal vulnerability with intermediate forcing level.
- SSP3-7.0 Regional Rivalry A Rocky Road: new in CMIP6, substantial land use change (decreased global forest cover), high NTCF (Near-Term Climate Forcers) emission.
- SSP5-8.5 (RCP85) Fossil-fueled Development Taking the Highway: strong economic and social developments, exploitation of abundant fossil fuel resources, adoption of resource and energy intensive lifestyles.

3. DATA AND RESULTS

The CMIP6 variables eastward zonal wind and surface temperature were used for the present investigation. CMIP6 is an ongoing effort, and at the time of the preparation of this work, these variables were available in terms of historical simulations and identified scenarios only for a few models, from which we chose the GFDL-ESM4 of the US National Oceanic and Atmospheric Administration (NOAA). We calculated trends in the zonal mean zonal wind fields at each pressure level, with pressure decreasing locally by height (19 levels from 1000 to 1 hPa). The trends from CMIP6 are shown in Figure 1 for the historical simulation and the four scenarios listed above.

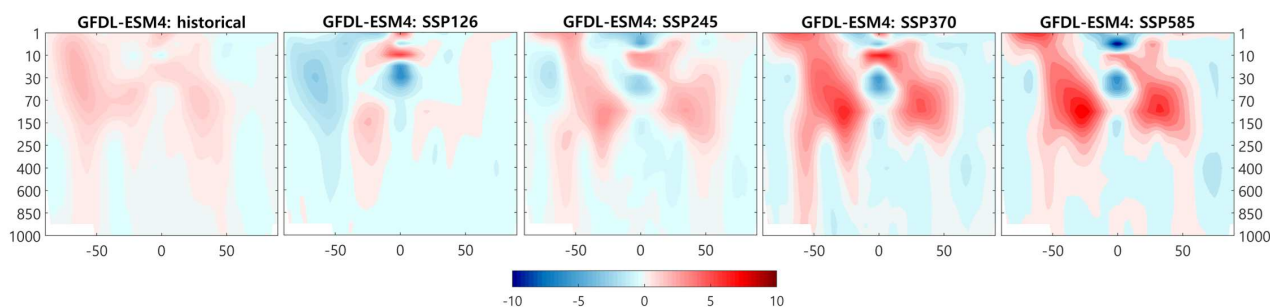


Figure 1: Trends in zonal means of zonal wind [m/s/century] from CMIP6 ScenarioMIP, model GFDL-ESM4 (John et al., 2018; Krasting et al., 2018), x-axis: latitude [degrees], y-axis: pressure [hPa].

In order to illustrate the relation with global warming, the trends in surface temperature for each grid point are presented in Figure 2.

Axial atmospheric angular momentum functions (AAMF) χ_3 were derived using the angular momentum approach (with vertical integration from 1hPa to 1000 hPa) to study the integral effect of changing zonal winds based on different scenarios. The resulting AAMF and trends for the GFDL-ESM4 model are shown in Figure 3. For comparison Figure 4 displays the AAMF and trends corresponding to a different model from CMIP5, which were obtained in a previous study by Salstein et al. (2012).

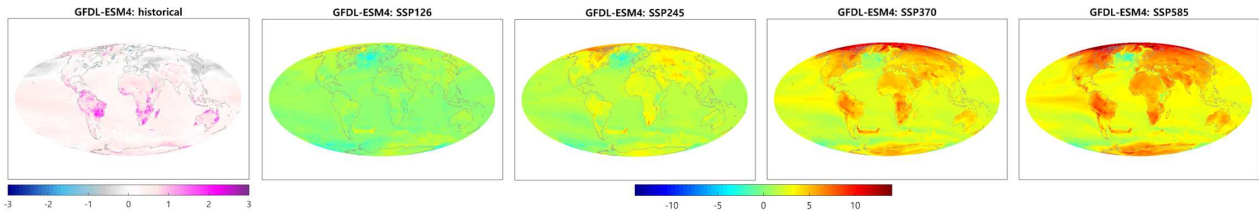


Figure 2: Trends in surface temperature [degrees Celsius/century] from CMIP6 - ScenarioMIP, model GFDL-ESM4.

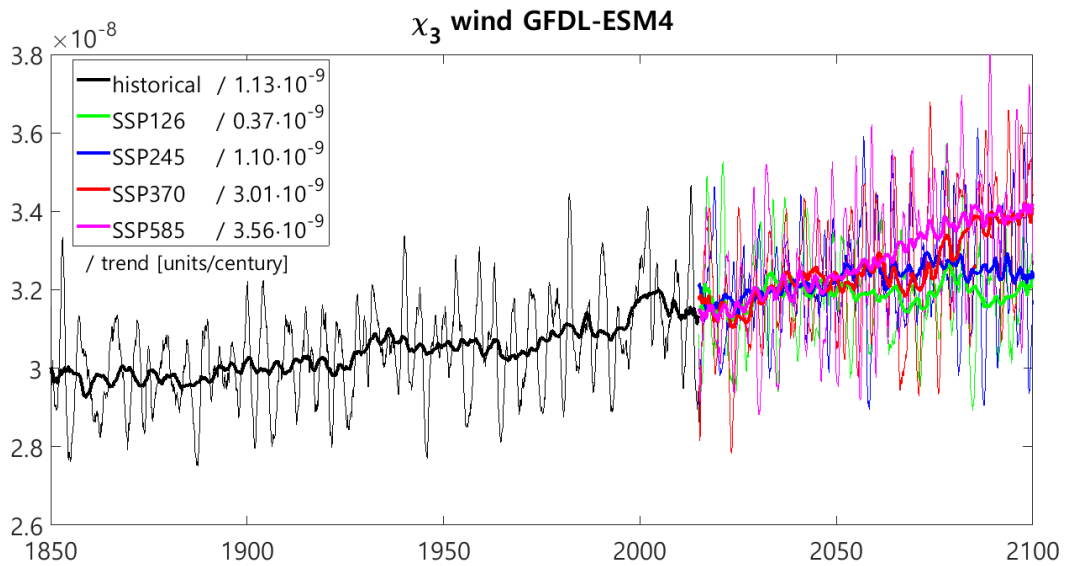


Figure 3: Axial atmospheric angular momentum functions χ_3 and trends from CMIP6 Scenario MIP, model GFDL-ESM4.

4. CONCLUSION

We can confirm a clear relationship between the rise in global temperature, and its geographic distribution, and the areas with increasing wind speed, leading to an increase in axial AAM (equivalent to an increase in length of day/slower rotation). More intense greenhouse gas emission scenarios would lead to slower terrestrial rotation.

The most important layers in terms of excitation of length of day are located in the upper atmosphere (around 100 hPa), in tropical to subtropical latitudes. Mean trends in zonal means of zonal wind are very similar from CMIP5 and CMIP6 in this respect (the picture for CMIP5 is not included in this paper but in the associated poster, which can be downloaded from <https://syrtel.obspm.fr/astro/journees2019/>).

The course of the AAMF over the 21st century from CMIP6 is somewhat different from that of CMIP5, whereas the overall trends and results in 2100 are again similar.

Global atmospheric angular momentum units increase from around 3.1×10^{-8} , in excitation units now to around 3.4×10^{-8} units in the year 2100 in the highest scenarios runs, approximately a 10 percent increase in overall relative axial angular momentum of the atmosphere.

The wind terms from CMIP6 show an offset with respect to the CMIP5 estimates, which is

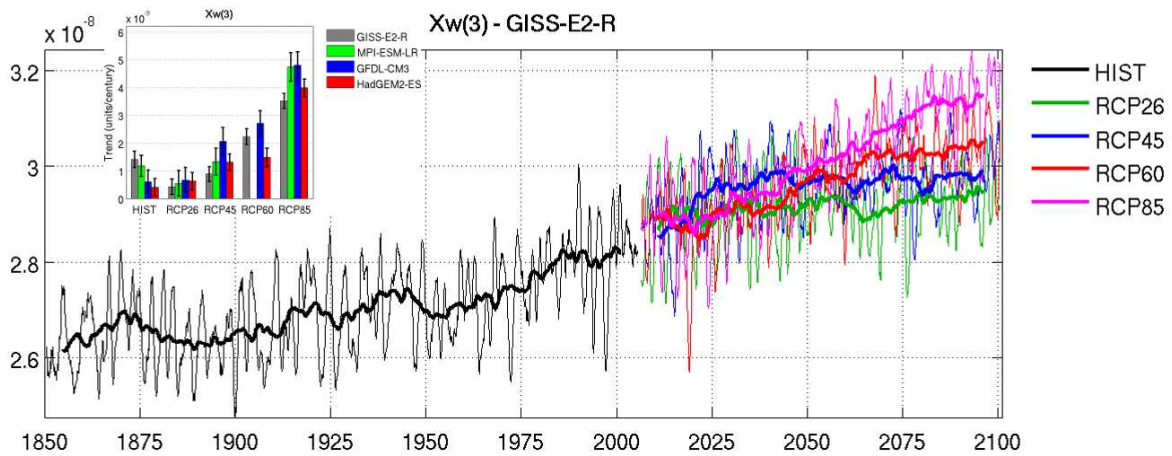


Figure 4: Axial atmospheric angular momentum functions χ_3 and trends from a CMIP5 model (Salstein et al., 2012).

likely due (at least in part) to differences in the vertical integration limits, but needs to be further investigated.

5. REFERENCES

- Eyring, V., Bony, S., Meehl, G.A., Senior, C.A., Stevens, B., Stouffer, R.J., and Taylor, K.E., 2016, "Overview of the Coupled Model Intercomparison Project Phase 6 (CMIP6) experimental design and organization", *Geosci. Model Dev.* 9, pp. 1937–1958, doi: 10.5194/gmd-9-1937-2016.
- O'Neill, B. C., Tebaldi, C., van Vuuren, D. P., Eyring, V., Friedlingstein, P., Hurtt, G., Knutti, R., Kriegler, E., Lamarque, J.-F., Lowe, J., Meehl, G. A., Moss, R., Riahi, K., and Sanderson, B. M., 2016, "The Scenario Model Intercomparison Project (ScenarioMIP) for CMIP6", *Geosci. Model Dev.*, 9, pp. 3461–3482, doi: 10.5194/gmd-9-3461-2016.
- Salstein, D., Quinn, K. J., and Abarca del Rio, R., 2012, "Using Coupled Climate Models for Predictions of Angular Momentum", presentation at the 92nd American Meteorological Society Annual Meeting, New Orleans.
- John, J. G., Blanton, C., McHugh, C., et al., 2018, "NOAA-GFDL GFDL-ESM4 model output prepared for CMIP6 ScenarioMIP ssp126, ssp245, ssp370, ssp570", Version 20180701, Earth System Grid Federation, doi: 10.22033/ESGF/CMIP6.8684, *.8686, *.8691, *.8706
- Krasting, J. P., John, J. G, Blanton, C., et al., 2018, "NOAA-GFDL GFDL-ESM4 model output prepared for CMIP6 CMIP historical", Version 20190726, Earth System Grid Federation, doi: 10.22033/ESGF/CMIP6.8597.

Session V

**SPACE NAVIGATION
&
SOLAR SYSTEM DYNAMICS**

INPOP NEW RELEASE: INPOP19a

A. Fienga^{1,2}, V. Viswanathan^{2,3}, P. Deram¹, A. Di Ruscio^{4,1}, L. Bernus^{2,1},
J. Laskar², M. Gastineau², N. Rambaux², O. Minazzoli⁵, D. Durante⁴, L. Iess⁴

¹ Géoazur-CNRS 7329, Université Côte d'Azur, Observatoire de la Côte d'Azur,
France - agnes.fienga@oca.eu

² IMCCE, CNRS, PSL University, Observatoire de Paris - France

³ Goddard Space Flight Center, Greenbelt - USA

⁴ Department of Mechanical and Aerospace Engineering, Sapienza University - Italy

⁵ Artemis, CNRS, Université Côte d'Azur, Observatoire de la Côte d'Azur - France

ABSTRACT. We present here the new planetary ephemeris INPOP19a for the orbits of the 8 planets of the solar system, the moon, Pluto as well as 14000 asteroids. It is fitted over about 155000 planetary observations including 9 positions of Jupiter deduced from the Juno mission, an extension of the Cassini data sample from 2014 to 2017 for the Saturn orbit and of the MEX data from 2016.4 to 2017.4 for the Mars orbit. The asteroid orbits were fitted on the almost 2 millions of observations obtained by the GAIA mission and delivered with the DR2. Finally a new bayesian procedure for the computation of the masses of 343 main-belt asteroids has been applied and leads to an important improvement in the accuracy of the Mars orbit and of its extrapolation capabilities. INPOP19a is available on www.imcce.fr/inpop.

1. INPOP19A : THE NEW PLANETARY EPHEMERIDES

1.1 Update of the data sample In this new ephemeris, the nine first perijove of Juno around Jupiter have been included improving the accuracy of the Jupiter barycentric orbit. Furthermore with the end of the Cassini mission in 2017, a new analysis of the data used for the navigation and for the radio experiment was proposed in order to benefit from the best knowledge in terms of gravity field and Cassini orbital systematics accumulated over the mission duration. In this context, new positions deduced from an independent analysis of Cassini data were obtained and taken into account into the INPOP construction, extending the time coverage for the Cassini data sample from 2014 to 2017. The full dataset used for the INPOP19a adjustment is presented in Table 1. In this table are given the periods of each data sample as well as the number of observations and their average accuracies. The last two columns give the weighted root mean square (WRMS) for each data sample estimated with INPOP19a and INPOP17a.

1.2 Postfit residuals and comparison to INPOP17a

The last two columns of Table 1 give the WRMS of the post-residuals obtained for INPOP19a and INPOP17a. As it can be seen the improvement is clear for Jupiter, Saturn and Mars.

For Mars, as explained in section and in (Fienga et, 2019), the gain in postfit residuals is significant, in particular for the MRO/MO residuals and is due to i) an improvement in the solar plasma correction ii) and mainly to a new method for constraining asteroid masses perturbing the Mars orbits. For MRO/MO, INPOP19a improves INPOP17a residuals by 44% on a common interval of fit.

For Jupiter the improvement is obviously brought by the Juno tracking data. It reaches 2 order of magnitude: from about 2 km for INPOP17a to 20 m for INPOP19a in keeping good residuals for the other flybys obtained between 1975 to 2001.

For Saturn, the prolongation of the data set from 2014 to 2017 was crucial to identify the

Table 1: INPOP19a data samples used for its adjustment. The columns 1 and 2 give the observed planet and an information on the source of the observations. Columns 3 and 4 provide the number of observations and the time interval, while the column 5 gives the *a priori* uncertainties provided by the space agencies or the navigation teams. Finally in the last two columns, are given the WRMS for INPOP19a and INPOP17a.

Planet / Type	#	Period	Averaged Accuracy	WRMS	
				INPOP19a	INPOP17a
Mercury					
Direct range [m]	462	1971.29 : 1997.60	900	0.95	0.96
Messenger range [m]	1096	2011.23 : 2014.26	5	0.82	1.29
Mariner range [m]	2	1974.24 : 1976.21	100	0.37	0.78
Venus					
VLBI [mas]	68	1990.70 : 2013.14	2.0	1.13	1.178
Direct range [m]	489	1965.96 : 1990.07	1400	0.98	0.98
Vex range [m]	24783	2006.32 : 2011.45	7.0	0.93	0.93
Mars					
VLBI [mas]	194	1989.13 : 2013.86	0.3	1.26	1.16
Mex range [m]	30669	2005.17 : 2017.37	2.0	0.98	3.37
		2005.17 : 2016.37	2.0	0.97	1.26
MGS range [m]	2459	1999.31 : 2006.70	2.0	0.93	1.31
MRO/MO range [m]	20985	2002.14 : 2014.00	1.2	1.07	1.91
Jupiter					
VLBI [mas]	24	1996.54 : 1997.94	11	1.01	1.03
Optical ra/de [arcsec]	6416	1924.34 : 2008.49	0.3	1.0	1.0
Flybys ra/de [mas]	5	1974.92 : 2001.00	4.0/12.0	0.94/1.0	0.58/0.82
Flybys range [m]	5	1974.92 : 2001.00	2000	0.98	0.71
Juno range [m]	9	2016.65 : 2018.68	20	0.945	116.0
Saturn					
Optical ra/de [arcsec]	7826	1924.22 : 2008.34	0.3	0.96/0.87	0.96/0.87
Cassini					
VLBI ra/de [mas]	10	2004.69 : 2009.31	0.6/0.3	0.97/0.99	0.92/0.91
JPL range [m]	165	2004.41 : 2014.38	25.0	0.99	1.01
Grand Finale range [m]	9	2017.35 : 2017.55	3.0	1.14	29.0
La Sapienza range [m]	614	2006.01 : 2016.61	6.0	1.01	2.64
Uranus					
Optical ra/de [arcsec]	12893	1924.62 : 2011.74	0.2/0.3	1.09 / 0.82	1.09 / 0.82
Flybys ra/de [mas]	1	1986.07 : 1986.07	50/50	0.12 / 0.42	0.42 / 1.23
Flybys range [m]	1	1986.07 : 1986.07	50	0.92	0.002
Neptune					
Optical ra/de [arcsec]	5254	1924.04 : 2007.88	0.25/0.3	1.008 / 0.97	1.008 / 0.97
Flybys ra/de [mas]	1	1989.65 : 1989.65	15.0	0.11 / 0.15	1.0/1.57
Flybys range [m]	1	1989.65 : 1989.65	2	1.14	1.42

contribution of TNOs into the perturbations to be applied on the Saturn orbit. Furthermore the introduction of data obtained between 2006 and 2016 and analyzed independently from JPL is also very important to confirm that these data obtained in between 2006 and 2007 have to be taken into account in the adjustment with a high level of weighting. The improvement between INPOP17a and INPOP19a is of a factor 30 for the Grand Finale and 2.6 for the period between 2006 and 2016.

2. ASTEROID MASSES

As described in (Fienga et, 2019), we combine knowledge of the physical properties of asteroids by spatial or ground-based surveys, in particular spectral classes, to planetary ephemerides determinations of masses in order to enlarge the set of estimated asteroid masses and study their consistency with the spectral classes of the asteroids. For the mass determination, we use a constrained least square method based on the BVLS (Bounded Values Least Squares) algorithm from (Lawson and Hanson, 1974) which limits the fitted parameters to given intervals. Bounds have been selected according to the parameters of the fit: for asteroid masses, the lower bounds and the upper bounds are chosen according to the *a priori* masses and the *a priori* uncertainties deduced from the literature. The selection of 343 asteroids perturbing the planetary orbits is done based on the method of (Kuchynka and Folkner, 2014) and (Folkner et al. 2014). For defining the bounds, we separate the sample in the three taxonomic complexes C, S, and X according to the spectral informations extracted from the M3PC data base (`mp3c.oca.eu`). *A priori* uncertainties on the initial guess values for the masses are deduced by considering random sampling of the density uncertainties and by including the $3\text{-}\sigma$ diameter uncertainties to the density lower bounds and the upper bounds. A detailed description of the method is given in (Fienga et, 2019). In Figure 1 are compared the densities obtained with INPOP19a and those deduced from INPOP17a and DE430. As one can see, the INPOP19a density distribution is far more realistic : when INPOP17a and DE430 may obtained densities up to several tens of $\text{g}\cdot\text{cm}^{-3}$, the maximum density obtained with INPOP19a is of about $6\text{ g}\cdot\text{cm}^{-3}$. Furthermore the INPOP19a distribution in term of taxonomic complexes is also closer from expected than the one of INPOP17a and DE430. At the end 103 asteroids have their masses determined with INPOP19a with an accuracy better than 30 %.

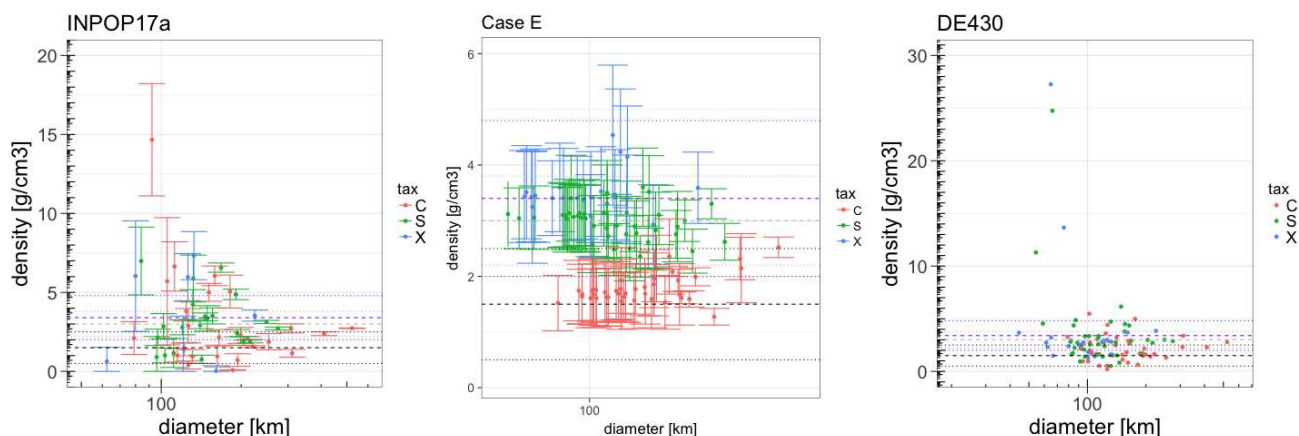


Figure 1: Comparisons between INPOP19a (Case E), INPOP17a and DE430. The x-axis gives the diameters in kilometers and y-axis indicates the densities in $\text{g}\cdot\text{cm}^{-3}$.

3. GAIA DR2 ASTEROID ORBITS

In 2013, was launched the astrometric satellite GAIA. Among observations of about 1 billion of stars with an accuracy down to $24\ \mu\text{arcseconds}$, the satellite also observed objects in the solar system. In 2018, were released positions and velocities of about 14 099 known Solar System objects

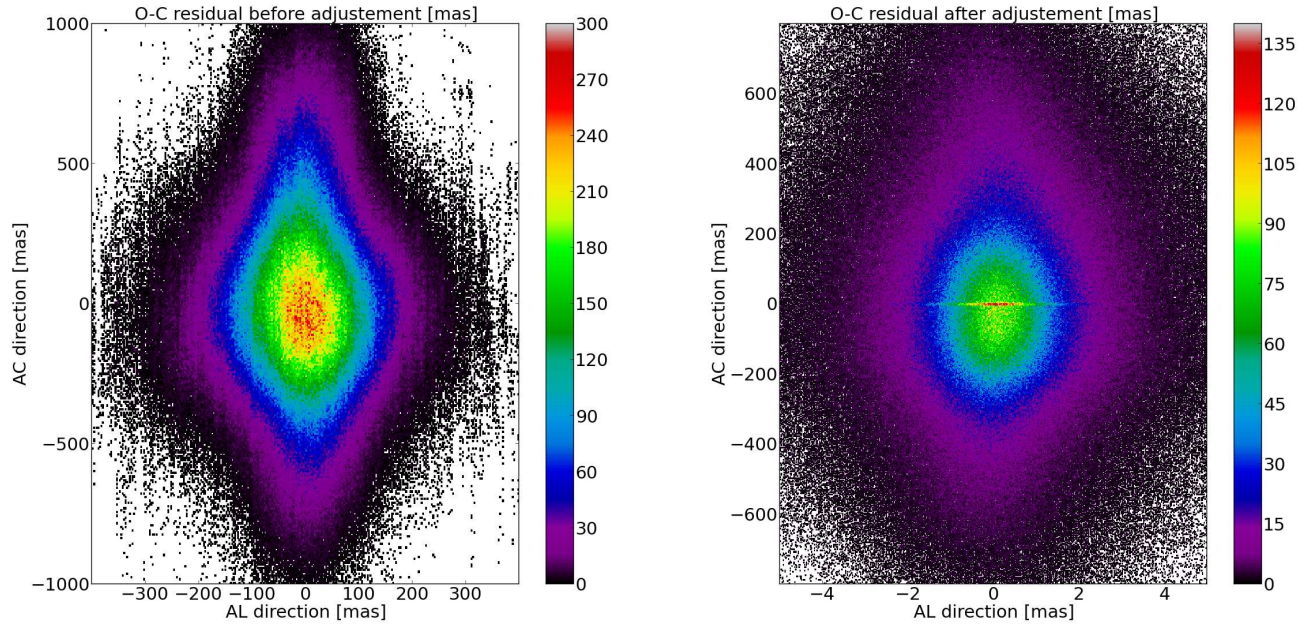


Figure 2: Density plot of the residuals in the (AL,AC) plane given in mas before and after the adjustment of the initial conditions. The colorbar and the axis range were chosen to be directly comparable with Figure 19 of (Gaia collaboration, 2018)

mainly main belt, Near-Earth and Kuiper belt asteroids based on nearly 2 millions observations. The positions were acquired in the GAIA specific coordinates AL and AC as described in (Gaia collaboration, 2018) with an optimal range of brightness $G=12-17$ where the accuracy in the AL-direction reaches the milliarcsecond (mas). As the error on AC remains considerably larger, the information provided by GAIA is essentially one dimensional. These particular features give rise to very strong correlations between right ascension and declination coordinates given in the barycentric reference system (BCRS) and have to be fully taken into account during the orbit determination process. 14099 orbits have then been integrated with INPOP together with the planetary and moon orbits. We fit these orbits to the GAIA data in using the correlation matrix provided by the DPAC. We did not fit the planetary orbits together with the asteroid orbits but we iterate the procedure in order to include the asteroid orbital improvements brought by the GAIA observations to the computation and the adjustment of the planet orbits. In order to integrate the motion of 14099 orbits in a reasonable time, we included the perturbations of the Sun and of the main planets but in a newtonian formalism and in taking into account only a reduced number of the biggest asteroids that can have an influence on the other asteroid orbits. For a sake of comparison, we chose the same list of perturbing asteroids (16) as in (Gaia collaboration, 2018). However, after testing different alternative lists of perturbers, due to the limited interval of time covered by the GAIA data (22 months), no differences are noticeable on the residuals after the fit. Figure 2 presents the residuals obtained before and after the fit of the 14099 asteroids in using INPOP19a. The obtained results are very similar to those published by (Gaia collaboration, 2018). The mean and the standard deviation of the residuals after the adjustment are respectively 0.08 and 2.13 mas in AL direction (compared to 0.05 and 2.14 in (Gaia collaboration, 2018)). 96% of the AL residuals fall in the interval $[-5,5]$ mas and 53% are at sub-mas level. 98% of the AC residuals fall

in the interval [-800 800] mas.

4. CONCLUSION

The INPOP19a planetary ephemeris is available on the IMCCE website www.imcce.fr/inpop with different formats: spice, calceph and the old JPL binary. A detailed documentation is also provided.

5. REFERENCES

- Fienga, A., Avdeïidou, C., Hanus., J., 2019, "Asteroid masses obtained with inpop planetary ephemerides", MNRAS , 3035.
- Kuchynka, P., Folkner, W. M., 2013, "A new approach to determining asteroid masses from planetary range measurements.", Icarus 222, pp. 243–253
- Folkner, W. M., Williams, J. G., Boggs, D. H., Park, R. S., Kuchynka, P., 2014, "The Planetary and Lunar Ephemerides DE430 and DE431", IOM-196:C1
- Gaia Collaboration, 2018, "Gaia Data Release 2. Observations of solar system objects", A&A 616, pp.A13.
- Lawson, C., Hanson, R., 1974, "Solving least squares problems", eds SIAM

IMPLEMENTATION OF IMPROVED MAGNITUDE PARAMETERS FOR SOLAR SYSTEM PLANETARY EPHEMERIDES

J.L. HILTON, S.G. STEWART

U.S. Naval Observatory - USA - james.l.hilton12.civ@mail.mil, susan.g.stewart@navy.mil

ABSTRACT. The joint publications of the U.S. Naval Observatory and Her Majesty's Nautical Almanac Office have integrated the Mallama & Hilton (2018) algorithms to improve planetary apparent magnitude and surface brightness values. Prior calculations were based on algorithms from the 1960s, except for Mercury and Venus (Hilton 2005). Physical ephemeris predictions are required for factors such as identification, exposure estimates, and offset between center-of-light and center-of-object. These improved algorithms will first appear in *The Astronomical Almanac* for 2021 and *Astronomical Phenomena* for 2022. The uncertainty in the V magnitude predictions ranges from 0.02 mag for Uranus to nearly 0.2 mag for Mars. There is room for improvement, and work is underway to further enhance these magnitude ephemerides is discussed. Renewed interest in planetary magnitude theory has implications for predictions of the characteristics of exoplanets and space navigation.

1. INTRODUCTION

Prediction of the apparent magnitudes and surface brightness of solar system bodies are required for factors such as identification, exposure estimates, and offset between center-of-light and center-of-object. Renewed interest in physics behind planetary magnitude has implications for predictions of the characteristics of exoplanets for missions such as HabEx (2019) and space navigation.

The joint publications of the U.S. Naval Observatory and Her Majesty's Nautical Almanac Office *The Astronomical Almanac* and *Astronomical Phenomena* provide these data. The algorithms used to predict the apparent magnitudes were, until recently, primarily drawn from Harris (1961). Hilton (2005) supplied the algorithms for Mercury and Venus. And the value $V(1,0)$ ¹ for Jupiter was drawn from Irvine et al. (1968).

The Harris algorithms were entirely empirical and ignored variations arising from albedo markings on the surfaces of Mercury and Mars. The predicted apparent magnitude for Mars had an uncertainty in V of about 0.3 mag. The uncertainty for the other planets was on the order of 0.1 mag. The large uncertainties made the predictions poor for planning purposes, and using empirical formulae, ignoring the physical properties of the planets made these algorithms useless as guides for applications to exoplanets.

2. NEW ALGORITHMS FOR THE ASTRONOMICAL ALMANAC

The 2007 edition of *The Astronomical Almanac* introduced the Hilton (2005) algorithms for predicting the apparent magnitudes of Mercury and Venus. Previous predicted apparent magnitude values for these planets were particularly inaccurate. The inferior positions of these two planets have made accurate photometric observations difficult because they must be made against a background that varies in both space and time. Figure 1 illustrates the problem. Modern data taken from CCD and spacecraft observations are compared to the older data referenced by Harris. At small phase

¹The body's apparent magnitude when it is 1 au from the Sun, 1 au from the observer, and at a phase angle of 0°.

angles there is an offset of about 0.1 mag and there is a nonlinear trend maximizing at difference of about 0.4 mag at a phase angle of 120°.

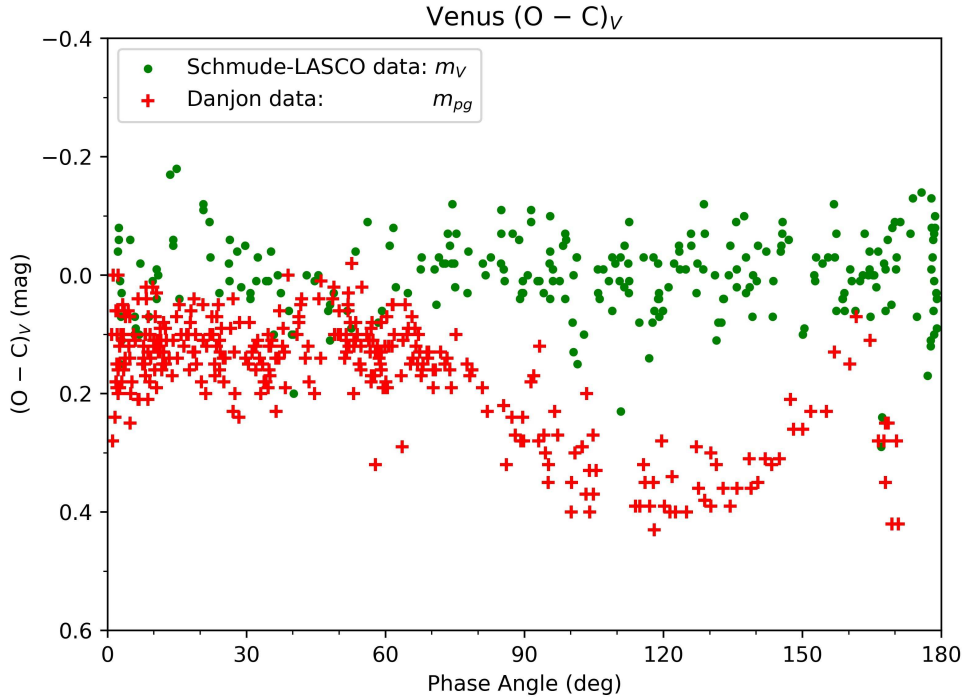


Figure 1: The $(O - C)_V$ s for the modern CCD (Schmude) and spacecraft (LASCO) data and the older Danjon (1949) data. The predicted values were calculated using the Mallama & Hilton (2018) algorithm.

Starting with the 2021 edition of *The Astronomical Almanac* all of the prediction algorithms will be replaced with those from Mallama & Hilton (2018). Table 1 gives the $1 \sigma_V$ uncertainties in the predicted apparent V magnitudes for these algorithms. Both Mercury and Mars have significant albedo markings. The algorithm for Mars attempts to correct for these (see § 2.1.), but no correction has been applied for Mercury. Venus has a glory near inferior conjunction (see § 3.1.) that was not incorporated into its algorithm.

2.1 Mars

Mars is still a significant problem. It is not clear that the current parameterization of Mars' algorithm is optimal. It contains terms to account for Mars' variation with sub-Earth longitude and season. The seasonal term includes changes such as changes in the size of its polar caps and cloud cover. It also accounts for changes in its sub-Earth latitude. The rate of change with longitude is variable and may be as great as $0.039 \text{ mag hr}^{-1}$ in V . The rate of change of the seasonal term also varies greatly. Its maximum rate of change is only $0.0042 \text{ mag day}^{-1}$ in V . The difference in the rates of change is primarily caused by the large difference in the rate of change of the angular velocity of rotation, $350^\circ.8 \text{ day}^{-1}$, compared to Mars' tropical year angular motion, $0^\circ.524 \text{ day}^{-1}$. The variations in magnitude are similar for the two terms. The difference between the minimum and maximum rotational magnitudes is 0.11 mag, and the difference for the seasonal magnitudes is 0.14 mag.

The tabular interval for the apparent magnitude of Mars in *The Astronomical Almanac* is four days, 3.8986 martian sidereal rotations. Thus the sub-Earth longitude at the tabulation interval is

Planet	σ_V
Mercury	0.079
Venus	0.069
Mars	0.074
Jupiter	0.042
Saturn (planet and rings)	0.042
Saturn (planet alone)	0.244
Uranus	0.024
Neptune	0.034

Table 1: Standard deviation uncertainties of the revised predictions for apparent V magnitudes of the planets.

slowly regressing on average. This regression could give the user a false idea of how Mars' apparent magnitude changes, so the sub-Earth longitude correction will not be included in the tabulation but will likely be included in other products with a finer time resolution.

Mars also has major dust storms that can obscure its entire disk and reduce its apparent V magnitude by up to 0.2 mag. These dust storms can also reveal and conceal albedo markings making semi-permanent changes in its albedo as a function of sub-Earth longitude and latitude.

3. FUTURE WORK

A predicted value accurate to 0.1 mag is likely adequate for planning purposes. However, the algorithms for Mars and the ball of Saturn alone do not meet this modest goal and the algorithms for Mercury and Venus are require an accuracy of 0.03 mag for our products. Improving the predictions will require developing improved algorithms, which will require knowledge of the light-scattering physics of the surfaces and/or atmospheres of the individual planets as input.

3.1 Exo-planets

Another aspect is the planets of the solar system can serve as a testbed for direct observation of exoplanets, *e.g.* HabEx (2019). Too little light is received to make spectroscopy or spectrophotometry possible. Leaving wideband photometry as the best tool to learn about their atmospheres.

For example, the uncertainty in the predicted apparent magnitude of Uranus is 0.02 mag in V . The algorithm for predicting its apparent magnitude is a function of the observer's sub-Earth latitude. Spectroscopy of Uranus shows that the proportion of methane in its atmosphere is a function of latitude and is the source of its change in apparent V magnitude.

Venus is another good example where incorporating our detailed knowledge of a solar system planet can lead to better understanding of an exo-planet through wideband photometry. Sulfuric acid droplets in its atmosphere contribute to two phenomena:

- First, excess light is scattered towards the observer at large phase angles resulting in an *increase* in its apparent magnitude at phase angles between about 165° and 172° .
- Second, a glory is observed at phase angles less than about 10° . Figure 2 is an example of a glory arising from water droplets viewed from an airplane. The physics of a glory are similar to that of a rainbow. Light is scattered away from a phase angle of 0° resulting in a wavelength dependent deficit at very small phase angles as opposed to a surge in the apparent magnitude.

The existence of the glory was only recently appreciated (García Muñoz et al. 2014), and the new



Figure 2: A glory arising from cloud water droplets. Photo credit: Brocken in a glory - Own work, CC BY-SA 3.0, <https://commons.wikimedia.org/w/index.php?curid=2204135>.

algorithm does not model it. A better algorithm including the glory should be able to significantly reduce the (O – C)s in Venus' V magnitude.

3.2 Other Wavelengths

The ability to predict the apparent magnitudes of the planets in other bands, particularly the near infra-red is significantly worse. The uncertainty in the apparent magnitudes of the outer planets is about 0.05 mag in R and 0.06 mag in I. The primary obstruction to improvement in these bands is insufficient data rather than the algorithms. There are insufficient data for Mercury, Venus, and Mars in R and I to provide even preliminary predictions.

4. REFERENCES

- Danjon, A., 1949, "Photométrie et colorimétrie des planètes Mercure et Venus", *Bull. Astron.* 14, pp. 315–345.
- García Muñoz, A. Pérez-Hoyos, P. & Sánchez-Lavega, A., 2014, "Glory Revealed in Disk-Integrated Photometry of Venus", *A&A* 566, L1.
- HabEx 2019, "HabEx Exoplanet Observatory Final Report", Pasadena, CA: Jet Propulsion Laboratory.
- Harris, D.L., 1961, "Photometry and Colorimetry of the Planets and Satellites", in *Planets and Satellites*, G.P. Kuiper & B.A. Middlehurst, eds. (Chicago: U of Chicago Press), pp. 272–342
- Hilton, J.L. 2005, "Improving the Visual Magnitudes of the Planet in The Astronomical Almanac. I. Mercury and Venus", *AJ* 129, pp. 2902–2906.
- Irvine, W.M., Simon, T., Menzel, D.H., Charon, J., Lecomte, G., Griboval, P., & Young, A.T. 1968, "Multicolor Photoelectric Photometry of the Brighter Planets. II. Observations from Le Houga Observatory", *AJ* 73, pp. 251–264.
- Mallama, A. & Hilton, J.L. 2018, "Computing Apparent Planetary Magnitudes for The Astronomical Almanac", *Astron. Comput.* 25, pp. 10–24.

A NEW DYNAMICAL MODEL OF THE LUNAR CORE AND IMPROVED OBSERVATIONAL CONSTRAINTS FROM LUNAR LASER RANGING

N. Rambaux¹, V. Viswanathan^(2,1), A. Fienga³, J. Laskar¹, M. Gastineau¹

¹ ASD/IMCCE, Observatoire de Paris, PSL Université, Sorbonne Université - France
Nicolas.Rambaux@obspm.fr

² NASA Goddard Space Flight Center, Greenbelt - USA

³ AstroGéo/Geoazur - CNRS/UMR7329, Observatoire de la Côte d'Azur - France.

ABSTRACT. Constraints on the interior structure of the Moon are revisited using gravity data from GRAIL, topography data from LRO-LOLA, Apollo seismic data and Lunar Laser Ranging data. Here, we present recent results obtained by Viswanathan et al. (2019) on the determination of the size and shape of the lunar fluid core through these dataset.

1. INTRODUCTION

Our Moon is one of the most studied objects in the Solar system; we benefit from chemical, geophysical, and geodetic observations achieved by multiple Earth ground-based telescopes, orbital and in situ missions. However, its deep interior properties remain a puzzle because the lunar core is very small, implying weak signature in the observational data set. This paper focuses on the description of a new lunar core rotational model included in INPOP (Viswanathan et al.2019) and used to provide a determination of the radius and geometry of the lunar core-mantle boundary (CMB) from the LLR observations. The obtained CMB radius is in full agreement with one seismological model (Garcia et al.2011).

2. LLR AND GRAIL OBSERVATIONS

The Moon's rotation is now measured with a remarkable accuracy of few milli-arcseconds thanks to the Lunar Laser Ranging (LLR) experiment that has been active since 1969 (e.g. Dickey et al.1994). This experiment consists of the measurement of the round-trip travel time of a short laser pulse between an Earth observatory and one of the five corner cube retroreflector arrays settled on the Moon (Williams et al. 2014; Pavlov et al., 2016; Viswanathan et al. 2018; Fienga et al. 2019). Earth observatories such as the APOLLO station (Murphy, 2013) and OCA station (Courde et al. 2017) regularly range to the retroreflectors for the collection of LLR data. The OCA laser station switched to ranging in infrared (1064 nm) allowing a better coverage of the retroreflectors and improving the precision of the LLR data (Courde et al. 2017). A strong interest from the laser ranging science has led to the emergence of new LLR stations Hartebeesthoek-South Africa (Munghemezulu et al., 2016), Yunnan-China, Wettzell-Germany (Eckl et al. 2019) and next-generation of retro-reflector developments (Dell'Agnello et al., 2018; Currie et al., 2013).

In addition, the Moon has been the target of the space mission Gravity Recovery and Interior Laboratory mission (GRAIL) that determined the gravity field of the Moon at an unprecedented accuracy (Konopliv et al., 2013; Lemoine et al., 2013, Konopliv et al., 2014). It has been obtained with an improved accuracy of 4-5 order of magnitude up to degree and order 1200-1500 (see e.g. Konopliv et al. 2014). In addition, the love number k_2 has been improved by a factor 5. Such

great accuracy is reached thanks to the intersatellite link based on a mission concept similar to GRACE. Also there were DSN two-way S-band doppler measurements for GRAIL (see Konopliv et al., 2013; Lemoine et al. 2013) and reference therein).

3. DYNAMICAL MODEL AND RESULTS

The lunar rotation is integrated numerically in INPOP ephemeris and fitted to the LLR observations (Viswanathan et al., 2019; Fienga et al. 2019). This model is obtained from a joint numerical integration of the orbits of the Moon, the Earth, the planets and asteroids, and of the lunar rotation. The dynamical partial derivatives of the orbits and lunar Euler angles with respect to solution parameters such as moment of inertia, gravity field, tides, dissipation, interaction with a fluid core and initial conditions are computed and the adjustment provides the determination of these geophysical parameters (for a complete description of the last INPOP version see Fienga et al. (2019) and references therein).

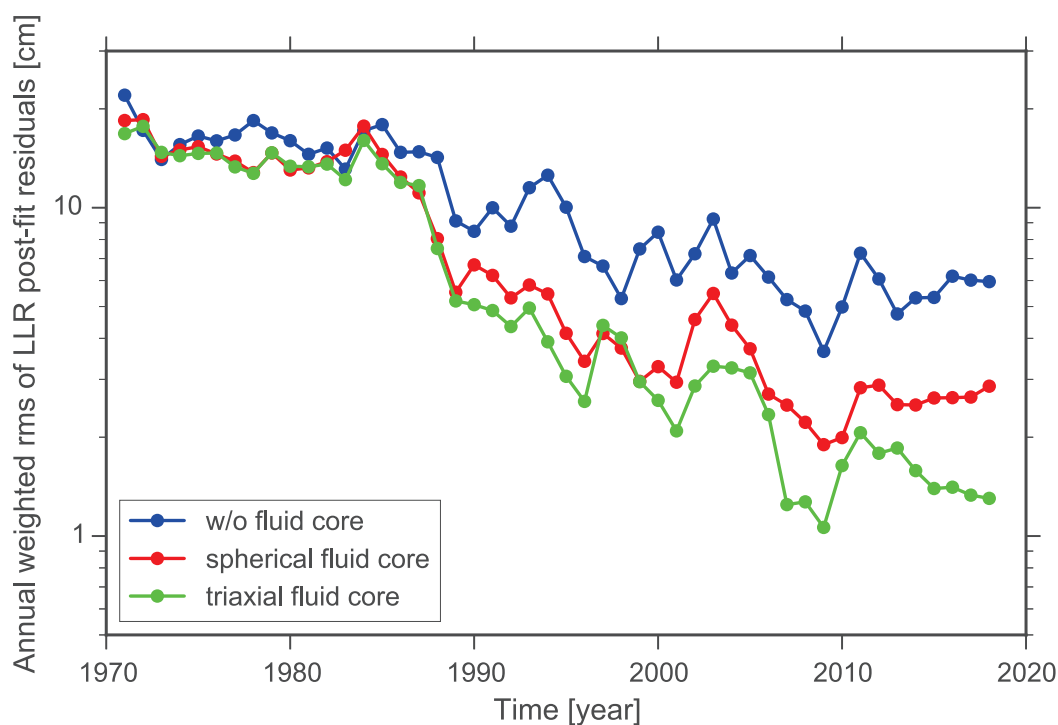


Figure 1: This plot shows the influence of the presence of the fluid core is sustained by a significant decrease in the annual wrms of the LLR over 50 years. In blue the solution without the fluid core provides a wrms of 5 cm, that reduces to 3 cm for a spherical fluid core with friction and further below 2 cm in the presence of a non-spherical fluid core.

A full set of rotational equations for the whole Moon and for the fluid-core that take into account the pressure torque due to the fluid core on the non-spherical CMB interface, including the triaxiality of this interface, has been developed. Such set of equations was used for Mercury (Rambaux et al., 2007) and icy satellites (Richard et al., 2014) studies and here extended to the

rotational motion of a differentiated Moon. The basic equations are

$$\frac{d[I]\boldsymbol{\omega}}{dt} + \boldsymbol{\omega} \wedge [I]\boldsymbol{\omega} = \boldsymbol{\Gamma} \quad (1)$$

$$\frac{d\mathbf{H}^c}{dt} + \boldsymbol{\omega} \wedge \mathbf{H}^c = \boldsymbol{\Gamma}_c \quad (2)$$

where $[I]$ is the inertia tensor of the Moon, $\boldsymbol{\omega}$ is the angular velocity vector, and $\boldsymbol{\Gamma}$ are the external gravitational torques, the \mathbf{H}^c is the angular momentum of the core and the $\boldsymbol{\Gamma}_c$ represents the interaction between the core and the mantle through two mechanisms. The first one is related to the friction at the CMB due to the differential rotation, that perturb the lunar Cassini state. The second one is due to the pressure of the fluid core on the core-mantle boundary and so it depends on the non-sphericity at the CMB.

The presence of fluid core has been identified few decades ago due its influence on the lunar Cassini state and the second clue has been the detection of the oblateness of the fluid core boundary that is an independent result of the existence of the fluid core (Williams et al., 2014). For example, in INPOP, the presence of the fluid core is sustained by significant decreases of the annual weighted root mean square (wrms) of the LLR post-fit residuals over 50 years. Figure 1 shows the influence of the non-sphericity and highlights the necessity to have accurate and long time series in order to separate the physical parameters of the lunar core.

The size of the lunar core, about 381 km, was determined in Viswanathan et al. (2019) by comparing flattening determined through LLR data and the theoretical flattening computed by assuming a hydrostatic CMB enclosed by a non-hydrostatic mantle and disturbed by tidal and centrifugal potentials. The bounded core size is consistent with an analysis of the seismic data (Garcia et al., 2011) and previous LLR model (Williams et al., 2014) but the accuracy of the core oblateness and radii of a presently-relaxed lunar core is improved by a factor of 3. This determination brings new constraints on the interior of the Moon. Notably, it allows to compute an estimation of the eigenfrequency and period of the free core nutation (FCN) of the Moon as shown in Figure 2. This figure shows the dependence of the FCN period onto interior parameters where a first order linear approach allow to estimate the FCN frequency equal to

$$\sigma_{\text{FCN}} = \frac{1}{2}n(\alpha''_c + \beta''_c) \quad (3)$$

with $\alpha''_c \sim \frac{AC_c - A_c B_c}{A - A_c}$ and $\beta''_c \sim \frac{BC_c - A_c B_c}{B - B_c}$ where (A, B, C) and (A_c, B_c, C_c) are the moment of inertia of the whole Moon and core, n is the lunar mean motion. This relationship is consistent with the estimation used in Rambaux and Williams (2011). However, in Rambaux and Williams (2011) the numerical value of the FCN was estimated based on DE421 flattening estimation and with the new determination of the flattening, the FCN is estimated at about 367 ± 100 years (Viswanathan et al., 2019).

Acknowledgments V.Viswanathan acknowledges the post-doctoral fellowship by ESEP for funding this research. The authors acknowledge the PINGRAM and PNP for funding this research. The computations were carried out on computational servers of Geoazur, OCA. This work benefited from the previous contribution of H. Manche to the INPOP ephemeris development. The LLR data were processed using CNES-GRGS software (GINS).

4. REFERENCES

Courde, C., Torre, J. M., Samain, E., Martinot-Lagarde, G., Aimar, M., Albanese, D., Exertier, P., Fienga, A., Maréchal, H., Metris, G., Viot, H., and Viswanathan, V. 2017, "Lunar laser ranging in infrared at the Grasse laser station", A&A 602:A90.

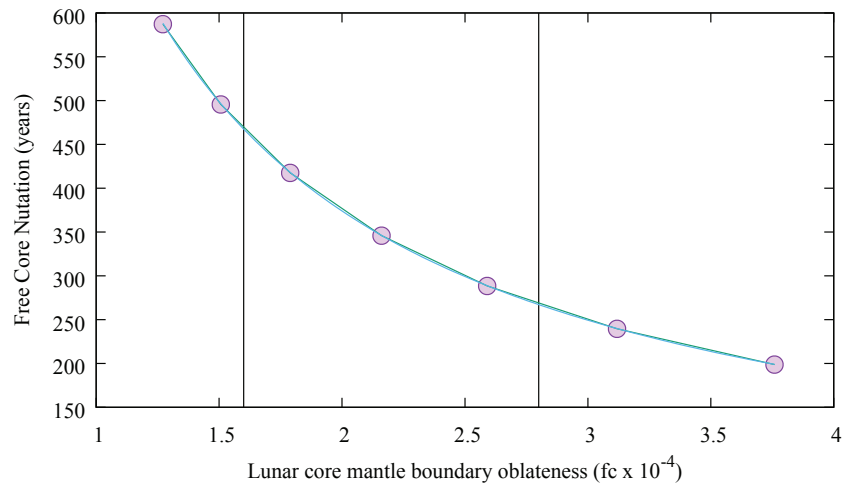


Figure 2: Period of FCN for the Moon as function of its oblateness. This gives a present-day $P_{FCN} \sim (367 \pm 100)$ years for the hydrostatic case, assuming a Poincaré flow within the lunar fluid core. The large value of P_{FCN} with respect to the mantle precession (18.6 years) confirms that the present-day lunar core should be decoupled with the mantle (Meyer and Wisdom, 2011).

- Currie, D. G., Dell’Agnello, S., Delle Monache, G. O., Behr, B., and Williams, J. G., 2013, "A Lunar Laser Ranging Retroreflector Array for the 21st Century", Nucl. Phys. B - Proc. Suppl. 243-244, pp. 218–228.
- Dell’Agnello, S., Boni, A., Cantone, C., Ciocci, E., Martini, M., Patrizi, G., Tibuzzi, M., Delle Monache, G., Vittori, R., Bianco, G., et al., 2018, "Next-generation laser retroreflectors for GNSS, solar system exploration, geodesy, gravitational physics and earth observation", in International Conference on Space Optics-ICSO 2014, volume 10563, p. 1056317. International Society for Optics and Photonics.
- Dickey, J. O., Bender, P. L., Faller, J. E., Newhall, X. X., Ricklefs, R. L., Ries, J. G., Shelus, P. J., Veillet, C., Whipple, A. L., Wiant, J. R., Williams, J. G., and Yoder, C. F., 1994, "Lunar Laser Ranging: A Continuing Legacy of the Apollo Program", Science 265, pp. 482–490.
- Eckl, J., Schreiber, U., and Schüler, T., 2019, "Lunar laser ranging utilizing a highly efficient solid-state detector in the near-IR", Quantum Optics and Photon Counting 2019, 1102708(April), p. 7.
- Fienga, A., Deram, P., Viswanathan, V., Di Ruscio, A., Bernus, L., Durante, D., Gastineau, M., and Laskar, J., 2019, "INPOP19a planetary ephemerides", Notes Scientifiques et Techniques de l’Institut de Mecanique Celeste 109.
- Garcia, R. F., Gagnepain-Beyneix, J., Chevrot, S., and Lognonné, P., 2011, "Very preliminary reference Moon model", Physics of the Earth and Planetary Interiors 188, pp. 96–113.
- Konopliv, A. S., Park, R. S., Yuan, D.-N., Asmar, S. W., Watkins, M. M., Williams, J. G., Fahnestock, E., Kruizinga, G., Paik, M., Strelakov, D., Harvey, N., Smith, D. E., and Zuber, M. T., 2013, "The JPL lunar gravity field to spherical harmonic degree 660 from the GRAIL Primary Mission", J. Geophys. Res. (Planets) 118, pp. 1415–1434.
- Konopliv, A. S., Park, R. S., Yuan, D.-N., Asmar, S. W., Watkins, M. M., Williams, J. G., Fahnestock, E., Kruizinga, G., Paik, M., Strelakov, D., Harvey, N., Smith, D. E., and Zuber, M. T., 2014, "High-resolution lunar gravity fields from the GRAIL Primary and Extended Missions", Geophys. Res. Lett. 41, pp. 1452–1458.
- Lemoine, F. G., Goossens, S., Sabaka, T. J., Nicholas, J. B., Mazarico, E., Rowlands, D. D.,

- Loomis, B. D., Chinn, D. S., Caprette, D. S., Neumann, G. A., Smith, D. E., and Zuber, M. T., 2013, "High-degree gravity models from GRAIL primary mission data", *Journal of Geophysical Research: Planets* 118(8), pp. 1676–1698.
- Meyer, J. and Wisdom, J., 2011, Precession of the lunar core, *Icarus* 211(1), pp. 921–924.
- Munghemezulu, C., Combrinck, L., and Botai, J. O. (2016), "A review of the lunar laser ranging technique and contribution of timing systems", *South African Journal of Science*, Volume 112 (Number 3/4), pp. 1–9.
- Murphy, T. W., 2013, "Lunar laser ranging: the millimeter challenge", *Reports on Progress in Physics* 76(7), p. 076901.
- Pavlov, D. A., Williams, J. G., and Suvorkin, V. V., 2016, "Determining parameters of Moon's orbital and rotational motion from LLR observations using GRAIL and IERS-recommended models", *Celest. Mech. Dyn. Astr.* 126(1-3), pp. 61–88.
- Rambaux, N., van Hoolst, T., Dehant, V., and Bois, E., 2007, "Inertial core-mantle coupling and libration of Mercury", *A&A* 468(2), pp. 711–719.
- Rambaux, N. and Williams, J. G., 2011, "The Moon's physical librations and determination of their free modes", *Celest. Mech. Dyn. Astr.* 109, pp. 85–100.
- Richard, A., Rambaux, N., and Charnay, B., 2014, "Librational response of a deformed 3-layer Titan perturbed by non-Keplerian orbit and atmospheric couplings", *Planetary and Space Science* 93, pp. 22–34.
- Viswanathan, V., Fienga, A., Minazzoli, O., Bernus, L., Laskar, J., and Gastineau, M., 2018, "The new lunar ephemeris INPOP17a and its application to fundamental physics", *MNRAS* 476, pp. 1877–1888.
- Viswanathan, V., Rambaux, N., Fienga, A., Laskar, J., and Gastineau, M., 2019, "Observational constraint on the radius and oblateness of the lunar core-mantle boundary", *Geophys. Res. Lett.* 46(13), pp. 7295–7303.
- Williams, J. G., Boggs, D. H., and Ratcliff, J. T. (2014), "Free Libration Modes of a Structured Moon", In *Lunar and Planetary Science Conference*, Lunar and Planetary Inst. Technical Report 45, p. 1579.

SOLID BODY TIDES IN THE DYNAMICAL MODEL OF THE MOON

D. Pavlov

Institute of Applied Astronomy - Russia - dpavlov@iaaras.ru

ABSTRACT. The dynamical model of the orbital-rotational motion of the Moon, used in numerically integrated lunar ephemeris, accounts for tidal dissipation. However, it does not explain some long-term signatures that are detected by lunar laser ranging (LLR) observations. One cause of those signatures may be that the lunar crust experiences tidal deformations at different bands, and tidal Q factor depends on band; however, the dynamical model has a single tidal delay and does not have a concept of tidal band. An attempt to improve the dynamical model, introducing two delays instead of one, is made in this work. One delay is applied to the diagonal elements of the inertia tensor, while the other delay is applied to the non-diagonal elements. It turns out that the two delays are well separated and some of the residual long-term signatures are significantly different from those obtained with one-delay model.

1. INTRODUCTION

Modern study of lunar interior is mainly based on three kinds of data:

- Gravimetry measurements done by the GRAIL mission and its predecessors;
- Earth-Moon lunar laser ranging (LLR) measurements which allow to validate hypotheses about lunar structure via the indirect effect on lunar orbital and rotational motion;
- Photometry, laser altimetry and other measurements of the lunar surface performed by the LRO spacecraft and its predecessors. Those measurements allow to explore the history of the formation of the Moon via the present state of its exterior.

While there are similarities between methods of study of Earth's and Moon's structure, the latter has two distinct features:

- The rotational model of the Moon, unlike that of the Earth, is modeled with a set of dynamical equations directly representing lunar figure, core, tidal and rotational dissipation.
- The observations of lunar orbiters, most importantly GRAIL, are not tied directly to the lunar surface. There is an indirect tie via Earth-spacecraft measurements and a geocentric lunar ephemeris which is built using the aforementioned dynamical model.

The most precise lunar reference frame to date contains five retroreflectors points on lunar surface whose positions are determined from LLR. The accuracy of this frame is presently estimated at 0.2 m (optimistic) or 2 m (pessimistic) (Pavlov 2020). While there are obvious technical ways to improve the accuracy (more LLR measurements, more lunar retroreflectors), it is no less important that further improvement of lunar reference frame should go together with the improvement of the lunar dynamical model.

LLR has existed for 50 years. A continuous orbit of the Moon is fit to 50 years of LLR observations to form lunar ephemeris. LLR has been proven sensitive not only to the initial conditions of the Earth-Moon dynamical system and positions of retroreflectors, but also to parameters of the

lunar core (Williams et al. 2001), low degree gravitational harmonics of the Moon, degree 2 tides on the Earth (Williams and Boggs 2016), and Earth’s orbit plane.

However, the lunar dynamical model in its present state does not explain all signatures that are visible in LLR residuals. One major direction of research to explain the signatures is the improvement of the model of the lunar core. Another part that could be improved, which this work is devoted to, is the model of the solid body tides on the Moon.

2. USAGE OF GRAIL’S RESULTS IN THE DYNAMICAL MODEL OF THE MOON

A particular inconsistency in the lunar gravitational field solutions obtained from GRAIL data indicates a problem in the lunar dynamical model. Selenocentric orbits of GRAIL spacecraft (Ebb and Flow) were determined by Doppler tracking from Earth and tied to a specific lunar ephemeris.

The lunar ephemeris is built in such a way that the coordinate axes are supposed to be the principal axes (PA) of the whole Moon. Under that assumption, the gravity field coefficients C21, S21, and S22 are supposed to be zero. However, different GRAIL solutions, which include the said coefficients, all have S21 equal approximately 1×10^{-9} (see Table 1).

Solution	Team	Ephemeris	C21	S21	S22
GL0660b	JPL	DE421	0.123×10^{-9}	0.101×10^{-8}	-0.249×10^{-9}
GRGM900c	GSFC	DE421	0.223×10^{-9}	0.101×10^{-8}	-0.105×10^{-9}
GRGM1200a	GSFC	DE430	0.147×10^{-10}	0.117×10^{-8}	0.908×10^{-9}
GL1500e	JPL	DE430	0.173×10^{-9}	0.104×10^{-8}	-0.102×10^{-9}

Table 1: Values of C21, S21, and S22 coefficients in different solutions obtained from GRAIL data

The nonzero GRAIL’s S21 value does not depend much of the used ephemeris, and does not differ much in solutions done by different teams. Most probably, the nonzero S21 indicates an inconsistency in the lunar dynamical model rather than an artifact in GRAIL data or processing.

Another fact that further supports that point: nonzero S21 can be detected from LLR itself. While normally S21 is fixed to zero in the lunar dynamical equations (together with C21 and S22), it is possible to add S21 into the set of determined parameters in the solution. Such an experiment has been done in a special test solution of EPM lunar ephemeris, with the result of

$$S21 = (0.74 \pm 0.05^{(1\sigma)}) \times 10^{-9}$$

which is reasonably close to the GRAIL’s value.

So, most probably the present lunar model (Folkner et al. 2014, Pavlov et al. 2016) has an inconsistency: a mass misalignment that manifests itself in the external torque but not in the mantle’s inertia tensor. Once supposed cause of that was the shape of the lunar core (Williams et al. 2014). A tilted core would make the mantle’s inertia tensor asymmetric, while not changing the external torque in the PA frame. Unfortunately, that hypothesis did not work out, because the supposed tilt would affect not only the inertia tensor, but the pressure torque, too. The effects nearly cancel each other out and the overall result of the titled core on lunar rotational dynamics would be very small (Pavlov 2018, Viswanathan et al. 2019).

It is also important that GRAIL solutions can have systematic biases that come from imperfections of the lunar rotational model. Also, fixing low-degree gravity coefficients to GRAIL values in the dynamical model can cause artificial “drag” of the resulting ephemeris towards the ephemeris consistent with the used GRAIL values. An attempt has been made (not shown here) to use the GRAIL gravity model in the DE430 frame while keeping the dynamical equations in their own

(determined) frame; the resulting orbit turned out to be very bad in terms of LLR fits. A further attempt, to not only use the GRAIL values in DE430 frame, but also use kinematic model of lunar solid body tides (Konopliv et al. 2013) instead of the dynamical equations of tidal variations, did not give an acceptable result, either.

At this point it seems reasonable to avoid using GRAIL values for low-degree harmonics in the lunar dynamical model until a more elaborate dynamical model appears. First, at least, the nonzero S21 problem should be resolved; afterward, it is recommended to re-obtain GRAIL solution using the ephemeris obtained with the improved dynamical model.

3. JPL DE430 MODEL OF (DELAYED) TIDAL DISSIPATION

The DE430 lunar model (Folkner et al. 2014) is presently accepted, with minor modifications, also in EPM (Pavlov et al. 2016) and INPOP (Viswanathan et al. 2018) lunar ephemeris.

Let $I^* = I + I_c$ be the inertia tensor of the whole Moon, consisting of the mantle and the core. The inertia tensor of the whole Moon, according to the model, obeys the following equation:

$$\begin{aligned} \frac{I^*}{m} = & \frac{I_0}{m} - k_2 \frac{\mu_E}{\mu_M} \left(\frac{R_M}{r} \right)^5 \begin{bmatrix} x^2 - \frac{1}{3}r^2 & xy & xz \\ xy & y^2 - \frac{1}{3}r^2 & yz \\ xz & yz & z^2 - \frac{1}{3}r^2 \end{bmatrix} + \\ & + k_2 \frac{R_M^5}{3\mu_M} \begin{bmatrix} \omega_x^2 - \frac{1}{3}(\omega^2 - n^2) & \omega_x\omega_y & \omega_x\omega_z \\ \omega_x\omega_y & \omega_y^2 - \frac{1}{3}(\omega^2 - n^2) & \omega_y\omega_z \\ \omega_x\omega_z & \omega_y\omega_z & \omega_z^2 - \frac{1}{3}(\omega^2 + 2n^2) \end{bmatrix}, \end{aligned} \quad (1)$$

where I_0 is the (diagonal) inertia tensor of the whole undistorted Moon; μ_E and μ_M are the gravitational parameters of the Earth and the Moon, respectively; R_M is the equatorial radius of the Moon; k_2 is the Love number; $\mathbf{r} = (x, y, z)^T$ is the geocentric position of the Moon; $\boldsymbol{\omega} = (\omega_x, \omega_y, \omega_z)^T$ is the angular velocity of the lunar mantle; n is the lunar mean motion.

The second and the third terms of Eq. (1) account for tidal and spin distortion, respectively. They come with a time delay: $I^*(t)$ depends not on $\mathbf{r}(t)$ and $\boldsymbol{\omega}(t)$, but on $\mathbf{r}(t - \tau)$ and $\boldsymbol{\omega}(t - \tau)$. τ is the time delay, a determined parameter.

The second-order gravitational potential varies over time accordingly with the inertia tensor:

$$\begin{aligned} C_{20} &= \frac{1}{R_M^2} \left[\frac{1}{2} \left(\frac{I_{11}^*}{m} + \frac{I_{22}^*}{m} \right) - \frac{I_{33}^*}{m} \right] \\ C_{22} &= \frac{1}{4R_M^2} \left[\frac{I_{22}^*}{m} - \frac{I_{11}^*}{m} \right] \\ C_{21} &= -\frac{1}{R_M^2} \frac{I_{13}^*}{m} \\ S_{21} &= -\frac{1}{R_M^2} \frac{I_{32}^*}{m} \\ S_{22} &= -\frac{1}{2R_M^2} \frac{I_{21}^*}{m} \end{aligned} \quad (2)$$

It is well known (Williams et al. 2013) that the described single-delay model is a compromise. In reality, the tidal delay strongly depends on the tidal band. The concept of band is not natural to the dynamical model. As a result, few-mas periodic longitudinal libration terms appear in the LLR residuals. Some of them are: $\cos l'$ term (1 year), $\cos(2l - 2D)$ (206 days), and $\cos(2F - 2l)$ (3 years). Another, not presently included into ephemeris solutions, is a 6-year term $\sin(F - l)$, relatively recently noted by James Williams from NASA JPL.

One approach to allow tidal delay to vary with frequency is using an orbital delay in addition to the rotational delay (Williams and Boggs 2016); however, that approach was developed for Earth tides and is not applicable to the Moon.

Irrespective to the tidal delay problem, the currently developed EPM lunar ephemeris (Pavlov 2020) accounts for the tides not only from the Earth, but from the Sun, too. The single delay τ is applied to tides from both bodies.

4. TWO-DELAY MODEL

First of all, the spin part of Eq. (1), while originally proposed to have a delay, is mathematically almost non-sensitive to the delay. So for further calculations $\omega(t)$ can be taken instead of $\omega(t - \tau)$ with negligible impact on the outcome.

As for the tidal distortions: (Williams and Boggs 2015, Table 1) lists an overview of variations of degree 2 spherical harmonic coefficients at different bands. There are monthly bands (F , I) and semi-monthly bands ($2D$, $2I$, $F+I$). There is also $2D-I$ band (31.812 days) and the aforementioned $F - I$ band (2190.350 days). All of them cause variations of second-degree coefficients; the set of affected coefficients depends on band. There are also other bands that cause smaller variations than the ones listed here.

Ideally, one would want to separate the bands entirely and use a dedicated delay for each band (and also separate the effect of tides of different bands on the inertia tensor). It does not seem to be easy, or possible at all. One small step towards the reduction of the disorder, however, is made in this work.

The idea is the following: use two delays τ_{02} and τ_1 instead of a single τ . Apply τ_{02} to the diagonal elements of the tidal part of I^* in Eq. (1), and apply τ_1 to the off-diagonal elements. Consequently, in Eq. (2), variations of C_{20} and C_{22} will depend on τ_{02} , while variations of C_{21} , S_{21} , and S_{22} will depend on τ_1 .

The ABMD numerical integrator (Aksim and Pavlov 2019), developed at the IAA RAS, can handle differential equations with arbitrary number of delays, and can integrate both forward and backwards in time. The source code of the integrator is available at <https://gitlab.iaaras.ru/iaaras/abmd>.

5. RESULTS

Two lunar solutions were obtained for comparison. The LLR observations used in the solutions, as well as the statistics of the residuals, are presented in (Pavlov 2020). Table 2 lists the determined values of the delays in the two solutions, and also the determined amplitudes of the kinematic longitudinal libration terms. Separate solutions were obtained where S_{21} coefficient was determined while $\sin(F - I)$ amplitude was not considered. The given errors are 1σ .

$\sin(F - I)$ amplitude and S_{21} are strongly correlated. If the lunar dynamical model is improved so that it naturally absorbs the $(F - I)$ longitudinal libration, the S_{21} frame misalignment problem will most likely be gone.

6. CONCLUSION

- In the lunar dynamical model, solid body lunar tides are of no less importance than the core.
- GRAIL data should be later reanalyzed with an improved underlying lunar dynamical model.
- 6-year period in longitude (discovered by James Williams) is strongly connected to the frame misalignment that results in nonzero S_{21} .

Fitted value	Single delay	Two delays
τ , days	0.098 ± 0.001	—
τ_{02} , days	—	0.068 ± 0.002
τ_1 , days	—	0.144 ± 0.002
$\cos l'$ amplitude, mas	4.2 ± 0.1	4.2 ± 0.1
$\cos(2l - 2D)$ amplitude, mas	1.6 ± 0.1	0.8 ± 0.1
$\cos(2F - 2l)$ amplitude, mas	-0.8 ± 0.3	-3.4 ± 0.3
$\sin(F - l)$ amplitude, mas	-9.0 ± 0.6	-7.2 ± 0.6
$S_{21} \times 10^9$ (separate solution)	0.74 ± 0.5	0.58 ± 0.5

Table 2: Comparison of solutions obtained with single-delay and two-delay models

- Two different delays can be detected from LLR data. Separation significantly affects 206 days and 3 year amplitudes, slightly affects S_{21} / 6-year amplitude.

Regardless of the tidal model, work should continue on improving the model of the lunar core. One particular hypothesis worth checking there is the shifted core, see e. g. (Wieczorek et al. 2019) where shifted core is derived from joint analysis of GRAIL and LOLA data.

7. REFERENCES

- Aksim, D., Pavlov, D., 2019, "On the extension of AdamsBashforthMoulton methods for numerical integration of delay differential equations and application to the Moon's orbit", *Math Comput Sci.*, doi: 10.1007/s11786-019-00447-y.
- Folkner, W., Williams, J., Boggs, D., Park, R., Kuchynka, P., 2014, "The Planetary and Lunar Ephemerides DE430 and DE431", IPN Progress Report 42-196, NASA JPL.
- Konopliv, A.S., Park, R.S., Yuan, D.N., Asmar, S.W., Watkins, M.M., Williams, J.G., Fahnestock, E., Kruizinga, G., Paik, M., Strelakov, D., Harvey, N., Smith, D.E., Zuber, M.T., 2013, "The JPL lunar gravity field to spherical harmonic degree 660 from the GRAIL Primary Mission", *J. Geophys. Res. (Planets)* 118(7), pp. 1415–1434, doi:10.1002/jgre.20097.
- Pavlov, D.A., Williams, J.G., Suvorin, V.V., 2016, "Determining parameters of Moon's orbital and rotational motion from LLR observations using GRAIL and IERS-recommended models", *Celest. Mech. Dyn. Astr.* 126, pp. 61–88, doi: 10.1007/s10569-016-9712-1.
- Pavlov, D., 2018, "Results of processing of the lunar laser ranging observations of 1970–2017", *Izvestia GAO 225* (in Russian).
- Pavlov, D., 2020, "Role of lunar laser ranging in realization of terrestrial, lunar, and ephemeris reference frames", *J Geod* 94(5), doi: 10.1007/s00190-019-01333-y.
- Williams, J.G., Boggs, D.H., Yoder, C.F., Ratcliff, J.T., Dickey, J.O., 2001, "Lunar rotational dissipation in solid body and molten core", *J. Geophys. Res. (Planets)* 106(E11), pp. 27933–27968, doi: 10.1029/2000JE001396
- Williams, J., Boggs, D., 2015, "Tides on the Moon: Theory and determination of dissipation". *J. Geophys. Res. : Planets* 120, pp. 689–724, doi: 10.1002/2014JE004755.
- Williams, J., Boggs, D., 2016, "Secular tidal changes in lunar orbit and Earth rotation". *Celest. Mech. Dyn. Astr.* 126:89, doi: 10.1007/s10569-016-9702-3
- Williams, J. G., Konopliv, A. S., Lemoine, F. G., Goossens, S., Asmar, S. W., Park, R. S., Yuan, D. -N., Boggs, D. H., Mazarico, E., Kiefer, W. S., Wieczorek, M. A., Watkins, M. M., Smith, D. E., Zuber, M. T., 2014, "A Glimpse of Lunar Core Shape and Deep Gravity Field", 45th Lunar and Planetary Science Conference.

- Williams, J.G., Boggs, D.H., Folkner, W.M., 2013, "DE430 Lunar Orbit, Physical Librations, and Surface Coordinates", JPL IOM 335, California Institute of Technology.
- Viswanathan, V., Fienga, A., Minazzoli, O., Bernus, L., Laskar, J., Gastineau, M., 2018, "The new lunar ephemeris INPOP17a and its application to fundamental physics", *Monthly Not R Astron Soc* 476(2), pp. 1877–1888, doi: 10.1093/mnras/sty096.
- Viswanathan, V., Rambaux, N., Fienga, A., Laskar, J., Gastineau, M., 2019, "Observational constraint on the radius and oblateness of the lunar core-mantle boundary", *Geophys Res Let* 46, pp. 7295–7303, doi: 10.1029/2019GL082677.

GEODETIC (RELATIVISTIC) ROTATION OF THE MARS SATELLITES SYSTEM

V.V. PASHKEVICH, A.N. VERSHKOV,

Central (Pulkovo) Astronomical Observatory of the Russian Academy of Science - Russia
pashvladvit@yandex.ru, avershkov@mail.ru

ABSTRACT. The relativistic effect of the geodetic rotation (which consist of two effects: the geodetic precession and the geodetic nutation) in the rotation of Mars satellites system for the first time was investigated. The most essential terms of the geodetic rotation were computed by the algorithm of Pashkevich (2016), which is applicable to the study of any bodies of the Solar system that have long-time ephemeris. As a result, a new high-precision values of the geodetic rotation for Mars dynamically adjusted to JPL DE431/LE431 ephemeris (Folkner et al., 2014) in Euler angles and for its satellites dynamically adjusted to Horizons On-Line Ephemeris System (Giorgini et al., 2001) in Euler angles and in the perturbing terms of its physical librations were calculated.

1. INTRODUCTION

The geodetic rotation of a body, first considered by Willem de Sitter in 1916 (De Sitter, 1916), is the most essential relativistic effect of its rotation. This effect consist of two effects: the geodetic precession, which is the systematic effect, and the geodetic nutation (Fukushima, 1991), which is the periodic effect. These effects have a formal similarity with the phenomena of precession and nutation, which are better-known events on the classical mechanics. In contrast to the above-mentioned classical events their emergence are not depend on from influences of any forces to body and represents only the effect of the curvature of space-time, predicted by general relativity, on a vector of the body rotation axis carried along with an orbiting body.

The main objectives of the present research are for the first time to study the effect of the geodetic rotation in the rotation of Mars satellites system and to obtain a new high-precision values of the geodetic rotation for Mars dynamically adjusted to JPL DE431/LE431 ephemeris (Folkner et al., 2014) in Euler angles and for its satellites dynamically adjusted to Horizons On-Line Ephemeris System (Giorgini et al., 2001) in Euler angles and in the perturbing terms of its physical librations.

For these purposes the algorithm of Pashkevich (2016), which is applicable to the study of any bodies of the Solar system that have long-time ephemeris will be used.

Mathematical model of the problem.- The problem of the geodetic (relativistic) rotation for Mars and for his satellites (Phobos and Deimos) is studied over the time span from AD1600 to AD2500 with one hour spacing with respect to the kinematically non-rotating (Kopeikin et al., 2011) proper coordinate system of the studied bodies. Body orientation parameters for Mars taken from Seidelmann et al. (2005) and for Mars satellites from Archinal et al. (2018).

The positions, velocities, physical parameters and orbital elements for Phobos and Deimos are taken from the Horizons On-Line Ephemeris System (Giorgini et al., 2001) and ones for the disturbing bodies: the Sun, the Moon, Pluto and the major planets are calculated using the fundamental ephemeris JPL DE431/LE431 (Folkner et al., 2014).

2. RESULTS

As a result of this investigation, in the perturbing terms of the physical librations and in Euler

angles for the Martian satellites (Phobos and Deimos), and in Euler angles for Mars the most significant systematic Δx_s (Table 1) and periodic Δx_p (Table 3) terms of the geodetic rotation are calculated:

$$\Delta x_s = \sum_{n=1}^N \Delta x_n t^n, \quad (1)$$

$$\Delta x_p = \sum_j^M \sum_{k=0}^M [\Delta x_{Sjk} \sin(\nu_{j0} + \nu_{j1} t) + \Delta x_{Cjk} \cos(\nu_{j0} + \nu_{j1} t)] t^k, \quad (2)$$

where $\Delta x = x_{relativistic} - x_{Newtonian}$, $x = \psi, \theta, \varphi, \tau, \rho, \sigma$; Δx_n are the coefficients of the systematic terms; $\Delta x_{Sjk}, \Delta x_{Cjk}$ are the coefficients of the periodic terms for sine and for cosine, respectively; ν_{j0}, ν_{j1} are phases and frequencies of the body under study, which are combinations of the corresponding Delaunay arguments (Smart, 1953) and the mean longitudes of the perturbing bodies; the summation index j is the number of added periodic terms, and its value changes for each body under study; t is the time in the Julian days.

Notes to tables. In Tables 1–3: T is the Dynamical Barycentric Time (TDB) measured in thousand Julian years (tjy) (of 365250 days) from J2000; a is orbital semi-major axis of Mars satellites taking from the Horizons On-Line Ephemeris System (Giorgini et al., 2001); $\Omega_{L41}, \Omega_{L42}$ are longitudes of the ascending node (Mars satellites orbits) on the Laplace plane for Phobos and Deimos, respectively; $D_{41} = \lambda_{41} - \lambda_4 + 180^\circ$, $D_{42} = \lambda_{42} - \lambda_4 + 180^\circ$ are mean elongations of Phobos and Deimos from the Sun, respectively; λ_4 is mean longitude of Mars; $\lambda_{41}, \lambda_{42}$ are marsocentric longitudes of Phobos and Deimos, respectively. The mean longitude of Mars was taken from (Brumberg and Bretagnon, 2000). The mean longitudes of the Martian satellites, their longitudes of the ascending node on the Laplace plane and mean elongations from the Sun are calculated using data from the Horizons On-Line Ephemeris System (Giorgini et al., 2001).

	Mars	Phobos ($a = 9376 km$)		Deimos ($a = 23458 km$)	
tjy	$\Delta\psi_s (\mu as)$	$\Delta\psi_s (\mu as)$	$\Delta\tau_s (\mu as)$	$\Delta\psi_s (\mu as)$	$\Delta\tau_s (\mu as)$
T	-7113935.6683	-209314864.7430	-95713236.3800	-27680096.2268	-15836815.1715
T^2	9758.6588	43043.9996	22074.5862	14436.8795	1970.5567
T^3	1328.3085				
tjy	$\Delta\theta_s (\mu as)$	$\Delta\theta_s (\mu as)$	$\Delta\rho_s (\mu as)$	$\Delta\theta_s (\mu as)$	$\Delta\rho_s (\mu as)$
T	119866.5547	109821.3069	109821.3069	118932.5546	118932.5546
T^2	-1065.6036	-79913.4426	-79913.4426	-5802.8941	-5802.8941
T^3	-57.9607				
tjy	$\Delta\varphi_s (\mu as)$	$\Delta\varphi_s (\mu as)$	$\Delta(\iota)_s (\mu as)$	$\Delta\varphi_s (\mu as)$	$\Delta(\iota)_s (\mu as)$
T	405134.4944	113601628.3630	94088505.4932	11843281.0553	12076398.3007
T^2	-11482.6140	-20969.4134	32232.9894	-12466.3227	640.6748
T^3	-280.3423				

Table 1: The secular terms of geodetic rotation of Mars and its satellites

The secular terms of geodetic rotation of some bodies of Solar system (Pashkevich and Verzhkov, 2019) represented in Euler angles (Table 2).

As can be seen from Tables 1 and 2, the values of the geodetic rotation of Mars satellites decrease with increasing their distance from Mars and the values of the geodetic rotation of planets decrease with increasing their distance from the Sun. The values of the geodetic rotation of the Earth and the Moon are very close. It is due to the fact that the Earth and the Moon have very close heliocentric orbit and the Sun has a greater influence on the geodetic rotation of the Moon

	The Sun	Mercury	Venus	The Earth	The Moon
tjy	$\Delta\psi_s (\mu\text{as})$	$\Delta\psi_s (\mu\text{as})$	$\Delta\psi_s (\mu\text{as})$	$\Delta\psi_s (\mu\text{as})$	$\Delta\tau_s (\mu\text{as})$
T	-870.0219	-426451032.8798	-156030839.3400	-19198865.6280	-19494124.5472
T^2	1.3770	-39215.8785	-687024.3196	50432.5497	-12.3454
T^3	-0.2568	14420.2934	78660.6535	-657.0605	565.0905
tjy	$\Delta\theta_s (\mu\text{as})$	$\Delta\theta_s (\mu\text{as})$	$\Delta\theta_s (\mu\text{as})$	$\Delta\theta_s (\mu\text{as})$	$\Delta\rho_s (\mu\text{as})$
T	-1.8891	36028.3827	-740880.9685	-10.7322	-297.2493
T^2	0.0809	-2910.6802	60179.7955	-1951.6003	-1779.1546
T^3	-0.0080	-193.9063	627.4990	-4125.4000	-3128.5299
tjy	$\Delta\varphi_s (\mu\text{as})$	$\Delta\varphi_s (\mu\text{as})$	$\Delta\varphi_s (\mu\text{as})$	$\Delta\varphi_s (\mu\text{as})$	$\Delta(l\sigma)_s (\mu\text{as})$
T	179.5703	214756196.8118	113009422.3955	-17.8008	6536.9172
T^2	-1.3915	2268.1428	687231.8895	-54775.6865	-36208.8512
T^3	0.0433	-12967.5814	-78746.0736	1245.0101	27296.6113

Table 2: The secular terms of geodetic rotation of some bodies of Solar system (Pashkevich and Vershkov, 2019)

than the Earth. At the same time, despite the fact that the heliocentric orbits of Mars and its satellites are also very close, the values of the geodetic rotation of Phobos and Deimos far exceed the value of the geodetic rotation of Mars. This is because Mars has a greater influence on the geodetic rotation of its satellites than the Sun on its and Mars by reason of the close distances between Mars and its satellites, than between the Earth and the Moon. The value of the geodetic rotation of Phobos is greater than ones values of the Earth and Venus; the value of the geodetic rotation of Deimos is greater than one value of the Earth. It is due to the fact that Mars has a greater influence on the geodetic rotation of its satellites than the Sun on some near planets by reason of very close distances between Mars and its satellites.

Mars and its satellites Phobos and Deimos (like the Earth and the Moon) are on average at the same distance from the Sun. As a result, their coefficients in $\Delta\psi_p$ and $\Delta\tau_p$ for periodic with argument λ_4 (Table 3) components are quite close to each other.

The geodetic rotations of Phobos and Deimos are determined not only by the Sun, but also by Mars. This fact is confirmed by the appearance of a harmonic with the argument D_{41} for Phobos and D_{41} for Deimos (Table 3).

In contrast to Phobos, located closer to the planet, the Sun has a greater influence on the geodetic rotation of Deimos. It is easy to see that the closer a satellite is located to the planet, the more the harmonic contribution depends on the mean longitude of the planet (see Phobos in Table 3). Therefore, the harmonic with a period of 1.881 years and the argument of λ_4 (Table 3) becomes predominant for Phobos. If the satellite is farther away from the planet, then more harmonic contribution depends on the precession orbit node in the Laplace plane¹ (see Deimos in Table 3). Therefore, the harmonic with a period of 54.537 years and the argument of Ω_{L42} (Table 3) becomes predominant for Deimos.

¹The Laplace plane is the plane normal to the satellite's orbital precession pole. It is a kind of "average orbital plane" of the satellite (between their planet's equatorial plane and the plane of its solar orbit), around which the instantaneous orbital plane of the satellite precesses, and to which it has a constant additional inclination (P. Kenneth Seidelmann (ed.), 1992).

Body	Angle	Period	Arg	Coefficient of $\sin(\text{Arg})$ (μas)	Coefficient of $\cos(\text{Arg})$ (μas)
Mars	$\Delta\psi_p$	1.881 yr	λ_4	$-543.438 - 22.455T + \dots$	$-241.415 + 40.433T + \dots$
	$\Delta\theta_p$	1.881 yr	λ_4	$9.157 + 0.241T + \dots$	$4.068 - 0.742T + \dots$
	$\Delta\varphi_p$	1.881 yr	λ_4	$30.949 - 0.392T + \dots$	$13.748 - 3.045T + \dots$
Phobos	$\Delta\psi_p$	1.881 yr	λ_4	$-537.291 + \dots$	$-238.028 + \dots$
		2.262 yr	Ω_{L41}	$-125.461 + \dots$	$680.758 + \dots$
		7.657 h	D_{41}	$-58.679 + 0.204T + \dots$	$59.450 - 0.022T + \dots$
	$\Delta\theta_p$	1.881 yr	λ_4	$9.448 + \dots$	$3.305 + \dots$
		2.262 yr	Ω_{L41}	$4.099 + \dots$	$1.339 + \dots$
		7.657 h	D_{41}	$-8.480 + 0.017T - \dots$	$-9.228 - 0.036T - \dots$
$\Delta\varphi_p$	1.881 yr	λ_4	$-29.698 + \dots$	$14.013 + \dots$	
	2.262 yr	Ω_{L41}	$-1.139 + \dots$	$-3.219 + \dots$	
	7.657 h	D_{41}	$21.359 - 0.129T - \dots$	$-22.722 - 0.036T - \dots$	
$\Delta\tau_p$	1.881 yr	λ_4	$-507.594 + \dots$	$-224.015 + \dots$	
	2.262 yr	Ω_{L41}	$-126.600 + \dots$	$677.538 + \dots$	
	7.657 h	D_{41}	$-37.319 + 0.074T - \dots$	$36.728 - 0.058T + \dots$	
$\Delta\rho_p$	1.881 yr	λ_4	$9.448 + \dots$	$3.305 + \dots$	
	2.262 yr	Ω_{L41}	$4.099 + \dots$	$1.339 + \dots$	
	7.657 h	D_{41}	$-8.480 + 0.017T - \dots$	$-9.228 - 0.036T - \dots$	
$\Delta(l\sigma)_p$	1.881 yr	λ_4	$250.815 + \dots$	$114.078 + \dots$	
	2.262 yr	Ω_{L41}	$-176.168 + \dots$	$935.392 + \dots$	
	7.657 h	D_{41}	$26.377 - 0.044T - \dots$	$-26.723 - 0.035T - \dots$	
Deimos	$\Delta\psi_p$	1.881 yr	λ_4	$-544.598 + \dots$	$-241.408 + \dots$
		54.537 yr	Ω_{L42}	$-2879.646 + \dots$	$757.953 + \dots$
		1.265 d	D_{42}	$-51.777 + 0.142T - \dots$	$11.009 + 0.007T + \dots$
	$\Delta\theta_p$	1.881 yr	λ_4	$9.220 + \dots$	$3.792 + \dots$
		54.537 yr	Ω_{L42}	$28.678 + \dots$	$106.025 + \dots$
		1.265 d	D_{42}	$-1.214 + 0.009T + \dots$	$-7.571 - 0.090T + \dots$
$\Delta\varphi_p$	1.881 yr	λ_4	$32.026 + \dots$	$13.676 + \dots$	
	54.537 yr	Ω_{L42}	$195.066 + \dots$	$-216.931 + \dots$	
	1.265 d	D_{42}	$19.149 - 0.045T - \dots$	$-4.576 - 0.042T - \dots$	
$\Delta\tau_p$	1.881 yr	λ_4	$-512.573 + \dots$	$-227.733 + \dots$	
	54.537 yr	Ω_{L42}	$-2684.581 + \dots$	$541.022 + \dots$	
	1.265 d	D_{42}	$-32.628 + 0.097T - \dots$	$6.433 - 0.035T + \dots$	
$\Delta\rho_p$	1.881 yr	λ_4	$9.220 + \dots$	$3.792 + \dots$	
	54.537 yr	Ω_{L42}	$28.678 + \dots$	$106.025 + \dots$	
	1.265 d	D_{42}	$-1.214 + 0.009T + \dots$	$-7.571 - 0.090T + \dots$	
$\Delta(l\sigma)_p$	1.881 yr	λ_4	$237.604 + \dots$	$105.749 + \dots$	
	54.537 yr	Ω_{L42}	$-5381.398 + \dots$	$1058.129 + \dots$	
	1.265 d	D_{42}	$22.601 + 0.174T - \dots$	$-4.805 - 0.053T + \dots$	

Table 3: The periodic terms of geodetic rotation of Mars and its satellites

In this investigation it was also carried out a study on the mutual relativistic influence of Mars satellites on each other and on Mars (i.e., the inclusion of another satellite in the number of perturbing bodies).

So, the change in Deimos geodetic rotation from Phobos relativistic influence: in the longitude of the node ψ is $-0.22 \mu\text{as/tjy}$, in the longitude τ is $-9.5 \cdot 10^{-2} \mu\text{as/tjy}$, in the inclination θ is $-9.3 \cdot 10^{-6} \mu\text{as/tjy}$, in the inclination ρ is $-9.3 \cdot 10^{-6} \mu\text{as/tjy}$, in the proper rotation angle φ is $0.12 \mu\text{as/tjy}$; in the node longitude $\iota\sigma$ is $9.4 \cdot 10^{-2} \mu\text{as/tjy}$.

The change in Phobos geodetic rotation from Deimos relativistic influence: in the longitude of the node ψ is $-5.3 \cdot 10^{-2} \mu\text{as/tjy}$, in the longitude τ is $-2.4 \cdot 10^{-2} \mu\text{as/tjy}$, in the inclination θ is $6.2 \cdot 10^{-6} \mu\text{as/tjy}$, in the inclination ρ is $6.2 \cdot 10^{-6} \mu\text{as/tjy}$, in the proper rotation angle φ is $2.9 \cdot 10^{-2} \mu\text{as/tjy}$; in the node longitude $\iota\sigma$ is $2.4 \cdot 10^{-2} \mu\text{as/tjy}$.

The change in Mars geodetic rotation from its satellites relativistic influence: in the longitude of the node ψ is $-0.62 \mu\text{as/tjy}$, in the inclination θ is $-1.2 \cdot 10^{-4} \mu\text{as/tjy}$, in the proper rotation angle φ is $0.35 \mu\text{as/tjy}$.

3. CONCLUSION

1. New high-precision values with the additions periodic terms of the geodetic rotation for Mars in Euler angles were obtained. These values are the dynamically adjusted to the DE431/LE431 ephemeris.

2. The systematic (Table. 1) and periodic (Table. 3) terms of the geodetic rotation of Martian satellites (Phobos and Deimos) are computed for the first time in the Euler angles and a perturbing terms of the physical libration. The mutual relativistic influence of the Mars satellites on each other in comparison with the Sun and Mars influences is insignificant. The obtained analytical values for the geodetic rotation of Phobos and Deimos can be used for the numerical study of their rotation in the relativistic approximation.

3. The secular terms of geodetic rotation of Mars satellites depend on their distance from the Sun and Mars, which masses are dominant in the Solar and Mars system, respectively. Mars has a greater influence on the geodetic rotation of its satellites than the Sun on the geodetic rotation of Phobos, Deimos and Mars.

4. The main periodic parts of the geodetic rotations for Mars satellites are determined not only by the Sun but also by Mars, which is the nearest planet to their satellites.

5. The values of the geodetic rotation of Mars satellites decrease with increasing their distance from Mars.

Acknowledgments. The investigation was carried out at Central (Pulkovo) Astronomical Observatory of the Russian Academy of Science (CAO) and the Space Research Centre of the Polish Academy of Science (SRC), under a financial support of the Cooperation between the SRC and CAO, and RFBR grant: the research project 19-02-00811.

4. REFERENCES

- Pashkevich V.V., 2016, "New high-precision values of the geodetic rotation of the major planets, Pluto, the Moon and the Sun", *Artificial Satellites* 51(2), doi: 10.1515/arsa-2016-0006, pp. 61–73.
- Folkner W.F., Williams J.G., Boggs D.H., Park R.S., and Kuchynka P., 2014, "The Planetary and Lunar Ephemerides DE430 and DE431", IPN Progress Report 42–196, February 15, 2014.
- Giorgini J.D., Chodas P.W., Yeomans D.K., 2001, "Orbit Uncertainty and Close-Approach Analysis Capabilities of the Horizons On-Line Ephemeris System", 33rd AAS/DPS meeting in New Orleans. LA. Nov 26. 2001 – Dec 01. 2001.

- De Sitter W., 1916, "On Einstein's Theory of Gravitation and its Astronomical Consequences", *MNRAS* 77, pp. 155–184.
- Fukushima T., 1991, "Geodesic Nutation", *A&A* 244(1), pp. L11–L12.
- Kopeikin S. Efroimsky M. and Kaplan G., 2011, "Relativistic Celestial Mechanics in the Solar System", Hoboken, NJ : John Wiley & Sons., pp. 1–894.
- Seidelmann P.K., Archinal B.A., A'Hearn M.F., Cruikshank D.P., Hilton J.L., Keller H.U., Oberst J., Simon J.L., Stooke P., Tholen D.J., and Thomas P.C., 2005, "Report of the IAU/IAG Working Group on Cartographic Coordinates and Rotational Elements: 2003", *Celest. Mech. Dyn. Astr.* 91, pp. 203–215.
- Archinal B.A., Acton C.H., A Hearn M.F. et al., 2018, "Report of the IAU Working Group on Cartographic Coordinates and Rotational Elements: 2015", *Celest. Mech. Dyn. Astr.* 130, 22, doi: 10.1007/s10569-017-9805-5 , pp. 21–46.
- Smart W.M., 1953, "Celestial Mechanics", Longmans, Green and Co, London-New York-Toronto.
- Brumberg V.A., Bretagnon P., 2000, "Kinematical Relativistic Corrections for Earth's Rotation Parameters", in *Proc. of IAU Colloquium 180*, eds. K. Johnston, D. McCarthy, B. Luzum and G. Kaplan, U.S. Naval Observatory, pp. 293–302.
- Pashkevich V.V., Vershkov A.N., 2019, "New High-Precision Values of the Geodetic Rotation of the Mars Satellites System, Major Planets, Pluto, the Moon and the Sun", *Artificial Satellites* 54(2), pp. 31–42, doi: 10.2478/arsa-2019-0004
- P. Kenneth Seidelmann (ed.), 1992, "Explanatory Supplement to the Astronomical Almanac", University Science Books, Sausalito (Ca).

POST-LINEAR METRIC OF A SOLAR SYSTEM BODY

S. Zschocke

Institute of Planetary Geodesy, TU Dresden - Germany - sven.zschocke@tu-dresden.de

ABSTRACT. A precise modeling of light trajectories in the solar system on the sub-micro-arcsecond and nano-arcsecond scale of accuracy requires the metric tensor of solar system bodies in post-linear approximation. The Multipolar Post-Minkowskian formalism represents a framework for determining the metric density in the exterior of a compact source of matter, which can be regarded as massive solar system body. The knowledge of the metric density, frequently been called gothic metric, allows to deduce the metric tensor. Some aspects are considered about how to determine the metric density and the metric tensor from the field equations of gravity.

1. INTRODUCTION

An advancement in astrometric science towards sub-micro-arcsecond and nano-arcsecond level in angular measurements of celestial objects requires considerable progress in the theory of light propagation through the curvilinear space-time of the solar system. In curved space-time the light signals propagate along null-geodesics, governed by the geodesic equation which reads $\ddot{x}^\alpha(\lambda) + \Gamma_{\mu\nu}^\alpha \dot{x}^\mu(\lambda) \dot{x}^\nu(\lambda) = 0$, where $x^\alpha(\lambda)$ is the four-coordinate of the light signal as function of the affine curve parameter λ , a dot means total derivative with respect to λ , and the Christoffel symbols $\Gamma_{\mu\nu}^\alpha = g^{\alpha\beta} (g_{\beta\mu, \nu} + g_{\beta\nu, \mu} - g_{\mu\nu, \beta}) / 2$ are functions of the metric tensor $g_{\alpha\beta}$, and a comma denotes partial derivative with respect to the four-coordinates, e.g. $f_{, \mu} = \partial f / \partial x^\mu$ and $f_{, \mu\nu} = \partial^2 f / \partial x^\mu \partial x^\nu$, etc. Accordingly, a precise modeling of light trajectories implies a precise knowledge of the metric of solar system bodies. The metric tensor can be series expanded in powers of the gravitational constant G , called post-Minkowskian expansion,

$$g_{\alpha\beta}(x) = \eta_{\alpha\beta} + \sum_{n=1}^{\infty} G^n h_{\alpha\beta}^{(n\text{PM})}(x) \quad (1)$$

where the first and second term, $h_{\alpha\beta}^{(1\text{PM})}$ and $h_{\alpha\beta}^{(2\text{PM})}$, are the linear and post-linear term of the metric perturbation, which are required for determining the light trajectory on the sub-micro-arcsecond and nano-arcsecond scale of accuracy. The orthogonality relation $g^{\alpha\rho} g_{\rho\beta} = \delta_\beta^\alpha$ enables to switch between the contravariant and covariant components of the metric tensor.

The Multipolar Post-Minkowskian (MPM) formalism represents a perturbative approach for determining the metric density, $\bar{g}^{\alpha\beta}$, in the exterior of a compact source of matter, defined by

$$\bar{g}^{\alpha\beta} = \sqrt{-g} g^{\alpha\beta} \quad \text{or} \quad g^{\alpha\beta} = \sqrt{-\bar{g}} \bar{g}^{\alpha\beta} \quad (2)$$

where $g = \det(g_{\rho\sigma})$ and $\bar{g} = \det(\bar{g}_{\rho\sigma})$ is the determinant of the covariant components of the metric tensor and metric density, respectively. The post-Minkowskian expansion of the metric density reads

$$\bar{g}^{\alpha\beta}(x) = \eta^{\alpha\beta} - \sum_{n=1}^{\infty} G^n \bar{h}_{(n\text{PM})}^{\alpha\beta}(x) \quad (3)$$

where the first and second term, $\bar{h}_{(1\text{PM})}^{\alpha\beta}$ and $\bar{h}_{(2\text{PM})}^{\alpha\beta}$, are the linear and post-linear term of the gothic metric perturbation. The orthogonality relation $\bar{g}^{\alpha\rho} \bar{g}_{\rho\beta} = \delta_\beta^\alpha$ enables to switch between the contravariant and covariant components of the gothic metric.

The MPM formalism determines the metric density in the exterior of a massive body, having arbitrary shape, inner structure, oscillations, and rotational motions. Due to Eq. (2) the knowledge of the metric density allows to deduce the metric tensor. In what follows, some aspects are considered about how to obtain the metric density and metric tensor from the field equations.

2. THE FIELD EQUATIONS OF GRAVITY

The field equations relate the metric tensor $g_{\mu\nu}$ to the stress-energy tensor of matter $T_{\mu\nu}$,

$$R_{\mu\nu} - \frac{1}{2} g_{\mu\nu} R = \frac{8\pi G}{c^4} T_{\mu\nu} \quad (4)$$

where $R_{\mu\nu} = \Gamma_{\mu\nu,\rho}^\rho - \Gamma_{\mu\rho,\nu}^\rho + \Gamma_{\sigma\rho}^\rho \Gamma_{\mu\nu}^\sigma - \Gamma_{\sigma\nu}^\rho \Gamma_{\mu\rho}^\sigma$ is the Ricci tensor and $R = g^{\mu\nu} R_{\mu\nu}$ is the Ricci scalar. The field equations constitute a set of ten coupled non-linear partial differential equations for the ten components of the metric tensor $g_{\mu\nu}$ of space-time, which in differential geometry is modeled by a semi-Riemannian manifold \mathcal{M} . The contracted Bianchi identities imply that only six of these field equations (4) are independent, which determine the ten components of the metric tensor up to a passive coordinate transformation (keep points of manifold fixed and change coordinates) from the old $\{y\}$ to the new coordinate system $\{y'\}$,

$$y^\mu \rightarrow y'^\mu. \quad (5)$$

The field equations (4) are invariant under these (infinitely many) coordinate transformations, known as passive general covariance of the field equations. That means, if the set $(\mathcal{M}, \mathbf{g})$ is a solution of the field equations, then the set $(\mathcal{M}, \mathbf{g}')$ is also a solution of the same field equations, where $g'_{\alpha\beta} = A_\alpha^\mu A_\beta^\nu g_{\mu\nu}$ is the metric tensor in these new coordinates with A_α^μ being the Jacobian matrix $A_\alpha^\mu = \partial y^\mu / \partial y'^\alpha$ of the passive coordinate transformation. These sets are physically equivalent and describe the same physical system. The metric tensors have different components in different coordinate systems, $g'_{\alpha\beta} \neq g_{\mu\nu}$, but as geometrical objects (Eq. (2.23) in *Hawking, Ellis (1974)*) they are equal, $\mathbf{g}' = \mathbf{g}$, because they attribute the same distance to the same pair of points \mathcal{P} and \mathcal{Q} of the manifold: $d_{g'}(\mathcal{P}, \mathcal{Q}) = d_g(\mathcal{P}, \mathcal{Q})$ (infinitesimal distance of these pairs is assumed). For later purposes it is useful to consider an active coordinate transformation (keep coordinates fixed and change points of manifold),

$$\Psi : \mathcal{M} \rightarrow \mathcal{M} \quad (6)$$

which is a C^∞ differentiable mapping of each point of the manifold reversibly unique to another image point of the same manifold, $\mathcal{P} \rightarrow \Psi(\mathcal{P})$. Hence, the coordinates are changed $y^\mu(\mathcal{P}) \rightarrow y'^\mu(\mathcal{P})$. The field equations (4) are invariant under these (infinitely many) diffeomorphisms, known as active general covariance of the field equations. That means, if the set $(\mathcal{M}, \mathbf{g})$ is a solution of the field equations, then the set $(\mathcal{M}, \mathbf{g}')$ is also a solution of the same field equations, where $\mathbf{g}' = \Psi^* \mathbf{g}$ is the pullback of the metric tensor, $g'_{\alpha\beta} = A_\alpha^\mu A_\beta^\nu g_{\mu\nu}$, with A_α^μ being the Jacobian matrix $A_\alpha^\mu = \partial y^\mu / \partial y'^\alpha$ of the active coordinate transformation. These sets are physically equivalent and describe the same physical system (Section 7.1 in *Hawking, Ellis (1974)*; for the associated problem of Leibniz Equivalence see *Earman, Norton (1987)* and *Lusanna, Pauri (2006)*). These metric tensors attribute the same distance of a pair of points of the manifold and their images, $d_{g'}(\mathcal{P}, \mathcal{Q}) = d_g(\Psi(\mathcal{P}), \Psi(\mathcal{Q}))$ (infinitesimal distance of these pairs and their images is assumed). But these metric tensors are not equal, $\mathbf{g}' \neq \mathbf{g}$, because they attribute different distances to the same pair of points of the manifold: $d_{g'}(\mathcal{P}, \mathcal{Q}) \neq d_g(\mathcal{P}, \mathcal{Q})$ (e.g. *Gaul, Rovelli, (2000)*). However, if a Killing vector field exists on \mathcal{M} and the diffeomorphism Ψ proceeds along the congruence of that Killing vector field, then the metric and pullback metric are equal, $\mathbf{g}' = \mathbf{g}$, and the diffeomorphism is an isometry (Section 2.6 in *Hawking, Ellis (1974)*).

3. LANDAU-LIFSCHITZ FORMULATION OF GRAVITY

The theory of gravity has a geometrical interpretation in physical curvilinear space-time and a field-theoretical interpretation in auxiliary flat space-time (e.g. text below Eq. (11) in *Gupta* (1954) or Section 8.4 in *Feynman* (1995) or part 5 in Box 17.2 in *Misner, Thorne, Wheeler* (1973)); for an excellent historical overview we refer to *Brian Pitts, Schieve* (2018). So one distinguishes between a physical manifold \mathcal{M} covered by curvilinear coordinates y^μ and endowed with metric $g_{\mu\nu}(y)$, a flat background manifold \mathcal{M}_0 covered by curvilinear coordinates x^α and endowed with metric $g_{\alpha\beta}^0(x)$, and a diffeomorphism

$$\Phi : \mathcal{M}_0 \rightarrow \mathcal{M} \quad (7)$$

which is a C^∞ differentiable mapping of each point $q \in \mathcal{M}_0$ of the flat background manifold \mathcal{M}_0 reversibly unique to another point $p \in \mathcal{M}$ of the physical manifold \mathcal{M} (hence $\dim \mathcal{M}_0 = \dim \mathcal{M}$); it is not relevant whether (7) exists everywhere or only on finite domains $\Phi : \mathcal{V} \subseteq \mathcal{M}_0 \rightarrow \mathcal{U} \subseteq \mathcal{M}$.

The field equations (4) are not invariant under (7), because the manifolds \mathcal{M} and \mathcal{M}_0 are different with respect to their geometrical properties: the curvature tensor of \mathcal{M} expressed in terms of $g_{\mu\nu}(y)$ is non-zero, $R_{\alpha\nu\beta}^\mu(y) \neq 0$, in any coordinate system $\{y\}$ which maps the physical manifold, while the curvature tensor of \mathcal{M}_0 expressed in terms of $g_{\alpha\beta}^0(x)$ vanishes, $R_{\alpha\nu\beta}^\mu(x) = 0$, in any coordinate system $\{x\}$ which maps the flat background manifold. In particular, the metric tensor \mathbf{g}^0 of \mathcal{M}_0 (e.g. in Cartesian coordinates \mathbf{g}^0 is given by $\eta_{\alpha\beta} = \text{diag}(-1, +1, +1, +1)$) and the metric tensor \mathbf{g} of \mathcal{M} can never be related by a pullback: $\mathbf{g}^0 \neq \Phi^*\mathbf{g}$.

But the diffeomorphism (7) is an active coordinate transformation, which makes it possible to pullback the metric tensor \mathbf{g} of the physical manifold \mathcal{M} (given by $g_{\mu\nu}(y)$) to the metric tensor $\Phi^*\mathbf{g}$ which propagates as tensorial field on the flat background \mathcal{M}_0 (given by $g_{\alpha\beta}(x)$)

$$g_{\alpha\beta}(x) = \frac{\partial y^\mu}{\partial x^\alpha} \frac{\partial y^\nu}{\partial x^\beta} g_{\mu\nu}(y) . \quad (8)$$

In the same way, the Ricci tensor and energy-momentum tensor on \mathcal{M} are pulled back on \mathcal{M}_0 . By means of these relations the field equations of gravity (4) on the physical manifold \mathcal{M} can be pulled back to field equations on the flat background manifold \mathcal{M}_0 . Then, the sets $(\mathcal{M}, \mathbf{g})$ and $(\mathcal{M}_0, \Phi^*\mathbf{g})$ are physically equivalent, iff the metric tensor \mathbf{g} on the physical manifold \mathcal{M} is determined by the field equations (4), while the pulled-back metric tensor $\Phi^*\mathbf{g}$ on the flat background manifold \mathcal{M}_0 (i.e. $g_{\alpha\beta} = \Phi^{*\mu\nu} g_{\mu\nu}$ in Eq. (8)) is determined by the pulled-back field equations on \mathcal{M}_0 (cf. Section 7 in *Hawking, Ellis* (1974), especially text below Eq. (7.51) in *Hawking, Ellis* (1974), as well as text below Eq. (7.10) in *Carroll* (2013)).

In the Landau-Lifschitz formulation one makes a detour and does not consider the metric tensor $g_{\mu\nu}(y)$ but the metric density $\bar{g}^{\mu\nu}(y)$, which is pulled back from the physical manifold to the flat background manifold. A detailed mathematical representation of the Landau-Lifschitz formulation is given by Sections 1 and 2 in *Petrov, Kopeikin, Lompay, Tekin* (2017) as well as by Section 7 in *Hawking, Ellis* (1974). These field equations take the following form (cf. Eqs. (20.20) - (20.22) in *Misner, Thorne, Wheeler* (1973), Eq. (6.6) in *Poisson, Will* (2014)),

$$H^{\alpha\rho\beta\sigma}{}_{,\rho\sigma}(x) = \frac{16\pi G}{c^4} (-g(x)) \left(T^{\alpha\beta}(x) + t_{LL}^{\alpha\beta}(x) \right) . \quad (9)$$

The l.h.s. is the Landau-Lifschitz superpotential, $H^{\alpha\rho\beta\sigma} = \bar{g}^{\alpha\beta} \bar{g}^{\rho\sigma} - \bar{g}^{\alpha\sigma} \bar{g}^{\beta\rho}$, while the r.h.s. is the Landau-Lifschitz complex, where $t_{LL}^{\alpha\beta}$ is the Landau-Lifschitz pseudotensor which represents, roughly to speak, the energy-momentum distribution of the gravitational fields. The field equations (9) are manifestly Lorentz-covariant and constitute a set of ten coupled non-linear partial differential equations for the ten components of the metric density $\bar{g}^{\alpha\beta}$. Because of the identity $H^{\alpha\rho\beta\sigma}{}_{,\rho\sigma\beta} = 0$ (implying energy-momentum conservation, cf. Eqs. (6.7) - (6.8) in *Poisson, Will* (2014)) only six

equations are independent, which determine the ten components of the metric density up to a passive transformation of coordinates which map the flat background manifold.

Thus far, no specific choice of the coordinates of the flat background manifold has been imposed. For practical calculations in celestial mechanics, in the theory of light propagation, or in the theory of gravitational waves, it is, however, very useful to choose harmonic coordinates to cover the flat background space-time \mathcal{M}_0 , which are introduced by the gauge condition

$$\bar{g}^{\alpha\beta}_{,\beta}(x) = 0 \quad \Longrightarrow \quad \square_g x^\alpha = 0 \quad (10)$$

where the relation on the r.h.s. follows from the relation on the l.h.s. where \square_g is the covariant d'Alembert operator which in harmonic coordinates reads $\square_g = g^{\rho\sigma} \nabla_\rho \nabla_\sigma$ and ∇_ρ denotes covariant derivative with respect to x^ρ . Harmonic coordinates are small deformations of the Minkowski coordinates, therefore it is useful to decompose the pulled-back metric density into the flat Minkowskian metric plus a small perturbation,

$$\bar{g}^{\alpha\beta}(x) = \eta^{\alpha\beta} - \bar{h}^{\alpha\beta}(x) \quad (11)$$

so that the gothic metric perturbation $\bar{h}^{\alpha\beta}$ propagates as dynamical field on the flat background space-time \mathcal{M}_0 (Section 7.1 in *Carroll (2013)* and Section 6.2 in *Poisson, Will (2014)*). By inserting (10) and (11) into (9) one obtains the Landau-Lifschitz field equations (also known as reduced field equations of gravity) in the following form (Eq. (5.2b) in *Thorne (1980)*)

$$\square \bar{h}^{\alpha\beta}(x) = -\frac{16\pi G}{c^4} (\tau^{\alpha\beta}(x) + t^{\alpha\beta}(x)) \quad (12)$$

where $\square = \eta^{\rho\sigma} \partial_\rho \partial_\sigma$ is the flat d'Alembert operator in terms of harmonic coordinates in the flat background space-time \mathcal{M}_0 . The terms on the r.h.s. in (12) are given by

$$\tau^{\alpha\beta} = (-g) T^{\alpha\beta} \quad \text{and} \quad t^{\alpha\beta} = (-g) t_{\text{LL}}^{\alpha\beta} + \frac{c^4}{16\pi G} \left(\bar{h}^{\alpha\rho}_{,\sigma} \bar{h}^{\beta\sigma}_{,\rho} - \bar{h}^{\alpha\beta}_{,\rho\sigma} \bar{h}^{\rho\sigma} \right). \quad (13)$$

The ten coupled non-linear partial differential equations (12) are exact field equations of gravity in the Landau-Lifschitz formulation in harmonic coordinates. Because of the gauge condition $\bar{h}^{\alpha\beta}_{,\beta} = 0$, which follows from (10) and (11), only six equations are independent of each other.

The harmonic gauge (10) does not uniquely select one harmonic coordinate system but a class of infinitely many harmonic systems, because it allows for a residual gauge transformation between two arbitrary harmonic reference systems $\{x\}$ and $\{x'\}$,

$$x'^\alpha = x^\alpha + \varphi^\alpha(x) \quad (14)$$

if the gauge vector φ^α satisfies the homogeneous Laplace-Beltrami equation $\square_g \varphi^\alpha = 0$; Eq. (14) has been elucidated by Fig. 1 in *Zschocke (2019)*. The field equations (12) are invariant under the residual gauge transformation (14), which permits extensive simplifications of the form of the metric density. Moreover, the calculations of the MPM formalism are considerably simplified by assuming that $\{x\}$ are just Minkowskian (i.e. straight harmonic) coordinates, while $\{x'\}$ are considered as curvilinear harmonic coordinates.

4. THE MULTIPOLAR POST-MINKOWSKIAN FORMALISM

The MPM approach has originally been introduced in *Thorne (1980)*, while considerable extensions and important advancements have later been worked out in *Blanchet, Damour (1986)* and in a

series of subsequent investigations. The MPM formalism is based on the post-Minkowski expansion of the field equations (12),

$$\bar{h}^{\alpha\beta} = \sum_{n=1}^{\infty} G^n \bar{h}_{(n\text{PM})}^{\alpha\beta} \quad \text{and} \quad \tau^{\alpha\beta} = T^{\alpha\beta} + \sum_{n=1}^{\infty} G^n \tau_{(n\text{PM})}^{\alpha\beta} \quad \text{and} \quad t^{\alpha\beta} = \sum_{n=1}^{\infty} G^n t_{(n\text{PM})}^{\alpha\beta}. \quad (15)$$

Inserting (15) into (12) yields a hierarchy of field equations,

$$\square \bar{h}_{(1\text{PM})}^{\alpha\beta}(x) = -\frac{16\pi}{c^4} T^{\alpha\beta}(x), \quad (16)$$

$$\square \bar{h}_{(2\text{PM})}^{\alpha\beta}(x) = -\frac{16\pi}{c^4} \left(\tau_{(1\text{PM})}^{\alpha\beta}(x) + t_{(1\text{PM})}^{\alpha\beta}(x) \right), \quad (17)$$

⋮

$$\square \bar{h}_{(n\text{PM})}^{\alpha\beta}(x) = -\frac{16\pi}{c^4} \left(\tau_{((n-1)\text{PM})}^{\alpha\beta}(x) + t_{((n-1)\text{PM})}^{\alpha\beta}(x) \right). \quad (18)$$

Each of the field equations (16) ⋯ (18) represents an equation in flat space-time. The MPM formalism is an approach for solving that hierarchy of field equations iteratively, starting with the first iteration (16), where $T^{\alpha\beta}$ is the energy-momentum tensor of matter in the approximation of special relativity. The general solution of the gothic metric in linear-order $\bar{h}_{(1\text{PM})}^{\alpha\beta}$ (Thorne (1980), Blanchet, Damour (1986), Damour, Iyer (1991)) is inserted into the second iteration (17) which yields the gothic metric in post-linear order, $\bar{h}_{(2\text{PM})}^{\alpha\beta}$, and so on. Using this iterative approach, it has been demonstrated in Blanchet, Damour (1986) that the general solution of these field equations depends on six source-multipoles, $I_L, J_L, W_L, X_L, Y_L, Z_L$, which are integrals over the energy-momentum tensor of the compact source of matter (cf. Eqs. (5.15) - (5.20) in Blanchet (1998)). Furthermore, using the residual gauge freedom (14), it has been demonstrated in Blanchet, Damour (1986) that the general solution of (16) ⋯ (18) can be written as follows,

$$\bar{g}^{\alpha\beta}[I_L, J_L, W_L, X_L, Y_L, Z_L] = \eta^{\alpha\beta} - \sum_{n=1}^{\infty} G^n \bar{h}_{(n\text{PM})}^{\alpha\beta \text{ can}}[M_L, S_L] + \text{gauge terms} \quad (19)$$

which is valid in the exterior of the body. The canonical piece, $\bar{h}_{(n\text{PM})}^{\alpha\beta \text{ can}}$, depends on two multipoles: mass-type multipole M_L (accounts for shape, inner structure, and oscillations of the body) and current-type multipole S_L (accounts for rotational motions and inner currents of the body), which are related to the source-multipoles via non-linear equations (Eqs. (6.1a) and (6.1b) in Blanchet (1998)). All those terms in the metric density which depend on the gauge vector φ^α are called gauge terms and represent unphysical degrees of freedom because they have no impact on physical observables which are, by definition, coordinate-independent scalars (Bergmann (1961)).

The MPM formalism has been developed for understanding the generation of gravitational waves by an isolated source of matter, like binary black holes. Gravitational waves decouple from the source in the intermediate zone and they do finally propagate with the speed of light into the far wave-zone of the gravitational system. In the far wave-zone the gravitational fields have two degrees of freedom, where the transverse traceless (TT) gauge of the metric tensor becomes relevant because the TT terms in the metric tensor carry the physical information (Blanchet, Kopeikin, Schäfer (2001)). In the far wave-zone, the TT projection of the metric density equals the TT projection of the metric tensor (cf. Eq. (7.119) in Carroll (2013)),

$$\bar{h}_{\alpha\beta}^{\text{TT}} = h_{\alpha\beta}^{\text{TT}} \quad \text{in the far - zone.} \quad (20)$$

That is why there is no need to determine the metric tensor in the far wave-zone of the system. The gothic metric perturbation in TT gauge in terms of radiative moments U_L and V_L , which are time-derivatives of source multipoles, is given by Eq. (64) in *Blanchet, Kopeikin, Schäfer (2001)*.

5. THE METRIC TENSOR

For determining light trajectories in the near-zone of the solar system one needs the metric tensor of solar system bodies. While in principle one might use the TT gauge, one should, however, not expect much simplification, because such a nice relation like (20) does not exist,

$$\bar{h}_{\alpha\beta}^{\text{TT}} \neq h_{\alpha\beta}^{\text{TT}} \quad \text{in the near - zone .} \quad (21)$$

Thus, relativistic astrometry necessarily requires the determination of the metric tensor in the near-zone of the gravitational system. The metric density and the metric tensor contain the same physical information about the gravitational system, because they are related to each other reversibly unique by Eqs. (2). Using these relations, it has been shown in *Zschocke (2019)* that the general form of the metric tensor in the exterior of a solar system body is given by

$$g_{\alpha\beta} [I_L, J_L, W_L, X_L, Y_L, Z_L] = \eta_{\alpha\beta} + \sum_{n=1}^{\infty} G^n h_{\alpha\beta \text{ can}}^{(n\text{PM})} [M_L, S_L] + \text{gauge terms} \quad (22)$$

where the canonical piece, $h_{\alpha\beta \text{ can}}^{(n\text{PM})}$, depends only on two multipoles M_L and S_L . The linear term and the post-linear term of the metric perturbation, $h_{\alpha\beta \text{ can}}^{(1\text{PM})}$ and $h_{\alpha\beta \text{ can}}^{(2\text{PM})}$, respectively, are explicitly given by Eqs. (109) - (111) and (115) - (117) in *Zschocke (2019)*. The gauge terms depend on the gauge vector φ^α and have no impact on physical observables.

6. CONCLUSION

Future astrometry at the sub-micro-arcsecond and nano-arcsecond level of accuracy in astrometric measurements requires considerable progress in modeling the trajectory of light signals through the curved space-time of the solar system. Such a precise determination of light trajectories implies the knowledge of the metric tensor $g_{\alpha\beta}$ of solar system bodies in the post-linear approximation. The Multipolar Post-Minkowskian formalism represents a framework for determining the metric density $\bar{g}^{\alpha\beta}$ in the exterior of a massive body having arbitrary shape and inner structure, oscillations and rotational motions. The knowledge of the metric density allows to deduce the metric tensor $g_{\alpha\beta}$. Some aspects of that approach have been considered which are relevant for future investigations in the theory of light propagation and relativistic astrometry.

7. REFERENCES

- Bergmann, P.G., 1961, "Observables in General Relativity", *Rev. Mod. Phys.* 33, pp. 510-514.
 Blanchet, L., 1998, "On the multipole expansion of the gravitational field", *Class. Quantum Grav.* 15, pp. 1971-1999.
 Blanchet, L., Damour, T., 1986, "Radiative gravitational fields in general relativity: I. General structure of the field outside the source", *Phil. Trans. R. Soc. London A* 320, pp. 379-430.
 Blanchet, L., Kopeikin, S.A., Schäfer, G., 2001, "Gravitational radiation theory and light propagation", *Lecture Notes in Physics* 562, pp. 141-166.
 Brian Pitts, J., Schieve W.C., 2018, "Null Cones in Lorentz-Covariant General Relativity", in *gr-qc/0111004*.
 Carroll, S., 2013, "Spacetime and Geometry: An Introduction to General Relativity", First Edition, Pearson New International, Edinburgh Gate, UK.

- Damour, T., Iyer, B.R., 1991, "Multipole analysis for electromagnetism and linearized gravity with irreducible Cartesian tensors", *Phys. Rev. D* 43, pp. 3259-3272.
- Earman, J., Norton, J., 1987, "What price spacetime substantivalism? The hole story", *The British Journal for the Philosophy of Science* 38(4), pp. 515-525.
- Feynman, R.P., 1995, "Lectures on Gravitation", First Edition, Addison-Wesley, Boston, U.S.
- Gaul, M., Rovelli, C., 2000, "Loop Quantum Gravity and the Meaning of Diffeomorphism Invariance", *Lect. Notes Phys.* 541, pp. 277-324.
- Gupta, S.N., 1954, "Gravitation and Electromagnetism", *Phys. Rev.* 96, pp. 1683-1685.
- Hawking, S.W., Ellis, G.F.R., 1974, "The large scale structure of space-time", First Edition, Cambridge University Press, New York, U.S.
- Landau, L.D., Lifschitz, E.M., 1971, "The Classical Theory of Fields", Third English Edition, Course of Theoretical Physics, Volume 2, Pergamon Press, Oxford, UK.
- Lusanna, L., Pauri, M., 2006, "The Physical Role of Gravitational and Gauge Degrees of Freedom in General Relativity - I,II" *Gen. Rel. Grav.* 38, pp. 187-227, pp. 229-267.
- Misner, C.W., Thorne, K.S., Wheeler, J.A., 1973, "Gravitation", First Edition, W.H. Freeman, New York, U.S.
- Petrov, A.N., Kopeikin, S.M., Lompay, R.R., Tekin, B., 2017, "Metric Theories of Gravity: Perturbations and Conservation Laws", First Edition, De Gruyter, Boston, U.S.
- Poisson, E., Will, C.M., 2014, "Gravity: Newtonian, Post-Newtonian, Relativistic", First Edition, Cambridge University Press, UK.
- Thorne, K.S., 1980, "Multipole expansions of gravitational radiation", *Rev. Mod. Phys.* 52, pp. 299-339.
- Zschocke, S., 2019, "Post-linear metric of a compact source of matter", *Phys. Rev. D* 100, 084005, pp. 1-32.

RECENT IMPROVEMENTS IN THE DETERMINATION OF TIME TRANSFER FUNCTIONS

P. TEYSSANDIER

Observatoire de Paris / SYRTE, PSL Research University, CNRS/UMR 8630 - pierre.teyssandier@obspm.fr

ABSTRACT. A few years ago, a new approach allowed to determine in an exact form the time transfer functions in Schwarzschild-like spacetimes within the weak-field, linearized approximation. We give a brief survey of the main results thus obtained and we indicate how the new procedure can be used to compute the contributions to the travel time of light rays due to the mass and spin multipoles of a rotating axisymmetric body.

1. INTRODUCTION

In the area of highly precise astrometry as well in a lot of experiments performed to test the metric theories of gravity in the Solar System, it is of crucial interest to know the travel time of a light ray between an emitter A and a receiver B as a function of the position of the emitter, the position of the receiver and the instant of reception. We call such a function “a reception time transfer function”. To be more precise, consider a light ray propagating through a vacuum in a region of spacetime covered by a coordinate system $x^\mu = (x^0, \mathbf{x})$, with $x^0 = ct$ and $\mathbf{x} = (x^i)$, $i = 1, 2, 3$, t being supposed to have the dimension of a time, and the x^i the dimension of a length for the sake of simplicity. Denote by (x_A^0, \mathbf{x}_A) the point-event where the ray is emitted and by (x_B^0, \mathbf{x}_B) the point-event where it is observed. The light ray joining (x_A^0, \mathbf{x}_A) and (x_B^0, \mathbf{x}_B) is a null geodesic of spacetime, which implies that the coordinate light travel time $(x_B^0 - x_A^0)/c = t_B - t_A$ is a function of \mathbf{x}_A , \mathbf{x}_B and t_B , so that we can write

$$t_B - t_A = \mathcal{T}_r(\mathbf{x}_A, t_B, \mathbf{x}_B). \quad (1)$$

Knowing the reception time transfer function (TTF) $\mathcal{T}_r(\mathbf{x}_A, t_B, \mathbf{x}_B)$ associated with a light ray enables us to model the time delay and the Doppler tracking along this ray. It also enables us to compute the propagation direction of the ray at the point of observation (Le Poncin-Lafitte et al 2004), which explains the relevance of the notion of TTF in relativistic astrometry (see, e.g., Hees et al 2014, Bertone et al 2017). Nevertheless, in spite of a large amount of works, the explicit computation of all the possible TTFs in a given spacetime remains an unsolved problem, even in the special case of static, spherically symmetric spacetimes. Only partial results have been obtained, using several methods which are in fact equivalent. We summarize here the procedure presented in Teyssandier and Le Poncin-Lafitte 2008.

It is supposed that the metric of spacetime may be expanded in a power series of the Newtonian gravitational constant G as follows:

$$g_{\mu\nu}(x; G) = \eta_{\mu\nu} + \sum_{n=1}^{\infty} G^n g_{\mu\nu}^{(n)}(x), \quad (2)$$

where $\eta_{\mu\nu}$ is the Minkowski metric: $\eta_{\mu\nu} = \text{diag}(1, -1, -1, -1)$. The procedure is based on the assumption that there exists at least a null geodesic linking the emitter and the receiver such that the corresponding reception TTF can be expanded in a power series of G as follows:

$$\mathcal{T}_r(\mathbf{x}_A, t_B, \mathbf{x}_B; G) = \frac{R_{AB}}{c} + \sum_{n=1}^{\infty} G^n \mathcal{T}_r^{(n)}(\mathbf{x}_A, t_B, \mathbf{x}_B), \quad (3)$$

where R_{AB} is the ‘Euclidean’ distance between the positions \mathbf{x}_A and \mathbf{x}_B , that is

$$R_{AB} = |\mathbf{x}_B - \mathbf{x}_A| = [(x_B^1 - x_A^1)^2 + (x_B^2 - x_A^2)^2 + (x_B^3 - x_A^3)^2]^{1/2}. \quad (4)$$

Under these assumptions, it may be shown that each perturbation term $\mathcal{T}_r^{(n)}$ is given by an integral involving only the metric perturbations $g_{\mu\nu}^{(1)}, \dots, g_{\mu\nu}^{(n)}$ and the functions $\mathcal{T}_r^{(1)}, \dots, \mathcal{T}_r^{(n-1)}$ taken on a Minkowskian null straight line passing through the spatial positions \mathbf{x}_A and \mathbf{x}_B .

However, two major problems are raised by the iterative procedure outlined above. First, the method yields a single TTF, thus excluding the possibility to model the gravitational lensing, where multiple images appear. Moreover, the perturbation functions $\mathcal{T}_r^{(n)}$ involve ‘enhanced terms’, namely terms which are infinite for some positions of the emitter and the receiver (for the pioneer work, see Klioner and Zschocke 2010; see also Teyssandier 2012). An example of this pathology is furnished by the TTF calculated with this procedure in a static spherically symmetric spacetime, as it may be seen in the next section.

2 CASE OF STATIC SPHERICALLY SYMMETRIC SPACETIMES

For an isolated spherically symmetric body of mass M , the coordinates (x^0, \mathbf{x}) may be chosen so that the metric takes the form

$$ds^2 = \left(1 - \frac{2m}{r} + 2\beta\frac{m^2}{r^2} - \frac{3}{2}\beta_3\frac{m^3}{r^3} + \dots\right) (dx^0)^2 - \left(1 + 2\gamma\frac{m}{r} + \frac{3}{2}\gamma_2\frac{m^2}{r^2} + \frac{1}{2}\gamma_3\frac{m^3}{r^3} + \dots\right) d\mathbf{x}^2, \quad (5)$$

where $m = GM/c^2$, $r = |\mathbf{x}| = [\sum_{i=1}^3 (x^i)^2]^{1/2}$, $d\mathbf{x}^2 = \sum_{i=1}^3 (dx^i)^2$, and $\beta, \beta_3, \gamma, \gamma_2, \gamma_3$ are post-Newtonian parameters equal to 1 in general relativity.

Owing to the static character of spacetime, each TTF for the metric (5) is independent of the reception time. So we shall henceforth omit the index r standing for ‘reception’. The procedure outlined in the Introduction yields a TTF as follows (for the terms in m^2 , see Le Poncin-Lafitte et al 2004 and Klioner and Zschocke 2010; for the terms in m^3 , see Linet and Teyssandier 2013):

$$\begin{aligned} \mathcal{T}_{\text{Spher}}(\mathbf{x}_A, \mathbf{x}_B) = & \frac{R_{AB}}{c} + \mathcal{T}_{\text{Shap}}(\mathbf{x}_A, \mathbf{x}_B) - \frac{m^2 R_{AB}}{c r_A r_B} \left[\frac{(\gamma + 1)^2}{1 + \cos \psi_{AB}} - \kappa_2 \frac{\psi_{AB}}{\sin \psi_{AB}} \right] \\ & + \frac{m^3 (r_A + r_B) R_{AB}}{c r_A^2 r_B^2 (1 + \cos \psi_{AB})} \left[\frac{(\gamma + 1)^3}{1 + \cos \psi_{AB}} - \kappa_2 (\gamma + 1) \frac{\psi_{AB}}{\sin \psi_{AB}} + \kappa_3 \right] + \mathcal{O}(m^4), \quad (6) \end{aligned}$$

where $r_A = |\mathbf{x}_A|$, $r_B = |\mathbf{x}_B|$, R_{AB} is defined by (4), ψ_{AB} is the measure of the angle between \mathbf{x}_A and \mathbf{x}_B laid down by

$$\cos \psi_{AB} = \frac{\mathbf{x}_A \cdot \mathbf{x}_B}{r_A r_B}, \quad 0 \leq \psi_{AB} \leq \pi, \quad (7)$$

$\mathcal{T}_{\text{Shap}}$ is the Shapiro time delay, namely (see, e.g., Blanchet et al 2001 and refs. therein)

$$\mathcal{T}_{\text{Shap}}(\mathbf{x}_A, \mathbf{x}_B) = \frac{(\gamma + 1)m}{c} \ln \left(\frac{r_A + r_B + R_{AB}}{r_A + r_B - R_{AB}} \right) \quad (8)$$

and κ_2 and κ_3 are constants defined by

$$\kappa_2 = 2(\gamma + 1) - \beta + \frac{3}{4}\gamma_2, \quad (9)$$

$$\kappa_3 = 4(\gamma - \beta + 1) - 2\beta\gamma + \frac{3}{2}\gamma_2 + \frac{1}{4}(3\beta_3 + \gamma_3). \quad (10)$$

An enhanced effect is ensured since each term in Eq. (6) – except R_{AB} – tends to infinity when $\psi_{AB} \rightarrow \pi$. This divergent behaviour is not surprising. If ψ_{AB} is sufficiently close to π , the straight

line joining \mathbf{x}_A and \mathbf{x}_B is passing through a region of strong field. Consequently, a convergent expansion in a series of powers of G cannot be reasonably expected for a TTF. Clearly, the second assumption is not realist in this case. Moreover, it is obvious that if r_A and r_B are sufficiently large and ψ_{AB} is sufficiently close to π , there exist at least two distinct light rays joining the emitter and the receiver and confined to the zone of weak field: this means that the usual theory of the time transfer functions does not work in a configuration of gravitational lensing. So, the theory summarized in the Introduction must be revised.

3. EXACT SOLUTIONS FOR LINEARIZED SPHERICALLY SYMMETRIC METRICS

3.1 The complete set of time transfer functions

In order to overcome the difficulties raised in the previous section, we can reason differently. The dominant divergent terms in Eq. (6) are manifestly linked to the linear part of the metric since they only involve the post-Newtonian parameter γ . So, in a first approach, we may be content with treating the problem in the weak-field, linearized approximation provided that we use the rigorous solutions to the null geodesic equations. This program has been successfully carried through for the Schwarzschild-like metrics in Linet and Teyssandier 2016. The main results of this paper are summarized in this section.

Since the terms of order m^2/r^2 in the metric are ignored in the linearized approximation, the initial metric (5) may be replaced by the metric

$$ds^2 = \left(1 - \frac{2m}{r}\right) \left\{ (dx^0)^2 - \left[1 + \frac{2(\gamma+1)m}{r}\right] d\mathbf{x}^2 \right\}. \quad (11)$$

However, it is well known that the null geodesics considered as points sets are identical for two conformal metrics (see, e.g. Joshi 2007). So the time transfer functions we are searching for coincide with the time transfer functions of the metric

$$d\tilde{s}^2 = (dx^0)^2 - \left[1 + \frac{2(\gamma+1)m}{r}\right] d\mathbf{x}^2. \quad (12)$$

Owing to the spherical symmetry of spacetime, each light ray joining \mathbf{x}_A and \mathbf{x}_B is confined to a plane passing through \mathbf{x}_A , \mathbf{x}_B and the origin O of the spatial coordinates (this plane is unique when the position vectors of the emitter and the receiver are not colinear). We adopt spherical coordinates (r, ϑ, φ) such that $\vartheta = \pi/2$ for the plane containing the light ray and $\varphi = 0$ for the point of emission.

A rigorous integration of the null geodesic equations of the metric (12) is easy to perform. It is shown that there exist two and only two light rays joining A and B , provided that \mathbf{x}_A and \mathbf{x}_B are not aligned with the origin O . We denote by $\Gamma_{AB}^{(0)+}$ (resp. $\Gamma_{AB}^{(0)-}$) the light ray joining \mathbf{x}_A and \mathbf{x}_B along which φ increases from 0 to ψ_{AB} (resp. decreases from 0 to $\psi_{AB} - 2\pi$). $\Gamma_{AB}^{(0)+}$ and $\Gamma_{AB}^{(0)-}$ are Keplerian hyperbolas having the origin O as a focus and respective impact parameters given by

$$b_{\pm} = \frac{r_A r_B \sqrt{1 - \cos \psi_{AB}}}{2R_{AB}} \left[\sqrt{1 + \cos \psi_{AB} + \frac{2(\gamma+1)m(r_A + r_B - R_{AB})}{r_A r_B}} \right. \\ \left. \pm \sqrt{1 + \cos \psi_{AB} + \frac{2(\gamma+1)m(r_A + r_B + R_{AB})}{r_A r_B}} \right]. \quad (13)$$

The time transfer functions which correspond to the light rays $\Gamma_{AB}^{(0)+}$ and $\Gamma_{AB}^{(0)-}$ will be denoted by T^+ and T^- , respectively. The full expression of these functions can be deduced in a closed form

from Eq. (13):

$$\begin{aligned}
T^\pm(\mathbf{x}_A, \mathbf{x}_B) = & \frac{1}{2c} \sqrt{r_A + r_B + R_{AB}} \sqrt{r_A + r_B + R_{AB} + 4(\gamma + 1)m} \\
& \mp \frac{1}{2c} \sqrt{r_A + r_B - R_{AB}} \sqrt{r_A + r_B - R_{AB} + 4(\gamma + 1)m} \\
& + \frac{2(\gamma + 1)m}{c} \ln \left(\frac{\sqrt{r_A + r_B + R_{AB} + 4(\gamma + 1)m} + \sqrt{r_A + r_B + R_{AB}}}{\sqrt{r_A + r_B - R_{AB} + 4(\gamma + 1)m} \pm \sqrt{r_A + r_B - R_{AB}}} \right). \quad (14)
\end{aligned}$$

These TTFs are regular everywhere: there is no appearance of any enhanced term.

3.2 Time transfer function relevant for the missions in the Solar System

The time transfer function relevant for the missions in the Solar System is T^+ , which corresponds to $0 \leq \varphi \leq \psi_{AB} \leq \pi$. This function may be expanded in a convergent series of powers of m if and only if

$$1 + \cos \psi_{AB} \geq \frac{4(\gamma + 1)m[r_A + r_B - 2(\gamma + 1)m]}{r_A r_B}. \quad (15)$$

Then:

$$\begin{aligned}
T^+(\mathbf{x}_A, \mathbf{x}_B) = & \frac{R_{AB}}{c} + \mathcal{T}_{\text{Shap}}(\mathbf{x}_A, \mathbf{x}_B) - \frac{(\gamma + 1)^2 m^2 R_{AB}}{c r_A r_B (1 + \cos \psi_{AB})} \\
& + \frac{(\gamma + 1)^3 m^3 (r_A + r_B) R_{AB}}{c r_A^2 r_B^2 (1 + \cos \psi_{AB})^2} + \mathcal{O}(m^4). \quad (16)
\end{aligned}$$

Thus we formally recover the dominant enhanced terms of orders m^2 and m^3 in expansion (6), but now we know that these terms cannot yield the correct behaviour of cT^+ when ψ_{AB} is very close or equal to π since the domain of validity of the expansion (16) is delimited by the condition (15). However, in the present state of the art, the differences $\pi - \psi_{AB}$ in the missions confined in the Solar System are not sufficiently close to zero to invalidate the use of (16) for estimating the gravitational time delay with the required accuracy. See, e.g., the discussion of the measurement of γ with the Cassini 2002 experiment given in Ashby and Bertotti 2010.

4. APPLICATION TO A SPINNING AXISYMMETRIC BODY

Consider now a spacetime containing a single axisymmetric body slowly spinning around its axis of symmetry. The results set out above can be used to find the TTFs of this spacetime which can be regarded as first-order perturbations of the spherically symmetric TTFs given by Eq. (14). We denote by \mathbf{S} the angular momentum of the body, we put

$$\mathbf{n} = \frac{\mathbf{x}}{r}, \quad \mathbf{s} = \frac{\mathbf{S}}{|\mathbf{S}|}$$

and we introduce the Kerr parameter a defined by

$$a = \frac{|\mathbf{S}|}{Mc} = \frac{G|\mathbf{S}|}{mc^3}. \quad (17)$$

Since the terms of order m^2/r^2 are neglected within the weak-field, linearized approximation, we start up from the metric

$$ds^2 = \left(1 - \frac{2W}{c^2}\right) \left\{ (dx^0)^2 + \frac{4(\gamma + 1)}{c^3} (\mathbf{W} \cdot d\mathbf{x}) dx^0 - \left[1 + \frac{2(\gamma + 1)W}{c^2}\right] d\mathbf{x}^2 \right\}, \quad (18)$$

where W is the Newtonian potential of the body and \mathbf{W} is the gravitomagnetic potential generated by the angular momentum. Outside any sphere of radius r_0 centered on the origin O and enclosing the central body, W and \mathbf{W} can be expanded as

$$\frac{1}{c^2}W(\mathbf{x}) = \frac{m}{r} \left[1 - \sum_{n=1}^{\infty} J_n \left(\frac{r_0}{r} \right)^n P_n(\mathbf{s} \cdot \mathbf{n}) \right] \quad (19)$$

and (see Linet and Teyssandier 2002):

$$\frac{1}{c^3}\mathbf{W}(\mathbf{x}) = \frac{ma(\mathbf{s} \times \mathbf{x})}{2r^3} \left[1 - \sum_{n=1}^{\infty} K_n \left(\frac{r_0}{r} \right)^n P'_{n+1}(\mathbf{s} \cdot \mathbf{n}) \right], \quad (20)$$

where $P_n(x)$ is the Legendre polynomial of degree n and $P'_n(x)$ its derivative with respect to x ; J_n and K_n are the mass-multipole and spin-multipole moments of order n , respectively.

According to a remark pointed out in subsect. 3.1, the problem comes down to determine TTFs of the conformal metric

$$d\tilde{s}^2 = (dx^0)^2 + \frac{4(\gamma+1)}{c^3}(\mathbf{W} \cdot d\mathbf{x})dx^0 - \left[1 + \frac{2(\gamma+1)W}{c^2} \right] d\mathbf{x}^2. \quad (21)$$

The metric (21) is supposed to be a small perturbation of the static spherically symmetric metric (12). So it is natural to assume that there exist time transfer functions \mathcal{T}^+ and \mathcal{T}^- which can be expanded as follows:

$$\begin{aligned} \mathcal{T}^{\pm}(\mathbf{x}_A, \mathbf{x}_B; J_n, \mathbf{S}, K_n) &= T^{\pm}(\mathbf{x}_A, \mathbf{x}_B) + \sum_{n=1}^{\infty} J_n \Delta \mathcal{T}_{J_n}^{\pm}(\mathbf{x}_A, \mathbf{x}_B) + a \Delta \mathcal{T}_{\mathbf{S}}^{\pm}(\mathbf{x}_A, \mathbf{x}_B) \\ &+ \sum_{n=1}^{\infty} K_n \Delta \mathcal{T}_{K_n}^{\pm}(\mathbf{x}_A, \mathbf{x}_B) + \dots, \end{aligned} \quad (22)$$

where the symbols $+\dots$ stand for the second-order perturbation terms which are neglected.

Substituting the right-hand side of Eq. (22) for \mathcal{T}^{\pm} into the eikonal equation satisfied by any TTF (cf. Teyssandier and Le Poncin 2008), and then separating the zeroth-order equation satisfied by T^{\pm} and the first-order equation satisfied by each perturbation term, it can be shown that each $\Delta \mathcal{T}^+$ (resp. $\Delta \mathcal{T}^-$) can be expressed by an integral taken along the unperturbed light ray $\Gamma_{AB}^{(0)+}$ (resp. $\Gamma_{AB}^{(0)-}$). These integrals can be calculated with any symbolic computer program.

Computing the contribution of the quadrupole J_2 is easy when the unperturbed light rays are confined to the equatorial plane, i.e. when $\mathbf{s} \cdot \mathbf{n}_A = \mathbf{s} \cdot \mathbf{n}_B = 0$. We have in this case

$$\begin{aligned} J_2 \Delta \mathcal{T}_{J_2}^{\pm}(\mathbf{x}_A, \mathbf{x}_B) &= \frac{(\gamma+1)m}{2c} J_2 \left(\frac{r_0}{b_{\pm}} \right)^2 \left[\left(\frac{b_{\pm}}{r_A} + \frac{b_{\pm}}{r_B} \right) \frac{1 - \cos \psi_{AB}}{\sin \psi_{AB}} \right. \\ &\left. + \frac{(\gamma+1)m}{b_{\pm}} \left(\psi_{AB}^{\pm} - 2 \frac{1 - \cos \psi_{AB}}{\sin \psi_{AB}} \right) \right], \end{aligned} \quad (23)$$

where b^{\pm} is given by Eq. (13) and ψ_{AB}^{\pm} is defined by

$$\psi_{AB}^+ = \psi_{AB}, \quad \psi_{AB}^- = \psi_{AB} - 2\pi. \quad (24)$$

When $\psi_{AB} \ll \pi$, only the unperturbed ray $\Gamma_{AB}^{(0)+}$ is relevant since $\Gamma_{AB}^{(0)-}$ is not confined in the zone of weak field $r \gg 2m$ (see Linet and Teyssandier 2016). As a consequence, only $J_2 \Delta \mathcal{T}_{J_2}^+$ has to be retained in this case. The impact parameter b_+ may be expanded as

$$b_+ = r_c \left[1 + \frac{(\gamma+1)m(r_A + r_B)}{r_A r_B (1 + \cos \psi_{AB})} + \mathcal{O}(m^2) \right], \quad (25)$$

where r_c is the ‘Euclidean’ distance between the origin O and the straight line passing through \mathbf{x}_A and \mathbf{x}_B , namely

$$r_c = \frac{r_A r_B \sin \psi_{AB}}{R_{AB}}. \quad (26)$$

Then, it follows from Eq. (23) that

$$J_2 \Delta \mathcal{T}_{J_2}^+(\mathbf{x}_A, \mathbf{x}_B) = \frac{(\gamma + 1)m}{2c} J_2 \frac{r_0^2 (r_A + r_B) R_{AB}}{r_A^2 r_B^2 (1 + \cos \psi_{AB})} + \mathcal{O}(m^2 J_2) \quad (27)$$

when ψ_{AB} is sufficiently far from π . The contribution of J_2 to the travel time of light given by Eq. (27) is equivalent to the one previously obtained in the literature (Klioner 1991, Linet and Teysandier 2002, Le Poncin-Lafitte and Teysandier 2008, Zschocke and Klioner 2011). The progress is that henceforth the enhanced effect apparently predicted by Eq. (27) when $\psi_{AB} \rightarrow \pi$ must be regarded as fictitious. This divergence is just warning us that the right-hand side of Eq. (23) cannot be expanded in a convergent series in powers of m for any value of ψ_{AB} . This feature does not prevent $J_2 \Delta \mathcal{T}_{J_2}^\pm$ from remaining bounded when $\psi_{AB} \rightarrow \pi$. Indeed, taking into account that

$$\lim_{\psi_{AB} \rightarrow \pi} b_\pm = \pm \sqrt{\frac{2(\gamma + 1) m r_A r_B}{r_A + r_B}}, \quad (28)$$

it may be inferred from Eq. (23) that

$$\lim_{\psi_{AB} \rightarrow \pi} \left[J_2 \Delta \mathcal{T}_{J_2}^\pm(\mathbf{x}_A, \mathbf{x}_B) \right] = \frac{J_2 r_0^2 (r_A + r_B)}{2c r_A r_B} \left[\sqrt{1 + \frac{2(\gamma + 1)m}{r_A + r_B}} + \frac{\pi}{2} \sqrt{\frac{(\gamma + 1)m(r_A + r_B)}{2r_A r_B}} \right]. \quad (29)$$

5. REFERENCES

- Asby, N., Bertotti, B., 2010, *Class. Quantum Grav.*, 27, 145013.
- Bertone, S., Vecchiato, A., Bucciarelli, B., Crosta, M., Lattanzi, M. G., Bianchi, L., Angonin, M.-C., Le Poncin-Lafitte, C., 2017, *A&A* 608, A 83.
- Blanchet, L., Salomon, C., Teysandier, P., Wolf, P., 2001, *A&A* 370, pp. 320-329.
- Hees, A., Bertone, S., Le Poncin-Lafitte, C., 2014, *Phys. Rev. D* 89, p. 064045.
- Joshi, P. S., 2007, “Gravitational Collapse and Spacetime Singularities”, Cambridge University Press, Cambridge, England.
- Klioner, S. A., 1991, *Sov. Astron.* 35, p. 523.
- Klioner, S. A., Zschocke, S., 2010, *Class. Quantum Grav.* 27, p. 075015; see also Zschocke, S., Klioner, S. A., 2010, arXiv:1007.5175 [gr-qc].
- Le Poncin-Lafitte, C., Linet, B., Teysandier, P., 2004, *Class. Quantum Grav.* 21, p. 4463.
- Le Poncin-Lafitte, C., Teysandier, P., 2008, *Phys. Rev. D* 77, p. 044029.
- Linet, B., Teysandier, P., 2002, *Phys. Rev. D* 66, p. 024045.
- Linet, B., Teysandier, P., 2013, *Class. Quantum Grav.* 30, p. 175008.
- Linet, B., Teysandier, P., 2016, *Phys. Rev. D* 93, p. 044028.
- Teyssandier, P., Le Poncin-Lafitte, C., 2008, *Class. Quantum Grav.* 25, p. 145020.
- Teyssandier, P., 2012, *Class. Quantum Grav.* 29, p. 245010.
- Zschocke, S., Klioner, S. A., 2011, *Class. Quantum Grav.* 28, p. 015009.

ANALYSIS AND NORMALIZATION OF GNSS ONBOARD CLOCKS

P. Movsesian¹, S. Petrov¹, D. Trofimov¹, I. Chekunov²

¹ Saint Petersburg State University - Russia - Movsesyanpv@gmail.com

² Bauman Moscow State Technical University - Russia

ABSTRACT. Nowadays determination of precise coordinates using GNSS (Global Navigation Satellite System) observations can be made with the differential method or with an absolute solution (PPP method - Precise Point Positioning). The precision of navigational data, such as satellite ephemerides and satellite clock biases, is very important when using the PPP method. Usually, satellite orbits are approximated with smooth functions, currently, their accuracy is about 2-3 cm. Unlike ephemerides satellite clock biases are not approximated with any function, also clock series are being processed not as a continuous time series but as daily fragments, which leads to jumps at 00:00 UTC. Processing methods that are currently used can also lead to clock jumps inside a day. Different studies propose a variety of satellite clock improvement methods but clock jump removal is performed manually. An automatic jump correction algorithm is proposed. About two years of satellite clock biases were processed. Usage of the algorithm allows removal of clock jumps on time intervals of any length..

1. INTRODUCTION

Nowadays determination of precise coordinates using GNSS (Global Navigation Satellite System) observations can be made with differential method or with absolute solution (PPP method Precise Point Positioning). Precision of navigational data is very important when using PPP method.

Currently GPS and GLONASS satellites are using rubidium (Rb) and cesium (Cs) clocks. GPS satellites use 10.23 MHz frequency sources [GPS-IS, 2019], GLONASS - 5 MHz [GLONASS-ICD, 2008]. Satellite clock biases are transmitted in navigational messages with ephemerides.

GNSS analysis centers provide satellite clock biases in form of unapproximated time series. This leads to clock biases having random jumps up to several ns.

Analysis of the aforementioned jumps shows that clock biases from different analysis centers have different jumps and a lot of these jumps are at 00:00 UTC.

This shows that most of the jumps are processing artifacts, as confirmed by other researchers [Prange, 2017].

Different methods of improving satellite clock biases are proposed [Shi, 2019, Hauschild, 2010, Hauschild, 2009], but they require manual correction of aforementioned jumps [Huang, 2012].

2. ALGORITHM DESCRIPTION

2.1 Global change detection

To get a more correct estimation of the quadratic trend of the clock bias series outliers need to be corrected. They are searched for and corrected by using the formula

$$b_j = \frac{b_{j+1} + b_{j-1}}{2}; \quad (1)$$

where b_j is a point of the series with number j .

If a trend change is present, the series is split and its parts are processed separately. Trend change algorithm contains the following steps:

1. The second derivative of the series is computed.
2. If the second derivative of the clock bias series is at least 500 times larger or smaller than its average, then we consider that a trend change has been detected.

2.2 Jump correction

The quadratic trend of the clock bias series is computed with the least squares method and removed. Then a search for significant (more than 0.55 ns for 30-second clock file) differences between neighbouring points is performed. When such difference is found (point with number k), search for next difference that is not further from point k than 3 days is performed. If the next difference is not found then the jump is absent. However if such difference is found (point n or the series ends before that, the right border of correction interval is the last point in the series (point n)).

Jumps are being corrected by adding a linear trend on the correction interval. Difference between borders of correction interval is computed ($\Delta b = b_k - b_n$). Correction on the interval from point k to point n is performed using formula (2)

$$b_{k+i} = b_{k+i} - \Delta b \cdot \frac{i}{n-k}, \quad 0 < i \leq n-k \quad (2)$$

2.3 Clock bias filtering

After jump correction filtering was performed. Kalman filter was used. Clock bias series were modelled as wiener process $\dot{b} = w$, where w is random function. The following Kalman filter model was used:

$$P = \begin{cases} \sigma^2 & , \text{ if error is present in clk file} \\ 10^{-24} \text{ s}^2 & , \text{ if error is absent in clk file;} \end{cases}$$

where P is error covariance. Predicted state estimate:

$$b_{k+1}^- = b_k$$

Predicted error covariance:

$$P_{k+1}^- = P_k$$

Updated state estimate:

$$\begin{aligned} b_{k+1} &= b_{k+1}^- + K_{k+1} v_{k+1} \\ v_{k+1} &= b_{k+1} - b_{k+1}^- \end{aligned}$$

Updated estimate covariance:

$$P_{k+1} = (1 - K_{k+1}) P_{k+1}^-$$

Optimal Kalman gain:

$$\begin{aligned} K_{k+1} &= \frac{P_{k+1}^- H^T}{H^T P_{k+1}^- H + R} \\ H &= 1, \quad R = 9 \cdot 10^{-23} \text{ s}^2 \end{aligned}$$

H is the observation model; R is the covariance of the observation noise; v_{k+1} is measurement pre-fit residual.

3. RESULTS

Analysis was performed on 2017 satellite clock biases from IAC. Figure 1 shows the beginning of a correction interval highlighted by the red vertical line. Figure 2 shows the end of the same correction interval as on the Figure 1. It is noticeable that the processed time series does not have a jump on 17.02.2017 at 11:39.

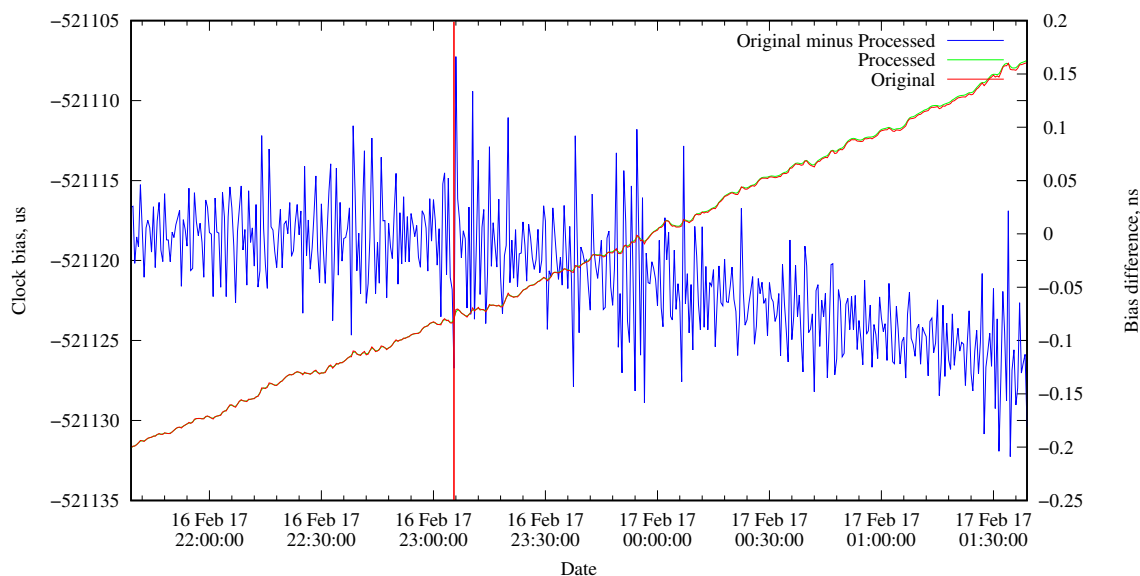


Figure 1: Start of correction interval for G21

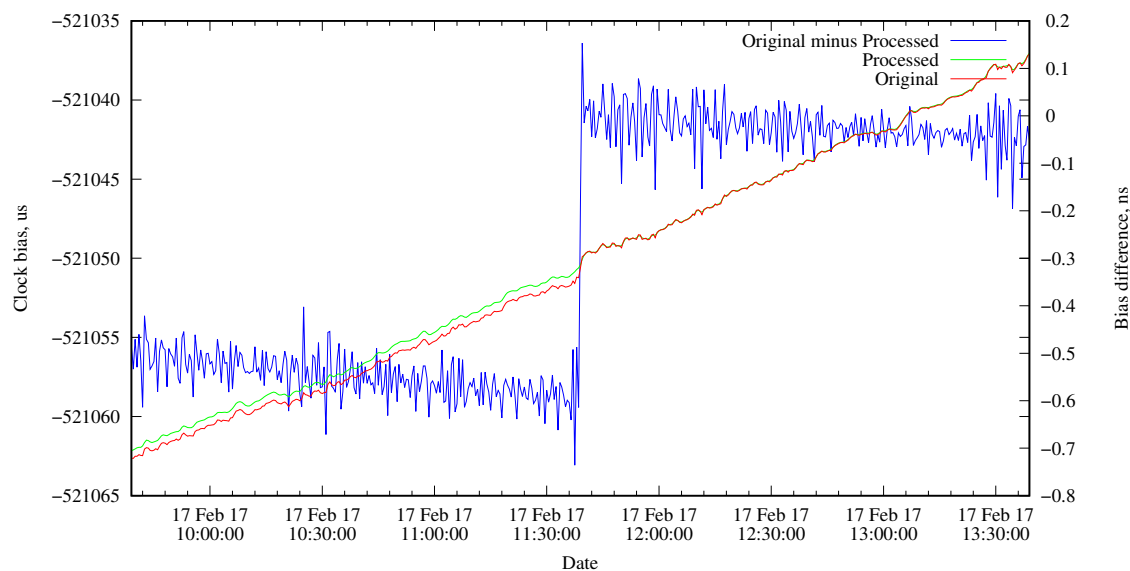


Figure 2: G21 clock bias

Absence of jumps on the processed biases can be seen on Figure 3. Original biases show multiple jumps on the same figure. It should be noted that differences are not accumulated.

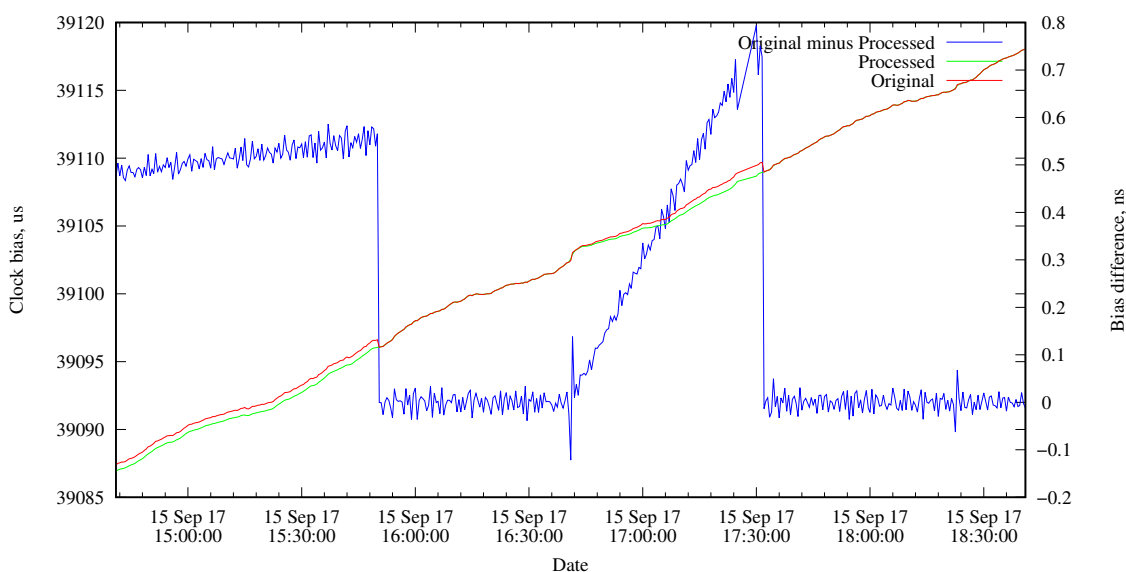


Figure 3: R09 correction

4. CONCLUSION

- Current processing methods for estimating satellite clock biases lead to jumps.
- The proposed correction algorithm allows to remove jumps in clock biases automatically.
- Applying this algorithm to processing of GNSS measurements leads to more precise results.

5. REFERENCES

- Prange L., Orliac E., Dach R., Arnold D., Beutler G., Schaer S., Jäggi A., 2017, "CODE's five-system orbit and clock solution—the challenges of multi-GNSS data analysis", *Journal of Geodesy*, 91, pp. 345–360, doi: 10.1007/s00190-016-0968-8.
- Shi C., Guo S., Gu S., Yang X., Gong X., Deng Z., Ge M., Schuh H., 2019, "Multi-GNSS satellite clock estimation constrained with oscillator noise model in the existence of data discontinuity", *Journal of Geodesy*, 93, pp. 515–528, doi: 10.1007/s00190-018-1178-3.
- Hauschild A., 2010, "Precise GNSS Clock-Estimation for Real-Time Navigation and Precise Point Positioning".
- Hauschild A, Montenbruck O., 2009, "Kalman-filter-based GPS clock estimation for near real-time positioning", *GPS Solutions*, 13, pp. 173–182, doi: 10.1007/s10291-008-0110-3.
- Huang G., Zhang Q., 2012, "Real-time estimation of satellite clock offset using adaptively robust Kalman filter with classified adaptive factors", *GPS Solutions*, 16, pp. 531–539, doi: 10.1007/s10291-012-0254-z.
- GPS-IS, 2019, "Interface Specification IS-GPS-200".
- GLONASS-ICD, 2008, "GLONASS interface control document".

CHAOS AND RELATIVISTIC EFFECTS IN THE ROTATIONAL DYNAMICS OF MINOR PLANETARY SATELLITES

A.V. MELNIKOV¹, V.V. PASHKEVICH², A.N. VERSHKOV³, G.M. KARELIN⁴

Central (Pulkovo) Astronomical Observatory of the Russian Academy of Science - Russia

¹melnikov@gaoran.ru, ²pashvladvit@yandex.ru, ³avershkov@mail.ru, ⁴karegosh@yandex.ru

ABSTRACT. The chaotic regime of rotation of minor planetary satellites taking place during tidal evolution is considered. The possibility of the formation of strange attractors in the rotational dynamics of all known minor planetary satellites of the Solar system is estimated. A detailed analysis of the presence of anisotropy in the orientation of the satellite figure during its chaotic rotation was carried out. The relativistic effect (the geodetic precession, which is the part of the effect of the geodetic rotation) in the rotation of some minor satellites for the first time is investigated. As a result, in Euler angles, the most significant systematic terms of the geodetic rotation are calculated.

1. INTRODUCTION

Currently, the total number of known planetary satellites is approaching two hundred (see JPL Solar System Dynamics, <https://ssd.jpl.nasa.gov>). Wisdom et al. (1984) showed that a satellite of a strongly non-spherical shape (a typical shape of the small satellites) in an elliptical orbit can rotate chaotically. It was found (Wisdom et al., 1984, Devyatkin et al., 2002, Harbison et al., 2011) that the satellite of Saturn Hyperion (S7) is in chaotic rotation mode; Prometheus (S16) and Pandora (S17) have a high probability (Kouprianov, Shevchenko, 2005; Melnikov, Shevchenko, 2008) of transition from synchronous to chaotic rotation. Studies (Khan et al., 1998; Beletskii, 2007; Melnikov, 2014) of the planar rotational motion of a satellite in the presence of tidal dissipation have shown that, in the phase space of rotational motion, a strange attractor can exist. Wisdom (1987) (see also Melnikov and Shevchenko (2008)) indicated that chaotic rotation of a satellite may result in a preferred orientation of the largest axis of the satellites figure toward the planet. If we consider the rotational motion of the satellite in the gravitational field of the planet in the post-Newtonian approximation, it is necessary to take into account the effects of geodetic precession and nutation, which together make up the geodetic rotation (De Sitter, 1916).

2. STRANGE ATTRACTORS IN THE ROTATION OF SATELLITES

Consider the plane (in the orbit plane) rotational motion of the satellite respect to its center of mass. The equation of motion taking into account tidal interaction (within the framework of the MacDonald model) has the form (Khan et al., 1998; Beletskii, 2007; Melnikov, 2014):

$$(1 + e \cos f) \frac{d^2\theta}{df^2} + [\beta(1 + e \cos f)^5 - 2e \sin f] \frac{d\theta}{df} + \omega_0^2 \sin \theta \cos \theta = 2e \sin f,$$

where e is the eccentricity, f is the true anomaly, $\omega_0 \simeq \sqrt{3(a^2 - b^2)/(a^2 + b^2)}$, $a > b > c$ are the semiaxes of a triaxial ellipsoid approximating the satellite figure; θ is the angle between the axis of the smallest principal central moment of inertia of the satellite (the largest axis of the triaxial ellipsoid) and the radius-vector "planet — the center of mass of the satellite"; the dimensionless parameter $\beta \geq 0$ characterizes the value of the tidal interaction. By calculating the Lyapunov exponents (LE), we found that for certain values of e , ω_0 and β in the phase space of rotational

motion there is a strange attractor for which the maximum LE is greater than zero, that is, the motion is chaotic. This conclusion is confirmed by the analysis of representative phase space sections constructed for the selected values of e , ω_0 and β . At the sections (see the example for Hyperion in Figure 1a, b), there is a structure characteristic of a strange attractor. The sections defined at the pericenter of the orbit; i.e., the variables are mapped each orbital period. For most planet satellites whose shape parameters are determined, the values of $\beta \in [10^{-6}, 10^{-4}]$ (Melnikov, 2014). If we place these satellites on the plane (ω_0, e) , where the regions of existence of the strange attractor are highlighted, then can be verify (see Figure 1c, d) that Hyperion (S7) and Phoebe (S9) fall into these regions. Phoebe is in fast non-synchronous rotation (Andersson, 1972) and it is located in the phase space far from the strange attractor that exists in the vicinity of synchronous resonance. Hyperion, for which $\beta \sim 10^{-6}$, is currently (Devyatkin et al., 2002, Harbison et al., 2011) in the chaotic rotation mode and, most likely, the rotation occurs on a strange attractor. Consequently, the probability that Hyperion can leave the chaotic rotation regime is very small.

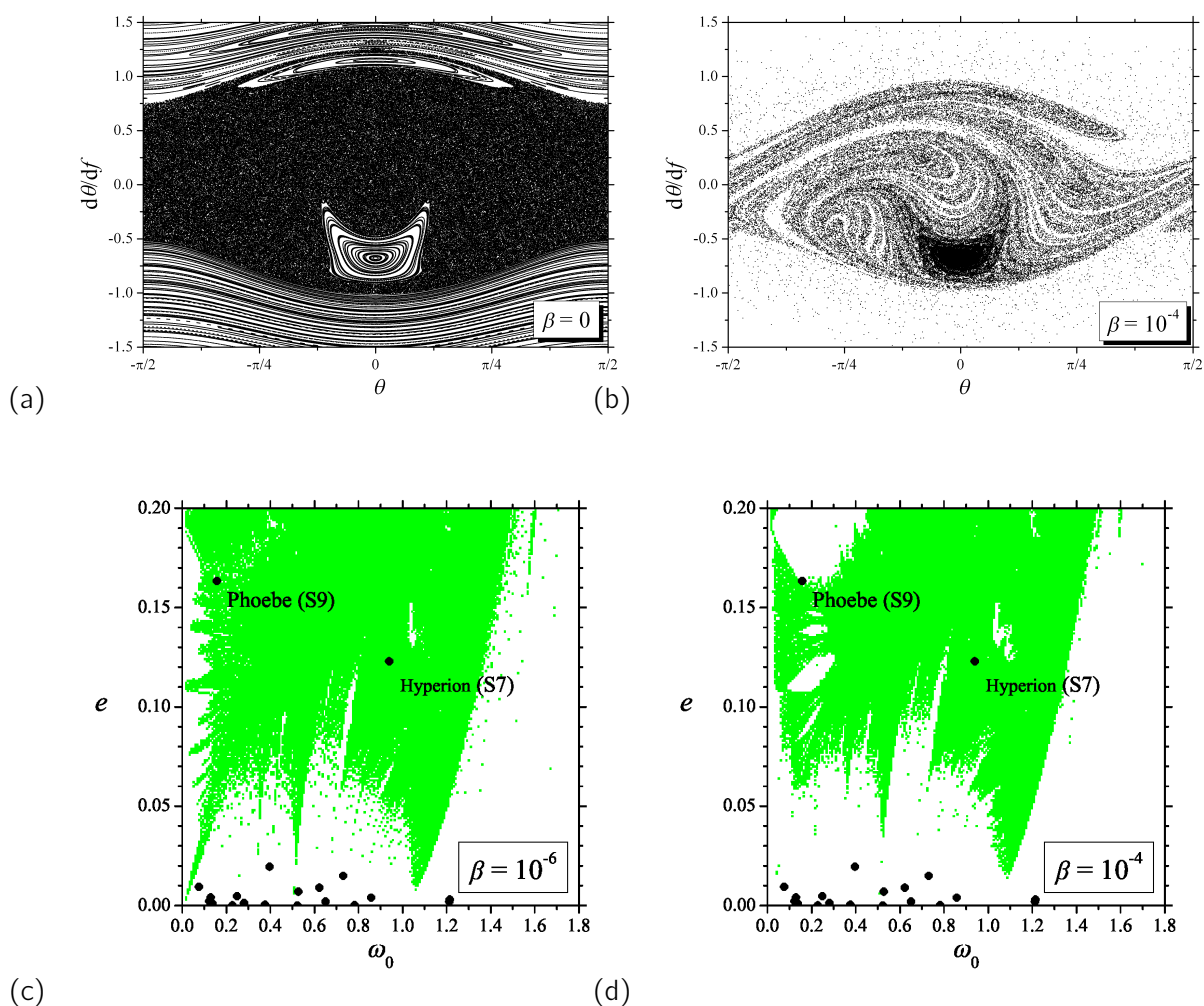


Figure 1: The phase space section of the planar rotational motion for $e = 0.123$, $\omega_0 = 0.936$ (Hyperion (S7)): (a) $\beta = 0$ there is no tidal interaction, (b) an example of a strange attractor for $\beta = 10^{-4}$. (c) and (d) are the regions of existence of the strange attractor (green) for different values of β . Dots mark the locations of a some of known planetary satellites.

3. ANISOTROPY IN THE CHAOTIC ROTATION OF SATELLITES

In (Kouprianov, Shevchenko, 2005; Melnikov, Shevchenko, 2008) it was shown that for two satellites of Saturn : Prometheus (S16) and Pandora (S17) there is a high probability of a transition from a synchronous rotation mode to a chaotic one. Our massive numerical experiments on modeling the spatial chaotic rotation of Prometheus and Pandora showed that the chaotic rotation of these satellites is similar to ordinary synchronous rotation. Namely, the satellites retain their preferred orientation over long time intervals (100–1 000 orbital periods) : the largest axis of the satellite's figure is directed mainly to Saturn (see the example for the case of Prometheus in Figures 2 and 3).

In Figure 3, on the integration time interval $t = 10^5$ of orbital periods, the behavior of σ is the relative amount of time during, which the largest axis of the satellite figure is oriented to Saturn on a segment of 1 000 of orbital periods is shown. It can be seen that the value $\sigma \simeq 9\%$, which in the case of Prometheus corresponds to "isotropic" chaotic rotation, is several times exceeded. The chaotic rotational dynamics of Pandora has a similar character. It is expected that in the chaotic rotational dynamics of other small planetary satellites in the vicinity of synchronous resonance effect should manifest predominant orientation of their largest axis of the figures.

The discovered phenomenon can make it difficult to detect chaotic rotation of small satellites, for which there are indications of a possible chaotic rotation, by analyzing observational data if the observation interval is not large enough.

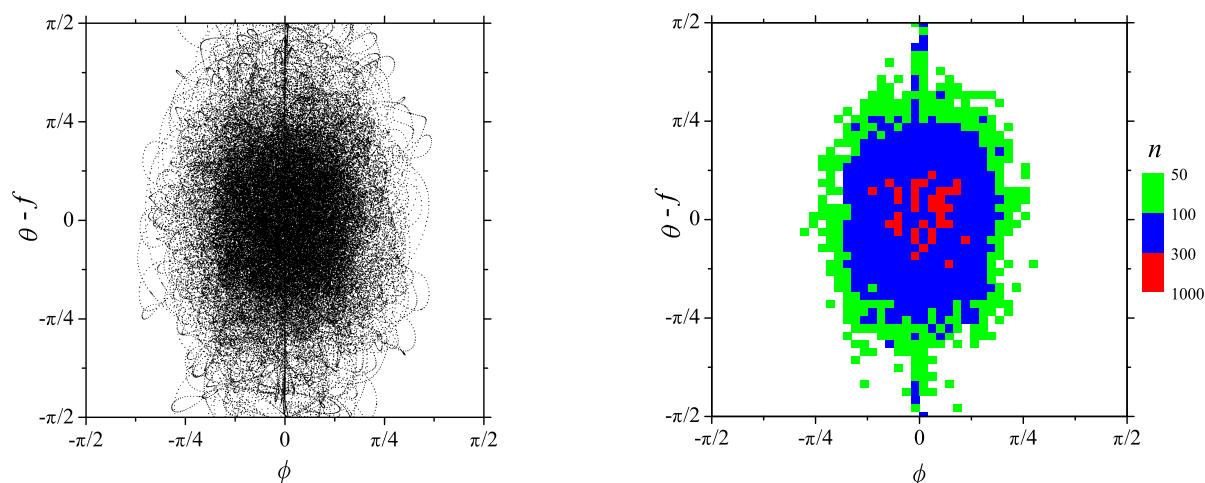


Figure 2: Orientation of Prometheus (S16) in chaotic rotation. (a) The projection of the chaotic trajectory to $(\phi, \theta - f)$ plane, where ϕ is the angle between the axis of rotation and the normal to the plane of the orbit, θ is the angle between the largest axis of the satellite's figure and the direction to Saturn, f is the true anomaly. The integration time is 1 000 orbital periods. (b) Density graph of discrete projections of a chaotic trajectory to $(\phi, \theta - f)$ plane. The integration time is 10 000 orbital periods. The white area corresponds to $n < 50$. The direction to Saturn corresponds to the point $(0, 0)$.

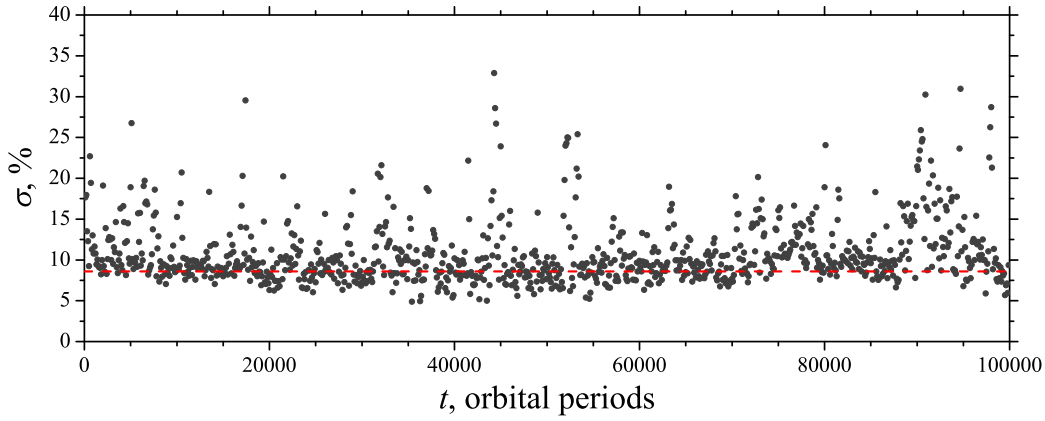


Figure 3: The relative percentage of time σ during which, with chaotic rotation, the largest axis of the figure of Prometheus (S16) is oriented to Saturn. Under “isotropic” chaotic rotation $\sigma \simeq 9\%$ (red dashed horizontal line).

4. GEODETIC ROTATION OF PLANET SATELLITES

The geodetic rotation of a body is the most essential relativistic effect of its rotation and consist of two effects: the geodetic precession is the systematic effect and the geodetic nutation is the periodic effect. These effects have some analogies with precession and nutation, which are better-known events on the classical mechanics. Their emergence, unlike the last classical events, are not depend on from influences of any forces to body, represents only the effect of the curvature of space-time, predicted by general relativity (De Sitter, 1916), on a vector of the body rotation axis carried along with an orbiting body.

Using the technique developed in (Pashkevich, 2016), we obtained estimates of the values of the systematic terms in the Euler angles (ψ , θ , ϕ) and the rates of their change for the geodetic rotation of a some of planetary satellites. Satellites were considered whose rotation parameters were well established (see Archinal et al., 2018).

Table 1 shows the differences $\Delta x = x_r - x_N = \Delta x_1 T + \Delta x_2 T^2 + \dots$ of the relativistic (x_r) and Newtonian Euler angles (x_N) of the body under study, where $x = \psi$, θ , ϕ . Only the first two terms of the expansion are presented, making the main contribution to the geodetic precession; Δx_i values are given in arc seconds per thousand years. Figure 4 shows the rate of change of the magnitude of the geodetic rotation.

Table 1: The systematic terms of geodetic rotation of Mercury and some planet satellites (in as/tjy). J5 — Amalthea, S16 — Prometheus, S17 — Pandora, S8 — Iapetus, S9 — Phoebe, U5 — Miranda.

	Mercury	J5	S16	S17	S8	S9	U5
$\Delta\psi_1$	-426.4	-22118.2	-205.6	-197.2	-0.924	-0.021	67.04
$\Delta\psi_2$	-0.039	-0.756	-1.623	-1.679	-0.656	-0.016	0.365
$\Delta\theta_1$	0.036	-0.092	-590.1	-566.0	-0.313	0.001	-0.472
$\Delta\theta_2$	-0.003	4.735	-3.283	-3.205	0.058	0.012	-0.0002
$\Delta\phi_1$	214.8	11055.2	-3275.7	-3142.2	-0.167	-0.005	-249.4
$\Delta\phi_2$	0.002	0.579	1.986	2.374	0.659	0.016	0.001

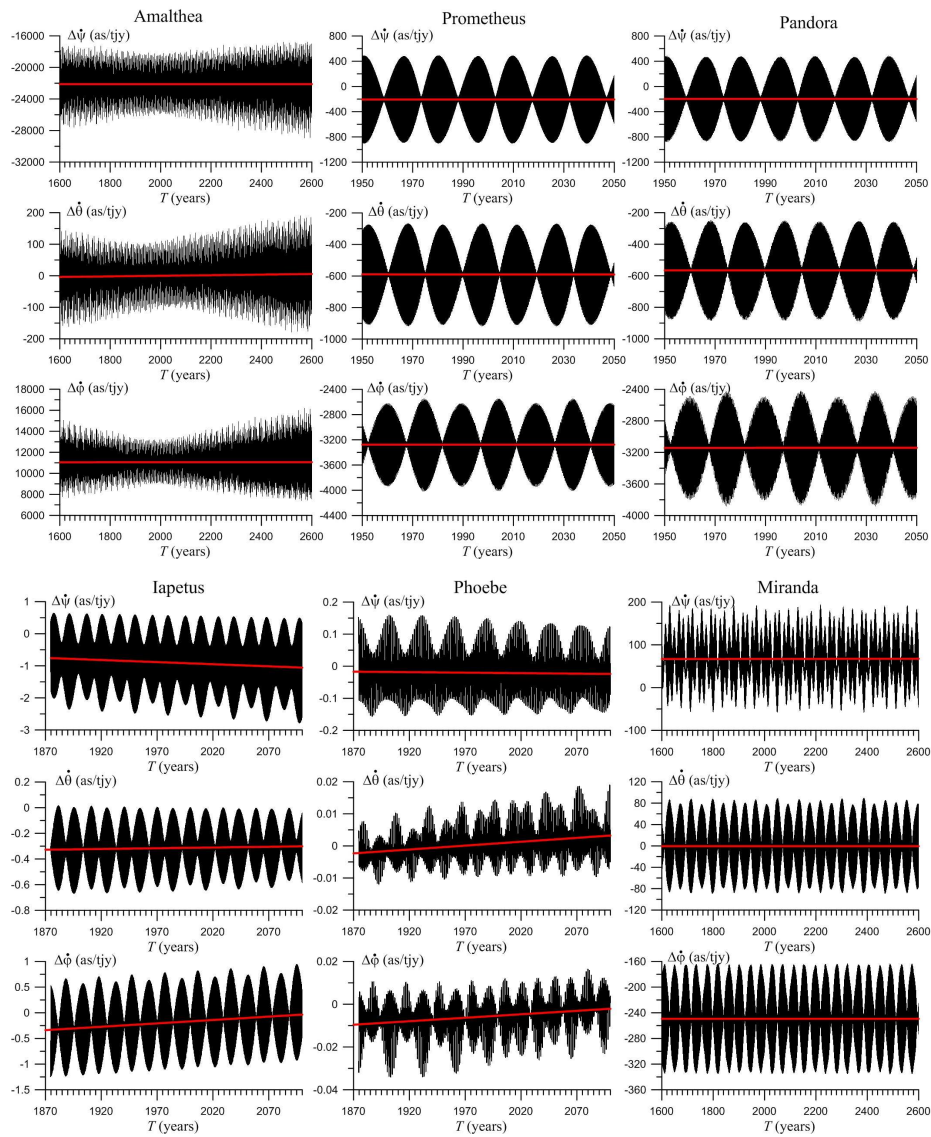


Figure 4: The values of the velocities of the change in full effect of the geodetic rotation (black) and in only geodetic precession of Mercury and some planet satellites (red line).

Despite the fact that the Sun (1000 times) is more massive than Jupiter, the value of the geodetic precession of the fifth satellite of Jupiter Amalthea is 50 times greater than the value of the geodetic precession of Mercury, which is the largest among ones values of major planets of Solar system (Pashkevich, 2016). Amalthea (J5) is 300 times closer to Jupiter than Mercury is to the Sun. Therefore, in this case, the value of the geodesic precession is greater for a satellite closer to a low-mass central body than for a planet located at a greater distance from the Sun. In the case of Amalthea, the geodetic precession we obtained is about 0.006 degrees of arc per year and must be taken into account in the existing ephemeris (Archinal et al., 2018).

Acknowledgement. The reported study was funded by RFBR according to the research project 19-02-00811.

5. REFERENCES

- Andersson, L., 1972, "Photometry of Jupiter VI and Phoebe (Saturn IX)", *BAAS* 4, pp. 313.
- Archinal, B.A., Acton, C.H., A'Hearn, M.F. et al., 2018, "Report of the IAU Working Group on Cartographic Coordinates and Rotational Elements: 2015", *Celest. Mech. Dyn. Astr.* 130, 22.
- Beletskii, V.V., 2007, "Regular and chaotic motions of solid bodies", Moscow–Izhevsk: IKM.
- De Sitter, W., 1916, "On Einstein's theory of gravitation and its astronomical consequences. Second paper", *MNRAS* 77, pp. 155–184.
- Devyatkin, A.V., Gorshanov, D.L., Gritsuk, A.N. et al., 2002, "Observations and theoretical analysis of lightcurves of natural satellites of planets", *Sol. Sys. Res.* 36, pp. 248–259.
- Harbison, R.A., Thomas, P.C., Nicholson, P.C., 2011, "Rotational modeling of Hyperion", *Celest. Mech. Dyn. Astr.* 110, pp. 1–15.
- Khan, A., Sharma, R., Saha, L.M., 1998, "Chaotic motion of an ellipsoidal satellite. I.", *Astron. J.* 116, pp. 2058–2066.
- Kouprianov, V.V., Shevchenko, I.I., 2005, "Rotational dynamics of planetary satellites: A survey of regular and chaotic behavior", *Icarus* 176, pp. 224–234.
- Melnikov, A.V., 2014, "Conditions for appearance of strange attractors in rotational dynamics of small planetary satellites", *Cosm. Res.* 52, pp. 461–471.
- Melnikov, A.V., Shevchenko, I.I., 2008, "On the rotational dynamics of Prometheus and Pandora", *Celest. Mech. Dyn. Astr.* 101, pp. 31–47.
- Pashkevich, V.V., 2016, "New high-precision values of the geodetic rotation of the major planets, Pluto, the Moon and the Sun", *Artif. Sat.* 51, pp. 61–73.
- Wisdom, J., 1987, "Rotational dynamics of irregularly shaped natural satellites", *Astron. J.* 94, pp. 1350–1360.
- Wisdom, J., Peale, S.J., Mignard, F., 1984, "The chaotic rotation of Hyperion", *Icarus* 58, pp. 137–152.

POSTFACE

Journées “Systèmes de Référence Spatio-temporels”

Previous editions

- September 25-27 2017, Universidad de Alicante : " Journées des Systèmes de Référence et de la Rotation Terrestre: Furthering our knowledge of Earth Rotation". <https://web.ua.es/journees2017/>
- September 22-24 2014, Pulkovskaya Observatoriya, St. Petersburg : "Furthering our knowledge of Earth Rotation". <https://syrtte.obspm.fr/jsr/journees2014/pdf/>
- September 16-18 2013, Observatoire de Paris-Meudon, France : "Scientific developments from highly accurate space-time reference systems". <https://syrtte.obspm.fr/jsr/journees2013/pdf>
- September 19-21 2011, TU Wien, Vienna: "Earth rotation, reference systems and celestial mechanics: synergies of geodesy and astronomy". <https://syrtte.obspm.fr/jsr/journees2011/pdf/>
- September 20-22 2010, Observatoire de Paris & Ecole Normale Supérieure, Paris: "New challenges for Reference Systems and Numerical Standards in Astronomy". <https://syrtte.obspm.fr/jsr/journees2010/pdf/>
- September 22-24 2008, Lohrmann Observatorium, TU Dresden: "Astrometry Geodynamics and Astronomical Reference Systems". <https://syrtte.obspm.fr/jsr/journees2008/pdf/>
- September 17-19 2007, Observatoire de Paris : "The Celestial Reference Frame for the Future". <https://syrtte.obspm.fr/jsr/journees2007/pdf/>
- September 19-21 2005, Centrum Badań Kosmicznych, Warsaw: "Earth dynamics an reference systems five years after adoption of the IAU 2000 resolutions". <https://syrtte.obspm.fr/jsr/journees2005/pdf/>
- September 2004 20-22, Observatoire de Paris: "Fundamental astronomy : New concepts and models for high accuracy observation". <https://syrtte.obspm.fr/jsr/journees2004/pdf/>
- September 22-25 2003, Institut Pribladnoy Astronomii, St. Petersburg: "Astrometry, Geodynamics and Solar System Dynamics : from milliarseconds to microarcseconds". <https://syrtte.obspm.fr/jsr/journees2003/pdf/>
- September 25-28 2002, Institutul Astronomic al Academiei Române, Bucharest: Astronomy from ground and from space. <https://syrtte.obspm.fr/jsr/journees2002/pdf/>

- September 24-26 2001, Observatoire Royal de Belgique, Brussels: Influence of geophysics, time and space reference frames on Earth rotation studies. <https://syrtel.obspm.fr/jsr/journees2001/pdf/>
- September 18-20 2000, Observatoire de Paris: "J2000, a fundamental epoch for origins of reference systems and astronomical models". Proceedings ed. by N. Capitaine.
- September 13-15 1999, Lohrmann Observatorium, TU Dresden: "Journées 1999 & IX. Lohrmann-Kolloquium: Motion of Celestial Bodies, Astrometry and Astronomical Reference Frames". Proceedings ed. by M. Soffel & N. Capitaine.
- September 21-23 1998, Observatoire de Paris: "Conceptual, conventional and practical studies related to Earth rotation". Proceedings ed. by N. Capitaine.
- September 22-24 1997, Astronomický ústav, Prague Planetarium: "Reference systems and frames in the space era: present and future astrometric programmes". Proceedings ed. by J. Vondrák & N. Capitaine.
- September 23-25 1996, Observatoire de Paris: "Deux siècles d'évolution du Système du Monde. Hommage Laplace". Proceedings ed. by N. Capitaine.
- September 18-20 1995, Centrum Badań Kosmicznych, Warsaw: "Earth Rotation, Reference Systems in Geodynamics and Solar System". Proceedings ed. by N. Capitaine, B. Kolaczek, S. Débarbat.
- June 13-14 1994, Observatoire de Paris: "Les systèmes de référence et les constantes astronomiques fondamentales". Proceedings ed. by N. Capitaine.
- June 1-2 1992, Observatoire de Paris: "Géodynamique Globale et Systèmes de Référence"
- June 3-4 1991, Observatoire de Paris: "Métrologie et Astrométrie". Proceedings ed. by N. Capitaine.
- May 28-30 1990, Observatoire de Paris: "Colloque André Danjon". Proceedings ed. by N. Capitaine & S. Débarbat.
- April 24-25 1989, Observatoire de Paris: "Astrométrie et relativité". Proceedings ed. by N. Capitaine.
- June 20-21 1988, Observatoire de Paris: "Journées Systèmes de référence spatio-temporels". Proceedings ed. by N. Capitaine.